SANDIA REPORT

SAND98–2537
Unlimited Release
Printed July 1999

Hydraulic Testing of Salado Formation Evaporites at the Waste Isolation Pilot Plant Site: Final Report

Randall M. Roberts, Richard L. Beauheim, and Paul S. Domski

Prepared by
Sandia National Laboratories
Albuquerque, New Mexico 87185 and Livermore, California 94550

Sandia is a multiprogram laboratory operated by Sandia Corporation, a Lockheed Martin Company, for the United States Department of Energy under Contract DE-AC04-94AL85000.

Sandia National Laboratories

Issued by Sandia National Laboratories, operated for the United States Department of Energy by Sandia Corporation.

Available to DOE and DOE contractors from
Office of Scientific and Technical Information
P.O. Box 62
Oak Ridge, TN 37831

Prices available from (703) 605-6000
Web site: http://www.ntis.gov/ordering.htm

Available to the public from
National Technical Information Service
U.S. Department of Commerce
5285 Port Royal Rd
Springfield, VA 22161

NTIS price codes
Printed copy: A03
Microfiche copy: A01

SAND98-2537
Unlimited Release
Printed July 1999

Hydraulic Testing of Salado Formation Evaporites at the Waste Isolation Pilot Plant Site: Final Report

Randall M. Roberts and Richard L. Beauheim
WIPP Regulatory Compliance Department
Sandia National Laboratories
P.O. Box 5800
Albuquerque, NM 87185-1395

Paul S. Domski
Duke Engineering & Services, Inc.
1650 University Boulevard NE, Suite 300
Albuquerque, NM 87102-1732

ABSTRACT

Pressure-pulse, constant-pressure flow, and pressure-buildup tests have been performed in bedded evaporites of the Salado Formation at the Waste Isolation Pilot Plant (WIPP) site to evaluate the hydraulic properties controlling brine flow through the Salado Formation. New numerical methods have been developed to interpret these tests that allow definition of the dimensionality of flow and quantification of uncertainty in parameter estimates. Vertically averaged hydraulic conductivities ranging from about 8×10^{-14} to 7×10^{-10} m/s (permeabilities of 1×10^{-20} to 1×10^{-16} m^2) have been interpreted from seven new sequences of tests conducted on six stratigraphic intervals within 22 m of the WIPP underground excavations. Modeled average values of specific storage range from 2×10^{-11} to 2×10^{-4} m^{-1}. However, these modeled specific-storage values include the effects of wellbore skin and are not, therefore, representative of actual formation conditions. Pore pressures in nine stratigraphic intervals range from approximately 4.0 to 10.3 MPa. Interpretations of two tests conducted on one halite interval and two tests conducted on two anhydrite intervals indicated that the hydraulic properties in those intervals were pressure-dependent. When the results of the recent testing are combined with those from previous tests, we find that the hydraulic conductivity of anhydrite typically ranges from 1×10^{-13} to 5×10^{-11} m/s (permeabilities of approximately 10^{-20} to 10^{-17} m^2). The hydraulic conductivity of halite is typically 10^{-16} to 10^{-13} m/s (permeabilities of approximately 10^{-23} to 10^{-20} m^2), but may be higher close to excavations or where clay is abundant. Flow in most of the tested intervals has been found to be nonradial, which may be caused by the complex stress regime around the excavations.

Analyses of brine samples collected from Marker Bed 140 in L4P51 showed that this brine has a chemistry that is different from that of all other brines collected around the WIPP site except for the brines sampled from the floor seep in Room G (GSEEP) and from boreholes G090 and H090, which also penetrate MB140. The brine chemistry suggests a dual marine and continental source for the solutes. Analyses of the gases that evolved from the brine when it was depressurized suggest that the brine may be saturated with respect to methane and nitrogen.

ACKNOWLEDGMENTS

The authors wish to thank Mike Fort, David Chace, Jeff Palmer, Ronnie Lewis, Wayne Stensrud, and Greg Martin for their efforts in fielding the tests discussed in this report. We would also like to thank Tom Doe, Jim Butler, and Bill Thompson for their helpful review comments. Lydia Biggs' and Jeff Palmer's assistance with figure preparation is greatly appreciated, as is Bob Jones' assistance with manuscript preparation.

CONTENTS

CONTENTS (continued)

Tables

Figures

Figures (continued)

Figures (continued)

Figures (continued)

Figures (continued)

Figures (continued)

1. INTRODUCTION

This report presents interpretations of hydraulic tests conducted in bedded evaporites of the Salado Formation from May 1992 through May 1995 at the Waste Isolation Pilot Plant (WIPP) site in southeastern New Mexico (Figure 1-1). The WIPP is a US Department of Energy research and development facility designed to demonstrate safe disposal of transuranic wastes from the nation's defense programs. The WIPP disposal horizon is located in the lower portion of the Permian Salado Formation. The hydraulic tests discussed in this report were performed in the WIPP underground facility by INTERA Inc. (now Duke Engineering & Services, Inc.), Austin, Texas, following the Field Operations Plan and Addendum prepared by Saulnier (1988, 1991) under the technical direction of Sandia National Laboratories, Albuquerque, New Mexico.

Hydraulic testing was performed to provide quantitative estimates of the hydraulic properties controlling brine flow through the Salado Formation. The specific objectives of the tests were:

- To quantify the hydraulic conductivity and specific storage of different stratigraphic intervals in the Salado Formation around the WIPP facility;
- To determine formation pore pressures within different stratigraphic intervals in the Salado Formation around the facility;
- To determine the radii of influence of the tests in order to define the scales at which the interpreted properties are representative;
- To determine how and to what distance(s) excavation effects around the WIPP facility have affected hydraulic properties and/or formation pore pressures in the surrounding rock; and
- To provide data to allow evaluation of the mechanisms controlling brine flow through evaporites.

This report represents a continuation of the work described by Beauheim et al. (1991, 1993a). Those reports presented preliminary interpretations of pressure-pulse, constant-pressure flow, and/or pressure-buildup tests completed in 14 isolated borehole intervals between September 1988 and July 1992. The testing program was expanded after May 1990 to include constant-pressure flow and pressure-buildup/falloff testing in an effort to provide estimates of hydraulic conductivity independent of test-zone compressibility and to allow determination of formation specific storage. New statistical analysis methods have demonstrated that hydraulic-conductivity estimates are greatly improved by conjunctive analysis of pulse, flow, and buildup/falloff tests. However, these statistical methods have also demonstrated that analysis of any single-hole test cannot be sufficiently constrained such that formation specific storage can be uniquely determined from test data possibly affected by borehole skin and compliance.

This report discusses testing completed between May 1992 and May 1995. In addition, re-analyses of all previous tests are included in Appendix A. The hydraulic testing reported herein consists of pressure-pulse, constant-pressure flow, and/or pressure-buildup/falloff

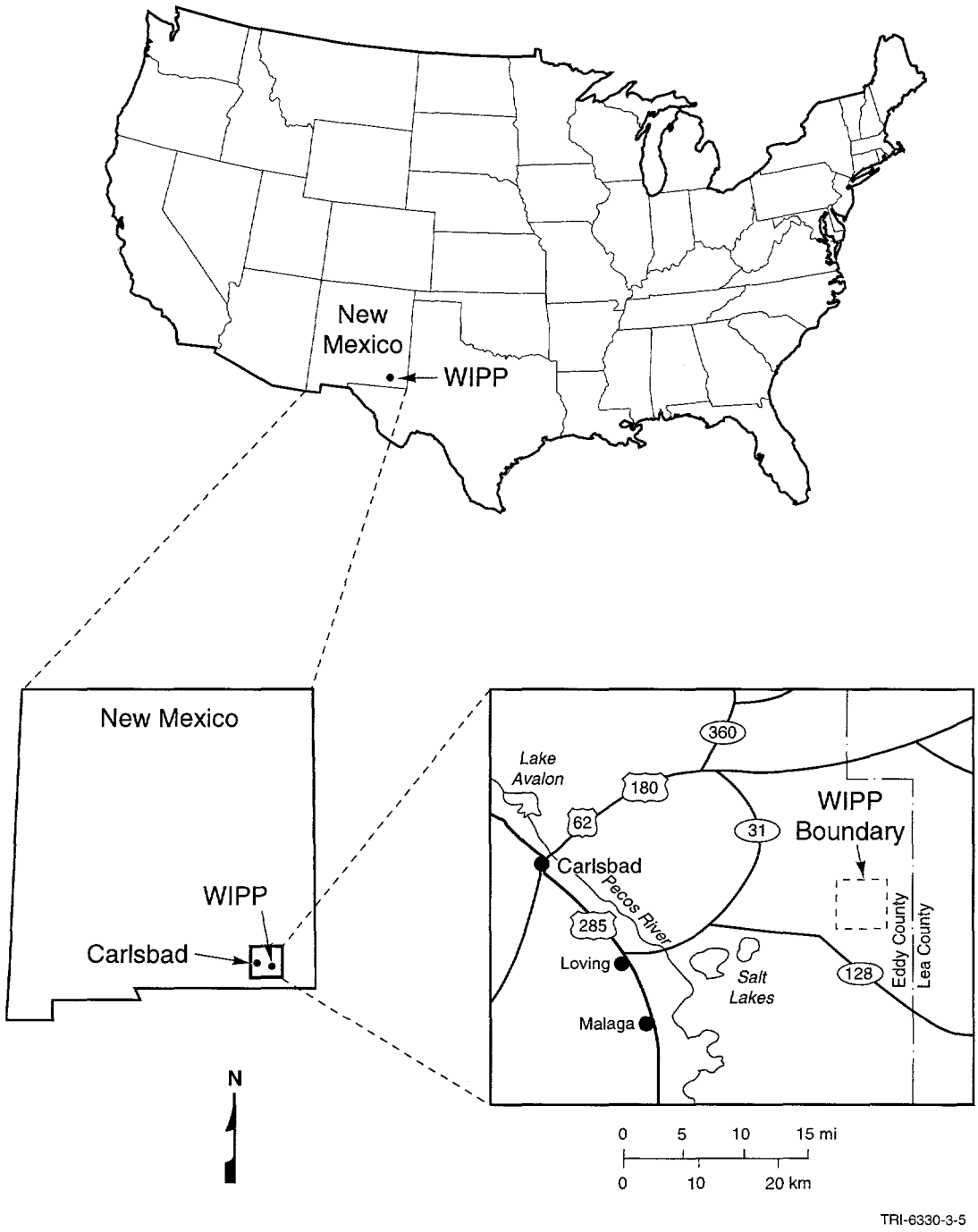

Figure 1-1. Location of the WIPP Site.

tests of six stratigraphic intervals at locations within 30 m of the WIPP excavations. The stratigraphic intervals tested included halite (both pure and impure) and anhydrite (with associated clay seams). The hydraulic tests that were amenable to analysis included five pressure-pulse tests completed in three different intervals and ten constant-pressure flow tests performed in four intervals, eight of which were followed by pressure-buildup/falloff tests. Equipment problems affected all of the tests of an argillaceous-halite unit below Marker Bed 140 to such a degree that no analysis of the data was possible.

The hydraulic-test analyses presented in this report were performed under the assumption that Darcy's (1856) law adequately describes flow through low-permeability evaporites. Previous analyses assumed that the transient fluid pressures observed during the tests were not affected by inelastic or nonlinearly elastic deformation of the rock. However, borehole-closure data collected from many of the tested intervals indicate that some amount of rock deformation occurs during testing, affecting the transient fluid pressures during the tests. The actual amount of deformation that occurs is difficult to quantify accurately, but the resulting uncertainty in the hydraulic-parameter estimates is small. The borehole-closure data are, therefore, not explicitly included in the analyses. The hydraulic-test analyses no longer assume cylindrical flow. The dimensionality of the flow can be treated as unknown and determined along with the other hydraulic parameters. Sensitivity-analysis techniques reported in Beauheim et al. (1991) have been significantly expanded for this report. The current methods allow quantification of the uncertainty in the fitting parameters resulting from data noise, formulation of the inverse problem (constraints), correlations among fitting parameters, and correlations among fitting and non-fitting parameters.

THIS PAGE INTENTIONALLY LEFT BLANK

2. GEOLOGIC SETTING AND LOCAL STRATIGRAPHY

The WIPP site is located in the northern part of the Delaware Basin in southeastern New Mexico. WIPP-site geologic investigations have concentrated on the upper seven formations typically found in that part of the Delaware Basin. These are, in ascending order, the Bell Canyon Formation, the Castile Formation, the Salado Formation, the Rustler Formation, the Dewey Lake Redbeds, the Dockum Group, and the Gatuña Formation (Figure 2-1). All of these formations are of Permian age, except for the Dockum Group, which is of Triassic age, and the Gatuña, which is a Quaternary deposit.

The WIPP underground facility lies in the lower part of the Salado Formation at an approximate depth of 655 m below ground surface. The Salado Formation is approximately 600 m thick at the WIPP site, and is composed largely of halite, with minor amounts of interspersed clay and polyhalite. The Salado also contains interbeds of anhydrite, polyhalite, clay, and siltstone. Many of these interbeds are traceable over most of the Delaware Basin. Jones et al. (1960) designated 45 of the continuous anhydrite and/or polyhalite interbeds as "Marker Beds", and numbered these Marker Beds (MB) from 100 to 144, increasing downward. The WIPP facility horizon (the stratigraphic location of the underground excavations) lies between MB138 and MB139.

A typical stratigraphic section of the Salado Formation in the vicinity of the WIPP underground facility, adapted from Deal et al. (1989), is shown in Figure 2-2. Deal et al. (1989) present a detailed description of stratigraphic units that correlate throughout most of the underground facility. The description has been extended to cover a 58-m interval of the Salado, centered approximately at the stratigraphic midpoint of the excavations (Appendix B). The description delineates 16 "map units" numbered 0 to 15 and 39 other identifiable units. The majority of the units are composed primarily of halite, and are differentiated principally on the basis of differing clay and polyhalite contents, which rarely exceed 5%. The halite units lacking integer map-unit designations are identified by H (pure halite), AH (argillaceous halite), or PH (polyhalitic halite) prefixes, followed by a number or letter ("m" for "minus")-number combination representing that unit's position with respect to the base of the sequence, which was arbitrarily defined as the halite unit immediately underlying anhydrite "c" and clay B. For example, AH-4 is the fourth argillaceous halite unit above the base of the sequence and H-m1 is the first halite unit below the base of the sequence. The remainder of the units are sulfatic interbeds, such as MB138 and MB139, and clay seams. The interbeds are composed primarily of anhydrite, with lesser amounts of polyhalite and halite. Thinner sulfatic interbeds and a number of the more continuous clay seams have also been given letter designations (e.g., anhydrite "a", clay B) to facilitate consistent referencing. These units are shown on Figure 2-2. The stratigraphic positions of the WIPP excavations with respect to the designated map units are shown in Figure 2-3.

The testing and guard-zone monitoring discussed in this report were carried out in H-m7, AH-m5, H-m6, H-m5, AH-m4, H-m4, H-m3, PH-m1, AH-m2, clay A-1, H-m3, AH-m1 (clay A), MB140, H-m2, H-m1, map units 6 through 12 (including anhydrites "a" and "b"), map units 14 and 15, AH-1 (clay J), H-5, AH-2, MB138, and H-6.

System	Series	Group	Formation	Member	Approximate Thickness (m)*
Recent	Recent		Surficial Deposits		3
Quaternary	Pleistocene		Mescalero Caliche		10
			Gatuña		
Triassic		Dockum	Undivided		3
Permian	Ochoan		Dewey Lake Redbeds		150
			Rustler	Forty-niner	18
				Magenta	7
				Tamarisk	26
				Culebra Dolomite	7
				unnamed	37
			Salado		600
			Castile		400
	Guadalupian	Delaware Mountain	Bell Canyon		310
			Cherry Canyon		335
			Brushy Canyon		550

* At center of WIPP site.

TRI-6115-38-0

Figure 2-1. WIPP area stratigraphic column.

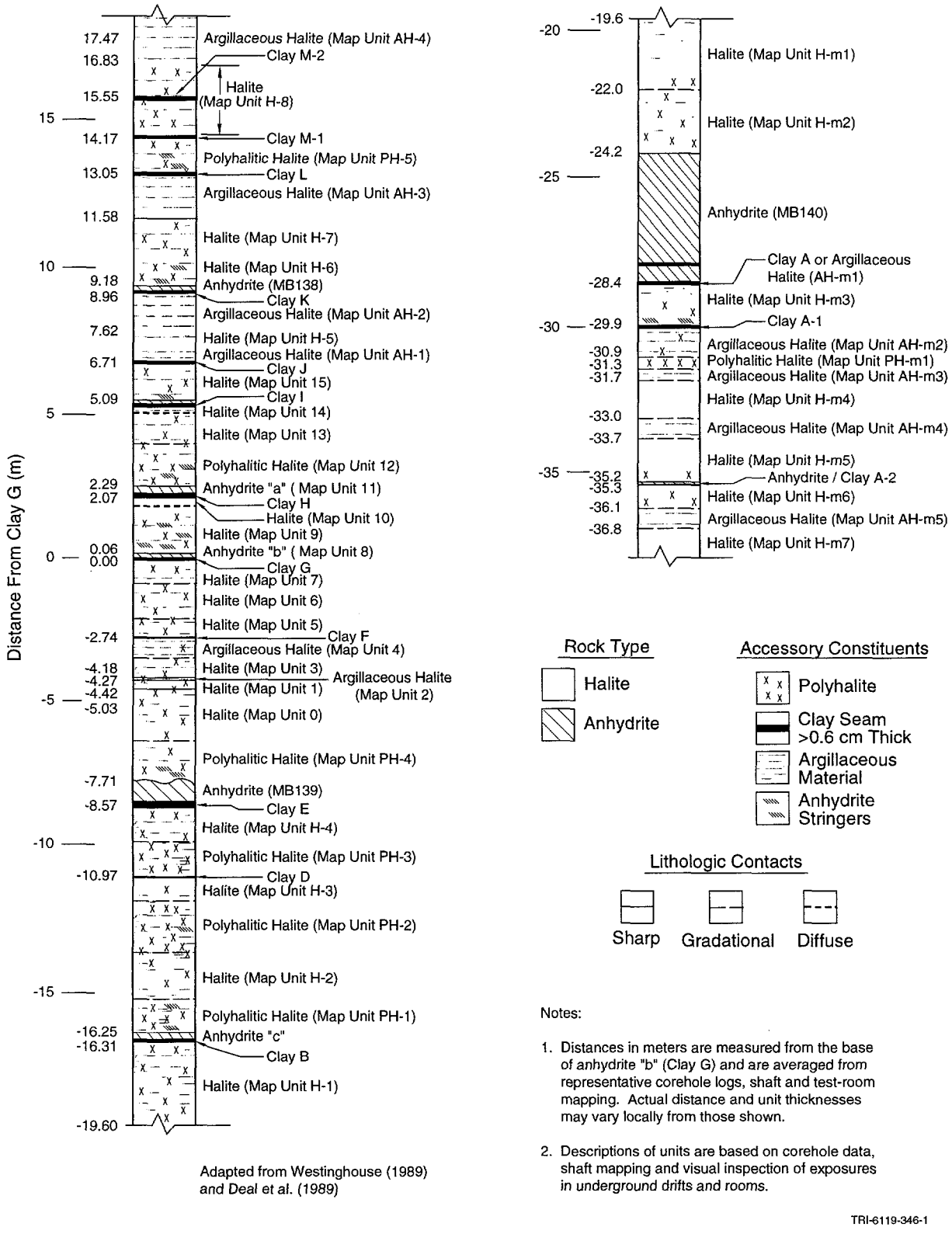

Adapted from Westinghouse (1989) and Deal et al. (1989)

Notes:

1. Distances in meters are measured from the base of anhydrite "b" (Clay G) and are averaged from representative corehole logs, shaft and test-room mapping. Actual distance and unit thicknesses may vary locally from those shown.

2. Descriptions of units are based on corehole data, shaft mapping and visual inspection of exposures in underground drifts and rooms.

TRI-6119-346-1

Figure 2-2. Detailed stratigraphy near the WIPP underground facility.

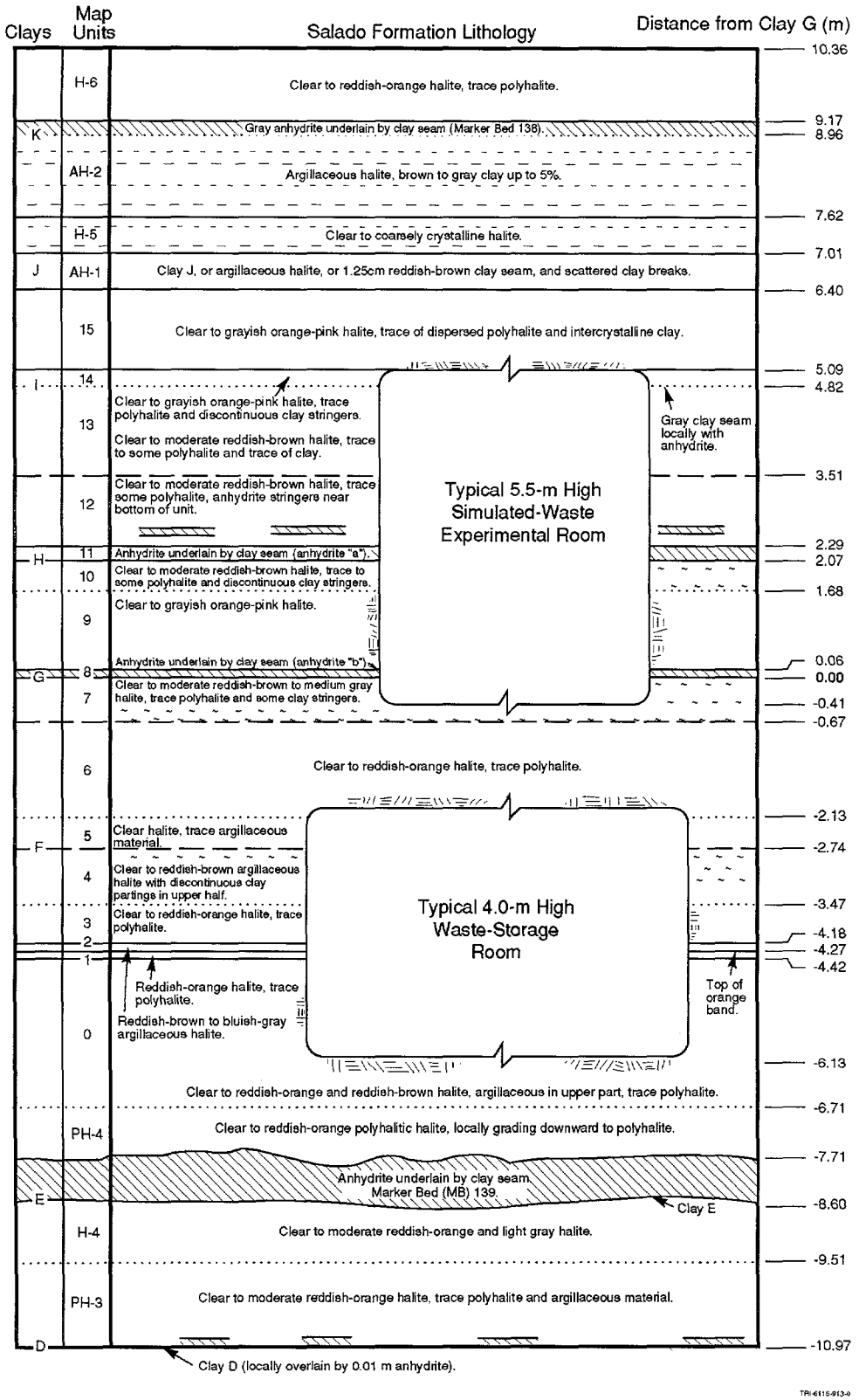

Figure 2-3. Schematic of typical WIPP underground rooms showing stratigraphic positions.

3. TESTING EQUIPMENT

The following sections briefly describe the equipment used in the permeability-testing program in the WIPP underground facility. The equipment included multipacker test tools, data-acquisition systems, pressure transducers, thermocouples, linear variable-differential transformers, a differential-pressure-transmitter panel, a tool to measure fracture dilation, a system to maintain packer pressures, compliance-testing equipment, and an apparatus to allow collection of brine and gas samples under pressure. More detailed descriptions of the testing equipment and the procedures and methods used to calibrate the equipment are presented in Stensrud et al. (1992) and Chace et al. (1998).

NOTE: The use of brand names in this report is for identification only, and does not imply endorsement of specific products by Sandia National Laboratories.

3.1 Multipacker Test Tool

The standard configuration of the multipacker test tool designed for this testing program, shown on Figures 3-1 and 3-2, had two sliding-end, 9.5-cm outside diameter (O.D.) inflatable packers mounted on a 4.83-cm O.D. mandrel and oriented with the packers' fixed ends toward the bottom-hole end of the test tool. The test tool's modular design allowed single- and triple-packer configurations to be assembled when necessary for a given testing scenario. The packers had 0.92-m-long inflatable elastic elements composed of natural rubber and synthetic materials. The packer elements had approximately 0.84-m seal lengths when inflated in 4-inch (10.2-cm) diameter boreholes. The test tool was restrained using a set of radially oriented tapered jaws or slips that tightened on the test-tool mandrel as the tool attempted to move out of the borehole in response to pressure buildup.

Each multipacker test tool was equipped with three sets of ports to the bottom-hole test zone and the guard zone between packers. One set of ports was used to transmit pressures from the test and guard zones to the transducers, which were mounted outside of the boreholes. A second set of ports was used to dissipate "squeeze" pressures created during packer inflation and to vent fluid from the isolated intervals during withdrawal tests. These two sets of ports were accessed by continuous lengths of 3/16-inch (0.48-cm) O.D. stainless-steel tubing. The third set of ports provided access for 1/8-inch (0.32-cm) diameter Type E thermocouples to measure temperatures in the test and guard zones. Packer-inflation pressures were monitored with transducers attached to the packer-inflation lines.

The test-interval section of some test tools was equipped with linear variable-differential transformers (LVDTs) to measure borehole deformation and test-tool movement during the testing period. Three radially oriented LVDTs were located below the test-interval packer, and one axially oriented LVDT was mounted at the bottom end of the multipacker test tool (Figure 3-2) to measure tool movement relative to the bottom of the hole during testing.

3.2 Data-Acquisition System

A computer-controlled data-acquisition system (DAS) monitored the progress of each test and recorded pressure, temperature, and borehole-deformation data (Figure 3-3). Each DAS consisted of an IBM PS/2 Model 50 or

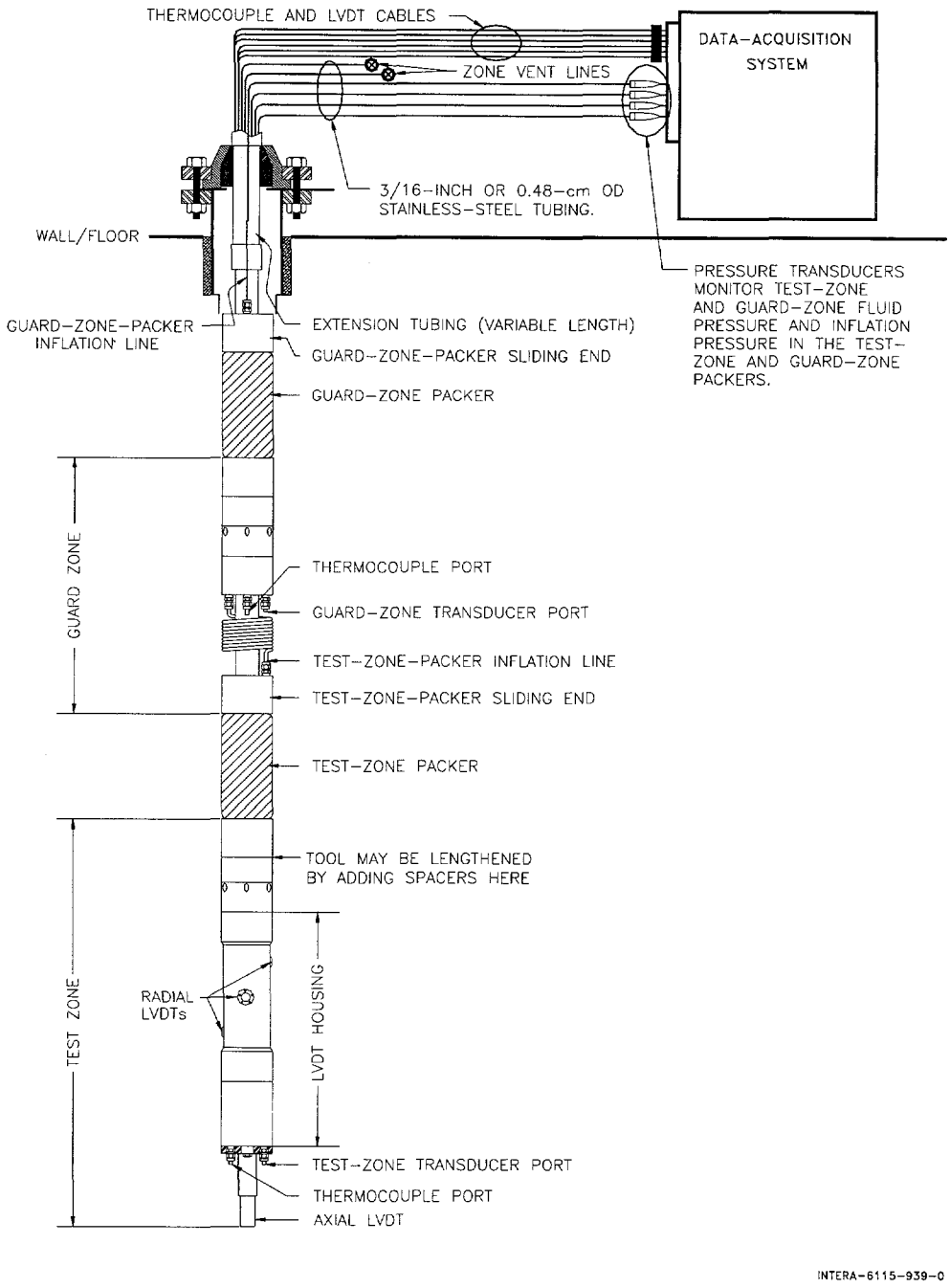

Figure 3-1. Typical configuration of the multipacker test tool used for hydraulic testing.

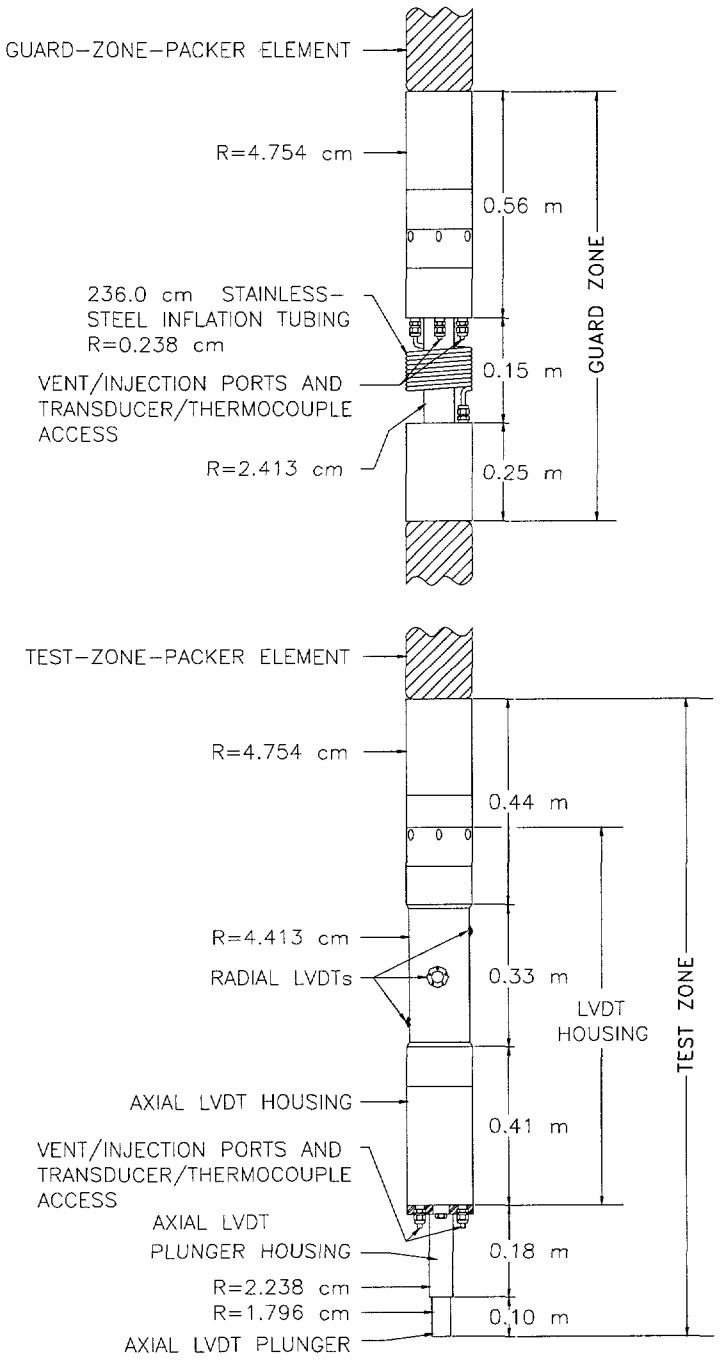

Figure 3-2. Detail of test- and guard-zone sections of the multipacker test tool.

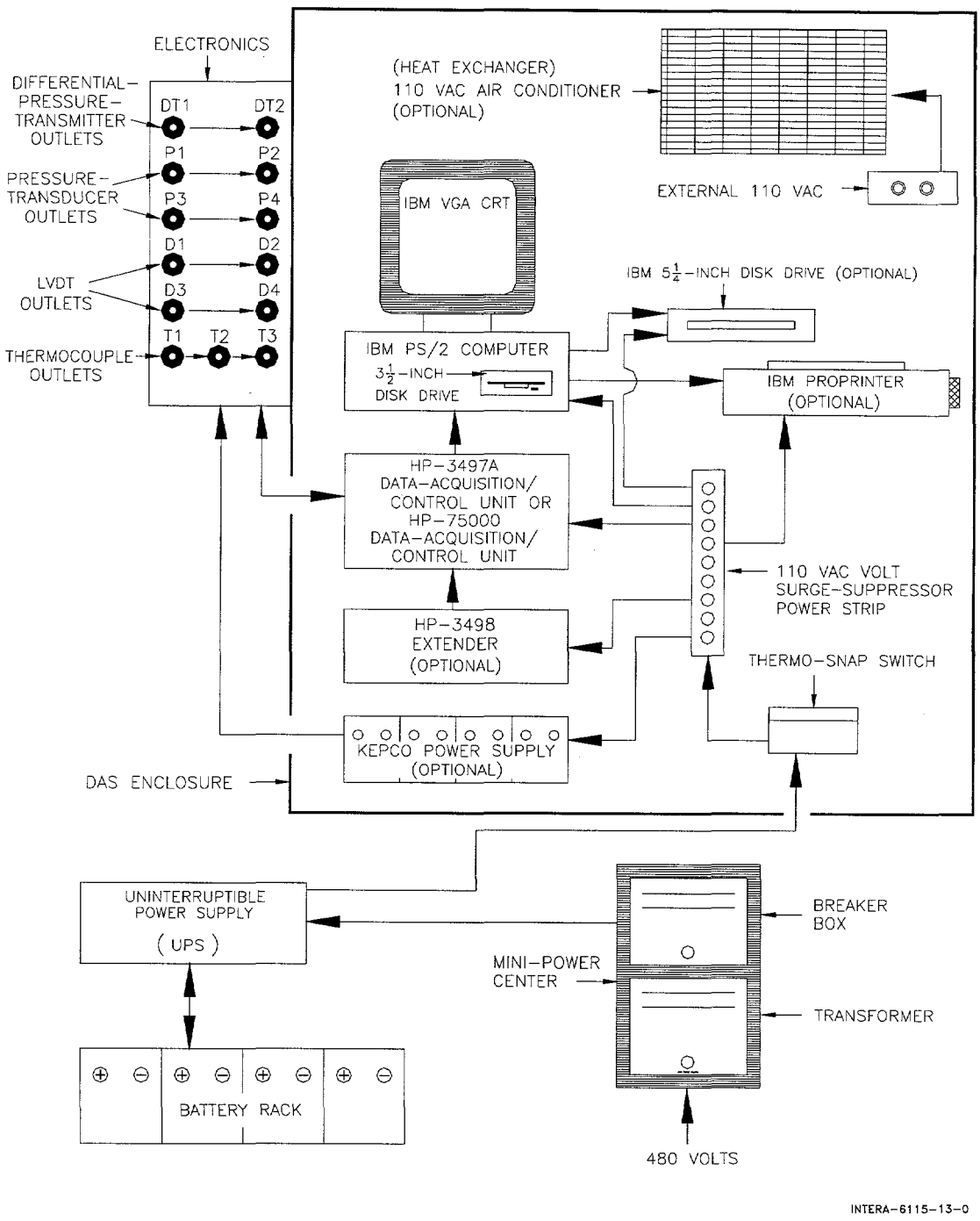

Figure 3-3. Schematic illustration of the data-acquisition system.

Gateway 386/25 desktop computer for system control and data storage, and a Hewlett Packard (HP) 3497A Data-Acquisition/Control Unit containing: power supplies to excite the transducers, thermocouples, and LVDTs; a signal scanner to switch and read channels; and a 5-1/2 digit voltmeter to measure the output from the transducers, thermocouples, and LVDTs. The data-acquisition software (PERM4F) allowed sampling of the sensors' outputs at user-specified time intervals ranging from 15 seconds to 24 hours. As data were acquired, they were stored both on the computer's hard disk and on 3.5-inch diskettes. Real-time listing of the data on an auxiliary printer and screen and/or printer plots of the accumulated data was also possible.

3.3 Pressure Transducers

Pressures in the test and guard zones and in the packers were monitored with various Druck strain-gage pressure transducers. Models PDCR-830, PDCR-10/D, and PDCR-910 were rated to monitor pressure from 0 to 2000 psi (0 to 13.8 MPa). Model PDCR-930 is rated to monitor pressures from 0 to 3000 psi (0 to 20.7 MPa). The transducers were mounted on instrument panels outside the boreholes and were connected to the isolated zones and the packers through 3/16-inch (0.48-cm) O.D. stainless-steel tubing that passed into and through the packer mandrels. The manufacturer's stated accuracy of models PDCR-830 and PDCR-910 is ±0.1% of full scale, or ±2 psi (0.014 MPa). The manufacturer's stated accuracy of model PDCR-930 is ±0.1% of full scale, or ±3 psi (0.021 MPa). The manufacturer's stated accuracy of model PDCR-10/D is ±0.2% of full scale, or ±4 psi (0.028 MPa).

Transducers were calibrated before and after each installation of a test tool according to procedures described in Stensrud et al. (1992) to determine their accuracies and to evaluate the magnitude of transducer drift during the testing periods. The sensitivity coefficients derived from the transducer calibrations are tabulated in Chace et al. (1998).

3.4 Thermocouples

Type E Chromel-Constantan thermocouples were used to monitor temperatures within the test and guard zones during the permeability tests. The thermocouples were 1/8 inch (0.32 cm) in diameter and were sheathed in Inconel 600. The thermocouples were reported to be accurate to within ±0.06 °C by the manufacturer, ARI Industries. The thermocouples were calibrated by Sandia National Laboratories.

3.5 Linear Variable-Differential Transformers

Open boreholes, rooms, and drifts in the underground facility exhibit closure, deformation, and differential movement between halite and anhydrite beds (Bechtel, 1986). Measurable borehole closure (on the order of a few tenths-of-a-millimeter change in borehole diameter) in a shut-in, fluid-filled test interval could raise the pressure in the hole. Axial movement of a multipacker test tool can be caused by changes in packer-inflation pressure, pressure buildup or withdrawal in the isolated intervals, and hole elongation resulting from creep closure of the excavations. The rate of rock creep decreases with increasing distance from an excavation (Westinghouse, 1990), causing boreholes drilled from an excavation to elongate. Axial movement of the test tool can change the test-zone volume, which, in low-permeability media, can affect the observed pressure response in an isolated borehole interval. Three Trans-Tek Model 241 LVDTs were radially mounted, with 120° separation, on the

test-interval part of the multipacker test tool to measure radial borehole deformation (Figures 3-1 and 3-2). These LVDTs can each measure a range of motion of 0.5 cm. An axially mounted Trans-Tek Model 245 LVDT on the bottom of the test tool measured tool movement along the borehole axis (Figures 3-1 and 3-2). This LVDT has a range of motion of 10 cm. The LVDT responses are reported by Trans-Tek to be linear within ±0.5% over their working ranges. Jensen (1990) discusses in detail the design, calibration, and use of the LVDTs.

3.6 Differential-Pressure-Transmitter Panel

Fluid volumes produced during constant-pressure flow tests were measured using a differential-pressure-transmitter panel (Figure 3-4). The panel consisted of a differential-pressure transmitter (DPT) and injection/withdrawal columns. Rosemount Alphaline Model 1151 DP DPTs were used in the WIPP permeability-testing program. The DPTs were calibrated from 0 to 100 cm of water (0-9.8 kPa). The manufacturer's stated accuracy of the DPTs is ±0.2% of the calibrated span, including the combined effects of hysteresis, repeatability, and independent linearity.

The DPT panel utilized for the tests included in this report had connectors for two columns. The panel was designed such that columns of various diameters could be interchanged, depending on the expected flow rate during testing. As fluid from the test zone entered and filled a column, voltage measurements were taken by the DAS from the DPT. The DPT measured the difference in the pressure exerted on two sides of a sensing diaphragm. On one side of the diaphragm was the ambient test pressure. On the other side of the diaphragm was the pressure exerted by the fluid in the column, plus the ambient pressure. The difference, or differential pressure, was equal to the pressure exerted by the fluid in the column. As the fluid level in the column changed (a change in fluid-column height corresponds to a linear change in the volume), the voltage output changed proportionally.

During constant-pressure flow tests, the pressure inside the injection/withdrawal column was maintained under near constant-pressure conditions. To maintain constant pressure, the injection/withdrawal column was connected to a nitrogen-gas reservoir or an electronic pressure controller. Before testing, the reservoir pressure or electronic pressure controller was set to the designated test pressure. During a constant-pressure injection/withdrawal test, fluid left/entered a designated column from the test zone, but little change in the gas pressure in the column occurred due to the buffering capacity of the gas reservoir or the response of the electronic pressure controller.

3.7 Fracture-Dilation Test Tool

Hydraulic responses during some of the permeability tests indicated that discrete fractures were opening and closing due to pressure changes in the test zone. The fracture-dilation test tool shown in Figure 3-5 was designed to measure changes in fracture apertures during testing and thereby allow correlation of permeability and porosity. However, the testing program was ended before the fracture-dilation tool was used to measure fracture dilation.

3.8 Packer-Pressure-Maintenance System

Packer pressures steadily declined during some testing sequences, potentially jeopardizing the isolation of test and/or guard zones.

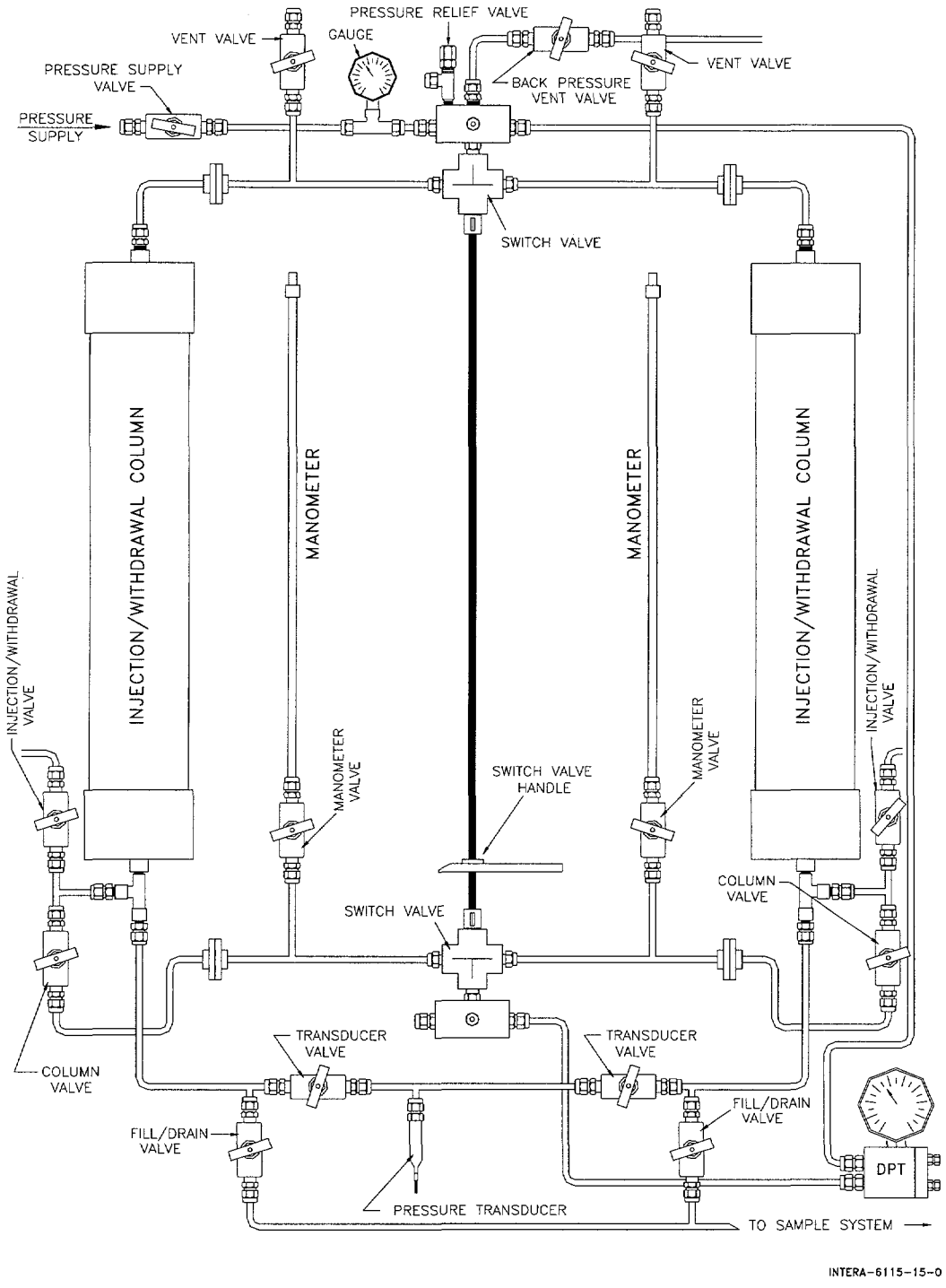

Figure 3-4. Differential-pressure-transmitter panel.

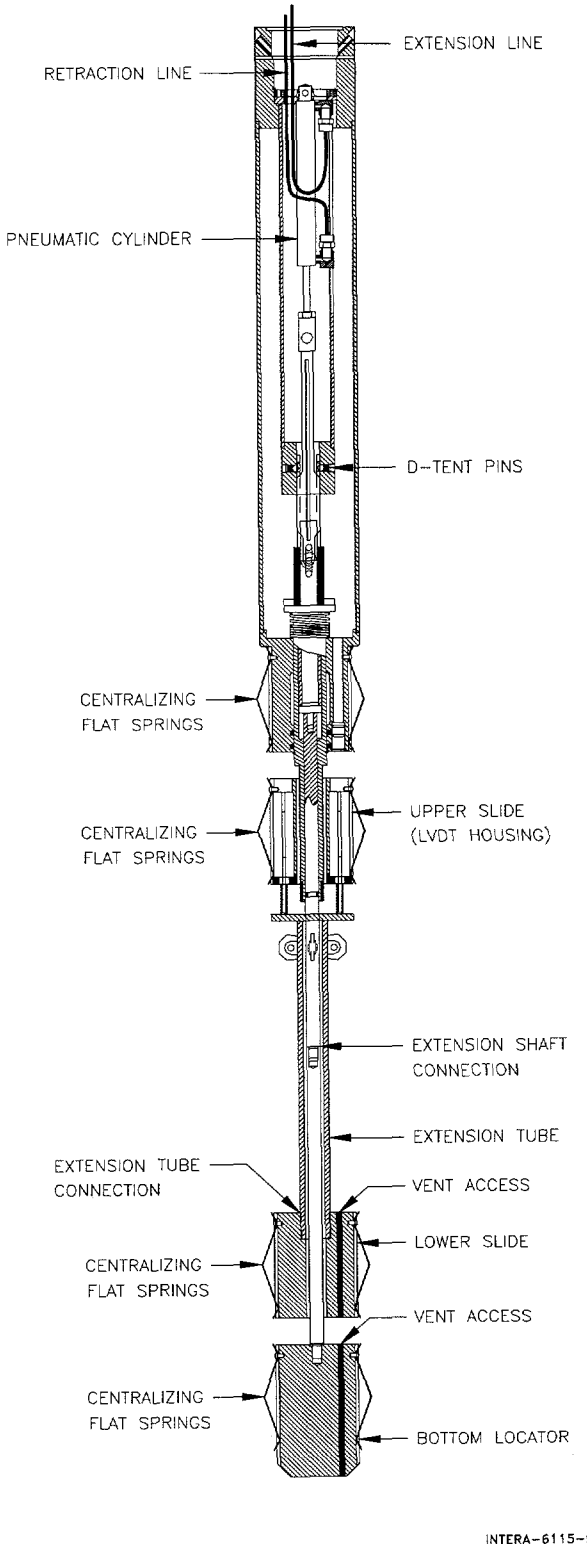

Figure 3-5. Detail of fracture-dilation test tool.

A pressure-maintenance system (Figure 3-6) was attached to various packers and zones during all of the testing sequences except S1P74-A. Details can be found in Chace et al. (1998).

The pressure-maintenance system served to hold the packer/zone pressure nearly constant during testing. A 1-gallon cylinder was filled approximately half-full with water and then pressurized with nitrogen to the desired pressure. The control valve between the cylinder and the nitrogen tank was closed when the desired pressure in the cylinder was achieved, and the control valve between the cylinder and the packer/zone was opened, allowing the pressures in the packer/zone and in the cylinder to equilibrate. The nitrogen in the cylinder served to increase the compressibility in the total system. Subsequent losses of fluid from the packer/zone resulted in smaller changes in pressure than would have otherwise occurred.

3.9 Compliance-Testing Equipment

Pickens et al. (1987) have shown that test-tool movement in response to packer inflation and fluid injection or withdrawal can affect pressure responses in isolated intervals in boreholes in low-permeability media. Figure 3-7 illustrates how packer movement due to packer inflation can cause the packer element to displace fluid in isolated intervals, causing changes in pressure. Changes in the shape, volume, or position of the test tool that affect pressure responses during testing are referred to as compliance. To evaluate the magnitude of compliance for the test tool, preinstallation compliance tests were conducted in the underground facility on all test tools according to procedures outlined in Section 3.1. Compliance tests were conducted in sealed and pressure-tested sections of 4.5-inch (11.43-cm) O.D. stainless-steel casing to differentiate test-tool-related phenomena from formation-related pressure responses observed in boreholes. The casing was intended to simulate a borehole with effectively zero permeability. The casing was placed in a borehole to minimize temperature fluctuations and associated pressure changes (Figure 3-8).

3.10 Pressurized-Fluid-Sampling Apparatus

Brine and gas samples from MB140 were collected under pressure during a constant-pressure flow event conducted at the end of test sequence L4P51-C1 (Chace et al., 1998). Figure 3-9 is a schematic of the pressurized-brine-sampling apparatus. The sampling apparatus was incorporated into the DPT panel and consisted of a Whitey sample cylinder, two Nupro non-rotating stem valves, and two Nupro rising-plug valves. The configuration of the sampling apparatus permitted replacement of the sample cylinder without affecting the zone pressure. The sampling apparatus and DPT panel were pressurized with argon rather than nitrogen for this exercise because nitrogen was expected to be one of the primary gases in solution. Each sample cylinder was flushed with argon prior to installation. Pressure in the sample cylinders was maintained at approximately 8 MPa during sample collection.

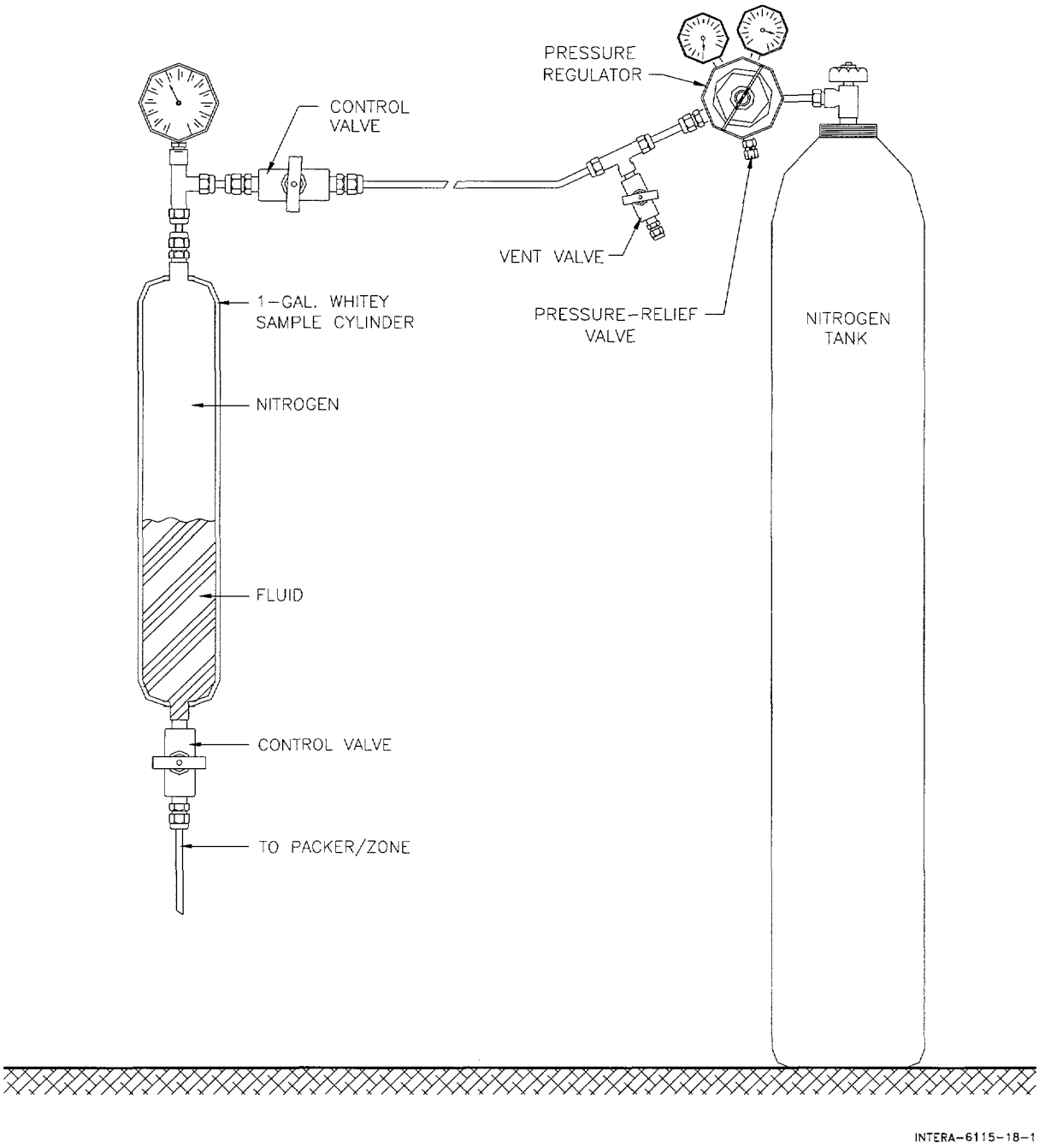

Figure 3-6. Pressure-maintenance system.

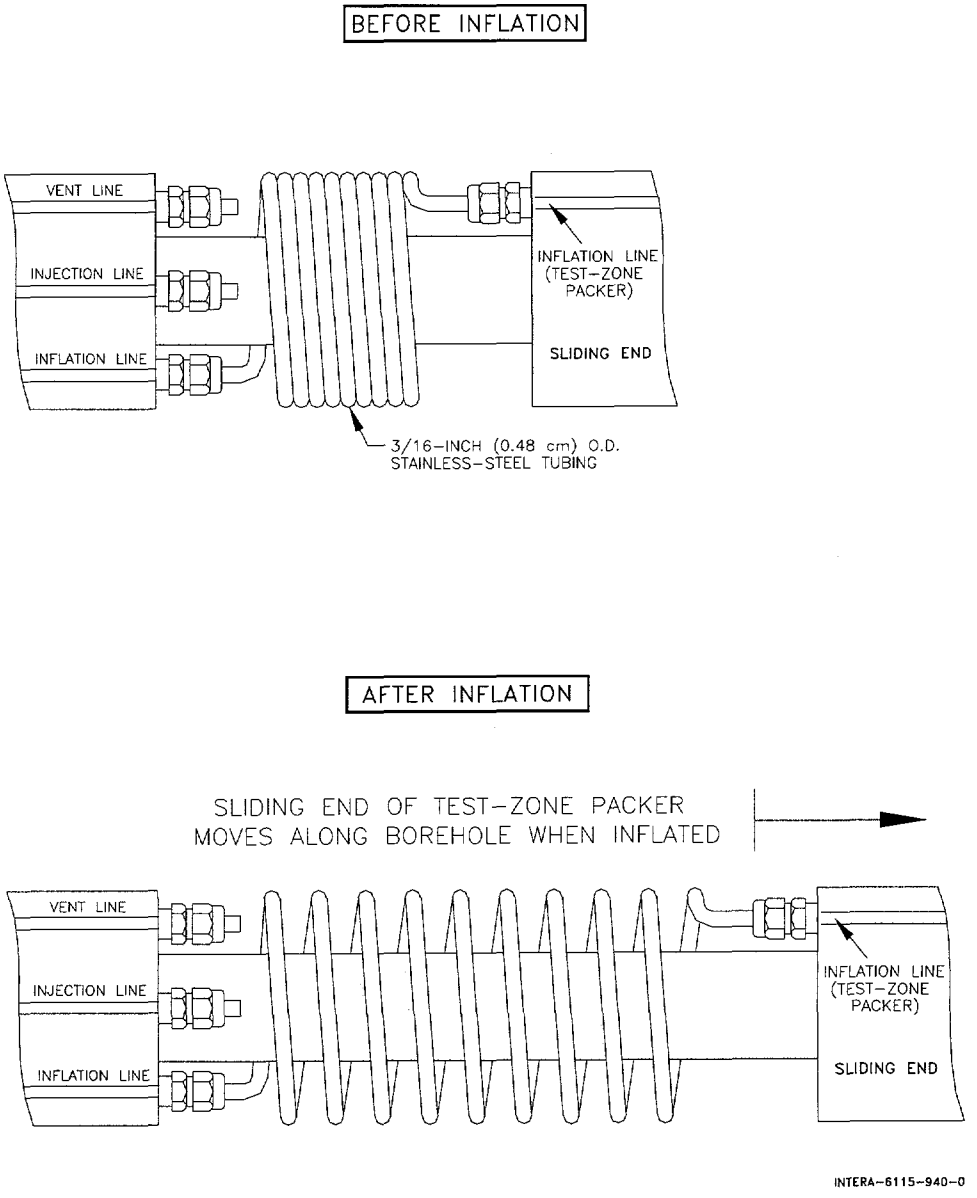

Figure 3-7. Movement of the sliding-end sub in the guard zone during packer inflation.

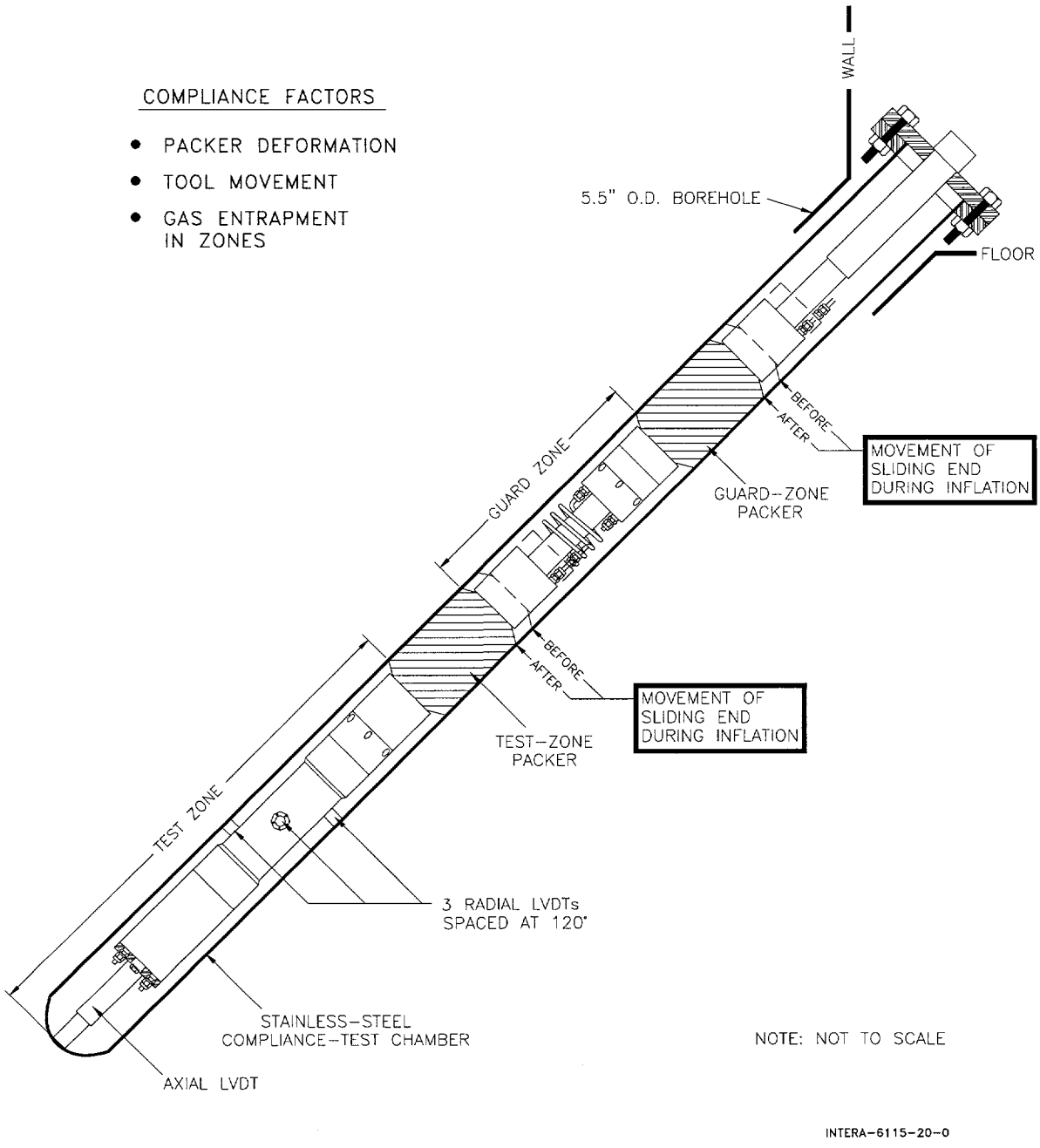

Figure 3-8. Cross-section view of the stainless-steel compliance-testing chamber in borehole P4P30.

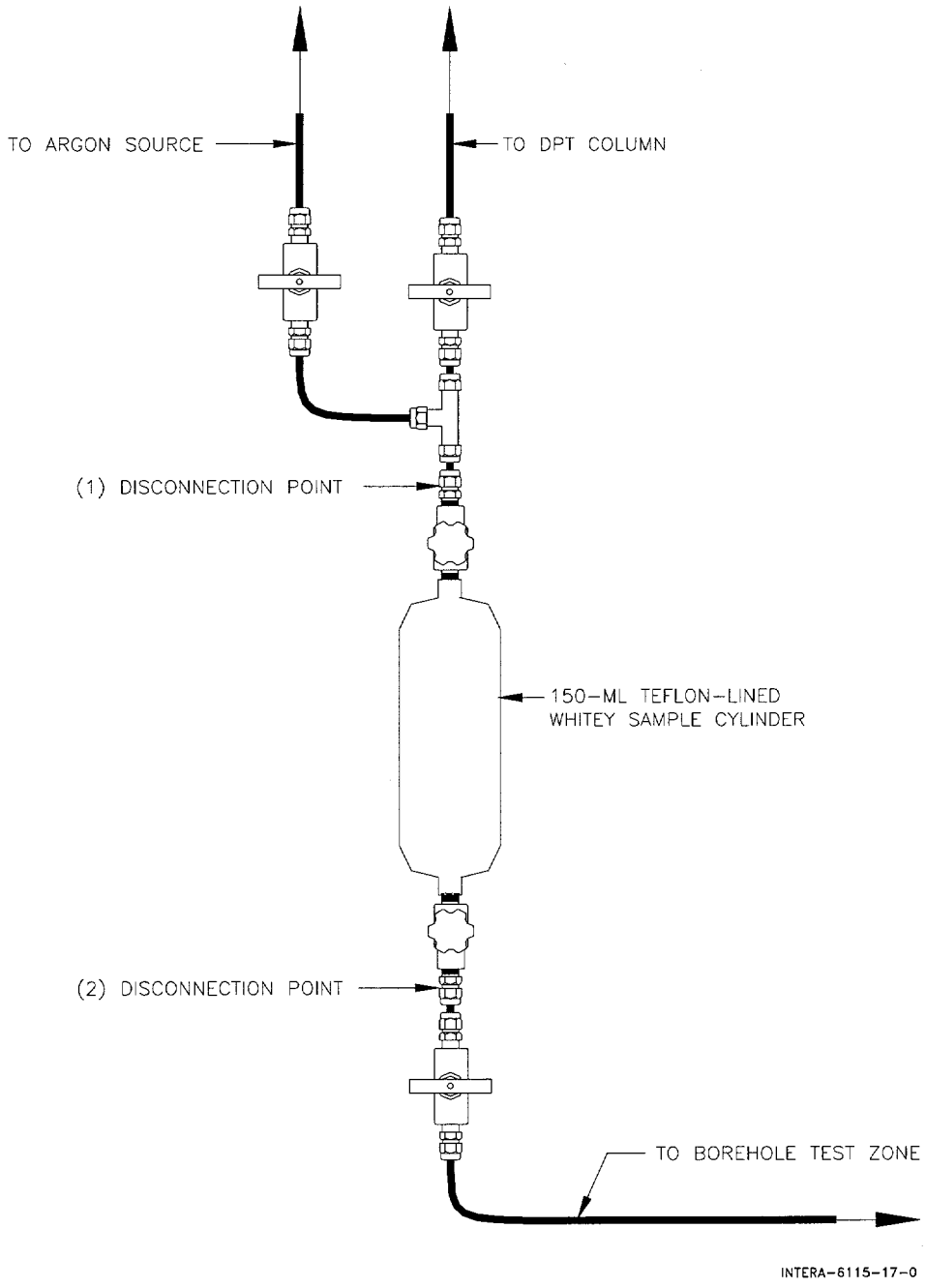

Figure 3-9. Pressurized-brine-sampling apparatus.

THIS PAGE INTENTIONALLY LEFT BLANK

4. TESTING PROCEDURES

The test tools were used to conduct hydraulic tests in boreholes drilled from the underground excavations. In low-permeability formations such as the Salado, changes in the volume or temperature of the test-zone fluid and/or the test tool can affect observed pressure responses, as described in Pickens et al. (1987). In addition, pressure changes in isolated sections of boreholes in low-permeability media can cause physical movement of the test tool. Changes in pressure can occur in response to temperature changes affecting the test-zone and/or packer-inflation fluids. Pressures in test intervals may also be affected by changes in packer-inflation pressures, and vice versa, as when a pulse injection in a test zone increases the forces acting against the outside of the test-zone packer, causing the packer-inflation pressure to increase.

Changes in the volume and pressure of the test-zone fluid that are not due to the formation's hydraulic response but instead to changes in the position of the test tool or deformation of the test tool or borehole are included under the term "compliance". Pickens et al. (1987) showed that compliance-related pressure changes during hydraulic tests of formations with hydraulic conductivities less than 10^{-12} m/s can obscure and/or dominate actual formation-related pressure changes and result in incorrect estimates of the formation's hydraulic properties. Test-tool-related compliance was empirically estimated by subjecting the testing equipment to simulated test conditions and observing the resulting pressure responses. These compliance tests provided data to understand and/or compensate for pressure changes resulting from compliance during actual hydraulic testing.

The test tool to be used for hydraulic testing in any borehole underwent compliance testing in a compliance-test chamber (Section 3.9) before being installed in the test borehole. Compliance testing quantified the response of the test tool to the types and magnitudes of pressure changes anticipated during hydraulic testing. After compliance testing was completed, the test tool was installed in the test borehole. A hydraulic testing sequence was then performed, consisting of a shut-in pressure buildup followed by some combination of pressure-pulse tests, constant-pressure flow tests, and pressure buildup/falloff tests. Compliance- and hydraulic-testing procedures are discussed below.

4.1 Compliance Testing

Compliance tests were performed for each test tool before the tool was installed in a test borehole. The purposes of the compliance testing were to: (1) establish that the test tools had been properly assembled and that all seals and fittings were performing as designed; and (2) evaluate test-tool responses to packer inflation and applied pressures in the intervals isolated by the inflated packers. For compliance tests, the test tools with all monitoring instruments were installed in test chambers in the same manner employed when installing the test tool in a borehole. The compliance chambers consisted of stainless steel well casing sealed at one end. The DAS was used to monitor and record the results of the compliance testing.

The test tool's packers were sequentially inflated, starting with the test-zone packer. Both packers were inflated to between 8 and 10 MPa, after which the pressures were monitored for 24 to 48 hours for evidence of

leaks or improper performance. Packer pressures usually decreased during this period due to the elasticity of the packer-element material, air that may have been entrapped during inflation going into solution, and other compliance-related phenomena. After monitoring this pressure decline for the initial 24- to 48-hour period, packer-inflation pressures were usually increased to 8 to 10 MPa and monitored for an additional 24 to 48 hours.

After the leak-check/packer-pressure-adjustment periods, the test zone was subjected to a pressure-injection pulse of at least 3.5 MPa. The pressure responses of both the test and guard zones were then monitored for evidence of leaks, and the associated packer-pressure responses were also monitored. After evaluation of test-zone integrity was completed, the same procedure was followed to evaluate the integrity of the guard zone.

In some instances, the test- and guard-zone pressures were increased and/or decreased in a series of step pressure-injection and/or withdrawal pulses to provide a range of test-zone and packer-pressure responses to pressure changes in neighboring zones and packers. During the withdrawals, the volume of fluid released during each pressure drop was measured to provide data with which to evaluate test-tool or system compressibility. In some instances, system compressibility was evaluated by continuously injecting and/or withdrawing brine into/from the test and/or guard zone using a DPT panel. This method gave a continuous measurement of compressibility versus pressure.

Figures 4-1 to 4-5 display the results of a typical compliance-test sequence. Figure 4-1 shows the pressures in the test and guard zones; Figure 4-2 shows the pressures in the

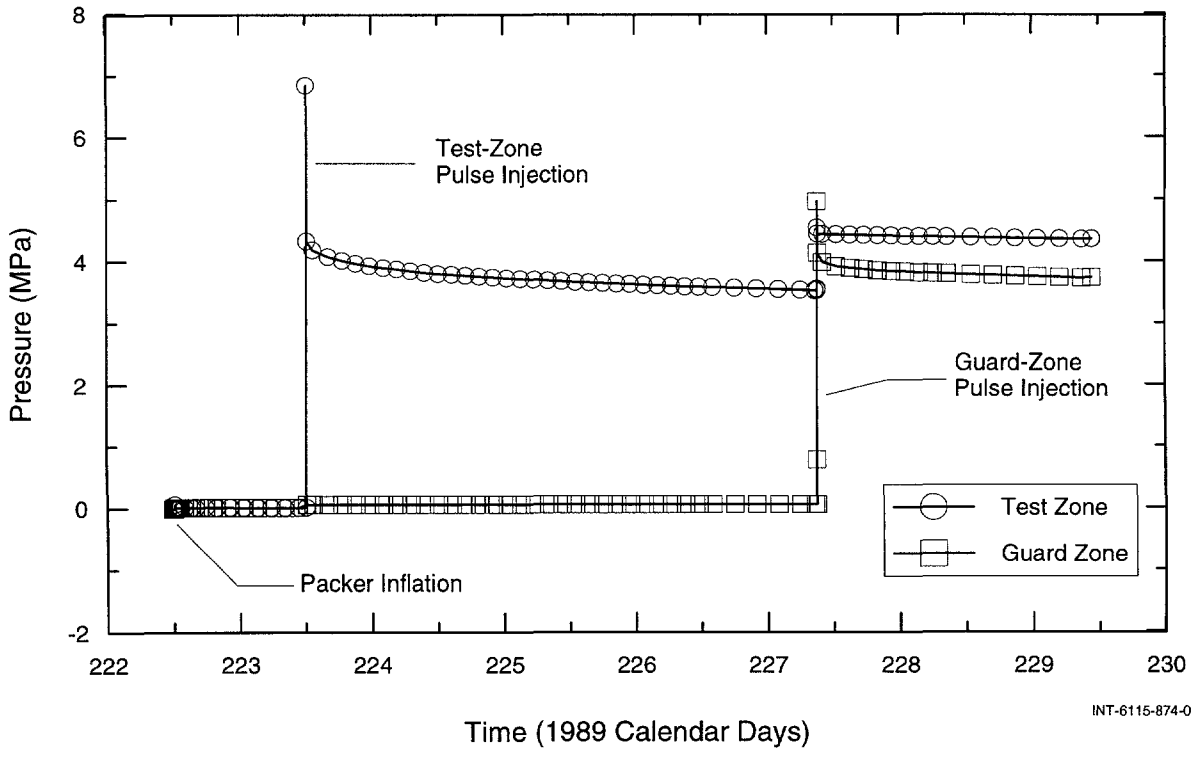

Figure 4-1. Zone pressures for compliance test COMP 16, multipacker test tool #5.

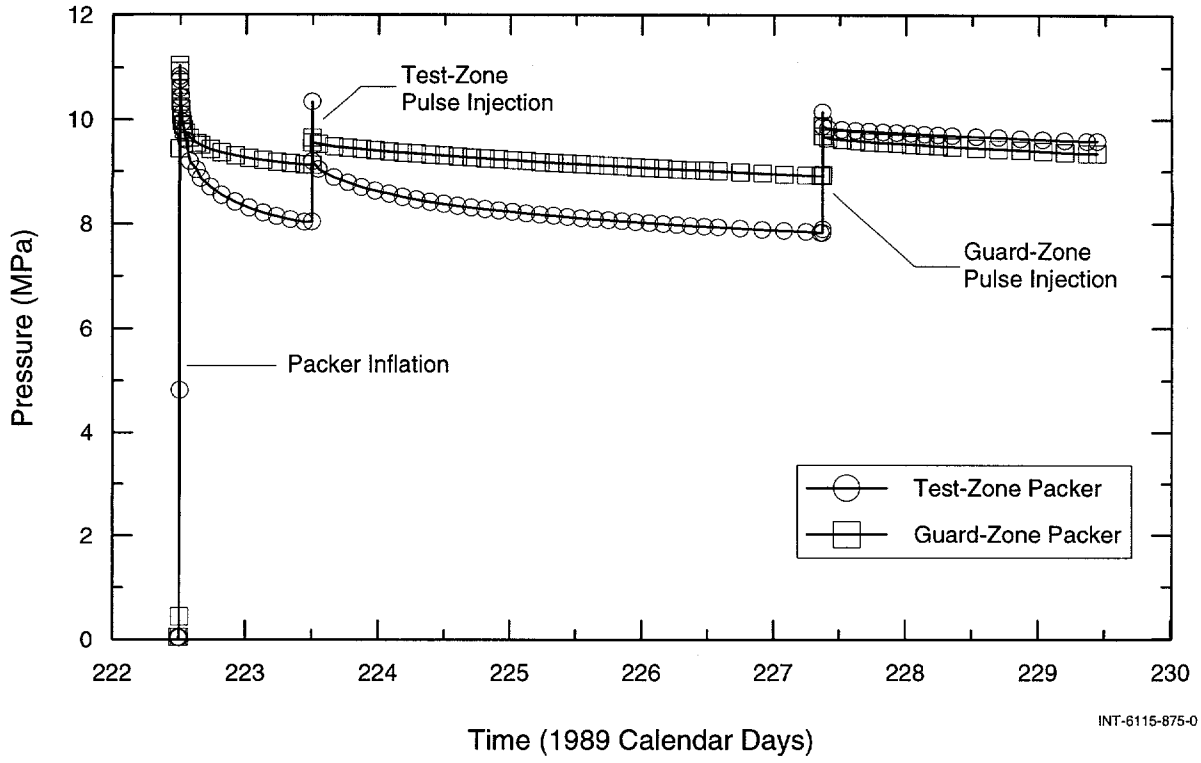

Figure 4-2. Packer pressures for compliance test COMP 16, multipacker test tool #5.

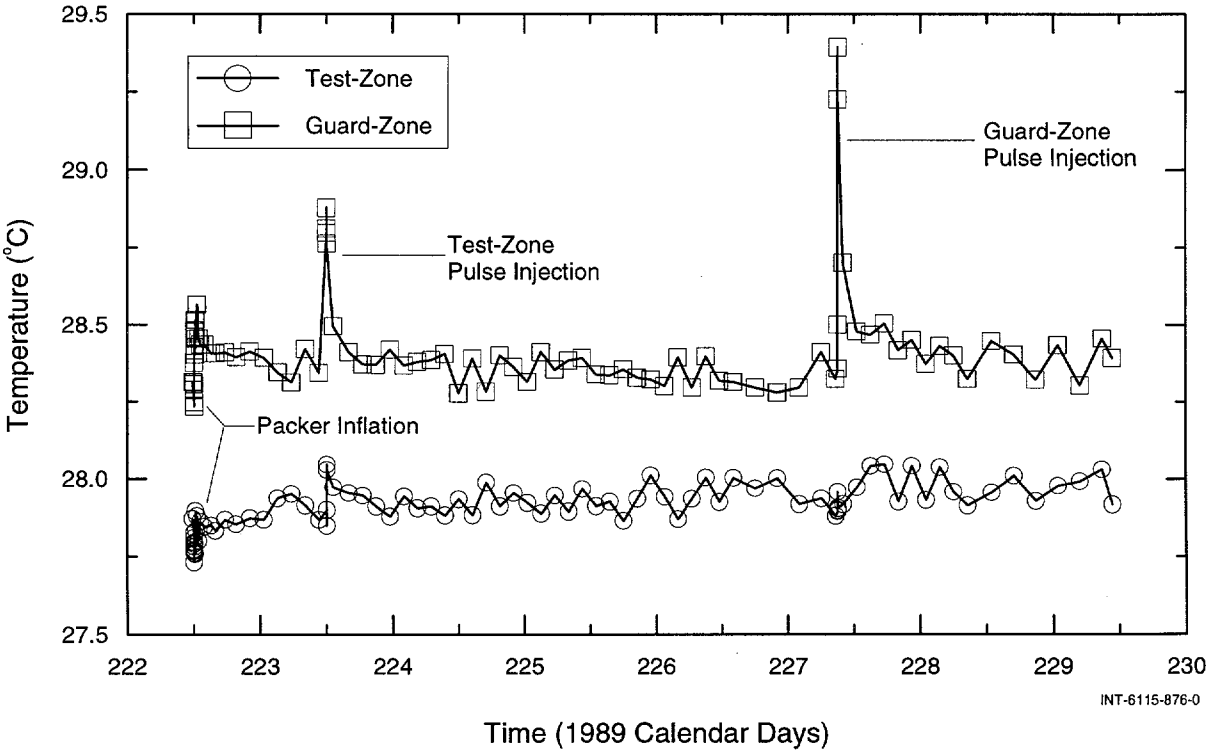

Figure 4-3. Zone temperatures for compliance test COMP 16, multipacker test tool #5.

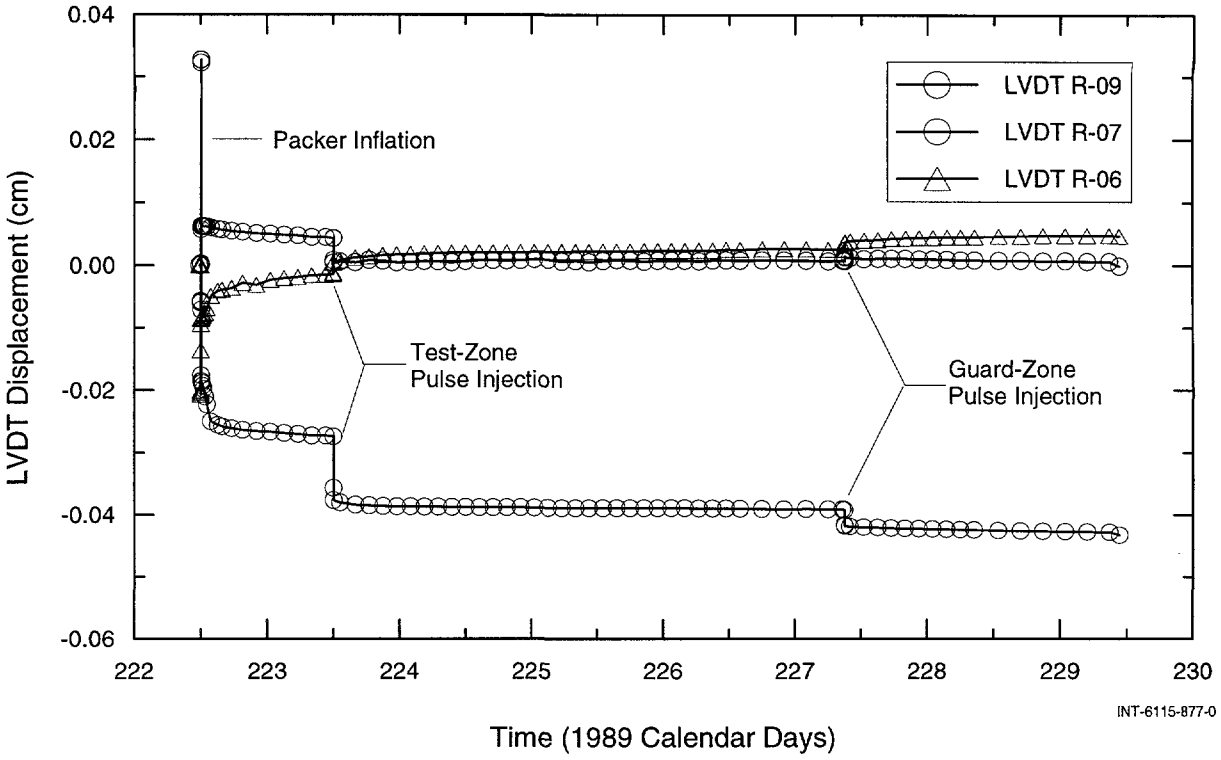

Figure 4-4. Radial-LVDT data for compliance test COMP 16, multipacker test tool #5.

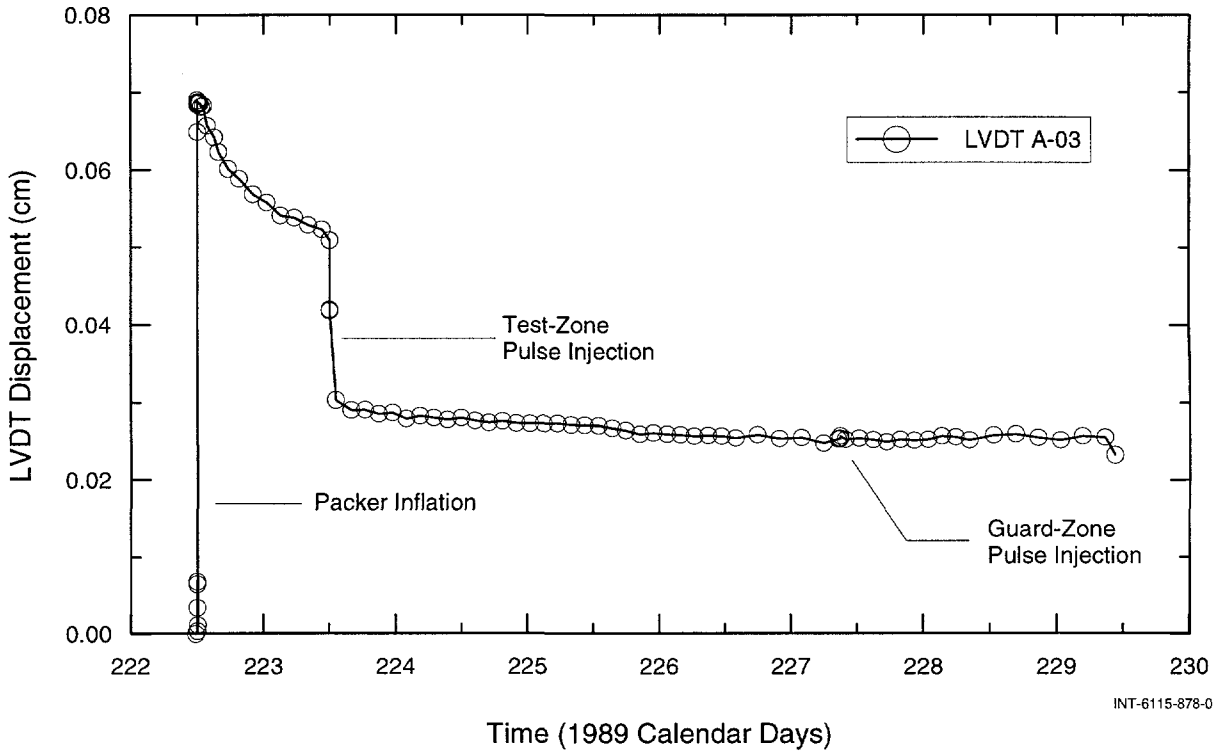

Figure 4-5. Axial-LVDT data for compliance test COMP 16, multipacker test tool #5.

test-zone and guard-zone packers; Figure 4-3 shows the fluid temperatures in the test and guard zones; Figure 4-4 shows the relative movement of the radial LVDTs; and Figure 4-5 shows the relative movement of the axial LVDT. Positive displacement in Figures 4-4 and 4-5 indicates that the LVDTs are being compressed.

During the compliance test depicted in Figures 4-1 to 4-5, the pressure in the test zone was increased from approximately 0 MPa to 7 MPa on Day 223 by injecting a small quantity of brine. The peak pressure quickly dissipated to about 4 MPa and then slowly decreased due to compliance effects, such as packer readjustment as stresses were redistributed through the entire test-tool string and axial test-tool movement. Figure 4-1 also shows that the guard zone received a pulse injection on Day 227 when the pressure was increased from 0 MPa to 5 MPa. The guard-zone pressure displayed similar behavior to that of the test zone. The pulse injections into the test and guard zones caused pressure changes throughout the system. As the pressure in a zone is increased, the adjacent packer(s) is compressed, causing its internal pressure to increase. The packer(s) also deforms slightly away from the zone being pressurized, which causes the pressure in the adjacent zone to rise slightly. This pressure increase can in turn be transmitted to another packer.

Figure 4-3 shows the temperatures measured in the test and guard zones during compliance testing. Temperatures were stable throughout the testing period except for short-lived increases in the guard-zone temperature following the pulse injections.

Figures 4-4 and 4-5 show the LVDT responses during compliance tests. The radial LVDTs (Figure 4-4) show that the test chamber's diameter in the test zone increased by about 0.04 mm during the pulse injection. This increase is consistent with the predicted diameter increase calculated from the material properties of the test chamber. Note that because of the LVDTs' orientation (see Section 3.5), the actual increase in diameter must be estimated by averaging the responses of all three radial LVDTs. Figure 4-5 shows that the axial LVDT was compressed (shortened) when the test-zone packer was inflated, but tended to lengthen as the test-zone-packer pressure declined. This response is probably due to some viscoelastic response of the packer element. During the pulse injection in the test zone, the axial LVDT lengthened as the increase in test-zone pressure forced the test tool upward in the compliance-testing chamber. The guard-zone pulse injection did not have the same effect on the axial LVDT response. Chace et al. (1998) present complete plots and tabulated data for the compliance tests performed before the hydraulic tests analyzed in this report.

4.2 Hydraulic Testing

A hydraulic-testing sequence began with the drilling of a nominal 10.2-cm (4-inch) diameter borehole. Downward-drilled boreholes were filled with brine shortly after drilling was completed. Upward-drilled boreholes were filled, after a test tool was installed and the packers were inflated, by injecting brine through an injection line until brine discharged from a vent line located at the top of the isolated interval. The brine used was collected from boreholes in the WIPP underground facility and, therefore, should already have been in chemical equilibrium with the Salado strata (Deal et al., 1991a). A test tool was installed in each test borehole as soon after drilling as possible to minimize pretest borehole history under non-shut-in conditions. The packers were sequentially inflated to approximately 11

MPa, starting with the lower-most packer. The packers were inflated with fresh water using a positive-displacement pressure-intensifier pump. The packer-inflation pressures were monitored closely for 24 to 48 hours after inflation. If compliance-related reductions in the packer-inflation pressures of greater than 3 MPa were observed, the packer-inflation pressures were increased to 11 MPa and observed for an additional 24 hours. After the initial transient decreases in packer pressures occurred and the packer-inflation pressures approached relative stability, valves on the test- and guard-zone vent lines were closed to shut in the test and guard zones. Once the test and guard zones were shut in, the pressures in the two zones increased as they equilibrated with the formation pore pressure in the vicinity of the borehole. After the rate of pressure increase in the test zone decreased and the pressure-recovery curve appeared to be on an asymptotic trend (Figure 4-6), hydraulic testing began.

4.2.1 Pressure-Pulse Testing

Pressure-pulse testing as described by Bredehoeft and Papadopulos (1980) was usually the first type of hydraulic test performed in a test interval. Pulse-withdrawal rather than pulse-injection tests were generally chosen for the Salado permeability testing because: they do not force fluids into the formation that may not be in complete chemical equilibrium with the rock; they do not overpressurize the formation, a process that could potentially open existing fractures or create new fractures by hydrofracture; and they more closely represent the hydraulic conditions expected shortly after closure of the WIPP underground facility when brine may be flowing from the host rock towards the relatively underpressurized rooms.

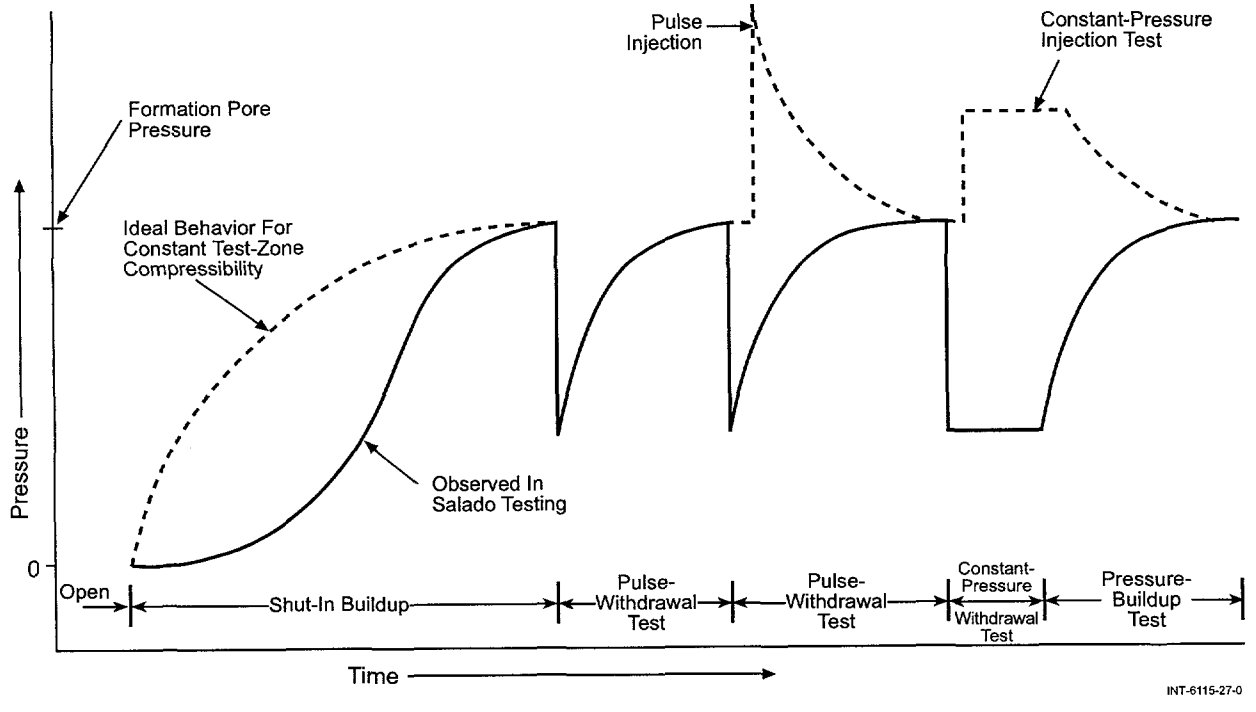

Figure 4-6. Typical permeability-testing sequence.

Pulse-withdrawal tests were initiated in a test or guard zone by opening the zone's vent valve and allowing fluid to flow from the zone until the desired fraction of the shut-in pressure had dissipated. After the desired pressure decrease had been achieved, the valve was then closed to shut in the zone. The volume of fluid released from the vent line during each pulse withdrawal was measured and recorded. Following the pulse withdrawal, the reequilibration of the zone's pressure and the formation pore pressure was monitored with the DAS. After the zone's pressure had recovered to approximately its pre-pulse value, the test was sometimes repeated (Figure 4-6) to provide assurance that the observed pressure responses were reproducible and were representative of formation responses.

4.2.2 Constant-Pressure Flow Testing

Constant-pressure flow tests were performed after pressure recovery from a pressure-pulse test was complete and the fluid pressure in the zone to be tested was relatively constant. The test zone was opened to one of the columns on the DPT panel (Section 3.6) that was pressurized to the constant pressure at which the test was to be conducted. The flow tests discussed in this report include both injection and withdrawal tests, and were conducted at constant pressures between 0.43 and 3.93 MPa above/below the pretest zone pressures. As a constant-pressure flow test proceeded, the change in fluid volume in the column was measured by the DPT. The test was terminated by shutting in the test zone after adequate flow data had been collected for analysis.

4.2.3 Pressure-Buildup/Falloff Testing

Pressure-buildup/falloff testing consisted of monitoring the pressure recovery after terminating a constant-pressure flow test and shutting in the test zone. A pressure-buildup/falloff test should generally last longer than the preceding flow test to provide adequate data for analysis. In low-permeability systems, buildup/falloff periods between two and ten times as long as the preceding flow periods are often required, and are always preferred.

THIS PAGE INTENTIONALLY LEFT BLANK

5. TEST LOCATIONS AND BOREHOLES

Figure 5-1 shows the locations of all of the boreholes drilled to date for the underground hydraulic-testing program. Boreholes were drilled in the experimental area, the operations area, and the waste-storage area. Borehole locations were chosen to provide access to different Salado Formation lithologies (Figure 2-3), to investigate whether or not the ages of excavations affect permeability in similar stratigraphic intervals, and to provide a representative distribution of data from a wide area of the underground facility. The tests discussed in this report were performed in boreholes L4P51, L4P52, and S1P74.

In some instances, holes were deepened and additional testing was performed after testing of the initial borehole configuration had been completed. In such a case, the first testing sequence performed in a borehole was given an "A" suffix, as in L4P51-A, and subsequent testing sequences were given "B", "C", etc. suffixes, as in L4P51-B and L4P51-C.

In two instances, additional testing was performed in a previously tested section of a borehole using a new test-tool configuration. The initial double-packer test tool used for testing sequence L4P51-C was replaced with a triple-packer test tool for additional testing of the halite directly above MB140. The initial triple-packer test tool used for testing sequence L4P51-D was replaced with a single-packer test tool for additional testing of the argillaceous halite at the bottom of the borehole. In these cases, a number was added to the existing suffix to indicate the sequence of the configurations, e.g., L4P51-C1 and L4P51-C2.

All of the boreholes were cored and/or drilled to a nominal 4-inch (10.2-cm) diameter. The boreholes were cored, when possible, to allow sample recovery. Compressed air was used as the circulation medium during the drilling of boreholes S1P74 and L4P52 while brine saturated with respect to sodium chloride was used as the drilling fluid when borehole L4P51 was deepened for testing sequences L4P51-C and L4P51-D. To provide an anchoring assembly for a test tool, a 5-inch (12.7-cm) I.D., 20-inch (51-cm) long, steel borehole collar was grouted to the formation in the top of each of the holes. The test tools were then bolted to the collars as described in Section 3.1 to reduce test-tool movement in response to packer inflation and pressure buildup in the guard and test zones.

Core samples were recovered from 98 percent of the drilled lengths of the test boreholes. The lithologies, fracturing, penetration times, and fluid occurrences noted in each borehole were recorded on core sample logs presented by Chace et al. (1998). The lithologies are referenced to the standard WIPP map units listed in Appendix B.

Descriptions of the drilling locations and individual boreholes are presented below. A summary of the configuration information for each test is presented in Table 5-1.

5.1 Room L4

Room L4 was excavated in February 1989 (Westinghouse, 1990) to nominal dimensions of 10.1 m wide, 3.7 m high, and 59.7 m long. After the L4P51-A and B testing sequences reported in Beauheim et al. (1991, 1993a) were completed, borehole L4P51 was deepened from 1 to 15 April 1992 (Calendar Days 92 to 106) to 22.35 m below the floor of Room L4. The deepening allowed testing of MB140 and the halite unit (H-m2) directly above MB140 during test sequence L4P51-C1.

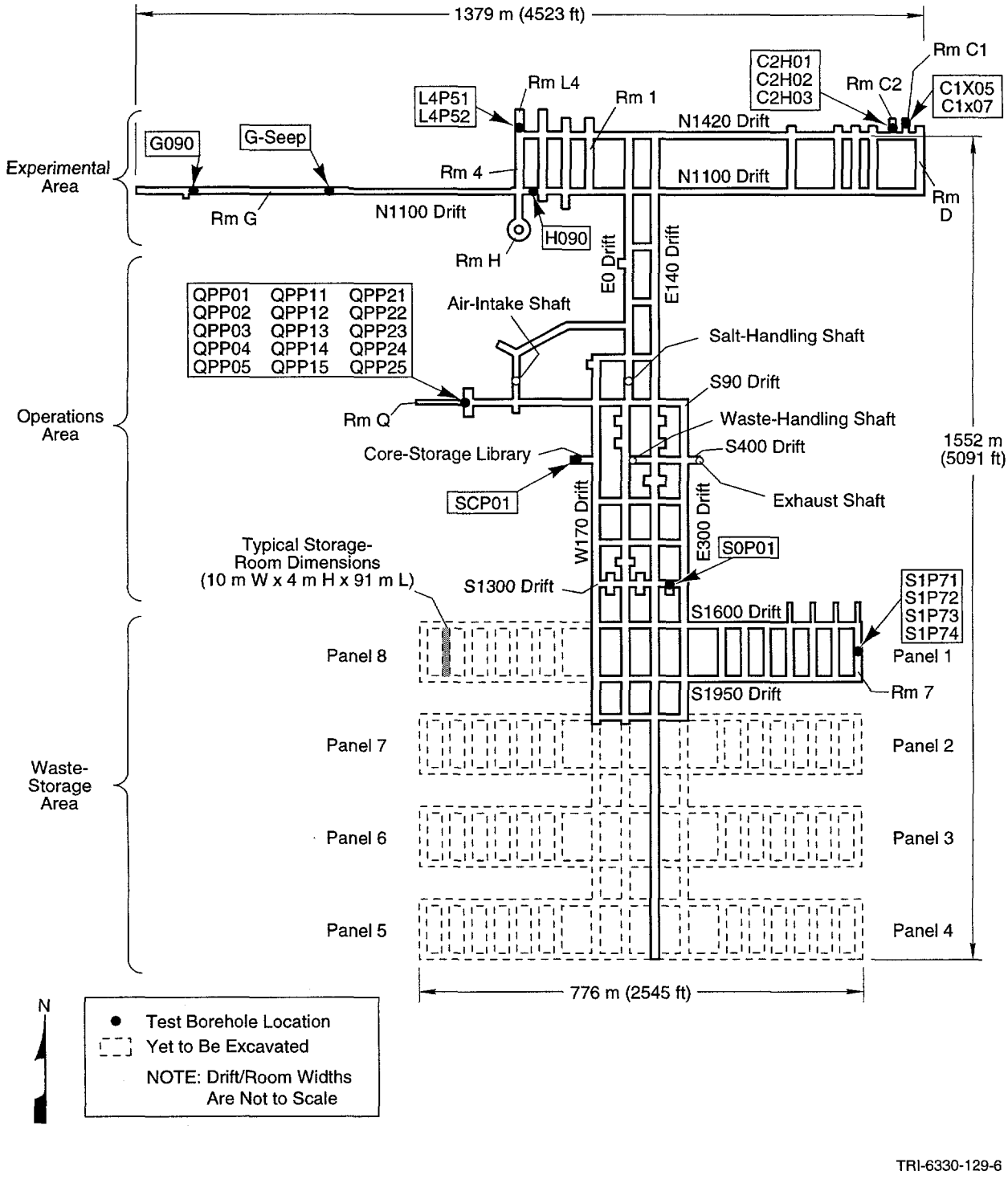

Figure 5-1. Map of the WIPP underground facility showing test locations.

Table 5-1. Summary of Test-Configuration Information

Hole	Orientation	Radius (cm)	Zone	Fluid Volume (cm^3)	Isolated Interval (m)	Map Units Tested
L4P51-C1	vertical down	5.560	guard	3967	15.56-16.60	H-m2
	vertical down	5.165	test	8784	17.43-22.20	H-m2, MB140, AH-m1, H-m3
L4P51-C2	vertical down	5.560	test 2	3967	15.55-16.59	H-m2
L4P52-B	upward 40° from vertical	5.075	guard	2128	10.83-11.88	AH-1, H-5, AH-2
	upward 40° from vertical	5.075	test	3134	12.71-14.12	AH-2, MB138, H-6
S1P74-A	upward 40° from vertical	5.174	guard	2135	4.38-5.40	7 (halite), 8 (anhydrite "b"), 9 (halite)
	upward 40° from vertical	5.174	test	3785	6.26-7.69	9 (halite), 10 (halite), 11 (anhydrite "a", clay H), 12 (polyhalitic halite)
S1P74-B	upward 40° from vertical	5.174	guard	2130	11.33-12.36	14 (halite), 15 (halite)
	upward 40° from vertical	5.174	test 2	2542	13.08-14.25	AH-1, H-5, AH-2
	upward 40° from vertical	5.174	test 1	8722	15.08-16.88	AH-2, clay K, MB138, H-6

H-m2 was encountered from 15.59 to 17.80 m, and MB140 was encountered from 17.80 to 21.97 m deep (Figure 5-2). The double-packer test tool used during test sequence L4P51-C1 was replaced with a triple-packer test tool on 17 November 1993 (Calendar Day 321) to allow further testing of H-m2 during test sequence L4P51-C2 (Figure 5-2).

Borehole L4P51 was again deepened on 20 to 22 September 1994 (Calendar Days 263 to 265) to 30.45 m below the floor of Room L4 to allow testing of an argillaceous halite unit (AH-m5) at a location where stress relief caused by the excavation was hoped to be insignificant. AH-m5 was encountered from 29.64 to 30.30 m deep (Figure 5-2). A triple-packer test tool was originally installed for this test sequence, designated L4P51-D1. Repeated problems with that tool led to its replacement with a single-packer test tool on 6 April 1995 (Calendar Day 96) to allow further testing of AH-m5 during test sequence L4P51-D2 (Figure 5-2).

Borehole L4P52 was drilled into the upper part of the west rib of Room L4 at an upward angle 40° from vertical on 1 and 2 April 1991 (Calendar Days 91 and 92) to a distance of 5.56 m. After the L4P52-A testing sequence reported in Beauheim et al. (1993a) was completed, the hole was deepened on 10 to 14 December 1992 (Calendar Days 345 to 349) to a distance of 14.18 m. The deepening allowed testing of MB138 during test sequence L4P52-B. MB138 was encountered from 13.89 to 14.02 m (Figure 5-2).

5.2 Room 7 of Waste Panel 1

Room 7 of Waste Panel 1 was excavated in March 1988 to nominal dimensions of 10.1 m wide, 4.1 m high, and 91.4 m long (Westinghouse, 1989). Borehole S1P74 was drilled on 27 to 29 July 1992 (Calendar Days 209 to 211). The hole was drilled into the upper part of the east rib of Room 7 at an upward angle 40° from vertical to a distance of 7.67 m. The borehole was drilled to allow testing of anhydrites "a" and "b" during test sequence S1P74-A. Anhydrite "b" was encountered from 4.56 to 4.64 m along the hole and anhydrite "a" was encountered from 7.15 to 7.41 m (Figure 5-3).

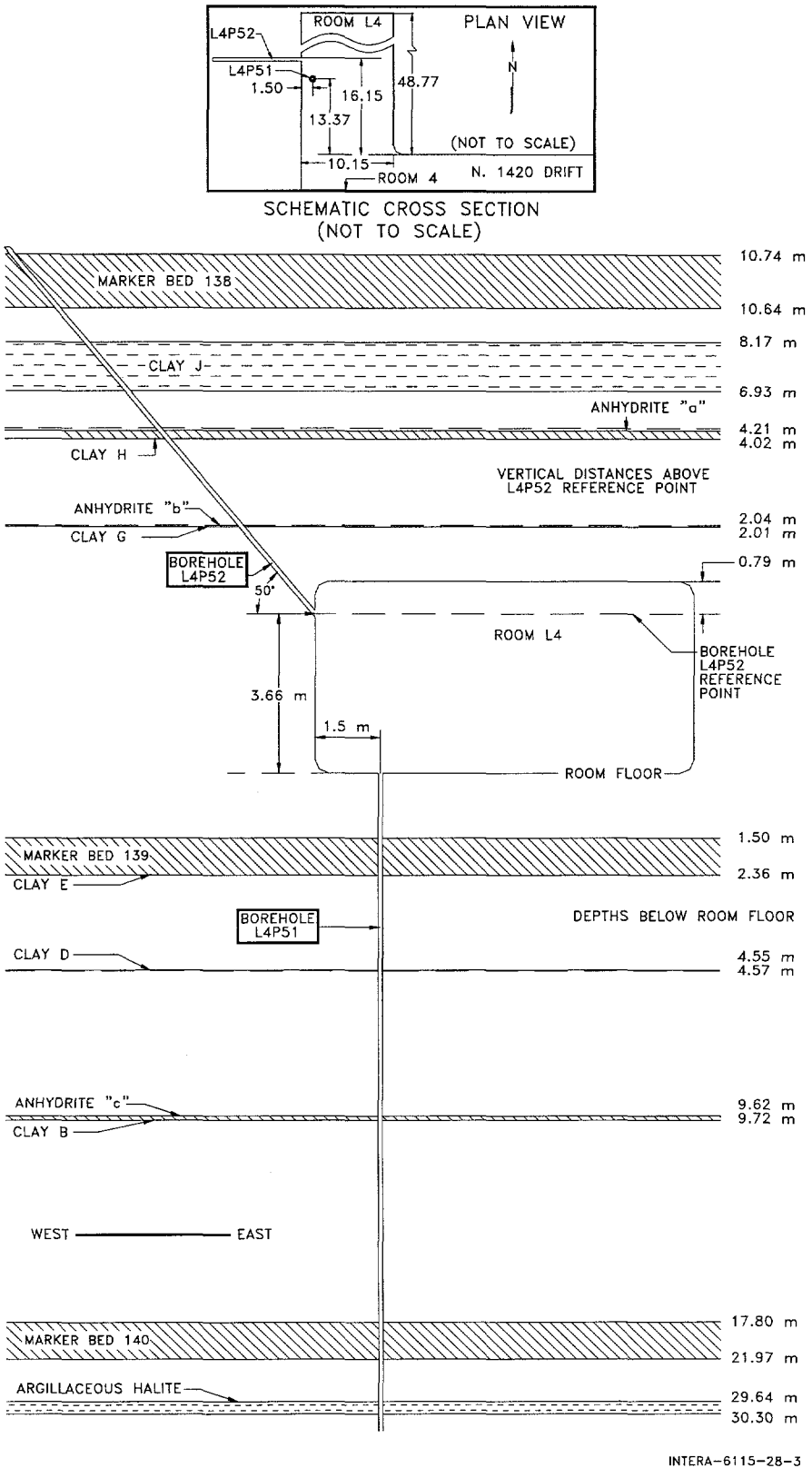

Figure 5-2. Schematic illustration of boreholes L4P51 and L4P52 in Room L4.

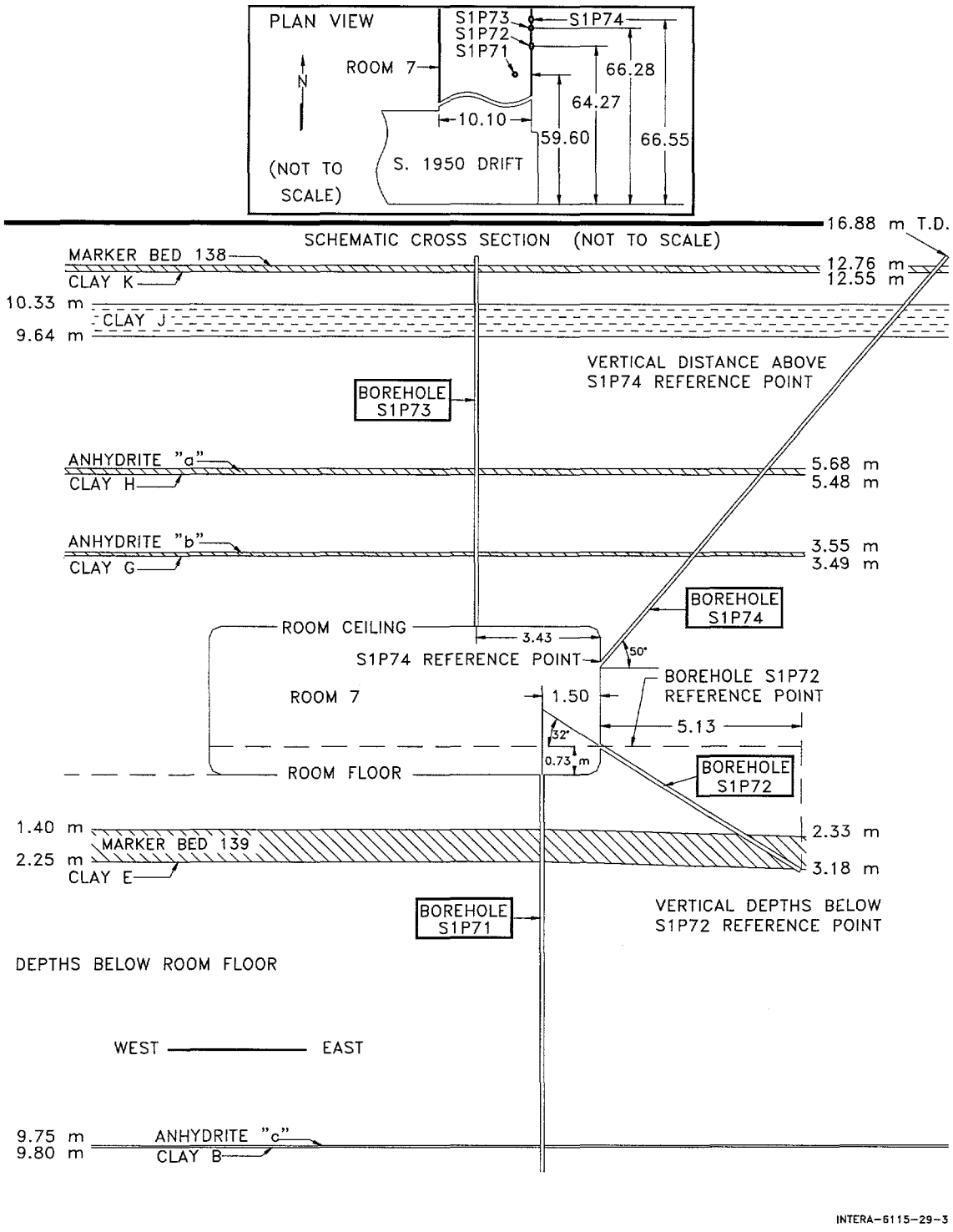

Figure 5-3. Schematic illustration of boreholes S1P71, S1P72, S1P73, and S1P74 in Room 7 of Waste Panel 1.

S1P74 was deepened on 26 to 31 January 1995 (Calendar Days 26 to 31) to a distance of 16.88 m. This allowed testing of clay J and MB138 during testing sequence S1P74-B. Clay J was encountered from 12.58 to 13.49 m along the hole and MB138 was encountered from 16.38 to 16.66 m (Figure 5-3).

6. INTERPRETATION METHODOLOGY AND OBJECTIVES

Interpretation of hydraulic tests is essentially an inverse problem. During a hydraulic test, one or more known stresses are applied to the system being studied, and the responses of the system are measured. Interpretation of the test consists of inferring the hydraulic properties and geometry of the system from its measured responses. Typically, a unique set of hydraulic properties cannot be inferred from a single test. As noted by Gringarten et al. (1979), however, increasing the number and types of stresses applied to a system provides an increase in information gained from the measured responses. By solving the inverse problem simultaneously or iteratively for a variety of different testing conditions, the number of viable alternative solutions can be greatly reduced for any specified system geometry. The problem becomes more complicated, however, when the system geometry cannot be specified with any reasonable certainty.

The three types of tests discussed in this report are amenable to interpretation using different techniques, providing the opportunity for cross-checking and cross-validation among results. Both analytical and numerical methods can be used. Discussions about the application of the analytical solutions and about the numerical techniques used to interpret the tests discussed in this report are presented below in Sections 6.1 and 6.2. The objectives of the different types of interpretations are also presented. Section 6.3 summarizes the major assumptions underlying the test interpretations. Section 6.4 discusses the values of material properties and experimental parameters needed as input in the test interpretations and how those values were determined.

6.1 Analytical Methods for Pressure-Buildup/Falloff Tests

Many authors in the fields of groundwater hydrology and petroleum reservoir engineering have studied the buildup of pressure in a well following a constant-rate flow period. The early studies of Theis (1935), Cooper and Jacob (1946), and Horner (1951) consider only the behavior of a well acting as a line source, with no wellbore storage or skin. Gringarten et al. (1979) included wellbore storage and skin in their analytical solution. Although the solution of Gringarten et al. (1979) was developed for the drawdown response of a well producing at a constant rate, it can be extended to analysis of the pressure buildup following a constant-pressure (multi-rate) flow test. This is done by subdividing the constant-pressure flow period into a number of shorter periods having constant, but different, rates and using linear superposition to combine the effects of all of the flow periods. This approach was verified theoretically by Ehlig-Economides (1979).

Bourdet et al. (1989) added pressure-derivative type curves to the analytical procedure of Gringarten et al. (1979). The derivative of pressure change with respect to the natural logarithm of elapsed time is a powerful tool used to diagnose well and formation conditions. On a log-log graph, pressure-derivative type curves begin with an initial segment with unit slope corresponding to early-time wellbore storage and skin effects (Figure 6-1). This segment reaches a maximum that is proportional to the amount of wellbore storage and skin, and then the curve declines and stabilizes at a constant value corresponding to late-time, infinite-acting, radial-flow effects. A minimum in the derivative at intermediate time indicates double-porosity

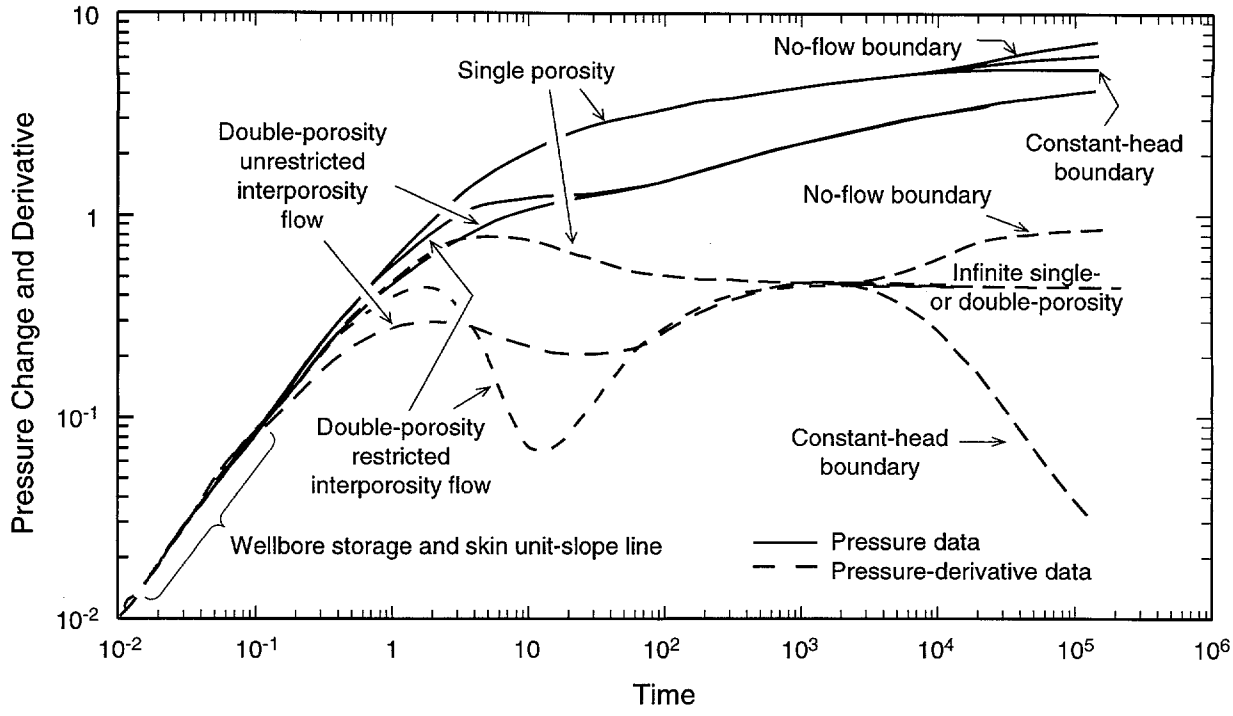

Figure 6-1. Effects of different conditions on pressure and pressure-derivative log-log plots.

(fracture + matrix) conditions, and deviations from a constant (horizontal) derivative at late time indicate the existence of hydraulic boundaries and/or non-radial flow.

Pressure-derivative data are typically plotted on a log-log graph to verify that the test has reached the infinite-acting, radial-flow period. The transmissivity (permeability-thickness product) can then be calculated from the following equation:

$$T = \frac{q\rho g}{4\pi m} \qquad (6\text{-}1)$$

where: T = transmissivity, L^2/T
q = flow rate (immediately prior to current rate for a multi-rate test), L^3/T
ρ = fluid density, M/L^3
g = gravitational acceleration, L/T^2
m = stabilized pressure-derivative value, M/LT^2

The wellbore-storage coefficient (C) can be calculated by first plotting pressure change (dP) versus elapsed time (dt) on a linear-linear graph and determining the slope (dP/dt) of the early-time data, i.e., the data that have a unit slope on a log-log graph. The wellbore-storage coefficient can then be calculated from the following equation:

$$C = \frac{q}{\frac{dP}{dt}} \qquad (6\text{-}2)$$

The interpretation of each pressure-buildup test had four principal objectives. First, we wanted to determine the transmissivity of the tested interval. Second, we wanted an estimate of the wellbore-storage coefficient to compare to the test-zone compressibility measurements made during pulse tests.

Third, we wanted to define the stabilized pore pressure in the tested stratum at the time of testing. Fourth, we wanted information on whether the tested stratum behaved hydraulically as infinite (on the scale of testing) or bounded, fully confined or leaky, and as a single-porosity medium or a double-porosity medium.

Estimation of transmissivity from pressure-buildup tests is independent of test-zone compressibility. Instead of needing a value of test-zone compressibility as model input, analysis of pressure-buildup tests provides an estimate of the wellbore-storage coefficient (the product of the test-zone compressibility and the shut-in test-zone volume) as described above. Stabilized pore pressure is readily determined by extrapolating the late-time pressure trend on a Horner (1951) plot to infinite recovery time. Information on the nature of the system tested comes from the pressure-derivative data.

6.2 Numerical Methods

A major limitation encountered when interpreting hydraulic tests with analytical solutions is that actual pretest conditions do not entirely match the idealized boundary conditions and initial conditions that underlie the analytical solutions. For this reason, a numerical model capable of dealing with complex pretest borehole history and variable boundary conditions was also used to interpret the Salado hydraulic tests. The general methods used by the numerical model chosen, GTFM 6.0 (Graph Theoretic Field Model), are described below in Section 6.2.1. Sections 6.2.2 and 6.2.3 describe flow-dimension and uncertainty analyses, respectively, and their implementation in GTFM 6.0. Section 6.2.4 discusses special concerns about the estimation of values for specific storage from single-hole tests.

6.2.1 GTFM 6.0

GTFM 6.0 simulates the hydraulic response of a single-phase, one-dimensional, radial/nonradial-flow regime to boundary conditions applied at a borehole located at the center of the modeled flow system. The problem domain is discretized by dividing the flow system into a series of concentric rings centered on the borehole, with each ring represented by a node. A constant multiplicative factor is used to increase the spacing between nodes with increasing distance from the origin (borehole). The model can simulate transient flow and pressure responses in a formation that has a varying thickness but assumes vertically homogeneous hydraulic properties. Formations may have single or double porosity, and may include radially centered heterogeneities (hydraulic conductivity (K) and/or specific storage (S_s) varying with radial distance) to simulate the presence of a "skin" zone adjacent to the borehole or more complex composite systems. K and S_s may also vary as a function of the calculated pressure at each node to simulate the effect of fractures opening/closing as a function of pressure.

GTFM can be used with assigned conditions of either fixed pressure or zero flow at the external boundary of the model. For all of the analyses in this report, a fixed-pressure boundary condition was specified at a distance from the borehole such that the type of boundary had no effect on the calculated pressure response in the borehole. In cases where boundary/nonradial-flow effects were indicated by the test data, the effects were simulated by varying the cross-sectional areas of the nodes at various distances. The parameter that determines the cross-sectional area at a given radius from the borehole is the flow dimension (n). This approach to simulating boundary/nonradial-flow effects

has been implemented for several reasons discussed in Section 6.2.2.

The model has wellbore (inner) boundary conditions that can be used to simulate pulse-injection/withdrawal tests, specified borehole-pressure conditions, specified formation flow rates, and slug-injection/withdrawal tests. The cumulative effects of consecutive tests are incorporated in the simulations. The model can also incorporate test-zone pressure changes resulting from temperature variations in the test zone as well as from test-equipment and/or formation-induced changes in the test-zone volume. The model output consists of simulated pressure responses in the borehole and at selected radial distances from the borehole. The model can also calculate formation flow rates and cumulative production based on the formation's estimated hydraulic properties.

The primary input parameters to GTFM include the formation's hydraulic properties (hydraulic conductivity, pore pressure, and specific storage or its constituent parameters), fluid properties (density, compressibility, and thermal-expansion coefficient), test-zone parameters (radius, length, contained fluid volume, and compressibility), flow dimension (geometry), and, if used, skin properties (radial thickness, hydraulic conductivity, and specific storage). Fitting parameters typically include the formation's hydraulic properties, and can also include (as determined by the conceptual model and available constraints) skin properties, flow dimension, and test-zone compressibility. All other parameters (non-fitting) are initially fixed at the best estimate of their true (but imperfectly known) values. The non-fitting parameters are sampled at a later stage of the analysis process to perform uncertainty analysis. Sampling of non-fitting parameters for uncertainty analysis is discussed in Section 6.2.3.7.

For the interpretations presented in this report, the individual testing periods were subdivided into discrete time intervals, called sequences. Sequences are differentiated by the wellbore boundary conditions in effect during those time periods. Sequences during which borehole pressures are prescribed in the model are referred to as history sequences. History sequences were used to represent: (1) the pressure in a test zone (often zero, or atmospheric) during the period between drilling and initial shut-in of the test zone; (2) time periods when external factors, such as changes in packer pressures, affected the observed test-zone pressures; and (3) test-zone pressures during constant-pressure flow tests. The pressures specified for history sequences are taken directly from the DAS records. Model output during history sequences consists of flow rates between the test zone and the surrounding formation and transient formation pore pressures. Sequences during which a test zone is shut in and pressures in the test zone and the surrounding formation are equilibrating are referred to as pulse sequences. Pulse sequences were used to represent: (1) periods immediately after test zones were shut in for the first time; (2) pressure-recovery periods following individual pulse injections and pulse withdrawals; and (3) pressure-buildup/falloff (recovery) periods following constant-pressure flow tests. Model output during pulse sequences consists of transient pressures in both the test zone and formation, as well as flow rates.

A description of the methodology, appropriate boundary conditions, and governing equations of GTFM can be found in Pickens et al. (1987). GTFM 6.0 has been fully verified as per Sandia QAP 19-1 Rev. 2.

6.2.2 Flow-Dimension Analysis

Estimating hydraulic parameters from test data is a multi-step process. The first step of the analysis process is to choose an appropriate conceptual model. Test data are utilized in this step by plotting them in specialized diagnostic formats that, by the shapes they reveal, suggest possible conceptual models. In the absence of complicating factors (temperature, compliance, etc.) and after the effects of wellbore storage are over, the shapes shown by these diagnostic plots depend on the geometry (n) of the flow system and the hydraulic parameters K and S_s. While the shape shown by a diagnostic plot is the result of some unique but unknown combination of these properties, the possible combinations of geometry and hydraulic properties that result in a given shape are non-unique.

The default assumption for most modeling approaches is that flow is radial (cylindrical geometry). However, the stress conditions and geology around the WIPP repository can result in flow geometries that are relatively complex and nonradial. Cores and video logs indicate that many of the tested intervals in the Salado Formation are fractured. Current and previous (Beauheim et al., 1993b) tests have suggested that some fracture apertures are pressure-dependent. Flow pathways in fractured units can be affected by proximity to the repository (changing stress with distance) and hydraulic testing (pressure-induced aperture changes). The flow geometry in some of the Salado tests should, therefore, be considered unknown. The resulting uniqueness problem (K, S_s, n) has been addressed in this report by expanding a methodology developed to deal with the flow-geometry issue in tests performed as part of the Swedish radioactive waste management/repository program (Barker, 1988).

6.2.2.1 Description

Well-test analysis methods have been developed primarily to investigate and characterize flow within idealized radial flow systems, i.e., flow within a homogeneous, isotropic, constant-thickness porous medium. Deviations from infinite radial flow are most commonly simulated using various configurations of image wells, a method adapted from heat-flow theory (Ferris et al., 1962). This method of simulating flow in more complex systems can be useful in some geological settings, but its application is often limited for the following reasons: 1) it assumes that flow always begins as radial and 2) it only works with transient pressure data, i.e., it cannot be applied to transient flow-rate data from a constant-pressure test.

Notable attempts to expand well-testing methodologies to characterize nonradial flow can be found in Black et al. (1986), Barker (1988), Noy et al. (1988), and Doe (1991), where the concept of a flow dimension (n) is introduced. Barker (1988) discussed flow systems with constant hydraulic properties (K and S_s) where the flow dimension of the system was related to the power by which the flow area changed with distance from the source and n described the geometry of the system. The flow area in this formulation is given by:

$$\text{Area}(r) = b^{3-n}\frac{2\pi^{\frac{n}{2}}}{\Gamma\left(\frac{n}{2}\right)}r^{n-1} \qquad (6\text{-}3)$$

where:
- n = flow dimension
- b = extent of the flow zone, L
- Γ = gamma function
- r = radial distance from borehole, L

The flow dimension n is related to the power-law relationship between flow area and radial distance from the borehole. The flow dimen-

sion is defined as the power of variation plus one. For example, the relationship between flow area and distance in a standard radial system is given by:

$$\text{Area}(r) = 2\pi rb \qquad (6\text{-}4)$$

The flow area is seen to vary linearly with distance (r^1), making the flow dimension, by definition, two. All of the diagnostic methods used to deduce radial flow, i.e., the shapes of various type curves, depend only on the relationship between flow area and distance (r). The shapes of the type curves are independent of the constant $2\pi b$.

Doe (1991) noted that identical hydraulic responses could be produced in both a homogeneous system with varying flow area ($n(r)$) and in a constant flow-area system with varying hydraulic properties ($K(r)$ and $S_s(r)$). This noted non-uniqueness means that, for any analysis in which K, S_s, and n are simultaneously treated as potentially spatially varying fitting parameters, an infinite number of hydraulic-parameter/flow-dimension combinations can be used to match any measured single-well hydraulic response.

The potential for an infinite number of solutions is simply a reflection of the lack of constraints, i.e., single-well hydraulic tests alone do not provide enough information about the flow system to constrain $K(r)$, $S_s(r)$, and $n(r)$ simultaneously. This problem can be addressed in two ways: the analyst can either obtain more information about the flow system or make assumptions about the flow system, being careful to understand the consequences of the assumptions. The following paragraphs discuss problems inherent in the well-test-analysis process for flow systems of increasing complexity.

In simple geologic systems, n is often known with reasonable certainty. If n is known, the corresponding estimates of K and S_s are relatively unique, i.e., the inverse problem is well-posed mathematically. Obtaining information about the flow geometry in complex fractured systems, however, is more problematic and n is often treated as a fitting parameter along with K and S_s. When the inverse problem is posed in this manner, i.e., K, S_s, and n are all fitting parameters, a reasonable but arbitrary approach is to assume that K and S_s are constant and only n can vary with distance, if necessary, to improve the fit to the data. This is the approach that was used for the analyses presented in this report. Again, this is a well-posed problem. The fitting parameters K, S_s, and $n(r)$ can usually be estimated with acceptable uncertainty. This small uncertainty does not guarantee that the estimated parameter values are correct. It simply means that the assumptions incorporated into the analysis (constant K and S_s) greatly reduce the possible number of solutions.

The situation is very different, as noted above, if one allows for the possibility that K and S_s can also vary with distance ($K(r)$ and $S_s(r)$). Consider a hypothetical example where a hydraulic-test response has been perfectly matched using constant values of K, S_s, and n. A simple transform of the initial solution can be used to generate an infinite number of alternative "perfect matches" using different combinations of $K(r)$, $S_s(r)$, and $n(r)$. Standard practice, however, is to use the simplest model that both adequately reproduces the measured hydraulic response and is in agreement with all other available information. Given that independent knowledge of how K, S_s, and n vary in space is generally not available, the simplest model is almost always constant K and S_s and constant or spatially varying n.

The inherent non-uniqueness described above combined with the assumption of constant K and S_s means that all real but unknown spatial variations in K, S_s, and n are lumped together in these analyses in the estimated value of n. The resulting "geometry" described by n can, therefore, be the actual geometry of the flow conduits in three-dimensional space or it can reflect a combination of factors. In addition to variations in K and S_s, these factors can include leakage from adjacent layers and constant-pressure and no-flow boundaries, resulting in a wide possible range of estimated n values.

The use of variable flow dimensions to describe complex flow regimes has several advantages over more traditional approaches. It is not limited by the assumption that all flow is radial until a boundary is encountered at some distance. It is easily applied to complex flow geometries or variable properties or any combination of the two. It can be applied to transient flow-rate (constant-pressure) data as well as transient pressure data. Once a system is described in terms of $n(r)$, a simple transform can be applied to define multiple combinations of flow geometries and hydraulic properties that would produce the observed response. This makes investigating a wide variety of possible conceptual models easy. Finally, given that the actual combination of flow geometry and properties that produces an observed response is unknown (particularly in a complex geologic setting), describing the combined effects in terms of a single parameter seems appropriate.

Using the analysis approach described above, flow systems may obviously exhibit a wide variety of flow dimensions. Even when geometry alone is considered, the flow dimension of a fracture system would not be expected to somehow be restricted to the integer values representing linear, radial, or spherical flow (n = 1, 2, or 3). Nor should the failure of a single flow dimension to describe flow in a complex system adequately be cause for surprise. Variations in geometry alone can result in values of n less than zero and greater than three for short periods of time. The arbitrary assumption of constant K and S_s further means that estimated values of n will not necessarily correspond to values typically associated with physical flow geometry.

The parameter-estimation process is further complicated if K, S_s, and n vary temporally as a function of pressure, as they appear to do in some of the Salado permeability tests. A system response cannot be determined to be pressure-dependent from any single hydraulic test. Pressure-dependence can be deduced, however, from the response to a combination constant-pressure/pressure-recovery test. Assume, for example, that data from a constant-pressure withdrawal test indicate that K (or n) decreases with distance from the borehole. If the subsequent pressure-recovery data indicate that K (or n) increases with distance from the borehole, then the simplest way to reconcile these seemingly contradictory responses is to assume that K or n is varying primarily as a function of pressure -- decreasing as the pressure in the test zone decreases and likewise increasing as the test-zone pressure increases.

The hydraulic conductivity of a fracture is related to the fracture aperture. If the fracture aperture varies as a function of pressure during a testing sequence, then K will vary temporally as a function of pressure. Variations in the fracture aperture could also alter the flow pathways within the fracture, thereby changing the flow geometry. This means that both K and n (and S_s) could vary temporally as a function of pressure.

Flow dimension cannot be specified as a pressure-dependent parameter in GTFM. Even if this were possible, sufficient constraints are not available from the Salado permeability-testing program to differentiate quantitatively among pressure-dependent variations in K, S_s, and n. At a minimum, changes in fracture aperture as a function of pressure would have to be known to go beyond the level of analysis presented in this report.

Flow dimensions were utilized in several different ways to analyze the pressure-dependent Salado responses. In some analyses, K and S_s were assumed to be both spatially and temporally constant and all real but unknown spatial and temporal changes in K, S_s, and n were simulated as spatial variations in n. This allows various scenarios to be investigated once a match to the data is obtained, i.e., for any assumed geometry (variation in n), corresponding variations in K and S_s can be calculated even if they are not explicitly modeled as pressure-dependent. In other analyses, K was explicitly modeled as a pressure-dependent parameter and single values of n and S_s were estimated.

Neither approach has any particular advantage over the other. Pressure-dependent responses for which the flow geometry appeared to be relatively constant were well matched simply by estimating $K(P)$ along with constant S_s and n. In the case of other pressure-dependent responses, n seemed to be highly variable, so all real but unknown parameter variations (both spatial and temporal) were lumped as spatial variations in n. These responses could not be matched using $K(P)$, S_s, and n.

The obvious difficulty with the analysis method described above is intuiting the physical reality from the many possibilities alluded to by the variations in n. No simple means of achieving this exists. Additional information apart from hydraulic tests, such as pressure-dependence of hydraulic apertures and statistical information on the distribution and orientation of fractures, would be necessary to limit the possible solutions.

Two final items related to nonradial flow analysis need to be addressed. The first item is the use of the term "transmissivity" (T). Traditionally, T has been associated with flow systems of constant thickness (b) where T is defined as the product of K and b. T represents a meaningful concept in radial ($n = 2$) systems in which flow is confined between two parallel boundaries, but loses meaning for other dimensions of flow. Therefore, we do not present results in terms of T in this report, but in terms of K (or k), recognizing that these results represent average values over the characteristic unit dimension of the particular flow geometry.

The second item is the assumed initial flow area at the borehole. The actual flowing area at the borehole face is never known exactly. It is particularly problematic in fractured systems, where flow most likely occurs only in discrete fractures. This problem is usually addressed by specifying that the initial flow area is equal to the entire borehole surface area within the test zone or some smaller part of it, e.g., the surface area of the exposed anhydrite. The estimates of the fitting parameters are then understood to be the average values of those parameters over the arbitrarily specified flow area. This is the approach that has been implemented in this report. In contrast, the initial flow area as defined by Barker (1988) is a function of the flow dimension (Eq. 6-3). The initial flow area in this formulation is not a specified constant, but varies with the estimated value of n. In Barker's formulation, the value of n at the

borehole cannot be negative because the initial flow area would also be negative (undefined). This is not true with the GTFM implementation of flow dimension. As stated above, the initial flow area in GTFM is specified by the analyst -- it is not a function of the flow dimension. A negative value of n at the borehole, in this case, simply means that the specified initial flow area is decreasing at some rate corresponding to n. Again, as flow dimensions are implemented in GTFM, they specify the rate at which the initial flow area changes, but the initial flow area is independent of the flow dimension.

6.2.2.2 Diagnostic Plots

Diagnostic plots to aid in obtaining initial estimates of n (or $n(r)$) can be made for each type of hydraulic test discussed in this report (pulse, constant-pressure, and pressure-recovery). Each of these diagnostic plots utilizes straight-line portions of the data or data derivatives that develop when certain test conditions are met. The slope (m) of these straight-line portions is directly related to the flow dimension of the system. Simple data transforms permit calculation and plotting of the flow dimension(s). Note that while the transforms discussed below are applied to the entire test response, the flow dimension can be visually estimated only from the straight-line portion of the transformed response, although non-linear regression permits estimation of the flow dimension prior to the development of the straight-line response.

The process begins by applying the appropriate transform to transient pressure and/or flow-rate data, resulting in a plot of flow dimension as a function of time ($n(t)$). This geometry/time function ($n(t)$) can then be transformed to a geometry/distance function ($n(r)$) for input into GTFM as an initial estimate of the system geometry. The transform from time to distance is given by Lee (1982) as:

$$d = \left(\frac{4Kt}{S_s}\right)^{0.5} + r_w \qquad (6\text{-}5)$$

where: d = distance from wellbore, L
t = elapsed time, T
r_w = wellbore radius, L

The diagnostic plots for each type of test are presented below.

Pulse Tests

To begin, the pulse-test data are converted to a normalized response using the following transform:

$$P_{\text{norm}} = \frac{P_i - P_t}{P_i - P_0} \qquad (6\text{-}6)$$

where: P_{norm} = normalized pressure response
P_i = initial pressure before pulse began, M/LT^2
P_t = pressure at time t, M/LT^2
P_0 = pressure at time t_0, M/LT^2

A log-log plot of the normalized pulse response (Eq. 6-6) for $n = 1$, 2, and 3 is shown in Figure 6-2. The late-time data plot as a straight line with slope (m) related to the flow dimension (n) of the system by:

$$m = \frac{-n}{2} \qquad (6\text{-}7)$$

Given this relationship between m and n, the log-log derivative of the normalized response can be scaled such that it will stabilize at a constant value equal to the dimension of the system. Figure 6-3 shows the scaled derivatives for $n = 1$, 2, and 3.

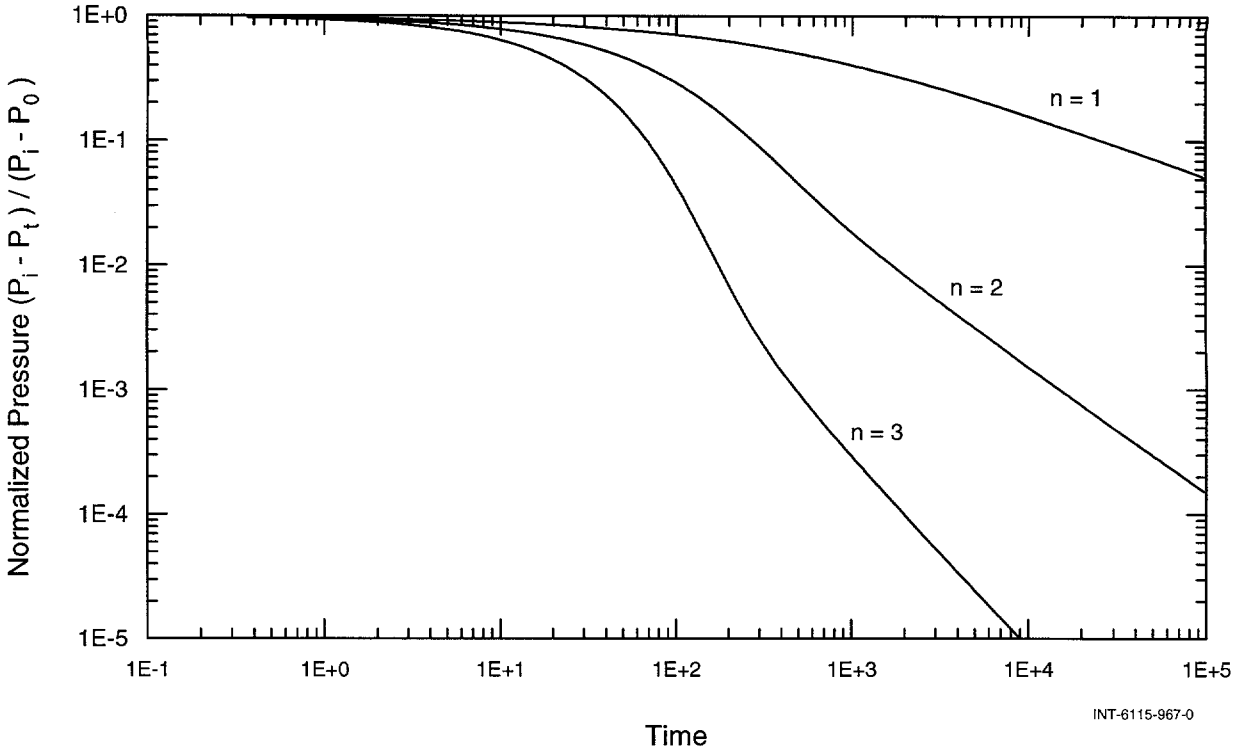

Figure 6-2. Log-log plot of normalized pulse responses for $n = 1$, 2, and 3.

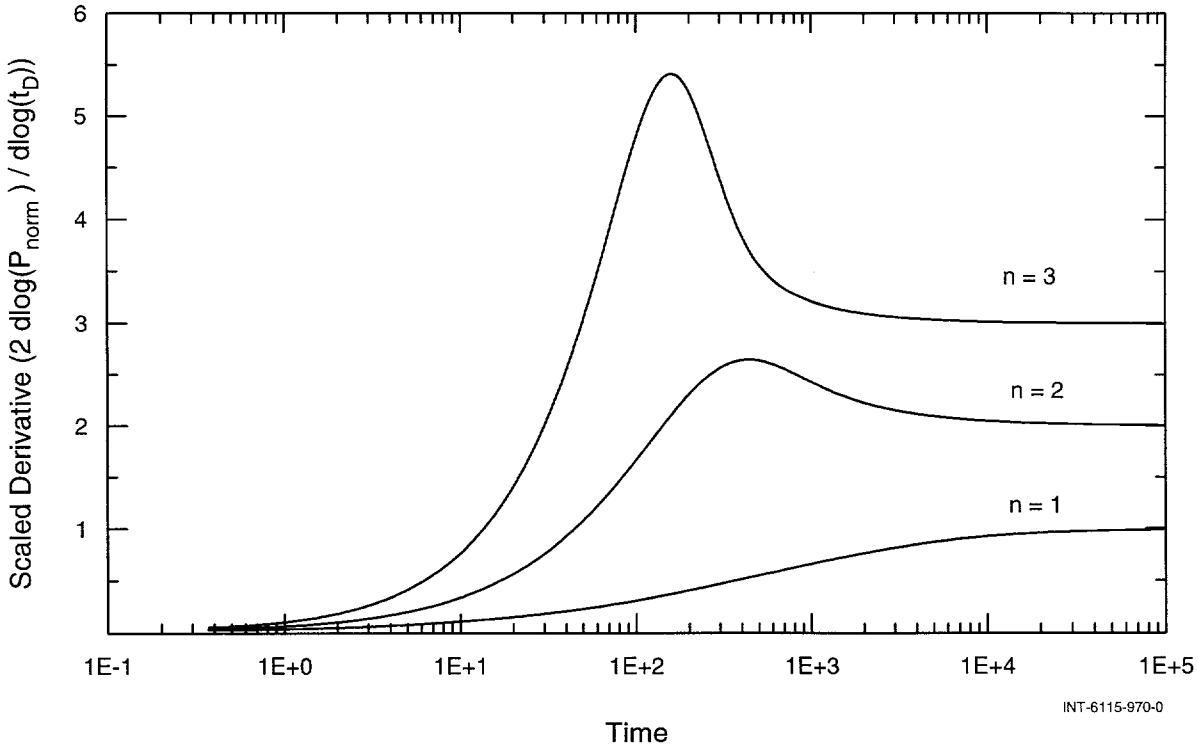

Figure 6-3. Semilog plot of scaled pulse-test pressure derivatives for $n = 1$, 2, and 3.

In practice, two aspects of this diagnostic technique limit its usefulness in low-permeability testing environments. First, the method is sensitive to pre-existing pressure transients in the system, i.e., the pressure around the borehole prior to the pulse tests must be fully stabilized for the flow dimension to be properly diagnosed. Figure 6-4 shows the diagnostic technique applied to a simulated pulse test in a radial system that was preceded by open-hole and shut-in periods typical of Salado testing sequences. Notice that the derivative does not stabilize at two (the input n value) before the pre-existing pressure transient causes a downward turn in the derivative.

The second problem in applying this technique is that the straight-line response develops only during the final 1% of the recovery. This means that pressure recovery must be complete (not always practical in low-permeability tests) and pressure resolution must be high.

Constant-Pressure Tests

Two types of flow-dimension diagnostic plots can be created using the flow-rate (q) data from constant pressure tests. In the first type, n can be calculated from the log-log derivative of the flow rate for all systems where $n < 2$. Figure 6-5 shows flow-rate data for various values of n. Flow-rate data for all $n < 2$ plot as a straight line on a log-log plot, with a unique slope for each value of n. Flow-rate data also plot as a straight line for all $n > 2$, but the slope is not unique, being zero for all $n > 2$. No straight line develops for $n = 2$. The relationship between the slope of the straight line and the flow dimension for all subradial systems is given by:

$$m = \frac{n}{2} - 1 \tag{6-8}$$

The log-log derivative of the flow rate in subradial systems can, therefore, be scaled such that it stabilizes at a constant value equal to the flow dimension of the system (Figure 6-6). For this type of diagnostic, the scaled derivative will stabilize at a value of two for all $n > 2$, and will never stabilize for $n = 2$ (Figure 6-6).

The second type of constant-pressure diagnostic plot displays a straight-line behavior for all values of n. The flow-rate data are plotted as $d(1/q)/d\log(t)$ versus dt (Geier et al., 1996) (Figure 6-7). The late-time data for all values of n will exhibit straight lines whose slopes are related to n by:

$$m = 1 - \frac{n}{2} \tag{6-9}$$

The flow dimension can be estimated from the slope of the straight line. If the data are relatively free of noise, the second derivative of $1/q$ can be calculated and the flow dimension plotted directly.

Pressure-Buildup/Falloff Tests

The derivatives of pressure-buildup/falloff data developed by Bourdet et al. (1989) display late-time straight lines with the slope/flow-dimension relationship given by Eq. 6-9 (Figure 6-8). The second derivative can, therefore, be scaled according to this relationship such that the late-time data will plot as a constant value equal to n (Figure 6-9).

6.2.2.3 Test Cases

The following test cases were designed to illustrate and investigate several aspects of the variable-flow-dimension approach. The

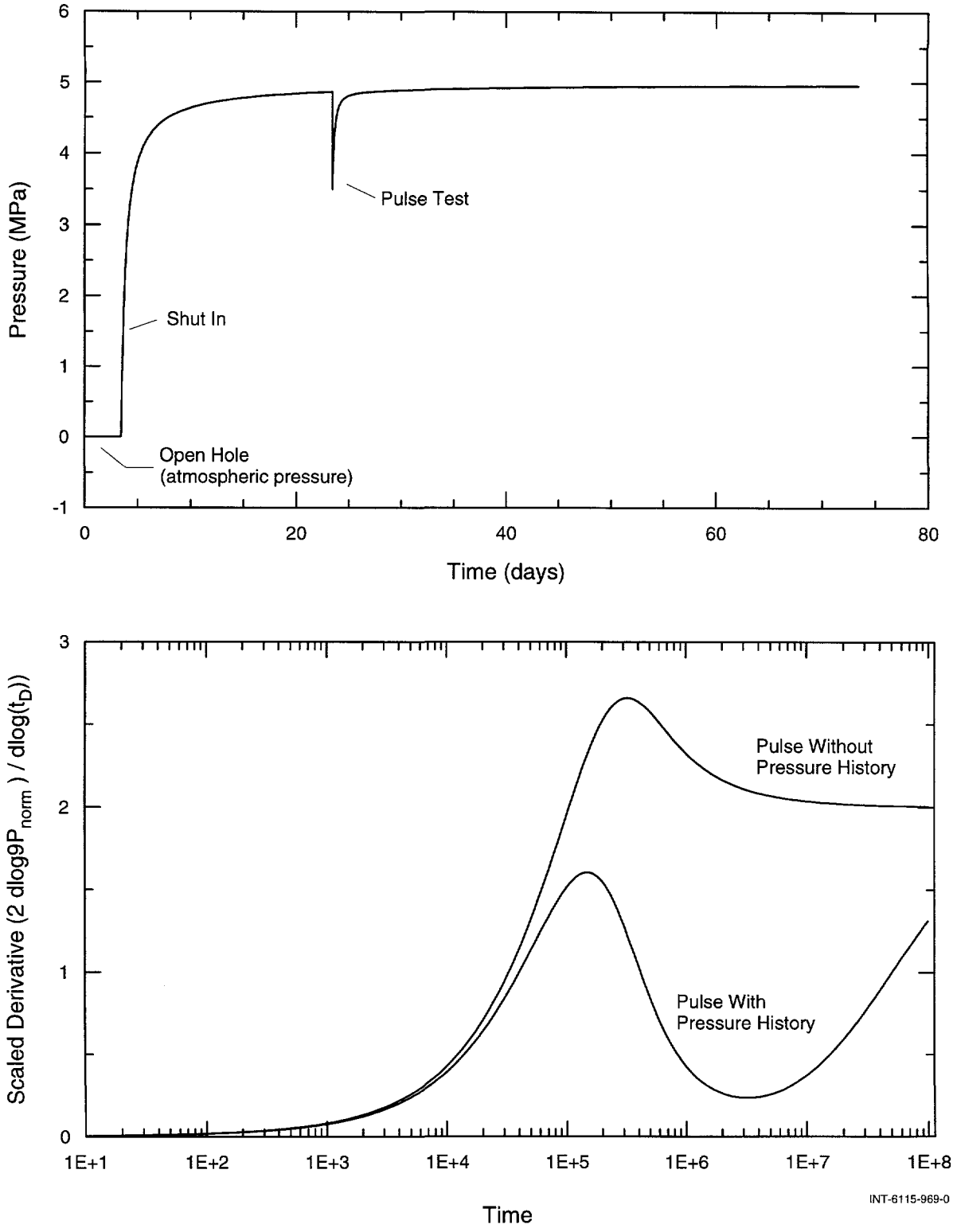

Figure 6-4. Simulated testing sequence showing the effect of pressure history on the pulse diagnostic plot.

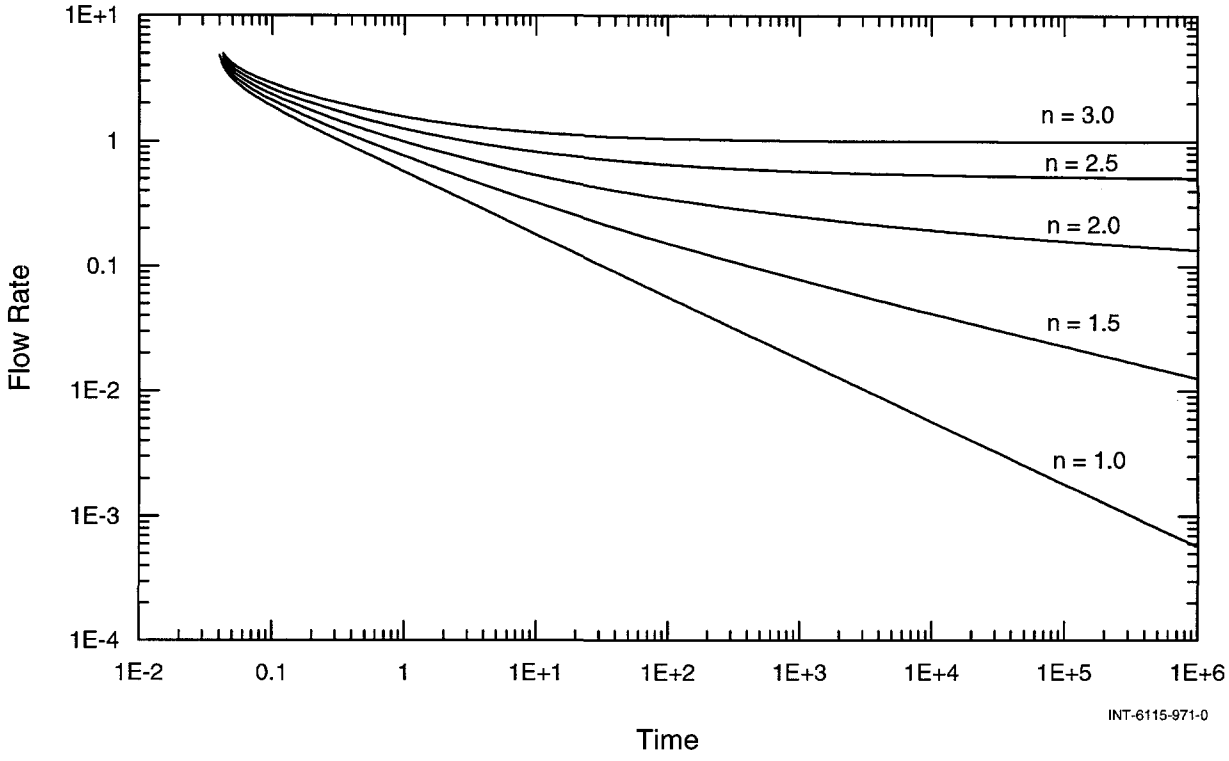

Figure 6-5. Log-log plot of flow rates during a constant-pressure test for selected values of *n*.

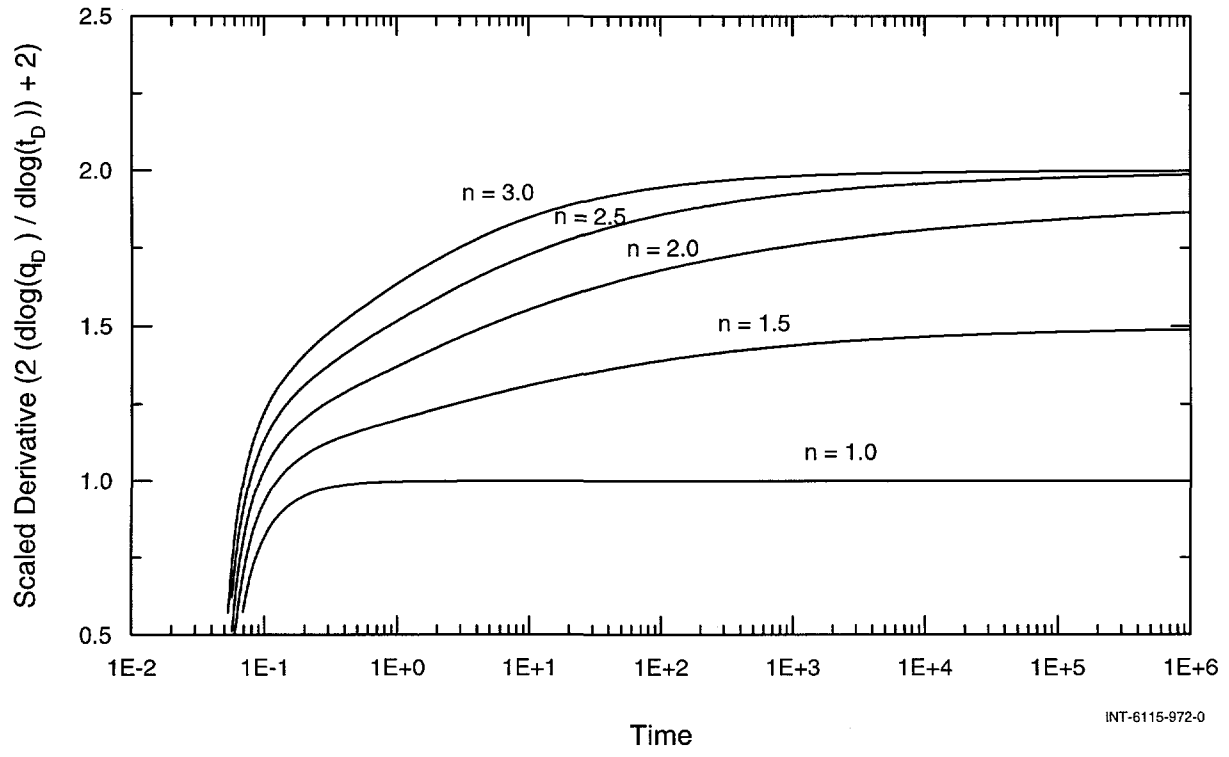

Figure 6-6. Scaled flow-rate derivative for a constant-pressure test for selected values of *n*.

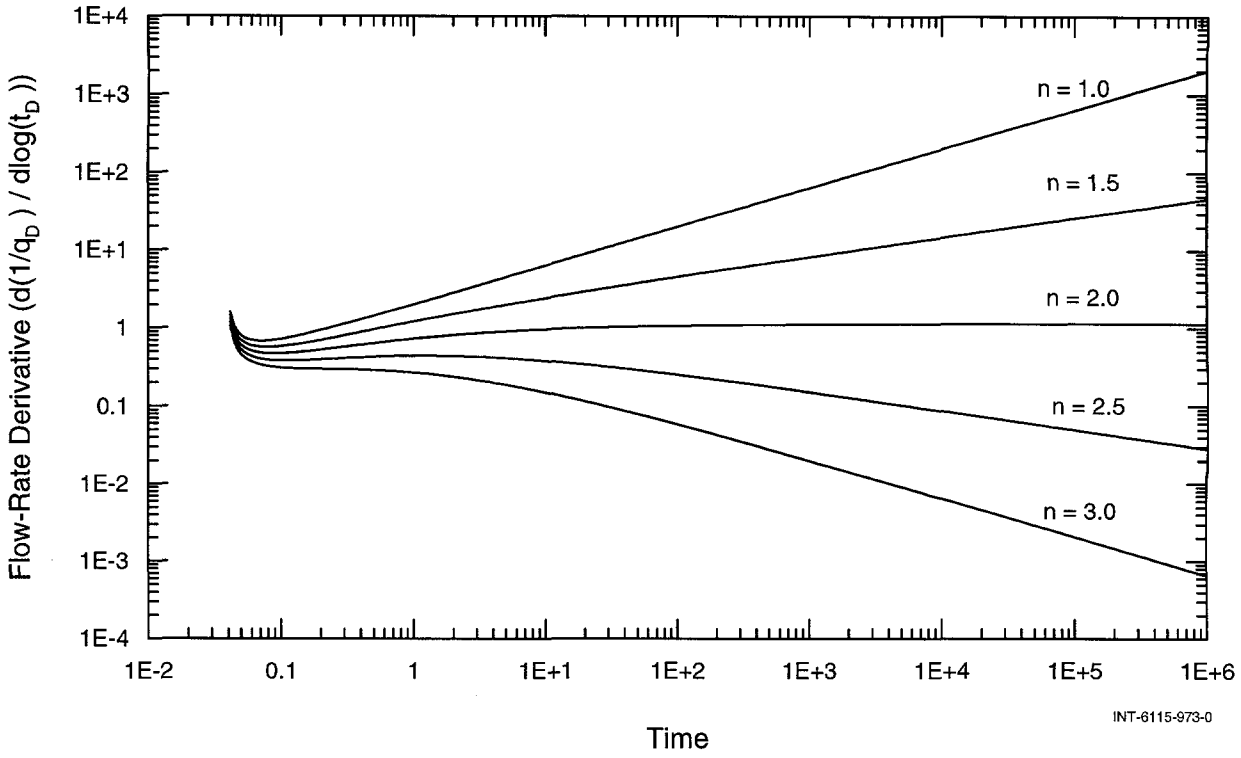

Figure 6-7. Derivative of $1/q_D$ for a constant-pressure test for selected values of *n*.

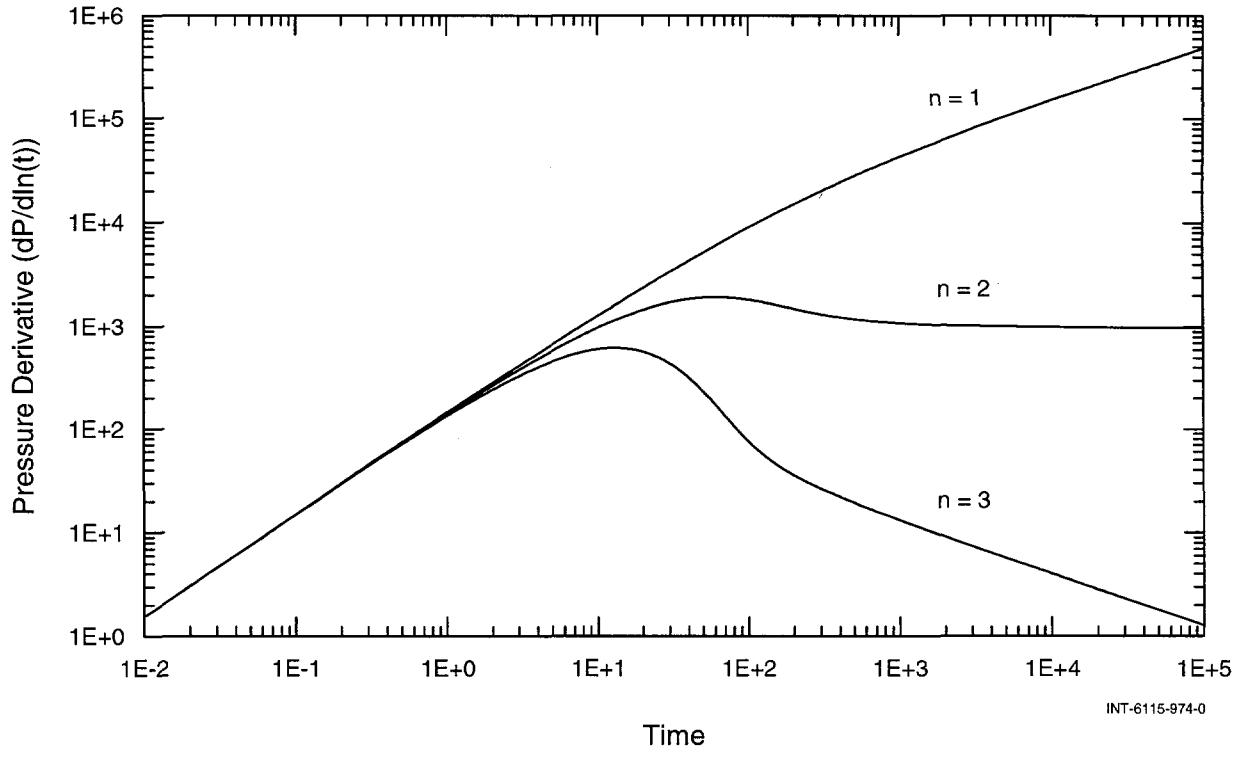

Figure 6-8. Example log-log plot of pressure-change derivative showing the late-time straight line for *n* = 1, 2, and 3.

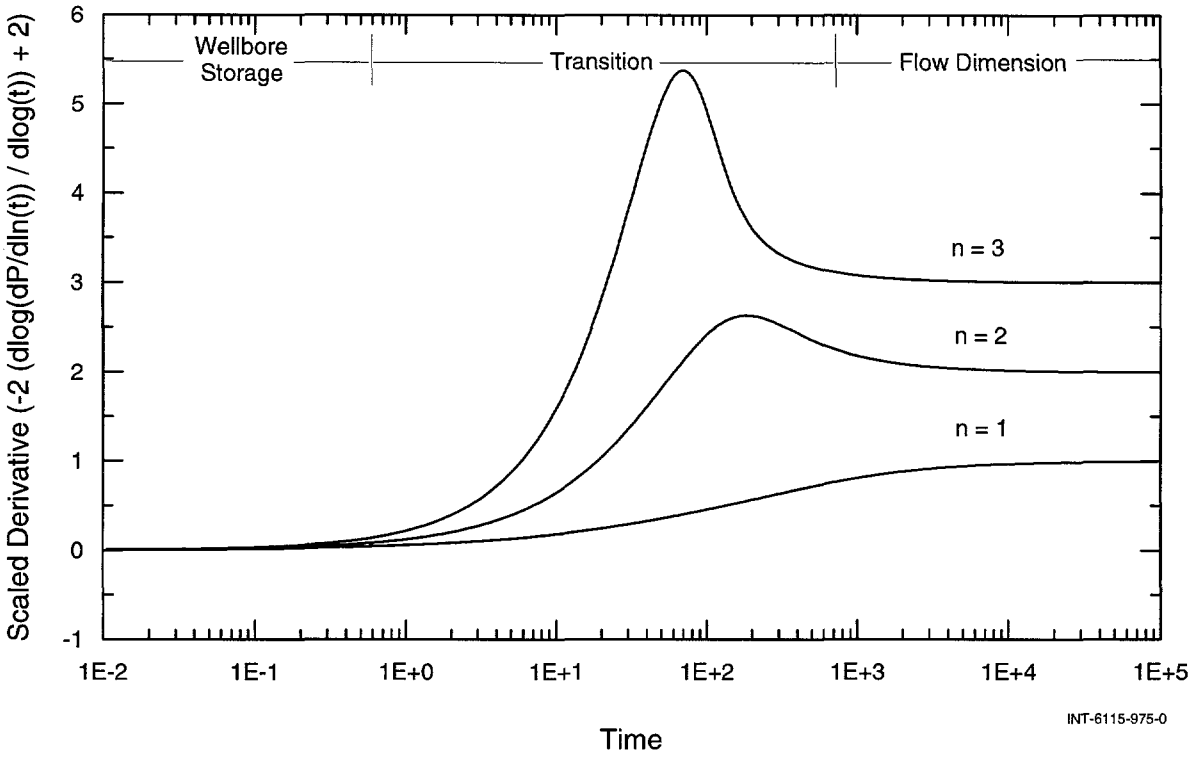

Figure 6-9. Semilog plot of the scaled second derivative of pressure-change for a constant-rate test.

first case illustrates the inherent non-uniqueness problem in well-test analysis. This, in turn, can be used to introduce a simple transform to calculate any number of geometry/parameter combinations that result in the same simulated response.

Consider a constant-rate pumping test performed in a fully penetrating, finite-radius well in a constant-thickness, fully confined, homogeneous, isotropic system of infinite extent. A standard diagnostic plot (dP and $dP/d\ln(t)$ vs. dt) of the pumping period for this type of test is shown in Figure 6-10. The horizontal late-time derivative is typically assumed to be indicative of infinite-acting radial flow. In terms of geometry and hydraulic properties, the flow area at any distance r from the well is given by Eq. 6-4 ($n = 2$) and K and S_s are constant. Now consider a new system where the available flow area at any distance r is constant and equal to the surface area of the wellbore, and K and S_s vary as a function of distance from the well in such a way that the response due to pumping is the same as before. The flow area of the new system at any distance r is given by:

$$\text{Area}_{new} = 2\pi r_w b \qquad (6\text{-}10)$$

where: r_w = wellbore radius

The new $K(r)$ and $S_s(r)$ values at any distance r from the well are given by:

$$K(r)_{new} = K_{old} \times \frac{2\pi rb}{2\pi r_w b} \qquad (6\text{-}11)$$

$$S_s(r)_{new} = S_{s\,old} \times \frac{2\pi rb}{2\pi r_w b} \qquad (6\text{-}12)$$

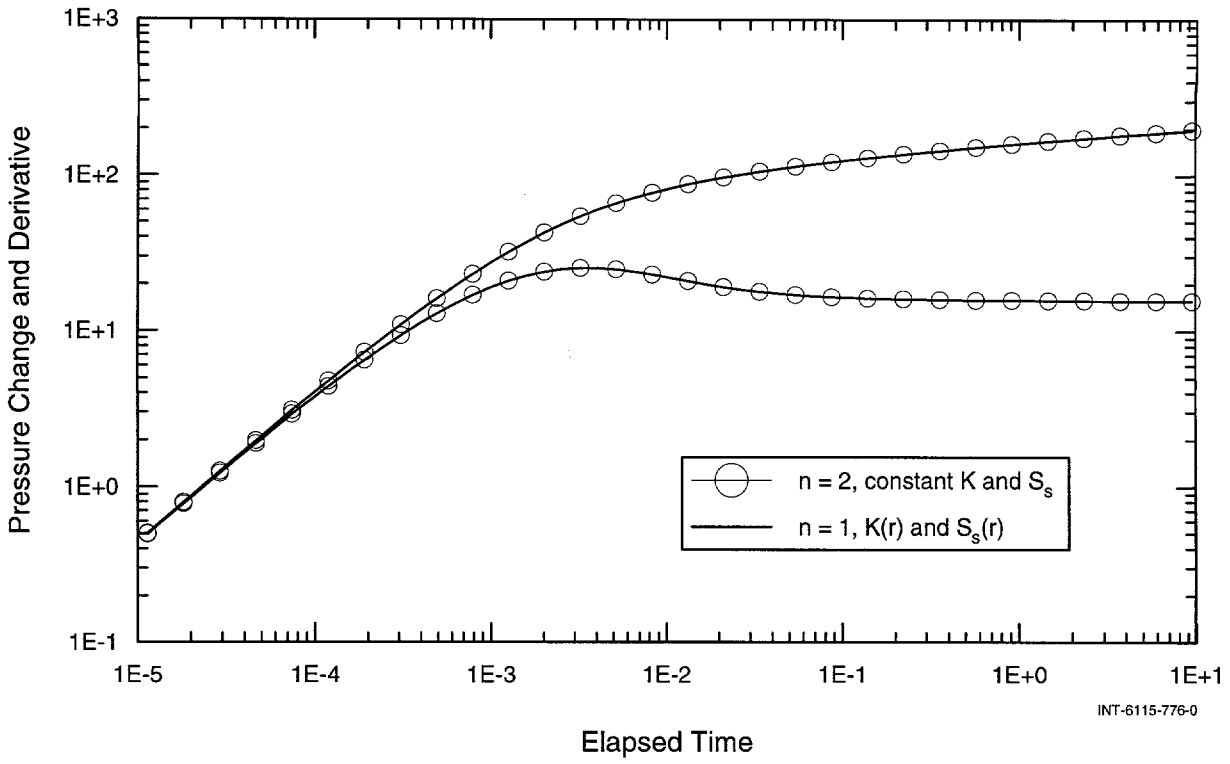

Figure 6-10. Diagnostic plot of a constant-rate pumping period in both a homogeneous radial system and a heterogeneous linear system.

If Eqs. 6-11 and 6-12 are rearranged, we see that the flow area-parameter products at any distance r simply remain constant. For example:

$$K(r)_{new} \times \text{Area}_{new} = K_{old} \times \text{Area}(r)_{old} \quad (6\text{-}13)$$

The pressure response in the new constant-area system will be identical to the response in the radial system (Figure 6-10). This example illustrates why estimates of K and S_s depend on the assumed flow geometry. In the transform presented above, $S_s(r)$ is assumed to vary by the same power as $K(r)$. Fortunately, any assumption made about S_s does not greatly affect the K estimate. Consider the previous example. If the hydraulic-parameter transform is applied only to K while S_s retains its original constant value, the calculated $K(r)$ function must be multiplied by a factor of two to obtain a reasonable match to the data. The uncertainty in $K(r)$ resulting from all other possible factors is probably much greater than this factor of two.

The second test case involves the use of radially varying flow dimensions to simulate a system with a linear no-flow boundary at some distance from the well. This simple geometry was chosen to show that the flow-dimension curve ($n(r)$) provides a description of the system geometry that would be intuitively expected.

A data set was generated in which the effect of a linear no-flow boundary on a constant-rate pumping test was simulated using an image well (Figure 6-11). The boundary effect was then simulated using an $n(r)$ curve instead of an image well. The estimated $n(r)$ curve is shown in Figure 6-12. At the boundary, $n(r)$ decreases rapidly but quickly returns

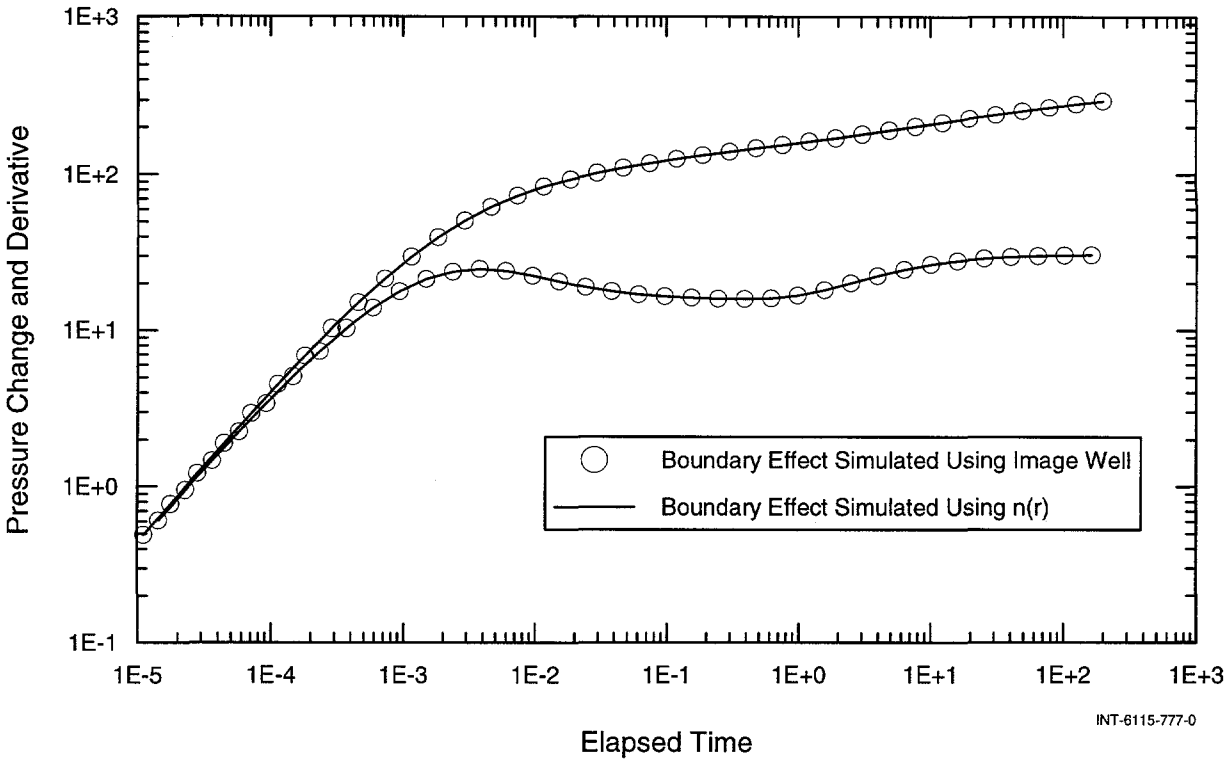

Figure 6-11. Diagnostic plot showing linear no-flow boundary effect simulated with both an image well and varying flow dimension.

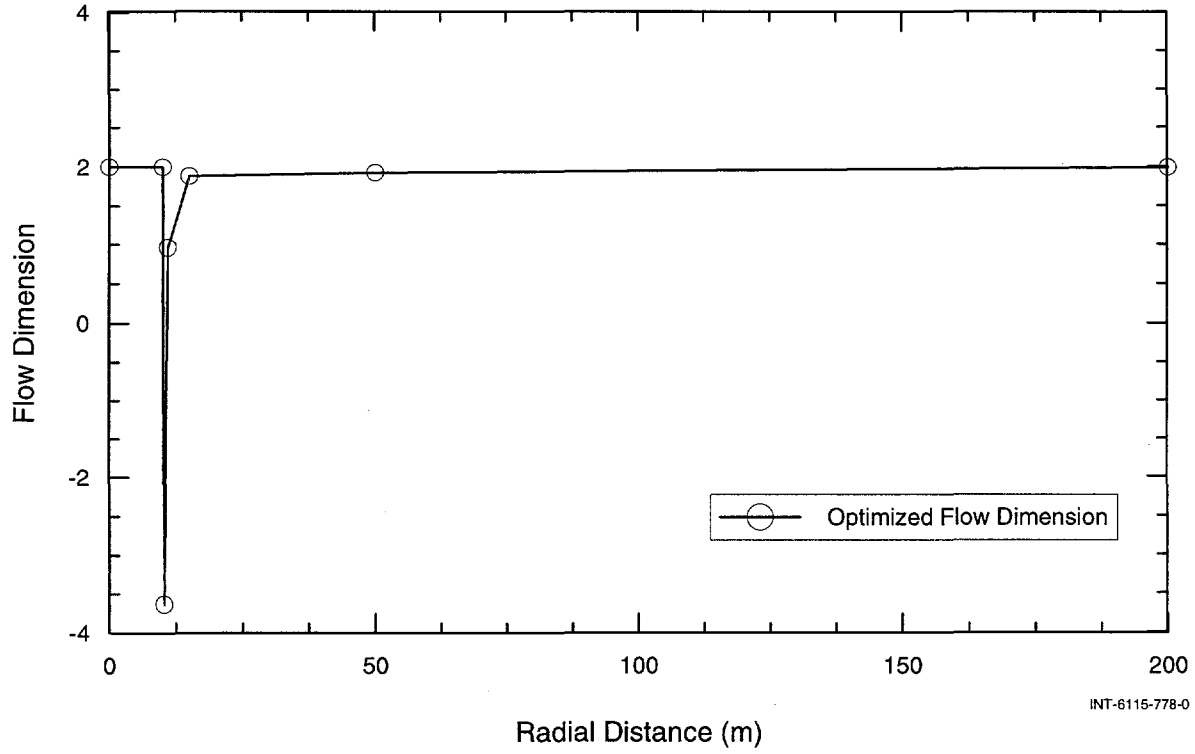

Figure 6-12. GTFM-calculated flow-dimension function representing a linear no-flow boundary.

to a value slightly less than 2. The flow-area-versus-distance function (*Area(r)*) calculated from *n(r)* for the bounded system is shown in Figure 6-13 along with the flow area function for an infinite radial system. Figure 6-14 shows the ratio of the flow areas of the two systems, the bounded-system area divided by the infinite-system area. From this plot, we can see that the flow-dimension curve defines a system in which flow area asymptotically approaches one half the flow area of an infinite cylindrical system as the radius of influence of the test increases. The *n(r)* description of the boundary, while appearing somewhat abstract at first, does provide meaningful information about the geometry of the flow system. As the radius of influence increases, the distance between the no-flow boundary and the well becomes less significant until the boundary effectively divides the system into two equal parts.

In the third test case, radially varying flow-dimension analysis is applied to the output from a semi-analytic solution (Butler and Liu, 1991) describing the drawdown produced by pumping from a fully penetrating well (line source) in the nonradial system shown in Figure 6-15. The configuration consists of an infinite strip of material (Region 2) separating two semi-infinite half-spaces (Regions 1 and 3) of material with the properties of each region shown in the figure. The diagnostic plot for the pumping period is shown in Figure 6-16. GTFM was used to match the data by assuming constant K and S_s and estimating *n(r)*. The match to the data is shown in Figure 6-16 and the estimated *n(r)* curve is shown in Figure 6-17. If the flow system was assumed to be a radial-composite system, the hydraulic conductivity for each of the regions would be estimated from the appropriate stabilization level of the pressure derivative as shown in Figure 6-18. Note that the

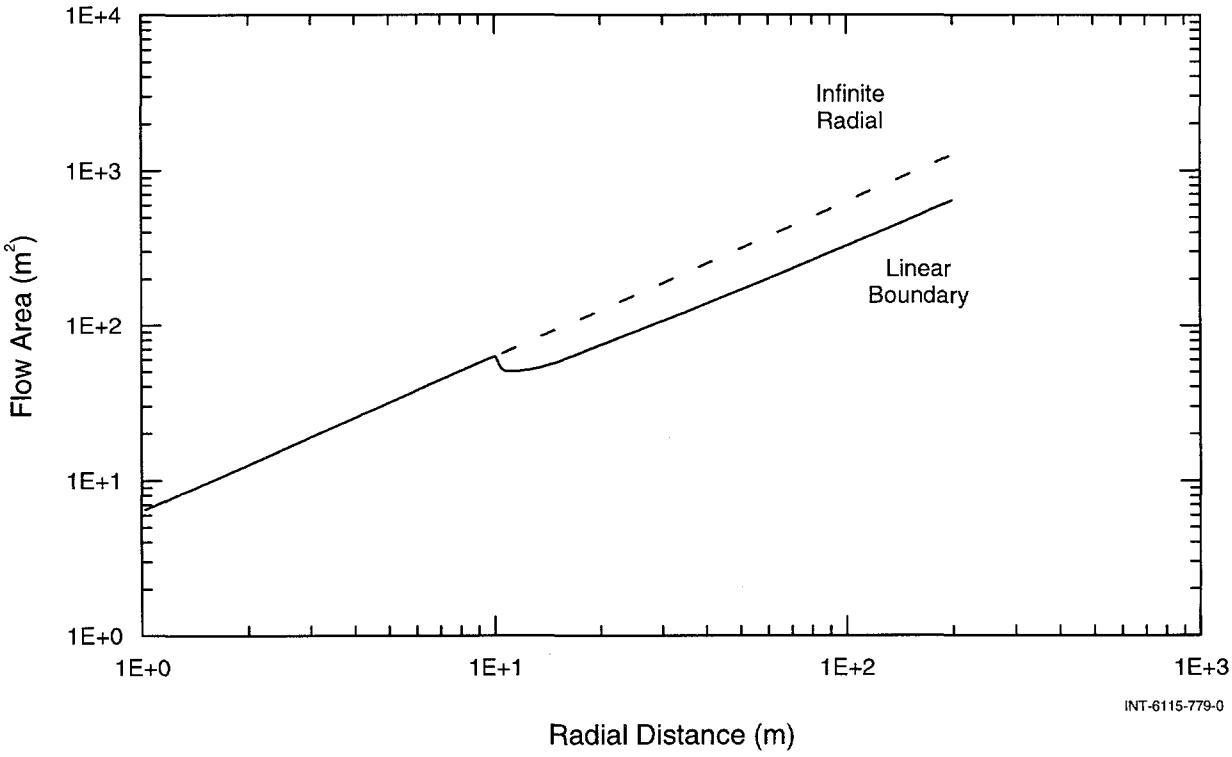

Figure 6-13. Flow area for an infinite radial flow system and a flow system with a linear no-flow boundary.

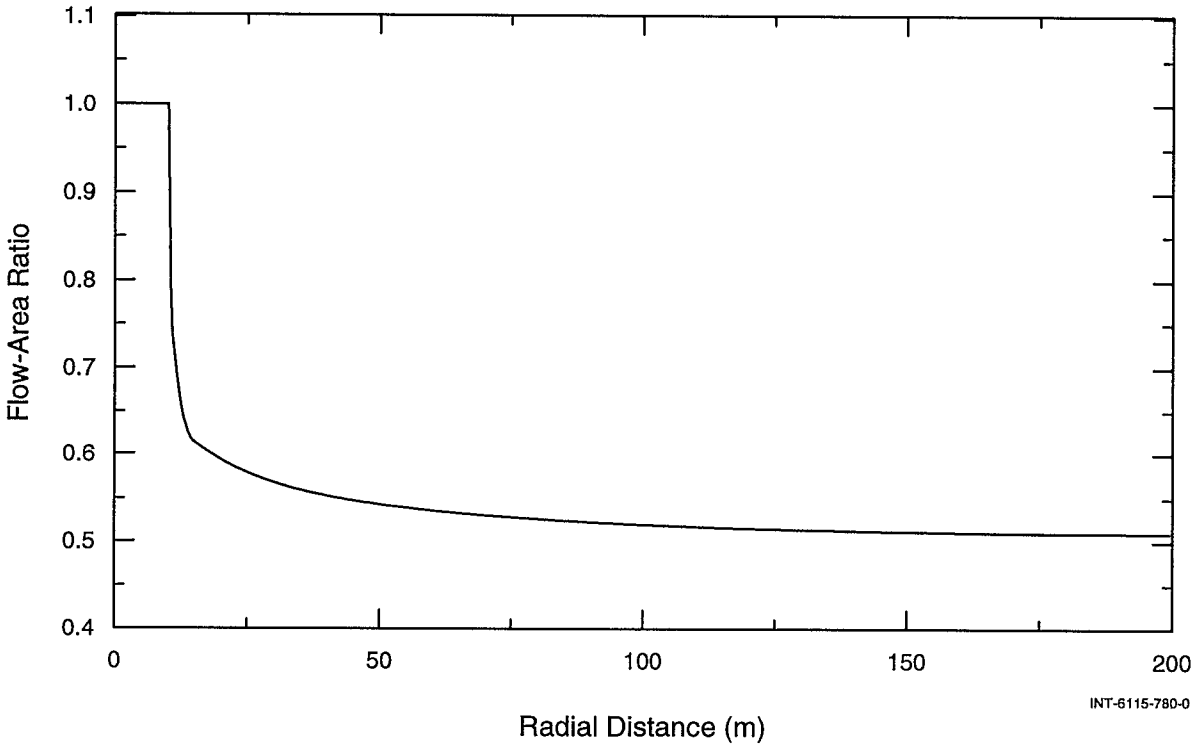

Figure 6-14. Ratio of bounded-system flow area to infinite-system flow area.

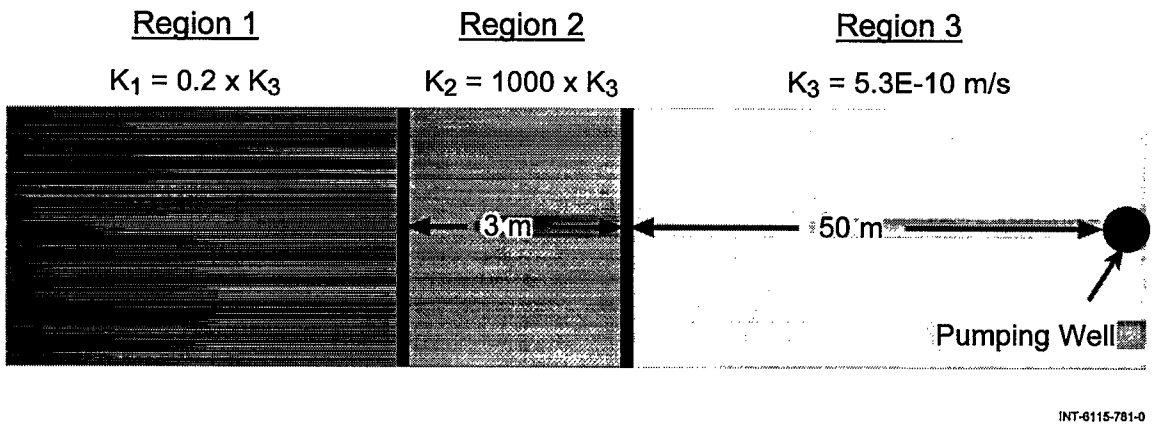

Figure 6-15. Schematic of 3-region flow system.

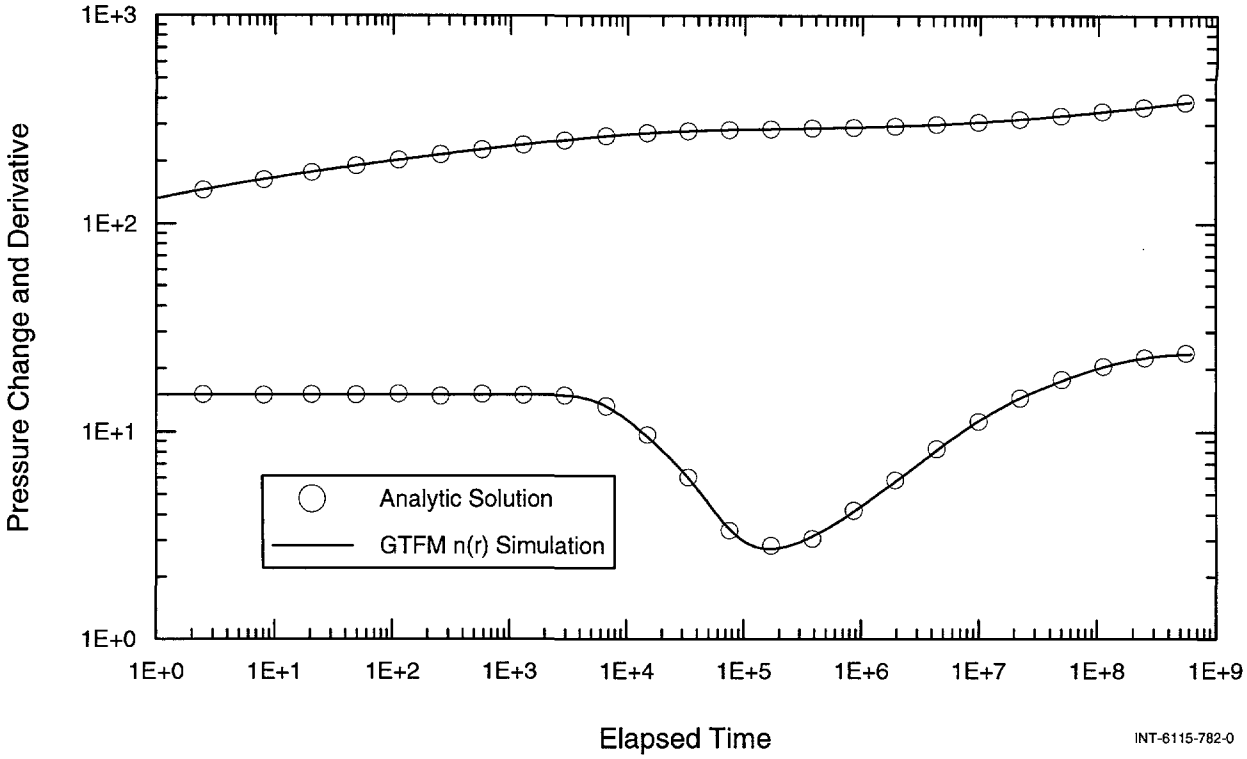

Figure 6-16. GTFM-varying flow-dimension simulation of pumping response in 3-region aquifer.

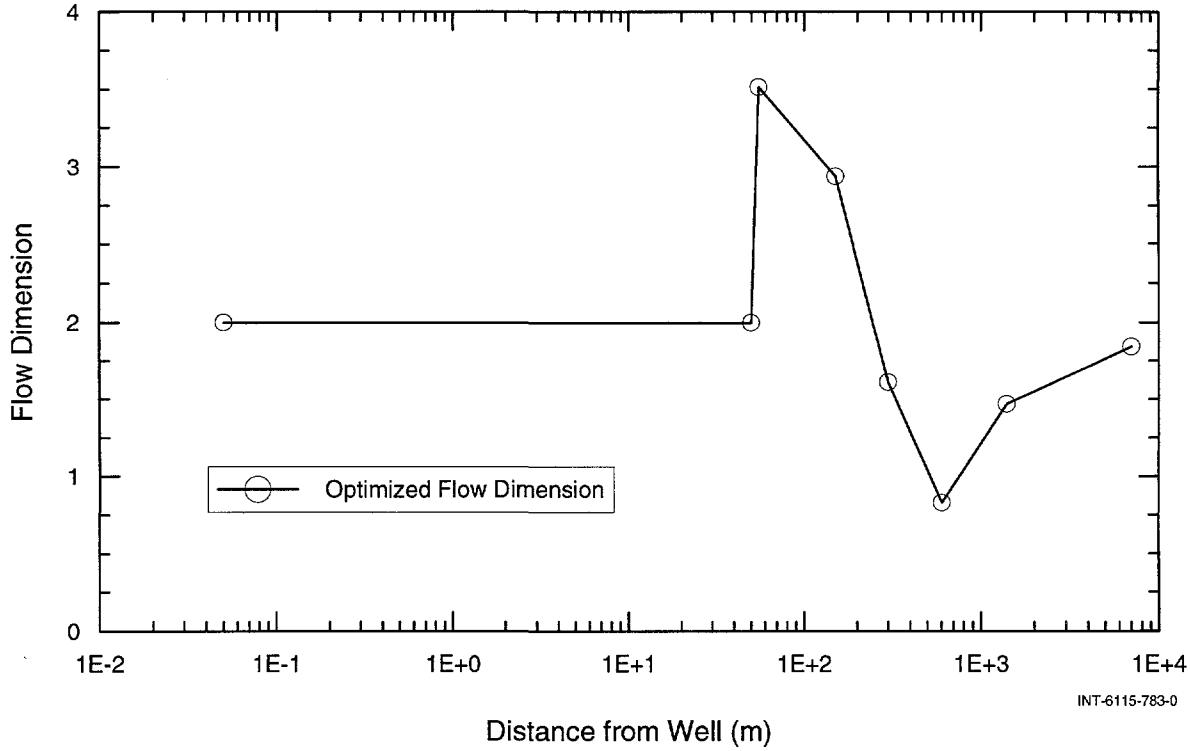

Figure 6-17. GTFM-calculated flow-dimension function representing changing hydraulic-properties in 3-region system.

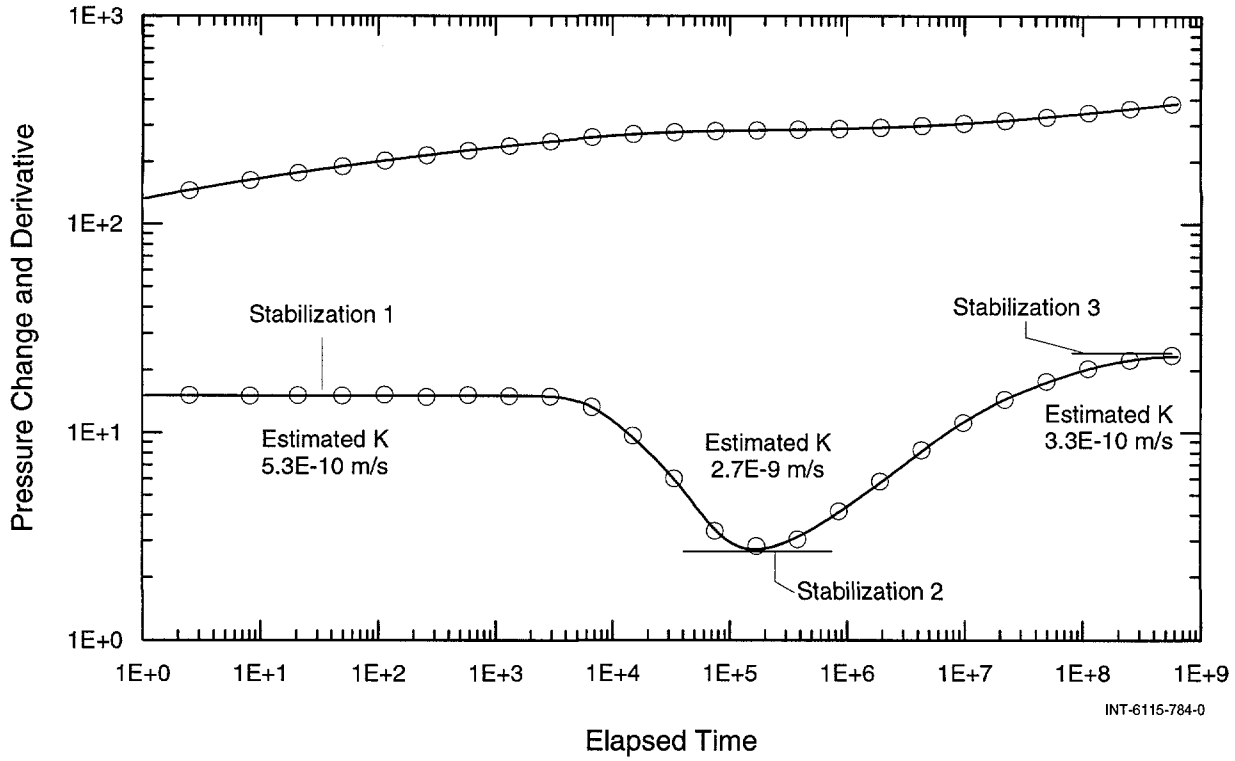

Figure 6-18. Pressure-derivative stabilization levels used to estimate hydraulic conductivity.

actual linear geometry of the system could not be determined from the single-well pumping-test data alone. A radial-composite system would be a reasonable and frequently used conceptual model. As explained above, if the flow geometry is assumed to be radial (n = 2), then the estimated $n(r)$ function (Figure 6-17) can be transformed into $K(r)$ and $S_s(r)$ functions such that the simulated response is unchanged. Figure 6-19 shows the $K(r)$ function calculated from $n(r)$ for the assumed radial-composite geometry along with the K values estimated analytically from the derivative-stabilization levels. The transformed $n(r)$ function (now assuming $n = 2$ and $K(r)$) provides K estimates that are equivalent to those estimated analytically from the derivative-stabilization levels.

Note that the estimated K value for the high-conductivity strip is two orders of magnitude lower than the actual K value due to the averaging nature of the well test. The early-time pressure response is influenced only by the Region 3 hydraulic parameters (Figure 6-15) and the estimated early-time K value (Figure 6-19) corresponds to the input value for that region. At no time, however, is the pressure response influenced only by the Region 2 hydraulic parameters. Once the pumping radius of influence extends beyond Region 3, the estimated K value is determined by some average of the properties of the different regions. Consequently, the actual Region 2 K value could never be estimated unless the true geometry of the system (Figure 6-15) was known. Butler and Liu (1991) note that the late-time K estimate for the configuration shown in Figure 6-15 will be independent of the Region 2 K value and will be equal to the arithmetic average of the Region 3 and Region 1 K values.

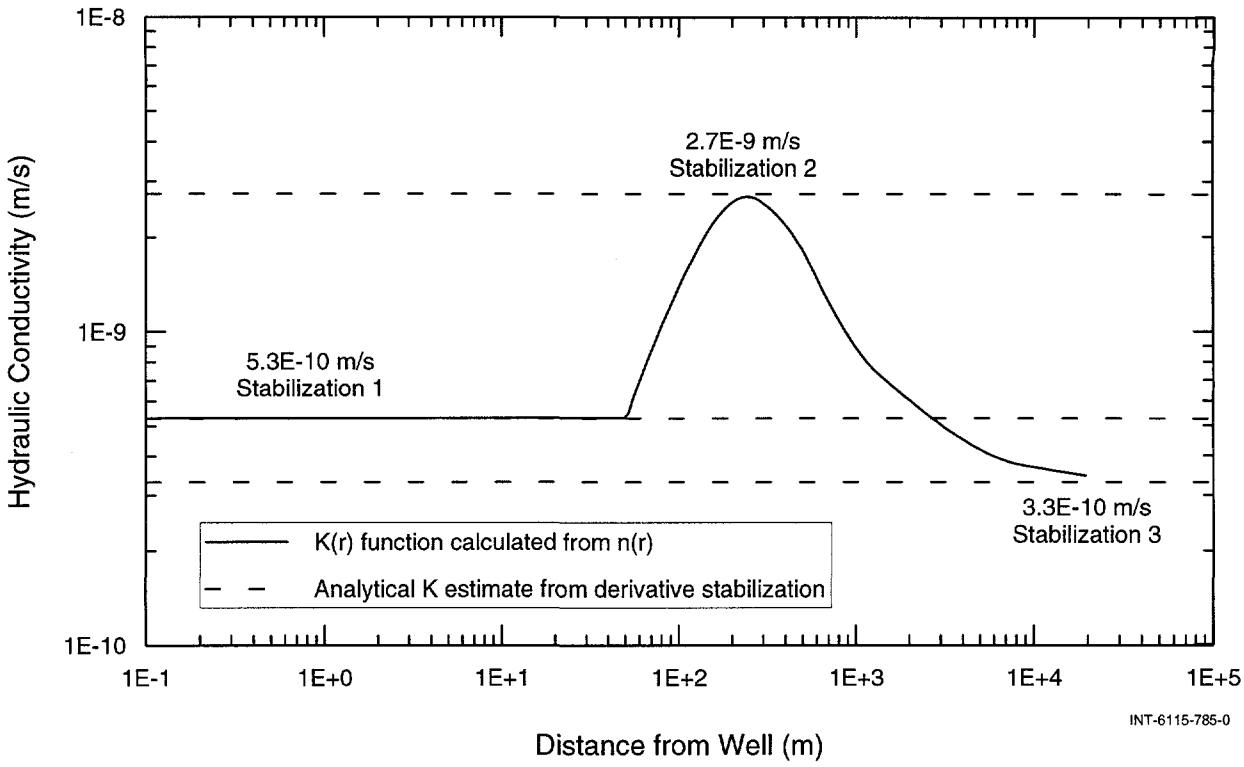

Figure 6-19. *K(r)* function for radial-composite system calculated from *n(r)* function from 3-region system and analytically derived *K* estimates.

6.2.3 Uncertainty Analysis

A methodology to quantify uncertainty in the estimates of fitting parameters has been developed and applied to the analyses presented in this report. The methodology incorporates diagnostic techniques, inverse-fitting routines, statistical analysis, and probabilistic techniques. Figure 6-20 shows a flowchart of the methodology. The methodology represents an advancement of the sensitivity analysis presented in Beauheim et al. (1991) and is explained in more detail in the following paragraphs.

6.2.3.1 Conceptual-Model Identification

Conceptual-model identification is the first step in the analysis procedure and is also the greatest source of uncertainty in the parameter-estimation process. Parameter values estimated using inverse methods are strictly model-related, i.e., changing the conceptual model can significantly change the estimated values of the fitting parameters. The best that can be done in this step of the analysis process is to choose a conceptual model with the following characteristics: it is the simplest model that accounts for all of the structure in the measured data (plots of simulated data should have the same characteristic shapes as the measured data) and it is supported by all other available information. This information would typically include some combination of core logs, video logs, geophysical logs, tracer-test data, and observation-well data. For the analyses in this report, only core logs and video logs were available.

Many of the analyses presented in this report were done assuming that K and S_s were

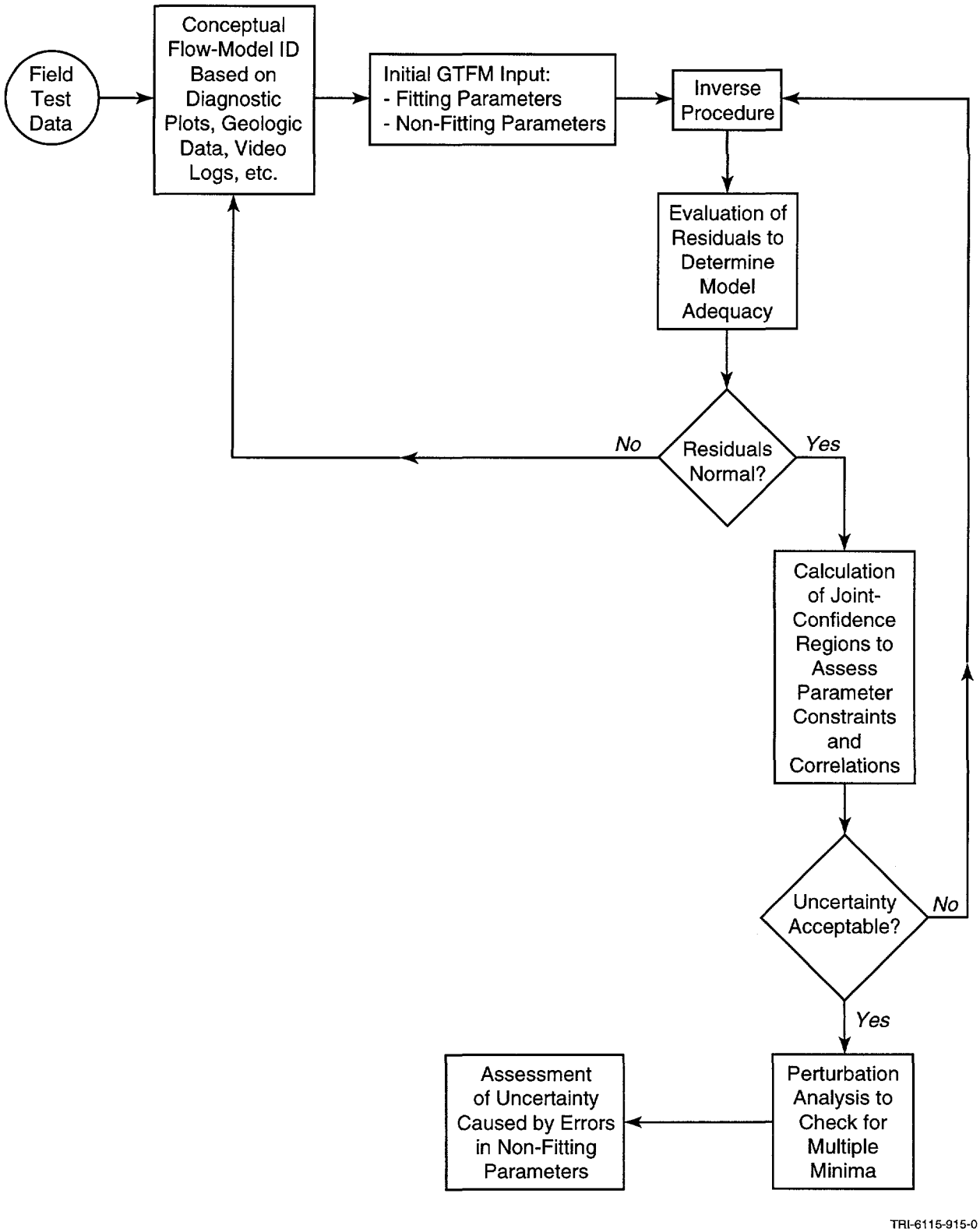

Figure 6-20. Flow chart of analysis methodology.

constant and only the geometry (n) was allowed, if necessary, to vary spatially to improve the match to the measured data. As discussed in Section 6.2.2, this is an arbitrary but reasonable assumption, given that nothing is typically known about the spatial variability of K, S_s, and n. This assumption is invoked, in part, simply to make analysis feasible. To always consider an infinite number of solutions makes no sense. Allowing only n to vary spatially is also typically the simplest conceptual model that satisfies the criteria listed in the paragraph above.

Another assumption incorporated into each of the analyses in this report was that no "skin zone" exists around the borehole, i.e., a zone of altered hydraulic conductivity surrounding the borehole resulting from drilling and/or stress relief. This assumption was made because no estimates of the skin-zone properties can be made from single-well test data without independently knowing the formation storage properties (S_s). Explicitly including skin-zone properties as fitting parameters would yield no additional defensible information from the analyses of the Salado data. However, the assumption of no skin zone will result in an error in the estimate of S_s if a significant skin zone does exist. If an increased-K skin is present around the borehole and not accounted for in the model, the estimated S_s value will be higher than the actual value. The opposite will be true if K near the borehole is decreased.

Well-test analysis is always performed using information that is limited in some respect. Consequently, assumptions (hopefully based on a synthesis of all the available information) are always made when well-test analysis is performed. These assumptions always affect the estimates of the fitting parameters. If the modeling assumptions are changed, the estimates of the fitting parameters will change. Therefore, the fitting-parameter estimates presented in this report must always be evaluated in light of the assumptions presented above.

All three types of tests performed as part of the Salado testing program are, in theory, conducive to conceptual-model identification. The diagnostic techniques related to each type of test are, however, affected to some degree by pressure transients that cannot, for various reasons, be properly accounted for in the technique. The technique described by Peres et al. (1989) can be used to identify the conceptual model in the case of pulse (pressurized slug) tests. This technique is used to convert a pulse test to its equivalent constant-rate response, thus allowing for conceptual model diagnostics using the pressure-derivative technique as described by Bourdet et al. (1989). Conversion to an equivalent constant-rate response is, however, a useful diagnostic technique only when the pulse is preceded by static pressure conditions -- a condition that occurred only during the L4P51-C1 guard zone and L4P51-C2 test zone 2 halite testing.

The pressure-derivative technique of Bourdet et al. (1989) can also be applied to pressure data from buildup/falloff tests following constant-pressure tests. Rate superposition is used in the pressure-derivative calculation to account for the changing rates during the preceding constant-pressure test. The shape of the pressure derivative and, therefore, the implied conceptual model may, however, be affected by pressure transients that preceded the constant-pressure test, e.g., the initial open-borehole period. Given that flow-rate data are not available for the open-borehole period, this pressure transient cannot be properly accounted for in the derivative calculation, thereby affecting the conceptual-model identification process.

Doe (1991) describes how constant-pressure tests provide transient flow-rate data that can be used to evaluate the system flow dimension. When using constant-pressure test data for conceptual model diagnostics, the test is assumed to have been preceded by static pressure conditions and the pressure during the test is assumed to have, in fact, remained constant. The potential error in diagnosing the proper conceptual model will roughly depend on the degree to which these assumptions are violated.

The conceptual-model identification techniques described above suffer from a common problem -- the inability to distinguish unambiguously among flow models. In light of this problem, the principle of parsimony should be applied to conceptual model identification, i.e., use the simplest model that the data will support. At a later step in the analysis, residual (the difference between simulated and measured values) distributions are checked to insure that the chosen conceptual model meets the minimum criterion of accounting for all of the structure in the data.

6.2.3.2 Definition of Initial Inputs

The second step in the analysis process is determining initial values for model input. Values must be determined for two types of parameters: 1) non-fitting parameters (e.g., borehole radius, flow rate, borehole pressure history, fluid density, etc.); and 2) fitting parameters (e.g., hydraulic conductivity, specific storage, static formation pressure, flow dimension, etc.). The non-fitting parameter values are determined directly from field measurements, equipment configurations, laboratory measurements, etc. Initial estimates of the fitting-parameter values are made using standard analytical techniques such as type-curve matching and straight-line analysis. Some parameters can be either fitting or non-fitting, depending on the type of test that is performed. Test-zone compressibility, for example, must be fixed (non-fitting) when analyzing a pulse test but can be a fitting parameter in the analysis of a pressure-buildup/falloff test. A parameter is specified as non-fitting when it cannot be constrained as a fitting parameter.

6.2.3.3 Inverse Procedure

After a conceptual model is chosen and initial parameter values are determined, the third step in the analysis process is setting up the inverse procedure. This step itself has three parts: specifying constraints, selecting a fitting algorithm, and choosing an objective function. The constraints are simply the different data plots to be matched by the fitting algorithm. These plots typically include some or all of the following data types: pressure, pressure derivative, cumulative production, and flow rates. The data are used to make specialized plots in an attempt to maximize sensitivity to the fitting parameters and combine parameter correlations such that relatively unique estimates of the fitting parameters are obtained.

Choosing optimal constraints is usually an iterative process. The fitting parameters are first optimized using some initial constraints. The Jacobian matrix, calculated during the optimization step, can then be used to assess the sensitivity of the fitting parameters to the chosen constraint(s). The Jacobian contains the sensitivity of each data point with respect to each fitting parameter. Figure 6-21 shows a Jacobian plot from a pressure-derivative match where K, S_s, C, and P_f were the fitting parameters. The pressure-derivative data points (constraints) are plotted above the Jacobian such that the sensitivity value on the Jacobian plot corresponds to the data point directly above. The Jacobian plot shows that the pressure derivative has both desirable

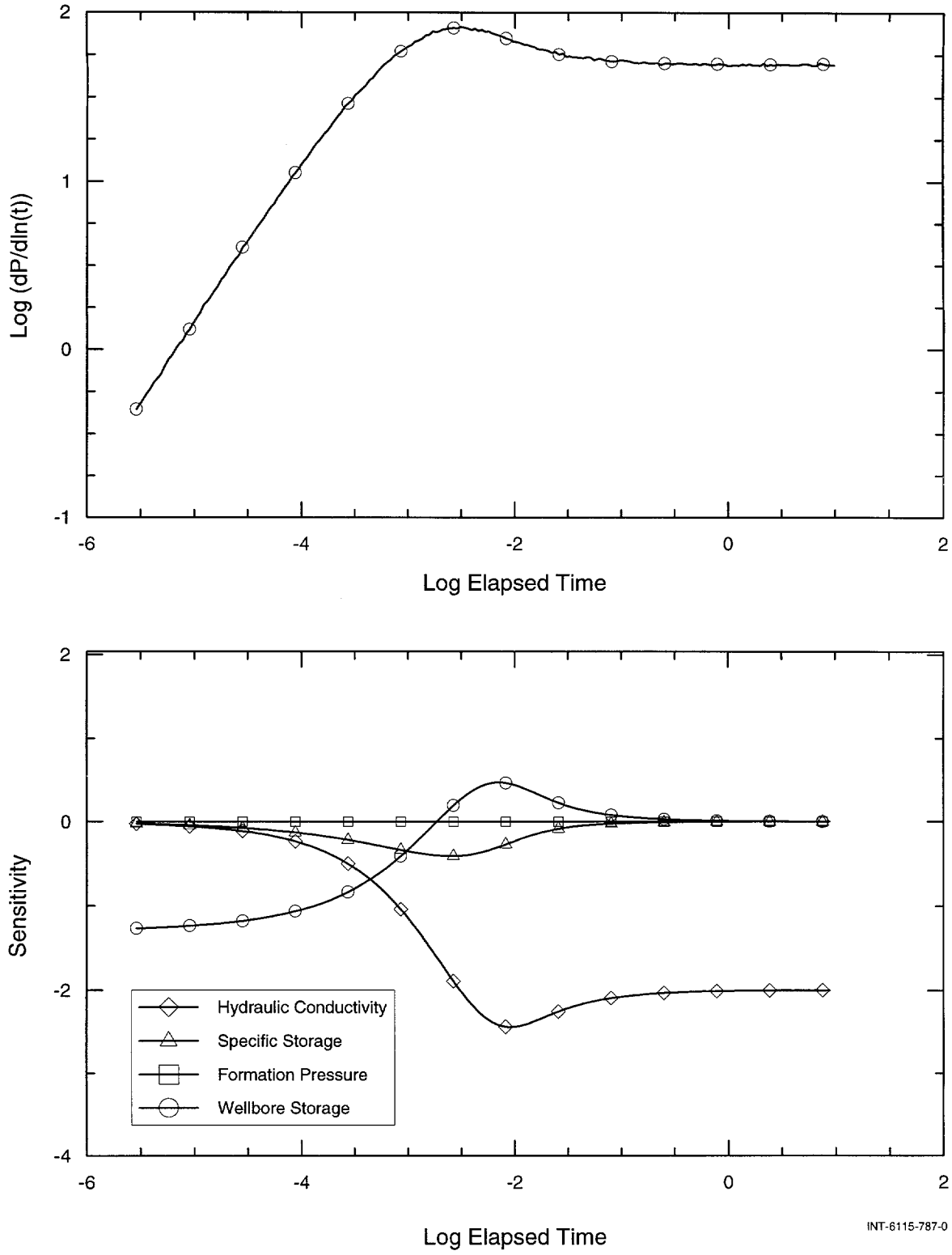

Figure 6-21. Pressure-derivative constraint and corresponding Jacobian plot.

and undesirable features as a constraint for estimating K, S_s, C, and P_f. The early-time match is seen to be sensitive only to C, the wellbore storage factor. By log elapsed time -3.5, sensitivity to C is decreasing and sensitivity to K and S_s is increasing. By log elapsed time -0.5, only sensitivity to K remains. Because the early and late-time matches are sensitive to only one parameter, C and K respectively, these parameters can be estimated independently of the other parameters, i.e., the parameters are uncorrelated in the matching process. This acts to reduce the uncertainty in the parameter estimates. Note, however, that no sensitivity to P_f ever exists, indicating that this parameter cannot be estimated by matching the pressure derivative.

Two inverse-fitting algorithms are available in GTFM: downhill simplex and Levenburg-Marquardt. A discussion of both methods can be found in Press et al. (1992). For many problems, either algorithm is acceptable, but for more complex conceptual models, the downhill simplex algorithm is generally used. The downhill simplex algorithm is slower to converge than the Levenburg-Marquardt algorithm, but it will generally converge to a solution regardless of the initial fitting-parameter estimates. The selected fitting algorithm is used to satisfy the specified objective function, i.e., in the case of all the analyses in this report, to minimize the sum of the squared errors (SSE). Horne (1995) provides an excellent summary of the strengths of using automated inverse techniques to estimate hydraulic properties. He states that compared with traditional methods of fitting a straight line to a portion of the data or manually shifting a type curve to obtain a pressure and time match, inverse methods are objective and able to consider all of the data.

6.2.3.4 Evaluation of Residuals

The results from the inverse procedure include a baseline set of values for the fitting parameters, the residual errors (differences between observed and calculated values), and the calculated joint-confidence regions for the fitting parameters. In step four of the analysis process, the residuals are analyzed to determine if the chosen conceptual model accounts for all of the structure in the observed data. If the chosen conceptual model adequately reproduces the observed response, the residuals should reflect random noise in the data and be approximately normally distributed (the random noise is assumed to have a normal distribution). If the residuals do not meet this criterion, then the analysis should be evaluated to determine if a different conceptual model should be used or if the residual distributions are being affected by some factor that cannot be included in the conceptual model, such as equipment problems/compliance.

Residual plots are the standard visual diagnostic to evaluate error distributions. Two type of residual plots were used during these analyses: a cumulative distribution function (CDF) plot and a quantile-normal plot. The two types of residual plots convey the same information, so the use of one over the other is a matter of personal preference. A normal distribution appears as an s-shaped curve on a CDF plot and as a straight line on a quantile-normal plot. Figures 6-22 and 6-23 show a CDF plot and a quantile-normal plot, respectively, of the residual distributions from the L4P51-C2 test zone 2 pulse-test GTFM simulation. The residuals are seen to have a reasonably normal distribution, indicating that the conceptual model adequately reproduces the observed response. This does not

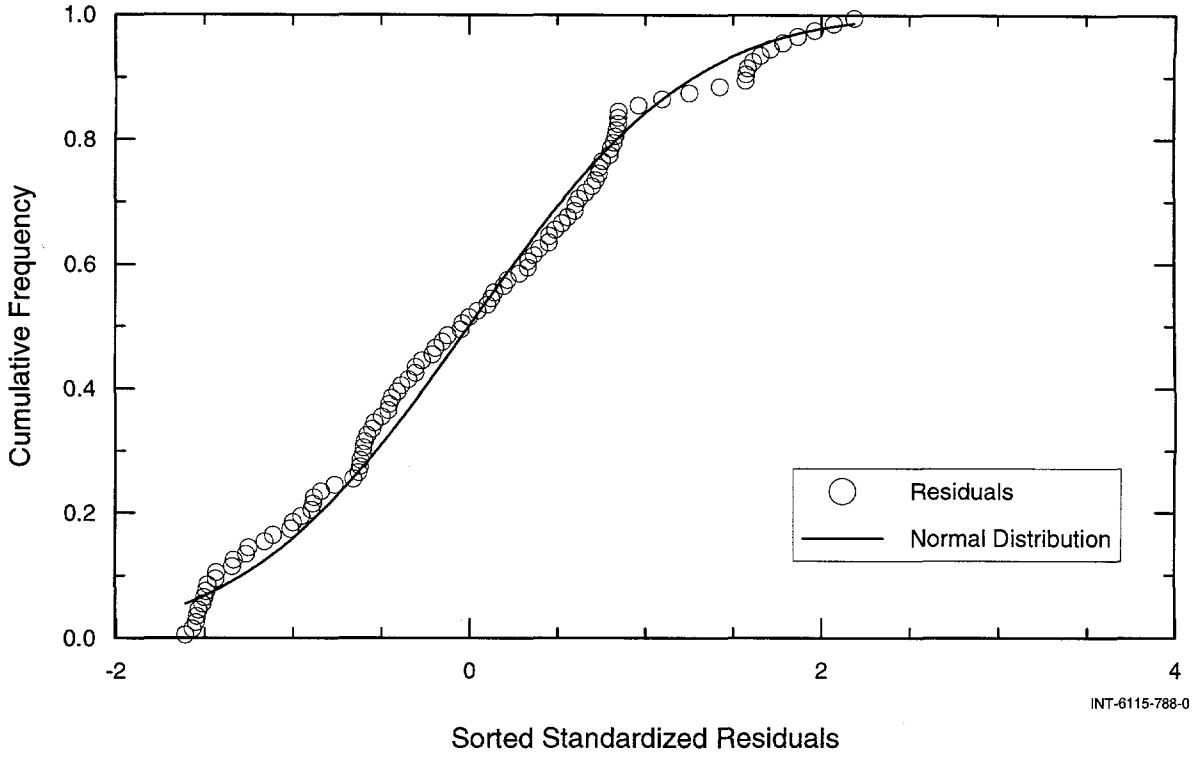

Figure 6-22. CDF plot from analysis of L4P51-C2 pulse test.

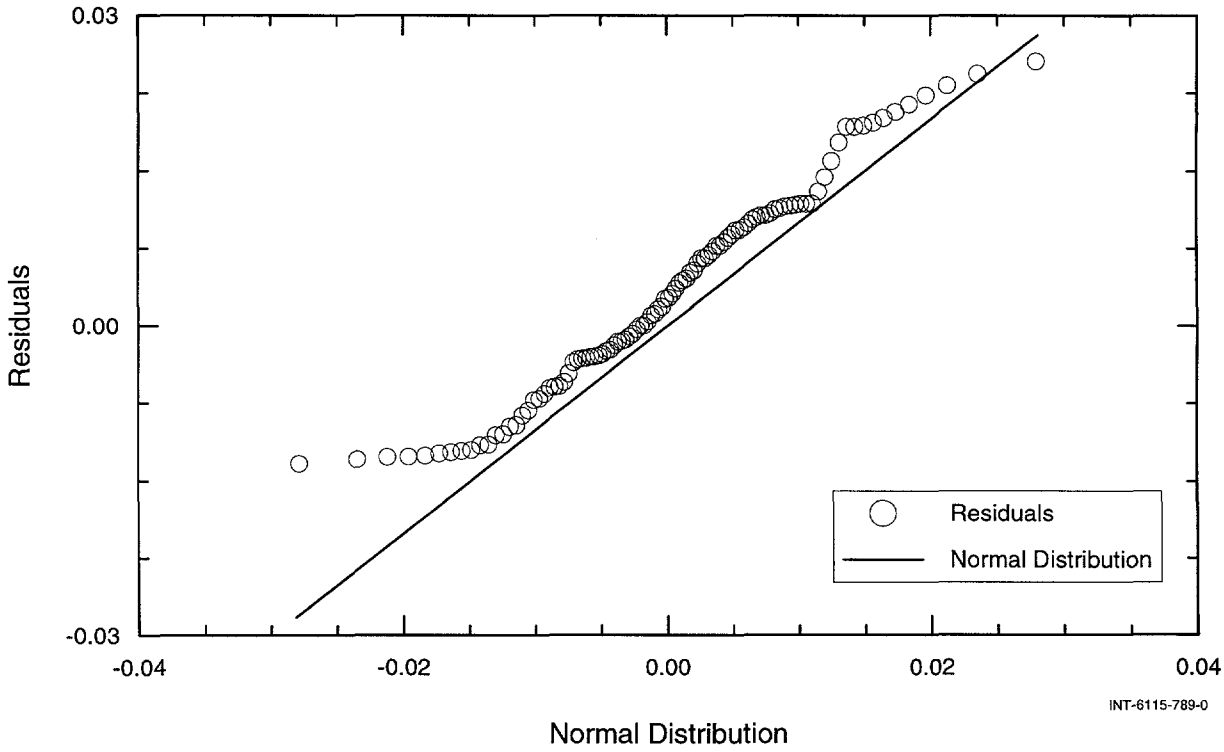

Figure 6-23. Quantile-normal plot from analysis of L4P51-C2 pulse test.

guarantee, however, that the conceptual model is correct.

In some cases, more than one conceptual model may adequately reproduce the observed system response and be plausible in light of the available geologic information. This is often the case in complex geologic settings. Also, one conceptual model may produce a quantitatively better fit to the observed data than another, but have more fitting parameters. In the absence of applying advanced methods to rank possible conceptual models, the principle of parsimony has been applied to the tests in this report: select the simplest model (least fitting parameters) that produces adequate results. Obviously, an "adequate result" is, to some degree, a matter of judgment. For the analyses presented in this report, an increase in model complexity was deemed acceptable if the increased complexity visibly improved the fit to the data and the additional fitting parameters could be constrained. The statistical methods discussed below (joint-confidence regions and perturbation analysis) were used to quantify the degree to which a parameter was constrained.

6.2.3.5 Joint-Confidence Regions

Once the conceptual model is deemed acceptable, the next part of the analysis process is quantifying the uncertainty in the estimates of the fitting parameters (see Figure 6-20). This is done in three steps: 1) joint-confidence regions are evaluated for the baseline fitting-parameter values; 2) the baseline fitting-parameter values are simultaneously randomly perturbed a specified number of times and re-optimized for each perturbation to investigate the uniqueness of the solution; and 3) uncertainty distributions are assigned to selected non-fitting parameters that are sampled a specified number of times. The fitting parameters are then re-optimized for each sampled set of non-fitting parameters. More detailed explanations and examples of each step are given in the following paragraphs.

In this report, joint-confidence regions are used to quantify the uncertainty in fitting-parameter values resulting primarily from fitting-parameter correlations and data noise. After the baseline fitting-parameter values are determined, GTFM uses numerical techniques to estimate the covariance matrix of the parameters. Joint-confidence regions are then calculated from the covariance matrix. The 95% joint-confidence regions for K and S_s from the L4P51-C2 test zone 2 pulse-test optimization are shown in Figure 6-24. The "95%" signifies that, for the problem as posed (conceptual model and constraints), the true answer has a 95% probability of being contained within the confidence region. The orientation of the joint-confidence region provides a qualitative indication of the type of correlation between the parameters displayed. The parameters are negatively correlated if the long axis of the region has a negative slope and positively correlated if the axis has a positive slope. Quantitative estimates of the type and degree of correlation between any two parameters can be calculated from the covariance matrix.

The normalized degree of correlation between any two parameters, A and B, ranges between 1 and -1 and is given by:

$$CORR = \frac{COV(A,B)}{VAR(A)^{1/2} \times VAR(B)^{1/2}} \qquad (6\text{-}14)$$

where: COV() = covariance of any two parameters
VAR() = variance of the given parameter

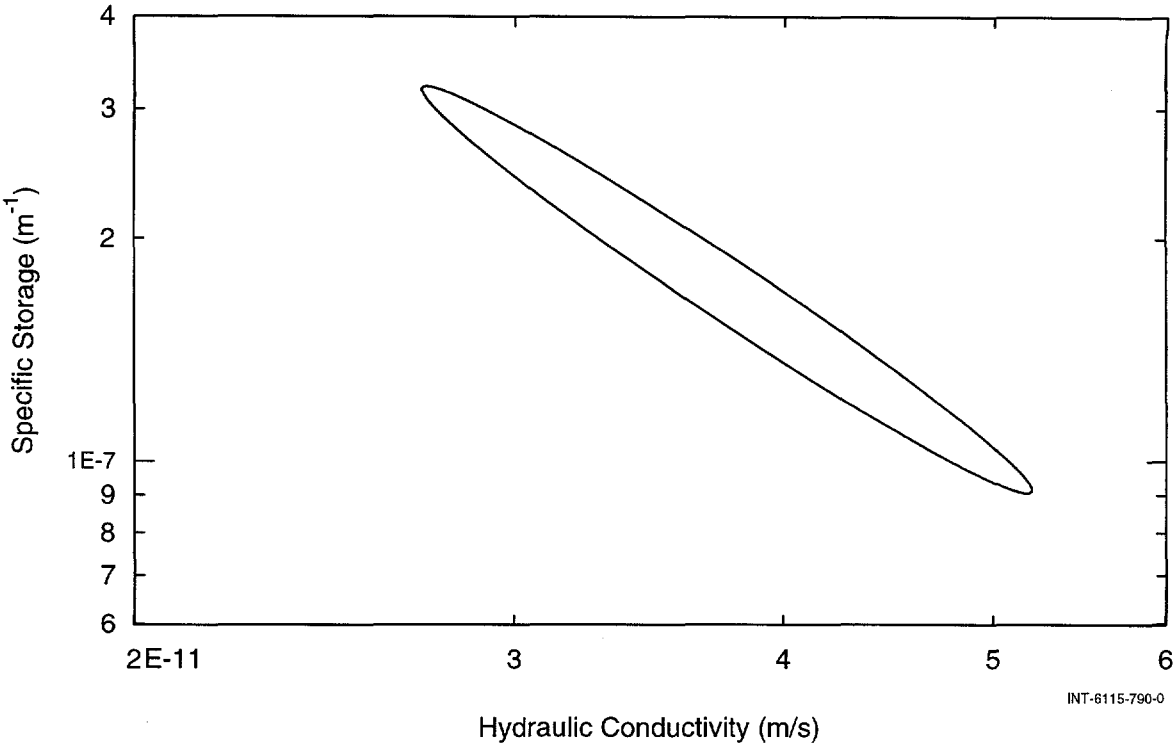

Figure 6-24. 95% joint-confidence region from analysis of L4P51-C2 pulse test.

The joint-confidence regions are actually linearized approximations of the true minima as they are defined in *n*-dimensional parameter space, where *n* corresponds to the number of fitting parameters (not flow dimension). Any 2-dimensional confidence-region plot will be a 2-dimensional projection of an *n*-dimensional confidence region. The complete fitting-parameter uncertainty and correlation information are combined in a single figure for each analysis in this report and are presented in Appendix C. Figure 6-25 is an example showing all the possible joint-confidence regions combinations and the corresponding correlation matrix for an optimization with six fitting parameters (C2H01-A).

Figure 6-26 shows a joint-confidence region (solid ellipse) superimposed on a contour map of an objective-function surface, i.e., the parameter space. The objective-function surface is from a synthetic test problem where K and S_s are being estimated by matching a Horner plot. The joint-confidence region is seen to correspond with the minimum of the objective-function surface. If the actual minimum is generally linear and smooth, then the calculated joint-confidence region will be a good approximation of the true minimum and consequently, the fitting-parameter uncertainty. When these criteria are not met, perturbation analysis is used to characterize the uncertainty and correlations among parameters. The limitations of joint-confidence regions are most easily discussed in conjunction with the information obtained from perturbation analysis. For this reason, these limitations are discussed in the perturbation-analysis section below.

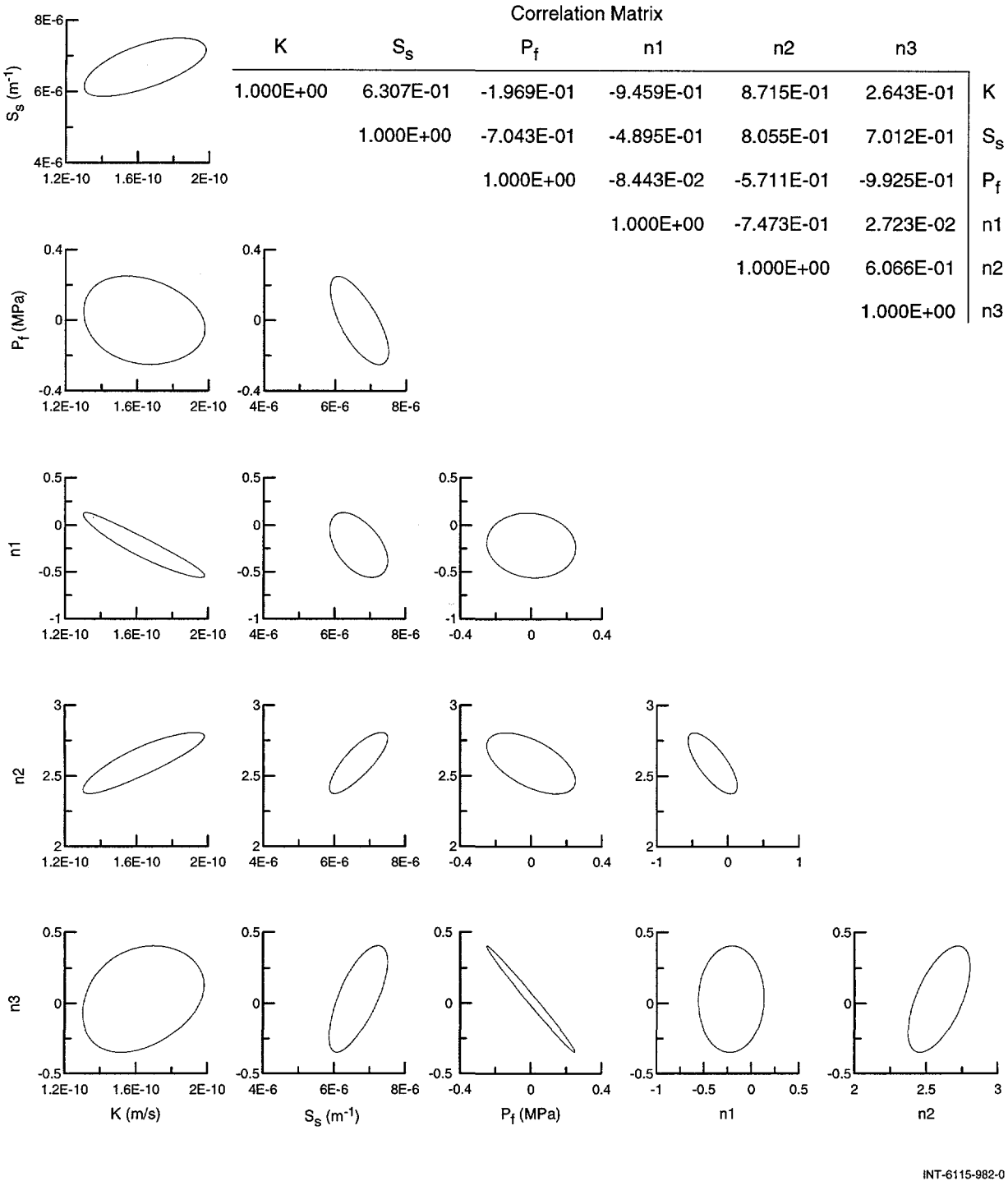

Figure 6-25. 95% joint-confidence regions and correlation matrix for all of the C2H01-A fitting parameters.

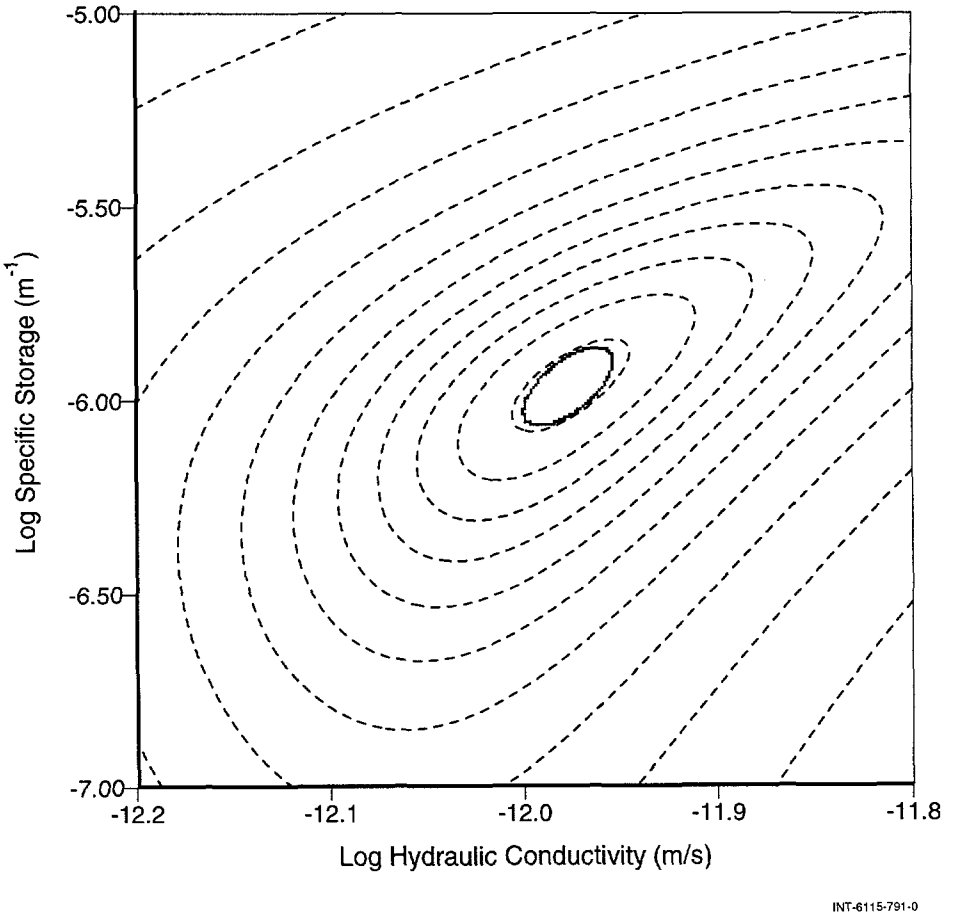

Figure 6-26. 95% joint-confidence region superimposed on contour plot of objective function.

6.2.3.6 Perturbation Analysis

Perturbation analysis is used to investigate the uniqueness of the solution and the correlations among the fitting parameters for the stated problem. As the name implies, perturbation analysis is performed by simultaneously applying random perturbations to all of the baseline values of the fitting parameters and then re-optimizing the values. The perturbed parameters will return to a value very close to their original baseline values if the solution to the problem is unique and well constrained. If more than one solution to the stated problem exists, or a single solution is not well constrained, it will be reflected in the results of the perturbation analysis.

Two types of plots are useful for examining perturbation results: a histogram and an xy-scatter plot. Figure 6-27 is a histogram of the optimized K values from 100 perturbations of the L4P51-C2 test zone 2 pulse-test baseline simulation values. Figure 6-28 is an xy-scatter plot of the optimized K and S_s values from the same 100 perturbations. The histogram shows that the estimated K value for more than 90 of the 100 perturbation results was about 3.8×10^{-11} m/s. The xy-scatter plot shows that a negative correlation exists between K and S_s and all of the perturbed solutions fall between 3×10^{-11} m/s and 5×10^{-11} m/s, indicating that the solution is well constrained. Figure 6-29 shows the 95% joint-confidence region for the L4P51-C2 test zone

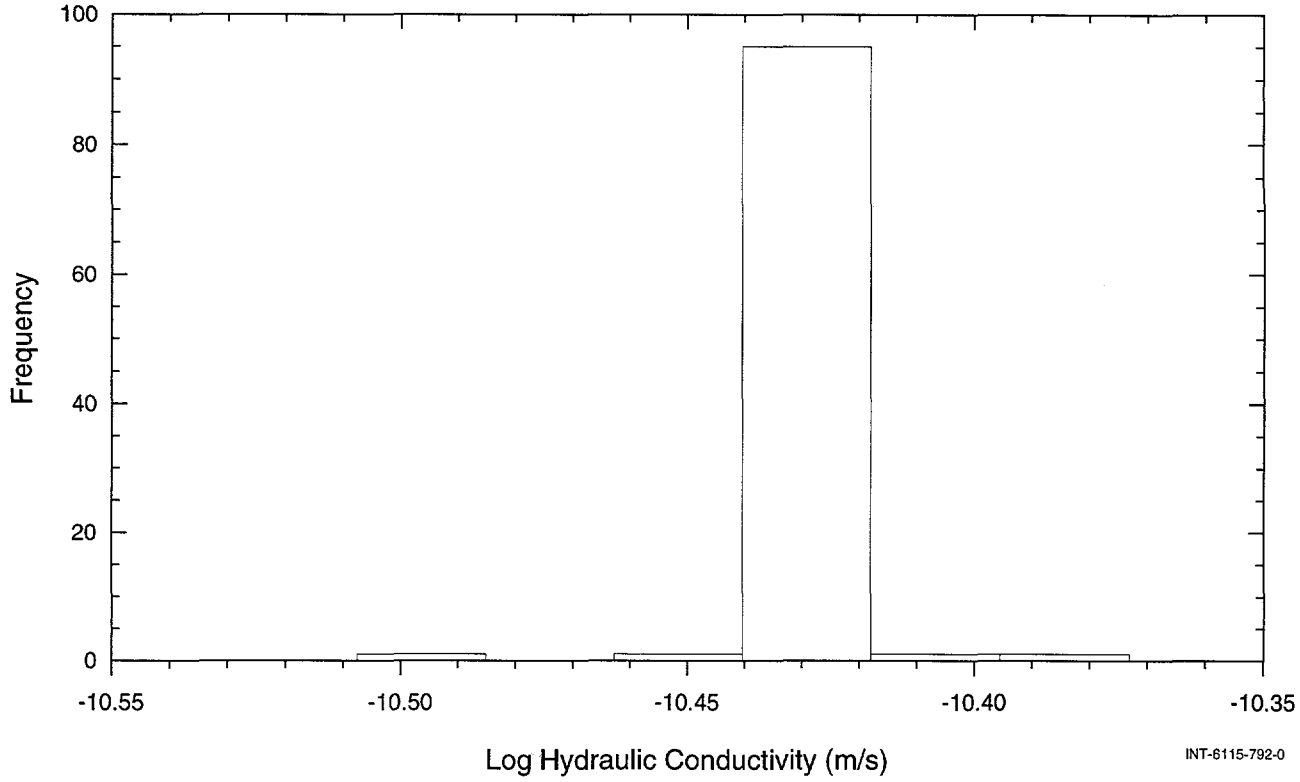

Figure 6-27. Histogram of optimized hydraulic conductivity values from perturbations of the L4P51-C2 pulse baseline optimization values.

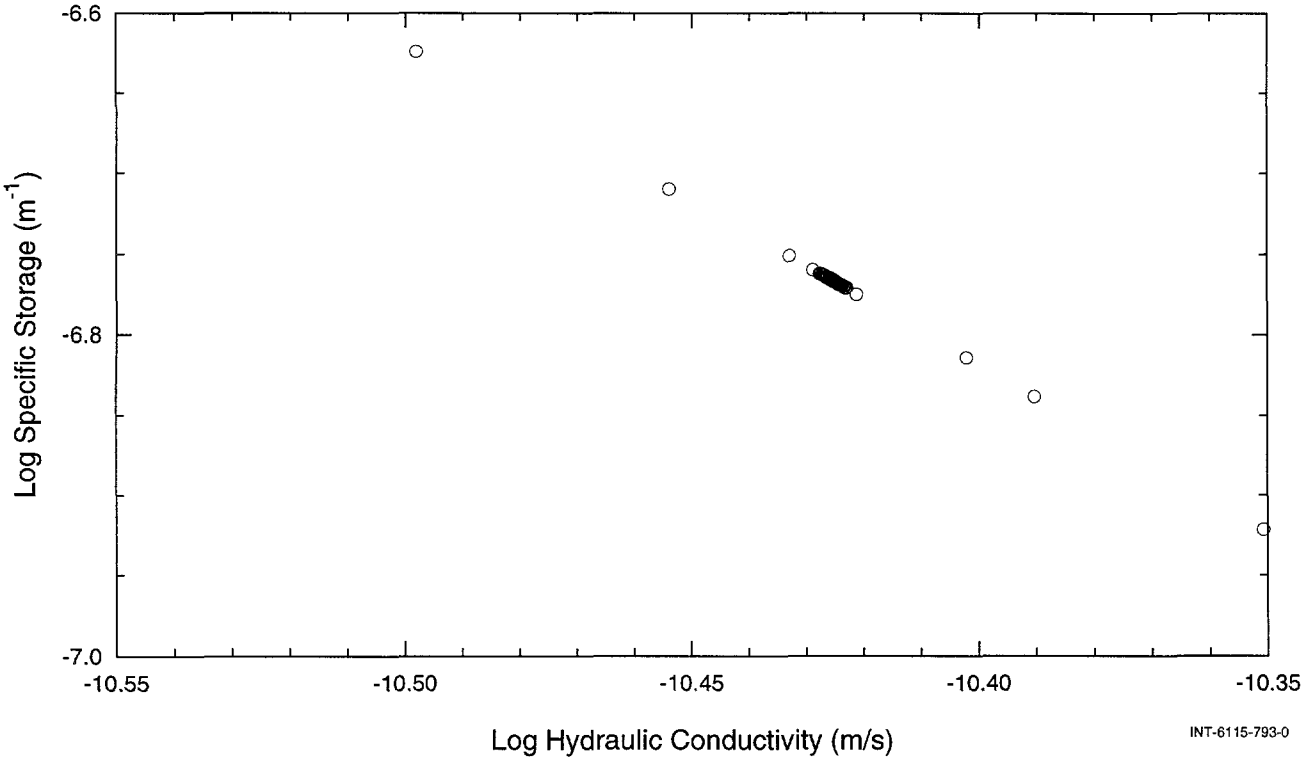

Figure 6-28. XY-scatter plot of optimized hydraulic parameter values from perturbations of the L4P51-C2 pulse baseline optimization values.

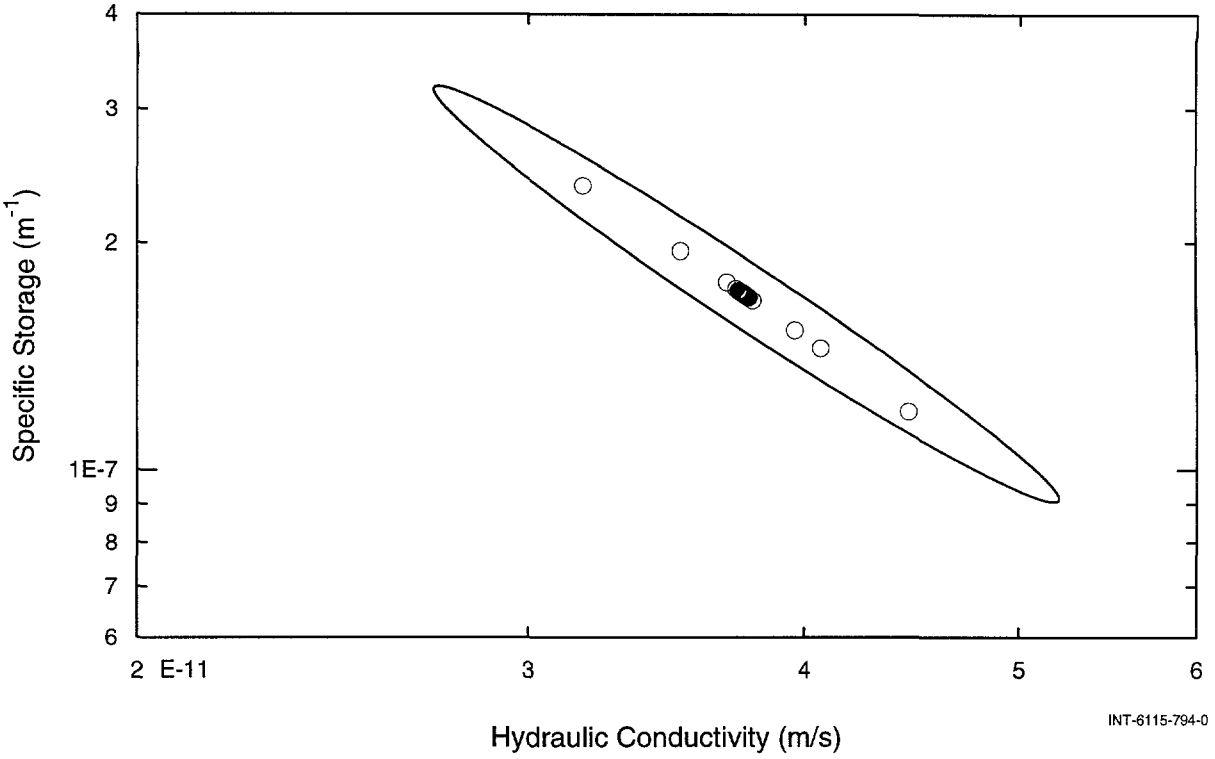

Figure 6-29. 95% joint-confidence region and perturbation results from analysis of L4P51-C2 pulse test.

2 pulse-test baseline K and S_s values along with the K and S_s perturbation results. The joint-confidence region and the perturbation data are seen to be in good agreement with respect to the parameter correlation and uncertainty information that they convey.

In contrast to the well-behaved problem shown above, Figure 6-30, a histogram of estimated K from 213 perturbations of the first L4P51-C1 test zone constant-pressure test baseline fitting-parameter values, shows that three distinct solution populations exist for theproblem as posed. Figure 6-31 is the corresponding xy-scatter plot showing the 213 optimized K and S_s values. The four fitting parameters in this problem were K, S_s, $n1$, and $n2$ (inner-region and outer-region flow dimensions). Figure 6-32 is a plot of the objective-function surface for K and S_s showing the locations of the 213 perturbation results. The objective-function surface shows that the three populations indicated on the histogram in Figure 6-30 correspond to a relatively broad global minimum and two local minima. Figure 6-33 shows the 213 optimized K and S_s perturbation values and the 95% joint-confidence region for the baseline K and S_s values. The joint-confidence region and the perturbation results convey the same K and S_s correlation information, but the perturbation results indicate a greater range of uncertainty than is indicated by the joint-confidence region. The smaller uncertainty range indicated by the joint-confidence region is probably due to the way in which the "bumpy" nature of the minimum affects the calculation of the joint-confidence region.

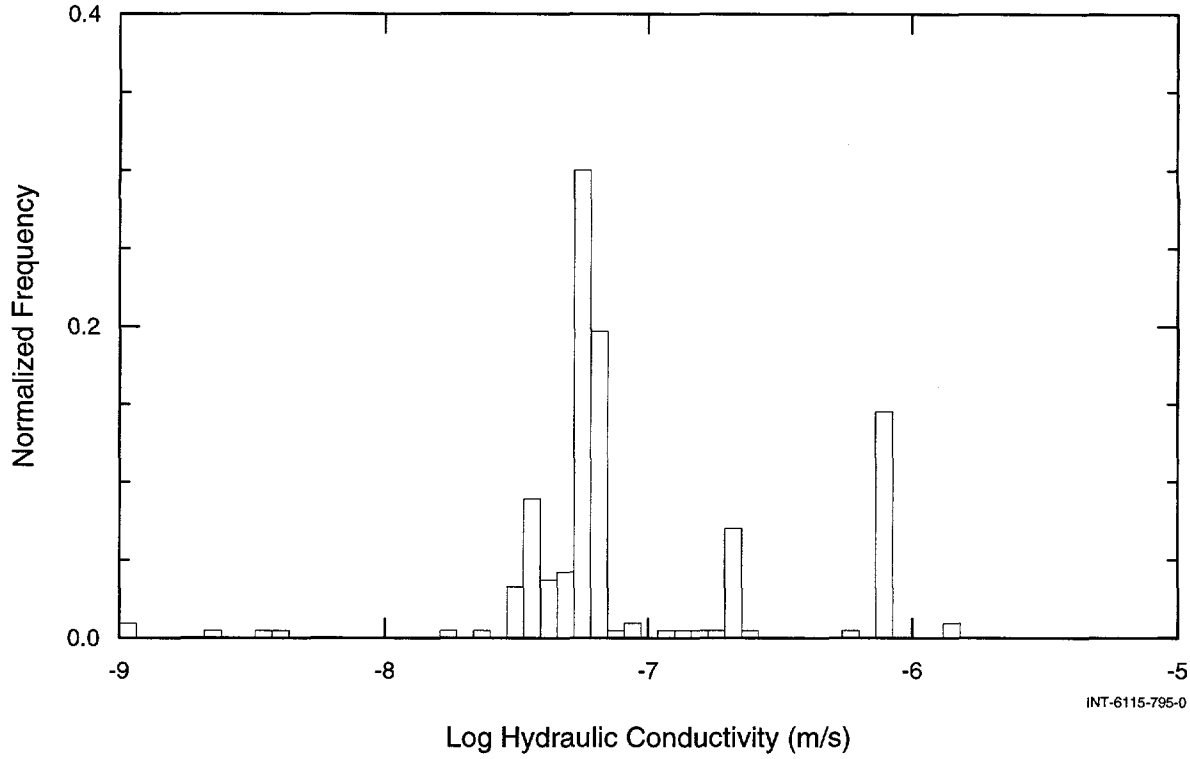

Figure 6-30. Histogram of estimated hydraulic conductivity from analysis of first L4P51-C1 constant-pressure test showing three solution populations.

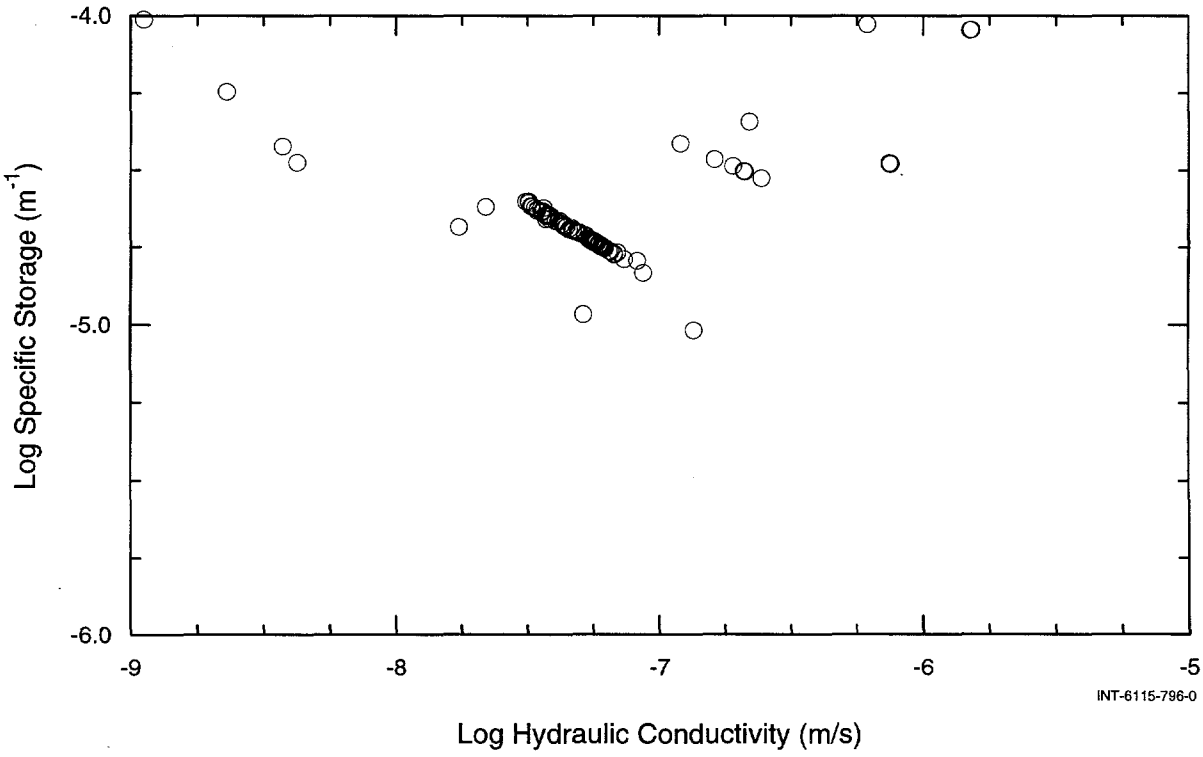

Figure 6-31. Perturbation results from analysis of first L4P51-C1 constant-pressure test.

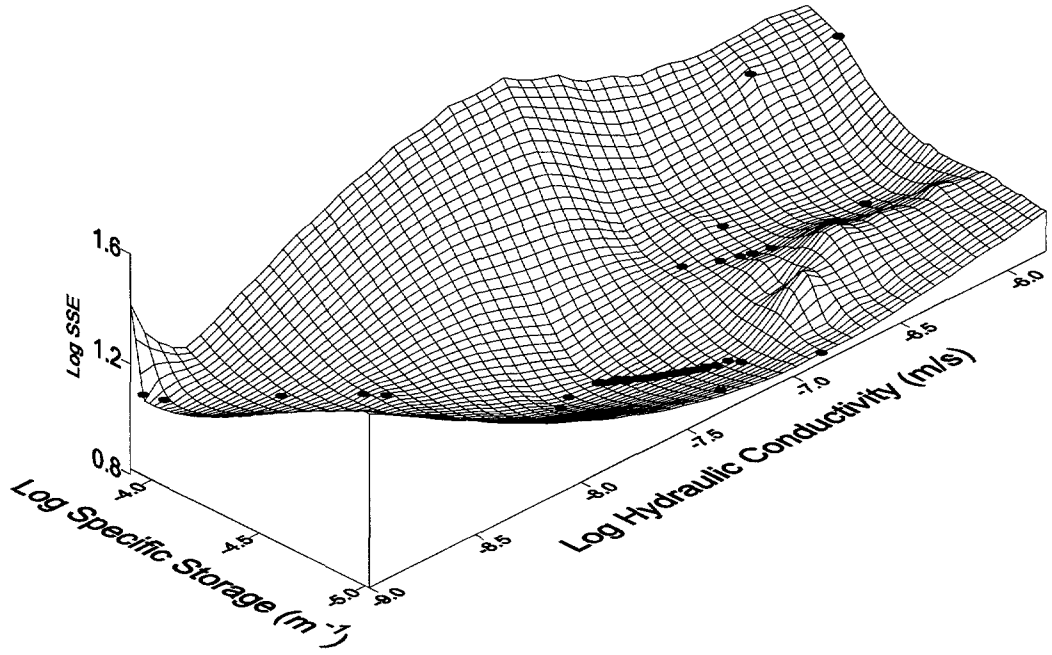

Figure 6-32. Objective-function surface and perturbation results from analysis of first L4P51-C1 constant-pressure test.

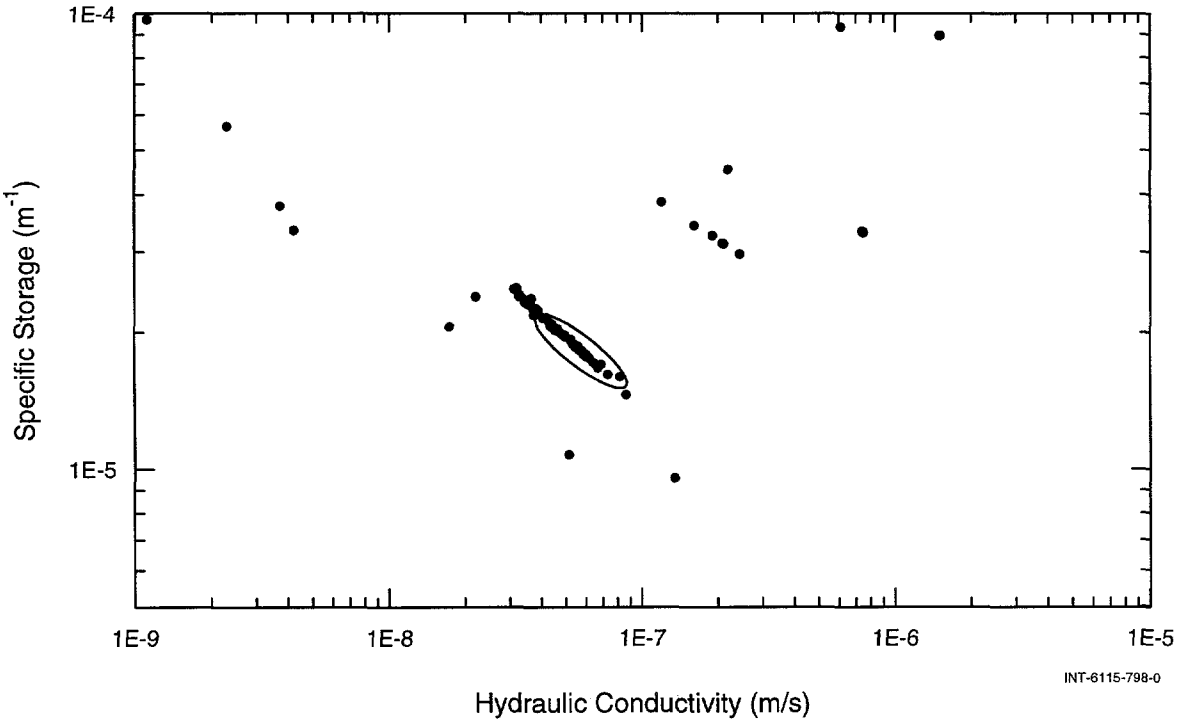

Figure 6-33. Perturbation results and 95% joint-confidence region from analysis of first L4P51-C1 constant-pressure test.

6.2.3.7 Uncertainty Distributions for Non-Fitting Parameters

The next step in quantifying fitting-parameter uncertainty (Figure 6-20) involves estimating the contribution of imperfectly known non-fitting parameters. Non-fitting parameters in GTFM typically include some combination of pressure history, borehole radius, test-zone length (isolated interval), fluid density, fluid thermal expansion coefficient, and test-zone compressibility. Non-fitting parameters are either measured directly and, therefore, have an uncertainty due to measurement error or are estimated from field notes as in the case of a pressure history during borehole drilling.

GTFM utilizes a Latin Hypercube sampling routine in a process to quantify the degree to which non-fitting parameter values affect the fitting-parameter values. Error distributions (normal, log normal, uniform, etc.) are specified for each of the non-fitting parameters. The non-fitting parameters are then sampled a specified number of times and the fitting parameters are optimized for each sampled set. The result is a distribution of joint-confidence regions that reflect both the uncertainty due to correlations among fitting parameters and correlations between fitting and non-fitting parameters.

Figure 6-34 shows the K and S_s estimates from 100 L4P51-C2 test zone 2 pulse analysis sampling/optimization runs. Also shown in the figure is the 95% joint-confidence region from the baseline analysis. Note that the K and S_s sampling/optimization estimates move almost orthogonally to the K and S_s correlation indicated by the joint-confidence region.

This indicates that the optimal K and S_s combinations are correlated to one (or more) of the sampled parameters. A plot of the optimal values for K, S_s, and the sampled parameter, C_{tz} (test-zone compressibility), clearly shows the correlation among the three parameters (Figure 6-35). The plot also shows why C_{tz} must be carefully measured when performing a pulse test. Figure 6-36 shows a plot of the sampled C_{tz} value versus the corresponding estimated n value. No correlation is seen, indicating that no direct correlation exists between the sampled non-fitting parameter (C_{tz}) and the optimized fitting parameter (n).

6.2.4 Uncertainty in Specific-Storage Estimates

Beauheim et al. (1991) report base-case values for halite and anhydrite specific storage of 9.0×10^{-8} m^{-1} and 1.3×10^{-7} m^{-1}, respectively. Values of S_s estimated from single-hole hydraulic tests for both halite and anhydrite, however, are often orders of magnitude greater than these base-case values. Several possible reasons for this have been adduced. McTigue et al. (1989) have suggested that the effects of deformation and creep around an opening might result in an apparent halite specific storage as much as three orders of magnitude greater than the base-case value given above. Stormont et al. (1991) found that borehole excavation (drilling) in halite resulted in increased permeability, i.e., a disturbed rock zone (DRZ), around the borehole to a distance of about three borehole radii. The presence of a DRZ around a borehole affects the borehole's effective hydraulic radius and, as discussed by Beauheim et al. (1993a), specific storage cannot be determined independently of radius.

The statistical features in GTFM can be used to demonstrate that S_s cannot be uniquely determined from single-well test data when a zone of increased (or decreased)

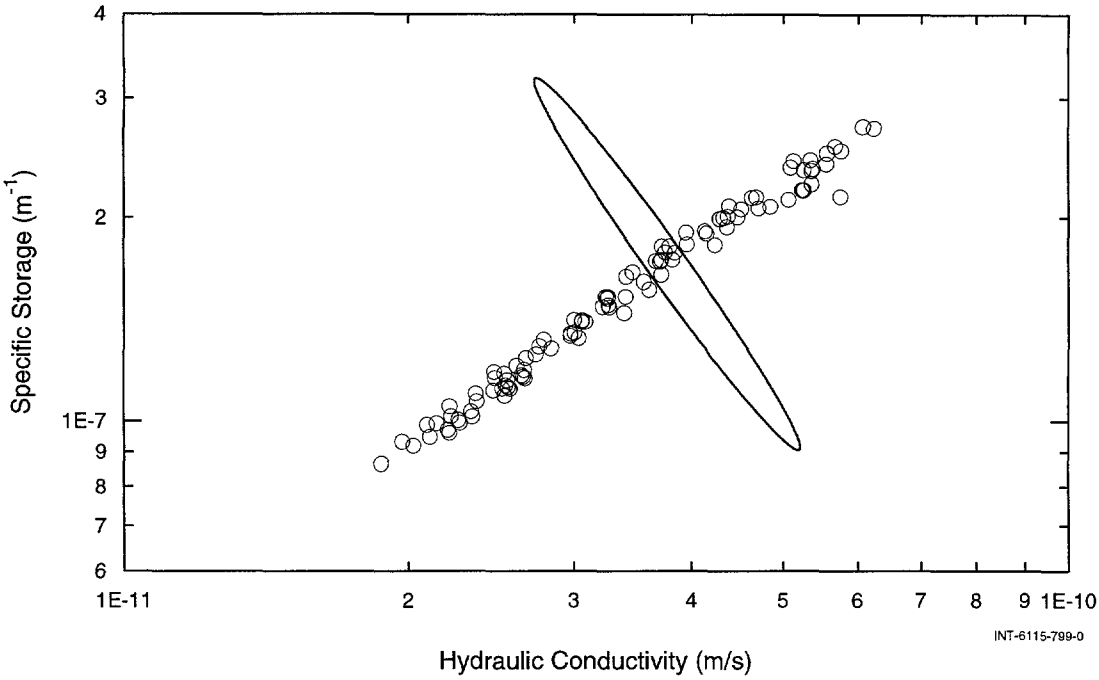

Figure 6-34. 95% joint-confidence region from baseline analysis and hydraulic conductivity and specific storage estimates from sampling analysis.

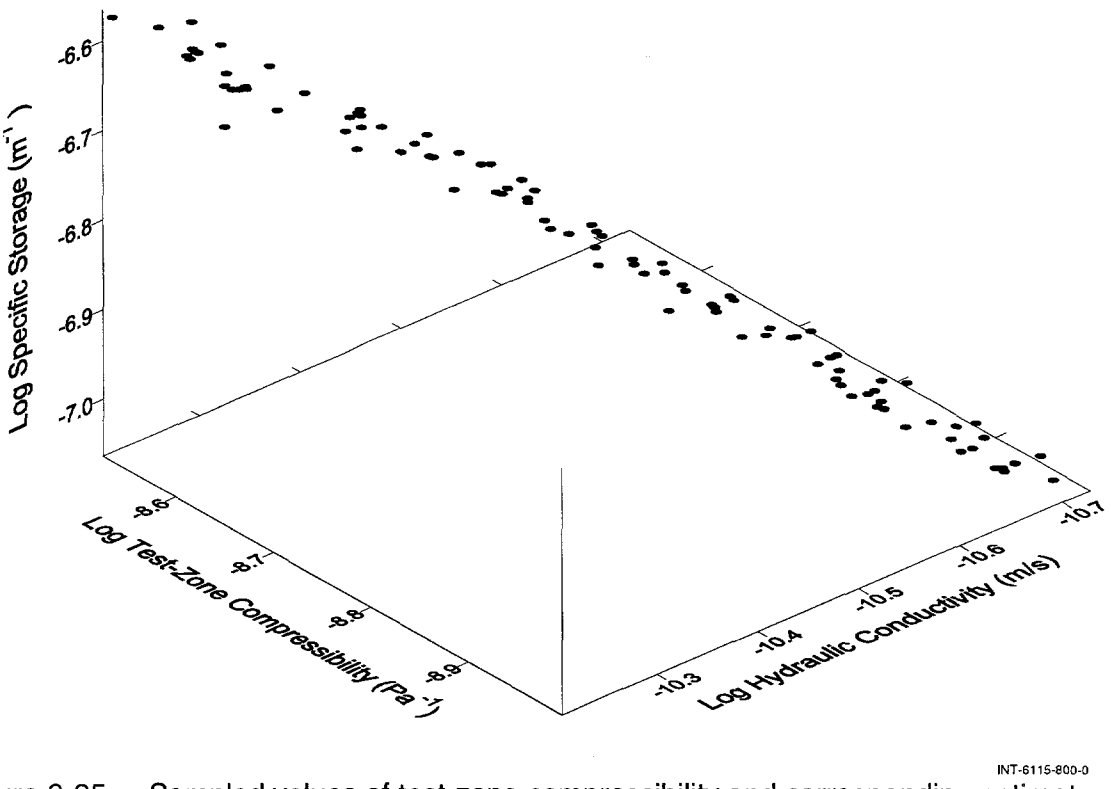

Figure 6-35. Sampled values of test-zone compressibility and corresponding estimates of hydraulic conductivity and specific storage.

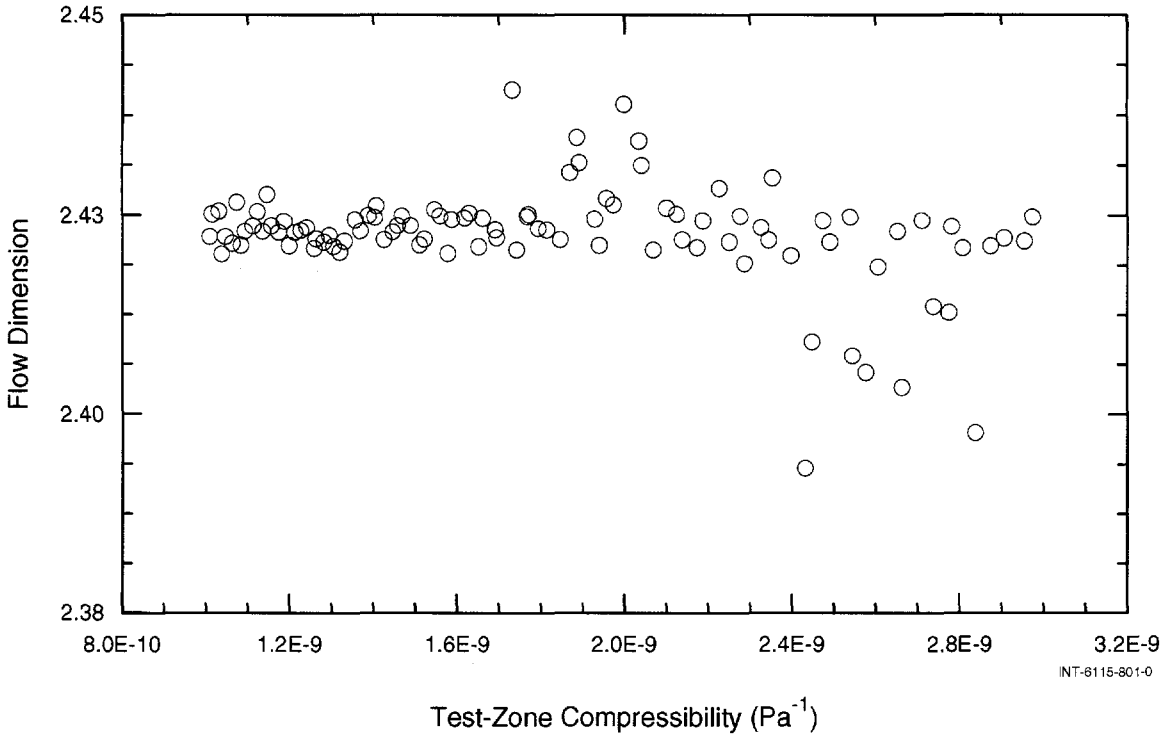

Figure 6-36. Sampled test-zone compressibility values and corresponding estimated flow-dimension values.

permeability develops around the borehole, a condition commonly known as a "skin".

Figure 6-37 shows a plot of parameter space for a problem where S_s and borehole skin properties (in this case, the thickness of the DRZ around the borehole) are being estimated from data from a single-borehole test. The optimal solution to the problem is represented by the black-shaded region on the figure (the SSEs have been normalized such that the minimum error corresponds to 1). The figure shows that no unique minimum (solution) exists for the problem as posed. All combinations of the two parameters that lie along the line of solutions (color index close to 1) provide effectively equivalent solutions to the problem. No combination of constraints from a single-borehole test can be found that are sufficient to define a unique solution. In contrast, Figure 6-38 shows the same problem with an additional constraint imposed, i.e., data from an observation borehole at some distance from the test borehole. The figure shows that the problem, as it is now posed, does have a unique solution. We believe that all of the S_s estimates that were made from tests performed during the Salado hydraulic testing program (all single-borehole tests) are potentially affected by skin (and compliance) effects, and should not be used quantitatively.

6.3 Assumptions Used In Test Analysis

The assumptions used in the test analyses presented in this report were:

- Darcy's law was valid for the conditions under which the tests were performed;
- The only factor causing transient pressure and flow responses was the pressure

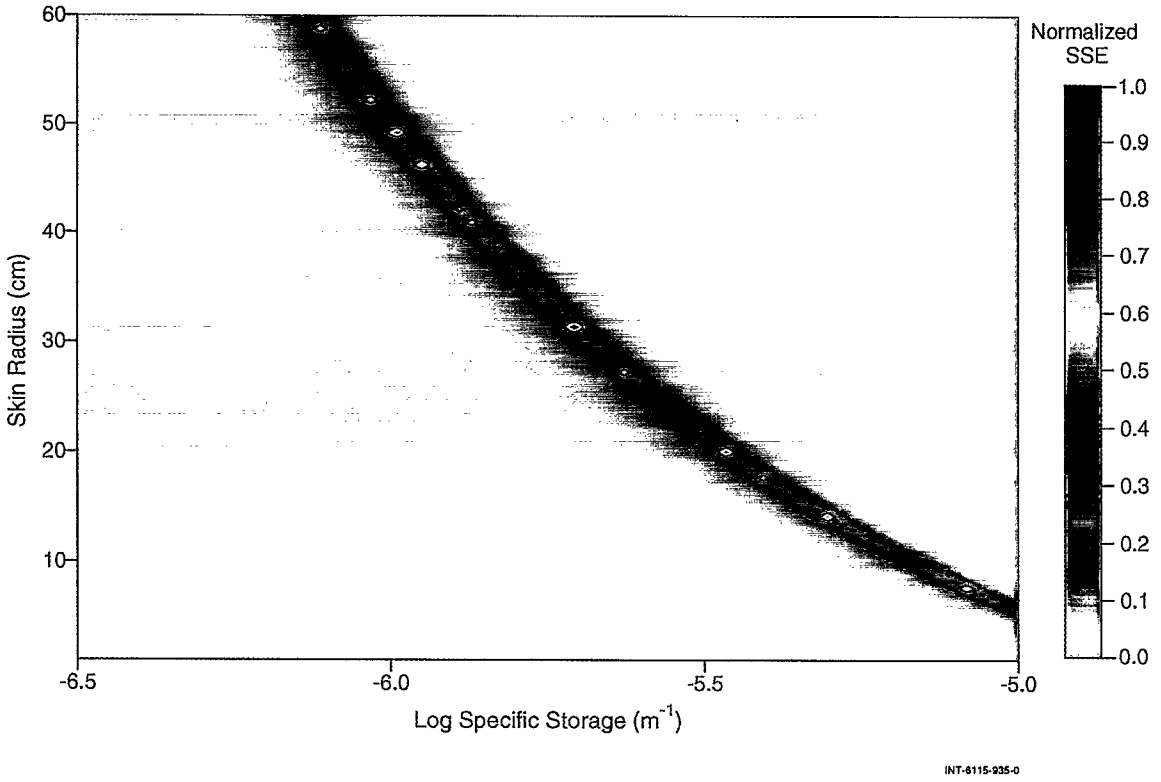

Figure 6-37. Parameter space showing continuous solution combinations of specific storage and skin (DRZ) radius.

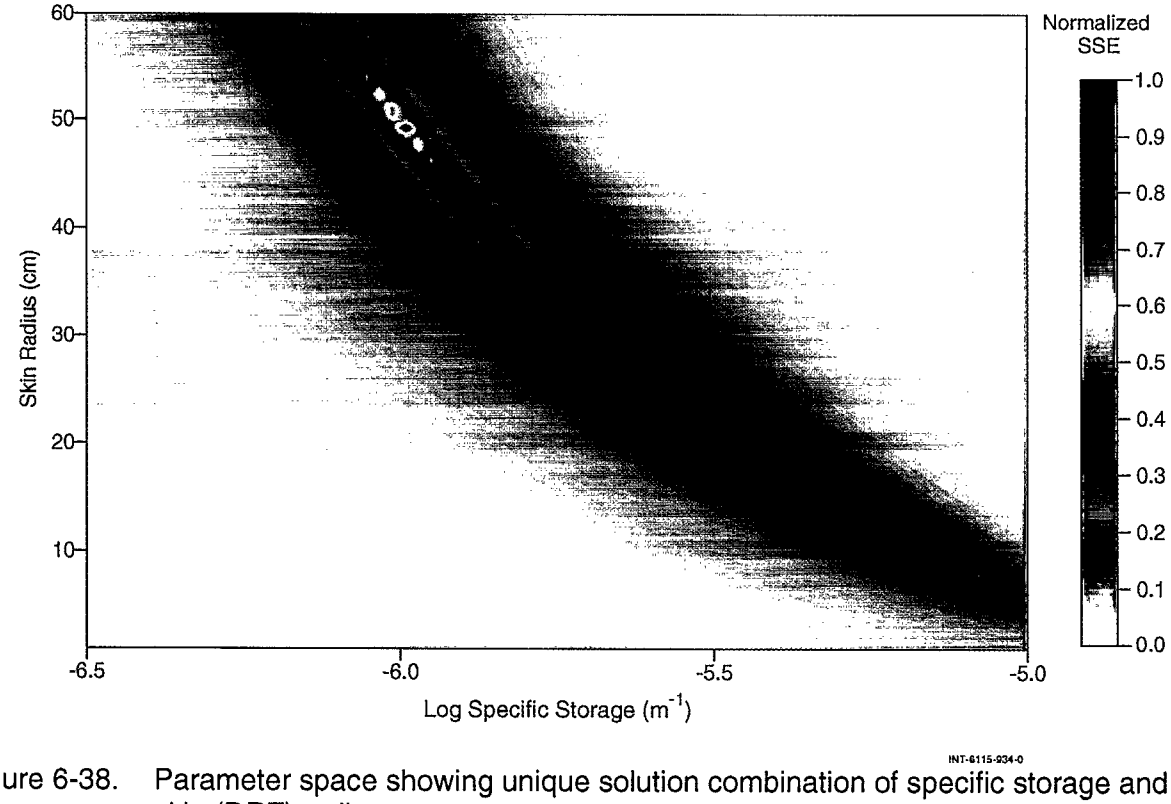

Figure 6-38. Parameter space showing unique solution combination of specific storage and skin (DRZ) radius.

disequilibrium between the borehole and the surrounding formation induced by the testing sequence;

- All flow was single-phase (brine) only;
- Test intervals of slanted boreholes could be treated as vertical cylindrical sections having thicknesses equal to the vertical thicknesses of the tested strata and effective radii calculated by averaging elliptical axes; and
- The pore pressure in each test horizon was static (constant with time), and radially and longitudinally (parallel to the borehole axis) invariant before drilling began.

Additional details and rationale related to these assumptions are presented in Beauheim et al. (1993a).

6.4 Material Properties and Experimental Parameters Used in Test Interpretations

To interpret hydraulic tests using either analytical solutions or GTFM, a number of material properties and experimental parameters must be specified. The specific properties and parameters required vary among the interpretive methods. These properties include the porosity and elastic moduli (drained bulk modulus, solids modulus, shear modulus, Young's modulus, and Poisson's ratio) of the lithology(ies) being tested, and the compressibility, density, viscosity, and thermal-expansion coefficient of the test-zone and formation brine. Porosity, elastic moduli, brine density, and brine compressibility are used to calculate the specific storage of the formation for GTFM. Brine viscosity is required to convert between hydraulic conductivity and permeability. The thermal-expansion coefficient of brine is used to incorporate the effects of variations in test-zone temperatures on test-zone pressures in GTFM. The thermal expansion of other materials present in test zones, such as stainless-steel tool components, is neglected because the thermal-expansion coefficients of these materials are all more than an order of magnitude lower than the thermal-expansion coefficient of brine. Experimental parameters important in test interpretation include the radius and length of each test zone, the volume of water contained within each test zone, and the aggregate compressibility of everything within each test zone.

6.4.1 Material Properties

Most of the values of the material properties necessary for test interpretation can be reliably estimated to within an order of magnitude or less. For a given rock type, estimates of specific storage based on values of its constituent parameters range over several orders of magnitude. However, because specific storage is treated as a fitting parameter in GTFM simulations rather than as a fixed parameter, the calculated ranges are used only to provide an initial focus for the GTFM simulations. Beauheim et al. (1991, 1993a) presented base-case values and ranges of values for the necessary input parameters, along with rationales for their selection. These parameters and their values are shown in Table 6-1.

6.4.2 Experimental Parameters

The experimental parameters needed for test interpretation include the dimensions of the borehole and test zone and the test-specific compressibility of each test zone. The radius of a test zone is determined from the radial-LVDT measurements, borehole caliper measurements, or assumed to be equal to the radius of the drill bit when no other information is available. Test-zone length is determined from the position of a test tool in a borehole, knowing the dimensions of the test-

Table 6-1. Material Properties Used in Test Interpretations[1]

Material	Parameter	Base-Case Value	Range of Uncertainty
halite	porosity	0.01	0.001 - 0.03
	Young's modulus	31.0 GPa	20.7 - 36.5 GPa
	Poisson's ratio	0.25	0.17 - 0.31
	drained bulk modulus	20.7 GPa	15.0 - 21.7 GPa
	solids modulus	23.4 GPa	22.8 - 24.0 GPa
	shear modulus	12.4 GPa	8.1 - 15.6 GPa
	specific storage	9.0E-8 m^{-1}	2.8E-8 - 3.5E-7 m^{-1}
anhydrite	porosity	0.01	0.001 - 0.03
	Young's modulus	75.1 GPa	59.0 - 78.9 GPa
	Poisson's ratio	0.35	0.31 - 0.42
	drained bulk modulus	83.4 GPa	68.1 - 85.0 GPa
	shear modulus	27.8 GPa	21.4 - 30.4 GPa
	specific storage	1.3E-7 m^{-1}	9.7E-8 - 2.3E-7 m^{-1}
Salado brine	density	1220 kg/m^3	1200 - 1250 kg/m^3
	compressibility (gas saturated)	2.7E-10 Pa^{-1}	2.5E-10 - 2.9E-10 Pa^{-1}
	viscosity[2]	2.1 cp	
	thermal-expansion coefficient	4.6E-4°C^{-1}	

[1] Data and rationales in Beauheim et al. (1991) except as noted
[2] McTigue (1993)

tool components. The volume of water contained within a test zone includes the water contained in injection and vent lines (tubing) between the test zone and valves positioned outside of the hole. The volume is calculated from the dimensions of the hole and tubing, and the known displacement volume of the test tool. Beauheim et al. (1991) discuss the calculation of test-zone volume in greater detail.

Test-zone compressibility is an important factor in permeability testing performed under shut-in conditions because, given the volume of a test zone, the test-zone compressibility governs the pressure change resulting from the flow of a given amount of fluid into or out of the test zone. Compressibilities calculated using data from pulse withdrawals, constant-pressure injections/withdrawals, and pressure buildups performed during permeability-testing sequences are presented in Table 6-2.

Beauheim et al. (1991, 1993a) discuss the factors that contribute to test-zone compressibility and methods used to quantify it. They noted from compliance tests that compressibility responses are not only instantaneous, but also include transient components as different materials respond at different rates. These transient compressibility effects are also reflected in measurements taken

Table 6-2. Summary of Test-Zone and Guard-Zone Compressibility Information

Test Sequence	Zone	Event	Initial Pressure (MPa)	Final Pressure (MPa)	Volume Produced (cm^2)	Zone Fluid Volume (cm^2)	Zone Compressibility (Pa^{-1})
L4P51-C1	guard	CPW	8.451	6.398	12	3967	1.5E-9
	guard	PB	—	—	—	3967	1.9E-9
	test	CPW1	8.831	8.771	295	8784	5.6E-7
	test	CPW2	9.039	8.872	177	8784	1.2E-7
	test	CPW3	9.200	9.183	23	8784	1.5E-7
L4P51-C2	test 2	PW	8.330	4.362	38	3967	2.4E-9
	test 2	CPW	8.336	4.378	29	3967	1.8E-9
	test 2	PB	—	—	—	3967	1.5E-9
L4P52-B	test	CPW	8.957	7.859	10	3134	2.9E-9
	test	CPI1	9.030	9.472	4	3134	2.9E-9
	test	CPI2	9.454	9.989	1.4	3134	8.3E-10
	test	CPI3	9.858	10.915	5	3134	1.5E-9
S1P74-A	test	CPW	6.420	5.621	6	3785	2.0E-9
S1P74-B	test 1	PW	9.105	7.820	9	8772	8.0E-10
	test 2	PW1	8.666	6.951	7	2542	1.6E-9
	test 2	PW2	8.678	4.591	21	2542	2.0E-9

during actual permeability testing. Figure 6-39 shows the test-zone pressures during the S1P73-B testing sequence along with the change in test-zone volume estimated from the radial LVDT borehole-closure data. Note that the change in test-zone volume is estimated assuming that borehole closure is uniform along the length of the test zone. Borehole-closure data from other testing sequences indicate that this is not true. Predicted volumes of fluid withdrawn based on borehole-closure data are sometimes greaterby more than a factor of two than the actual measured volumes. This indicates that closure is greater at the point of measurement than it is at other places along the test zone, such as at the borehole terminus or near the packer. The amount of closure may also vary with rock type; the LVDTs during the S1P73-B testing were in contact with argillaceous halite (clay J), not MB138. Even with this uncertainty, we can investigate, in a qualitative manner, how borehole compliance will affect different types of hydraulic tests.

The S1P73-B testing sequence was chosen because all the Salado hydraulic test types (pulse, constant pressure, and pressure recovery) are represented and the radial LVDT data are of good quality. Figures 6-40 to 6-43 show simulated test responses with and without the borehole closure shown in Figure 6-39. The effects of borehole compliance are most easily seen in the normalized pulse response (Figure 6-40) and the early-time portion of the constant-pressure flowrate data (Figure 6-41). The LVDT data indicate that, during a pulse-withdrawal test, the borehole radius initially decreases in response to the pressure decrease (Figure 6-39). As the pressure begins to recover, the borehole radius also increases for some period of time,

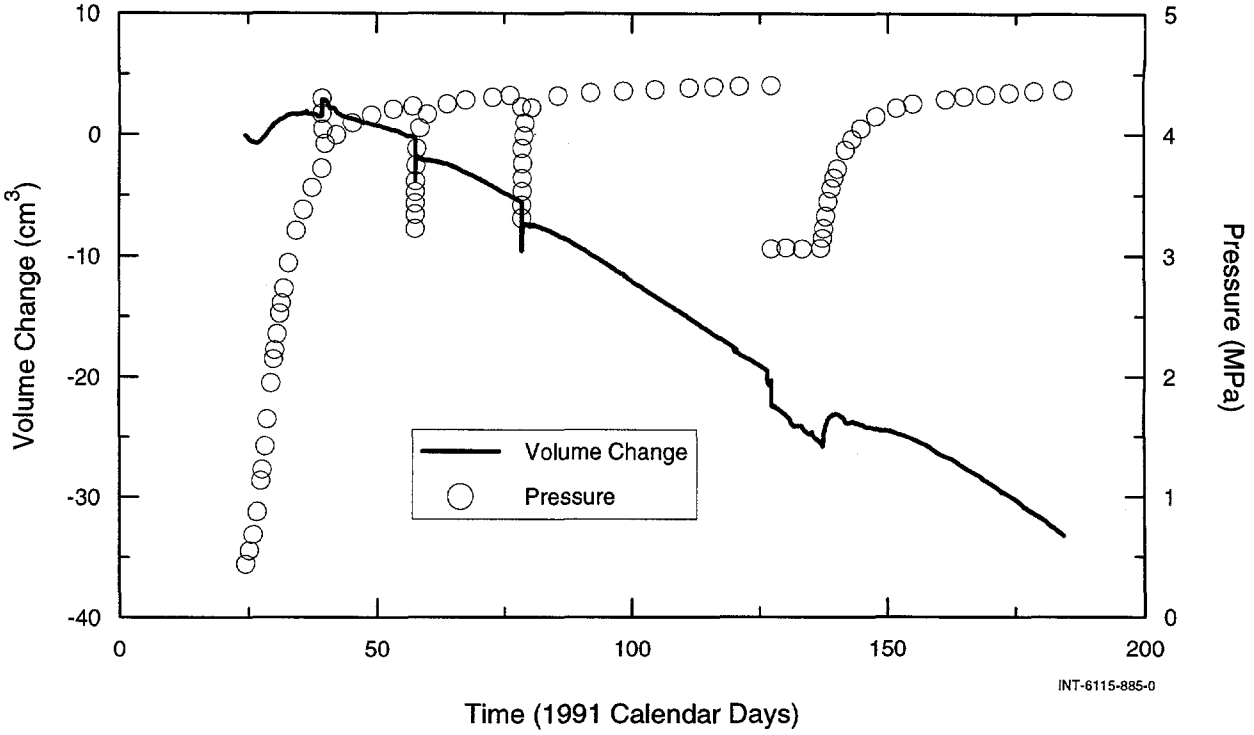

Figure 6-39. Estimated test-zone volume change and concurrent test-zone pressure during S1P73-B testing.

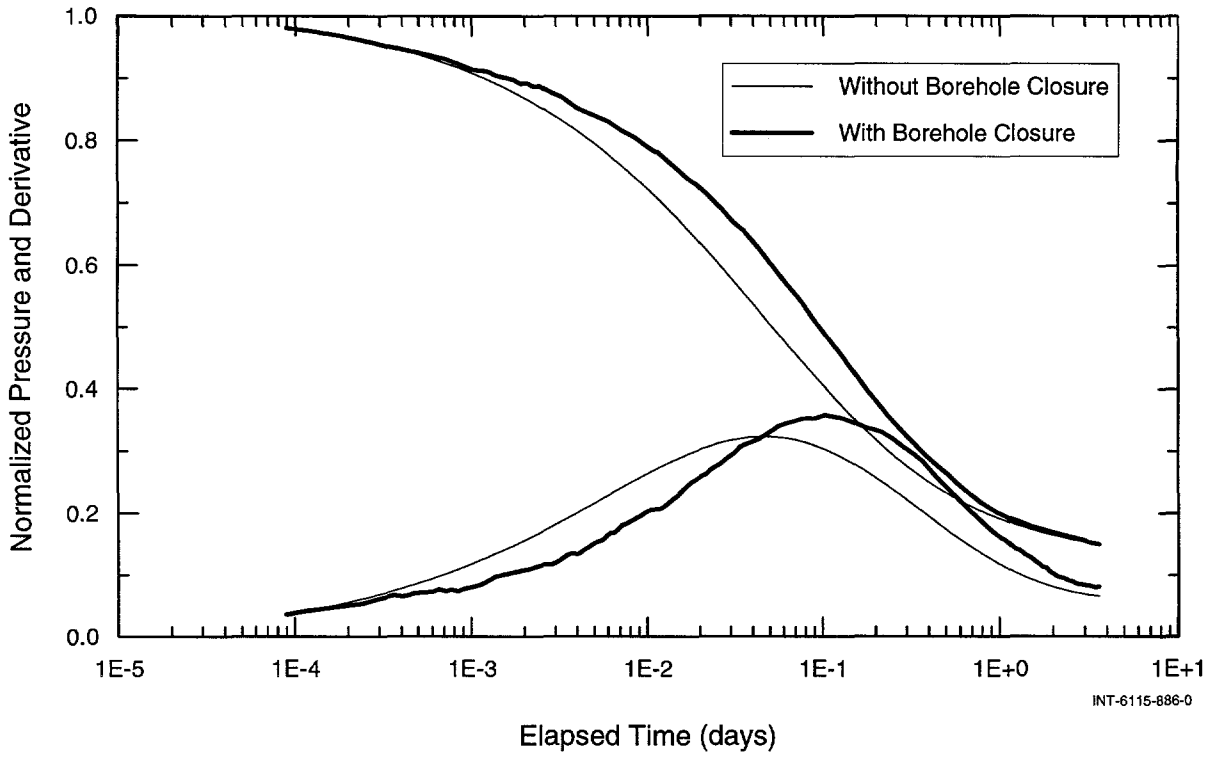

Figure 6-40. Simulated pulse responses with and without borehole closure.

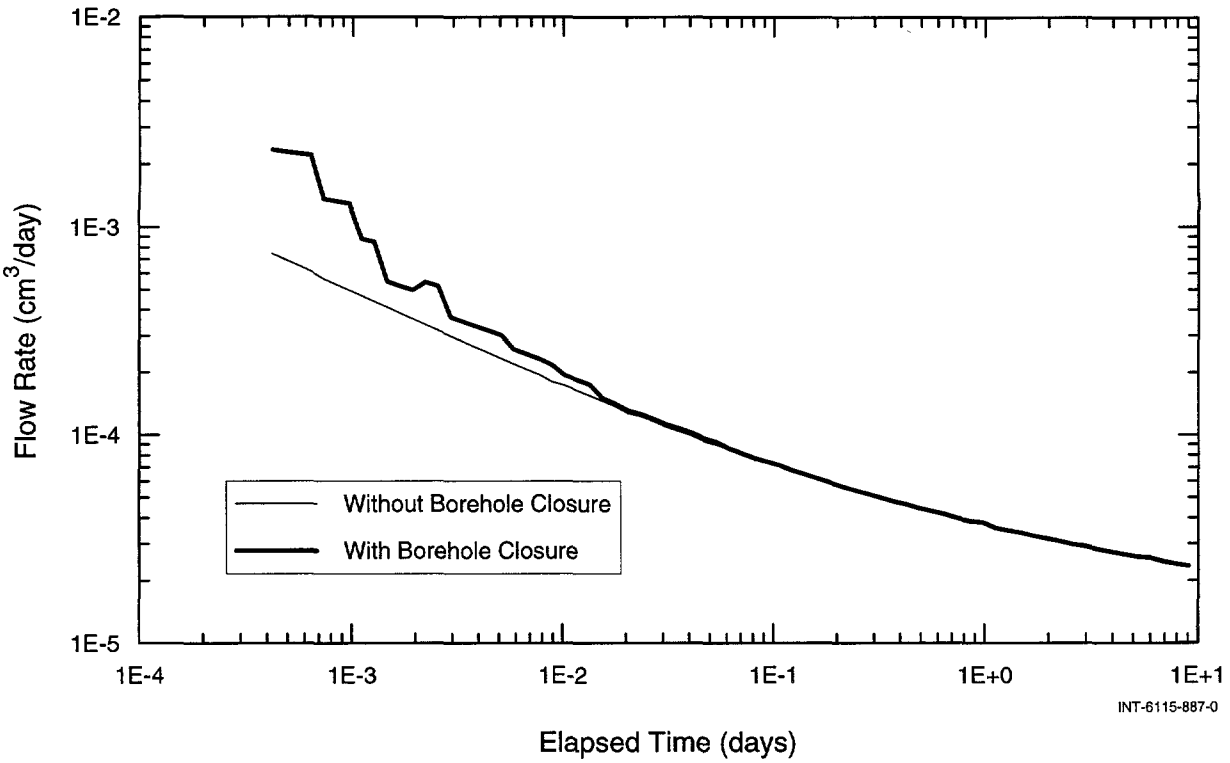

Figure 6-41. Simulated constant-pressure flow rate with and without borehole closure.

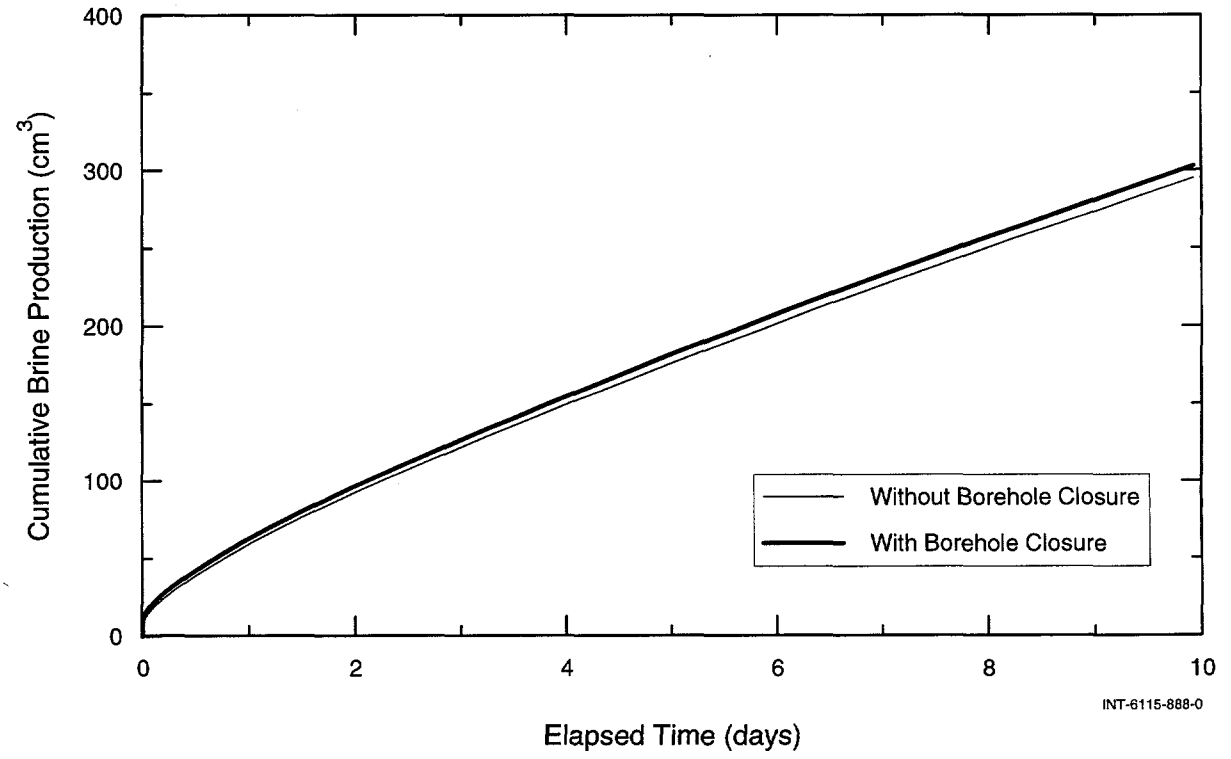

Figure 6-42. Simulated constant-pressure production with and without borehole closure.

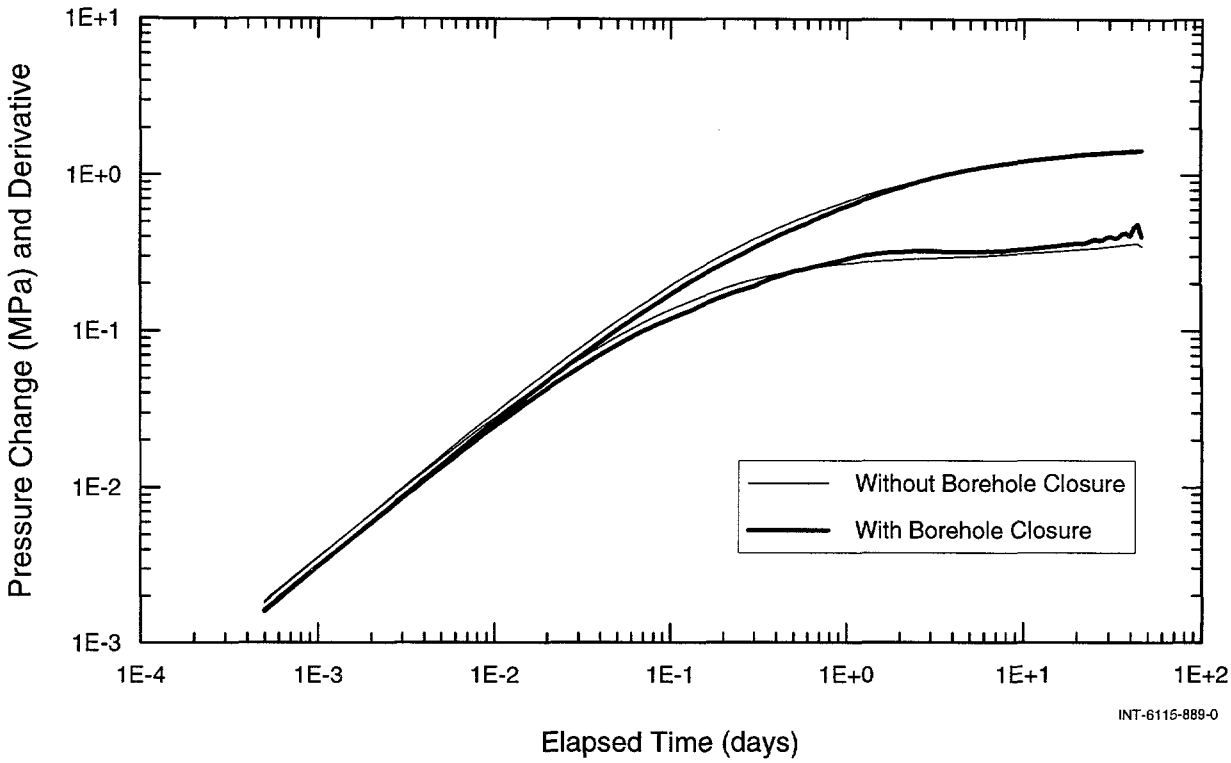

Figure 6-43. Simulated pressure-buildup test with and without borehole closure.

which, in turn, acts to slow the pulse recovery. This type of behavior was observed during the S1P74-B test zone 2 testing, where two pulse tests of different magnitudes were performed. The initial pressure change for the second pulse was greater than that of the first by a factor of 2.4. Borehole compliance appeared to affect the second pulse to a greater degree, and a plot of the two normalized pulse responses showed the same differences exhibited by the two responses in Figure 6-40.

The LVDT data also indicate that the rate of borehole closure increases during the early-time portion of the constant-pressure withdrawal test. This closure acts to increase the early-time flow rates. Beauheim et al. (1993a) noted that the early-time constant-pressure responses were difficult to match during the modeling process.

Borehole compliance appears to affect some types of tests more than others. While the effect is easily seen in the pulse response, it would be difficult to detect in the pressure-buildup test (Figure 6-43) if the typical amount of data noise were present. This would, in turn, make matching the responses with a consistent set of hydraulic-parameter values difficult unless the compliance effects were explicitly included in the simulation. Including the LVDT data in the simulation is also problematic, however, given that the measured changes in radius do not appear to be uniform along the borehole. At this point in the evolution of the Salado permeability testing analyses, LVDT data typically are not included in the simulation, both for the reasons discussed above and also because the LVDT data are often noisy. The differences in the simulated pulse responses shown in Figure 6-40 reflect a 0.0006-cm change in borehole

radius over the duration of the test. The magnitude of this value makes it sensitive to irregularities in the wall of the borehole. The radial LVDTs slide along the wall of the borehole due to axial test-tool movement during testing. This movement is reflected as noise in the LVDT data. Even with these problems, we believe that the LVDT data provide important insights into the Salado test responses, providing explanations for observed responses which might otherwise require exotic (and incorrect) conceptual models.

THIS PAGE INTENTIONALLY LEFT BLANK

7. ESTIMATION OF HYDRAULIC PROPERTIES

This section presents individual interpretations of the pressure-pulse, constant-pressure flow, and pressure-buildup/falloff tests conducted in the boreholes discussed in Section 5. Both analytical and numerical (GTFM) interpretations of the tests and estimates of the hydraulic parameters of the tested intervals are given. A summary of the interpreted results is presented in Table 7-1.

7.1 L4P51-C1 AND 2

Borehole L4P51 was originally drilled vertically downward into the floor of Room L4 in October 1989 to allow testing of MB139, PH-3, and clay D (L4P51-A) and was deepened in October 1990 to allow testing of anhydrite "c" and clay B (L4P51-B). For permeability-testing sequence L4P51-C, the borehole was deepened between 1 and 15 April 1992 to 22.20 m below the room floor, allowing testing of MB140 and H-m2 (the halite directly above MB140). The "C1" suffix designates the double-packer test-tool configuration shown in Figure 7-1 and the "C2" suffix designates the triple-packer test-tool configuration shown in Figure 7-2. The triple-packer test-tool configuration was installed on 13 May 1992 to determine if pressure bypass was occurring around the guard-zone packer of the double-packer test tool. The same intervals were tested during both installations and, therefore, the tests are discussed together.

Figure 7-3 shows a plot of the pressure data from the test and guard zones collected during L4P51-C1 testing. Figure 7-4 shows a plot of the pressure data from the test zone 1, test zone 2, and guard zone collected during L4P51-C2 testing. The pressure values presented in Figures 7-3 and 7-4 have been compensated for the elevation differences between the locations of the pressure transducers and the centers of the tested units in the test and guard zones. The test-zone and guard-zone pressures from L4P51-C1 were compensated by adding 0.247 and 0.204 MPa, respectively, to the pressures measured by the pressure transducers and reported by Chace et al. (1998). The test zone 1, test zone 2, and guard-zone pressures from L4P51-C2 were compensated by adding 0.247, 0.204, and 0.185 MPa, respectively, to the pressures measured by the pressure transducers and reported by Chace et al. (1998). Packer pressures during the L4P51-C1 and C2 testing are shown in Appendix D.

7.1.1 Halite (H-m2) Testing (L4P51-C1 Guard Zone and L4P51-C2 Test Zone 2)

Two series of tests were performed in H-m2: the L4P51-C1 guard-zone tests and L4P51-C2 test zone 2 tests. Each of the two series of tests consisted of a pulse-withdrawal (PW) test followed by a constant-pressure-withdrawal (CPW) and a subsequent pressure-buildup test. The L4P51-C1 tests, performed using a double-packer test tool, were repeated using a triple-packer test tool (L4P51-C2) because the responses observed in the first series of tests were unlike any that had been observed in previous Salado permeability tests and we wished to rule out the possibility that the responses were due to packer bypass and not formation response.

The initial shut-in preceding the L4P51-C1 tests was on 30 April 1992 (Calendar Day 121). The pulse-withdrawal test was initiated on 7 May 1992 (Calendar Day 128). The test tool was then removed on 11 May and reinstalled on 13 May (Calendar Days 132 and 134) and the guard zone was again shut in (13 May). A 13-day constant-pressure-

Table 7-1. Summary of Test-Interpretation Results

Hole/Zone	Map Unit	Test	Analysis Method	Map Unit Thickness (m)	Average Hydraulic Conductivity K (m/s)	Average Permeability k (m^2)	Average* Specific Storage S_s (m^{-1})	Formation Pore Pressure P_f (MPa)	Test Pressure (MPa)	Outer Flow Dimension
L4P51-C1/guard	H-m2	CPW	GTFM	1.05	6.7E-10	1.2E-16	2.1E-7	--	6.25	1.1
		PB	analytic	1.05	1.1E-10	2.0E-17	--	>8.5	--	2
L4P51-C2/test 2	H-m2	CPW	GTFM	1.05	1.6E-10	2.8E-17	5.4E-9	--	4.4	1.3
L4P51-C1/test	MB140	SI	--	4.17	--	--	--	>9.25	--	--
		CPW 1	GTFM	4.17	3.2E-13	5.6E-20	9.1E-11	--	8.30	2.8
		CPW 2	GTFM	4.17	8.0E-14	1.4E-20	1.7E-11	--	8.62	2.9
		CPW 3	GTFM	4.17	7.1E-13	1.2E-19	4.0E-8	--	8.70	2.8
L4P52-B/guard	AH-1, H-5, AH-2	SI	--	1.05	--	--	--	8.2	--	--
L4P52-B/test	MB138, clay K	CPW	type curve	0.10	6.1E-12	1.1E-18	--	--	7.9	2
		CPI 1	type curve	0.10	7.7E-12	1.4E-18	--	--	9.5	2
		PB	analytic	0.10	1.3E-11	2.3E-18	--	--	9.08	2
		through	GTFM	0.10	1.0E-11	1.8E-18	1.6E-4	9.08	7.85†	1.64
		CPI 3		0.10	1.8E-11	3.1E-18	1.6E-4	9.08	8.50†	1.64
				0.10	2.1E-11	3.7E-18	1.6E-4	9.08	9.47†	1.64
				0.10	4.9E-11	8.7E-18	1.6E-4	9.08	9.95†	1.64
				0.10	8.4E-11	1.5E-17	1.6E-4	9.08	10.83†	1.64
		PF	GTFM	0.10	2.0E-11	3.6E-18	6.3E-5	9.08	9.18†	1.77
				0.10	2.0E-11	3.5E-18	6.3E-5	9.08	9.47†	1.77
				0.10	3.6E-11	6.3E-18	6.3E-5	9.08	9.95†	1.77
				0.10	8.4E-11	1.5E-17	1.6E-4	9.08	10.83†	1.77
S1P74-A/guard	anhydrite "b"	SI	--	0.06	--	--	--	>4	--	--
S1P74-A/test	anhydrite "a"	PB	analytic	0.20	2.1E-13	3.6E-20	--	--	6.54	2
		all	GTFM	0.20	4.7E-17	8.3E-24	2.8E-5	6.73	2†	2
			GTFM	0.20	1.1E-14	1.9E-21	2.8E-5	6.73	4†	2
			GTFM	0.20	2.2E-13	3.9E-20	2.8E-5	6.73	5†	2
			GTFM	0.20	4.3E-13	7.5E-20	2.8E-5	6.73	6.5†	2
S1P74-B/guard	14, 15	SI	--	0.79	--	--	--	>4.77	--	--
S1P74-B/test 1	MB138, clay K	PW	GTFM	0.31	3.3E-11	5.8E-18	2.4E-5	10.27	--	1.2
S1P74-B/test 2	clay J	PW 1	GTFM	0.81	2.0E-11	3.5E-18	3.8E-8	8.67	--	1.5
		PW 2	GTFM	0.81	2.0E-11	3.5E-18	3.6E-7	8.72	--	1.3

Key: PB = pressure-buildup test; SI = shut-in pressure buildup; PF = pressure-falloff test; PW = pulse-withdrawal test; CPW = constant-pressure-withdrawal test; CPI = constant-pressure-injection test.

*All of the specific-storage estimates are potentially affected by skin effects and should not be used quantitatively.

†Indicates pressure specified in model for given hydraulic conductivity.

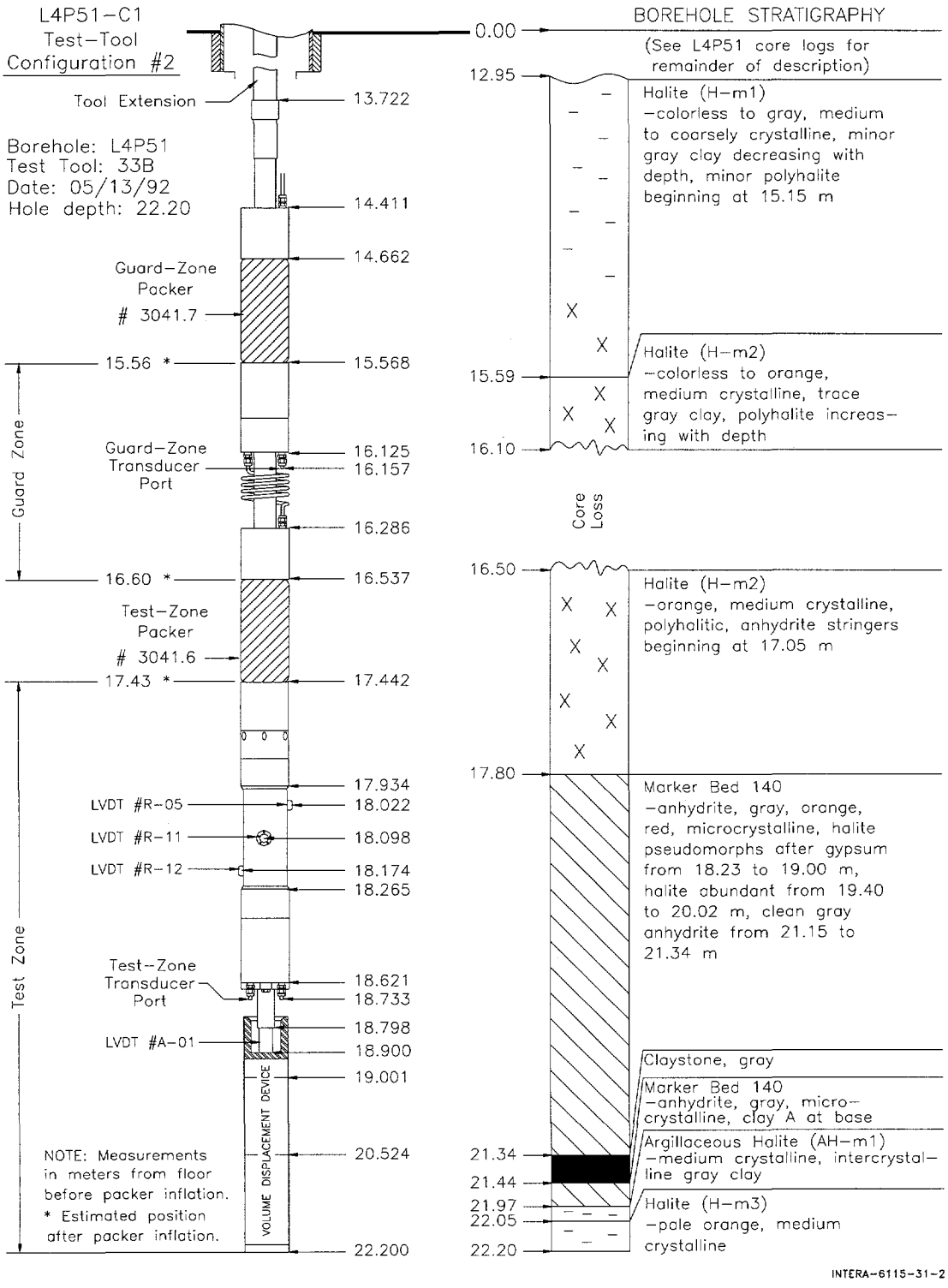

Figure 7-1. Configuration #2 of the tool in borehole L4P51 for testing sequence L4P51-C1.

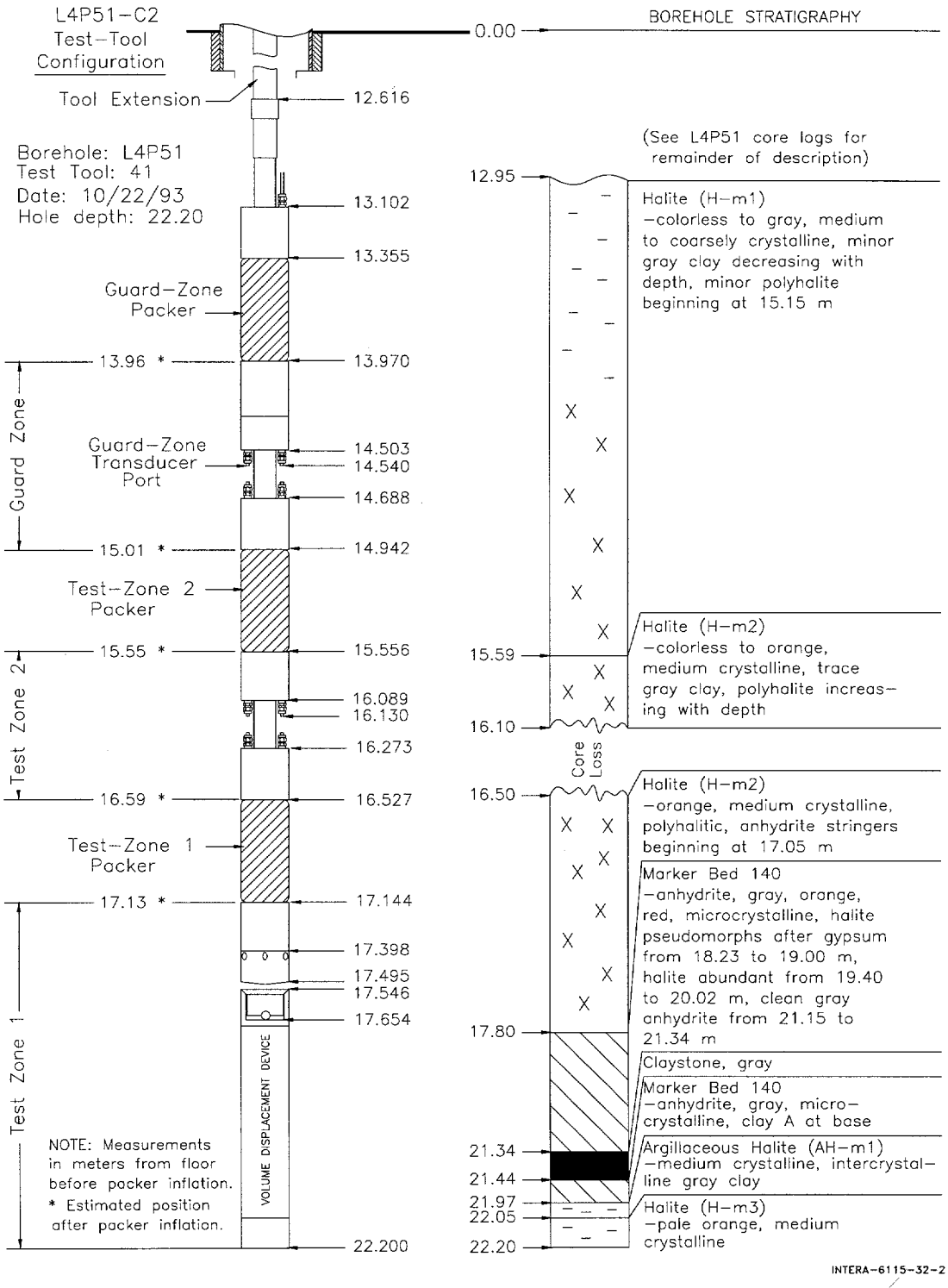

Figure 7-2. Configuration of the tool in borehole L4P51 for testing sequence L4P51-C2.

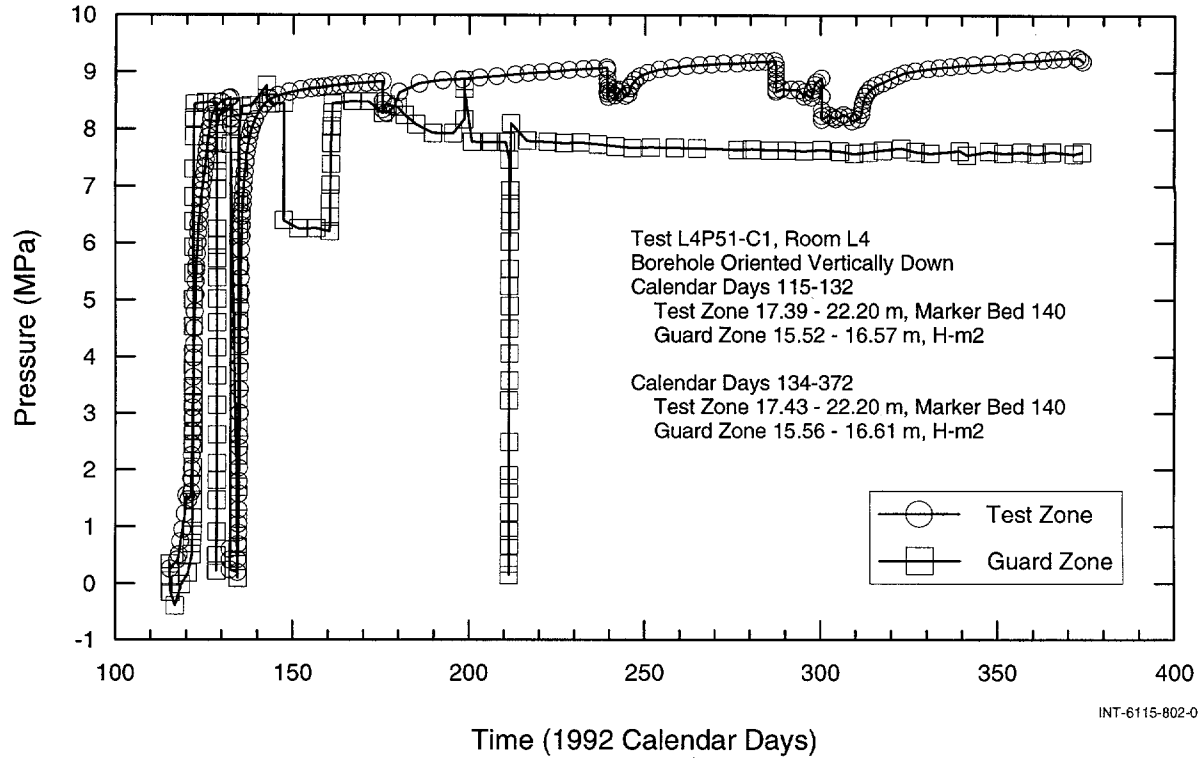

Figure 7-3. Test- and guard-zone pressures during L4P51-C1 testing.

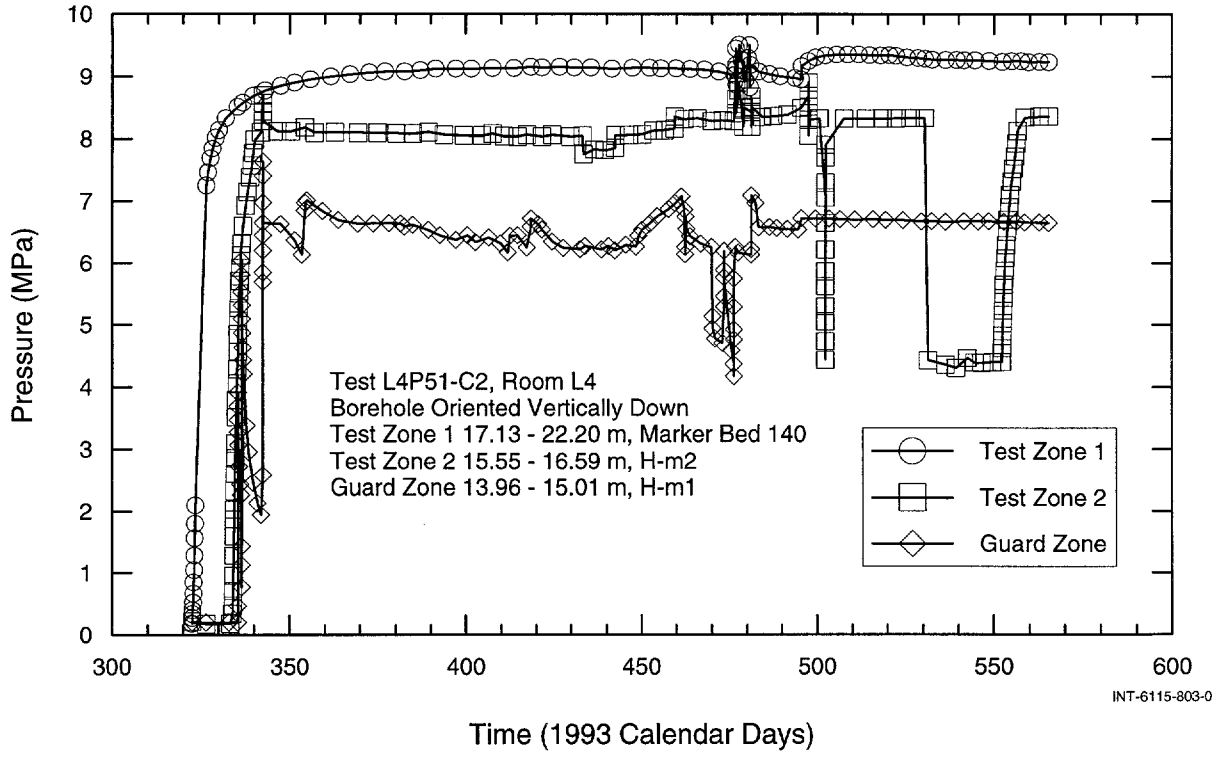

Figure 7-4. Test- and guard-zone pressures during L4P51-C2 testing.

withdrawal test was conducted between 26 May and 8 June 1992 (Calendar Days 147 to 160). The pressure-buildup test began on 8 June and continued until 18 June 1992 (Calendar Day 170), at which time the pressure in the guard zone began to fluctuate.

The double-packer test tool (Figure 7-1) was removed from the borehole on 11 November 1993 (1992 Calendar Day 681) following an extended program of brine sampling from MB140. To begin the L4P51-C2 testing, a triple-packer test tool (Figure 7-2) was installed on 17 November 1993 (1993 Calendar Day 321) and test zone 2 (which corresponds geologically to the guard zone in the previous installation) was shut in on 29 November 1993 (1993 Calendar Day 333). A pulse test was initiated on 17 May 1994 (1993 Calendar Day 501) and a 22-day constant-pressure-withdrawal test was conducted between 14 June and 6 July 1994 (1993 Calendar Days 530 to 552). The pressure-buildup test began on 6 July and continued until 19 July 1994 (1993 Calendar Day 565).

The cumulative-production data from the L4P51-C1 and C2 CPW tests are shown in Figures 7-5 and 7-6, respectively. A total of approximately 1,750 cm^3 of brine was produced during the 13-day C1 test and a total of approximately 3,470 cm^3 of brine was produced during the 22-day C2 test.

The compressibility of the L4P51-C1 guard zone was calculated from the data collected at the beginning of the CPW test and also from the subsequent pressure-buildup test. The calculated compressibilities were 1.5 x 10^{-9} and 1.9 x 10^{-9} Pa^{-1} for the CPW test and pressure-buildup test, respectively (Table 6-2). No single estimate of compressibility was available from the L4P51-C1 PW test because compressibility varied as a function of pressure during the test. The compressibility of the L4P51-C2 test zone 2 was

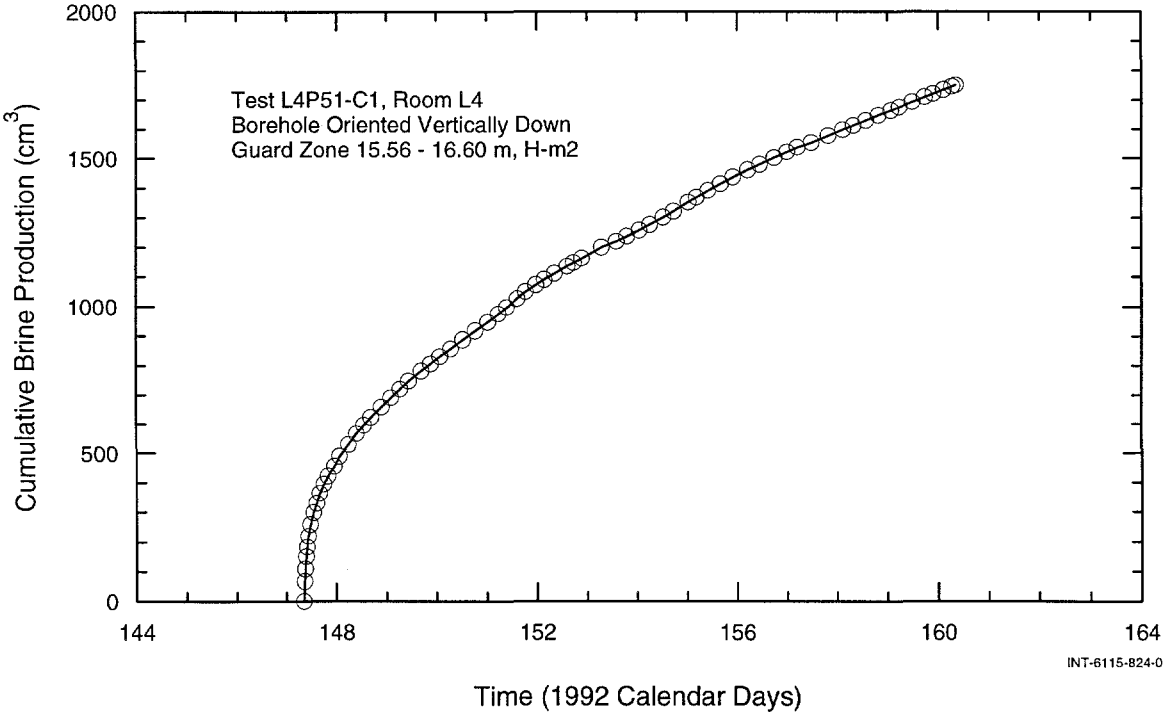

Figure 7-5. Cumulative brine production during the L4P51-C1 guard zone constant-pressure-withdrawal test.

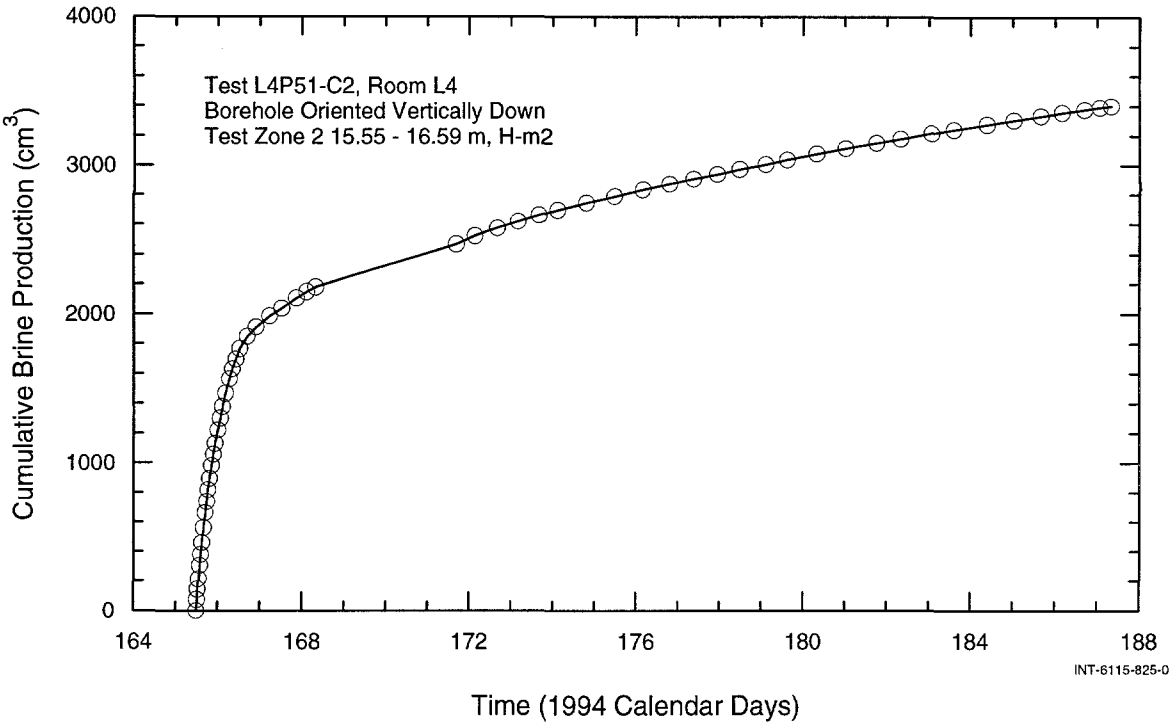

Figure 7-6. Cumulative brine production during the L4P51-C2 test zone 2 constant-pressure-withdrawal test.

calculated from the data collected at the beginning of the PW and CPW tests and also from the pressure-buildup test. The calculated compressibilities were 2.4 x 10^{-9}, 1.8 x 10^{-9}, and 1.6 x 10^{-9} Pa^{-1} for the PW, CPW, and pressure-buildup tests, respectively (Table 6-2).

The pressure behavior in L4P51-C2 test zone 2 was similar to the L4P51-C1 guard-zone response (rapid increase and stabilization followed by long-term decline, Figures 7-3 and 7-4). Both responses indicated that a leak developed once the pressure in the system exceeded approximately 8.3 MPa. The PW tests were, therefore, not amenable to analysis. The CPW tests were analyzed even though the leaks precluded accurate estimation of the static formation pressure. For each of the CPW analyses, the static formation pressure was assumed to be the actual initial pressure prior to flow. The resulting hydraulic-conductivity (K) estimate may be in error due to this assumption by a factor not greater than the percentage difference between the assumed (measured initial pressure minus flowing pressure) and actual (true formation pressure minus flowing pressure) driving pressures for the test. Two additional CPW tests and two constant-pressure-injection (CPI) tests were performed during the L4P51-C2 testing sequence, but due to equipment problems and/or the duration of the tests, none of the four tests were amenable to analysis.

Log-log plots of the calculated flow rates from the two CPW tests (Figures 7-7 and 7-8) suggest a system in which K decreases with either time or distance from the borehole. Pressure-derivative plots of the pressure buildups after each of the CPW tests, however, suggest a system in which K increases with time or distance from the borehole (Figures 7-9 and 7-10). The only conceptual model that appears to reconcile both types of

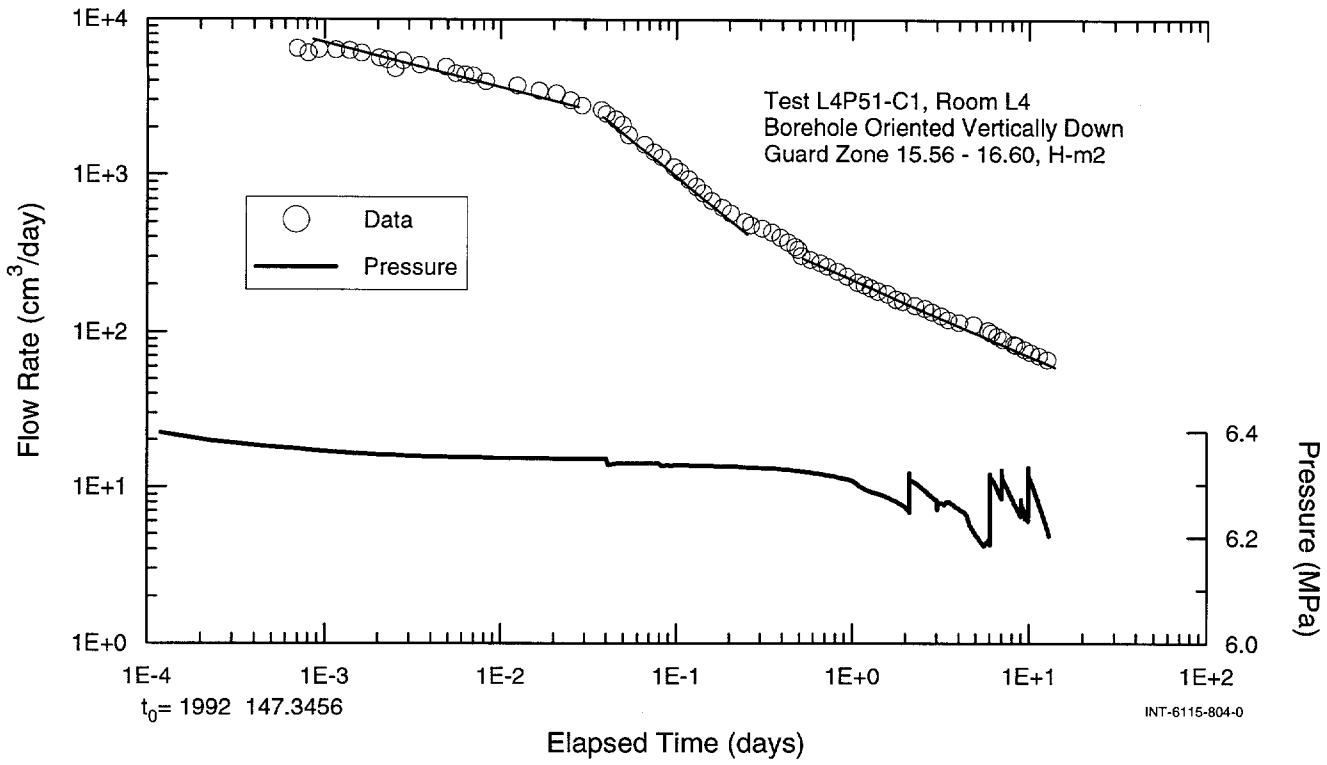

Figure 7-7. Flow rate and guard-zone pressure during the L4P51-C1 guard zone constant-pressure-withdrawal test.

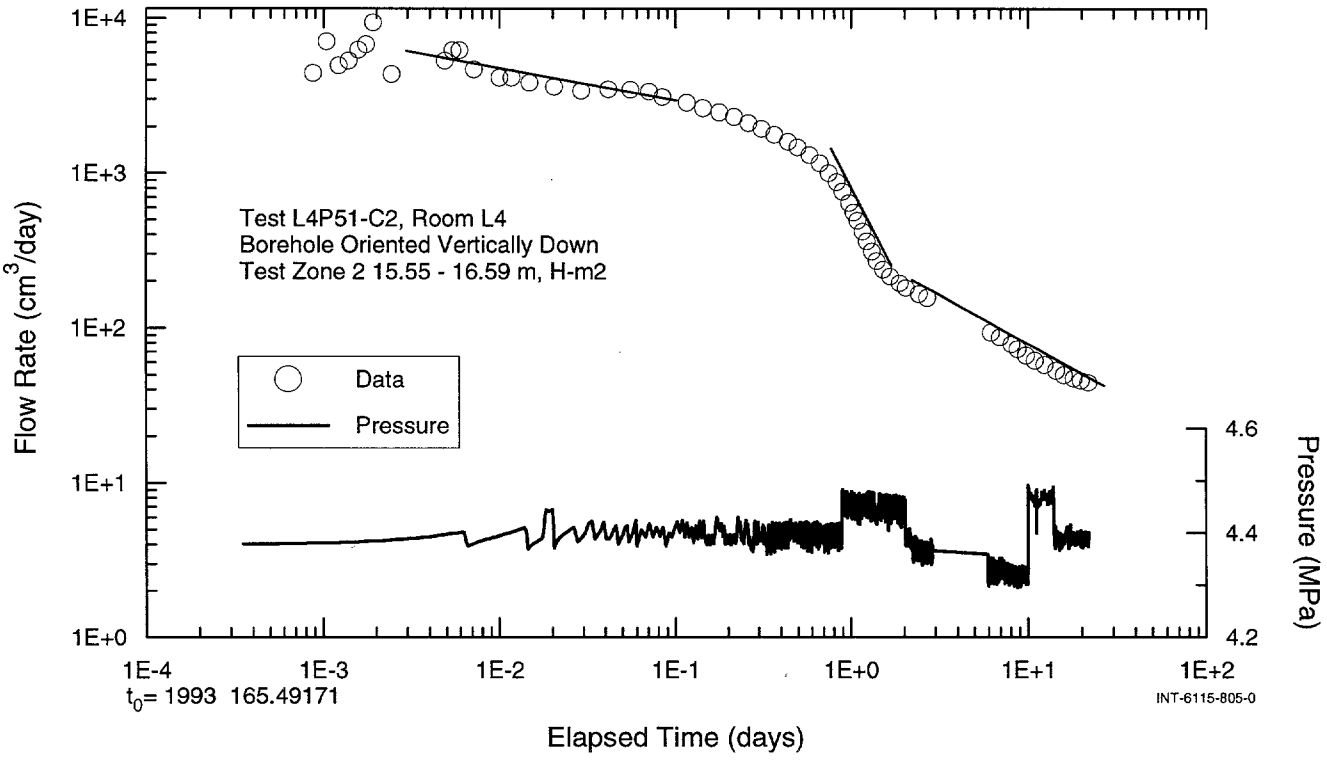

Figure 7-8. Flow rate and test zone 2 pressure during the L4P51-C2 test zone 2 constant-pressure-withdrawal test.

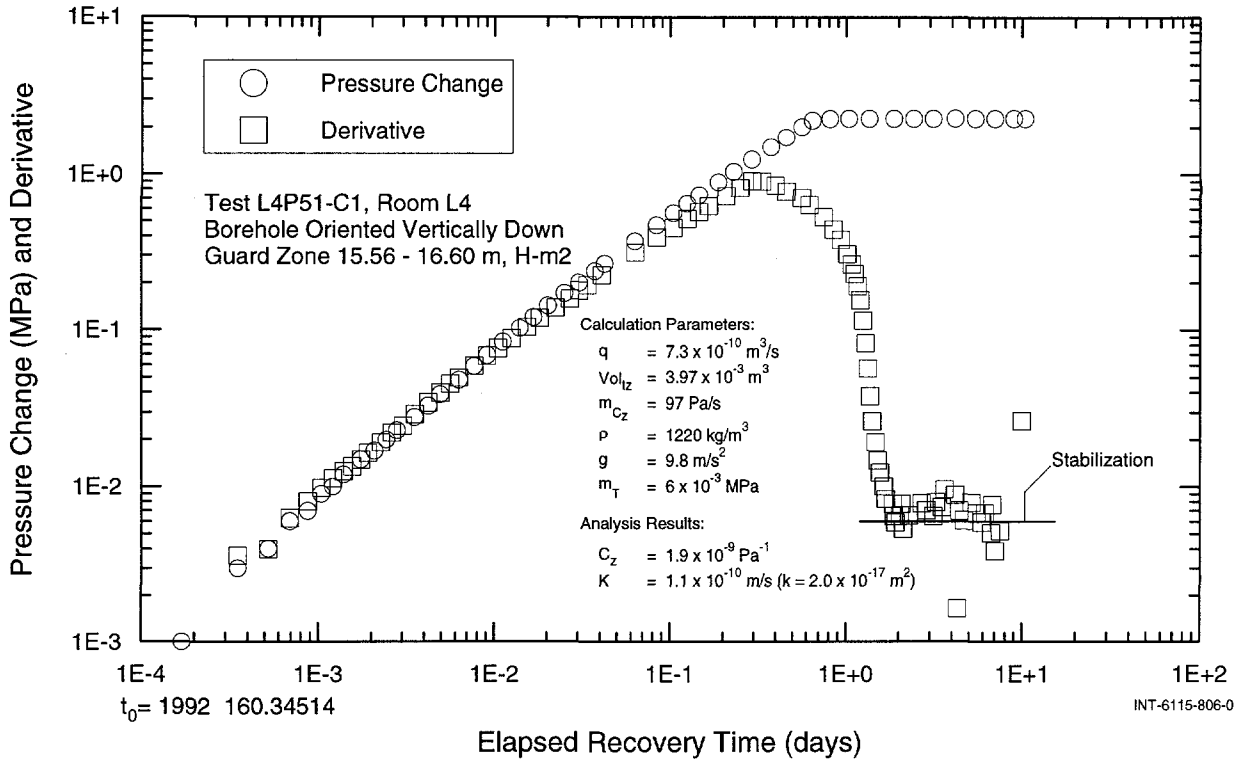

Figure 7-9. Analytical estimates of hydraulic conductivity and zone compressibility from the L4P51-C1 guard zone pressure-buildup test.

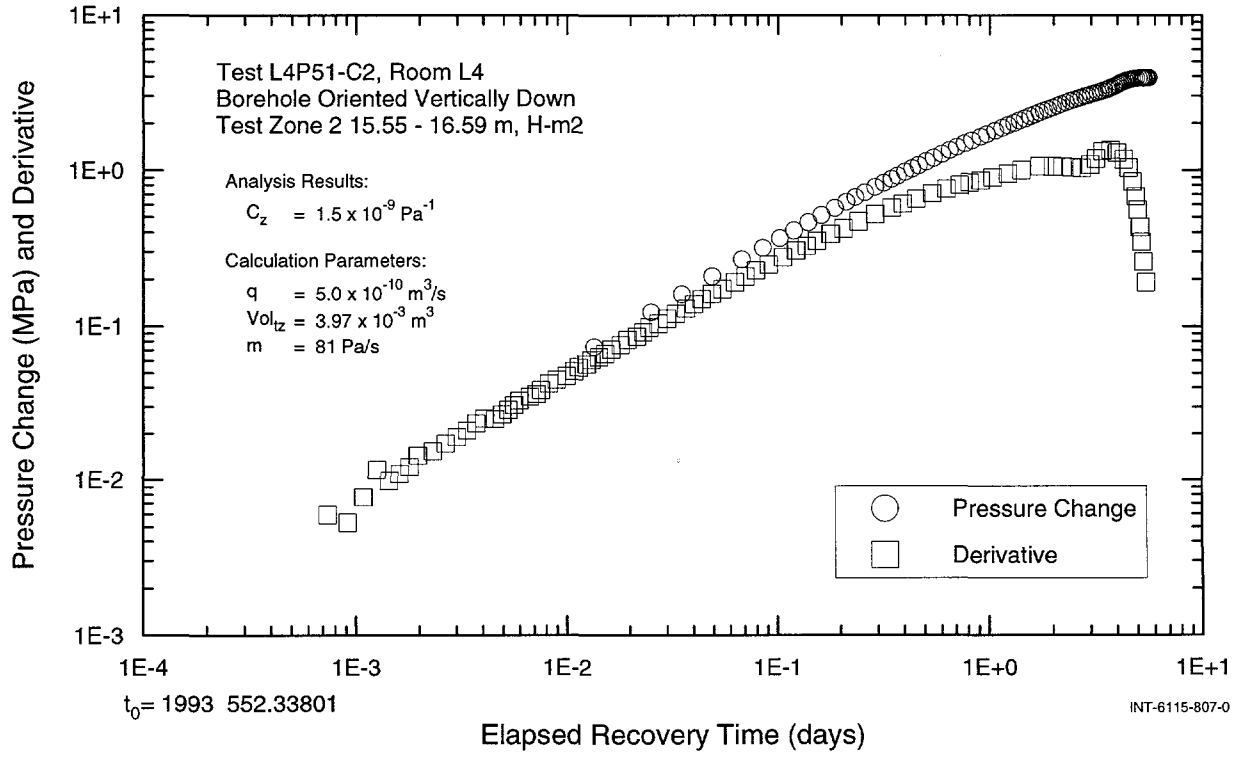

Figure 7-10. Analytical estimate of zone compressibility from the L4P51-C2 test zone 2 pressure-buildup test.

tests would be one in which K changes as a function of pressure, most likely a fracture(s) in which aperture changes as the fluid pressure in the fracture changes.

While GTFM can be used to simulate pressure-dependent effects (K is specified as a function of the pressure in each node), the application of this conceptual model for analysis of these tests is not straightforward. K appears to change primarily with time as a function of pressure. However, K could still be changing to a lesser degree with distance. If it were, the distance-varying effects would be superimposed on the time-varying effects. Further analysis of the log-log flow-rate plots from the CPW tests suggests yet another complication.

Doe (1991) discusses the relationship between the flow dimension (n) (Section 6.2.2) of a system and the observed flow rates during a constant-pressure test. He states that, for flow dimensions between 1 and 2, the flow rate declines along a straight line with a slope equal to $\frac{n}{2}-1$. In fact, this is true for all flow dimensions less than 2. Figures 7-7 and 7-8 show that linear portions of the flow-rate plots from both of the CPW tests indicate that the flow dimension for the system is not only subradial ($n < 2$), but changes concurrently with the fracture conductivity (assuming the conceptual model is correct). If only K were changing as a function of pressure, the straight lines drawn through the flow-rate data would be offset in the Y-direction, but the slopes of the lines would be the same. The fact that the slopes of the two straight-line portions of the data are different implies that n is pressure-dependent as well.

Flow dimension cannot be specified as a function of pressure in GTFM. Given that limitation, the following approach was adopted for analysis of these tests. Recall that the flow dimension of a system describes some non-unique combination of *hydraulic* properties and flow geometry (Section 6.2.2). All variations in K and n as a function of pressure (assumed true conceptual model) were, therefore, simulated as variations only in n as a function of distance, i.e., all time-dependent variations were simulated as spatially dependent variations. The transform between any assumed flow dimension and the subsequent conductivity function discussed in Section 6.2.2 can then be used to investigate various combinations of K and n. Even if the mechanism by which K and n vary is not modeled discretely, the estimated values of the parameters should not be affected regardless of whether they are specified to be changing with time or distance. This approach can obviously be applied only to individual test sequences where the pressure is constant or continuously increasing or decreasing. Any change in the direction of the pressure change will cause the flow-dimension function to reverse directions. The approach was applied only to the individual CPW tests where the initial conditions (static pressure) were known. No hydraulic properties were estimated numerically (using GTFM) from the L4P51-C1 guard zone and C2 test zone 2 pressure-buildup tests. We believe that no additional quantitative information would be gained by attempting to apply the approach described above to the pressure-buildup tests, given that the (unknown) initial conditions for the tests could not be implemented in GTFM.

Figure 7-11 shows a GTFM simulation of a pressure-buildup test after a CPW test, where both K and n are variable. The figure is shown only to demonstrate that the conceptual model discussed above does produce a response similar to the actual response observed during testing (see Figure 7-10).

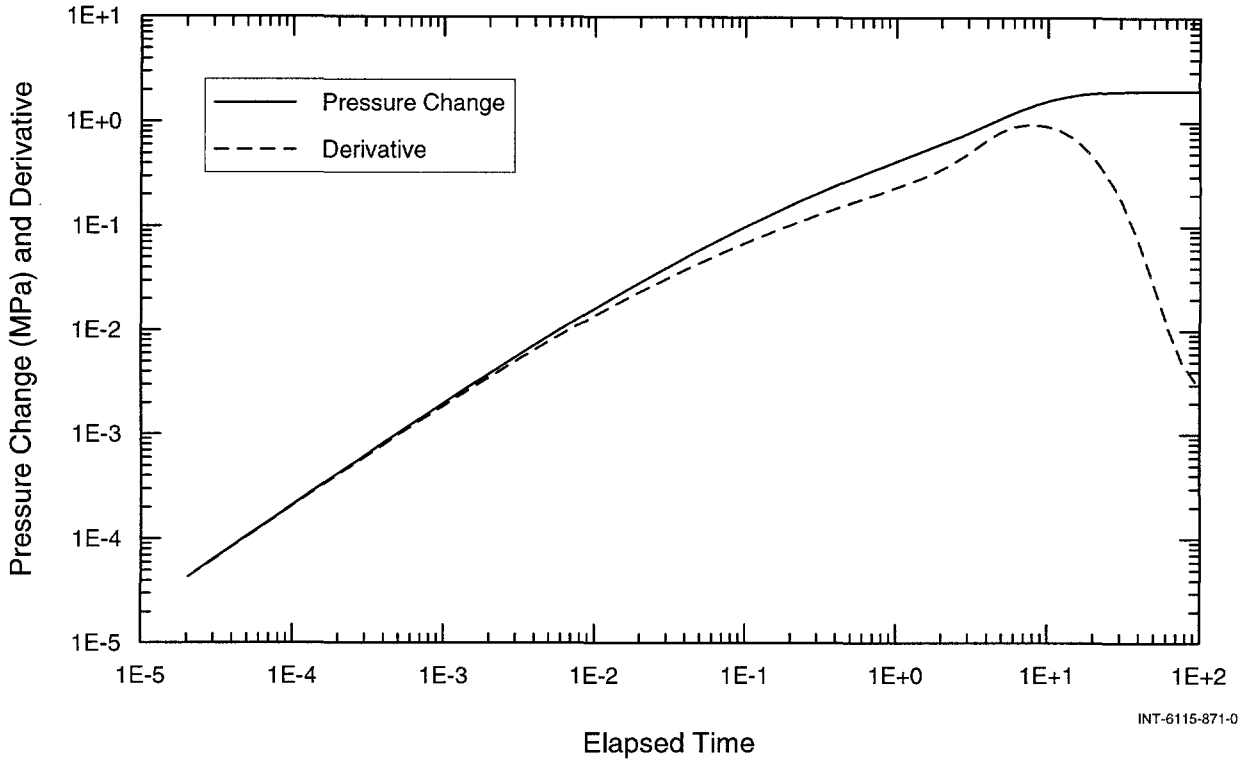

Figure 7-11. GTFM simulation of a pressure-buildup test showing the effect of variable hydraulic conductivity and flow dimension.

7.1.1.1 Analytical Interpretations

The data from the L4P51-C1 guard zone pressure-buildup test were used to estimate the zone compressibility and *K*. The estimated compressibility of the L4P51-C1 guard zone was 1.9 x 10^{-9} Pa^{-1} and the estimated *K* was 1.1 x 10^{-10} m/s (k = 2.0 x 10^{-17} m^2). Figure 7-9 shows a diagnostic plot of the pressure buildup and the values used to calculate these parameters.

A log-log plot of the pressure derivative from the L4P51-C2 test zone 2 pressure-buildup test and the corresponding zone-compressibility estimate are shown in Figure 7-10. The test-zone compressibility calculated from the wellbore-storage period was 1.5 x 10^{-9} Pa^{-1} (Table 6-2). The pressure derivative appeared to stabilize for a short period approximately two days after the pressure-buildup test began. This was followed by a sudden increase in the pressure-recovery rate, after which the derivative decreased. The "kink" in the recovery pressure is characteristic of tests performed in this halite unit (H-m2) and tests performed in MB140. In both geologic units, this distinctive pressure response is related to a preceding underpressurization period. The magnitude of the response increases with the duration of the underpressurization period.

7.1.1.2 Numerical Interpretations

A CPW test was initiated in the L4P51-C1 guard zone by decreasing the pressure from 8.45 MPa to an average pressure of 6.25 MPa on 26 May 1992 (Calendar Day 147). The test lasted approximately 13 days. The best-fit GTFM simulations compared to the cumulative-production and flow-rate data are shown in Figures 7-12 and 7-13, respectively. The estimated flow-dimension function is also

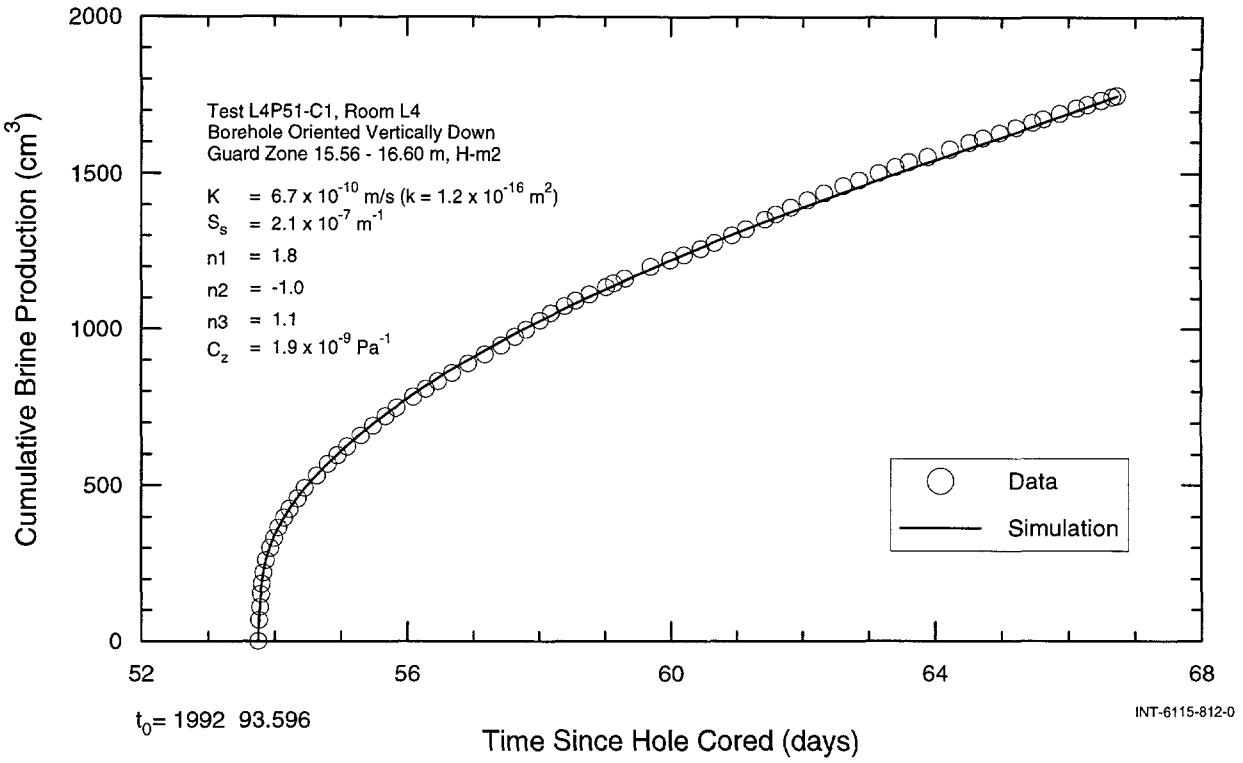

Figure 7-12. Linear-linear plot of GTFM simulation of brine production during the L4P51-C1 guard zone constant-pressure-withdrawal test.

shown in Figure 7-13. As explained above, data from the tests performed in this zone suggest a flow system in which geometry and hydraulic properties change with pressure. All temporal changes in geometry and hydraulic properties due to time-varying pressures were simulated by varying the flow dimension with distance.

For analysis, the CPW test was conceptualized as consisting of three periods represented by three different flow dimensions. Each period is characterized by a change in slope of the flow-rate data (Figure 7-7). The first period of the CPW test (0.0 to 0.02 days) has a slope corresponding to a flow dimension of about 1.5. The first period is followed by a transitional period (0.02 to 0.2 days) during which the slope increases, corresponding to a flow dimension of about -0.5. This transitional period is assumed to correspond to the partial closing of a pressure-sensitive fracture. The transitional period is followed by a final period of constant slope corresponding to a flow dimension of about 1.0. The optimized flow-dimension function converted from distance to time using Eq. 6-5 is shown in Figure 7-13 and is seen to be in good agreement with the initial estimates of *n*. The flow-dimension function calculated from the second derivative of *1/q* (Section 6.2.2.2) is also in good agreement with the optimized flow-dimension function (Figure 7-14). The optimized values of K and S_s for the optimized outer flow dimension of approximately 1.1 were 6.7 x 10^{-10} m/s (k = 1.2 x 10^{-16} m^2) and 2.1 x 10^{-7} m^{-1}, respectively. Formation pore pressure and zone compressibility were specified to be 8.5 MPa and 1.9 x 10^{-9} Pa^{-1}, respectively. Perturbation analysis (Section 6.2.3.6) indicated that this problem, as posed, had a well-constrained solution.

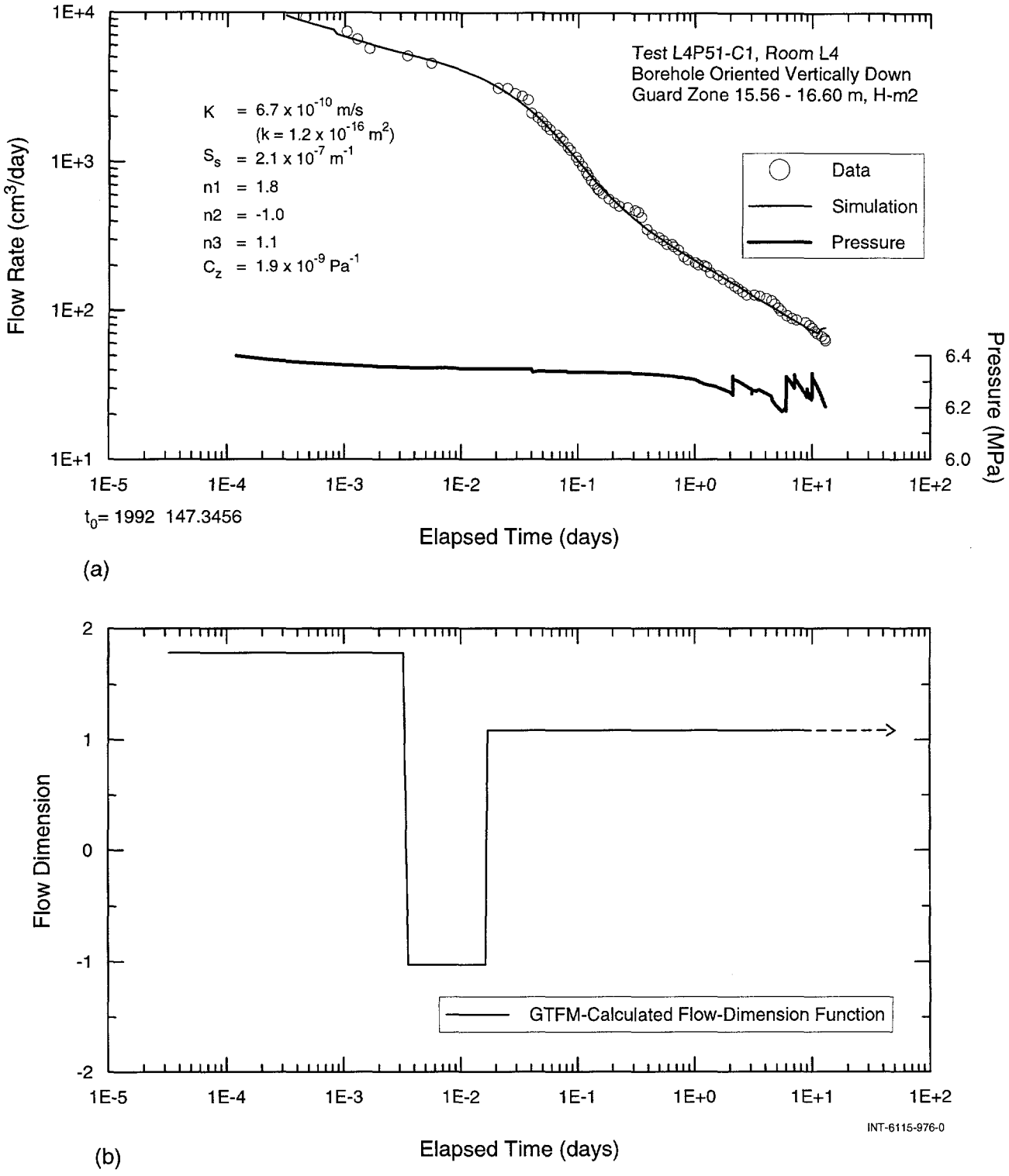

Figure 7-13. Log-log and semilog plots of GTFM simulation of flow rates along with the zone pressure (a) and flow-dimension function (b) during the L4P51-C1 constant-pressure-withdrawal test.

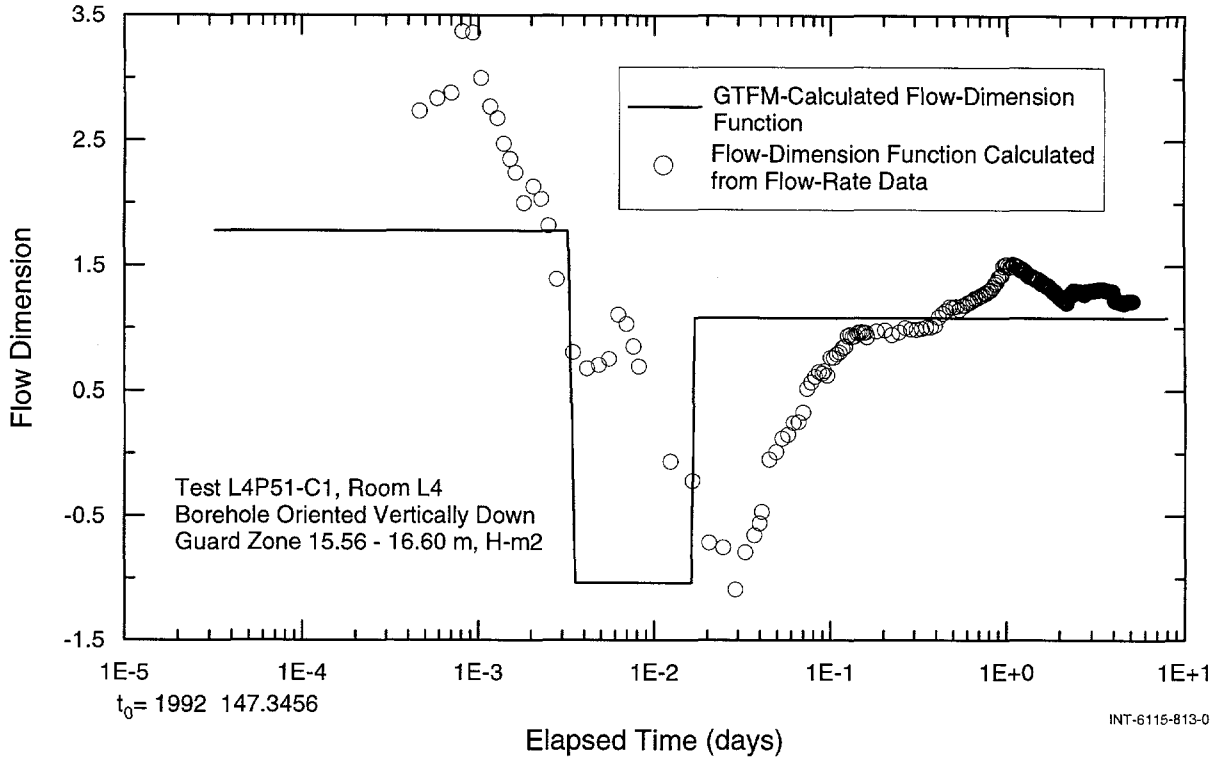

Figure 7-14. Comparison of optimized and calculated flow-dimension functions from the L4P51-C1 guard zone constant-pressure-withdrawal test.

The double-packer test tool was removed from borehole L4P51 on 11 November 1993 and replaced with a triple-packer test tool (Figure 7-2) on 18 November 1993 to begin permeability-testing sequence L4P51-C2. Test zone 2, however, was not shut in until 29 November 1993 and was, therefore, at or near atmospheric pressure for 18 days. The test sequence performed in the guard zone of the double-packer test tool was then repeated in test zone 2 of the triple-packer configuration, i.e., a pulse-withdrawal test followed by a constant-pressure-withdrawal test and a pressure-buildup test. The PW and pressure-buildup tests were not analyzed because the same apparent leak occurred above approximately 8.3 MPa as was observed during the L4P51-C1 guard zone tests. The starting times for the L4P51-C1 guard zone and L4P51-C2 test zone 2 pulse-withdrawal tests were separated by a period of slightly more than two years. The similarities of the responses suggest that they were true formation responses and not equipment-related. Increasing amounts of noise were observed in the pressure data approximately 45 days after shut in. The problem was found to be a faulty Data Control Unit (DCU), which was replaced on 12 May 1994, prior to starting the L4P51-C2 CPW test analyzed for this report. Three constant-pressure tests performed prior to replacing the DCU and one abbreviated CPW test performed immediately after the DCU was replaced were not suitable for analysis. A plot of the pressure in test zone 2 during the L4P51-C2 permeability-testing sequence is shown in Figure 7-4.

A constant-pressure-withdrawal test was initiated in test zone 2 by decreasing the pressure from 8.33 MPa to an average pressure of 4.4 MPa on 14 June 1994 (1994 Calendar

Day 165). The test lasted approximately 22 days. The best-fit GTFM simulations compared to the cumulative-production and flow-rate data are shown in Figures 7-15 and 7-16, respectively. The estimated flow-dimension function converted from distance to time using Eq. 6-5 is also shown in Figure 7-16. The estimated values of K and S_s corresponding to the best-fit match and a flow dimension of 1.3 were 1.6 x 10^{-10} m/s (k = 2.8 x 10^{-17} m^2) and 5.4 x 10^{-9} m^{-1}, respectively.

Figure 7-17 shows a plot of flow rate versus elapsed time for this CPW test and the L4P51-C1 CPW test. The early-time flow rates are similar, but the transition-period and late-time flow rates are different. The L4P51-C2 flow rate remained higher for a longer period of time but then decreased more rapidly during the transition period. The late-time L4P51-C2 flow rate decreased 50% faster than the L4P51-C1 flow rate, suggesting that the flow dimension depends on the imposed gradient (4 MPa versus 2 MPa).

7.1.1.3 Summary

Analytical and numerical interpretations of the tests of H-m2 in L4P51 provided estimates of K that ranged between 1.1 x 10^{-10} and 6.7 x 10^{-10} m/s (k = 2.0 x 10^{-17} to 1.2 x 10^{-16} m^2) and estimates of S_s ranging from 5.4 x 10^{-9} to 2.1 x 10^{-7} m^{-1}. Quantitative estimates of the fitting-parameter uncertainty (95% joint-confidence regions) and the corresponding correlation matrices are presented in Appendix C. The range of K values is believed to result from pressure-dependent changes in the aperture(s) of single or multiple fractures in the isolated test zone.

The pressure responses during the testing of H-m2 appeared to be affected by leaks at pressures greater than approximately 8.3

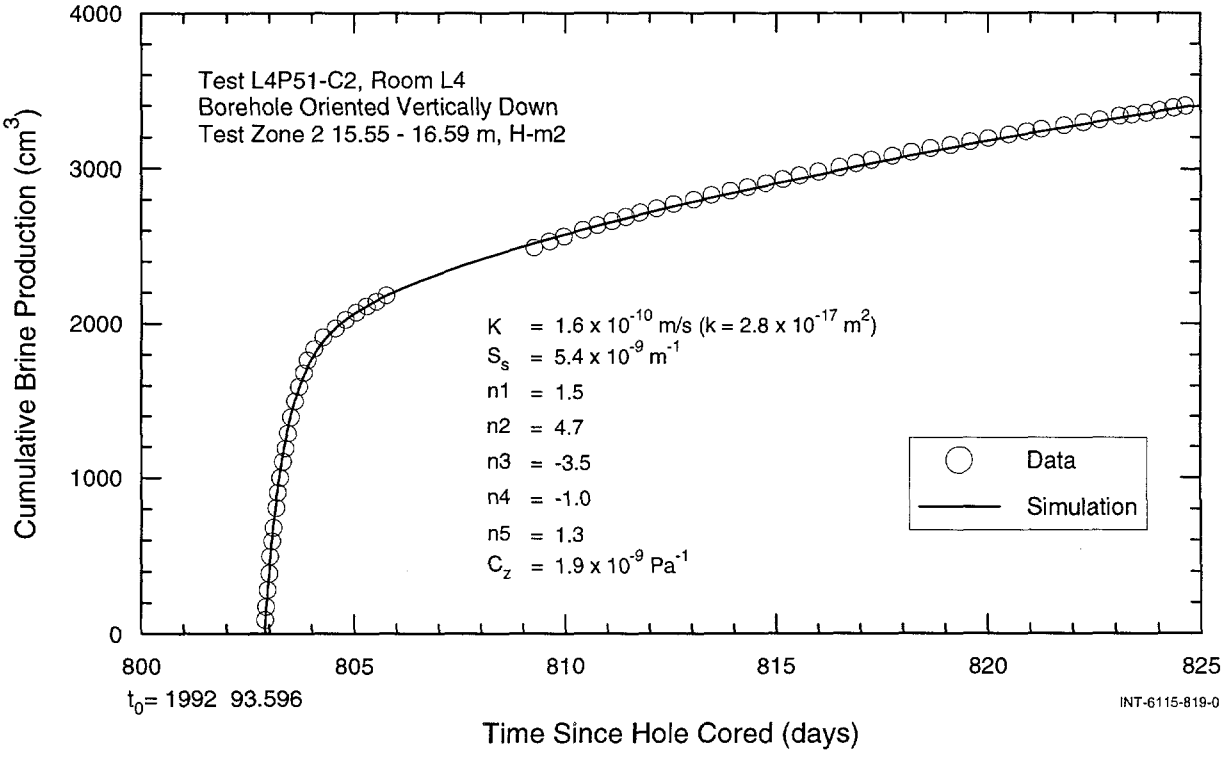

Figure 7-15. Linear-linear plot of GTFM simulation of brine production during the L4P51-C2 test zone 2 constant-pressure-withdrawal test.

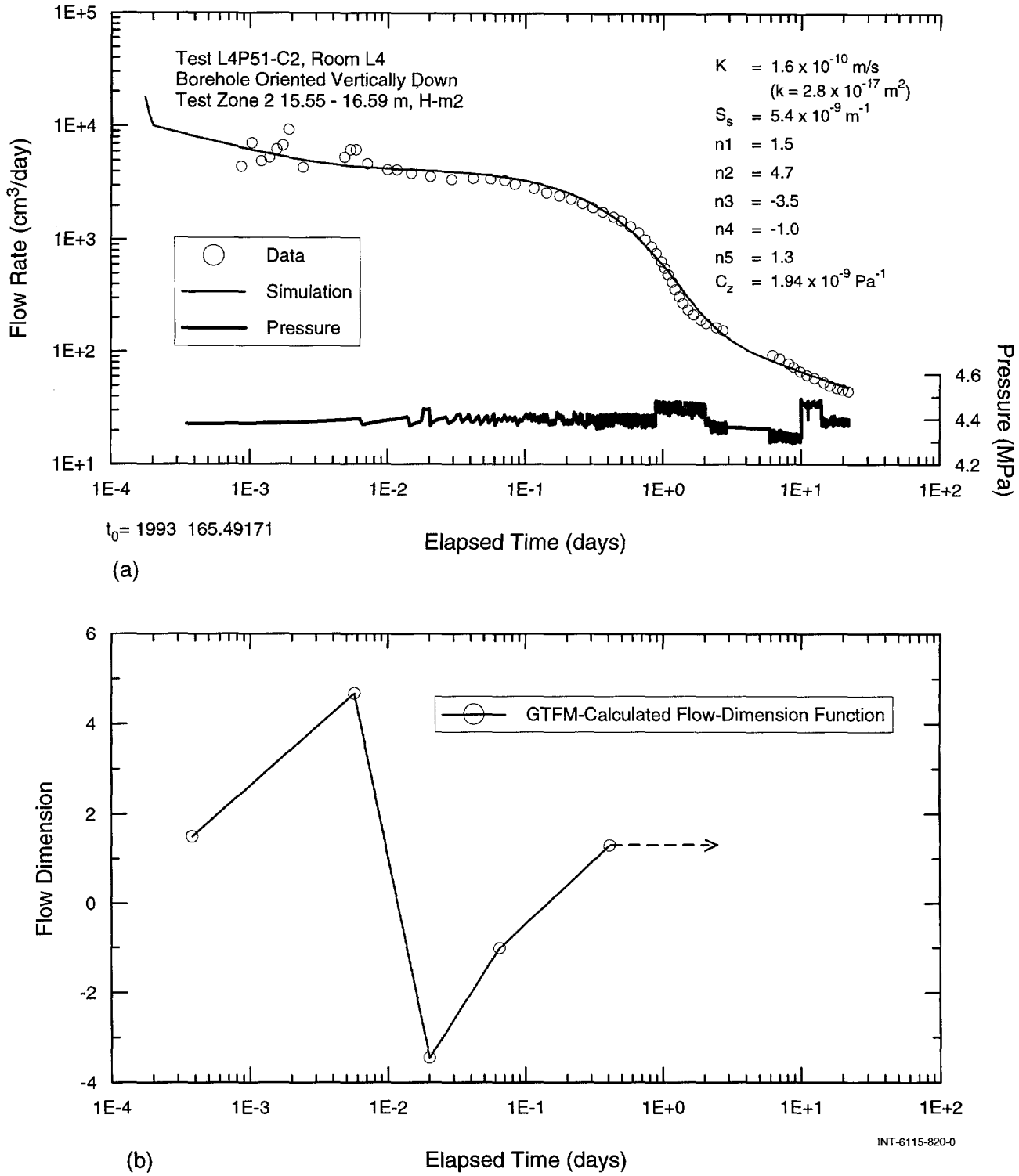

Figure 7-16. Log-log and semilog plots of GTFM simulation of flow rates along with the zone pressure (a) and flow-dimension function (b) during the L4P51-C2 test zone 2 constant-pressure-withdrawal test.

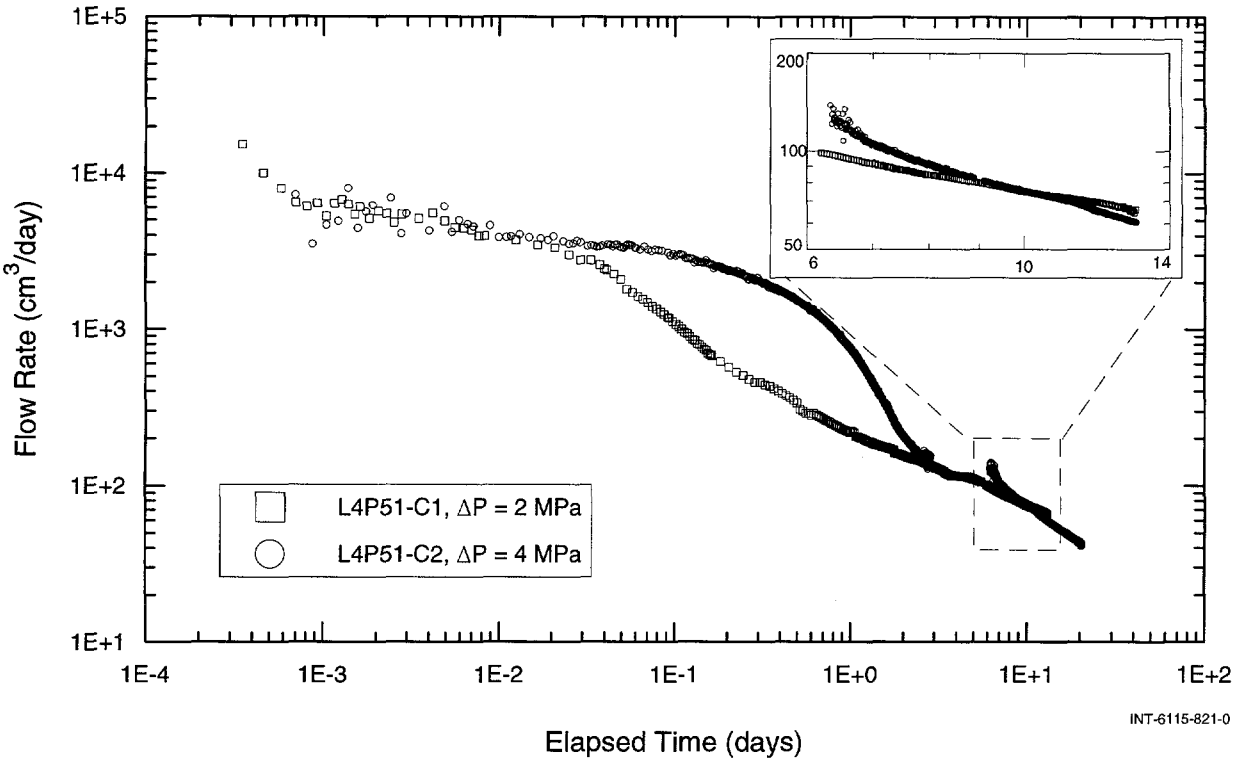

Figure 7-17. Flow rates during the L4P51-C1 guard zone and L4P51-C2 test zone 2 constant-pressure-withdrawal tests.

MPa. Consequently, no optimized estimate of the formation pore pressure was made. The highest pressure measured during the testing of H-m2 in L4P51 was 8.5 MPa on 17 June 1992 (Calendar Day 169).

7.1.2 Marker Bed 140 Testing (L4P51-C1 Test Zone)

The L4P51-C1 test zone was initially shut in on 24 April 1992 (Calendar Day 115). The test tool was subsequently removed from the borehole on 11 May 1992 (Calendar Day 132) for repairs and then re-installed on 13 May 1992 (Calendar Day 134). The test zone was shut in on the same day (134). Three CPW tests followed by pressure-buildup tests were performed in this zone during the L4P51-C1 permeability-testing sequence. Each of the CPW tests was performed at a pressure approximately 0.5 MPa below the pre-test pressure. CPW1, a 3-day constant-pressure-withdrawal test, was conducted between 23 and 26 June 1992 (Calendar Days 175 to 178). The pressure was reduced from 8.83 to 8.30 MPa for this test, which produced 9,360 cm^3 of brine. Figure 7-18 shows cumulative brine production plotted as a function of time during this test. The pressure-buildup test began on 26 June 1992, and continued until 26 August 1992 (Calendar Day 239). CPW2, a 6-day constant-pressure-withdrawal test, was conducted between 26 August and 1 September 1992 (Calendar Days 239 to 245). The pressure was reduced from 9.10 to 8.62 MPa for this test, which produced 8,160 cm^3 of brine. Figure 7-19 shows the cumulative brine production plotted as a function of time during this test. The pressure-buildup test began on 1 September 1992 and continued until 13 October 1992 (Calendar Day 287). CPW3, a 24-day constant-pressure-withdrawal test, was conducted between 13

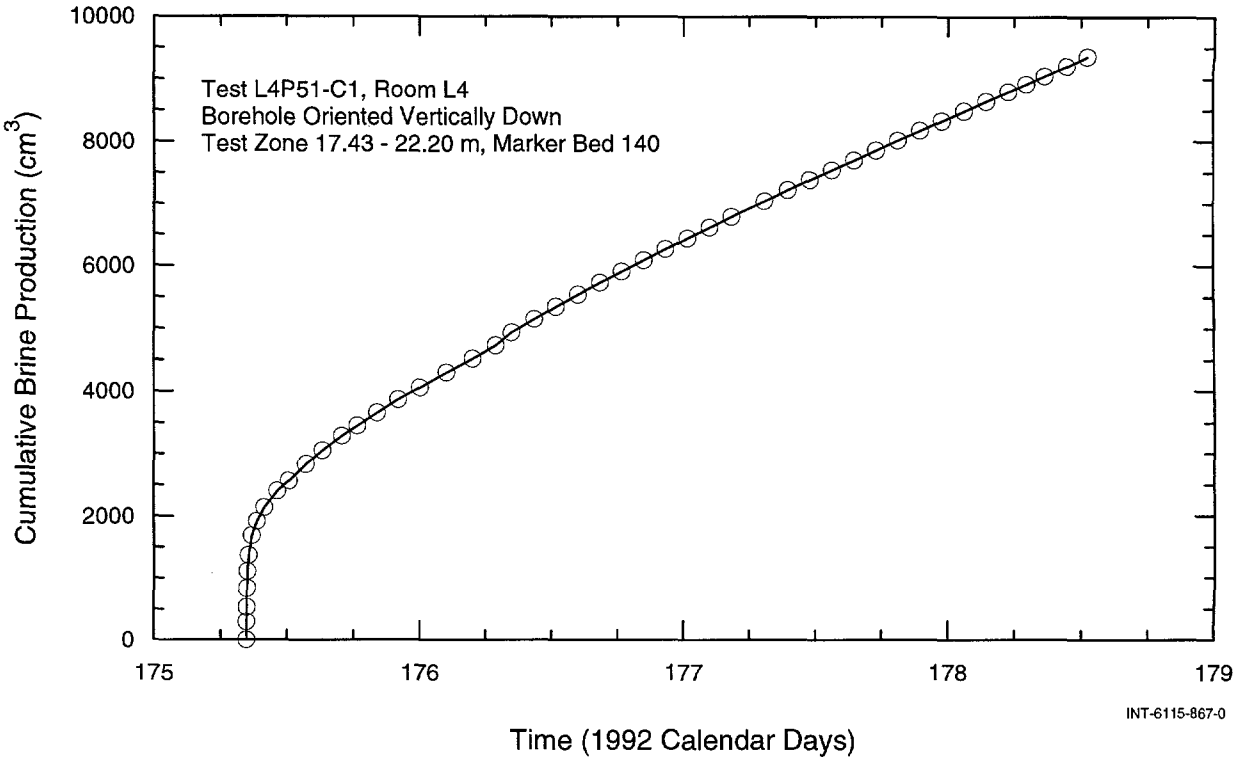

Figure 7-18. Cumulative brine production during the first L4P51-C1 test zone constant-pressure-withdrawal test in Marker Bed 140.

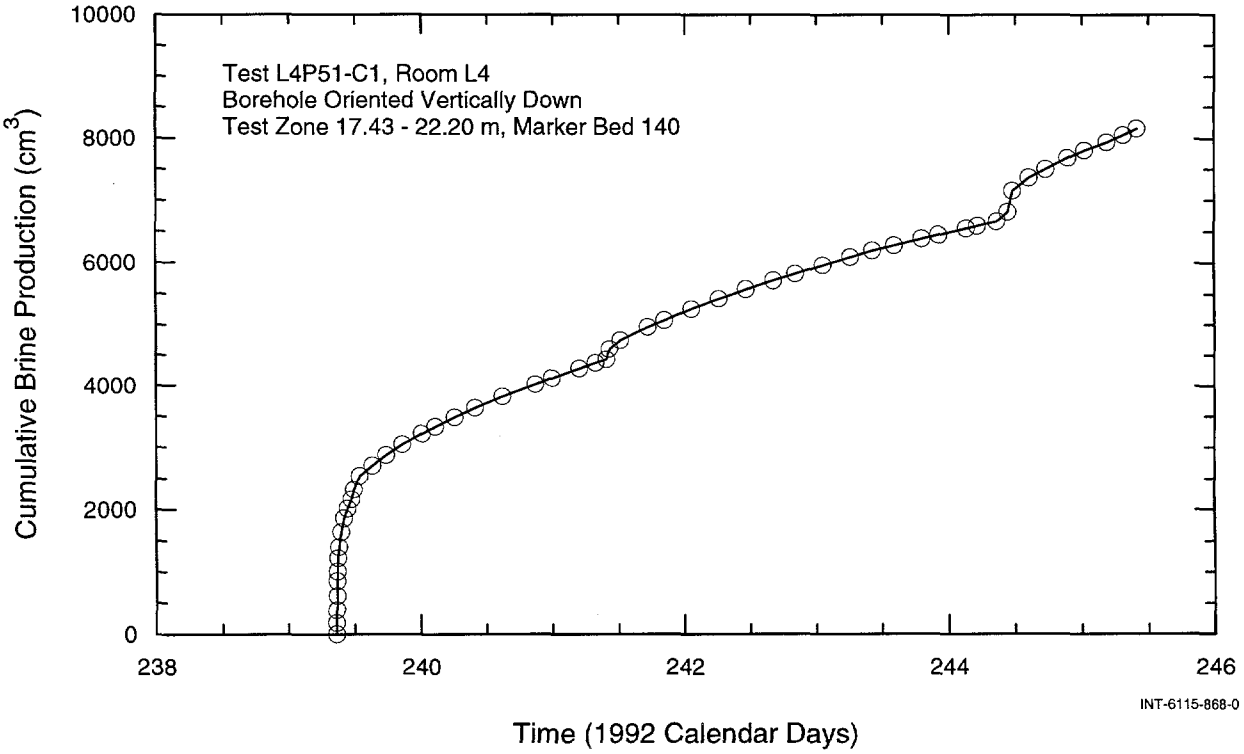

Figure 7-19. Cumulative brine production during the second L4P51-C1 test zone constant-pressure-withdrawal test in Marker Bed 140.

October and 6 November 1992 (Calendar Days 287 to 311). The pressure was reduced from 9.20 to 8.70 MPa for this test, which produced 37,400 cm^3 of brine. Figure 7-20 shows the cumulative brine production plotted as a function of time during this test. The pressure-buildup test began on 6 November 1992 and continued until 6 January 1993 (1992 Calendar Day 372), when a leak developed in the system.

The compressibility of the L4P51-C1 test zone was evaluated with data collected at the beginning of the constant-pressure-withdrawal tests. The test-zone compressibilities calculated using these data ranged from 1.2×10^{-7} to 5.6×10^{-7} Pa^{-1} (Table 6-2). These test-zone compressibilities are approximately two orders of magnitude greater than the average test-zone compressibility (at pressures greater than 3 MPa). The reason for this difference is unknown.

The durations of the constant-pressure-withdrawal tests appeared to affect the behavior of the system during the subsequent pressure-buildup tests. Each successive CPW test was run for a longer period of time than the previous test; the first test lasting three days, the next lasting six days, and the final CPW test lasting for 24 days. Figure 7-21 shows the pressure buildups following the three CPW tests performed in this zone. A distinct change in slope can be seen at about 7 days in the recovery following the 24-day CPW test (PBU3). A similar change in slope is barely discernible at about 2.5 days in the recovery following the 6-day CPW test (PBU2) and is not seen at all following the 3-day CPW test (PBU1). Figure 7-22 shows the pressure buildup following the initial shut-in on Calendar Day 115 and the pressure buildup after the test tool was re-installed on Calendar Day 134, each plotted with respect

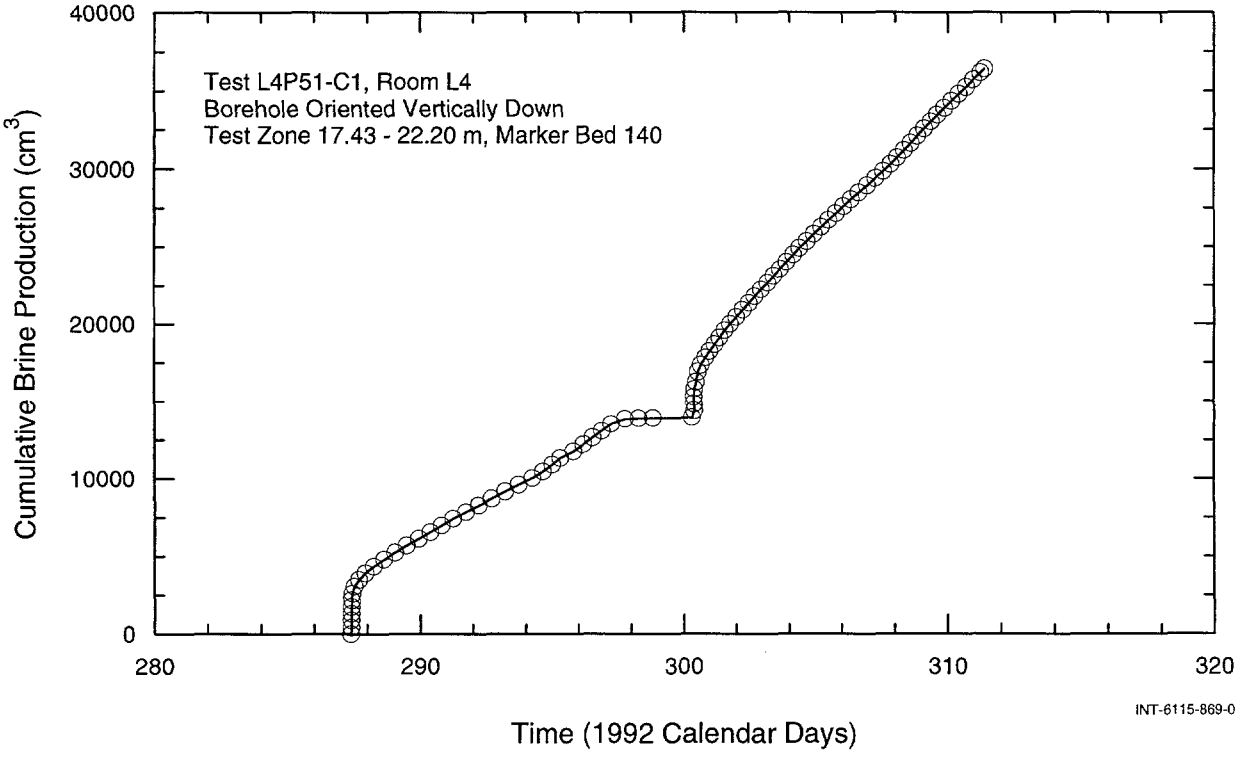

Figure 7-20. Cumulative brine production during the third L4P51-C1 test zone constant-pressure-withdrawal test in Marker Bed 140.

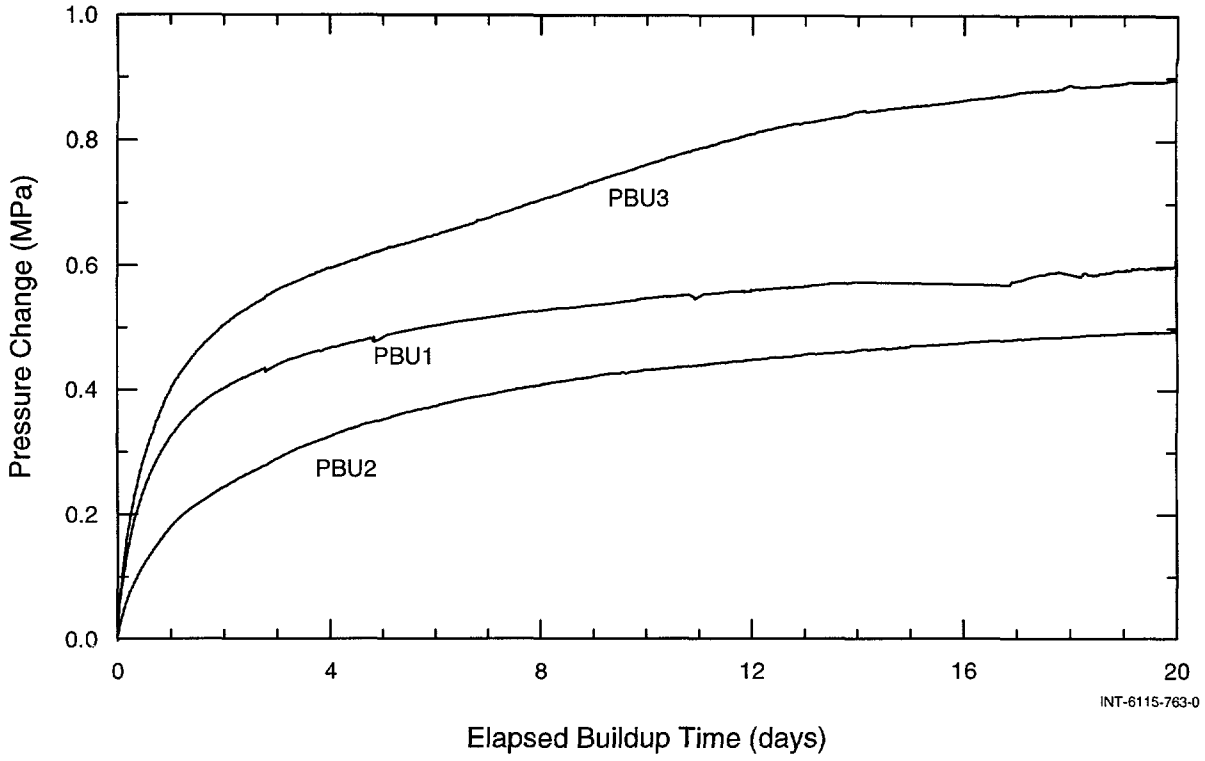

Figure 7-21. Pressure buildups following each of the three test zone constant-pressure-withdrawal tests in Marker Bed 140 during the L4P51-C1 testing sequence.

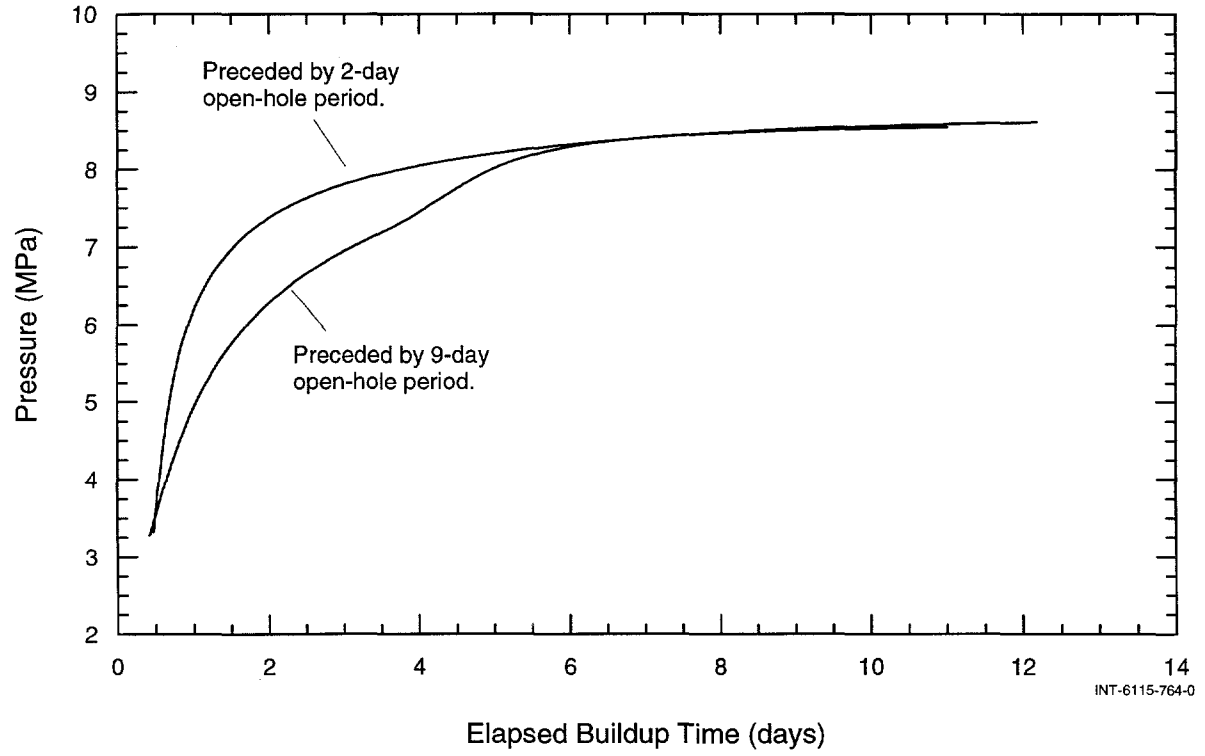

Figure 7-22. Test-zone pressure buildups following each of the two open-borehole periods during the L4P51-C1 testing sequence.

to elapsed shut-in time. The initial shut-in on day 115 was preceded by a nine-day open-hole period during which the zone was at or near atmospheric pressure. The shut-in on day 134 was preceded by a two-day open-hole period. Again, the abrupt change in slope during the pressure-buildup period, in this case seen only after the initial shut-in on Calendar Day 115, appears to be related to the amount of time the formation was under-pressurized. This same response was observed during the testing of H-m2 in L4P51 discussed in Section 7.1.1. There also, the magnitude of this anomalous response depended on the duration of the preceding underpressurization period. Modeling studies and test data (Beauheim et al., 1993b) suggest that this response results from changing properties in fractures with pressure-varying apertures. Core recovered during the drilling of borehole L4P51 indicated that fractures exist along several intervals of MB140.

In addition to the pressure-dependent behavior discussed above, the MB140 pressure response exhibited another unusual behavior. During the entire 259-day testing period, the pressure never appeared to be stabilizing (Figure 7-3). The pressure displays a long-term increasing trend that was not observed during any other Salado permeability-testing sequence. The cause of this response is unknown. It may be a long-term, stress-related transient resulting from the excavation of the WIPP repository.

MB140 includes layers of fractured and non-fractured anhydrite containing variable amounts of halite and a 10-cm-thick mudstone seam. The hydraulic properties of each of these layers could be quite different and the observed responses during testing could be a superposition of the different responses from each layer. Given the potential complexity of this system, the modeling approach used for the H-m2 testing analysis (Section 7.1.1.2) was also used for the analysis of the MB140 response. System responses were matched by optimizing K, S_s, and the flow-dimension function. Radially varying flow-dimension values could represent nonradial flow, time-varying fracture properties, a multi-layer response, or any combination of these responses. Because the flow system is not well understood and the flow dimension of a system, by definition, is determined by some unknown combination of flow geometry and hydraulic properties, this approach seemed to be the most reasonable.

None of the attempts to simulate the observed long-term increasing pressure response was successful. We decided, therefore, to simulate only the CPW responses for reasons discussed in the next paragraph. Each of the three CPW tests was treated as an isolated test event preceded by static pressure conditions. The formation pore pressure for each of the analyses was assumed to be the pressure just before the start of each test.

One might ask if the analysis approach outlined in the previous paragraph can provide any useful information about the hydraulic properties of MB140. The following discussion addresses some of the rationale for the modeling approach that was adopted. The rate of pressure change of the long-term response was less than 0.005 MPa/day. Given this rate of change with respect to the duration of the CPW tests, the assumption that the static formation pressure was the pressure that immediately preceded each CPW test should have relatively little effect on the estimated parameters. If the response is truly a multi-layer response where each layer has a different set of hydraulic properties, then the hydraulic properties estimated with the current modeling approach obviously repre-

sent an integrated value of that property over the entire length of the test zone. This, however, is true for any hydraulic test. The extent to which flow occurs through different sections of the test interval is never known with certainty. Is constructing a numerical model in which each of the assumed flow mechanisms (multi-layer, fracture flow, pressure-dependent properties) is explicitly modeled worthwhile? A model of this type is useful for investigating potential mechanisms for observed system responses, but it is of limited value for estimating hydraulic-parameter values. The more accurate (complex) the model becomes, the less unique (more uncertain) the parameter estimates become, i.e., constraining the parameter estimates becomes very difficult. Constraining parameter estimates using such a model would require many tests performed over much smaller sections of MB140. The level of analysis presented in this report is, therefore, probably the most appropriate for the type of data that were collected. In general, the MB140 flow system appears to be fairly complex and is poorly understood.

7.1.2.1 Analytical Interpretations

No analytical straight-line estimates of hydraulic conductivity were made from the three pressure-buildup tests. Pressure change and derivative plots of the first, second, and third pressure-buildup tests are shown in Figures 7-23, 7-24, and 7-25, respectively. Each of the test responses was detrended to remove the long-term transient discussed above. The pressure derivatives from each of the pressure-buildup tests displayed a response similar to that observed during the L4P51-C halite testing (Section 7.1.1). As discussed previously, this response appears to be related to pressure-dependent fracture properties and is affected by the duration of the preceding constant-pressure test.

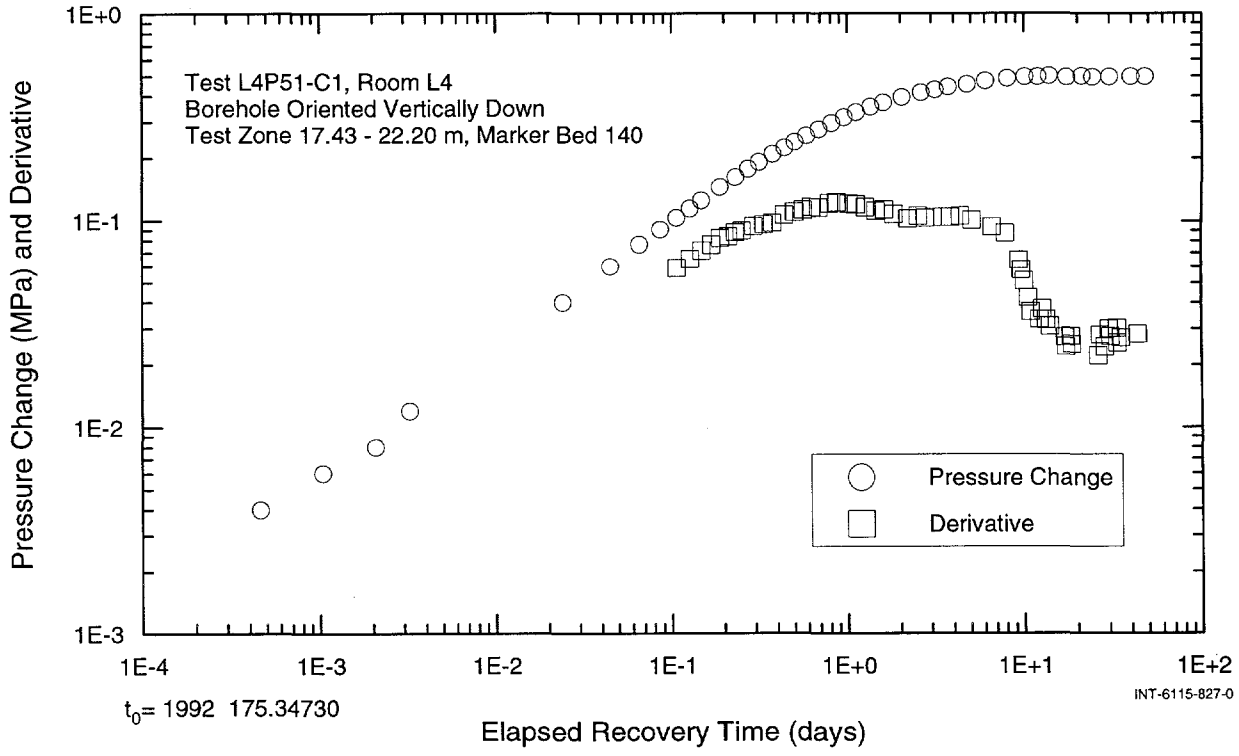

Figure 7-23. First L4P51-C1 test-zone pressure-buildup test.

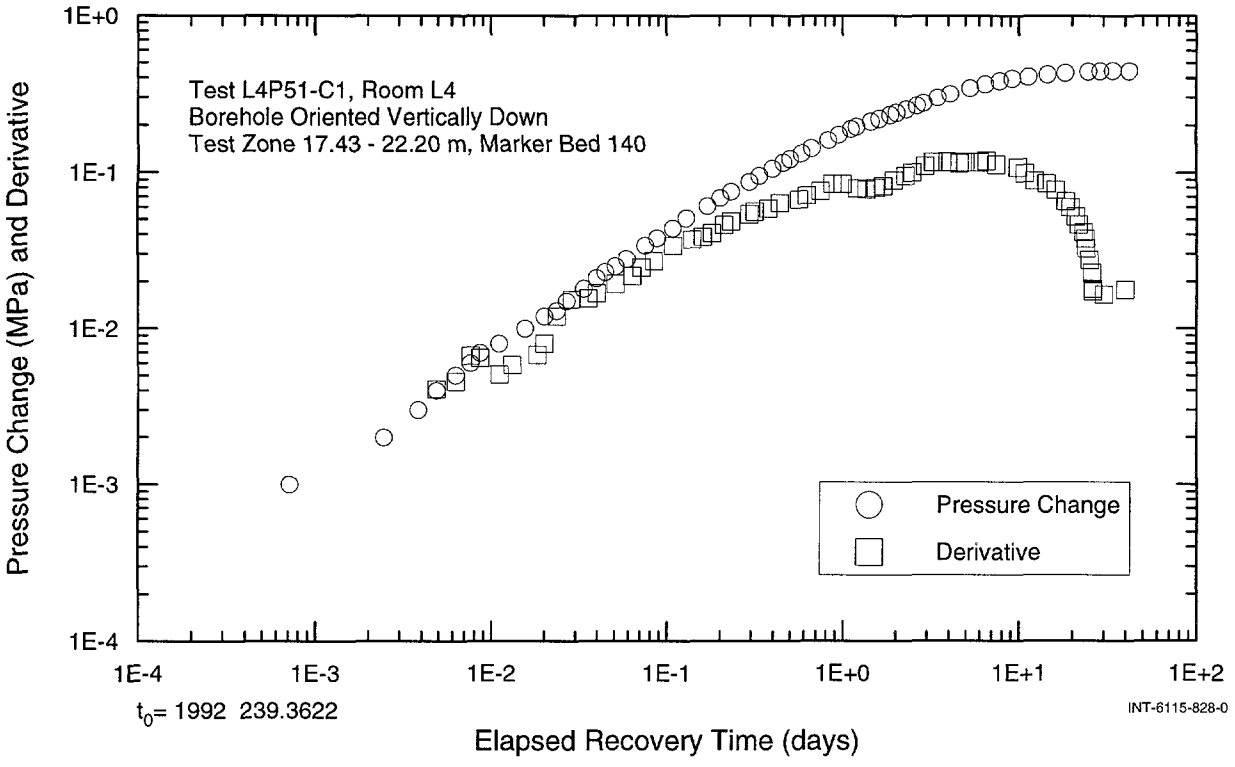

Figure 7-24. Second L4P51-C1 test-zone pressure-buildup test.

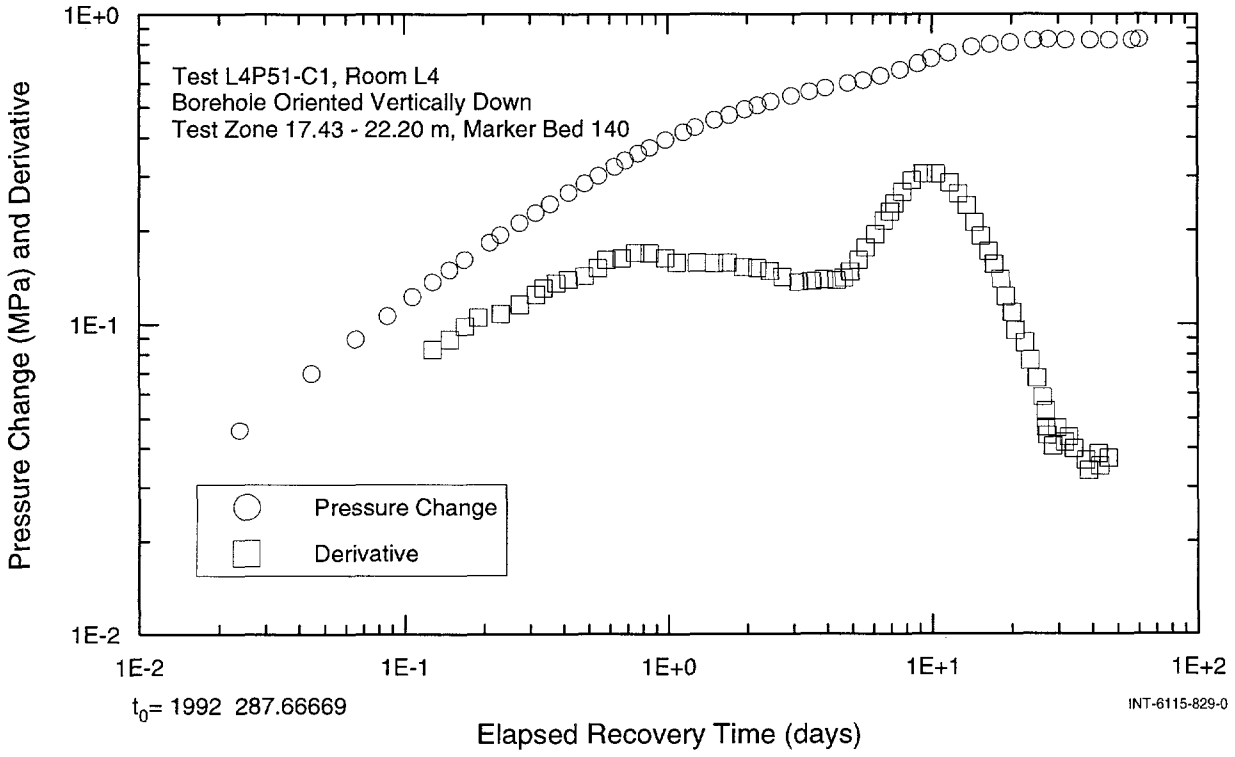

Figure 7-25. Third L4P51-C1 test-zone pressure-buildup test.

7.1.2.2 Numerical Interpretations

Residual analysis indicated that the measured responses during the MB140 CPW tests could not be adequately simulated using a homogeneous radial model. The fit was improved slightly by adding a skin to the model, but the results were still unsatisfactory. GTFM analysis indicated that each of the three CPW tests exhibited the same general characteristics. The early-time flow dimension was sublinear ($n < 1$) while the estimated late-time flow dimension was nearly 3. One possible explanation for this trend would be that MB140 is sparsely fractured in the immediate vicinity of the borehole, but that fracturing increases toward the front of the room and adjacent drift intersection where the vertical stress relief would be greatest (Argüello, 1990), which is reflected in a high flow dimension as a pressure transient propagates into it. Beauheim et al. (1993b) and Wawersik et al. (1997) discuss a similar situation in more detail in connection with hydraulic-fracturing experiments in MB139 and MB140 in Room C1.

The estimated K values were 3.2×10^{-13}, 8.0×10^{-14}, and 7.1×10^{-13} m/s ($k = 5.6 \times 10^{-20}$, 1.4×10^{-20}, and 1.2×10^{-19} m^2) for the first, second, and third tests, respectively. The S_s estimates were 9.1×10^{-11}, 1.7×10^{-11}, and 4.0×10^{-8} m^{-1} for the first, second, and third tests, respectively. The corresponding values of the outer flow dimension were 2.8, 2.9, and 2.8, and optimized values of C_{tz} were 1.0×10^{-7}, 3.1×10^{-8}, and 3.4×10^{-8} Pa^{-1} for the first, second, and third tests, respectively. Figures 7-26 through 7-31 show plots of the best-fit GTFM simulations compared to the observed cumulative production and flow rates for the first, second, and third L4P51-C1 CPW tests,

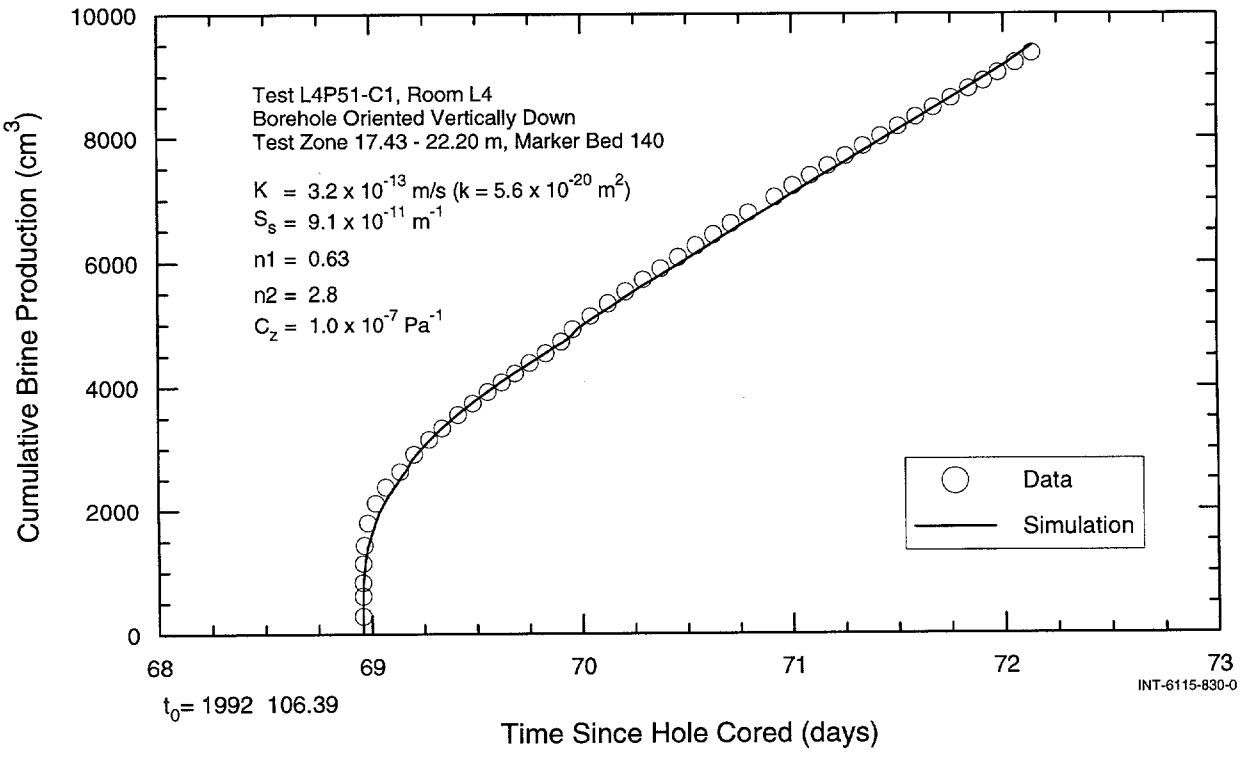

Figure 7-26. Linear-linear plot of GTFM simulation of brine production during the first L4P51-C1 test zone constant-pressure-withdrawal test.

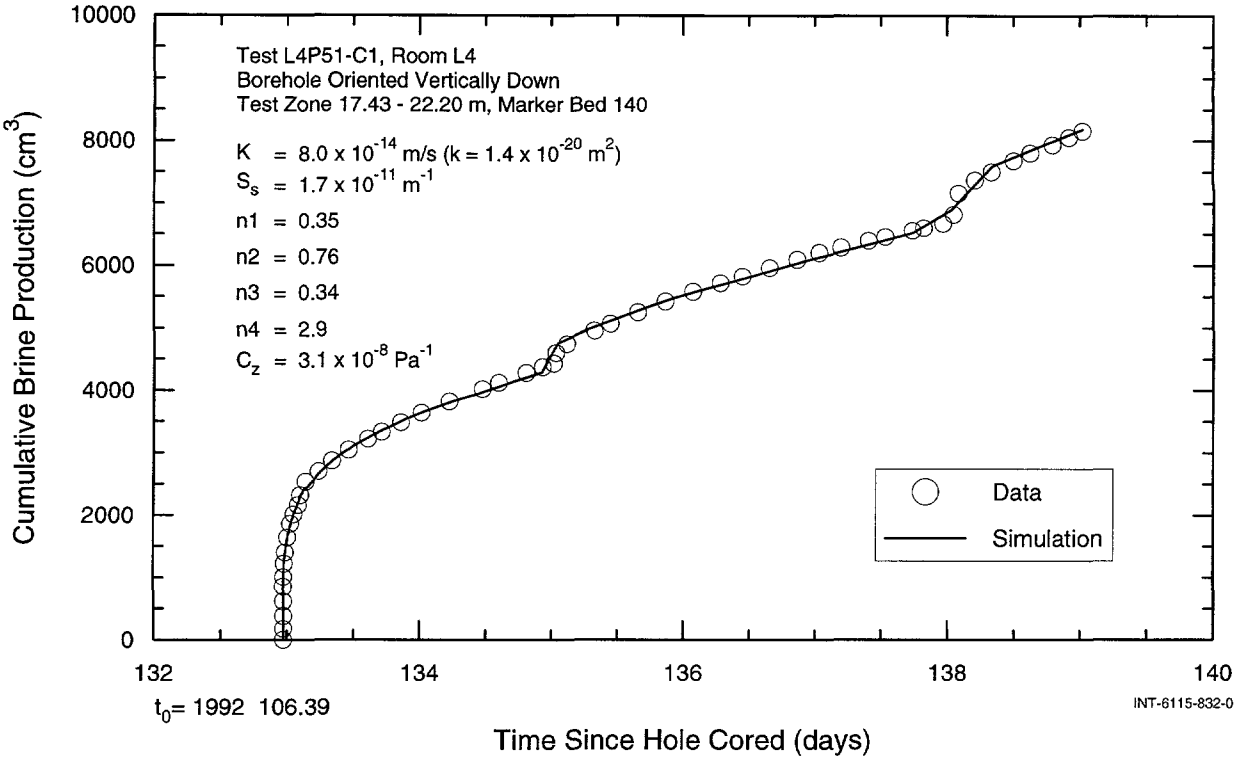

Figure 7-27. Linear-linear plot of GTFM simulation of brine production during the second L4P51-C1 test zone constant-pressure-withdrawal test.

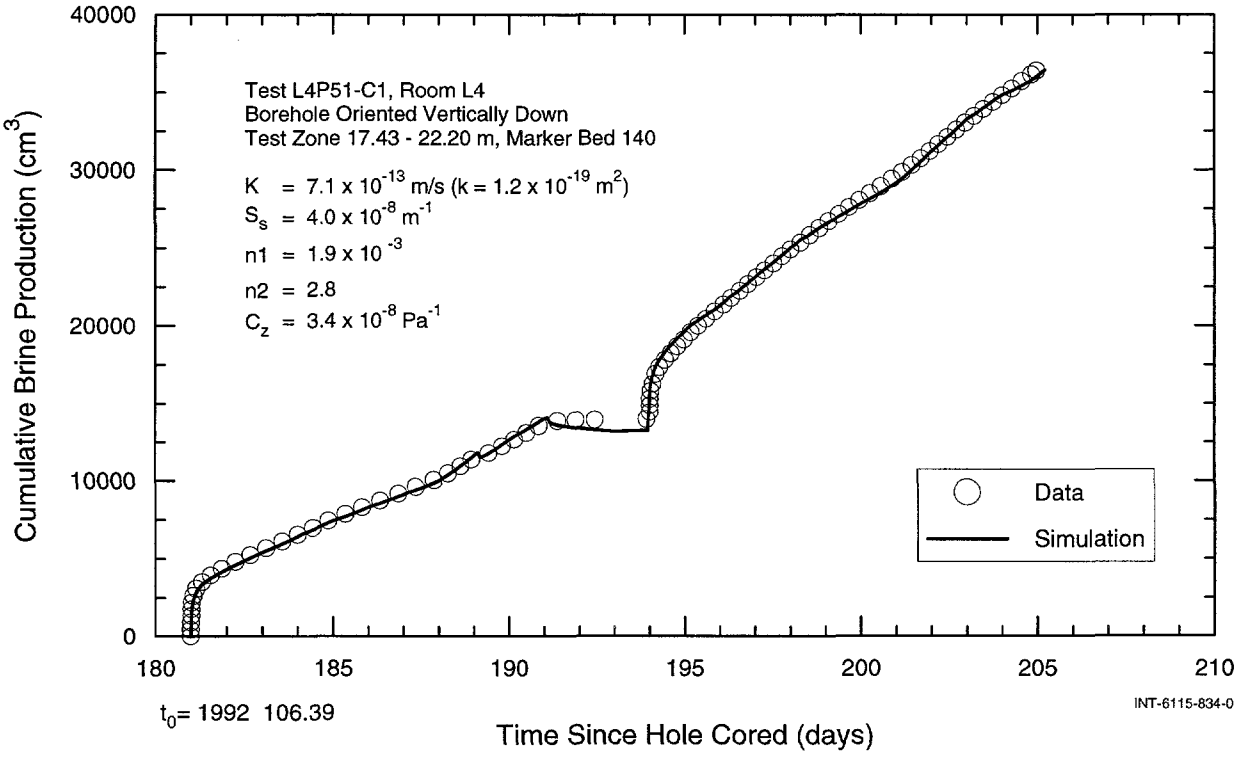

Figure 7-28. Linear-linear plot of GTFM simulation of brine production during the third L4P51-C1 test zone constant-pressure-withdrawal test.

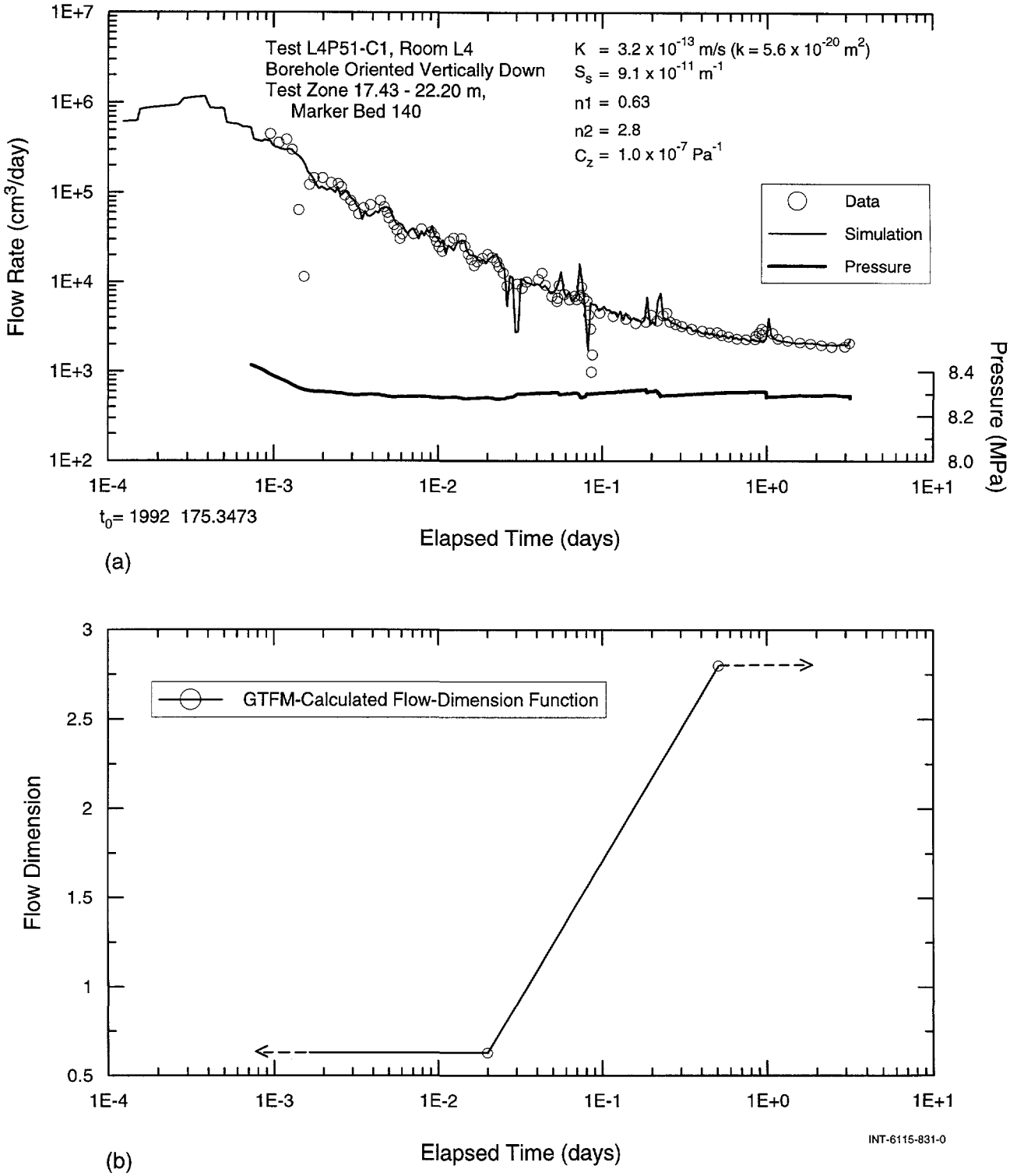

Figure 7-29. Log-log and semilog plots of GTFM simulation of flow rates along with the zone pressure (a) and flow-dimension function (b) during the first L4P51-C1 test zone constant-pressure-withdrawal test.

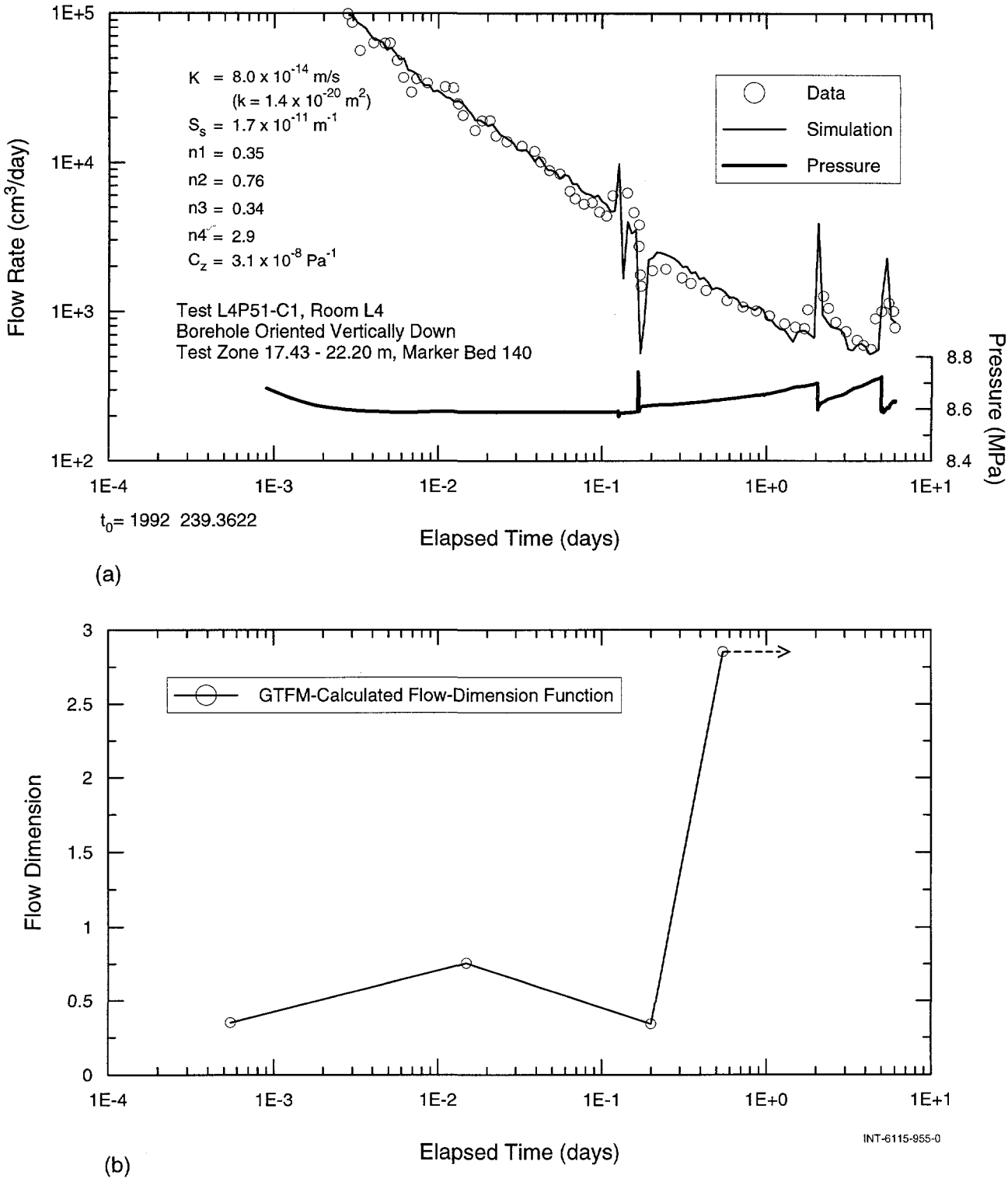

Figure 7-30. Log-log and semilog plots of GTFM simulation of flow rates along with the zone pressure (a) and flow-dimension function (b) during the second L4P51-C1 test zone constant-pressure-withdrawal test.

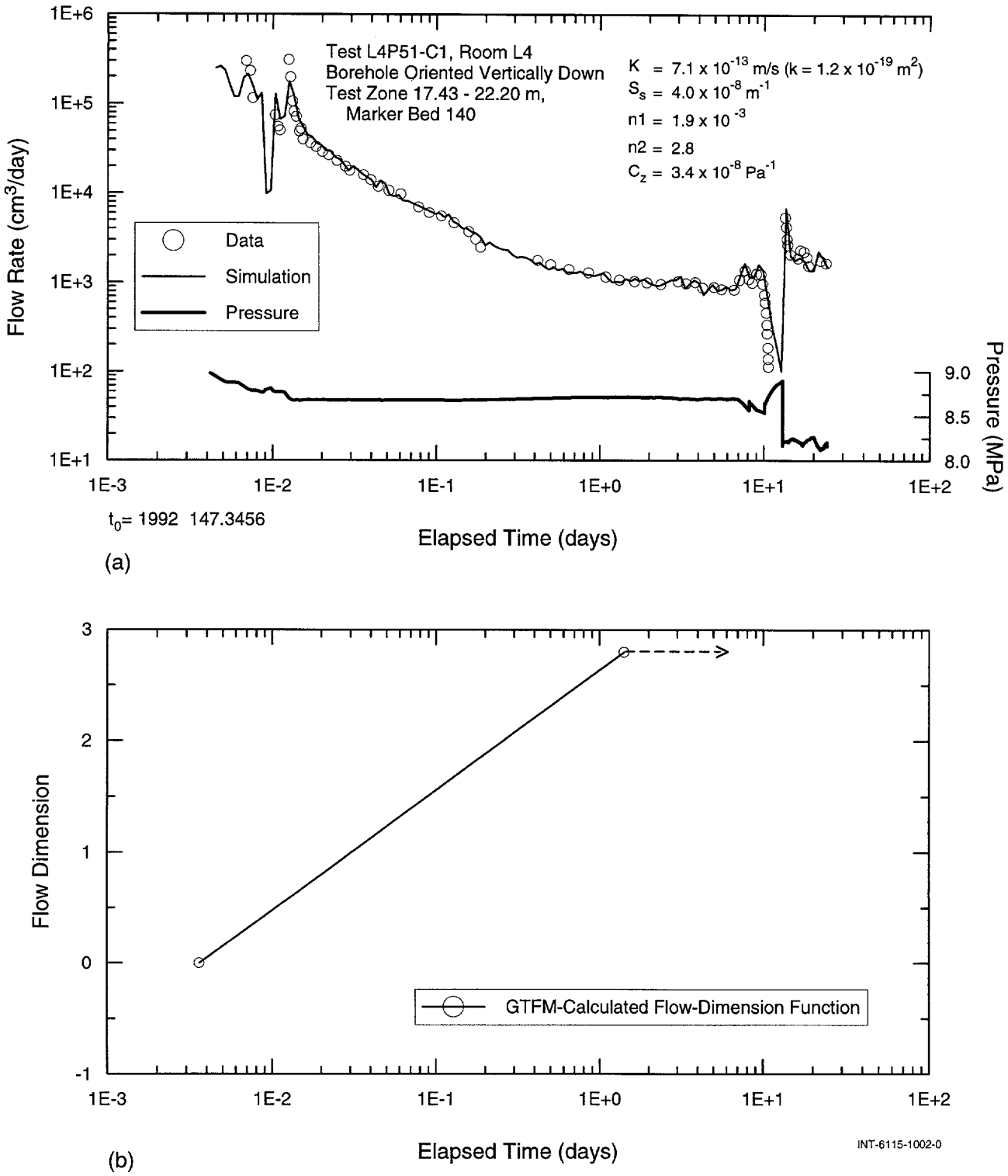

Figure 7-31. Log-log and semilog plots of GTFM simulation of flow rates along with the zone pressure (a) and flow-dimension function (b) during the third L4P51-C1 test zone constant-pressure-withdrawal test.

respectively. Figures 7-29 through 7-31 also show the corresponding flow-dimension functions converted from distance to time using Eq. 6-5.

7.1.2.3 Summary

Numerical interpretations of the L4P51-C1 MB140 constant-pressure-withdrawal tests provided estimates of hydraulic conductivity ranging from 8.0×10^{-14} to 7.1×10^{-13} m/s ($k = 1.4 \times 10^{-20}$ to 1.2×10^{-19} m^2). The flow dimension for the numerical analysis transitioned from sublinear to spherical as the flow tests progressed. Numerical analyses of the CPW tests provided specific-storage estimates ranging from 1.7×10^{-11} to 4.0×10^{-8} m^{-1}. As discussed in Section 6.2.4, specific storage cannot be reliably estimated from single-hole tests that may be influenced by a skin around the borehole. Therefore, the estimates of specific storage are considered meaningless. Quantitative estimates of the fitting-parameter uncertainty (95% joint-confidence regions) and the corresponding correlation matrices are presented in Appendix C.

No estimate of formation pore pressure was made from the MB140 tests. The pressure in the test zone continued to increase during the entire 266-day testing period. The highest pressure measured in the test zone was 9.25 MPa on 6 January 1993. At this time, the pressure was still increasing at a rate of approximately 4.5 kPa/day.

7.2 L4P51-D1 and 2

Borehole L4P51 was deepened from 22.2 m to 30.48 m below the floor of Room L4 on 20 to 22 September 1994 (Calendar Days 263 to 265). The hole was deepened to allow testing of an argillaceous halite unit (AH-m5) at a location where stress relief caused by the excavation was hoped to be insignificant. Figure 7-32 shows the initial configuration of the test tool in L4P51 for the L4P51-D testing, and indicates the lengths and stratigraphic locations of the guard and test zones. The guard zone extended from 17.05 to 26.19 m below the floor of Room L4 and included MB140, various halite units, and one unnamed anhydrite unit. Test zone 2 extended from 27.02 to 28.15 m and included halite with varying amounts of clay and polyhalite. Test zone 1 extended from 28.97 to 30.48 m and included halite and the target horizon, AH-m5.

The test tool was initially installed on 29 September 1994 (Calendar Day 272). The pressure response in test zone 1 (Figure 7-33) indicated that a leak existed somewhere in the system, so the test tool was removed on 11 October 1994 (Calendar Day 284). At this time the LVDT housing was replaced with a volume-displacement device in an attempt to reduce the number of potential pressure leaks. The test tool shown in Figure 7-34 was then re-installed on 13 October 1994 (Calendar Day 286). The pressure response continued to indicate that a leak existed and the test tool as configured in Figure 7-34 was subsequently removed and re-installed three more times over the next two months. All attempts to locate and correct the test-zone leak appeared to be unsuccessful, although the lack of any significant pressure response in the L4P51-D1 guard zone was found to be due to the failure of the o-ring seals in the 2-inch couplings joining the tool extensions in the guard zone (Figure 7-32). The test tool was again removed on 20 March 1995 (1994 Calendar Day 444) and was replaced on 5 April 1995 (1994 Calendar Day 460; 1995 Calendar Day 95) with a single-packer configuration shown in Figure 7-35 to begin the L4P51-D2 testing sequence. The pressure in the test zone increased too slowly for any testing to be performed in the

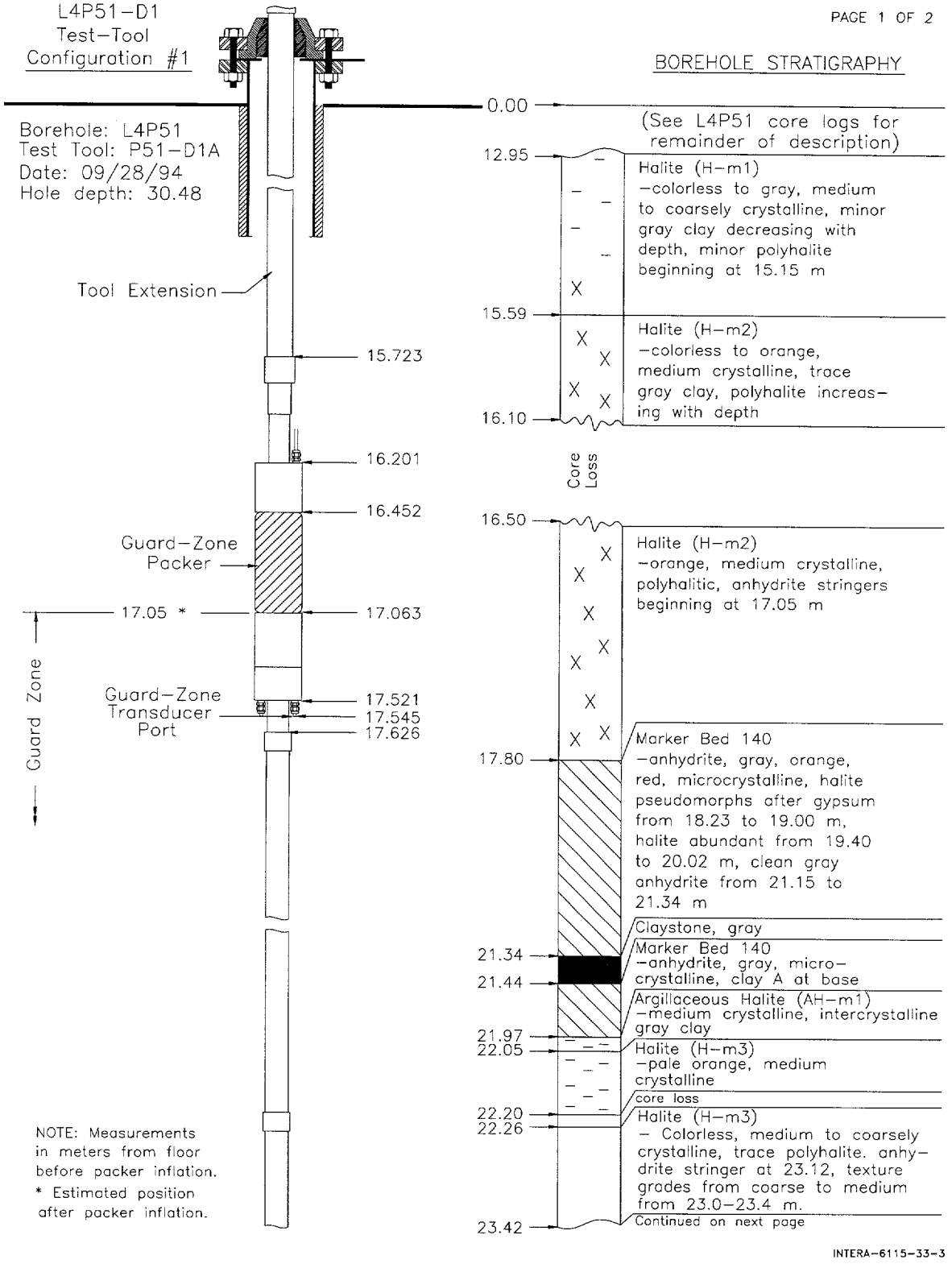

Figure 7-32a. Configuration #1 of the tool in borehole L4P51 for testing sequence L4P51-D1.

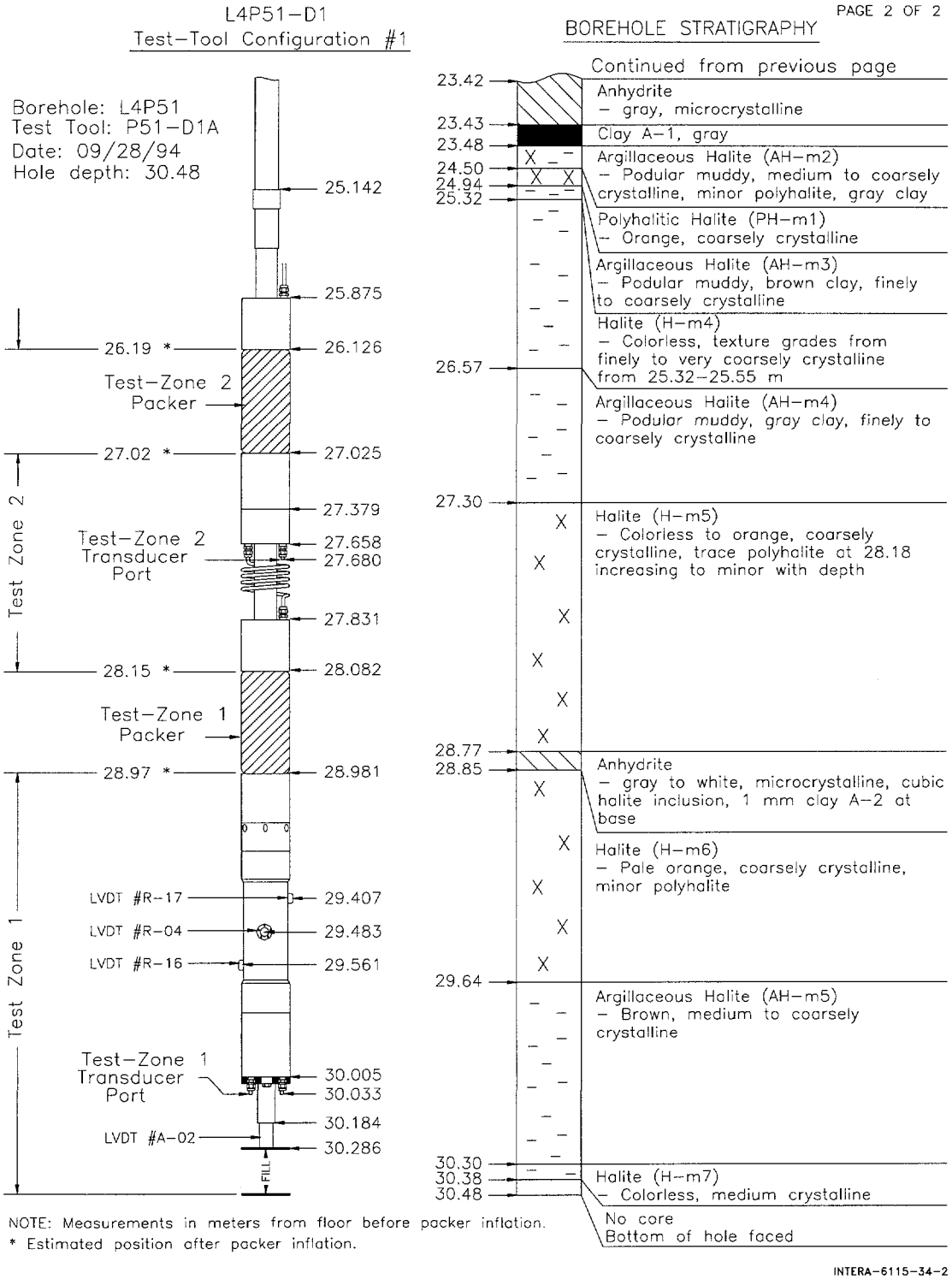

Figure 7-32b. Configuration #1 of the tool in borehole L4P51 for testing sequence L4P51-D1 (continued).

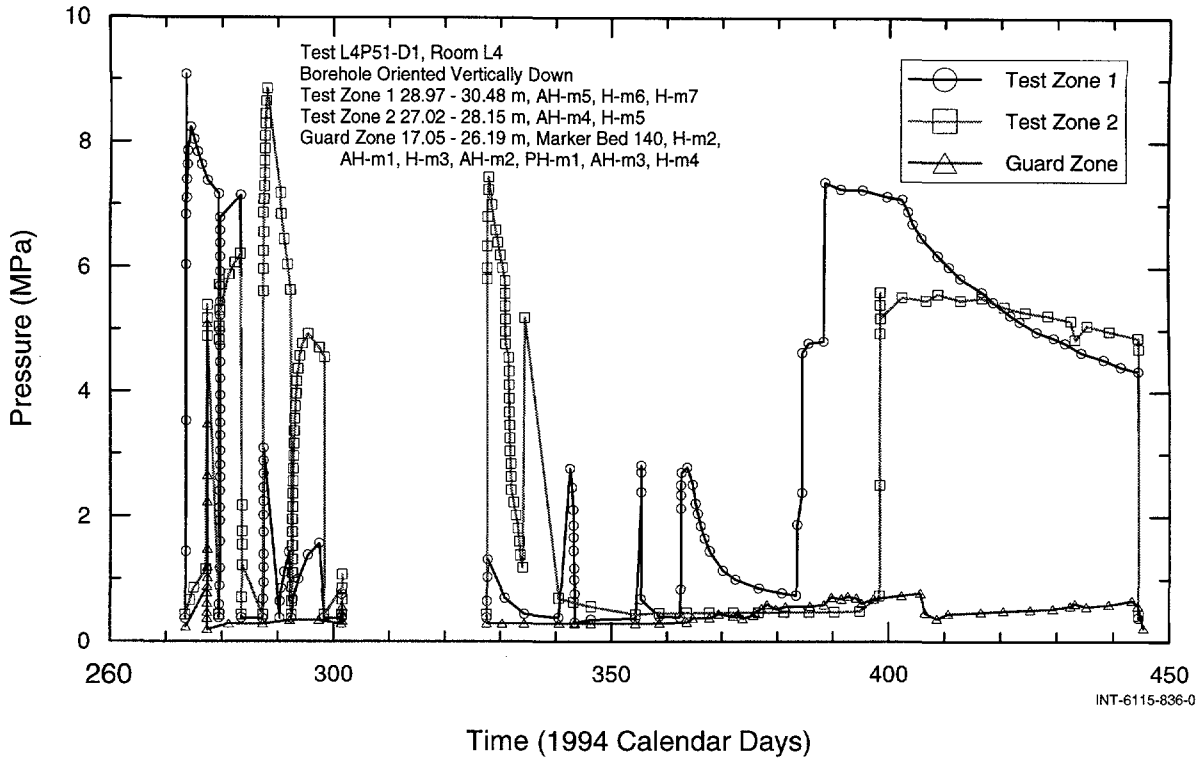

Figure 7-33. Test- and guard-zone pressures during L4P51-D1 testing.

time available. By the time the test tool had to be removed from the borehole on 25 October 1995 (Calendar Day 298), the pressure had reached only 4.81 MPa (Figure 7-36).

The pressure values presented have been compensated for the elevation differences between the locations of the pressure transducers and the centers of the tested units in the test and guard zones. The L4P51-D1 guard-zone, test zone 2, and test zone 1 pressures were compensated by adding 0.280, 0.342, and 0.370 MPa, respectively, to the pressures measured by the pressure transducers and reported by Chace et al. (1998). The L4P51-D2 test-zone pressures were compensated by adding 0.370 MPa to the pressures measured by the pressure transducer. Packer pressures during the L4P51-D1 and D2 monitoring are shown in Appendix D.

7.3 L4P52-B

Borehole L4P52 was originally drilled during April 1991 into the upper part of the west rib (wall) of Room L4 at an angle of 40° below vertical for permeability-testing sequence L4P52-A. The borehole was subsequently deepened from 5.56 m to 14.12 m on 10 to 14 December 1992 (Calendar Days 345 to 349) for testing sequence L4P52-B. The hole was deepened to allow testing of MB138. Figure 7-37 shows the configuration of the test tool in L4P52 for the L4P52-B testing, and indicates the lengths and stratigraphic locations of the guard and test zones. The guard zone extended from 10.83 to 11.88 m and included the upper 0.45 m of map unit AH-1 (clay J), the entire 0.52 m of map unit H-5 (halite), and the lower 0.08 m of map unit AH-2 (argillaceous halite). The test zone extended from 12.71 to 14.12 m and included the upper 1.18 m of map unit AH-2, the entire

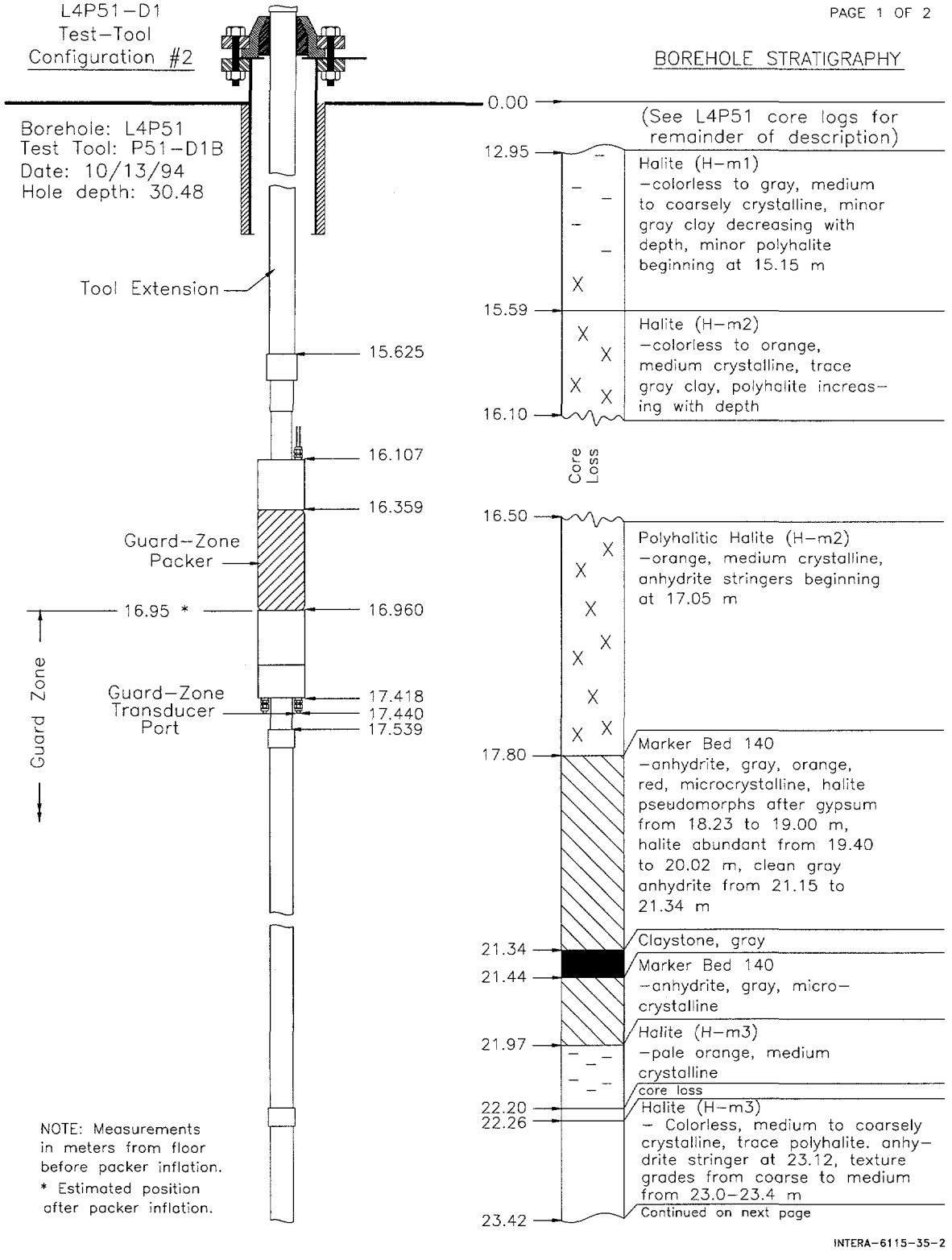

Figure 7-34a. Configuration #2 of the tool in borehole L4P51 for testing sequence L4P51-D1.

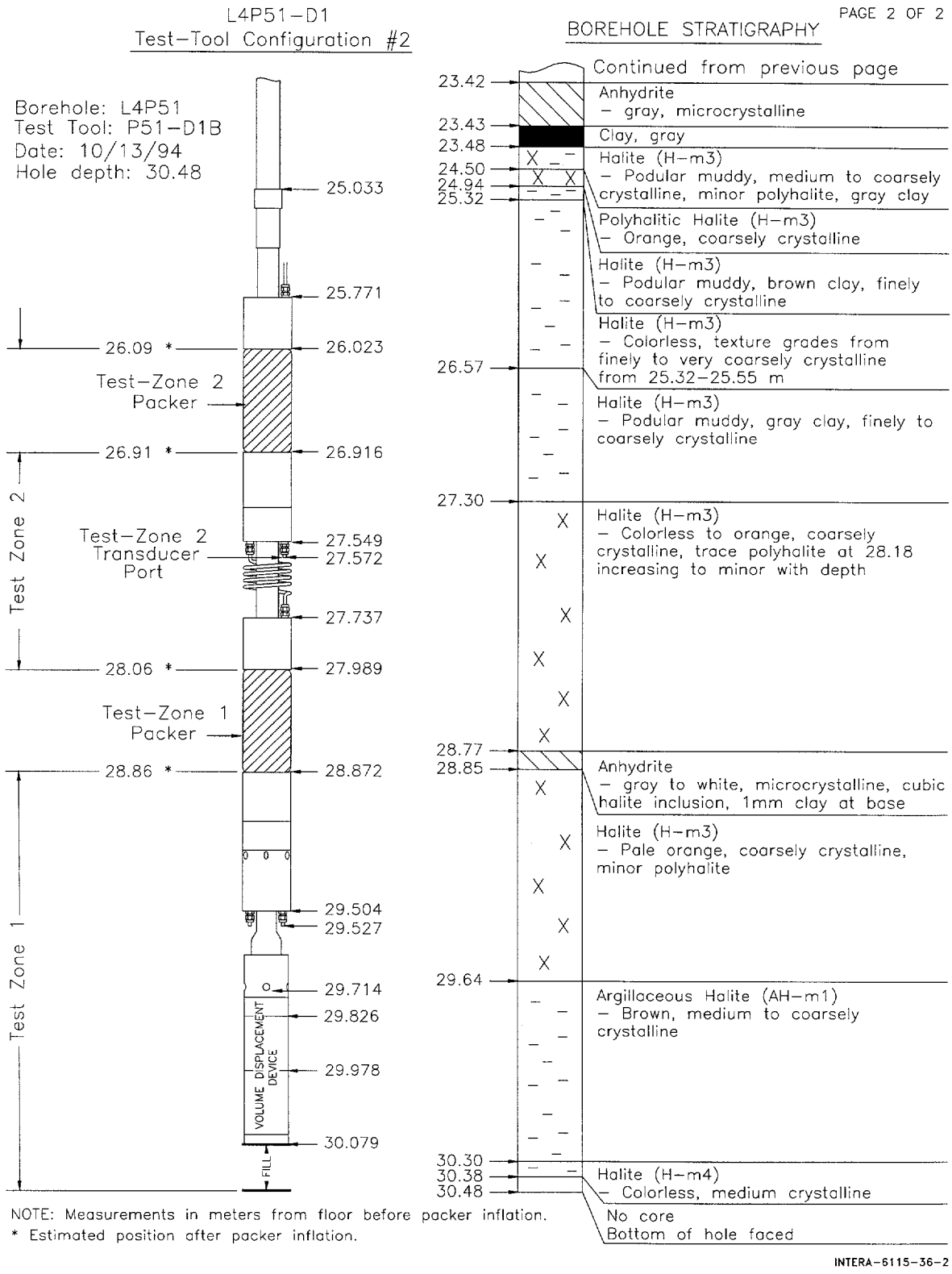

Figure 7-34b. Configuration #2 of the tool in borehole L4P51 for testing sequence L4P51-D1 (continued).

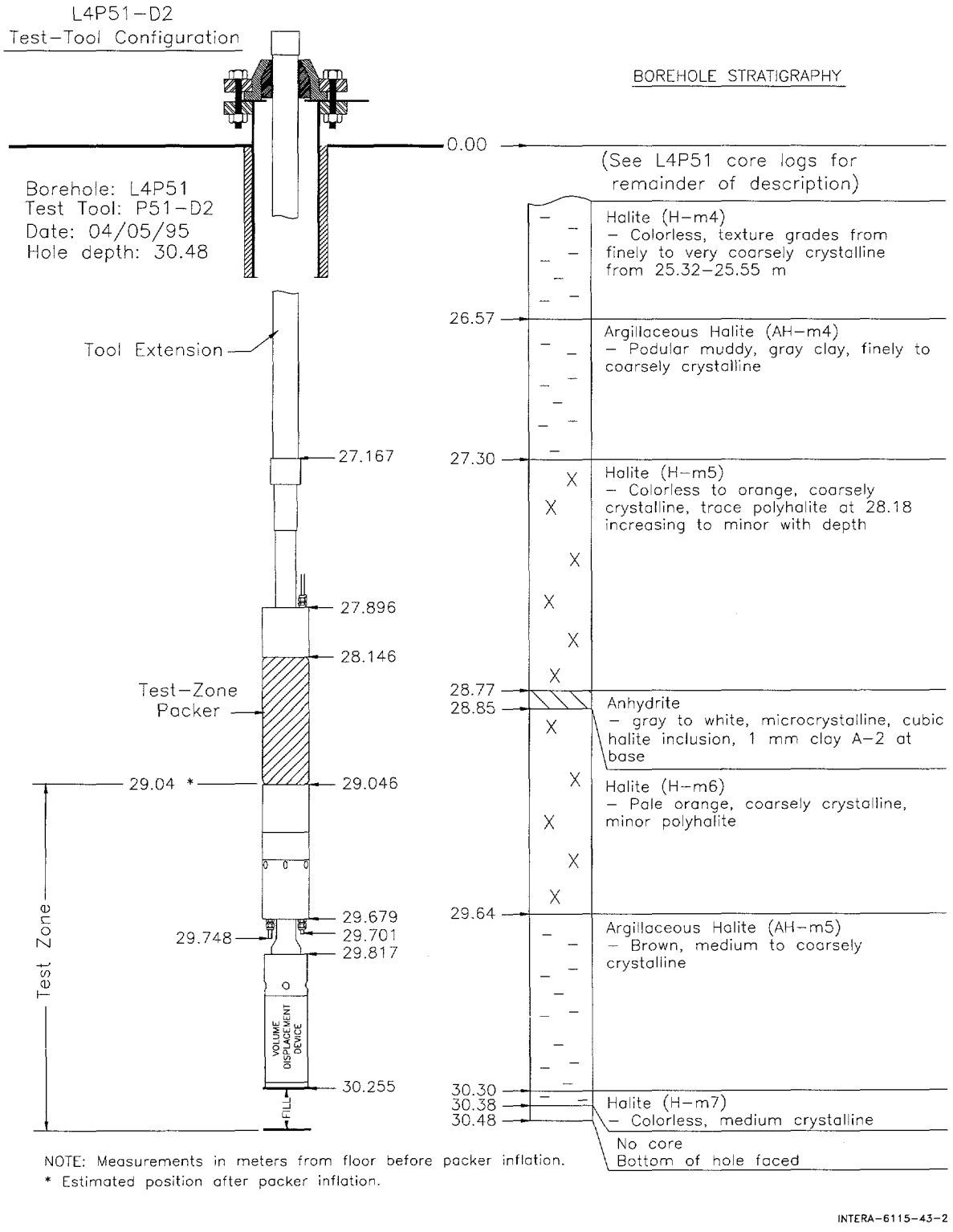

Figure 7-35. Configuration of the tool in borehole L4P51 for testing sequence L4P51-D2.

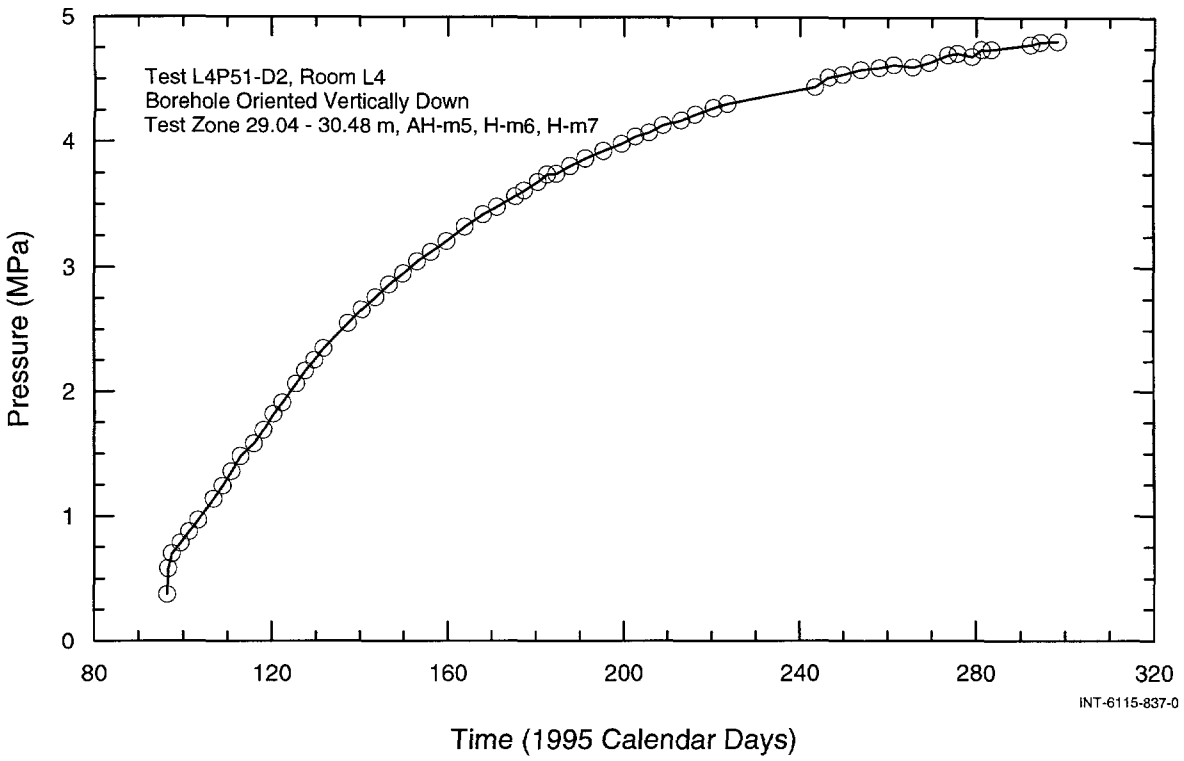

Figure 7-36. Test-zone pressure during L4P51-D2 testing.

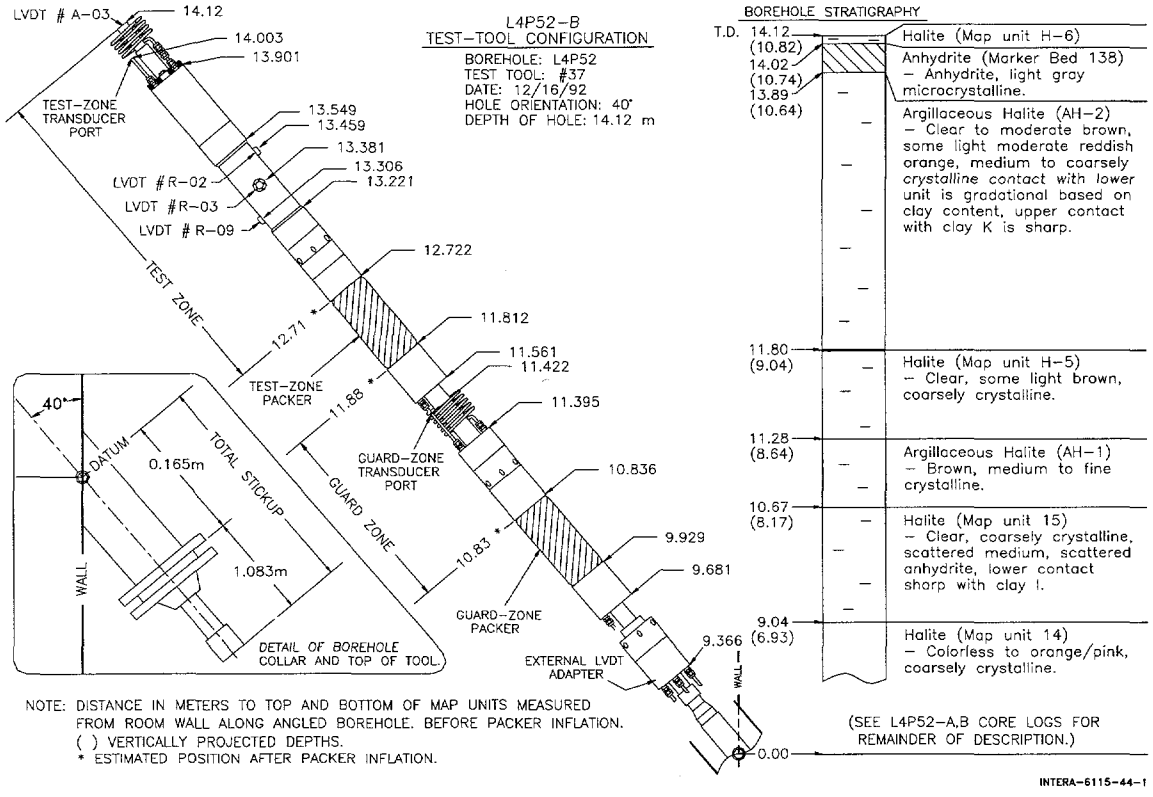

Figure 7-37. Configuration of the test tool in L4P52 for testing sequence L4P52-B.

0.13 m of MB138 and clay K, and the lower 0.10 m of map unit H-6 (halite). (All thicknesses listed above are as measured along the inclined borehole.) Figure 7-38 shows the test- and guard-zone pressures recorded during the monitoring period. All of the pressure data from the L4P52-B testing sequence presented in this report have been compensated for the elevation differences between the locations of the pressure transducers and the centers of the tested units in the test and guard zones. The test- and guard-zone pressures were compensated by subtracting 0.125 and 0.110 MPa, respectively, from the pressures measured by the pressure transducers and reported by Chace et al. (1998). Packer pressures during the L4P52-B testing are shown in Appendix D.

The test and guard zones were shut in on 18 December 1992 (Calendar Day 353). Following a pressure-buildup period, four constant-pressure flow and two pressure-recovery tests were conducted in the test zone. No testing was performed in the guard zone. During some of the testing period, the pressure in the guard zone was maintained by a pressure-maintenance system. Following the completion of the permeability testing, a gas-threshold-pressure test was conducted on MB138 in the L4P52-B test zone. This test is discussed in Appendix E.

7.3.1 Test Zone

The testing sequence in the L4P52-B test zone consisted of an open borehole period lasting from 14 to 18 December 1992 (Calendar Days 349 to 353), an initial shut-in period from 18 December 1992 to 11 February 1993 (1992 Calendar Days 353 to 408), a constant-pressure-withdrawal test lasting from 11 to 24 February 1993 (1992 Calendar Days 408 to 421), a pressure-buildup test lasting until 7 June 1993 (1992 Calendar Day 524), a constant-pressure-injection test at

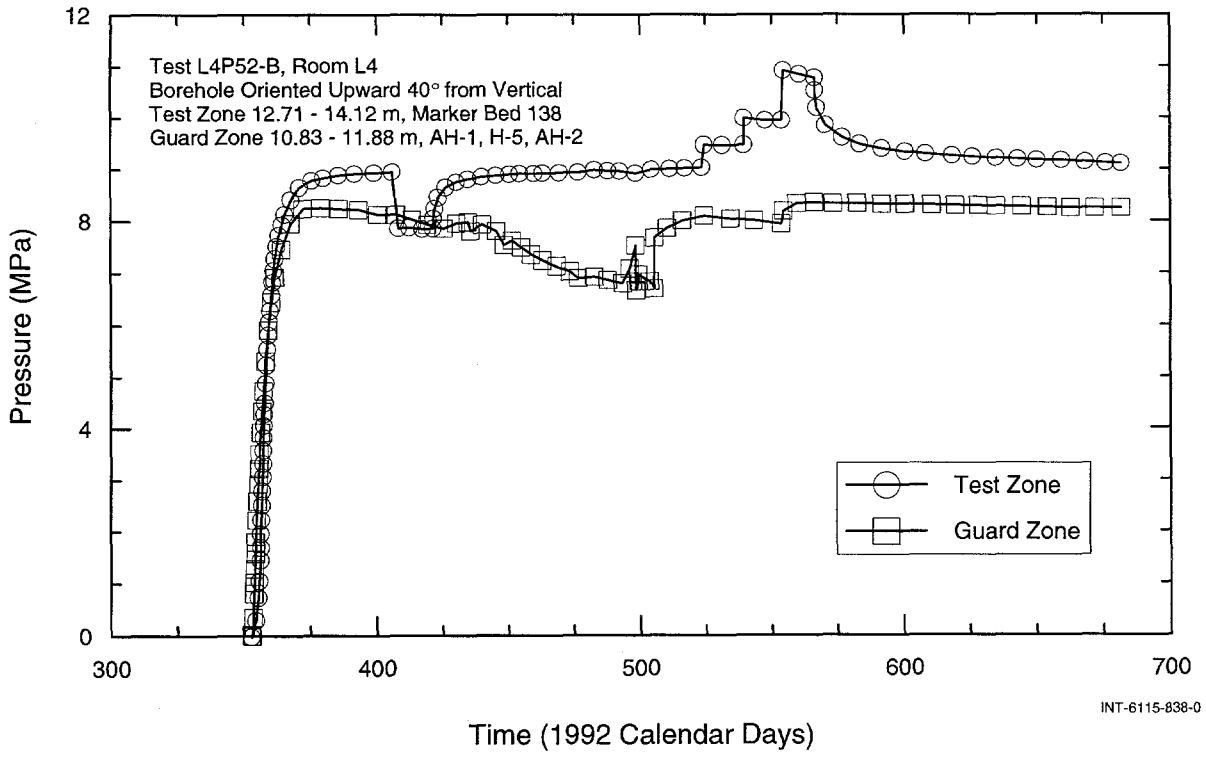

Figure 7-38. Test- and guard-zone pressures during L4P52-B testing.

about 0.4 MPa above static formation pressure lasting from 7 to 22 June 1993 (1992 Calendar Days 524 to 539), a constant-pressure-injection test at about 1 MPa above static formation pressure lasting from 22 June to 7 July 1993 (1992 Calendar Days 539 to 554), a constant-pressure-injection test at about 2 MPa above static formation pressure lasting from 7 to 19 July 1993 (1992 Calendar Days 554 to 566), and a pressure-falloff test lasting until 10 November 1993 (1992 Calendar Day 676).

The fluid-production data from the constant-pressure-withdrawal test and the injection data from the series of constant-pressure-injection tests are shown in Figures 7-39 and 7-40, respectively. Approximately 436 cm^3 of brine were produced during the 13-day constant-pressure-withdrawal test. The individual volumes of brine injected for the first, second, and third constant-pressure-injection tests were about 226, 496, and 1,247 cm^3, respectively.

The compressibility of the L4P52-B test zone was calculated from the data collected at the beginning of each constant-pressure test. The test-zone compressibility was also specified as a fitting parameter during numerical (GTFM) simulations. The compressibility values calculated from the constant-pressure data ranged from 8.2×10^{-10} to 2.9×10^{-9} Pa^{-1}. The optimized compressibility value of 2.5×10^{-9} Pa^{-1} was in good agreement with these calculated values.

The L4P52-B tests were analyzed using an idealized test-zone geometry as described in Section 6.3. Flow from MB138 to the borehole was assumed to be horizontal only, and the test zone was modeled as a vertical cylindrical borehole with a radius of 5.850 cm.

Preliminary analysis of the L4P52-B test data indicated that the hydraulic conductivity of the system was changing when the pressure in the test zone changed. The difference

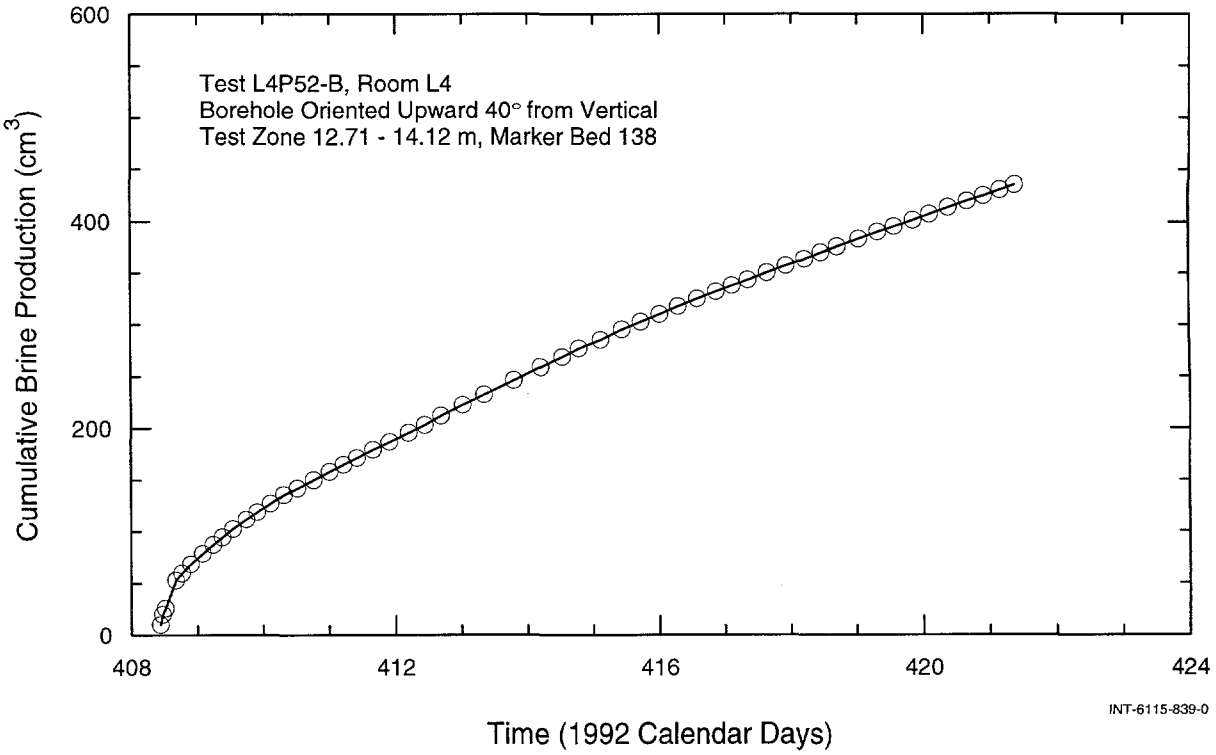

Figure 7-39. Cumulative brine production during the L4P52-B constant-pressure-withdrawal test.

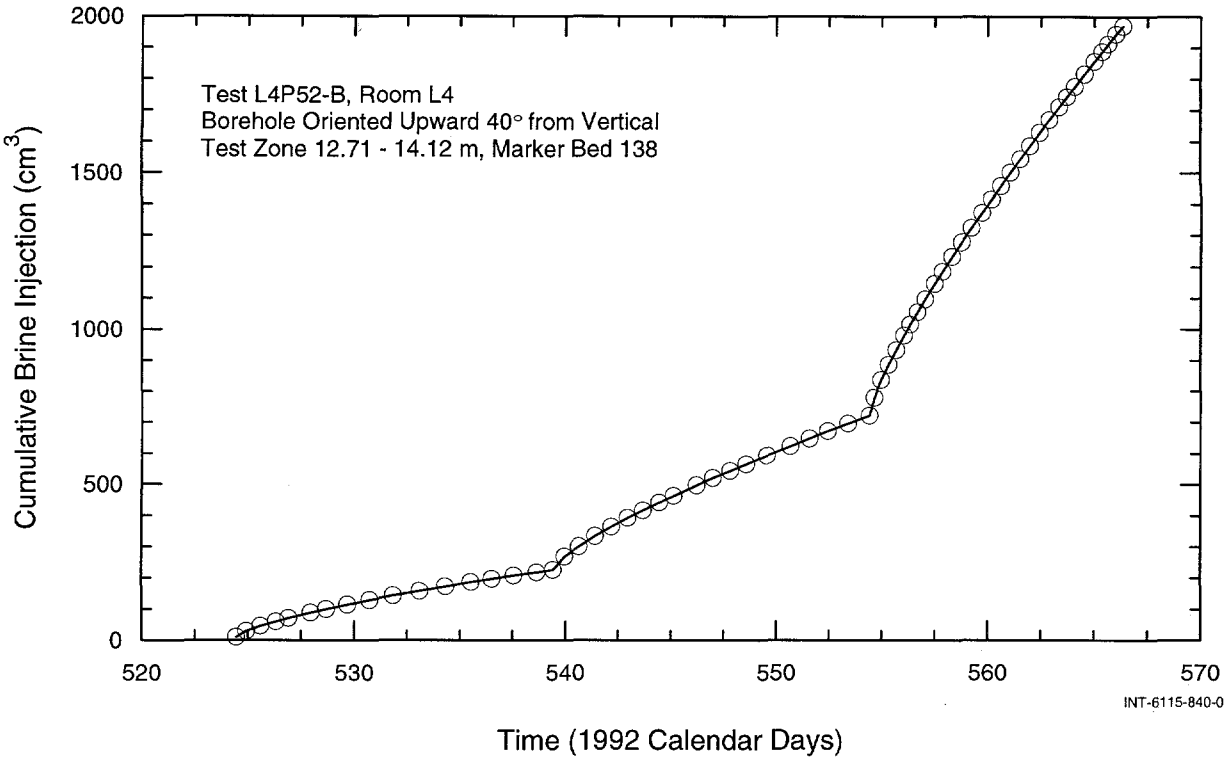

Figure 7-40. Cumulative brine injection during the L4P52-B constant-pressure-injection tests.

between the responses of the constant-pressure-withdrawal test and the first constant-pressure-injection test, in fact, prompted the addition of the second and third constant-pressure-injection tests to the testing sequence. The chosen conceptual model was, therefore, one in which K varied as a function of pressure. In GTFM, this is implemented by specifying that the K value at each node depends on the pressure calculated at that node. Specific storage was assumed to be constant because we are uncertain if or how it varies with pressure.

Log-log plots of the flow-rate data from the first three constant-pressure tests displayed a distinctive linear trend, indicating that flow in the system was subradial, i.e., the flow dimension was less than 2. Figure 7-41 shows the flow dimension during each of the constant-pressure-injection tests and the subsequent pressure-falloff test calculated from the second derivatives of $1/q$ and pressure (data from the CPW test were too noisy to be used). As the injection pressure was increased from CPI1 to CPI3, the flow dimension clearly increased, but appeared to remain relatively constant during each CPI test. A decrease in the dimension can then be seen during the pressure-falloff test. The flow dimension during the pressure-falloff test initially matched the CPI3 flow dimension. After approximately two days, the flow dimension transitioned to a lower dimension equal to that observed during CPI2. At ten days, the dimension began to decrease again, eventually reaching the CPI1 value.

Flow dimension was specified as a fitting parameter during the optimization process, but a single flow dimension was used to fit all of the constant-pressure tests. This was done primarily to simplify, as much as possible, an

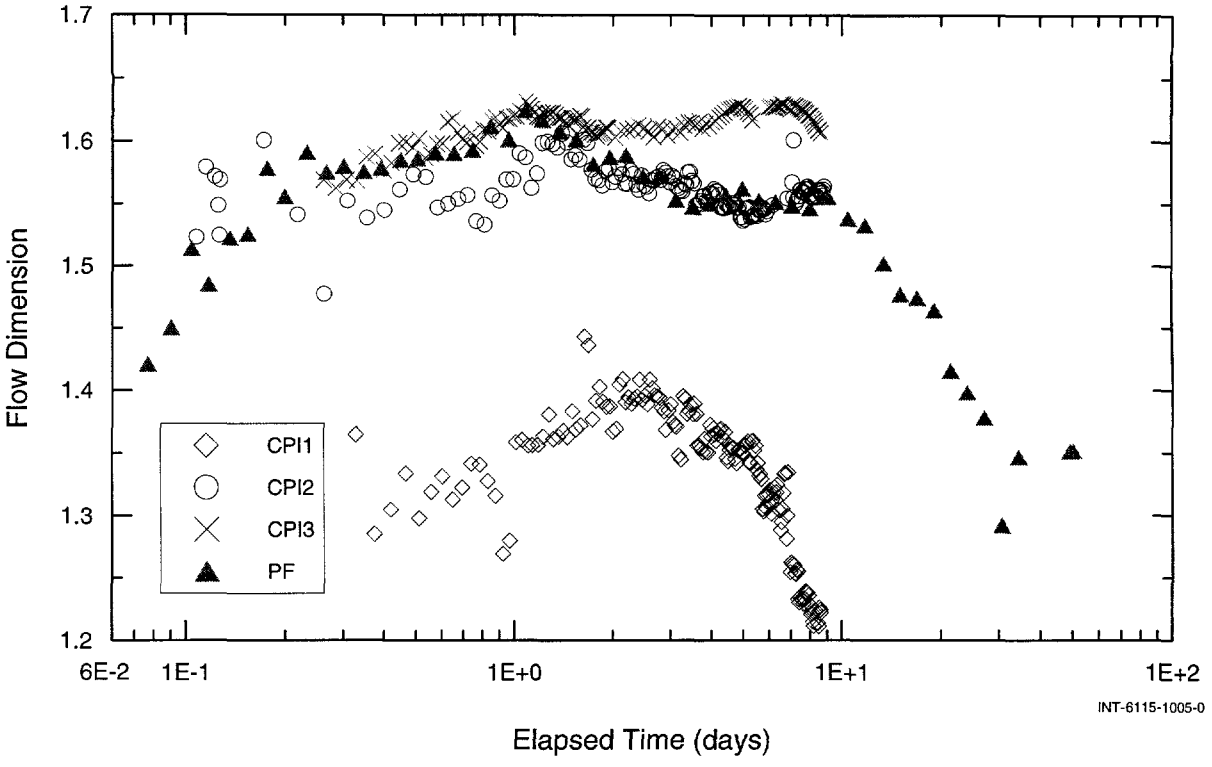

Figure 7-41. Calculated flow dimensions during the specified L4P52-B test sequences.

already complex conceptual model. Remember that a unique combination of pressure-dependent K and n cannot be obtained from well-test analysis. Conceptually, however, we see no reason to assume that both parameters don't change simultaneously. The calculated flow dimensions shown in Figure 7-41 should reflect both the geometry of the system and the rate of change of K as a function of pressure. To the extent that n was changing but assumed to be constant, the estimates of $K(P)$ will be affected.

The modeling/analysis approach described above resulted in a single parameter set that provided a good fit to the data through the final constant-pressure-injection test. This parameter set did not, however, provide a good fit to the final pressure-falloff data. The entire testing sequence was, therefore, divided into two parts with one parameter set for the test data through the final constant-pressure-injection test and another optimized parameter set for the final pressure-falloff test. This is done in GTFM by using the modeled pressure distribution at the end of the final constant-pressure-injection test as the initial conditions for estimating new fitting parameters for simulation of the pressure-falloff test.

7.3.1.1 Analytical Interpretations

Type-curve analysis was performed on the flow-rate data from the constant-pressure-withdrawal test and the first constant-pressure-injection test. Hydraulic-conductivity estimates from this type-curve analysis are made assuming that flow is radial. While subsequent numerical analysis indicated that the flow-rate data are better fit with a subradial model, this analysis is presented to see if a "moderate" violation of this assumption results in hydraulic-conductivity estimates that

differ greatly from the numerical interpretations.

The type-curve matches to the data from the constant-pressure-withdrawal and injection tests, respectively, are shown in Figures 7-42 and 7-43. The estimated K values for the match parameters indicated on the figures are 6.1×10^{-12} m/s ($k = 1.1 \times 10^{-18}$ m^2) and 7.7×10^{-12} m/s ($k = 1.4 \times 10^{-18}$ m^2) for the withdrawal and injection tests, respectively.

A K value of 1.3×10^{-11} m/s ($k = 2.3 \times 10^{-18}$ m^2) was estimated from the pressure-buildup test following the constant-pressure-withdrawal test using Eq. 6-1. The pressure derivative is shown in Figure 7-44 along with the parameter values used to estimate K. The pressure derivative from the pressure-falloff test never stabilized, so no analytical estimation of K was possible.

7.3.1.2 Numerical Interpretations

The pressure buildup observed after initially shutting in the test zone on 18 December 1992 (Calendar Day 353) exhibited increasing-rate behavior (Figure 7-38) indicative of pressure-dependent test-zone compressibility (Beauheim et al., 1991). The buildup is probably also affected by the pressure-dependent behavior of the formation (assuming the conceptual model is correct). Given the potential superposition of these two phenomena during the pressure buildup, the fact that test-zone compressibility becomes relatively constant above pressures of 3 MPa, and the relatively stabilized test-zone pressure (well above 3 MPa) immediately prior to the constant-pressure-withdrawal test, we decided to simplify the analysis by excluding all test events prior to the constant-pressure-withdrawal from the simulation. Subsequent

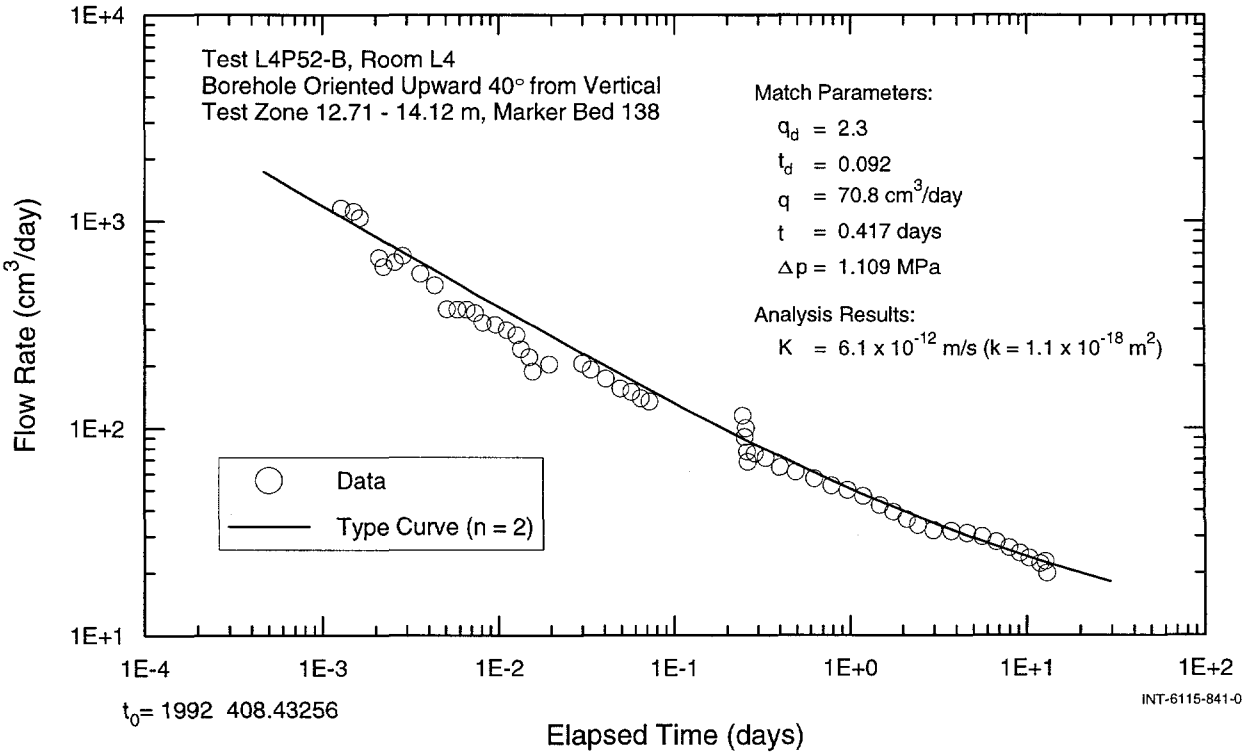

Figure 7-42. Log-log type-curve match to flow rates during the L4P52-B constant-pressure-withdrawal test.

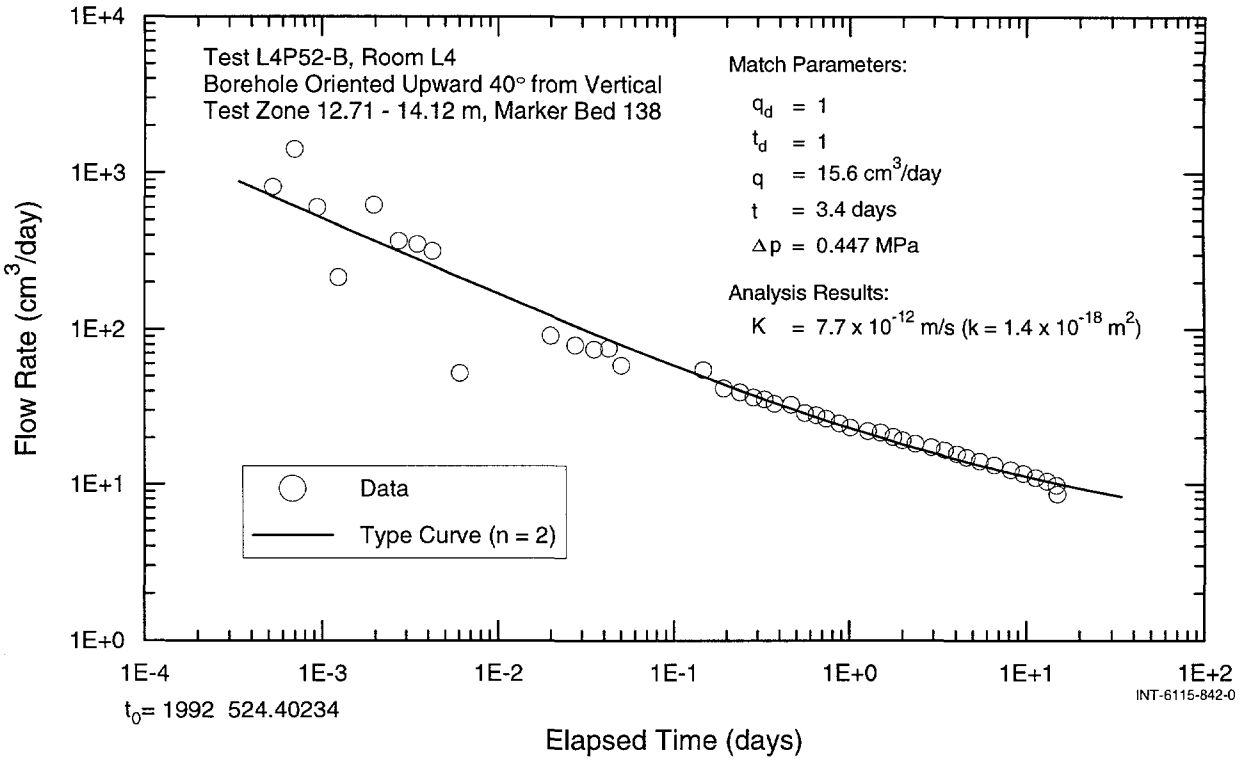

Figure 7-43. Log-log type-curve match to flow rates during the first L4P52-B constant-pressure-injection test.

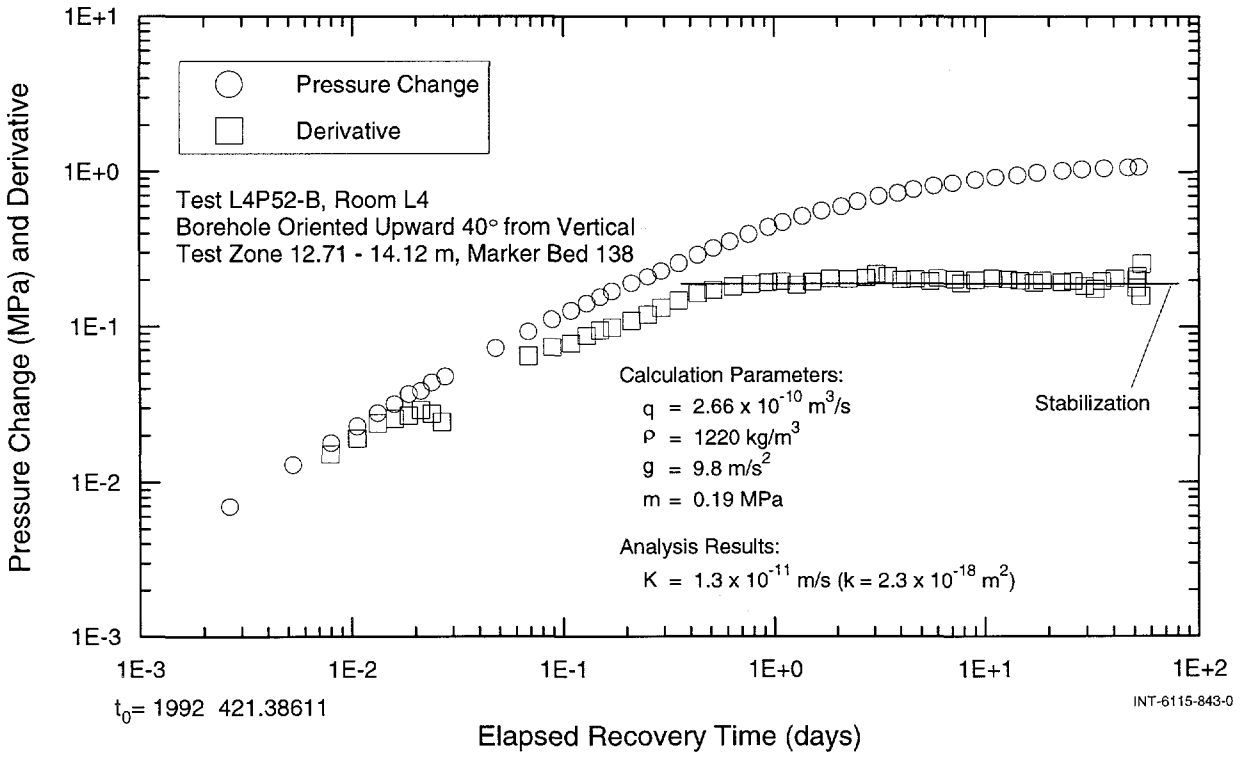

Figure 7-44. Analytical estimate of transmissivity from the L4P52-B pressure-buildup test.

sensitivity analysis indicated that the simulation results were not sensitive to the excluded test events.

The constant-pressure tests were simulated using specified-pressure sequences and hydraulic parameters were estimated by matching the brine-production data and the subsequent pressure-recovery tests. Analysis indicated that the measured test responses through the third constant-pressure-injection test could be matched with a single parameter set. However, a different set of parameters was needed to match the final pressure-falloff test. This could result from hysteresis in the opening/closing behavior of the fracture(s) and/or from simplifying assumptions made regarding the system geometry.

Initial attempts to match the data were made by specifying K, S_s, C_{tz}, and P_f as fitting parameters, allowing K to vary as a function of pressure while assuming that flow was radial (n = 2). The match to the data was greatly improved, however, when the flow dimension was added as a fitting parameter. Figure 7-45 shows the best-fit GTFM simulation compared to the flow-rate data from the four constant-pressure tests for n = 2 (radial flow). Figure 7-46 shows the best-fit GTFM simulation compared to the same data with a fitted flow-dimension value of 1.64. Given the estimated flow dimensions shown in Figure 7-41, an improved fit to the data using a subradial flow dimension would be expected. Although the subradial characteristic of the flow-rate data had been noted during the early simulation attempts, n was initially fixed at a value of 2 to see if the subradial behavior could be simulated simply by varying K as a function of pressure.

The fitted parameter values for simulations of all of the test events up to the final pressure-falloff test were a $K(P)$ function given by (all pressures in MPa) $K(7.85) = 1.0 \times 10^{-11}$ m/s, $K(8.5) = 1.8 \times 10^{-11}$ m/s, $K(9.47) = 2.1 \times 10^{-11}$ m/s, $K(9.95) = 4.9 \times 10^{-11}$ m/s, and $K(10.83) = 8.4 \times 10^{-11}$ m/s ($k = 1.8 \times 10^{-18}$, 3.1×10^{-18}, 3.7×10^{-18}, 8.7×10^{-18}, and 1.5×10^{-17} m^2, respectively), a specific storage of 1.6×10^{-4} m^{-1}, a formation pore pressure of 9.1 MPa, a test-zone compressibility of 2.5×10^{-9} Pa^{-1}, and a flow dimension of 1.64. Using these parameter values, the best-fit GTFM simulations compared to the observed flow for the constant-pressure-withdrawal test, the pressure and pressure derivative from the pressure-buildup test, and the cumulative injection for the three constant-pressure-injection tests are shown in Figures 7-47, 7-48, and 7-49, respectively.

The pressure-falloff test response was matched by fixing K(10.83 MPa) and P_f at their values given above and then optimizing the values of K(9.95), K(9.47), K(9.179), S_s, C_{tz}, and n. Figure 7-50 shows a plot of the best-fit GTFM simulation compared to the pressure and pressure derivative for the pressure-falloff test. The fitted parameter values were a K(9.95) of 3.6×10^{-11} m/s, a K(9.47) of 2.0×10^{-11} m/s, a K(9.18) of 2.0×10^{-11} m/s ($k = 6.3 \times 10^{-18}$, 3.5×10^{-18}, and 3.6×10^{-18} m^2, respectively), a specific storage of 6.3×10^{-5} m^{-1}, a test-zone compressibility of 1.3×10^{-9} Pa^{-1}, and a flow dimension of 1.77.

Figure 7-51 shows GTFM simulations and observed pressures for the L4P52-B testing period (excluding the open-hole and initial shut-in periods) using the two parameter sets described above.

Figure 7-52 shows the fitted $K(P)$ curves for both parameter sets and the associated uncertainties for those values. The uncertainties shown correspond to the limits of the 95% joint-confidence ellipses. Note that no uncertainty is given for K(10.83) for the following reasons. GTFM run-time messages

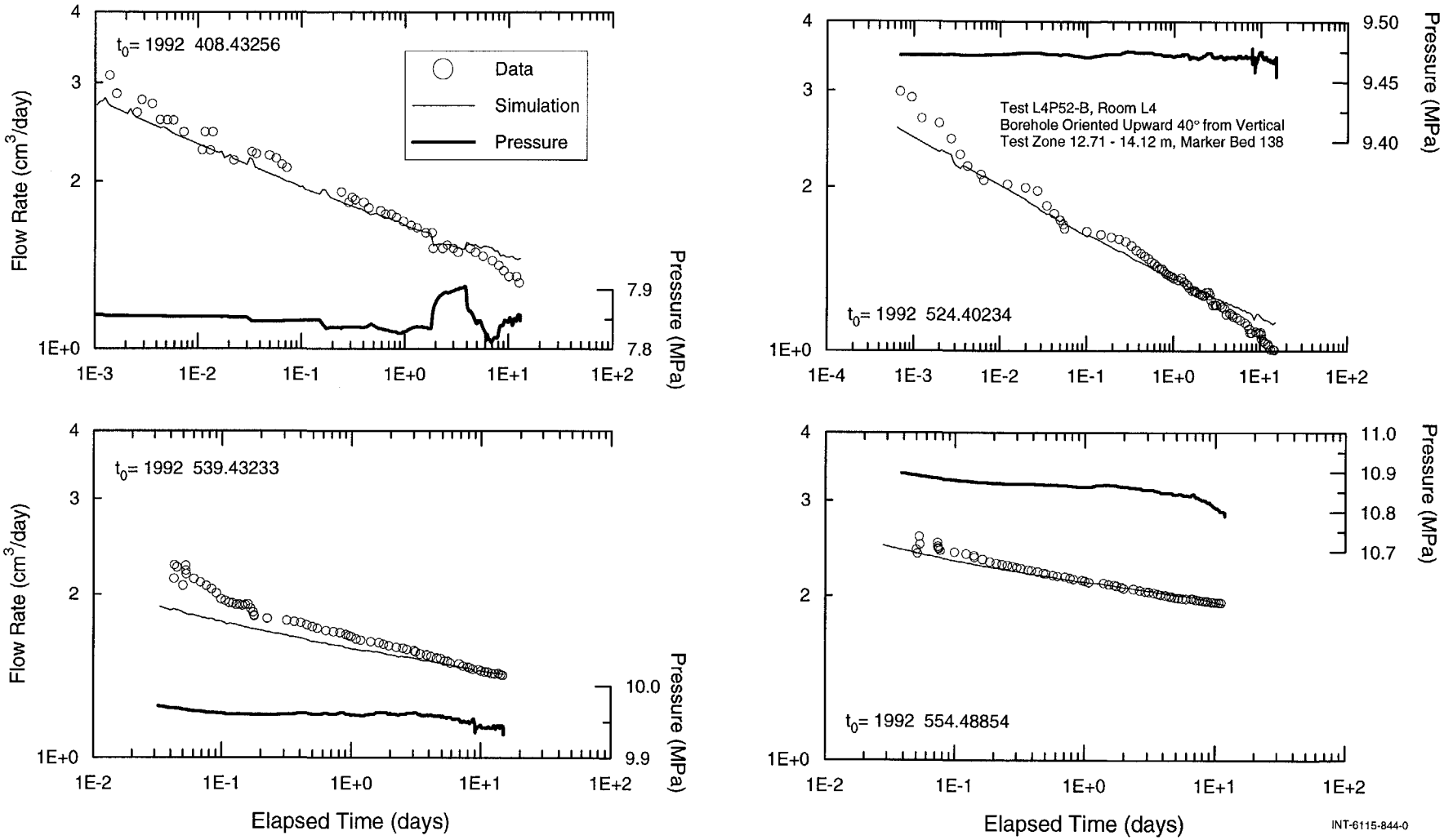

Figure 7-45. Log-log plots of GTFM simulations of flow rates during the L4P52-B constant-pressure tests with *K(P)* and $n = 2$.

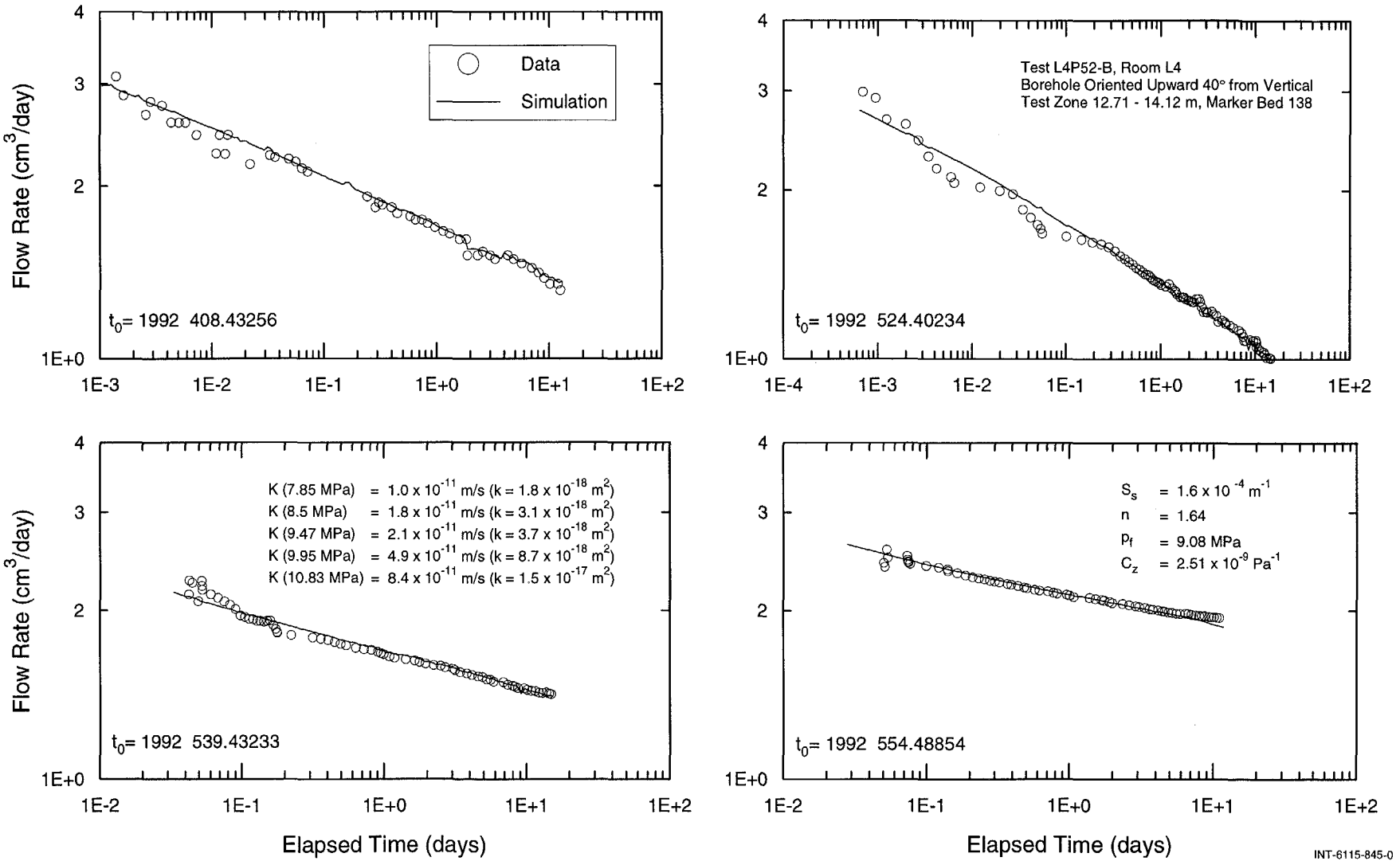

Figure 7-46 Log-log plots of GTFM simulations of flow rates during the L4P52-B constant-pressure tests with *K(P)* and $n = 1.64$.

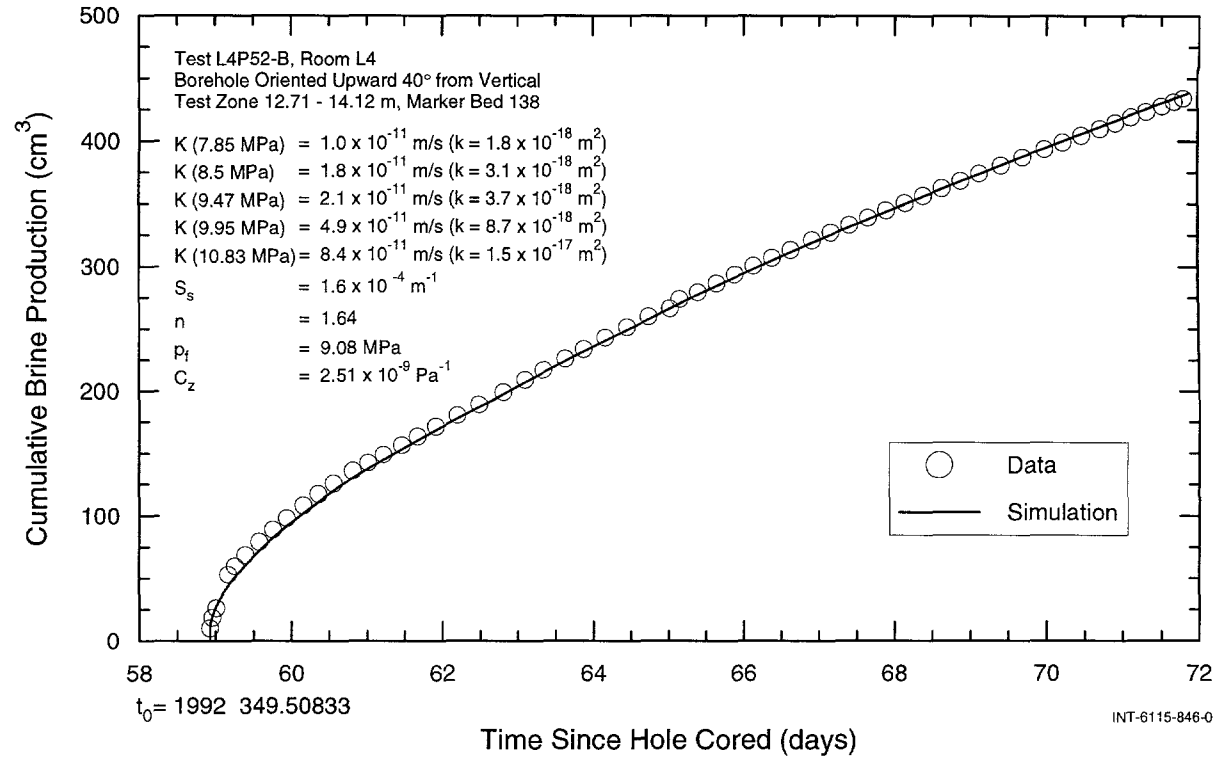

Figure 7-47. Linear-linear plot of GTFM simulation of brine production during the L4P52-B constant-pressure-withdrawal test.

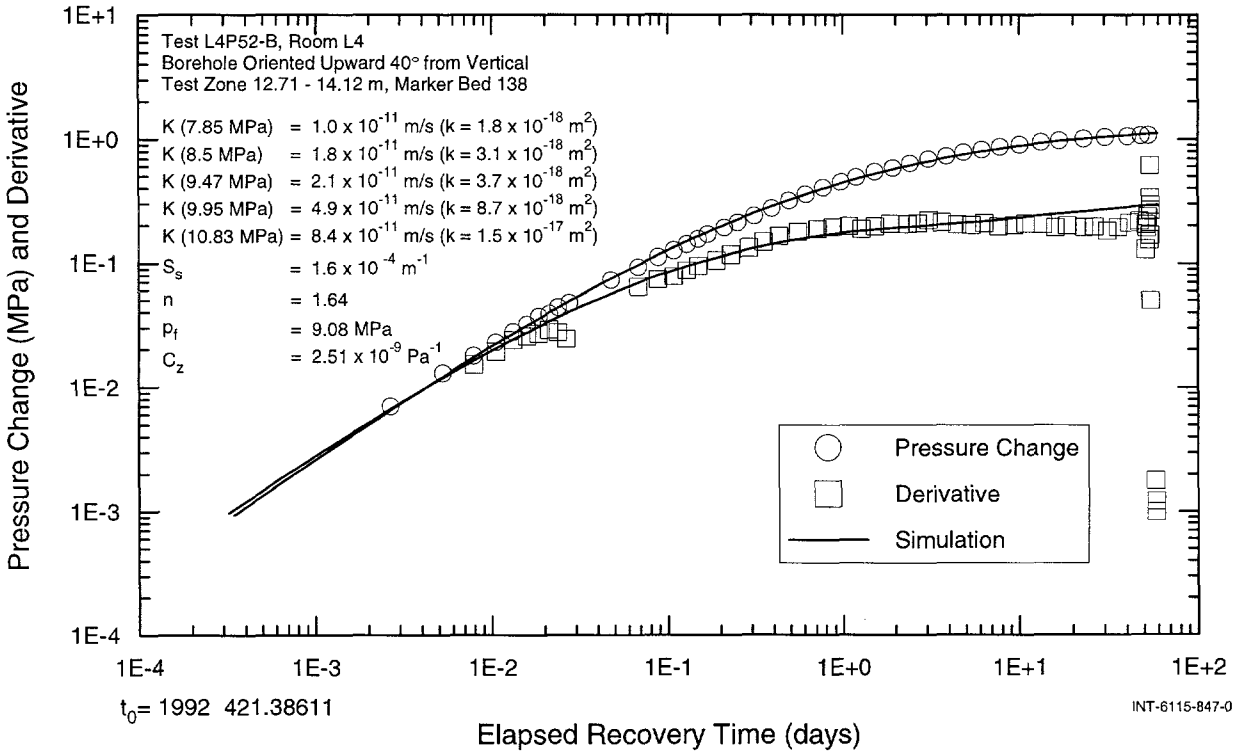

Figure 7-48. Log-log plot of GTFM simulation of pressure change and derivative during the L4P52-B pressure-buildup test.

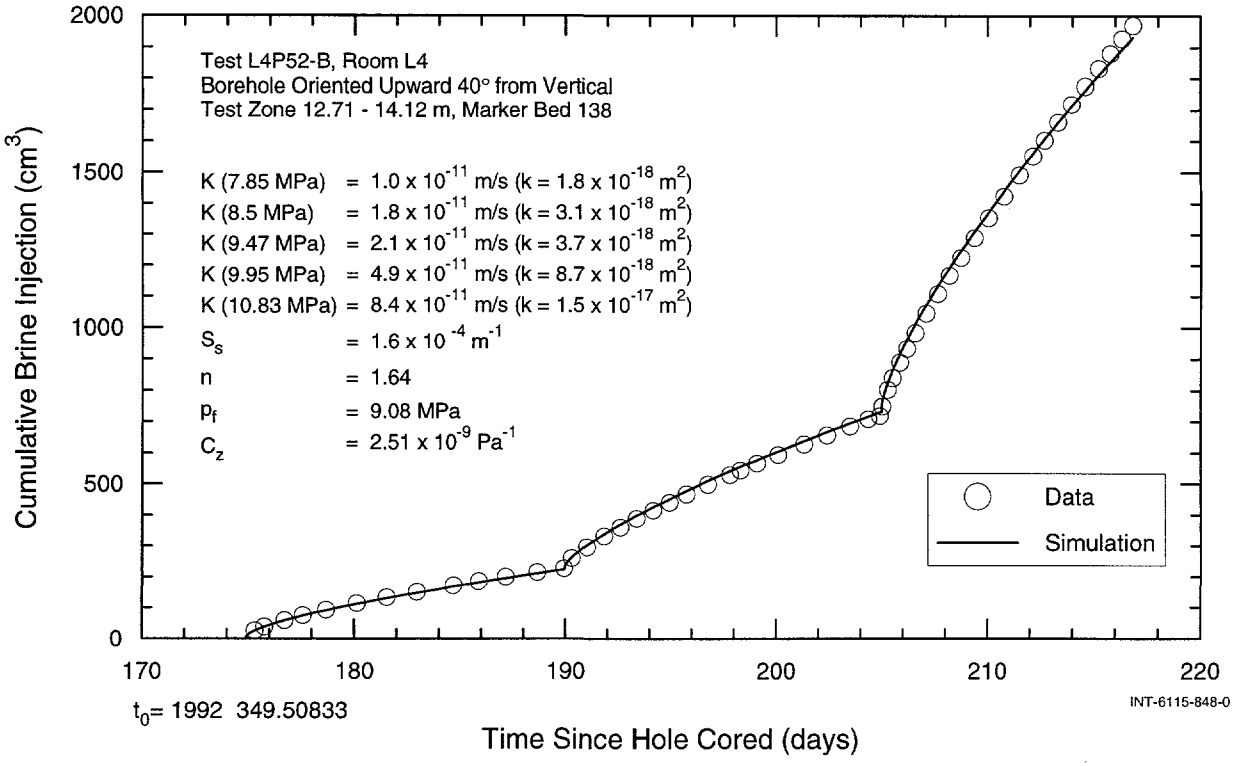

Figure 7-49. Linear-linear plot of GTFM simulation of brine injection during the L4P52-B constant-pressure-injection tests.

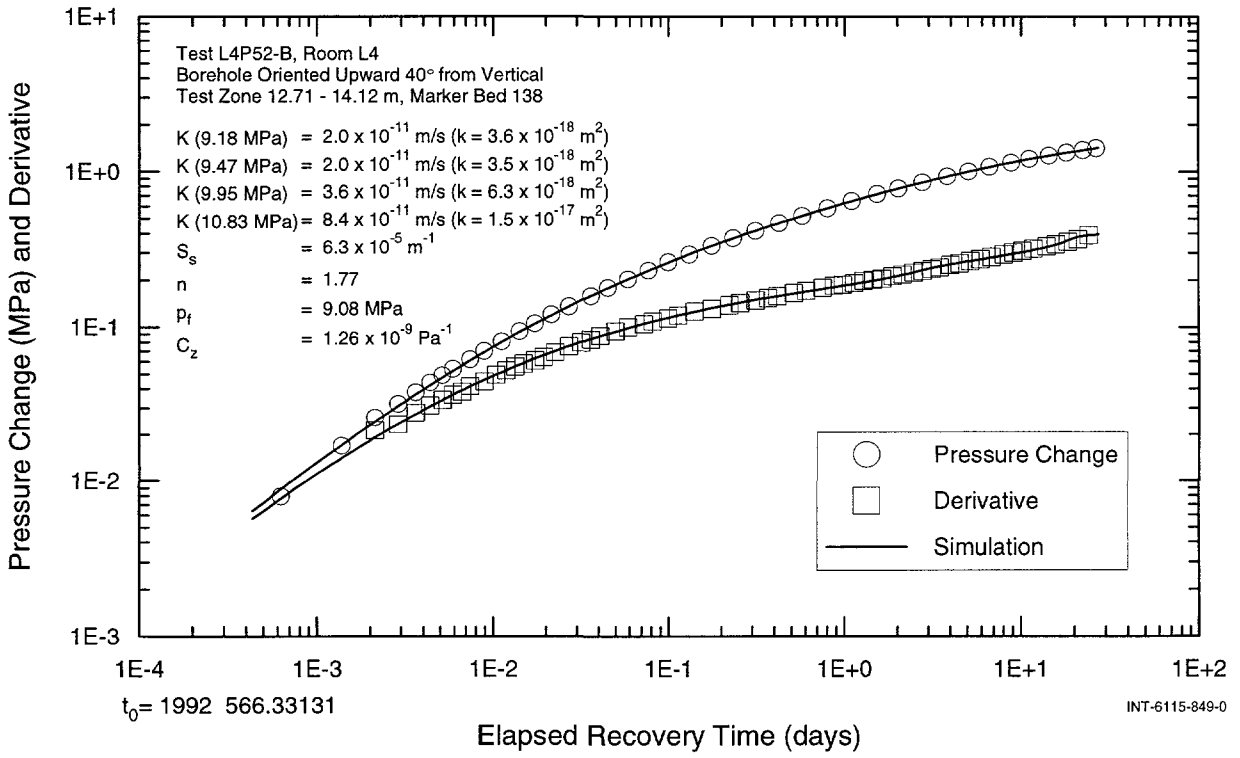

Figure 7-50. Log-log plot of GTFM simulation of pressure change and derivative during the L4P52-B pressure-falloff test.

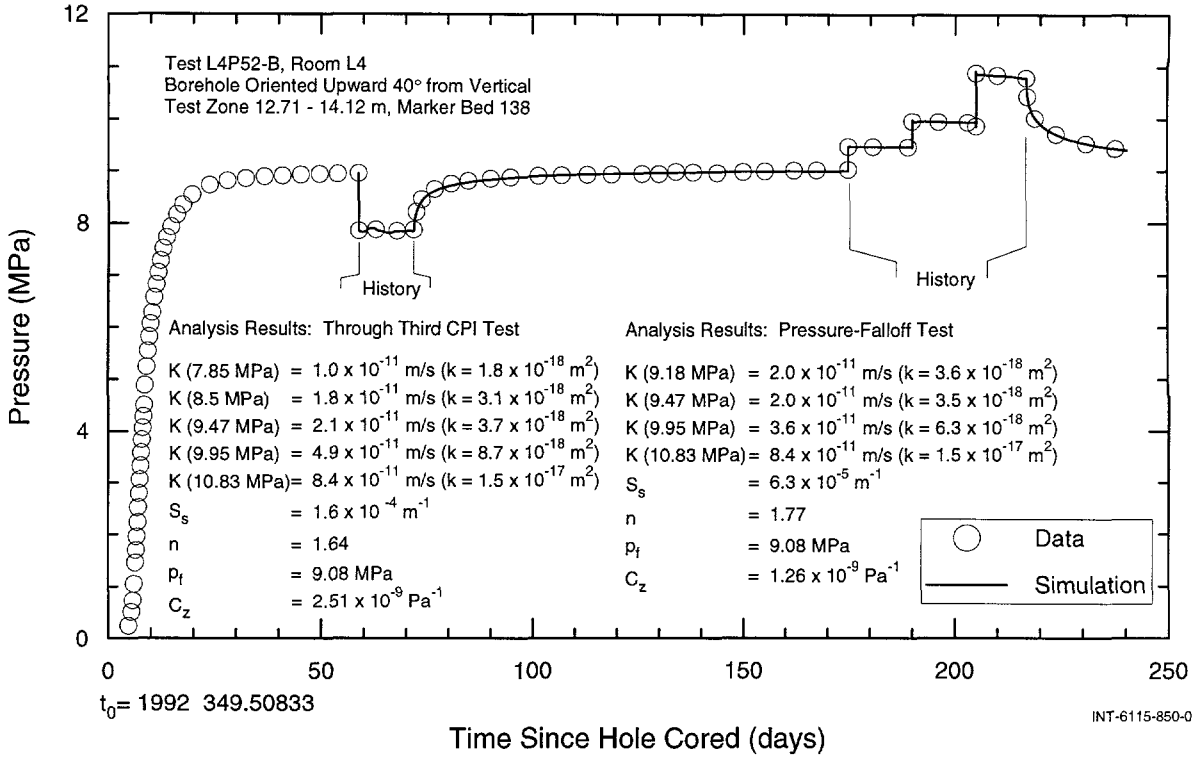

Figure 7-51. Linear-linear plot of GTFM simulation of the L4P52-B testing sequence.

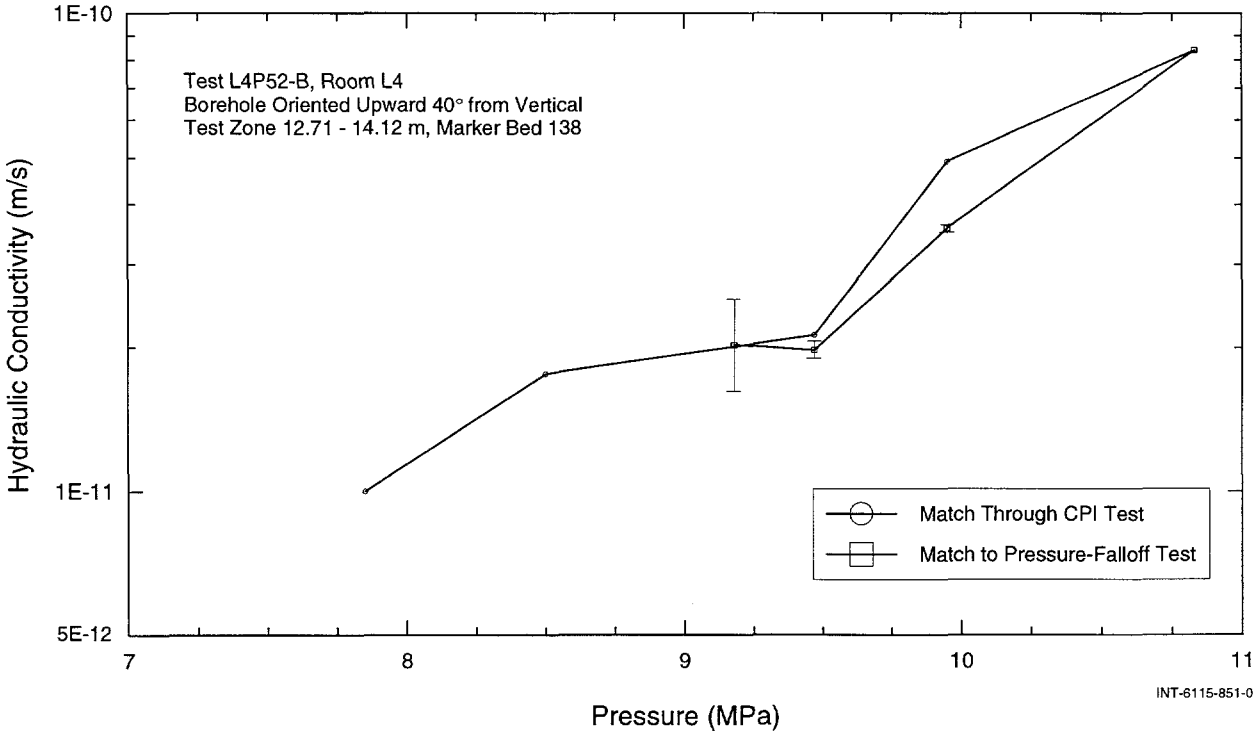

Figure 7-52. GTFM *K(P)* functions and calculated uncertainty for the L4P52-B test sequence.

indicated that no uncertainty calculations could be made for the fitted parameters used to simulate the test events through the constant-pressure tests. This typically happens when a problem is not well posed (very non-unique solution). Uncertainty estimates could be calculated for the fitting parameters from the pressure-falloff test simulation. The problem appears to become well posed if one of the *K(P)* values is specified (for this analysis, *K*(10.83)). This in turn means that the uncertainty ranges given in Figure 7-52 reflect the uncertainty in the fitting parameters assuming the hydraulic conductivity at some pressure is known. While this is not true, the numerically estimated *K(P)* values are seen to be in good agreement with the analytically derived estimates. The estimated values for S_s, C_{tz}, n, and P_f are all well constrained for the conditions discussed above.

7.3.1.3 Summary

Analytical and numerical interpretations of the L4P52-B data provided pressure-dependent hydraulic-conductivity estimates that ranged from 6.1×10^{-12} to 8.4×10^{-11} m/s ($k = 1.1 \times 10^{-18}$ to 1.5×10^{-17} m^2) for tests performed between approximately 7.8 and 10.8 MPa. Hydraulic-conductivity estimates from both analytical and numerical analyses are in good agreement where they can be compared, differing by less than a factor of three (note that flow was assumed to be radial for the analytical analyses, but not for the numerical analyses).

The range of numerically estimated *K* values (1.0 to 8.4×10^{-11} m/s) is larger by more than a factor of four than the estimated uncertainty for any of the individual *K* estimates at a given pressure, indicating that, for the numerical model as formulated, the *K* values *must* vary at different pressures to match the observed responses. While this does not guarantee that the hydraulic conductivity of the tested interval is truly pressure-dependent, it does rule out the possibility that the range of *K* estimates simply reflects large uncertainties in a poorly constrained problem.

The fit to the data was noticeably improved when a subradial flow dimension was used in addition to varying *K* as a function of pressure. Initially, the flow had been specified as radial to see if the measured responses could be matched simply by varying *K* as a function of pressure. Diagnostic plots indicated that the flow dimension increased as the injection pressure was increased and then decreased during the pressure-falloff test.

The fitted *K(P)* curve used to match the responses up to the pressure-falloff test did not provide a good match to the pressure-falloff test itself, suggesting some amount of hysteresis in the opening/closing behavior of the fracture(s) or possibly resulting from the assumption of constant *n*. The specific-storage estimates for the tests up to the pressure-falloff and the pressure-falloff test were 1.6×10^{-4} and 6.3×10^{-5} m^{-1}, respectively. Good fits to the data were obtained without varying specific storage as a function of pressure. A single value of formation pore pressure (9.1 MPa) was used for all of the GTFM simulations.

7.3.2 Guard Zone

Pressure in the guard zone increased to about 8.2 MPa after shut-in but then began to decrease, possibly due to bypass around the guard-zone packer. For this reason, a pressure-maintenance system was eventually used to stabilize the guard-zone pressure and no testing could be performed.

7.4 S1P74-A

Borehole S1P74 was drilled on 27 to 29 July 1992 (Calendar Days 209 to 211) into the upper part of the east rib (wall) of Room 7 in

Waste Panel 1 at an angle of 40° below vertical to allow testing of anhydrites "a" and "b". Figure 7-53 shows the configuration of the test tool in S1P74, and indicates the lengths and stratigraphic locations of the test and guard zones. The test zone included the lower 0.26 m of map unit 12 (polyhalitic halite), the combined 0.26-m thickness of anhydrite "a" and clay H, the 0.36-m thickness of map unit 10 (halite), and the upper 0.53 m of map unit 9 (halite). The guard zone included the lower 0.76 m of map unit 9, the 0.09-m thickness of anhydrite "b", and the upper 0.19 m of map unit 7 (halite). (All thicknesses listed above are as measured along the inclined borehole.)

Figure 7-54 shows the test- and guard-zone pressure responses recorded by the DAS during the monitoring period. The pressure values presented in Figure 7-54 and subsequent figures have been compensated for the elevation differences between the locations of the pressure transducers and the centers of the tested units in the test and guard zones. The test-zone and guard-zone pressures were compensated by subtracting 0.083 and 0.063 MPa, respectively, from the pressures measured by the pressure transducers and reported by Chace et al. (1998). Packer pressures during the S1P74-A testing are shown in Appendix D.

The test tool was installed and removed several times to make adjustments and repair leaks between 31 July and 7 August 1992 (Calendar Days 213 to 220). The test and guard zones were shut in on 7 August 1992. The test-zone pressure was increased to 2.27 MPa on 22 September 1992 (Calendar Day 266) to bypass the pressure range over which compressibility is highly pressure dependent

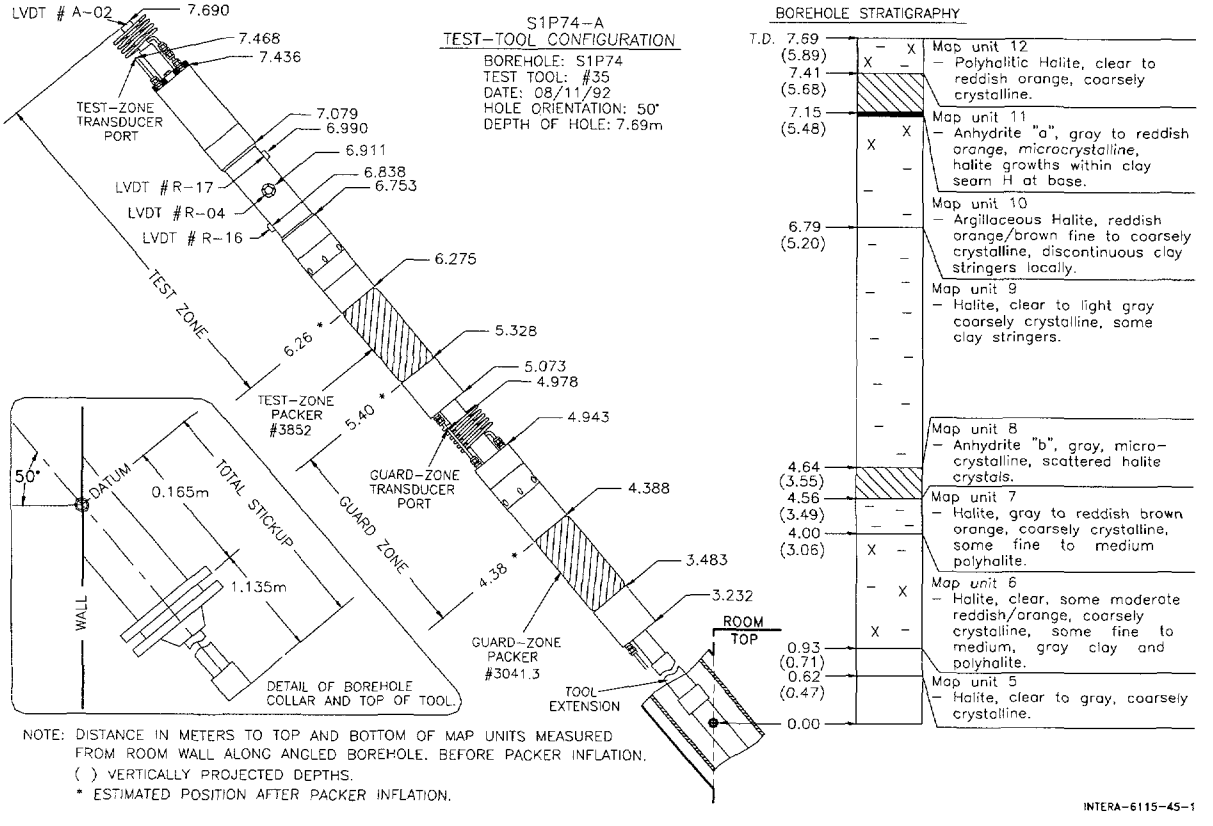

Figure 7-53. Configuration of the tool in borehole S1P74 for testing sequence S1P74-A.

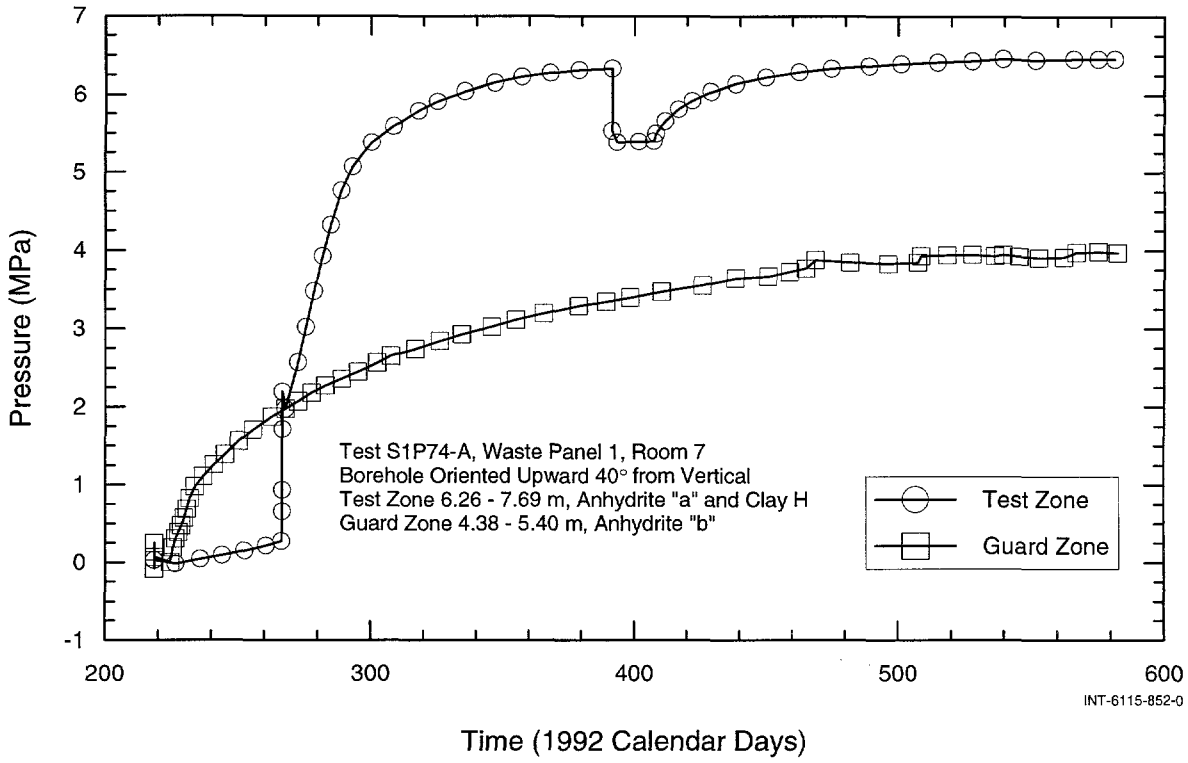

Figure 7-54. Test- and guard-zone pressures during S1P74-A testing.

and thereby decrease the time necessary for the pressure to stabilize. Following the pressure-buildup period, constant-pressure flow and pressure-buildup tests were conducted in the test zone. No testing was conducted in the guard zone.

7.4.1 Test Zone

The testing sequence in the S1P74-A test zone consisted of an open-borehole period lasting from 29 July to 7 August 1992 (Calendar Days 211 to 220), an initial shut-in period from 7 August 1992 to 25 January 1993 (1992 Calendar Days 211 to 391), a constant-pressure-withdrawal lasting from 25 January to 10 February 1993 (1992 Calendar Days 391 to 407), and a pressure-buildup test lasting until 3 August 1993 (1992 Calendar Day 581). The pressures observed during the testing sequence are shown in Figure 7-54.

The cumulative-production data from the constant-pressure-withdrawal test are shown in Figure 7-55. A total of about 73 cm^3 of brine was produced during the 16-day test. The constant-pressure test was interrupted for approximately 6 minutes on 26 January 1993 (Calendar Day 392) to reconfigure the DPT panel.

The compressibility of the S1P74-A test zone was evaluated both during and after testing was complete. Calculations of test-zone compressibility were made using the pressure-change-versus-volume-removed data collected at the initiation of the constant-pressure-withdrawal test and at the conclusion of testing. The value of test-zone compressibility calculated from the constant-pressure-withdrawal test was 2.0×10^{-9} Pa^{-1} (Table 6-2). The DPT panel was used at the end of testing to provide a continuous

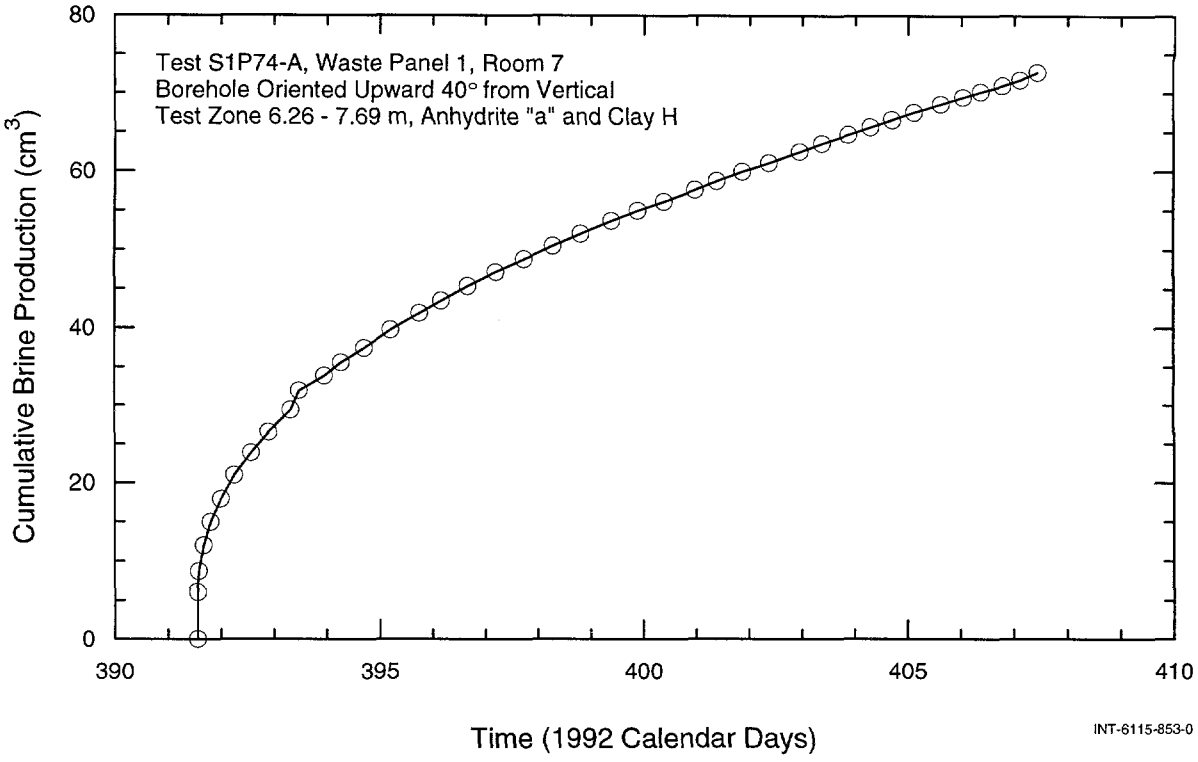

Figure 7-55. Cumulative brine production during the S1P74-A constant-pressure-withdrawal test.

measure of test-zone compressibility both as the test-zone pressure was decreased from 6.5 to 0.0 MPa and increased from 0.0 to 8.8 MPa. Note that these *in situ* continuous compressibility measurements are calculated assuming that no formation flow occurs during the measurement. Given that this is not true, the error in the calculation is proportional to the amount of formation flow that occurs. In general, the higher the hydraulic conductivity, the greater the error. This inherent error means that, while this type of compressibility measurement is of interest because it provides insight into the relationship between pressure and compressibility, it cannot be used for analysis. During numerical simulations, test-zone compressibility varied as a function of pressure according to the compressibility curve shown in Figure 7-56. The compressibility for all pressures above 2 MPa was specified to be 2.0×10^{-9} Pa^{-1}, the measured test-zone compressibility. The compressibilities for all pressures below 2 MPa were the approximate compressibilities for those pressures based on measurements obtained from compliance testing.

The S1P74-A tests were analyzed using an idealized test-zone geometry as described in Section 6.3. Flow from anhydrite "a" to the borehole was assumed to be horizontal only, and the test zone was modeled as a vertical cylindrical borehole with a radius of 5.964 cm.

7.4.1.1 Analytical Interpretations

A hydraulic-conductivity value of 2.1×10^{-13} m/s ($k = 3.6 \times 10^{-20}$ m^2) was estimated from the pressure-buildup test following the constant-pressure-withdrawal test using Eq. 6-1. The pressure derivative is shown in Figure 7-57 along with the parameter values used to estimate hydraulic conductivity.

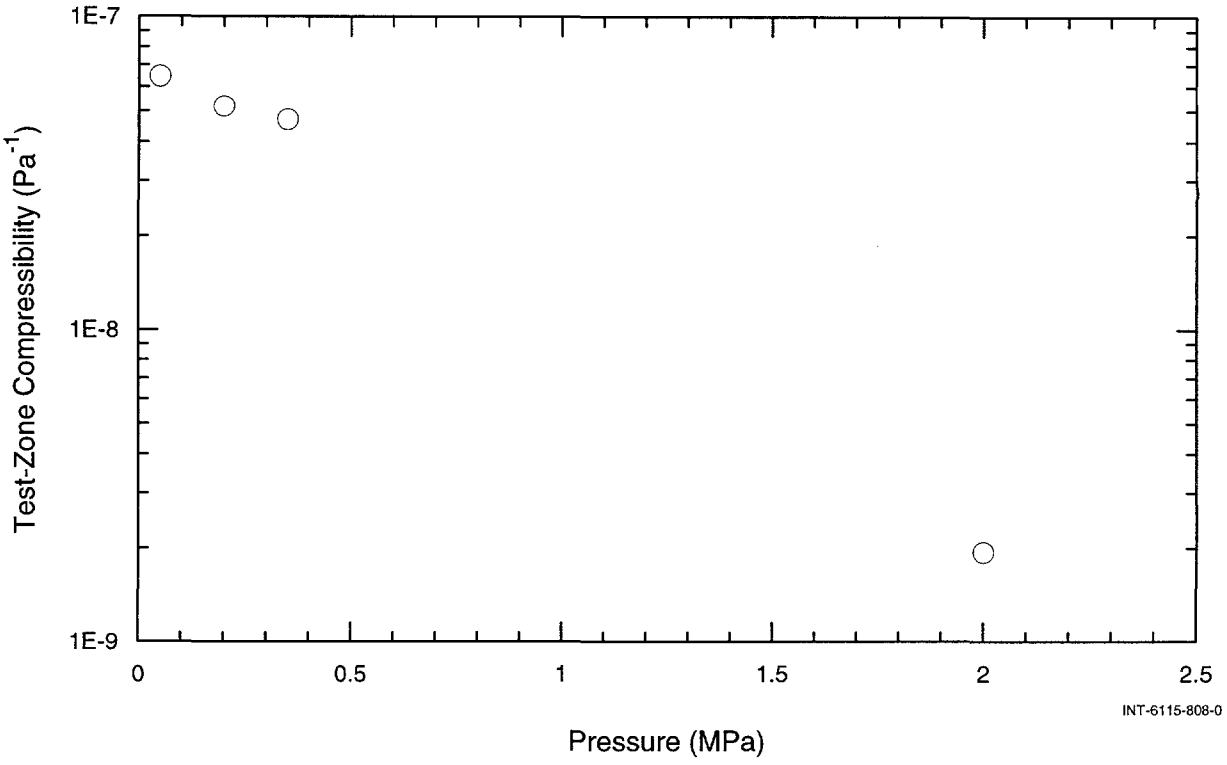

Figure 7-56. The test-zone-compressibility-versus-pressure function used in the S1P74-A GTFM simulations.

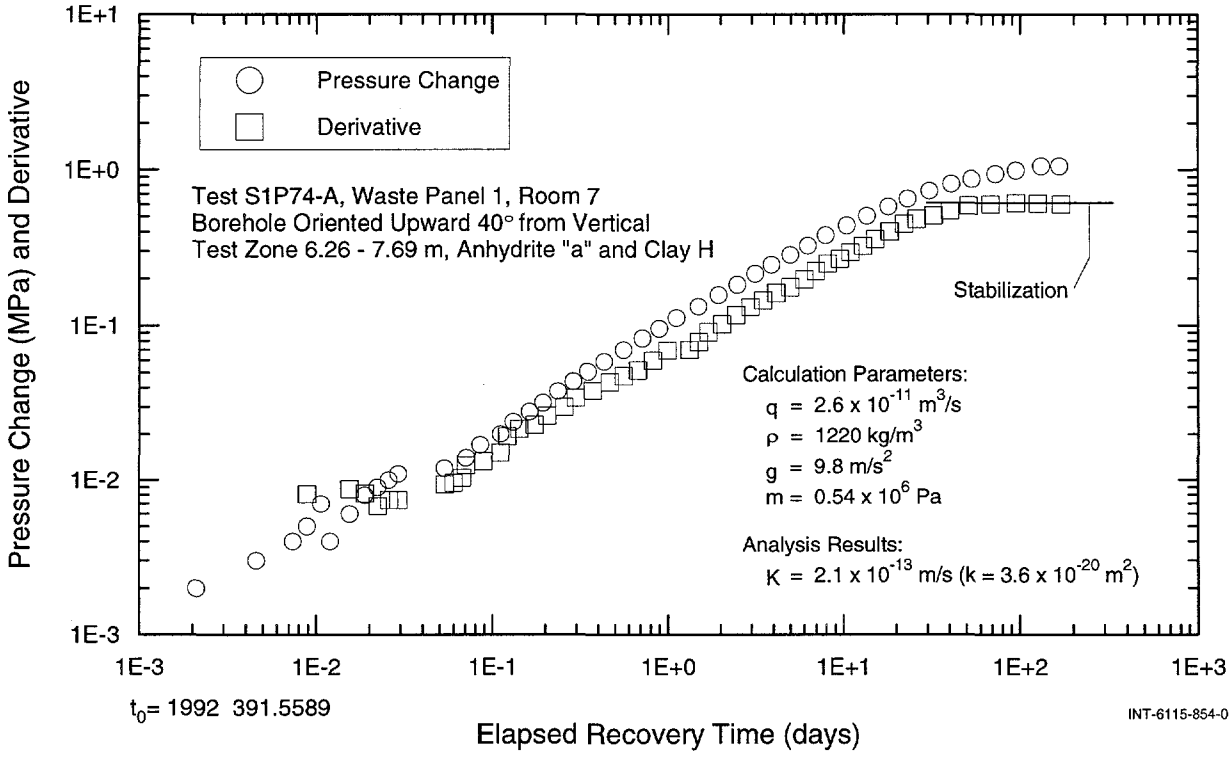

Figure 7-57. Analytical estimate of hydraulic conductivity from the S1P74-A pressure-buildup test.

No reasonable radial-flow type-curve match to the flow-rate data from the constant-pressure-withdrawal test could be made, so no hydraulic-conductivity estimate was possible. Subsequent numerical analysis suggested that the poor quality of the type-curve match was due to the pressure-dependent nature of the hydraulic conductivity.

7.4.1.2 Numerical Interpretations

The pressure increased slowly after the original shut-in on 7 August 1992 (Calendar Day 211) (Figure 7-54). Believing that this slow increase was due to pressure-dependent test-zone compressibility, the test-zone pressure was increased to 2.27 MPa on 22 September 1992 (Calendar Day 266) by injecting a small amount of brine. Previous compliance tests had shown that test-zone compressibility becomes relatively constant at pressures greater than 2 MPa. Before the pressure increase, the pressure in the test zone was changing at a rate of about 0.009 MPa/day. After the pressure increase, the pressure in the test zone began to increase at a rate of about 0.15 MPa/day.

The only conceptual model that reproduced the observed pressure response was one in which hydraulic conductivity changed as a function of pressure. Numerical modeling suggested that, if the hydraulic conductivity did not decrease in response to a decrease in the test-zone pressure, the formation in the vicinity of the borehole during the 11.7-day open-borehole period would have been depressurized to such a degree that the observed pressure response after the pressure increase on September 22 would not have occurred. If the hydraulic conductivity in the model is decreased as the test-zone pressure decreases, the nodes near the borehole are not depressurized and the observed response can be matched by the model.

In addition to varying hydraulic conductivity with pressure, the match to the observed response was greatly improved by including a small region around the borehole within which the hydraulic conductivity was constant (not pressure-dependent). What this skin zone represents is unclear. The stress state around the borehole may be such that the fracture(s) does not close near the borehole. A skin zone was not necessary, however, to achieve a match with the pressure-dependent model used to simulate the responses of MB138 in L4P52 (Section 7.3.1.2).

The open-borehole period was included in the GTFM simulation as a specified-pressure sequence. The fitted formation (outer-zone) parameters were a hydraulic-conductivity function (pressure in MPa) $K(2.0) = 4.7 \times 10^{-17}$ m/s, $K(4.0) = 1.1 \times 10^{-14}$ m/s, $K(5.0) = 2.2 \times 10^{-13}$ m/s, $K(6.5) = 4.3 \times 10^{-13}$ m/s ($k = 8.3 \times 10^{-24}$, 1.9×10^{-21}, 3.9×10^{-20}, and 7.5×10^{-20} m^2, respectively), a specific storage of 2.8×10^{-5} m^{-1}, and a formation pore pressure of 6.73 MPa. The fitted skin-zone (inner-zone) parameters were a hydraulic conductivity of 6.7×10^{-13} m/s ($k = 1.2 \times 10^{-19}$ m^2), a specific storage of 1.1×10^{-4} m^{-1}, and a radial thickness of 2.9 cm.

The best-fit GTFM simulation compared to the cumulative production for the constant-pressure-withdrawal test, the calculated flow rates during the constant-pressure-withdrawal test, the pressure and pressure derivative from the pressure-buildup test, and the observed pressures for the S1P74-A testing period are shown in Figures 7-58, 7-59, 7-60, and 7-61, respectively.

All of the pressure-dependent hydraulic-conductivity estimates were well constrained, with uncertainties less than a factor of two indicated by the 95% joint-confidence regions. The uncertainty in the estimated formation pore pressure was about ±0.02 MPa.

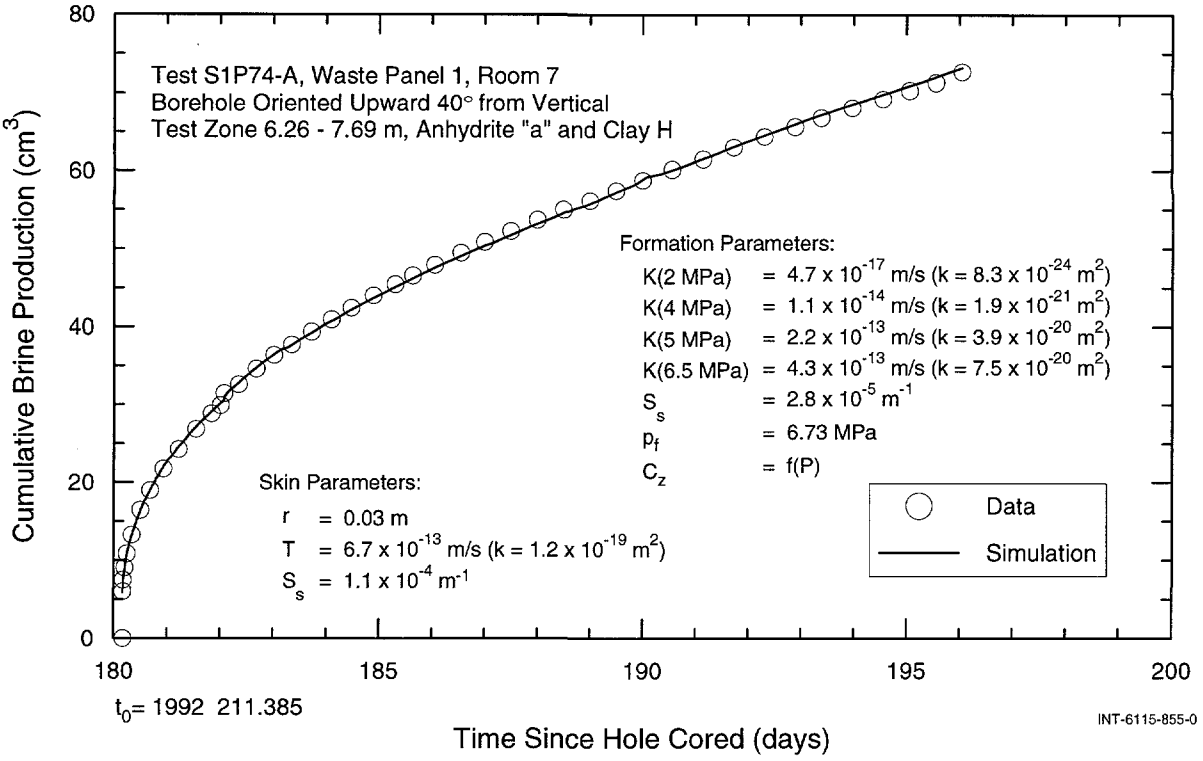

Figure 7-58. Linear-linear plot of GTFM simulation of brine production during the S1P74-A constant-pressure-withdrawal test.

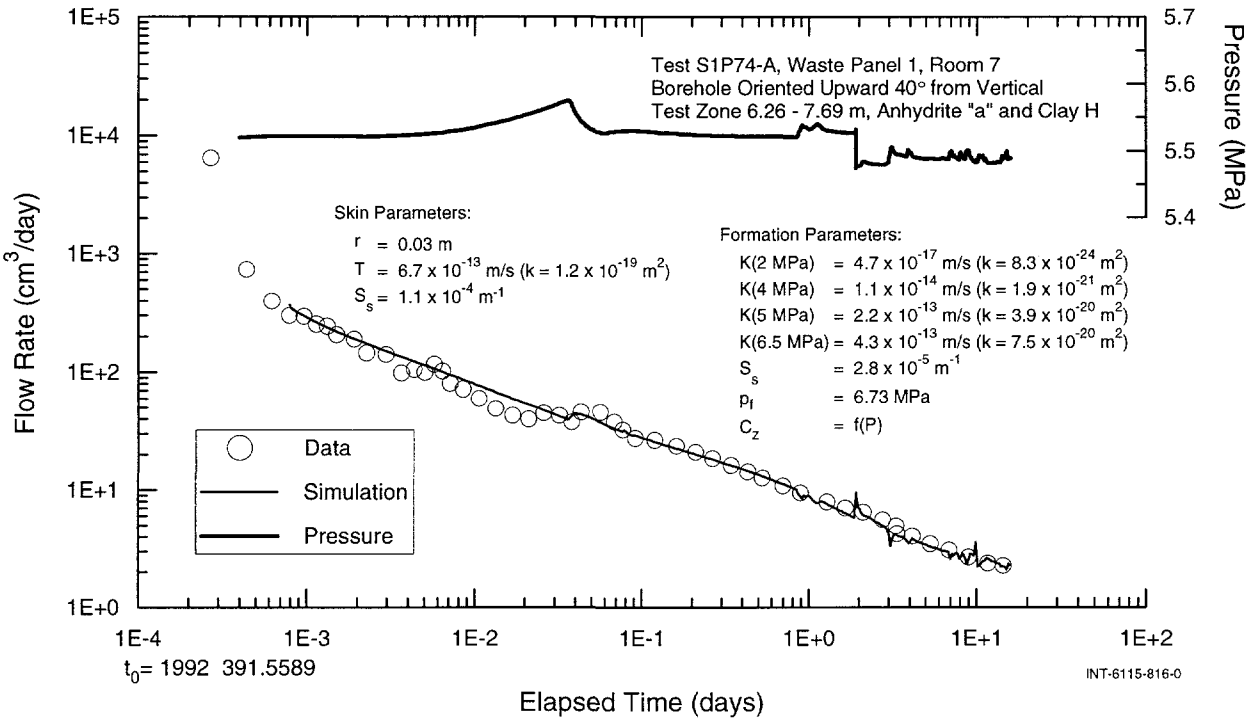

Figure 7-59. Log-log plot of GTFM simulation of flow rates during the SIP74-A constant-pressure-withdrawal test.

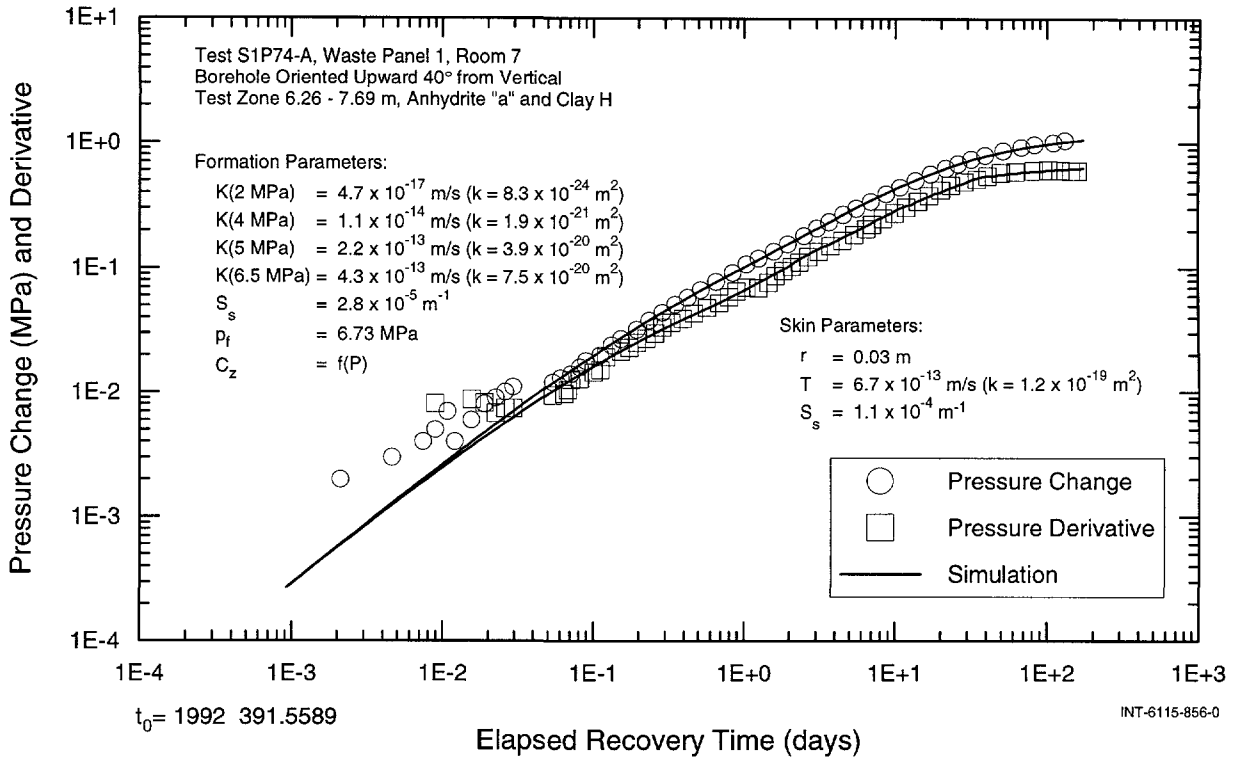

Figure 7-60. Log-log plot of GTFM simulation of pressure change and derivative during the S1P74-A pressure-buildup test.

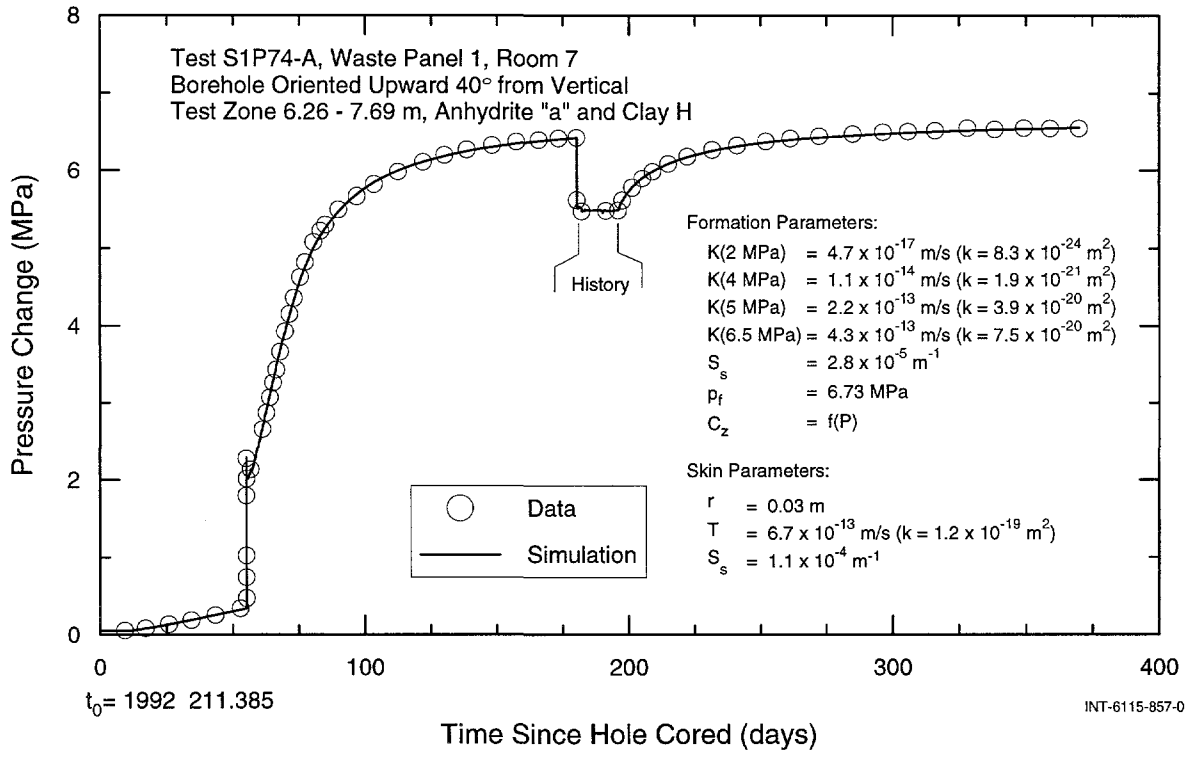

Figure 7-61. Linear-linear plot of GTFM simulation of the entire S1P74-A testing sequence.

The skin parameters are highly correlated to the formation specific storage and, consequently, are not well constrained.

7.4.1.3 Summary

Analytical and numerical interpretations of the S1P74-A data provided pressure-dependent hydraulic-conductivity estimates that ranged from 4.7×10^{-17} to 4.3×10^{-13} m/s ($k = 8.3 \times 10^{-24}$ to 7.5×10^{-20} m^2) for pressures ranging from approximately 2 to 6.5 MPa. A single value of formation pore pressure (6.73 MPa) was used for all of the GTFM simulations.

A single estimate of specific storage of 2.8×10^{-5} m^{-1} was obtained from numerical analysis. This specific-storage value was the estimated value prior to adding a skin zone to the numerical conceptual model. As with all other specific-storage estimates from the Salado testing program, this estimate is possibly affected by the development of a skin zone around the borehole.

Quantitative estimates of the fitting-parameter uncertainty (95% joint-confidence regions) and the corresponding correlation matrices are presented in Appendix C.

7.4.2 Guard Zone

No testing was performed in the guard zone, but pressure monitoring (Figure 7-54) indicated that the formation pore pressure of anhydrite "b" at S1P74 was at least 4 MPa.

7.5 S1P74-B

Borehole S1P74 was drilled upward into the east rib of Room 7 in Waste Panel 1 to a depth of 7.69 m in July 1992 for testing sequence S1P74-A (Section 7.4). S1P74 was deepened to 16.88 m on 26 to 31 January 1995 (Calendar Days 26 to 31) for testing sequence S1P74-B. Figure 7-62 shows the test-tool configuration for S1P74-B, and indicates the lengths and stratigraphic locations of the guard and test zones. Test zone 1 extended from 15.08 to 16.88 m into the east rib and included the lower 0.22 m of map unit H-6 (halite), the 0.28-m thickness of MB138, the 0.13-m thickness of clay K, and the upper 1.17 m of map unit AH-2 (argillaceous halite). Test zone 2 extended from 13.19 to 14.25 m into the east rib and included the lower 0.05 m of map unit AH-2, the 0.71-m thickness of map unit H-5 (halite), and the upper 0.30 m of map unit AH-1 (clay J). The guard zone extended from 11.33 to 12.36 m into the east rib and included 1.03 m of map units 14 and 15 (both are halite units that could not be differentiated based on visual inspection of core).

S1P74-B testing in test zone 1 consisted of a shut-in period followed by a pulse-withdrawal test. The test zone 2 testing consisted of a shut-in period followed by two pulse-withdrawal tests. No testing was performed in the guard zone. The pressures in the test and guard zones during S1P74-B testing are shown in Figure 7-63. The pressure values presented in Figure 7-63 and subsequent figures have been compensated for the elevation differences between the locations of the pressure transducers and the centers of the tested units in the test and guard zones. The test zone 1, test zone 2, and guard zone pressures were compensated by subtracting 0.168, 0.136, and 0.118 MPa, respectively, from the pressures measured by the pressure transducers and reported by Chace et al. (1998). Packer pressures during the S1P74-B testing are shown in Appendix D.

The S1P74-B tests were analyzed using an idealized test-zone geometry as described in Section 6.3. Flow to the borehole was assumed to be horizontal only, and the test zones were modeled as vertical cylindrical boreholes with radii of 5.964 cm.

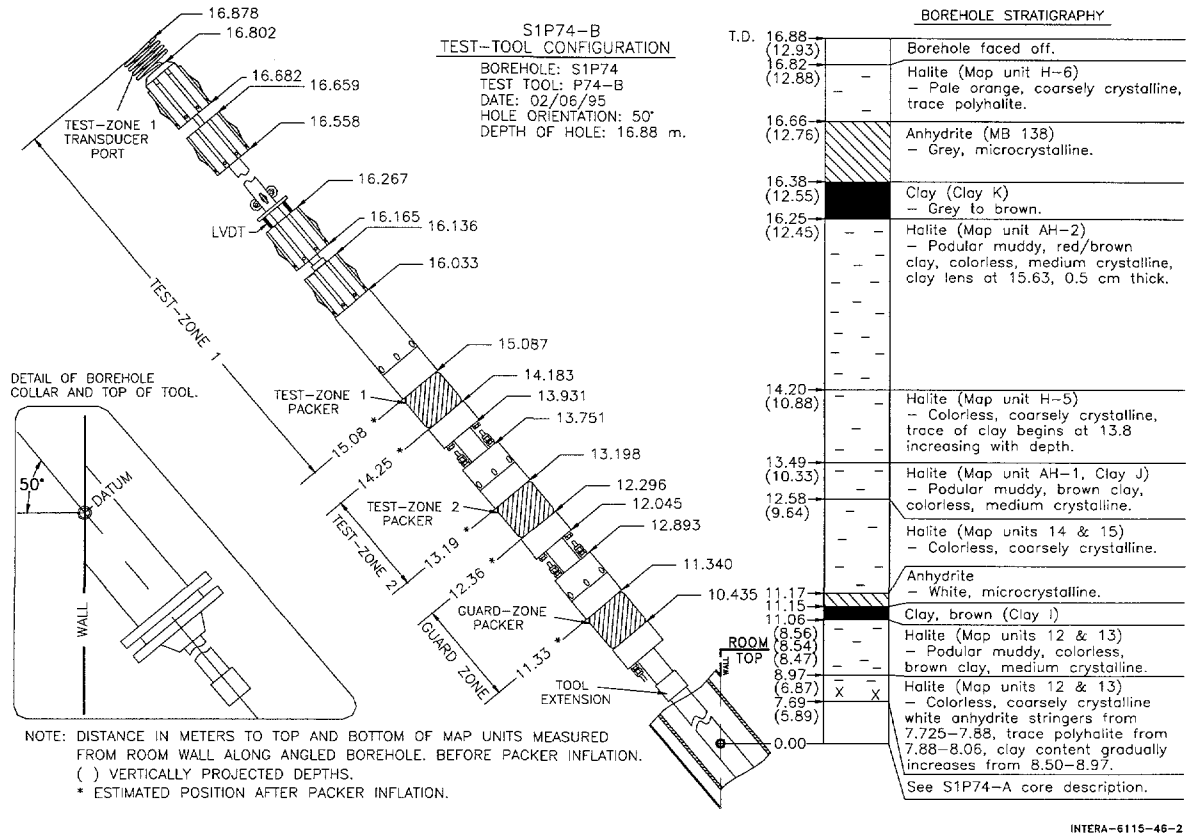

Figure 7-62. Configuration of the tool in borehole S1P74 for testing sequence S1P74-B.

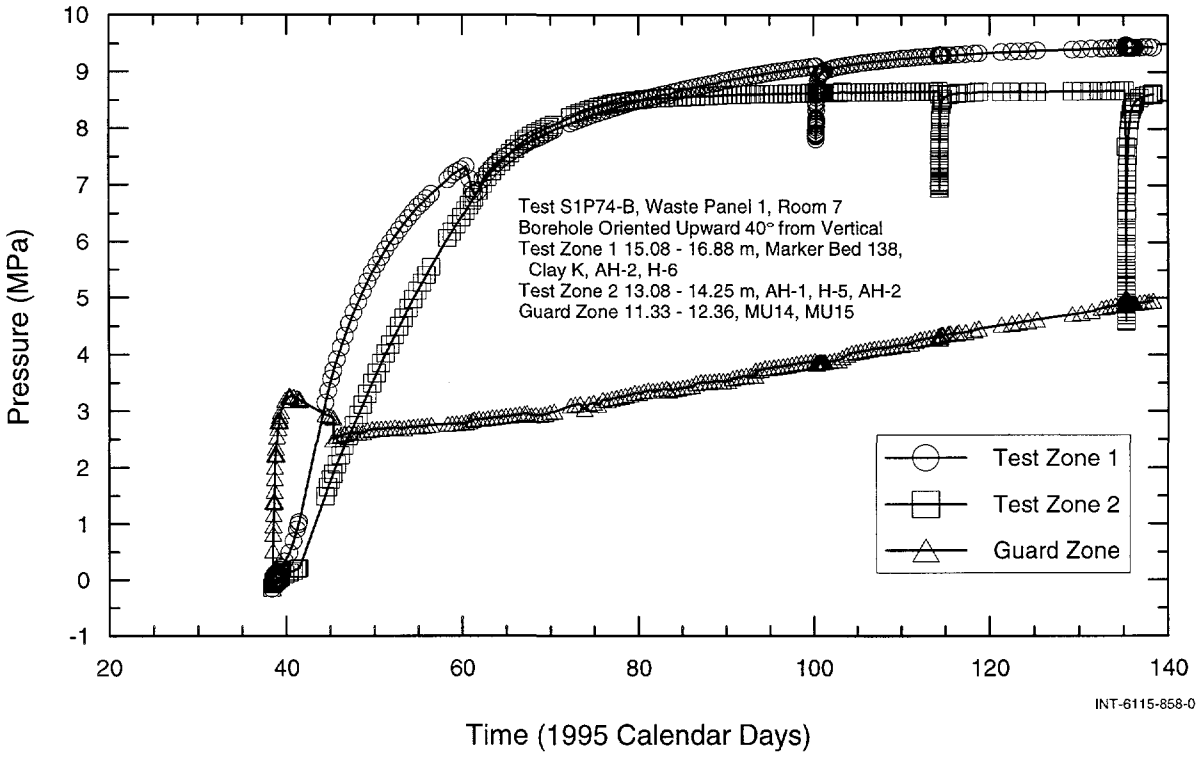

Figure 7-63. Test- and guard-zone pressures during S1P74-B testing.

7.5.1 Test Zone 1

The test tool used for the S1P74-B testing was originally designed to measure changes in MB138 fracture apertures during a series of constant-pressure tests performed at different pressures. This test program, however, was canceled and only a pulse test was performed in test zone 1. Test zone 1 was shut in on 7 February 1995 (Calendar Day 38). The pulse-withdrawal test was initiated on 10 April 1995 (Calendar Day 100). Leaks were noted in the test zone 1 injection line several times during the initial shut-in period. The degree to which the pressure response was affected by the leaks is unknown, but the effect is clearly evident on Calendar Day 60 (Figure 7-63). Given that the formation response prior to the pulse-withdrawal test was masked to some unknown degree by leaks in the system, the entire initial shut-in period was simulated as a specified-pressure sequence in GTFM. Only the pulse-test response was matched by estimating hydraulic parameters. The compressibility of the S1P74-B test zone 1 was evaluated with data collected during the initiation of the pulse withdrawal. The test-zone compressibility calculated from these data was 8.0×10^{-10} Pa^{-1} (Table 6-2).

The pulse-test data were not amenable to type-curve matching. Consequently, no analytical interpretations were performed.

Figure 7-64 shows the best-fit GTFM simulation compared to the normalized pulse response and its derivative plotted above the optimized flow-dimension function. Figure 7-65 shows the best-fit GTFM simulation compared to the observed test zone 1 pressures for the S1P74-B testing period. The fitted parameters were a hydraulic conductivity of 3.3×10^{-11} m/s ($k = 5.8 \times 10^{-18}$ m^2), a specific storage of 2.4×10^{-5} m^{-1}, a flow-dimension function $n1 = 1.8$, $n2 = -0.41$, $n3 = 3.9$, $n4 = 1.2$ (Figure 7-65), and a formation pore pressure of 10.27 MPa. The estimates of K and S_s correspond to an n of 1.2.

7.5.2 Test Zone 2

Test zone 2 was shut in on 7 February 1995 (Calendar Day 38). The first pulse-withdrawal test was initiated on 24 April 1995 (Calendar Day 114) and the second pulse-withdrawal test was initiated on 13 May 1995 (Calendar Day 135). The compressibility of the S1P74-B test zone 2 was evaluated with data collected during both pulse withdrawals. The test-zone compressibilities calculated from the first and second pulse withdrawals, respectively, were 1.6×10^{-9} and 2.0×10^{-9} Pa^{-1} (Table 6-2).

The magnitude of the pulse for the second test was greater than that for the first test by a factor of about 2.4. This difference in magnitudes appears to have affected the pulse responses to such a degree that they are visibly different. Figure 7-66 shows the normalized pulse responses and derivatives for the two pulse tests. Axial and radial LVDT data from previous tests suggest that the difference between the responses results from compliance effects, i.e., changes in borehole radius and test-tool movement. Because no LVDTs were installed in test zone 2, no compliance data were available for use in the simulation. The compliance effects were, therefore, incorporated into the numerical simulations as geometry variations, i.e., as variations in n. Similar to the approach used for the L4P51-C Hm-2 test analysis, time-varying geometry effects (compliance) were simulated as spatially varying geometry effects. The belief was that hydraulic parameters could be accurately estimated even if certain aspects of the response were not explicitly modeled. In this case, time variations were modeled as spatial variations.

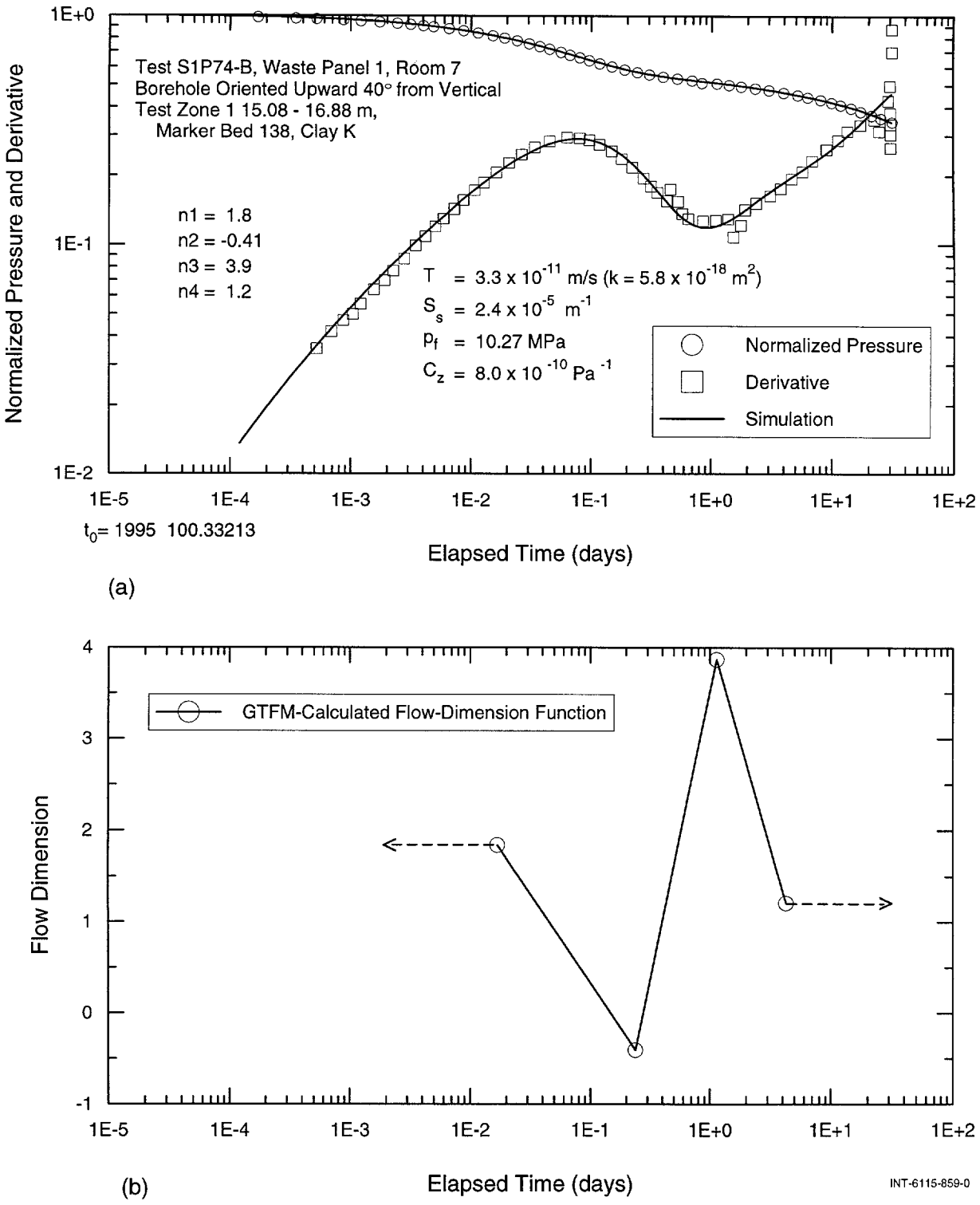

Figure 7-64. Log-log and semilog plots of GTFM simulation (a) and flow-dimension function (b) of the S1P74-B test zone 1 pulse-withdrawal test.

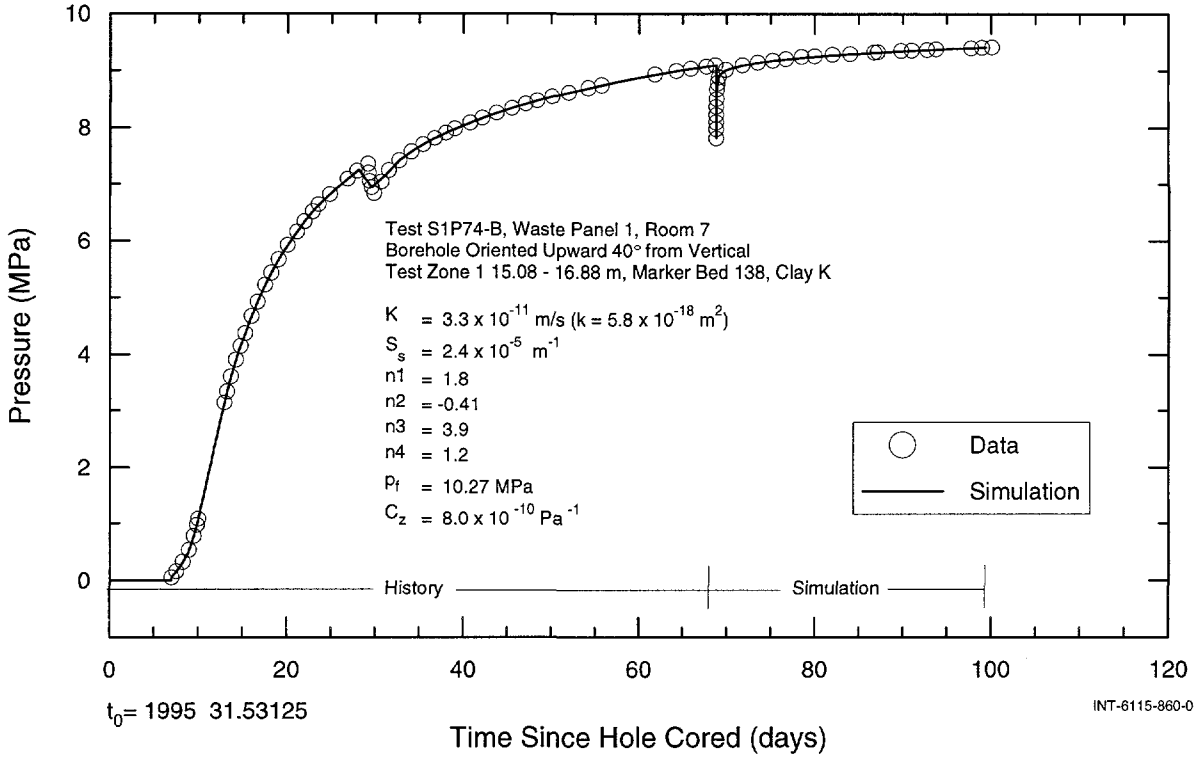

Figure 7-65. Linear-linear plot of GTFM simulation of the entire S1P74-B test zone 1 testing sequence.

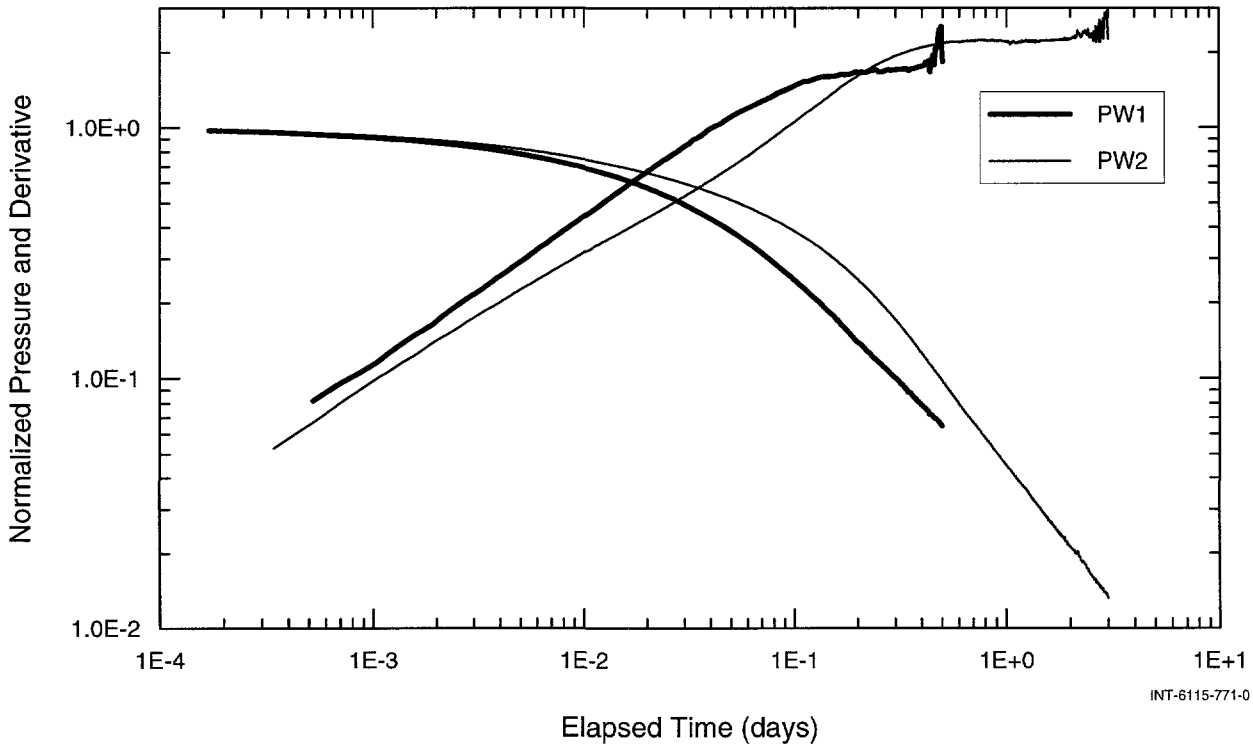

Figure 7-66. Normalized pressure and derivative responses during S1P74-B test zone 2 pulse tests.

Analytical interpretations of the test data were not considered warranted because of the inferred compliance effects. No attempt was made with GTFM to match the two pulse responses simultaneously with a single parameter set. The stability of the test-zone pressure preceding each pulse test allowed each pulse test to be analyzed independently with minimal effect on the fitted parameters.

Figure 7-67 shows the best-fit GTFM simulation compared to the normalized pressure response and derivative from the first pulse test. The fitted parameter values were a hydraulic conductivity of 2.0 x 10^{-11} m/s (k = 3.5 x 10^{-18} m^2), a specific storage of 3.8 x 10^{-8} m^{-1}, a flow dimension of 1.5, and a formation pore pressure of 8.67 MPa.

Figure 7-68 shows the best-fit GTFM simulation compared to the normalized pressure response and derivative from the second pulse test plotted above the optimized flow-dimension function. The fitted parameters were a hydraulic conductivity of 2.0 x 10^{-11} m/s (k = 3.5 x 10^{-18} m^2), a specific storage of 3.6 x 10^{-7} m^{-1}, a flow-dimension function of $n1$ = 1.3, $n2$ = 0.87, $n3$ = 3.1, $n4$ = 1.3 (Figure 7-68), and a formation pore pressure of 8.72 MPa.

The outer flow dimension for the second PW test (n = 1.3) was in good agreement with the single estimated value of n for the first PW test (n = 1.5). The estimated hydraulic conductivities for the two PW tests were the same, indicating that the analysis approach discussed above behaved as expected – time-varying changes (compliance) were simulated as spatially varying changes (n) and the estimate of K was unaffected. In contrast, the estimates of S_s for the two PW tests differed by a factor of 10, indicating that

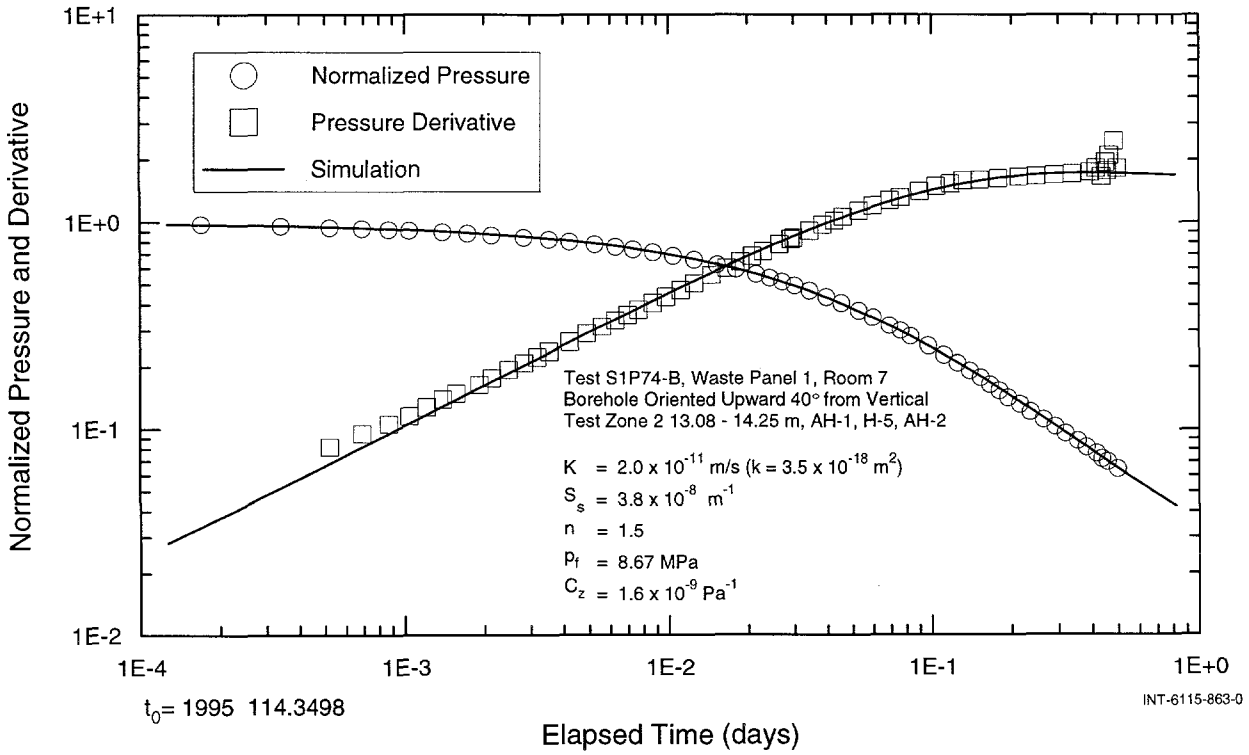

Figure 7-67. Log-log plot of GTFM simulation of the first S1P74-B test zone 2 pulse-withdrawal test.

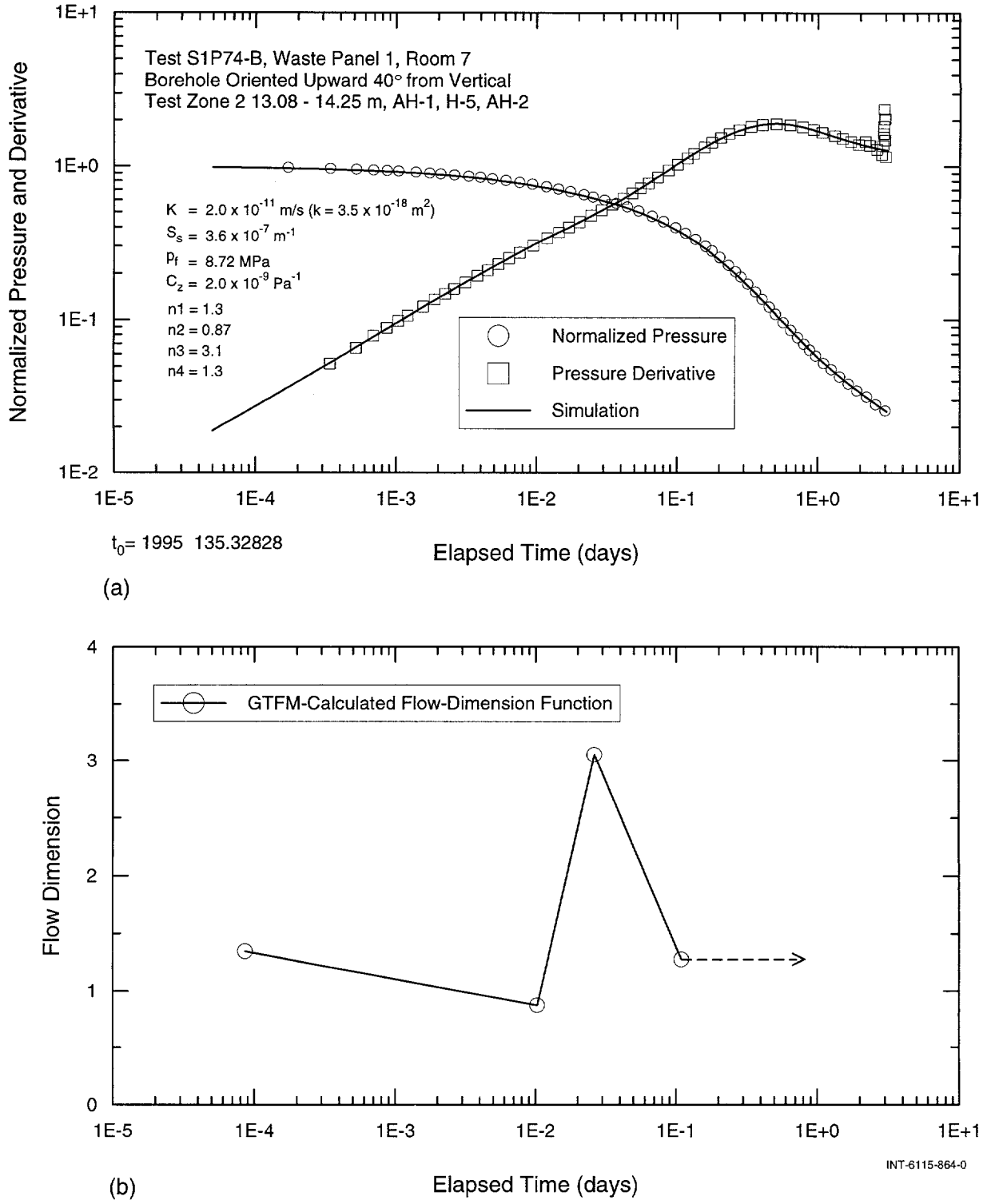

Figure 7-68. Log-log and semilog plots of GTFM simulation (a) and flow-dimension function (b) of the second S1P74-B test zone 2 pulse-withdrawal test.

near-borehole effects (skin) and/or early-time effects (compliance) render single-borehole estimates of S_s unreliable, as discussed throughout this report.

Figure 7-69 shows the GTFM simulations compared to the observed pressures in test zone 2 using the two parameter sets given above. Quantitative estimates of the fitting-parameter uncertainty (95% joint-confidence regions) and the corresponding correlation matrices are presented in Appendix C.

7.5.3 Guard Zone

The guard zone was shut in on 7 February 1995 (Calendar Day 38). The pressure in the zone had increased to 3.26 MPa by 9 February 1995 (Calendar Day 40), but then *began* decreasing. Repair of a leaking guard-zone pressure line was attempted on 14 February (Calendar Day 45). The pressure in the zone again began to increase (Figure 7-63), but the response indicated that equipment problems still existed. No analysis was done due to the poor quality of the data, but the formation pore pressure in the guard zone appears to have been at least 4.77 MPa, the maximum recorded pressure.

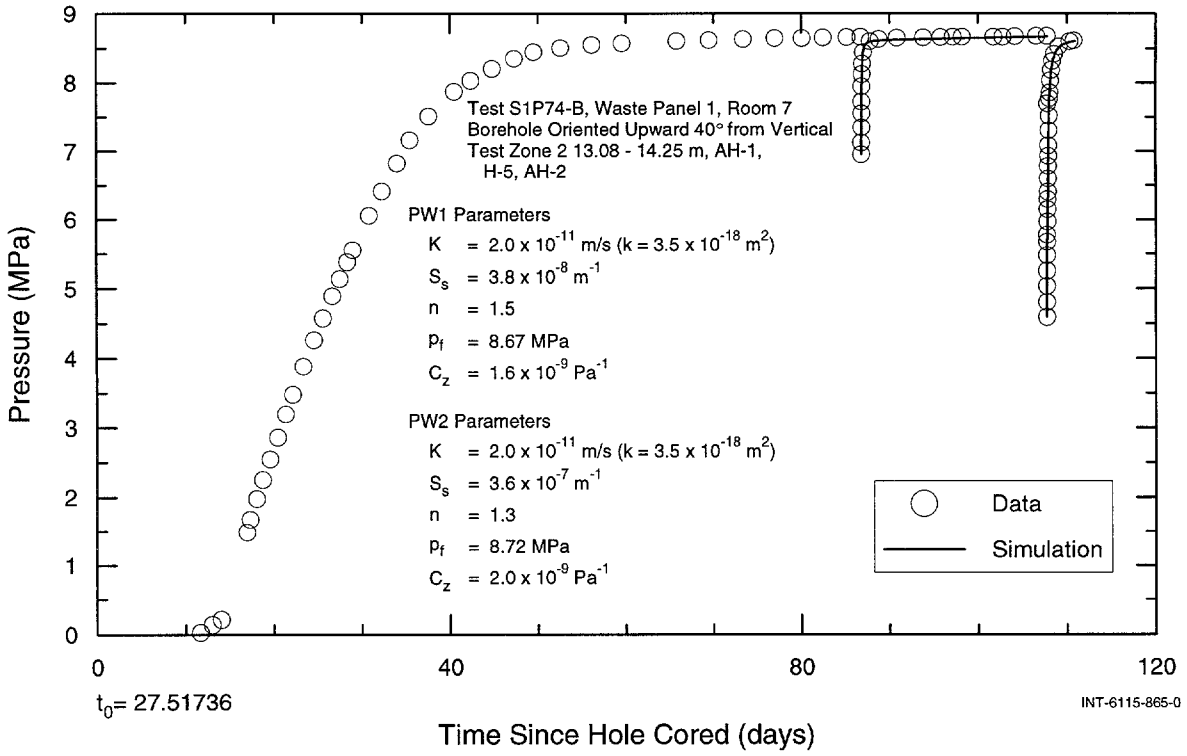

Figure 7-69. Linear-linear plot of GTFM simulation of the S1P74-B test zone 2 pulse-withdrawal tests.

8. DISCUSSION OF RESULTS

Beauheim et al. (1991) discussed how the disturbed-rock zone (DRZ) that forms around underground excavations might affect the parameters interpreted from hydraulic testing in the Salado Formation, identified a number of factors relating to DRZ development, and sought to establish relationships among those factors and hydraulic properties based on the limited data available at that time. Subsequent testing provided additional data, which were discussed in Beauheim et al. (1993a). Those factors and relationships can now be examined with all of the data from the Salado permeability-testing program and related to flow dimensions and pressure/stress-dependent properties. The implications of the current understanding of brine flow through the Salado with respect to modeling of flow and transport are discussed below.

8.1 Evaluation of Evaporite Flow Regime

Two aspects of flow in the Salado have been presented in this report that were not discussed in previous reports: pressure-dependent hydraulic conductivity and flow dimensions. Our recent findings relative to these two factors and their relationship to excavation effects are discussed below.

8.1.1 Pressure-Dependent Hydraulic Conductivity

Many researchers (e.g., Warpinski et al., 1991; Cook, 1992) have studied and reported on the effects of varying stress and pore-pressure conditions on the hydraulic properties of fractures in laboratory tests. They found that increasing the effective stress, whether by increasing the stress normal to the fracture while holding pore pressure constant or by decreasing pore pressure while holding the normal stress constant, resulted in decreases in fracture aperture and permeability. Similarly, field tests such as those described by Gale (1977) and Rutqvist et al. (1992) have shown that fracture permeability increases as pore pressures are raised in constant-pressure flow tests due to increases in fracture aperture. Depending on rock properties, timing, and other conditions, these permeability changes may be largely reversible by changing the effective stress in an opposite direction.

Beauheim et al. (1993a) concluded that the magnitude of the initial pressure differential appeared to have no effect on the hydraulic properties interpreted from tests in different intervals of the Salado. However, the responses observed during the constant-pressure flow tests performed on MB138 and clay K in L4P52 and on anhydrite "a" in S1P74 could only be matched with a model in which hydraulic conductivity was pressure-dependent. (Pressure-dependent hydraulic conductivity might more accurately be called effective-stress-dependent hydraulic conductivity. However, when tests are conducted at a single location where only pore pressure, and not confining stress, is changing, the phenomenon can reasonably be termed pressure-dependent.)

Hydraulic conductivities estimated from the constant-pressure tests of MB138 in L4P52 increased from 1×10^{-11} to 8×10^{-11} m/s as the test pressure increased from 7.9 to 10.8 MPa. The geometry (flow dimension) of the system was consistently subradial, but appeared to increase slightly as the test pressure increased. The *K(P)* function used to simulate the response as pressure increased did not provide as good a fit to the data when the pressure in the system was decreasing. This may result from an actual opening/

closing hysteresis effect or it may be an artifact of the simplified pressure-dependent model implemented in GTFM.

The pressure-buildup and constant-pressure responses of anhydrite "a" at S1P74 were matched using a hydraulic-conductivity function that increased from 5×10^{-17} to 4×10^{-13} m/s as the pressure increased from 2.0 to 6.5 MPa. A good match to the data was obtained in this case using a constant radial-flow geometry.

Pressure-dependent hydraulic conductivity may also have been indicated by the constant-pressure flow tests of H-m2 in L4P51. The flow rates during the two constant-pressure tests were similar during the early-time periods, but then displayed quite different behaviors during the transition to the lower, late-time flow rates (Figure 7-17). The rate decreased much more rapidly during the transition period of the second test, which was conducted at a pressure approximately 1.8 MPa below the pressure of the first test. For similar subradial (almost linear) flow dimensions, the late-time hydraulic conductivity was over a factor of four lower for the second test conducted at the lower pressure. These differences are believed to indicate that the system of pores and/or fractures providing permeability to H-m2 is pressure-dependent.

8.1.2 Flow Dimensions

Flow-dimension analysis of the tests discussed in this report, including the reinterpretations presented in Appendix A, provided information useful in understanding flow through the Salado. As discussed in detail in Section 6.2.2.1, however, flow dimensions are somewhat problematic in that radial (dimension = 2) flow in a system with distance-varying hydraulic parameters cannot be distinguished from nonradial flow in a system with constant hydraulic parameters (in a single-well test). In addition, time-varying (or pressure-dependent) properties can be difficult to distinguish from spatially varying properties. To deal with these ambiguities, the concept of variable flow dimensions was broadened to include the non-unique combinations of temporal and spatial variations in flow geometries and hydraulic parameters. The baseline analysis of any test could then be transformed into different, nonunique combinations of geometries and hydraulic parameters as desired.

The pattern of flow-dimension changes interpreted from the constant-pressure-withdrawal responses of H-m2 in L4P51 is consistent with an essentially two-dimensional (planar) system in which flow is initially radial to slightly channelized (not completely space-filling) and then encounters a discontinuity that causes it to be more strongly channelized. When a propagating pressure transient reaches some type of discontinuity that restricts flow, such as a zone of decreased permeability or, in the extreme, a no-flow boundary, the flow dimension initially decreases rapidly, as illustrated in Figure 6-12. The exact value to which it decreases is non-intuitive and, within GTFM, non-unique. A transition to a sublinear to negative flow dimension is probably best interpreted as a qualitative indication of a reduction in permeability and/or flow area at some distance from the test hole. As shown in Figure 6-12, the flow dimension may increase with time/distance to a value representing the rate at which the permeability-area product continues to increase as the transient propagates further. The flow dimensions shown in Figures 7-13 and 7-16 from the first and second CPW tests of H-m2 in L4P51, respectively, illustrate these points. The flow dimension was initially between 1.5 and 1.8 during both tests, reflecting slightly subradial to radial conditions. The flow dimensions then decreased to

negative values, reflecting some restriction to flow with distance from the borehole. After a transition period, the flow dimension rose and stabilized at a value greater than 1 but less than the initial value, reflecting the loss in permeability and/or area.

As suggested in Section 7.1.2.2, the flow dimensions interpreted from the CPW tests of MB140 in L4P51 may reflect sublinear fracture flow close to the borehole and/or at early time, followed by increasing fracture connectivity and/or conductivity toward the front of the room and connecting drift where vertical stress relief would be greater. The subradial flow dimensions interpreted from the tests of MB138 in L4P52 and S1P74 and of clay J in S1P74 are consistent with a sparsely fractured medium in which fractures are poorly interconnected or a medium in which flow is channeled through those portions of fractures having the largest apertures. The tests in anhydrite "a" in borehole S1P74, on the other hand, were well represented by models using pressure-dependent hydraulic conductivity and a flow dimension of two, representing simple space-filling flow in a two-dimensional system.

8.1.3 Excavation Effects and Flow Dimensions

The flow-dimension interpretations presented in the previous section present a complex picture of flow in the Salado. Some of these complexities may be related to alteration of conditions in the Salado around the WIPP repository. A variety of interrelated processes occur around a mined opening that can affect permeability instantaneously and/or as a function of time. These processes include stress changes and associated deformation (both elastic and inelastic), and changes in pore pressure (which affects gas and mineral solubilities as well as effective stress).

When an opening is mined or drilled out of rock, the stress field around the opening is altered from its virgin state, causing changes in rock properties. Detournay and Cheng (1993) note that a compressive tangential stress concentration occurs at the wall of a borehole (or other opening) when it is first drilled and exposed to no load other than atmospheric pressure. This compressive tangential stress concentration also extends for some distance into the rock mass around the borehole (or other opening). As the rock drains with time, the tangential stress becomes increasingly compressive, approaching an asymptotic value. This compressive stress concentration can be reduced by applying fluid pressure within the borehole. Thus, we would expect to observe significant permeability reduction around a borehole or other opening maintained at low or atmospheric pressure relative to a borehole maintained at the far-field pore pressure.

This expectation is supported by field evidence. No long-term brine flow is observed in boreholes or shafts open to atmospheric pressure that penetrate MB139, although flow is observed when the holes are first drilled. In holes in which MB139 is kept isolated by packers, on the other hand, pore pressures and permeability are maintained (e.g., C2H02 and SCP01).

Decreased permeability caused by increased compressive stress in the immediate vicinity of a low-pressure opening may also explain, in part, the observations discussed by Deal et al. (1993) that wet areas in halite appearing on the walls of new excavations in the WIPP facility tend to dry up after a few years. The initial wet period probably corresponds to the period of draining before the compressive stress reaches its maximum. However, decreased permeability close to an excavation may also be caused by other factors in addi-

tion to increased compressive stress. Permeability may also be reduced during the drainage period by precipitation of halite within the pore space close to the excavation surface, because of decreased solubility at lower pressure and/or evaporation. Additionally, the relative permeability to brine of the rock may be reduced if the relative brine saturation in the pores is reduced by degassing of brine as pore pressure decreases. The apparent cessation of flow to an excavation surface may also be related to the formation of relatively high permeability extension fractures parallel to the surface, which intercept the brine flowing from the far field and divert it into fractures below the floor of the excavation. Deal et al. (1993) recount one case in which a dried-up surface was mined back an additional meter, after which the new surface was wet for a few years. Clearly, brine had been present all along in the halite a meter or more from the surface of the excavation, but had been unable to flow to the surface. The new mining altered the stress field, probably allowing a new volume to drain before the maximum compressive stress was again reached, and may also have removed the extension fractures acting as drains as well as halite that had undergone permeability reduction by precipitation and degassing.

The halite surrounding the WIPP excavations is also altered by inelastic processes such as creep and shear failure. These processes occur because of the deviatoric stress created by mining an excavation. Stresses in the radial direction away from an opening are reduced when an opening is created, while stresses in the tangential or circumferential direction are increased (Detournay and Cheng, 1993). The resulting difference between the stresses is a measure of the deviatoric stress. Halite creeps under deviatoric stress and fails through shear when the stress exceeds the strength of the rock. In the WIPP facility, shear offset of halite occurs only relatively near (within one or a few meters of) the surface of an excavation where deviatoric stresses are very high. Creep occurs at greater distances from the excavation surface and causes grain-boundary readjustment and microfracturing. Both grain-boundary readjustment and microfracturing can lead to increased permeability if they create a more connected network of pores than existed before. If grain-boundary readjustment results in a pore network that is less well-connected than before, however, permeability may be reduced. Also, fractures in halite will tend to heal with time if any compressive stress normal to the fractures is present. Thus, creep of halite may result in time-dependent increases **or** decreases in permeability.

Olsson and Brown (1993) compared the relative effects of normal-stress changes and shear on fractures, and found that shear accompanied by slip (offset) had greater potential to create irreversible and higher magnitude changes in fracture permeability. Shear offset alters the positions of the sides of a fracture. Fracture permeability is heavily dependent on how well the two sides fit together. If the two sides fit together very well, the open, interconnected space may be small, with correspondingly low permeability. If the two sides are not well matched, many asperities may hold the fracture open, leading to high permeability. In general, shear will have a greater long-term effect on the permeability of fractures in anhydrite than of fractures in halite, because fractures in halite are more likely to heal.

Where shear is intense, the rock may become decoupled from the surrounding rock mass and its associated stress field, preventing healing of fractures from occurring. In these areas, permeabilities are high but

pore pressures are low to nonexistent because the adjacent rock cannot provide adequate brine to pressurize, or in some cases fill, the high porosity present. Tests C2H01-A (guard zone), L4P51-A (guard zone), S0P01 (guard zone), S1P71-A (guard zone), and S1P73-A provide examples of these conditions in the DRZ.

All of these processes are location-specific and time-dependent and affect flow dimensions around an excavation in a variety of ways. If hydraulic properties in an individual layer change with distance from an excavation, a hydraulic test conducted in that layer will certainly show a nonradial flow dimension. Whether the specific flow dimension is greater or less than radial will depend on the specific spatial pattern of variation of hydraulic properties. If a propagating pressure transient encounters a region of decreased permeability, the flow dimension will decrease, while a region of increased permeability will have an opposite effect. Fractures connecting two permeable layers that are otherwise separated will tend to increase the flow dimension.

Flow dimensions that change as the "radius" of influence of a test expands should be expected. For instance, stress relief directly above or below an excavation may result in a zone of increased permeability within the "footprint" (vertical projection) of the excavation. Argüello (1990) showed that stress relief is not uniform below an individual room, but is greater where the room intersects a drift and is less at the back of a room where no further excavation has occurred. A test conducted near the front of a room might, therefore, show one flow dimension until the pressure transient propagated into the higher permeability region below the intersection of the room with its access drift, at which time a higher flow dimension would be evident. The tests of MB140 in L4P51 may provide an example of this. Conversely, a test conducted near the back of a room might show a decreasing flow dimension for some period of time as the pressure transient propagates into the lower permeability rock beyond the footprint of the excavation. At some later time, the flow dimension might increase if the pressure transient propagated into a higher permeability region toward the front of the room. Flow dimensions should also be expected to change with time where hydraulic properties are pressure-dependent. Non-uniform (i.e., high-gradient) pressure fields in regions with varying hydraulic properties must also affect inferred flow dimensions.

8.2 Spatial Variations in Hydraulic Properties

Inferred values of hydraulic conductivity, pore pressure, and specific storage of tested intervals are discussed below in the context of the foregoing discussion and plotted versus distance from an excavation. We cannot be certain that any of our test results are representative of conditions in the far field, completely unaffected by the presence of the WIPP excavations. The hydraulic conductivity of anhydrite is typically higher than that of halite. Only pore pressure appears to be related to distance from an excavation. Specific-storage values are too poorly defined to determine reasons for differences.

8.2.1 Hydraulic Conductivity

Figure 8-1 presents a plot of average hydraulic conductivities versus test-interval distances from an excavation from GTFM simulations of the tests discussed in this report and in Beauheim et al. (1991, 1993a) and Domski et al. (1996). The tests discussed in Beauheim et al. (1991, 1993a) have been reinterpreted for this report, with results presented in Appendix A. The hydraulic conductivities of

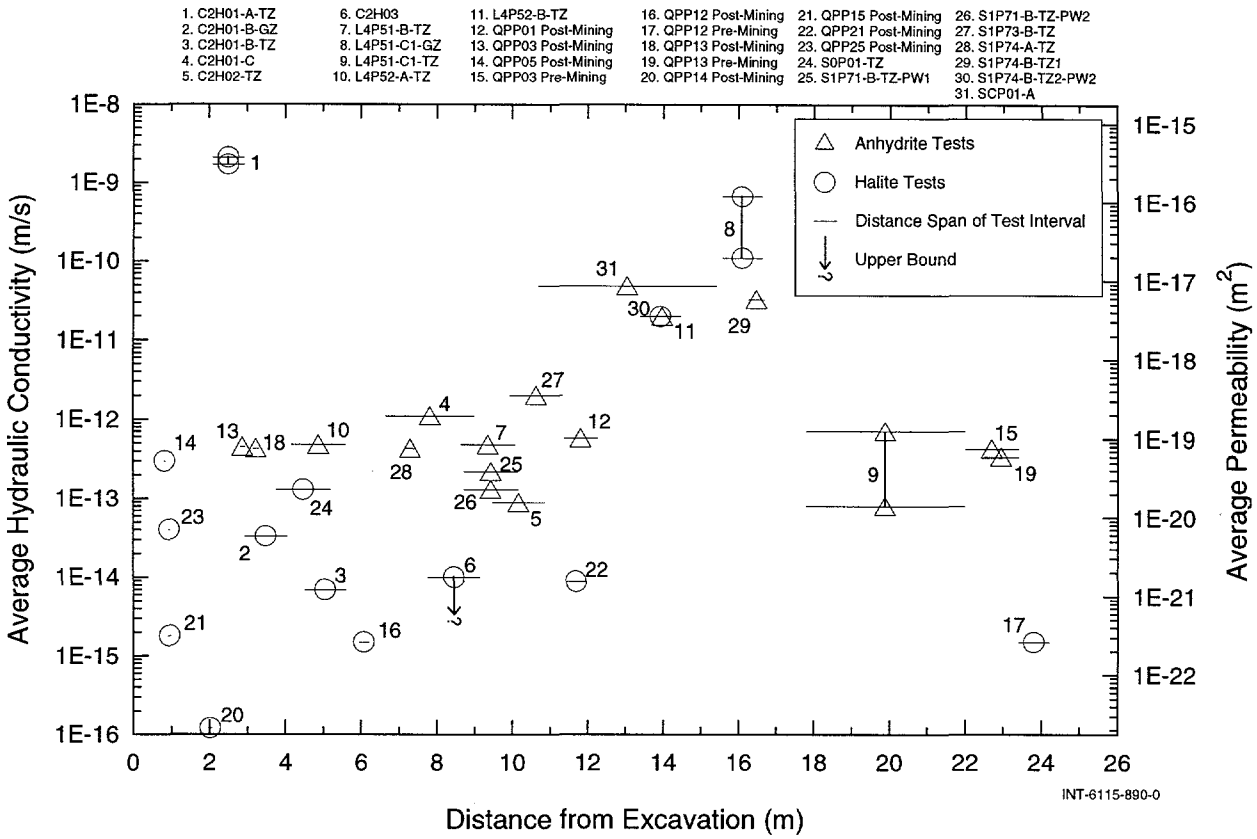

Figure 8-1. Interpreted average hydraulic conductivities versus distances from excavations to the tested intervals.

several of the tested units discussed in this report and shown on Figure 8-1 are believed to be pressure-dependent. The hydraulic conductivities shown on Figure 8-1 for these tests are the conductivities corresponding to static formation pressure in the tested unit. Testing sequences performed in the L4P51-C1 guard zone and L4P51-C2 test zone 2 were tests of the same halite interval over different time periods, so the estimated hydraulic-conductivity values are shown as a range for a single interval on the figure. Ranges are also shown for other intervals (e.g., MB140 in L4P51) for which different hydraulic-conductivity estimates were obtained.

Figure 8-1 shows 14 values of halite hydraulic conductivity and 17 values of anhydrite hydraulic conductivity. No correlations are evident between estimated halite or anhydrite hydraulic conductivity and distance from an excavation, regardless of the borehole orientation. The lowest estimate of halite hydraulic conductivity, 1×10^{-16} m/s ($k = 2 \times 10^{-23}$ m^2), is from QPP14 after the mining of Room Q, approximately 2 m from the excavation. The highest estimate, 2×10^{-9} m/s ($k = 3 \times 10^{-16}$ m^2), is from the C2H01-A test zone, also approximately 2 to 3 m below an excavation. The lowest estimate of anhydrite hydraulic conductivity, 9×10^{-14} m/s ($k = 2 \times 10^{-20}$ m^2), is from the C2H02 test zone, approximately 10 m from the excavation in a borehole angled downward under the rib. All eight estimates of anhydrite hydraulic conductivity from distances greater than 10 m, both in angled and vertical boreholes, are greater than this value.

The highest estimate of anhydrite hydraulic conductivity, 5×10^{-11} m/s ($k = 9 \times 10^{-18}$ m^2), is from MB139 in the SCP01 test zone, approximately 11 to 15 m below and beyond an excavation.

As noted by Beauheim et al. (1993a), estimated hydraulic conductivities such as those presented in Figure 8-1 represent average values assuming that the tested intervals are homogeneous. If the observed responses are dominated by singular features (such as fractures) rather than by uniform properties, then the average hydraulic-conductivity values shown in Figure 8-1 might not be meaningful. Another factor complicating the comparison of hydraulic-conductivity values is the relationship between hydraulic conductivity and flow dimension. As discussed in Section 6.2.2.1, flow dimension is used in this report to represent the combined effects of changes in hydraulic conductivity and flow geometry. Thus, the reported value of hydraulic conductivity depends on the value used for flow dimension. For a given response, as the value of flow dimension used to interpret that response increases, the estimated hydraulic conductivity decreases, and vice versa. Even when flow dimension is clearly defined, as on one of the diagnostic plots discussed in Section 6.2.2.2, we cannot tell without additional information if the dimension is caused by changes in hydraulic conductivity or changes in the geometry of flow. The reported hydraulic-conductivity values are based on an assumption that the flow dimension represents the flow geometry only. That assumption may or may not be valid.

The hydraulic conductivity of anhydrite appears to be generally higher than that of halite. The lowest anhydrite hydraulic conductivity inferred, 9×10^{-14} m/s ($k = 2 \times 10^{-20}$ m^2), is nearly three orders of magnitude higher than the lowest halite hydraulic conductivity, 1×10^{-16} m/s ($k = 2 \times 10^{-23}$ m^2). In general, anhydrite hydraulic conductivities are greater than 10^{-13} m/s ($k > 2 \times 10^{-20}$ m^2) and halite hydraulic conductivities are generally less than that value.

Only five of fourteen halite hydraulic conductivities are equal to or greater than 10^{-13} m/s: those from L4P51-C1-GZ (#8 on Figure 8-1), C2H01-A (#1), S1P74-B-TZ2 (#30), QPP05 post mining (#14), and S0P01-TZ (#24). The L4P51-C1 guard zone was unlike any other zone tested and the reason for high hydraulic conductivity in halite H-m2 is unknown. The other four halite hydraulic conductivities greater than 10^{-13} m/s all come from test intervals that are within approximately 5 m of an excavation and/or contain significant clay seams. The C2H01-A test interval was approximately 2 to 3 m below the floor of Room C2, a location where excavation-induced disturbance would be expected. The C2H01-A tests were also the first tests performed under this program, and later experience has shown that pulse tests conducted over a 0 to 3.5 MPa absolute pressure range are likely to be significantly affected by pressure-dependent test-zone compressibility. The data necessary to evaluate test-zone compressibility were not collected during the C2H01-A testing and, therefore, the parameters estimated from those tests are considered to have high uncertainty. The S1P74-B test zone 2 interval was approximately 14 m from the excavation, but included AH-1, the most clay-rich halite interval near the repository horizon. The QPP05 test interval was only approximately 0.8 m from Room Q, and the S0P01 test interval included clay D.

Hydraulic-conductivity values for anhydrite range from approximately 10^{-13} to 5×10^{-11} m/s (permeabilities of approximately 10^{-20} to 10^{-17} m^2). The three values greater than 10^{-11} m/s ($k > 2 \times 10^{-18}$ m^2) were from tests con-

ducted in boreholes angled away from the excavations (SCP01-A, S1P74-B, and L4P52-B), suggesting that the inferred high hydraulic conductivities are not necessarily caused by responses to the excavations, but may be representative of far-field properties.

For the WIPP Compliance Certification Application (CCA), halite in the far field was assigned a hydraulic-conductivity range from 5.7×10^{-18} to 5.7×10^{-15} m/s ($k = 10^{-24}$ to 10^{-21} m^2; US DOE, 1996, Table 6-14) and far-field anhydrite was assigned a hydraulic-conductivity range from 5.7×10^{-15} to 4.5×10^{-11} m/s ($k = 10^{-21}$ to 7.9×10^{-18} m^2; US DOE, 1996, Table 6-15). All rocks within the DRZ around the repository were assigned a single hydraulic-conductivity value of 5.7×10^{-9} m/s ($k = 10^{-15}$ m^2; US DOE, 1996, Table 6-17).

8.2.2 Pore Pressure

At equilibrium, pore pressures around an excavation should reflect steady flow toward the excavation driven by the difference between the far-field pore pressure in the formation and the pressure in the excavation. The time required for this equilibrium condition to be established after an excavation is opened is dependent on the mechanical and hydraulic properties of the rock. When an excavation is first opened, a disequilibrium condition is created between the atmospheric pressure in the excavation and the pore pressure initially present in the surrounding rock. This disequilibrium leads to flow from the rock into the excavation, causing the pore pressure in the rock to decrease. With time, the pore pressure in the rock is decreased to greater and greater distances from the excavation. In addition to the changes in pore pressure caused by flow, the mining of an excavation also changes pore pressures by changing the state of stress in the surrounding rock mass. The change in the stress in the rock has both instantaneous and time-dependent components that cause deformation of the rock, which in turn induces changes in pore pressures throughout the affected volume of rock. The pore-pressure change is given by Skempton's (1954) coefficient as some fraction of the stress change. Skempton's coefficient is inversely proportional to the strength of the rock matrix and is, therefore, higher in halite than in anhydrite. Because the change in stress is a time-dependent process, changes in pore pressures have two transient components: one arising from the evolution of the flow field and one arising from the evolution of the stress field. Which, if either, of these components dominates the pore-pressure response at a given time and place depends on the hydraulic and mechanical properties of the medium.

In a medium such as halite that is not linearly elastic, pore pressures may also change during deformation caused by creep, which is itself a time-dependent process. Thus, the evolution of pore pressures in halite is dependent on multiple processes, most of which are affected, to some degree, by distance from an excavation, but on different time scales. Developing a full understanding of those processes is beyond the scope of the work discussed in this report.

Figure 8-2 presents a plot of estimated formation pore pressures versus test-interval distances from an excavation for 23 halite intervals and 24 anhydrite intervals (Beauheim et al., 1991, 1993a; Domski et al., 1996; this report). The pore pressures were estimated from GTFM simulations or from maximum observed pressures in a zone for all of the Salado permeability tests. A general trend of increasing pore pressure with increasing distance from an excavation can be seen for both anhydrite and halite intervals. Comparing pore pressures between test zones and guard zones in individual boreholes in

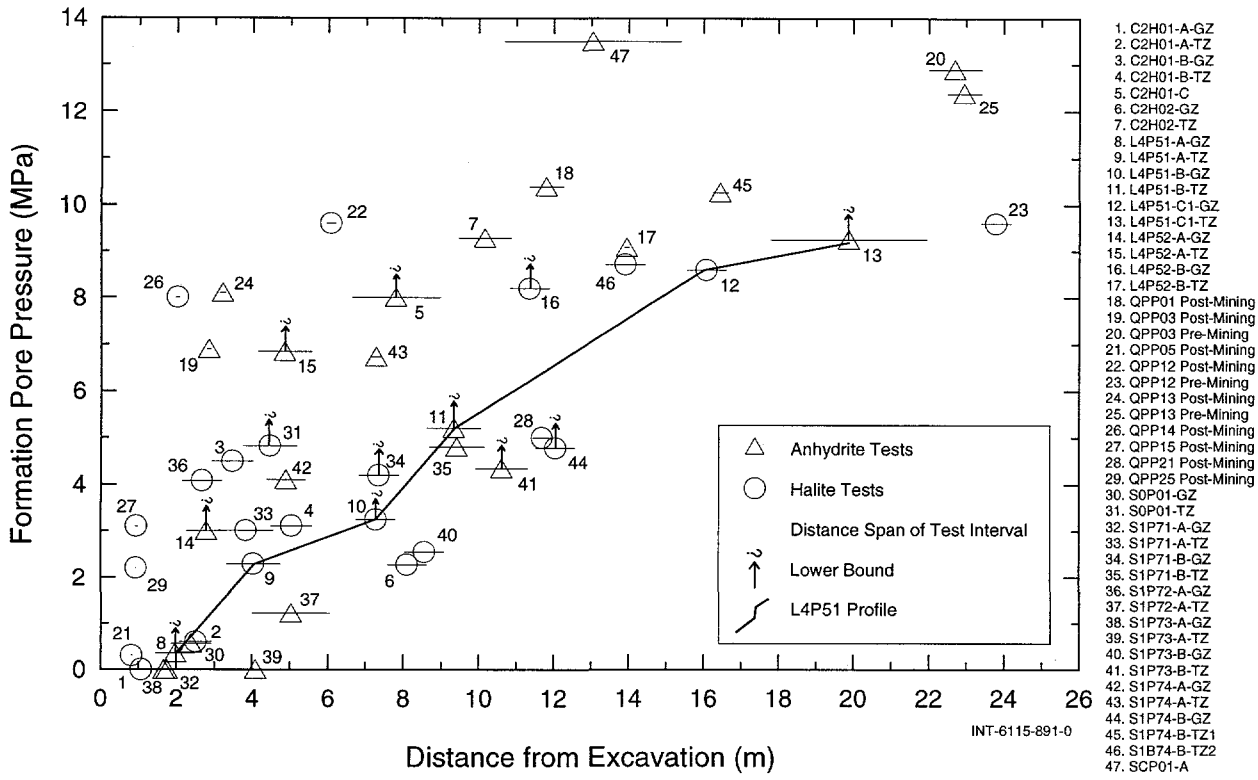

Figure 8-2. Interpreted pore pressures versus distances from excavations to the tested intervals.

Figure 8-2, we see that, with the exceptions of S1P72 and C2H01 (discussed in Beauheim et al., 1993a), pore pressures in test zones (at the ends of holes) are higher than pore pressures in guard zones (closer to the excavations). Pore-pressure estimates are available from more intervals (six) in borehole L4P51 than in any other hole, and show a clear trend of increasing pressure with distance from the excavation. This observation, along with the overall trend in the data, supports the hypothesis that the Salado becomes progressively depressurized with closer proximity to the repository.

8.2.3 Specific Storage

Beauheim et al. (1991) estimated baseline values for the specific storage of halite and anhydrite based on laboratory measurements of the material properties of those types of rocks (Table 6-1). The ranges given for the material properties were used to calculate corresponding ranges for halite and anhydrite specific storage. These ranges, along with the estimates of halite and anhydrite specific storage from GTFM simulations of the Salado permeability tests, are shown in Figure 8-3. Specific-storage values are given only for analyses in which the conceptual model did not explicitly include a skin, for reasons discussed in Section 6.2.3.8. Figure 8-3 shows that most of the specific-storage estimates are not within the theoretical limits.

In Section 6.2.3.8, estimates of formation specific storage were demonstrated to be in error if a zone of increased or decreased permeability develops around the borehole due to drilling and/or stress changes. This error occurs because sufficient constraints do not exist from single-borehole test data to estimate near-borehole permeability changes and formation specific storage simultaneously,

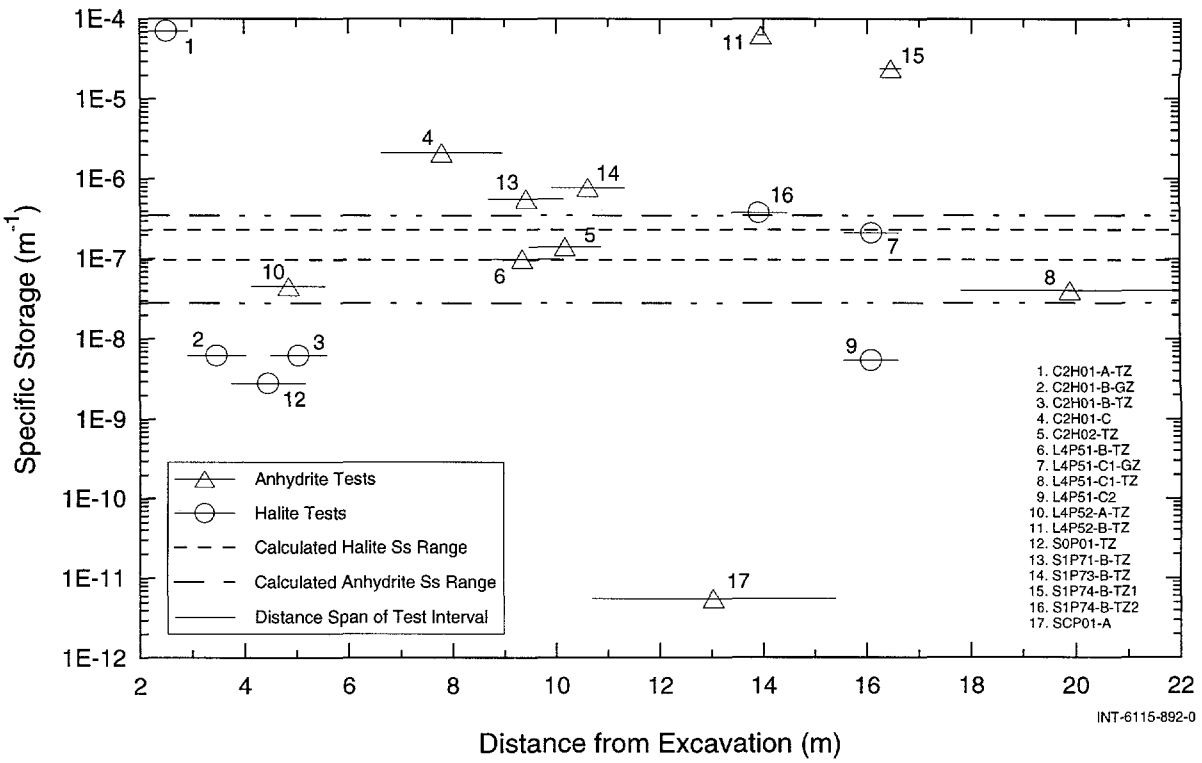

Figure 8-3. Interpreted average specific storages versus distances from excavations to the tested intervals.

i.e., this inverse problem is not well posed. Equivalent matches to test responses can be obtained by simultaneously varying three parameters in GTFM: skin (near-borehole) hydraulic conductivity, skin thickness, and formation specific storage. Figure 6-37 showed that matches to a test response could be obtained while varying specific storage over several orders of magnitude by simultaneously varying the other parameters. Therefore, the apparently anomalous specific-storage values interpreted from the majority of the tests may be taken as indications of the existence of skins around the boreholes and not as representations of the actual specific storage of the tested strata. The lack of accurately defined specific-storage values also precludes determination of the radii of influence of these tests.

8.2.4 Discussion

The pore pressure in a medium, such as halite, that undergoes creep might be expected to be equal to the lithostatic pressure because creep will continue until the deviatoric stress is zero. Pore pressures in anhydrite interbeds overlain and underlain by halite might also be expected to be equal to lithostatic pressure. Even at the greatest distance from the WIPP excavations at which tests have been conducted, 24 m, observed halite pore pressures are less than 10 MPa (Figure 8-2). Pore pressures approaching 13 MPa have been observed in anhydrite interbeds, still below the approximately 15 MPa considered to represent undisturbed lithostatic pressure at the WIPP horizon (Wawersik and Stone, 1989). Furthermore, Wawersik and Stone (1989) reported that an isotropic stress field in halite at the WIPP, representative of conditions unaffected by the

presence of excavations, was encountered only at distances greater than 50 m from the excavations. Therefore, none of the tests we have conducted may be outside the region of stress relief around the WIPP repository and we cannot be certain that any of the hydraulic properties we have inferred are representative of conditions in the far field. However, the consistency of the inferred anhydrite permeability values over a wide range of pore-pressure conditions suggests that far-field values would likely be similar. Appropriate values for the permeability of halite in the far field are less certain.

8.3 Implications for Modeling

The existence/occurrence of pressure-dependent hydraulic conductivity and nonradial flow dimensions in the Salado has implications with regard to modeling of flow and transport. If hydraulic properties are dependent on effective stress, hydraulic-conductivity values derived from tests conducted at locations under a given stress regime cannot be assigned throughout a modeling domain with a variable stress regime. A rigorous model should include a coupling between hydraulic properties and the stress field, with a full recognition of the time-dependence of conditions and properties.

Finite-difference and finite-element models constructed with homogeneous layers have implicit flow dimensions of 2 if the permeable layers are completely confined or some value between 2 and 3 if different layers have different properties or properties are anisotropic. Incorporating heterogeneity in permeability within layers can alter the flow dimension. We now recognize that no inferred value of hydraulic conductivity can be separated from its associated flow dimension. If a hydraulic conductivity estimated assuming a subradial flow dimension is used as input to a homogeneous flow model, flow will be overestimated. Flow may, likewise, be underestimated if a hydraulic conductivity estimated assuming a greater-than-radial flow dimension is used in a model having an implicit dimension of 2.

Each of the layers of the Salado represented in the modeling for the WIPP CCA (US DOE, 1996) was treated as homogeneous. As a result, the CCA modeling calculated a larger brine flux towards and away from the WIPP repository than would have been calculated had conditions giving the subradial flow dimensions observed in these tests been implemented. However, the same CCA modeling would, for a given flux, underestimate the distance to which brine would flow away from the repository because it would assume that the brine was spread evenly through the entire volume of rock instead of being channeled within some smaller percentage of the volume. Based on the test results presented in this report, the Salado might better be modeled as a heterogeneous medium with a subradial flow dimension.

All of the Salado permeability tests discussed in this and previous reports were conducted under conditions of high hydraulic gradients. Success in applying a Darcy-flow model to the interpretation of these tests does not necessarily imply that the model would provide a valid description of flow through the Salado under natural low-gradient conditions, as discussed by Beauheim et al. (1993a). The available data suggest that a Darcy-flow model should adequately describe flow in the near-field around the WIPP repository so long as gradients are high, but flow may be overestimated after the repository pressurizes and gradients decrease.

THIS PAGE INTENTIONALLY LEFT BLANK

9. GAS AND BRINE CHEMISTRY OF MARKER BED 140 IN BOREHOLE L4P51

Relatively large volumes of brine with abundant dissolved gas were produced during constant-pressure flow testing of MB140 in borehole L4P51 (Section 7.1.2). Inasmuch as the available information on Salado gas and brine chemistry was limited, particularly regarding MB140, a sampling campaign was initiated to collect gas and brine samples at pressures and temperatures as close to formation conditions as possible.

9.1 History

Borehole L4P51 was deepened from 10.06 m to 22.20 m between 1 and 15 April 1992 for hydraulic test sequence L4P51-C on the 4-meter-thick anhydrite interbed, MB140 (Chace et al., 1998). Figure 7-2 shows the configuration of the triple-packer tool installed for the testing and its position relative to the test-interval stratigraphy. The core log of borehole L4P51 is presented in Chace et al. (1998). The depth of MB140, 17.80 - 21.97 m below the floor of Room L4, required the use of brine as the drilling fluid rather than air. The drilling brine was made by dissolving 99% pure NaCl water-softener salt in fresh water heated using an electric water heater. The final density of the drilling fluid was 1.22 g/cm^3 at ambient repository temperature. Immediately upon reaching final depth, the borehole was bailed to 28 cm above the bottom of the hole.

Contamination of the formation with drilling fluid was expected to have been minimal due to the low pressure of the drilling fluid relative to the initial formation pressure of MB140. At full-borehole conditions, the pressure exerted at the midpoint depth of MB140 by brine with a density of 1.22 g/cm^3 was calculated to be 0.24 MPa while the initial formation pressure of MB140 is approximately 9 MPa. Therefore, the pressure gradient under full-borehole conditions is from the formation toward the borehole, thus minimizing the chance of drilling fluid invading the formation.

9.2 Gas and Brine Sampling and Analysis

Hydraulic testing revealed that MB140 has a high initial formation pressure (9.0 to 9.5 MPa) and relatively high permeability ($k \approx 10^{-19}$ m^2) (Section 7.1.2), which made sampling a large volume of brine possible. On 14 April 1993, a 203-day sampling campaign was initiated in the L4P51-C test zone with the goal of collecting several gas and brine samples for chemical analysis. The sample identification numbers, collection dates, cumulative flow volumes from the test zone, and number of extracted borehole volumes are listed in Table 9-1. Figure 9-1 displays the cumulative volume and the times at which samples were taken and Figure 9-2 shows the test-zone pressure during sampling.

Gas and brine samples were collected during a constant-pressure flow event at approximately 8 MPa pressure using in-line stainless-steel sample cylinders. This method allowed samples to be collected at pressure conditions near that of the formation pressure, thus preventing degassing. Figure 3-9 is a schematic drawing of the sample-collection apparatus. The sample cylinder was positioned in-line between the test zone and the constant-pressure panel to maximize the flow-through volume to collect samples representative of MB140. The design of the sampling apparatus allowed sample cylinders to be changed without interruption of the flow test. Each sample cylinder was flushed and pre-

Table 9-1. Sample Collection Information

Sample ID	Collection Date	Cumulative Volume (mL)	# Borehole Volumes[1]
13105-1	04/15/93	0.0	0
13123-1	05/03/93	32,650	3.70
13152-1	06/01/93	61,022	6.95
13167-1	06/25/93	83,577	9.51
13176-1	07/02/93	91,410	10.40
13183-1	07/09/93	96,041	10.93
13190-1[2]	07/15/93	99,349	11.31
13258-1[2]	09/15/93	139,126	15.84
13281-1	10/08/93	147,628	16.80
13294-1	10/21/93	154,983	17.64
13302-1	10/29/93	157,830	17.97
13308-1	11/04/93	162,375	18.48
13320	11/28/93	Post Testing	

[1] the borehole fluid volume for the test zone of L4P51-C was 8,785 mL
[2] only gas analysis available

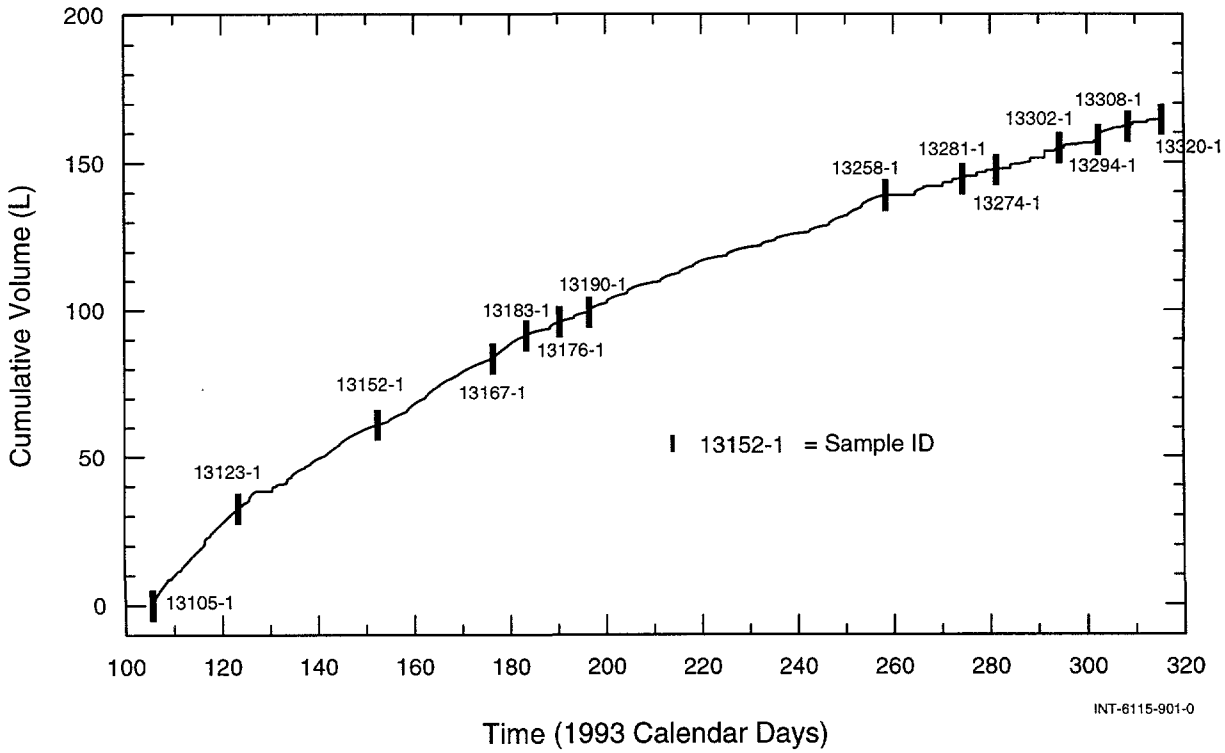

Figure 9-1. Cumulative volume of brine removed from the L4P51-C test zone and sampling times.

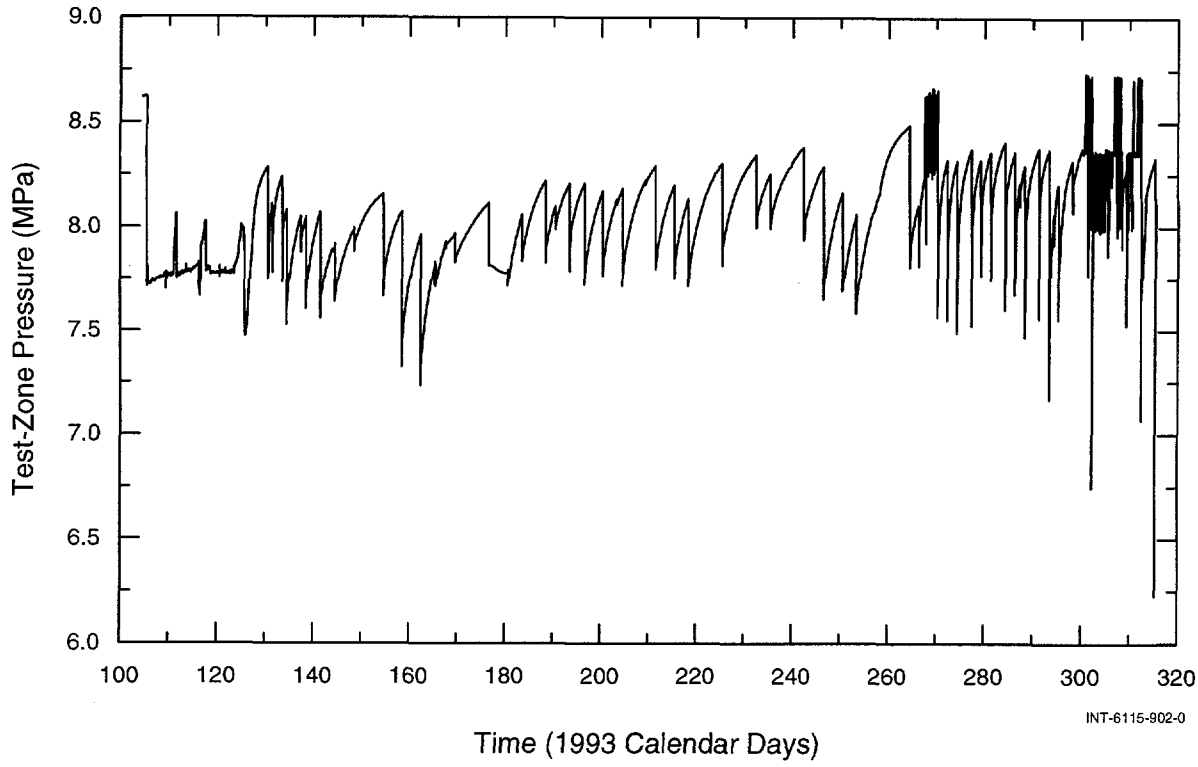

Figure 9-2. Test-zone pressure during the L4P51-C sampling.

pressurized with argon (Ar) prior to installation. This procedure helped to avoid atmospheric contamination of the gas samples, but also made interpretation of the Ar abundance questionable.

Following collection, the samples were sent to the New Mexico Institute of Mining and Technology for gas analysis. The pressurized sample cylinders were vented into an evacuated vessel, which allowed the gas to exsolve. The gas sample was analyzed using a quadrapole mass spectrometer. Difficulties were encountered extracting the gas from some of the sample cylinders, leading to gas loss or gas contaminated by the atmosphere. The resealed sample cylinder was sent to Chem-Nuclear Geotech Analytical Laboratory in Grand Junction, CO, for brine analysis.

9.3 Data Interpretation

Gas and brine analytical results are presented below. The data were used to develop hypotheses concerning the origin and history of the fluids.

9.3.1 Gas Chemistry

The results of the gas analyses are given in Table 9-2. The analytical data were evaluated using three techniques: 1) the temporal evolution of the gas chemistry was evaluated by plotting gas abundances versus collection date; 2) the saturations of N_2, CH_4, and CO_2 were calculated for the P-T conditions of MB140; and 3) the origin of the gases is discussed by comparison to atmospheric composition and possible geochemical processes.

Table 9-2. Gas Analytic Data in Mole Percent Dry Gas

Sample	Collection Date	N_2	CH_4	CO_2	C_2H_6	C_3H_8	C_4H_{10}	C_7H_8	Ar*	Ne	He	H_2S
13105-1	4/15/93	61.20	28.60	0.11	0.33	0.16	0.00E+0	0.00E+0	9.41	0.00E+0	5.34E-2	1.23E-4
13123-1	5/3/93	69.00	30.10	0.11	0.36	0.17	0.00E+0	0.00E+0	0.13	3.84E-3	1.93E-2	0.00E+0
13152-1	6/1/93	68.10	30.70	0.02	0.34	0.27	0.00E+0	0.00E+0	0.24	5.27E-3	6.83E-2	4.09E-5
13167-1	6/16/93	51.22	47.12	0.42	0.22	0.26	1.02E-3	6.72E-2	0.37	0.00E+0	0.00E+0	0.00E+0
13176-1	6/25/93	53.38	44.75	0.35	0.17	0.29	1.26E-3	6.96E-2	0.63	5.41E-2	2.22E-1	0.00E+0
13183-1	7/2/93	58.32	40.54	0.14	0.00	0.18	1.23E-3	6.70E-2	0.44	1.74E-2	2.40E-1	0.00E+0
13190-1	7/9/93	32.88	66.11	0.71	0.03	0.06	0.00E+0	1.00E-2	0.00	0.00E+0	1.83E-1	0.00E+0
13258-1	9/15/93	72.66	25.88	0.28	0.53	0.19	0.00E+0	0.00E+0	0.20	5.00E-2	2.30E-1	0.00E+0
13281-1	10/8/93	52.97	46.08	0.24	0.14	0.05	0.00E+0	0.00E+0	0.27	0.00E+0	2.10E-1	0.00E+0
13302-1	10/29/93	70.94	28.22	0.01	0.28	0.21	0.00E+0	0.00E+0	0.17	0.00E+0	1.70E-1	0.00E+0
13308-1	11/4/93	64.12	34.22	0.20	0.29	0.21	0.00E+0	0.00E+0	0.79	0.00E+0	1.60E-1	0.00E+0
13320-1	11/24/93	53.30	44.96	0.03	0.45	0.26	1.00E-2	0.00E+0	0.80	0.00E+0	2.00E-1	0.00E+0
Average:		59.01	38.94	0.22	0.26	0.19	1.13E-3	1.78E-2	1.12	1.09E-2	1.46E-1	1.36E-5
Atmosphere		78.08	1.6E-4	0.034	0.00	0.00	0.00E+0	0.00E+0	0.93	1.82E-3	5.24E-4	0.00E+0

* Sample cylinders were pressurized with argon.

9.3.1.1 Temporal Evolution

Figures 9-3 through 9-10 show mole percents as a function of the collection date for the gas phases identified in the samples. The error bars represent twice the population standard deviation, which is probably a conservative estimate of the analytical uncertainty. Although the sample analyses show scatter, all of the error bars for each phase's concentration overlap to some degree. This simple analysis suggests that the composition of gas dissolved in the MB140 brine was relatively constant over the sampling period.

9.3.1.2 Gas-Saturation State of MB140 Brine

Neither of the available geochemical codes for high-ionic-strength solutions, PHRQPITZ (Plummer et al., 1988) and EQ3/6 (Wolery, 1983), include the gas phases measured in the MB140 brine in their thermochemical databases. Therefore, rigorous calculations of the gas saturations could not be performed. Rather, the levels of gas saturation were calculated by converting the analyzed mole percent gas values to mole fractions of the gaseous components in the liquid phase using the method outlined below, and comparing them to data published by Cygan (1991), who also reports gas solubility in this manner. This calculation was possible only for those samples where the total volume of liberated gas was measured and a chemical analysis of the brine was performed. The results of the calculations are presented in Table 9-3.

Calculation of gas mole fraction:

1) Calculate Moles of Gas i in Sample

$$V_i = x_i V_{gas}$$
$$n_i = V_i/V_{mi}$$

where:

x_i = mole fraction of gas i in dry gas mixture
V_{gas} = total volume of gas in sample at STP
V_i = volume of gas I
V_{mi} = molar volume of gas i at STP
n_i = moles of gas i in sample

2) Calculate Moles of Water in Sample

$$M_{solutes} = V_{sample}\, c_i$$
$$M_{H2O} = V_{sample}\, \rho_{fluid} - M_{solutes}$$
$$n_{H2O} = M_{H2O}/GFW_{H2O}$$

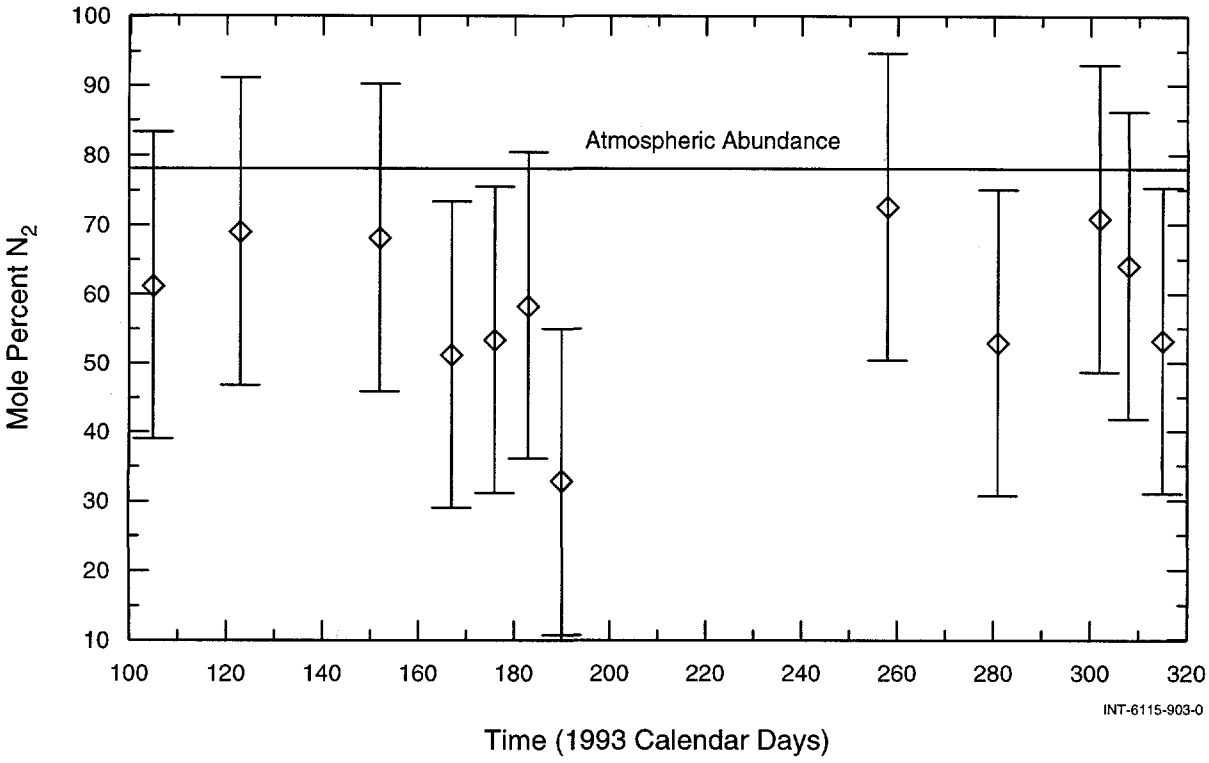

Figure 9-3. N_2 versus sample date.

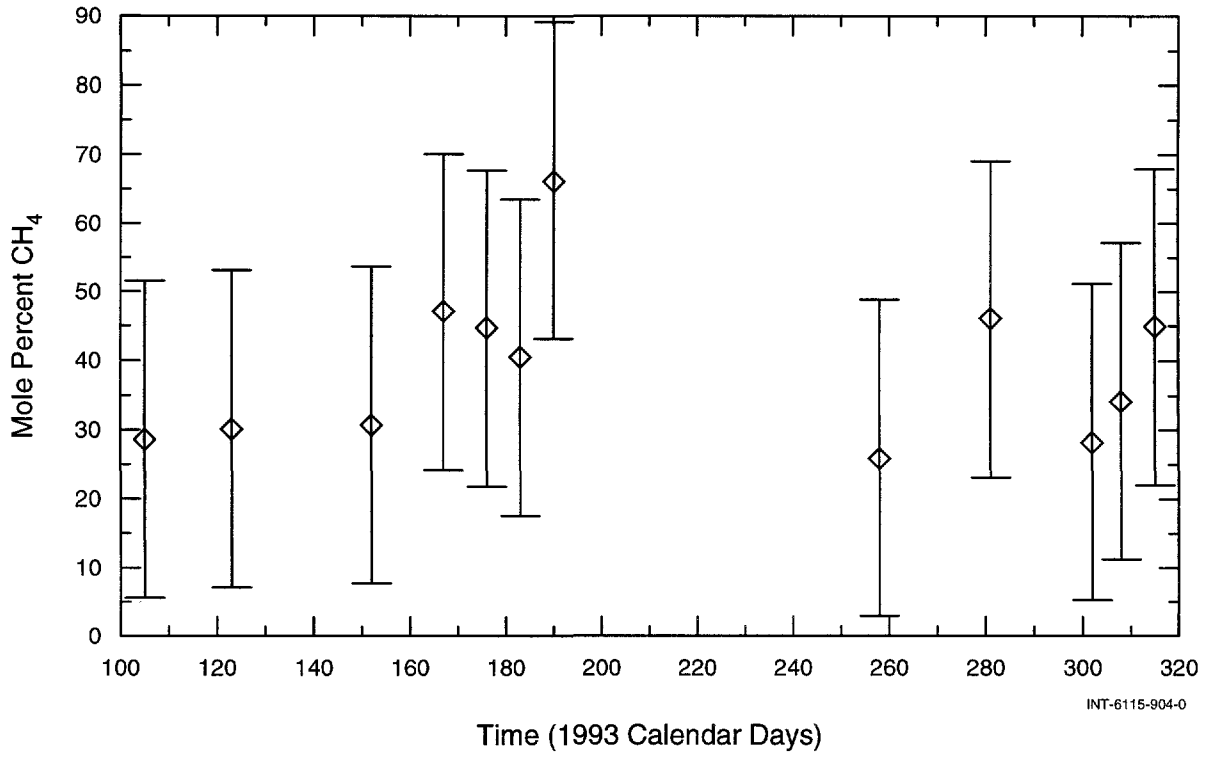

Figure 9-4. CH_4 versus sample date.

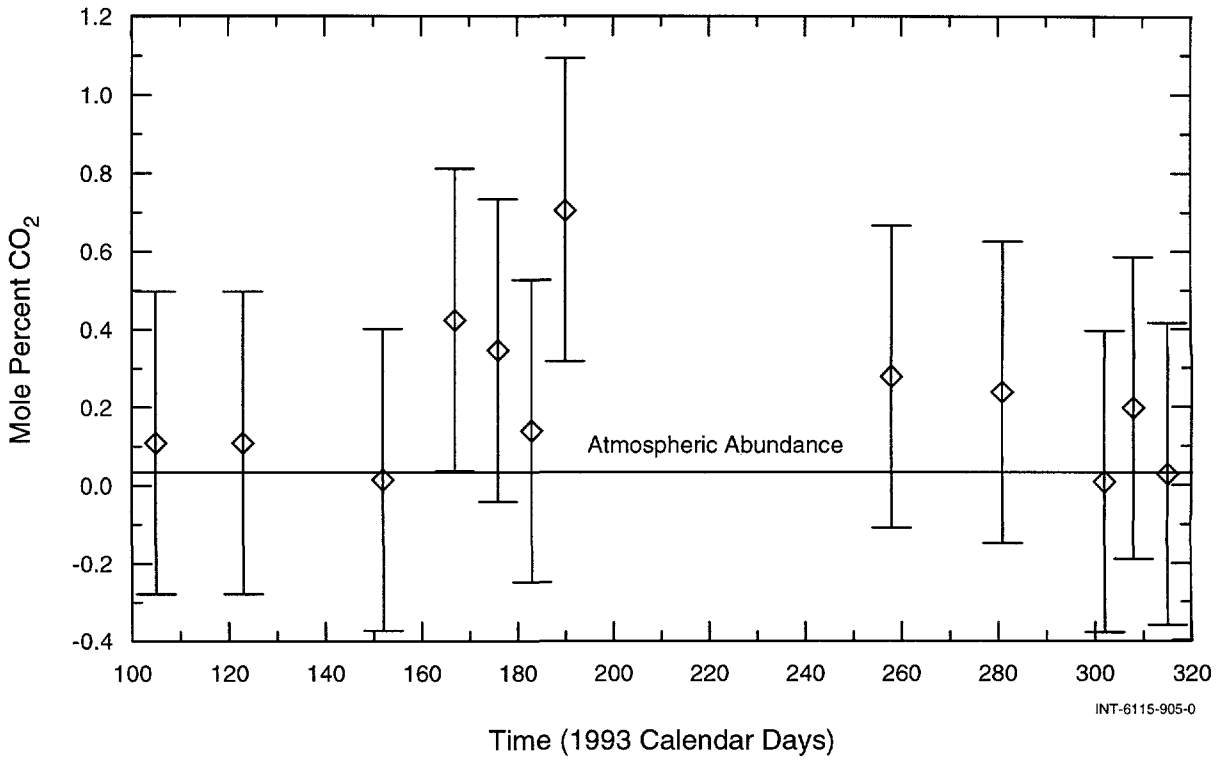

Figure 9-5. CO_2 versus sample date.

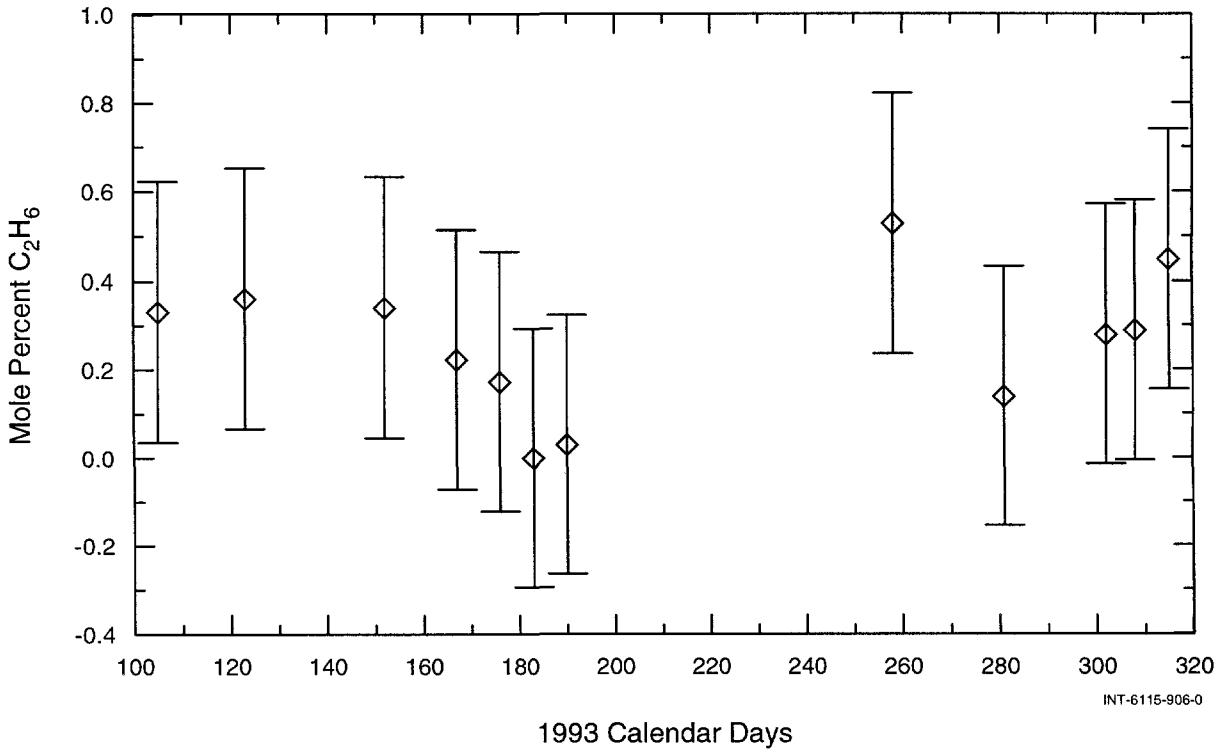

Figure 9-6. C_2H_6 versus sample date.

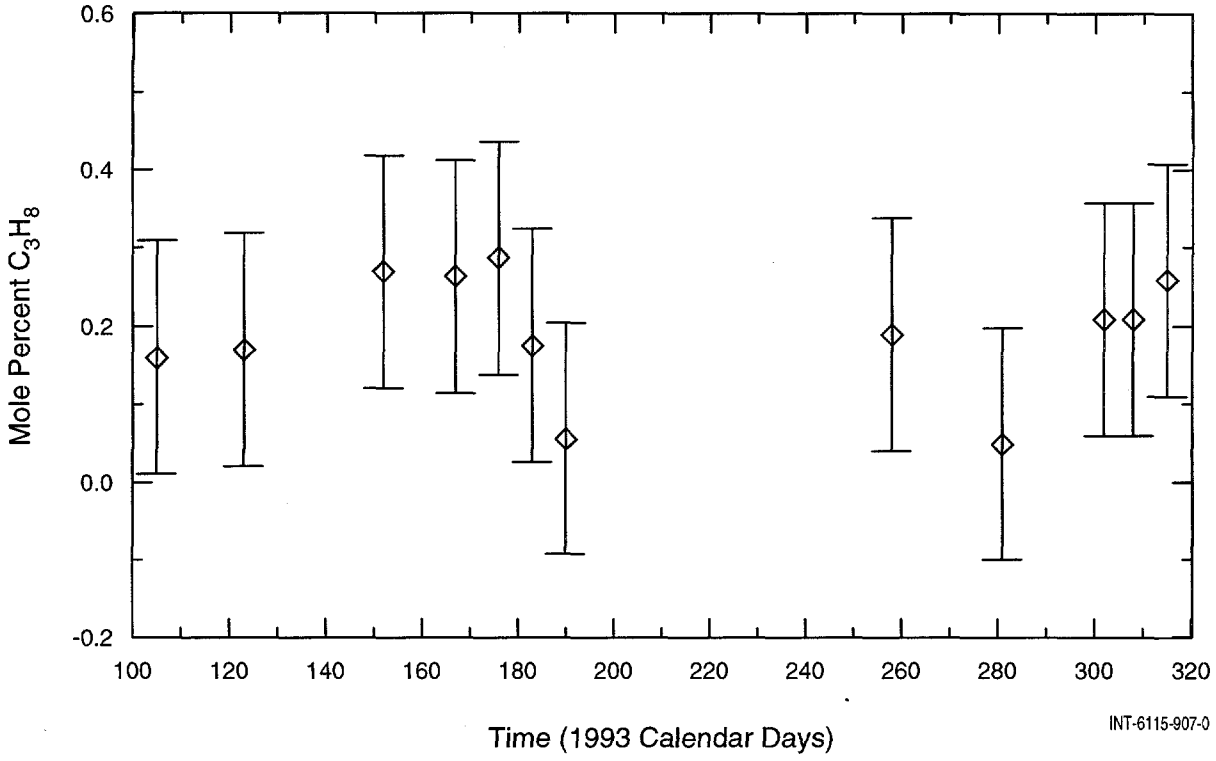

Figure 9-7. C_3H_8 versus sample date.

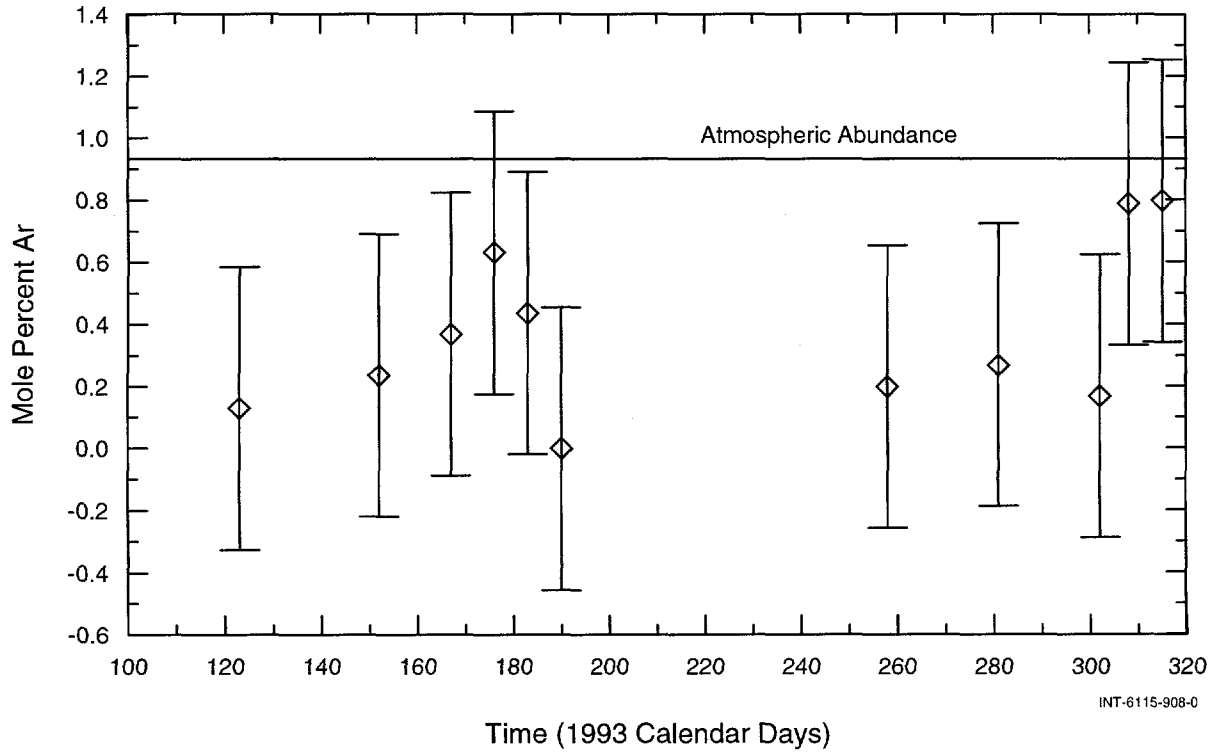

Figure 9-8. Ar versus sample date.

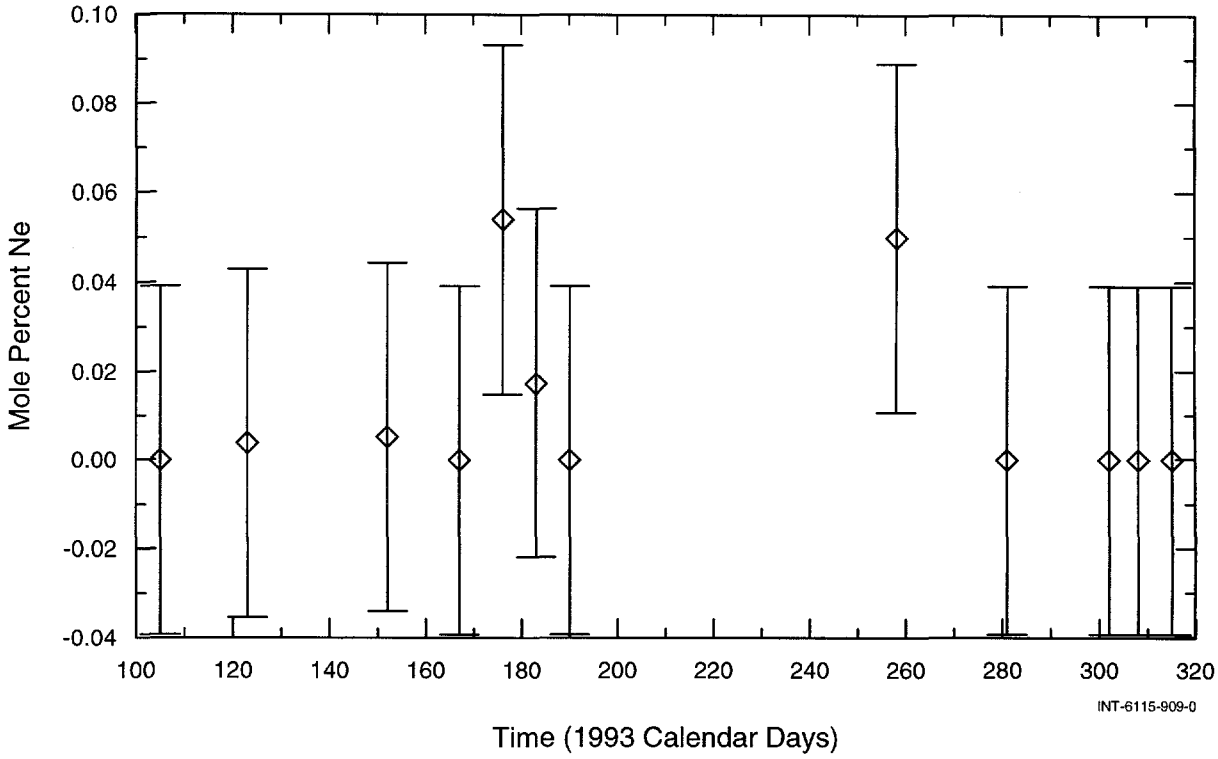

Figure 9-9. Ne versus sample date.

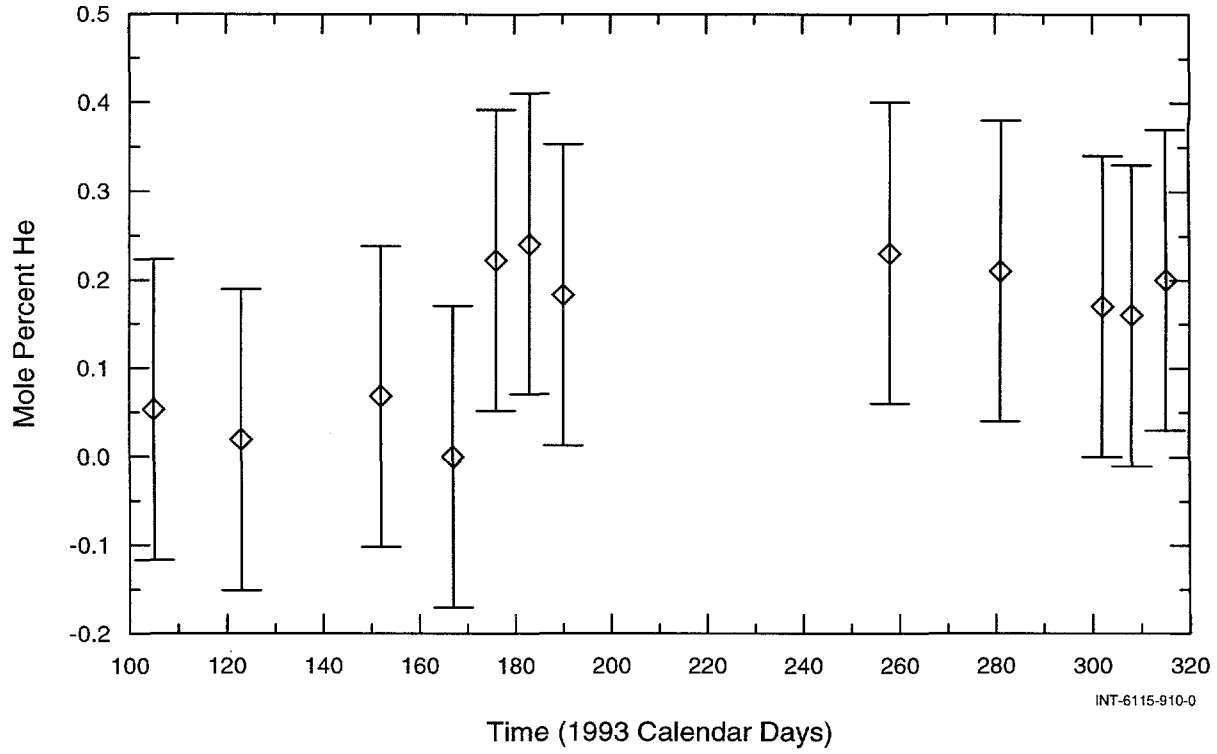

Figure 9-10. He versus sample date.

Table 9-3. Gas-Saturation Data for the MB140 Brine in Units of Mole Fraction

SAMPLE	N_2	CH_4	CO_2
13105-1	2.66E-5	1.24E-5	4.80E-8
13123-1	NA	NA	NA
13152-1	NA	NA	NA
13167-1	(3.99E-6)	(3.67E-6)	(3.33E-8)
13176-1	(5.27E-6)	(4.42E-6)	(3.45E-8)
13183-1	1.88E-5	1.30E-5	4.55E-8
13190-1	NA	NA	NA
13258-1	NA	NA	NA
13281-1	5.06E-5	4.41E-5	2.31E-7
13302-1	1.45E-4	5.78E-5	2.06E-8
13308-1	1.40E-4	7.45E-5	4.38E-7
13320	6.35E-5	5.36E-5	3.60E-8

( ) - low relative confidence

where:

V_{sample} = volume of the sample cylinder
c_i = concentration of ionic species i (mg/L)
$M_{solutes}$ = mass of solutes
ρ_{fluid} = density of brine sample
M_{H2O} = mass of water in sample
GFW_{H2O} = gram formula weight of water
n_{H2O} = moles of water in sample

3) Calculate the Mole Fraction of Gas i Dissolved in Sample

$$X_i = n_i/(n_i + n_{H2O})$$

where:

X_i = mole fraction of gas i dissolved in brine sample

Cygan (1991) does not provide data over the specific parameter ranges for which the solubility data are required. Theoretical gas saturations were, therefore, extrapolated from the graphs presented in Cygan (1991) and compared to those calculated for MB140 brine. Cygan (1991) presents gas saturation as a function of temperature, pressure, and normal NaCl units for N_2, CH_4, and CO_2. The conditions assumed for MB140 gas data were P = 9 MPa, T = 303.15 °K, and NaCl normality was set to a range between the average NaCl normality of samples, 4.3 N, and the average ionic strength of the samples, 7.5 N. The range of normality was used because Cygan (1991) reports gas-solubility data only for NaCl brine, not for multiple-solute brines. The extrapolated solubilities for N_2, CH_4, and CO_2 are reported in Table 9-4.

Comparison of the calculated saturation values in Table 9-3 with those extrapolated from Cygan (1991) in Table 9-4, and assuming some uncertainty in the values, indicates that both N_2 and CH_4 were approaching saturation in the MB140 brine. On the other hand, CO_2 appears to be far below saturation and significant amounts of CO_2 would be required to bring the MB140 brine to saturated conditions. Although this analysis is somewhat crude, it does provide some information on the state of saturation of primary gases collected from MB140.

Table 9-4. Gas-Solubility Data Extrapolated from Cygan (1991)

Gas	P (MPa)	T (°K)	NaCl (N)	Solubility (X_{gas})	Figure in Cygan (1991)
N_2	9.0	303.15	4.3	5E-4	25
			7.5	2E-4	
CH_4	9.0	303.15	4.3	7E-4	27
			7.5	2E-4	
CO_2	9.0	303.15	4.3	3E-3	35
			7.5	NA	

9.3.1.3 Possible Origins of the MB140 Gases

The gases present in MB140 could originate from several sources and/or processes such as atmospheric gas trapped at the time of deposition and isolated by subsequent burial, gas generated *in situ* from diagenetic reactions or microbial degradation of organic matter, gas generated as a daughter product in the decay chain of a naturally occurring radionuclide, or gas that has migrated from a deeper source reservoir. All of these processes could have been active to some degree in MB140.

Because the composition of the gas is dominated by nitrogen and methane, higher molecular weight hydrocarbons are present, and hydrogen sulfide appeared in three samples, the redox conditions of MB140 are most probably reducing. Therefore, a case can be made that N_2, CH_4, and the other reduced gases formed *in situ* from the degradation of organic matter. Gas migration from a deeper source reservoir is highly unlikely given the low permeability of the Salado and the observation that brines with unique chemical signatures coexist within a few vertical meters of one another in the Salado (Krumhansl et al., 1991).

Nitrogen is a common gas in the Salado Formation at the repository horizon, and is referred to as the WIPP "mine gas". Zartman et al. (1961) cite several possible sources of nitrogen in natural gas deposits: 1) Incorporation of atmospheric N_2 at the time of deposition; 2) the release of nitrogen by bacterial-mediated denitrification of organic-derived nitrate ion and organic matter; 3) the release of N_2 by inorganic breakdown of organic compounds; and 4) the liberation of N_2 from igneous and metamorphic rocks.

Figure 9-3 shows that N_2 concentrations in the samples were less than atmospheric concentrations, but not sufficiently less to dismiss atmospheric nitrogen as the potential source. Zartman et al. (1961) used the ratio of N_2:Ar_{air} (Ar_{air} = Ar concentration in modern air, 0.93%) as a means of determining if the N_2 in natural gas samples originated from incorporation of atmospheric N_2 or from other sources. They concluded that if the $N_2/Ar_{air} >> 84$, the value in modern air, then the N_2 was from a source other than the atmosphere. The N_2:Ar_{air} ratio in the MB140 samples ranges from 35 to 78, which suggests that an atmospheric source for the N_2 is possible. This analysis is somewhat suspect because Ar was used to purge the sample cylinders and could be a source of contamination.

Examination of Figure 9-5 reveals that the concentrations of CO_2 measured in the samples lie closely about the atmospheric concentration. Therefore, the CO_2 in the MB140

brine may have originated as trapped atmospheric carbon dioxide.

Figures 9-8, 9-9, and 9-10 show the concentrations of Ar, Ne, and He in the brine samples. Caution should be exercised in the interpretation of the Ar abundance because the sample cylinders were purged with Ar prior to sampling. However, several volumes of brine were run through the sample cylinders prior to sample collection. Both Ne and He are enriched in the samples relative to atmospheric concentrations. The average Ne concentration in the samples was 0.011 mole%. Helium is enriched by a factor of 250 in the samples compared to the atmospheric abundance. A likely source for the excess He is radioactive decay of naturally occurring ^{238}U, ^{235}U, and ^{232}Th in which ^{4}He is a daughter product (Faure, 1986). Matthess (1982) states that Ar and He concentrate in deep, confined groundwater systems with low flow rates as daughter products of radioactive decay, Ar from the decay of ^{40}K, and He from the decay of ^{238}U, ^{235}U, and ^{232}Th. This model of helium accumulation has been used to explain natural gas deposits with He contents as high as 10% (Zartman et al., 1961). This is the most plausible model to explain the accumulation of He in the MB140 brine. The source of He and Ar in the brine could be better defined with isotope data.

9.3.2 Brine Chemistry

Results of the brine analyses are shown in Table 9-5. The brine-chemistry data were evaluated using three techniques: 1) The time-dependent evolution of the brine chemistry was evaluated by plotting element concentrations, element ratios, mineral-saturation indices, and normative salt assemblages as a function of time; 2) the state of mineral saturation was calculated using the computer program PHRQPITZ 1.10 (Plummer et al., 1988) to evaluate if the brine was in equilibrium with the host rock; and 3) normative mineral assemblages were calculated using SNORM (Bodine and Jones, 1986) to determine the origin(s) of the solutes contained in the brine.

Table 9-5. Brine Analytic Data

Sample	13105-1	13123-1	13152-1	13167-1	13176-1	13183-1	13281-1	13294-1	13302-1	13308-1	13320-1
B (mg/L)	1,700	1,720	1,720	1,670	1,660	1,640	1,680	1,630	1,660	1,640	1,660
Br (mg/L)	1,320	1,320	1,320	1,310	1,310	1,310	1,310	1,310	1,310	1,300	1,310
Ca (mg/L)	203	196	193	229	236	232	232	229	231	232	233
Cl (mg/L)	182,000	186,000	183,000	181,000	180,000	180,000	179,000	180,000	181,000	180,000	180,000
F (mg/L)	4.2	3.8	3.6	3.8	3.9	3.8	3.9	4.1	3.7	3.8	3.9
Fe (mg/L)	1.06	3.37	<0.50	1.90	0.74	<0.50	1.26	1.23	2.23	1.44	0.87
K (mg/L)	12,600	12,600	12,600	12,400	12,500	12,400	12,400	12,400	12,400	12,200	12,400
Mg (mg/L)	14,500	14,400	14,300	14,700	14,400	14,800	15,000	14,700	14,700	14,700	14700
Na (mg/L)	98,000	98,000	98,000	101,000	98,000	101,000	101,000	101,000	100,000	101,000	100,000
SO_4 (mg/L)	27,600	27,700	27,500	27,200	27,100	27,200	27,200	27,200	27,200	27,100	27,200
Sr (mg/L)	1.18	1.01	0.98	1.01	1.02	1.03	1.01	1.01	1.02	1.03	1.03
pH	6.08	6.17	6.16	6.2	6.1	6.2	6.1	6.1	6.2	6.2	6.1
SG[1]	1.24	1.23	1.23	1.22	1.22	1.23	1.22	1.21	1.22	1.22	1.22
TDS[2] (mg/L)	350,600	357,200	356,200	354,200	356,000	359,600	357,200	356,200	356,800	355,600	357,400
TIC[3] (mg/L)	18.2	21.1	22.4	1.2	2.3	0.7	1	1.5	1.4	1.4	2.1

[1] Specific gravity
[2] Total dissolved solids
[3] Total inorganic carbon

9.3.2.1 Temporal Evolution

We assumed that prior to drilling through MB140, chemical equilibrium existed between the liquid and solid phases in terms of dissolution/precipitation and adsorption/desorption reactions. After drilling, disequilibrium was introduced in the form of drilling fluid of a different chemistry and exposure of MB140 to atmospheric gases and pressure conditions. We expected that if the pre-drilling conditions were restored in the borehole by pressurization by a packer system and removal of foreign fluid by a flow test, then the chemistry would return to the pre-drilling steady-state condition. Figures 9-11 to 9-19 show the major anion and cation concentrations (or ratios) plotted as a function of sample date. The error bars represent two times the population standard deviation for any given ion, which is probably a conservative estimate.

Chloride and Bromide: Chloride and bromide concentrations are good indicators of changes in the brine chemistry as a function of time because of their conservative geochemical and hydrologic behavior. Because the borehole was drilled with a pure NaCl concentration solution, contamination by drilling fluid would be indicated by an initial high Cl concentration that gradually decreased over time. The late-time samples from MB140 have Cl concentrations on the order of 4 mol/kg (180,000 mg/L) while water equilibrated with halite has a Cl concentration of 4.7 mol/kg (204,000 mg/L). The opposite trend would be expected for Br, where initially Br concentration would be low and increase with time. Figures 9-11 and 9-12 show Cl and Br concentrations as functions of time, respectively. Figure 9-11 shows no obvious trend of decreasing Cl concentration with time. The second through fifth Cl measurements could suggest a decreasing trend, although this apparent trend results in large part from the relatively high second measurement (186,000 mg/L), which we *consider* anomalous and discount from interpretation. The Br concentration was stable throughout the sampling period (Figure 9-12), further indicating that the chemical composition of the brine was constant and not contaminated by the drilling fluid. Figure 9-13 is a plot of the weight ratio of Cl to Br versus sampling date. If the formation fluid had been contaminated with a NaCl solution, then the Cl/Br ratio should exaggerate the Cl trend. This is clearly not the case, because Figure 9-13 shows that the Cl/Br ratio remained relatively constant between 137 and 141, further evidence that the samples were representative of formation fluids. The geochemical implications of the Cl/Br ratio will be discussed in a later section.

Sodium and Potassium: Sodium and potassium concentrations are plotted in Figures 9-14 and 9-15, respectively. Similar to the chloride concentration, the sodium concentration would decrease over time if the formation fluid were contaminated by the NaCl drilling fluid. Figure 9-14 shows that the Na concentration was constant during the sampling period within the uncertainty of the measurements. The same can be said for the potassium concentration — it would follow the same expected trend as Br had the formation been contaminated with NaCl drilling fluid. However, Figure 9-15 shows that the potassium concentration remained constant throughout the sampling period.

Calcium, Magnesium, Sulfate, and Total Inorganic Carbon: Plots of Ca, Mg, SO_4, and total inorganic carbon (TIC) concentration versus sampling date are presented in Figures 9-16 through 9-19, respectively. Based on the reasoning used thus far, the concentrations of these ions were constant, i.e., within the measurement uncertainty, during the

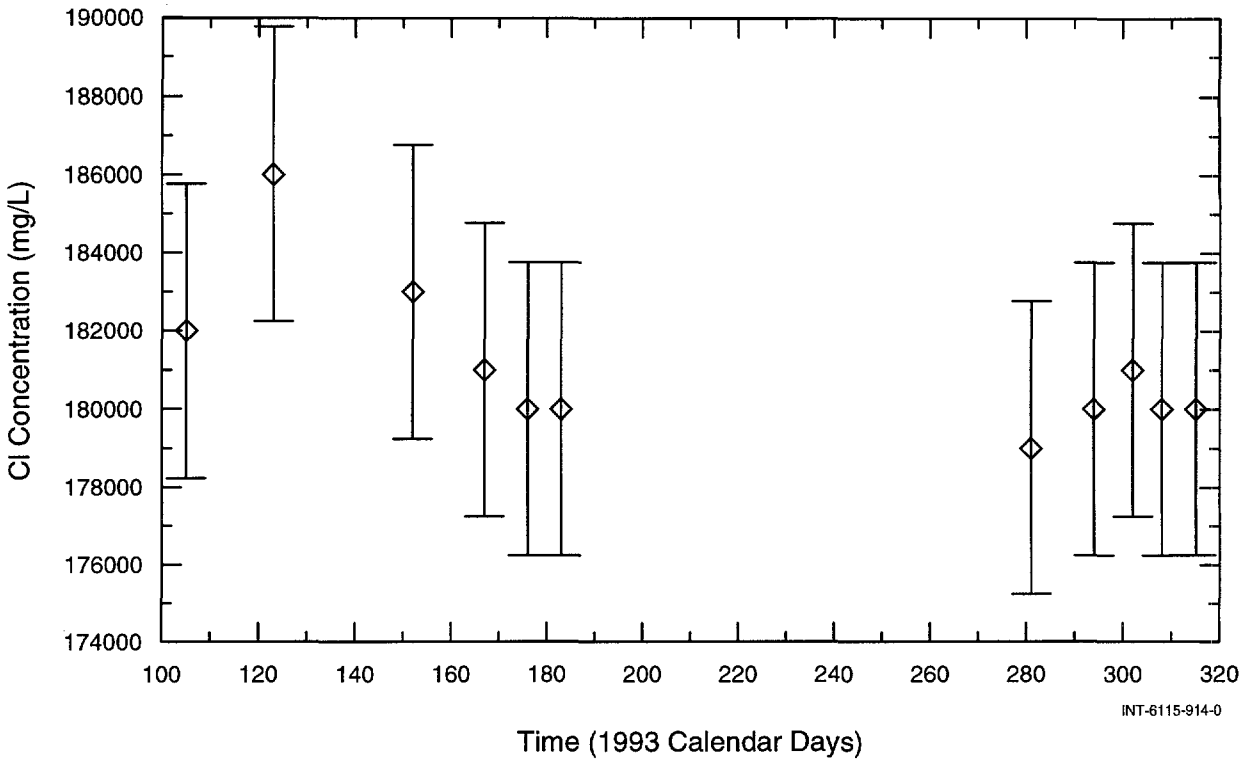

Figure 9-11. Cl concentration versus sample date.

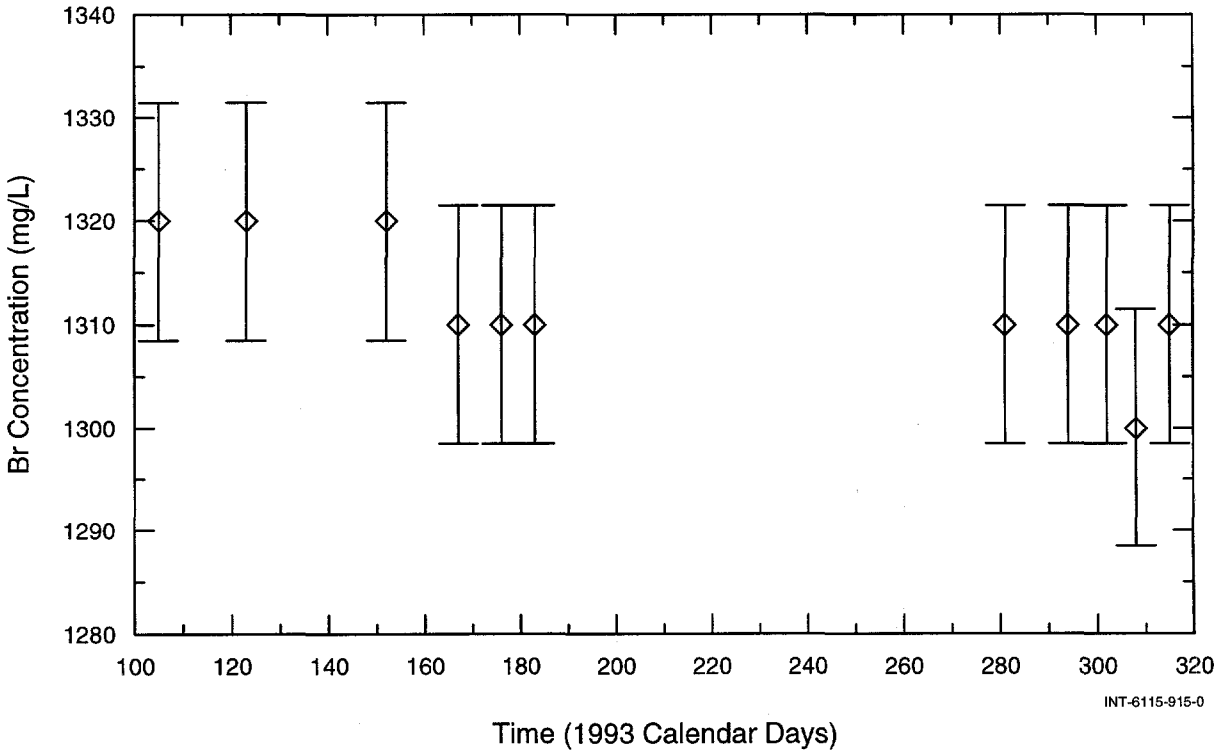

Figure 9-12. Br concentration versus sample date.

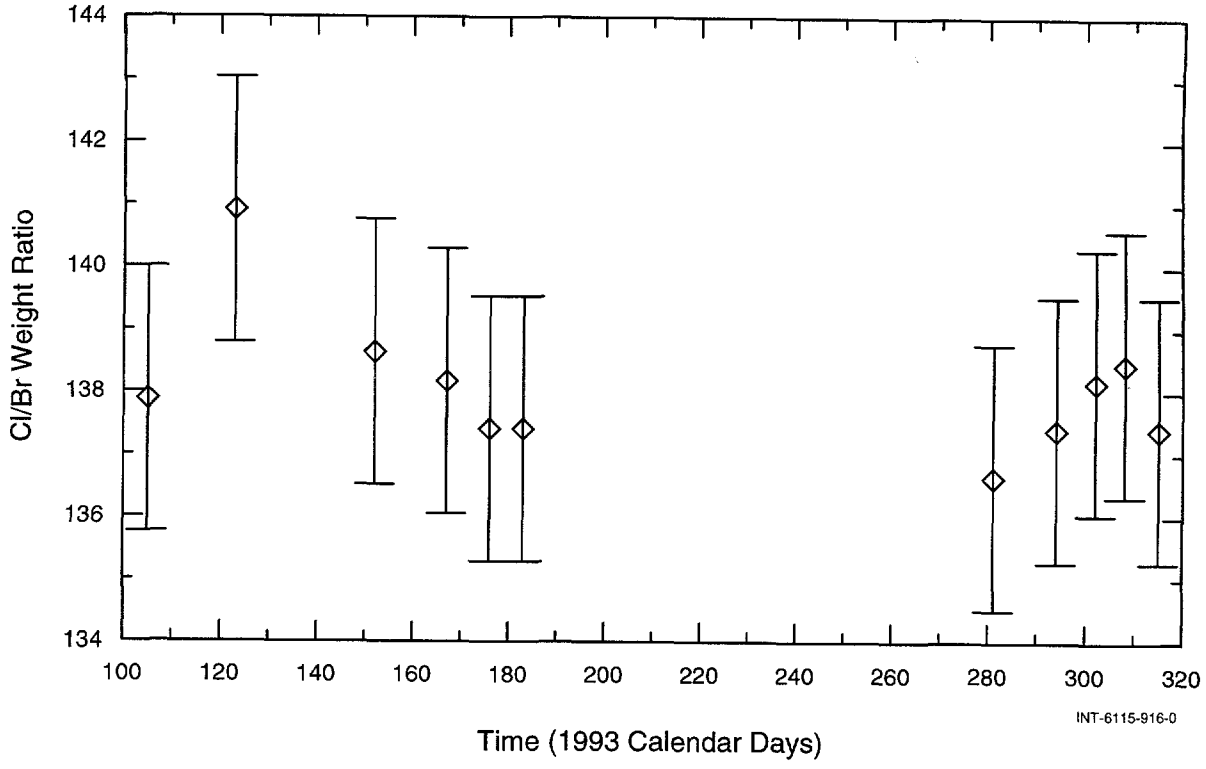

Figure 9-13. Cl/Br weight ratio versus sample date.

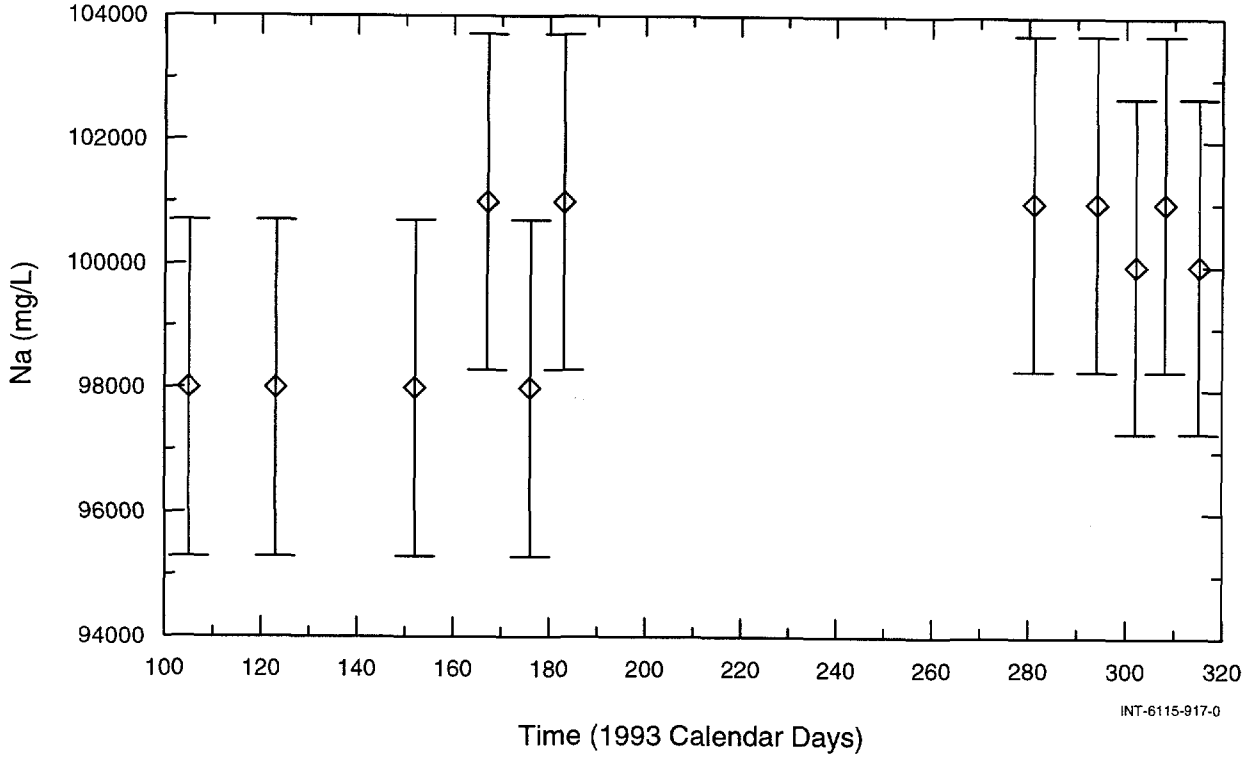

Figure 9-14. Na concentration versus sample date.

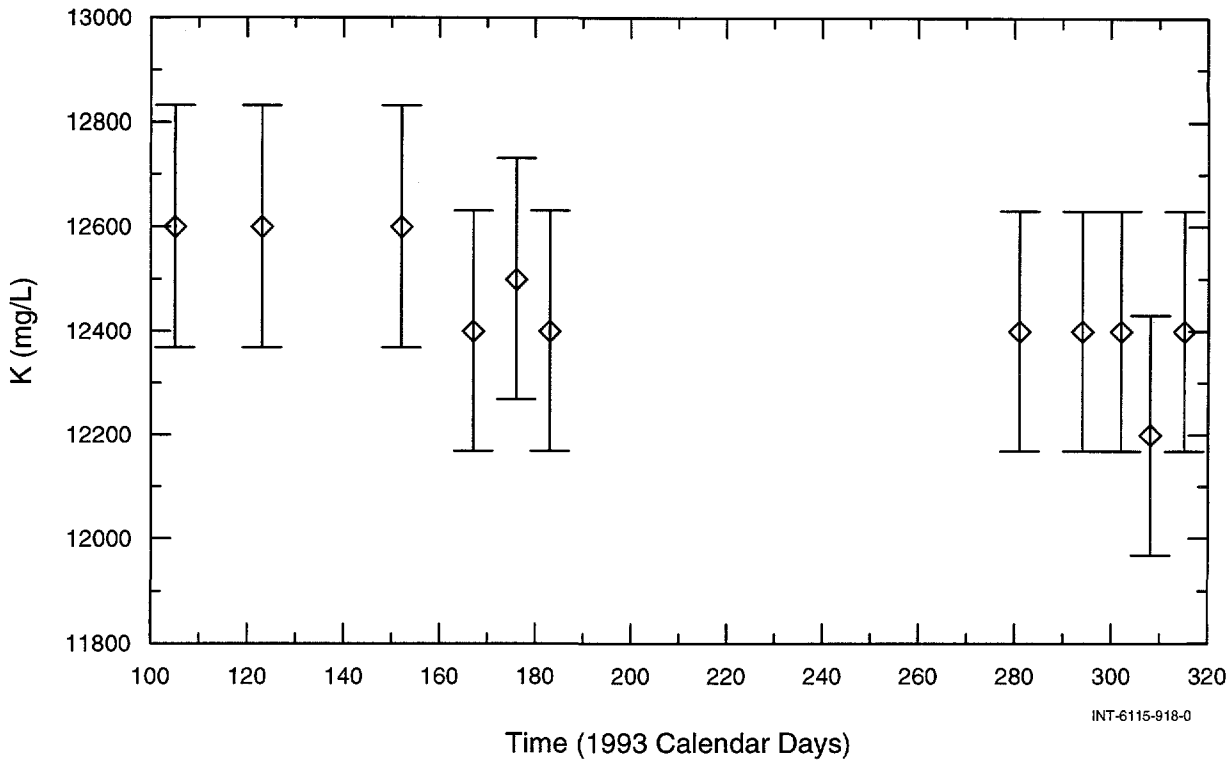

Figure 9-15. K concentration versus sample date.

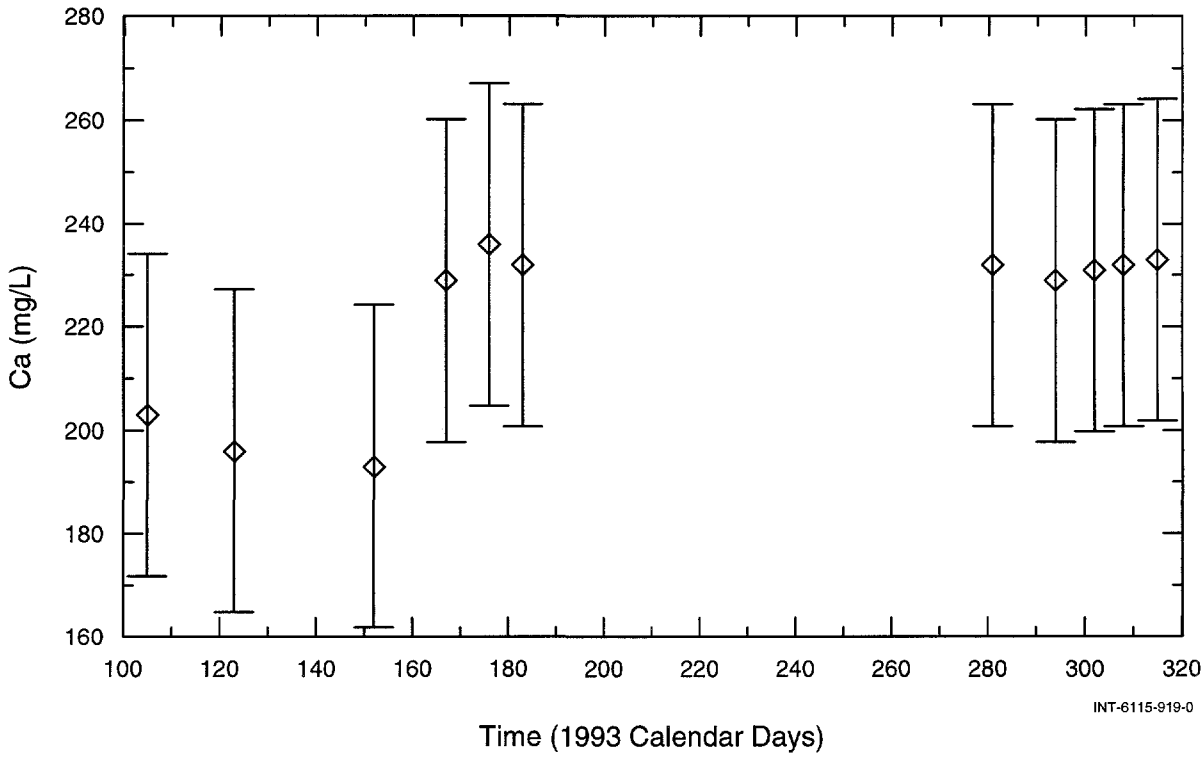

Figure 9-16. Ca concentration versus sample date.

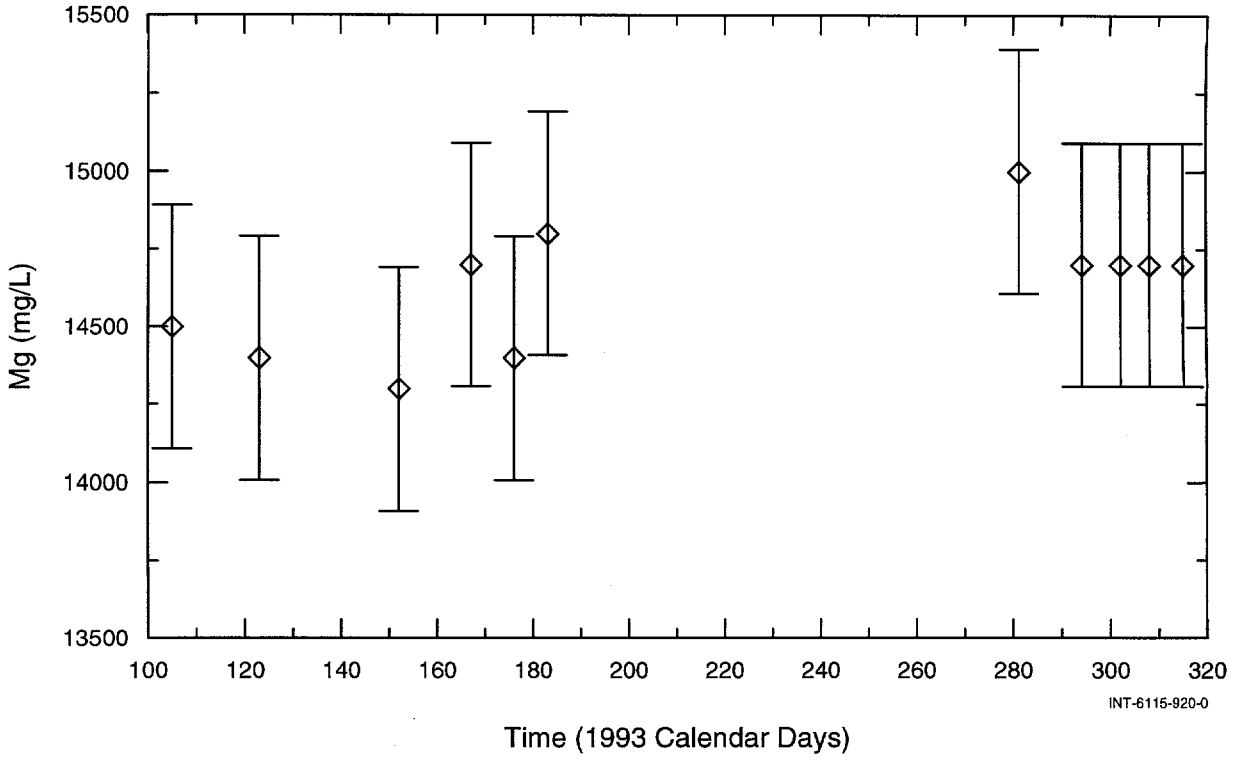

Figure 9-17. Mg concentration versus sample date.

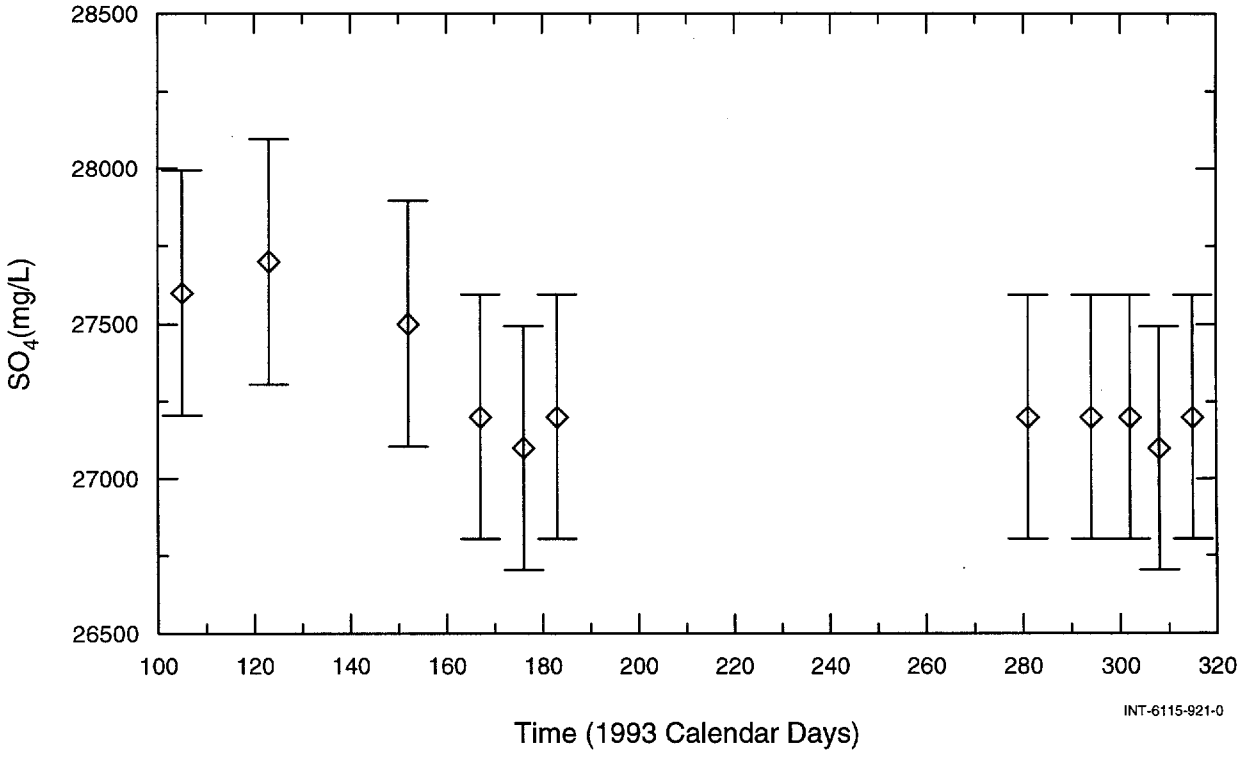

Figure 9-18. SO_4 concentration versus sample date.

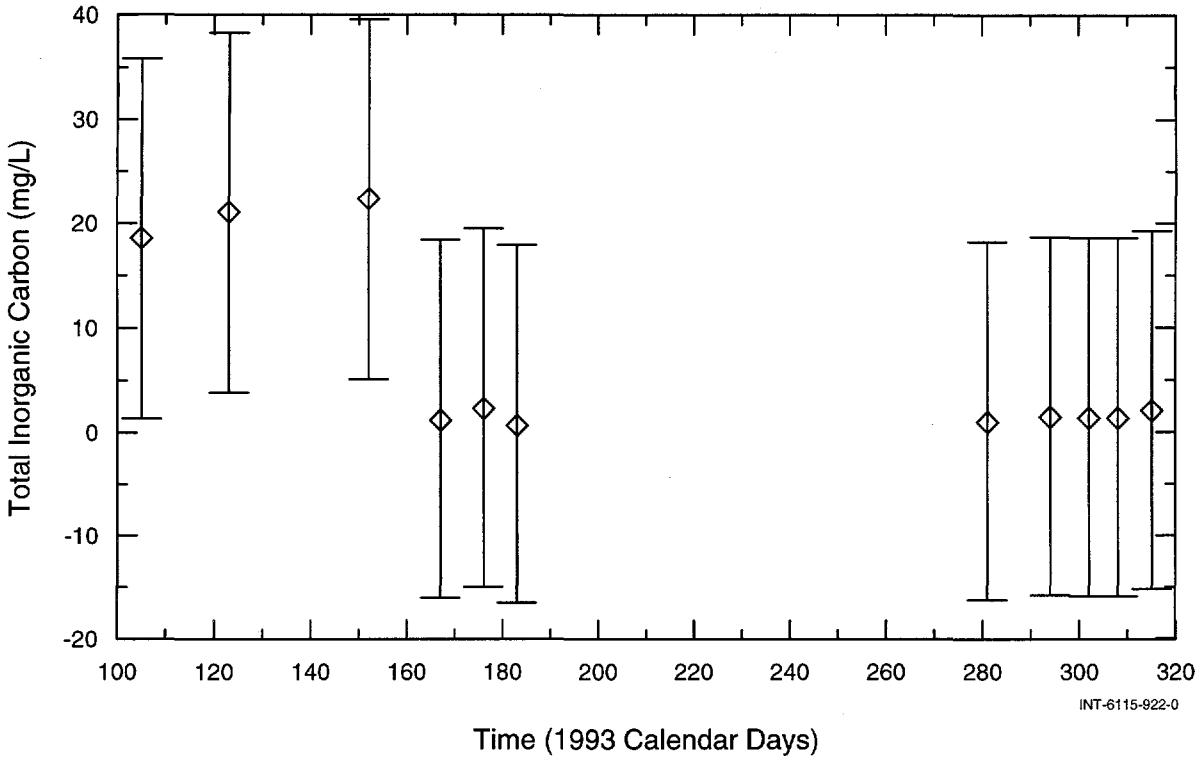

Figure 9-19. Total inorganic carbon concentration versus sample date.

sampling campaign. However, detailed inspection of these plots reveals a systematic concentration variation for the first three sample dates. The observed concentration variations of Ca, Mg, and SO_4 (and to a lesser degree Br, Na, and K) are correlated with the concentration of TIC. The cause of the increased carbon concentration in the first three samples is not readily apparent. A natural localized heterogeneity in the chemistry of the sampled brine could have existed, which is possible but unlikely given the low flow rates expected in MB140. Carbon may also have been introduced in the form of CO_2 gas through contact of the sample with the atmosphere after dissolved gas was removed for analysis. Because we have no way to determine what caused the disequilibrium in the carbonate system, we will not discuss it further.

9.3.2.2 Mineral Saturation State of MB140 Brine

The mineral saturation states of the samples were evaluated using the computer program PHRQPITZ 1.10 (Plummer et al., 1988). PHRQPITZ uses the Pitzer virial-coefficient approach for activity-coefficient corrections for high ionic strength solutions. Input consisted of the elemental concentrations in mg/L, the solution density (g/cm^3), and solution pH. Output consisted of an echo of the input data and a listing of the solution properties: activity of water, solution speciation, activity coefficients, and mineral saturation information. PHRQPITZ also has the capacity to solve complex hypothetical calculations such as mixing, evaporation-dilution, solubility, reaction paths, and temperature dependency.

The equilibrium state of an ionic solid in contact with aqueous solution can be characterized by its saturation index. The saturation index is defined by the following mass-action expression using calcite solubility as an example:

$$CaCO_3 \Leftrightarrow Ca^{2+} + CO_3^{2-}$$

At equilibrium, the solubility product may be defined:

$$K_{sp} = a_{Ca2+}\, a_{CO3\,2-} \quad (a = \text{activity})$$

The ion activity product (IAP) is a measure of disequilibrium and is defined the same as the solubility product.

$$IAP = a_{Ca2+}\, a_{CO3\,2-}$$

$$K_{sp} \neq IAP$$

The $\log_{10}$ of the ratio of the IAP to K_{sp} is termed the saturation index (SI).

$$SI = \log_{10}(IAP/K_{sp})$$

Thus, at equilibrium IAP is equal to K_{sp} and SI = 0. If IAP < K_{sp}, then SI is < 0 and the solution is undersaturated. Likewise, if IAP > K_{sp}, then SI is > 0 and the solution is supersaturated. However, given that K_{sp} values are determined experimentally and errors are associated with all chemical analyses, a range of SI must be used when assigning saturation states. Saturation will be considered to exist within the range -0.25 < SI < 0.25. Therefore, undersaturation SI < -0.25 and supersaturation SI > 0.25. Table 9-6 is the PHRQPITZ 1.10 output of saturation indices for selected minerals.

Figure 9-20 shows the saturation indices of the three most saturated phases, halite, anhydrite, and glauberite, as plotted against sampling date. The saturation indices of calcite, dolomite, magnesite, and pCO_2 are shown in Figure 9-21. With the exception of the first three samples, the saturation indices of the minerals shown in Figure 9-21 are stable throughout the sampling period. The constancy of the mineral saturation states is strong evidence that steady chemical conditions prevailed during the sampling period and that brine representative of MB140 had been sampled.

Table 9-6. Saturation Indices for Mineral Phases Calculated by PHRQPITZ 1.10

Sample	Anhydrite	Bischofite	Calcite	Carnallite	Celestite	Dolomite	Glauberite	Halite	Kainite	Kieserite	Magnesite	Mirabilite	pCO_2	Sylvite
13105-1	-0.17	-3.50	-1.22	-3.36	-0.73	0.19	-0.21	-0.10	-2.34	-2.18	0.56	-0.96	-1.74	-0.88
13123-1	-0.13	-3.43	-1.02	-3.25	-0.75	0.61	-0.14	-0.05	-2.26	-2.12	0.78	-0.97	-1.76	-0.85
13152-1	-0.16	-3.47	-1.03	-3.31	-0.79	0.57	-0.19	-0.07	-2.30	-2.16	0.76	-0.97	-1.72	-0.86
13167-1	-0.09	-3.45	-2.18	-3.27	-0.78	-1.78	-0.06	-0.04	-2.29	-2.15	-0.44	-0.95	-3.04	-0.85
13176-1	-0.09	-3.48	-2.00	-3.32	-0.79	-1.45	-0.11	-0.07	-2.31	-2.17	-0.29	-0.96	-2.65	-0.86
13183-1	-0.11	-3.49	-2.44	-3.33	-0.80	-2.30	-0.11	-0.06	-2.33	-2.17	-0.71	-0.95	-3.27	-0.87
13281-1	-0.09	-3.46	-2.37	-3.29	-0.80	-2.16	-0.08	-0.04	-2.30	-2.15	-0.63	-0.95	-3.03	-0.85
13294-1	-0.07	-3.43	-2.17	-3.25	-0.77	-1.76	-0.03	-0.02	-2.26	-2.13	-0.43	-0.95	-2.85	-0.84
13302-1	-0.08	-3.45	-2.11	-3.28	-0.78	-1.64	-0.07	-0.04	-2.29	-2.15	-0.38	-0.96	-2.97	-0.85
13308-1	-0.09	-3.46	-2.11	-3.30	-0.78	-1.66	-0.07	-0.04	-2.31	-2.16	-0.39	-0.95	-2.97	-0.86
13320-1	-0.09	-3.46	-2.04	-3.29	-0.78	-1.51	-0.08	-0.05	-2.30	-2.15	-0.31	-0.96	-2.70	-0.86

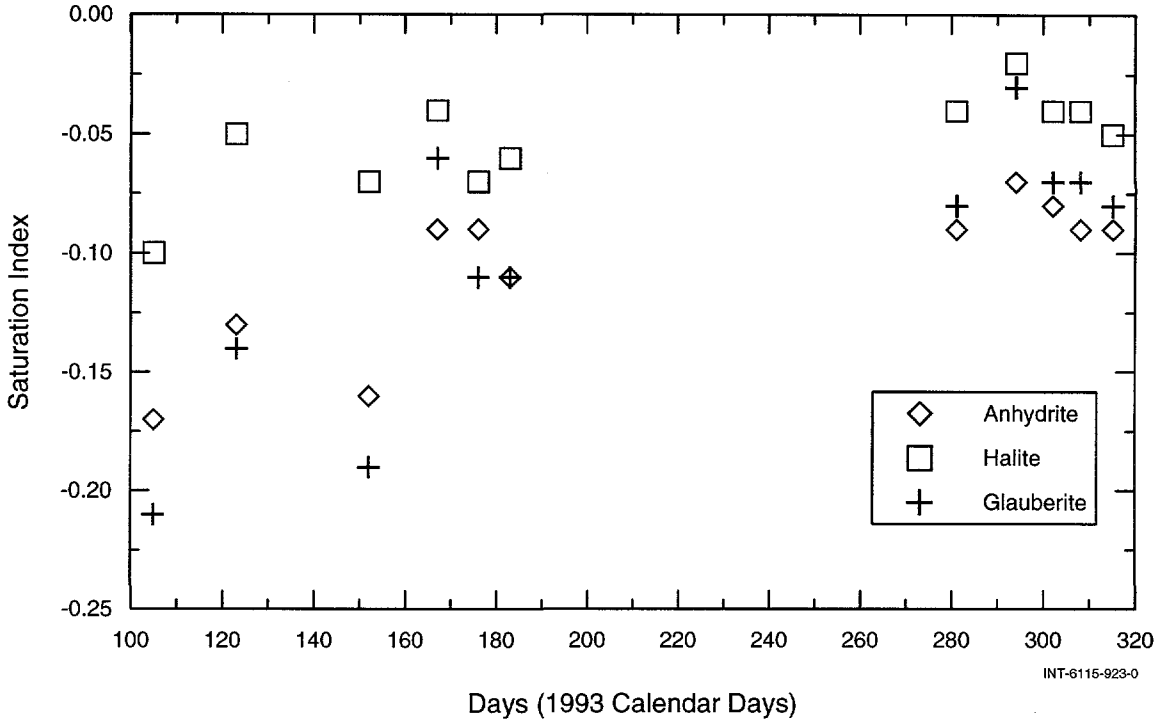

Figure 9-20. Saturation indices of anhydrite, halite, and glauberite calculated with PHRQPITZ versus sample date.

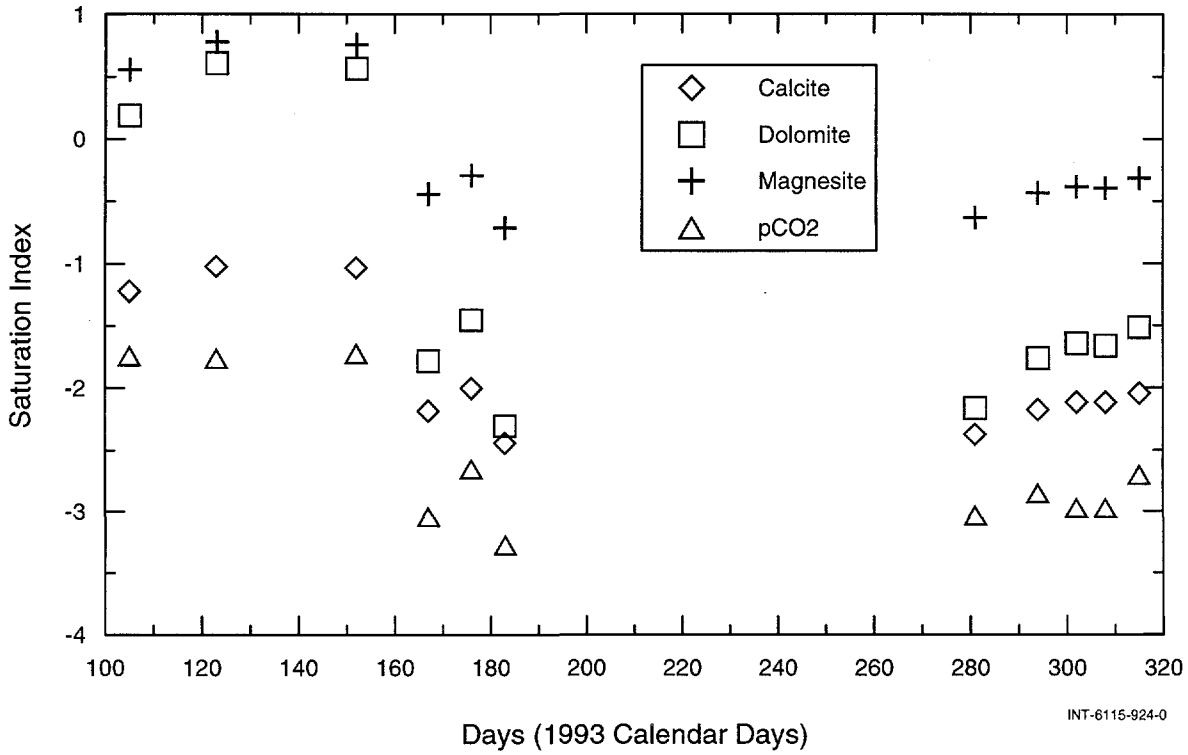

Figure 9-21. Saturation indices of calcite, dolomite, magnesite, and pCO_2 calculated with PHRQPITZ versus sample date.

9.3.2.3 MB140 Brine Salt Norm

As a means of characterizing the composition and evaluating the origins of the solutes in the MB140 brines, the salt norm approach of Bodine and Jones (1986) was used. As described in Bodine and Jones (1986): "The salt norm is the quantitative ideal equilibrium assemblage that would crystallize if the water evaporated to dryness at 25 °C and 1 bar pressure under atmospheric partial pressure of CO_2."

The salt norm is calculated with the computer code SNORM. SNORM distributes 18 solutes into normative salts from 63 possible normative salts based on three criteria: 1) the Gibb's phase rule; 2) free energy values; and 3) observed low-temperature mineral associations. The reader is referred to Bodine and Jones (1986) for a detailed discussion of the theory behind the calculation of the normative salt assemblage. Unlike geochemical codes that model the evaporation of a solution by following reaction paths, SNORM evaporates a solution in a single step with no back reactions. Thus, the resulting mineral assemblage from a SNORM run would differ from that calculated using a code such as PHRQPITZ for the same starting solution.

Characterization and interpretation of the salt norm of a water analysis is based primarily on the major cation - major anion salts in the norm and less so on salts of the minor ions. The reasons for this are that the major ions are better indicators of the important mineral reactions that took place during the evolution of the water and the major ions are less subject to analytical errors than trace constituents.

Based on the normative salt associations, three major solute sources may be identified: 1) meteoric or weathering; 2) marine-derived; and 3) diagenetic. Diagnostic minerals and their relative abundances in the normative mineral assemblage are indicative of the solute source and/or reaction process within each of the three groups.

A useful analogy to conceptualize how the normative salt assemblage differs from the equilibrium mineral assemblage (i.e., that calculated from PHRQPITZ) is that of the crystallization of two magmas of different compositions. For example, think of two magmas, one of granitic composition and the other of basaltic composition both of which intrude the earth's crust at similar depths and times. If we sample the liquid portion from both types of magma at any point in time and quench the sample, i.e., drop its temperature so as to crystallize it in a single step without allowing equilibrium conditions to develop between solid phases and the remaining liquid, we would not expect to have the same mineral assemblage from both. The mineral assemblages would represent a snapshot of the chemistry and processes that the magma had undergone up until the point in time that the sample was removed. They do not necessarily represent the phases with which the magmas were in equilibrium prior to sampling, but are indicative of the composition and processes the magmas went through up until the time the samples were taken.

A parallel line of reasoning can be applied to the use of the salt norm for the interpretation of groundwater samples. For the Salado brines, the salt norm from a particular layer will reflect the chemical environment and processes that have been active up until the time the sample was taken. At the time of deposition of the Salado Formation, the Delaware Basin was receiving solute input from continental meteoric-driven flood events and marine eustatic sea level changes (Holt and Powers, 1990). Both of these sources

have associated with them diagnostic normative mineral phases which, when present in a norm, point to the source of the solutes. Therefore, we may be able to distinguish which brines were derived from either marine or continental sources.

Input for the SNORM runs consisted of sample identifiers, major ion concentrations (Ca, Mg, Na, K, Cl, and SO_4), minor ion concentrations (CO_3, HCO_3, Br, B, Sr, and F), solution pH, and solution density. Output from the SNORM runs consists of a file listing the input, various ionic ratios, normative salt assemblage, and simple salt assemblage. Only the normative salt assemblage will be discussed here because of its diagnostic strength.

Table 9-7 lists the anhydrous weight percent of the normative minerals calculated for the MB140 brine samples. Figure 9-22 is a column bar chart of the normative mineral assemblage for each of the samples. Inspection of Table 9-7 and Figure 9-22 reveals that the normative salt assemblages and percents for the MB140 samples were constant through time. The disequilibrium in the carbonate system for the first three samples is reflected in the salt norm by the higher percentage relative to the later samples of normative magnesite ($MgCO_3$), the only carbonate phase in this normative assemblage.

The diagnostic normative minerals present in the MB140 salt norm are halite, carnallite ($KMgCl_3 \cdot 6H_2O$), kieserite ($MgSO_4 \cdot H_2O$), kainite ($KMg(SO_4)Cl \cdot 3H_2O$), polyhalite ($K_2Ca_2Mg(SO_4)_4 \cdot 2H_2O$), and magnesite. This mineral assemblage is indicative of a marine-source water that has undergone evaporative concentration in a hypersaline environment and mixed with a solution derived from weathering of sulfatic evaporite rocks. The absence of anhydrite in the MB140 norm (~4% in seawater norm) indicates that it has been fractionally removed from solution (Bodine and Jones, 1986). As a result of anhydrite removal from solution, potassium and magnesium become enriched in the residual solution and are expressed in the salt norm as excess carnallite, ~13% in the MB140 norm in contrast to ~5% in the seawater norm (Bodine and Jones, 1986) Evidence in the normative mineral assemblage for mixing of a hypersaline liquor with a sulfatic weathering solution is expressed by the presence of the diagnostic mineral kainite, the presence of polyhalite, and excess kieserite, ~8%. compared to ~5% in seawater (Bodine and Jones, 1986). The presence of these three phases in the MB140 salt norm is consistent with

Table 9-7. Normative Mineral Assemblages (Anhydrous Weight Percent) for MB140 Samples

Sample	Halite	Carnallite	Kieserite	Kainite	Indirite	Polyhalite	Magnesite	Sellaite	Celestite
13105-1	73.24	13.28	7.91	2.92	2.21	0.42	1.6E-2	2.0E-3	7.3E-4
13123-1	73.36	13.36	7.79	2.88	2.19	0.41	1.9E-2	1.8E-3	6.2E-4
13152-1	73.39	12.92	7.62	3.40	2.24	0.40	2.1E-2	1.7E-3	6.1E-4
13167-1	73.69	13.18	8.19	2.29	2.19	0.46	1.1E-3	1.8E-3	6.1E-4
13176-1	73.36	13.28	7.92	2.77	2.19	0.49	2.1E-3	1.9E-3	6.3E-4
13183-1	73.60	13.25	8.34	2.18	2.17	0.47	6.6E-4	1.8E-3	6.2E-4
13281-1	73.40	13.43	8.54	1.93	2.23	0.47	9.3E-4	1.9E-3	6.0E-4
13294-1	73.69	13.09	8.22	2.39	2.15	0.46	1.4E-3	2.0E-3	6.1E-4
13302-1	73.51	13.36	8.27	2.21	2.18	0.47	1.3E-3	1.8E-3	6.2E-4
13308-1	73.77	13.16	8.39	2.04	2.17	0.47	1.3E-3	1.8E-3	6.2E-4
13320-1	73.50	13.27	8.26	2.30	2.19	0.48	2.0E-3	1.9E-3	0.0

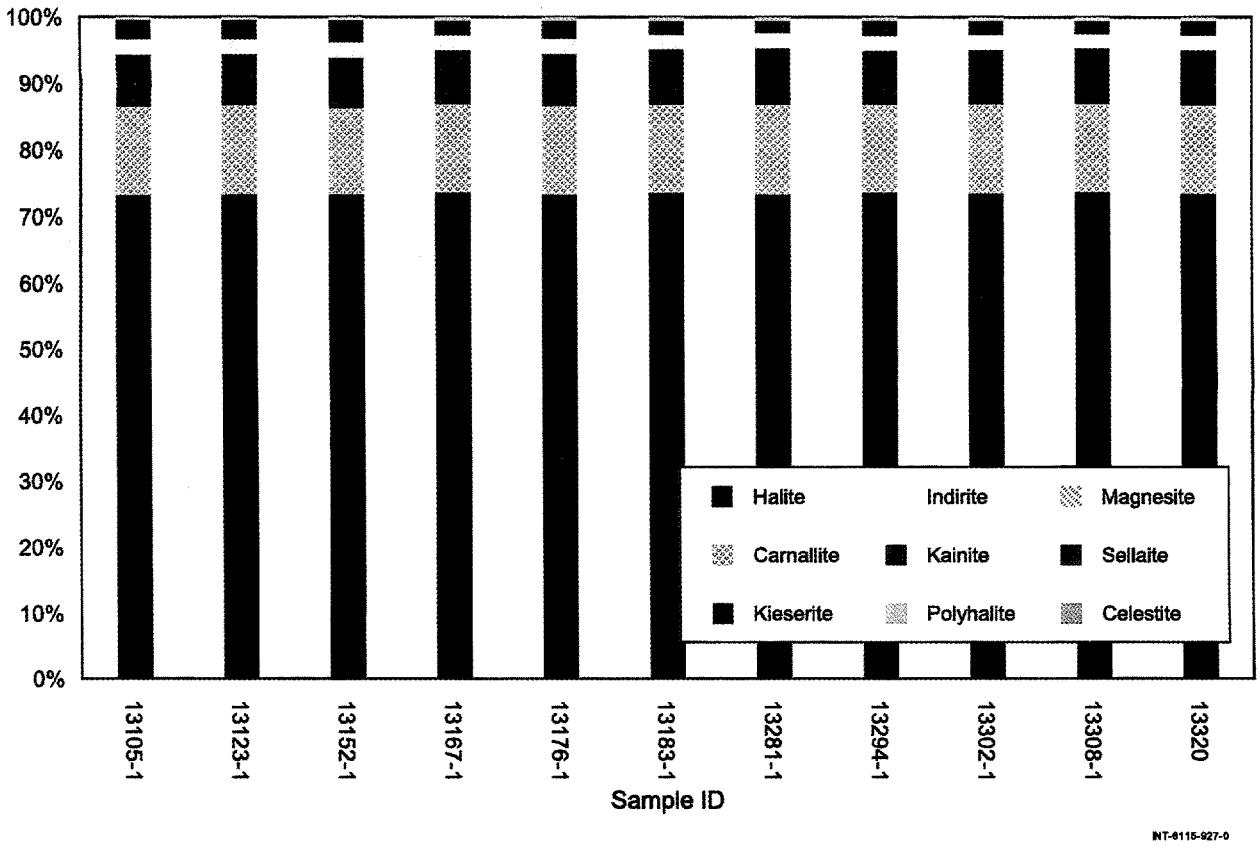

Figure 9-22. Normative mineral assemblages for Marker Bed 140 brine.

the addition of excess sulfate to a hypersaline brine while maintaining the proportions of K, Na, and Mg. Jones and Anderholm (1996) reached similar conclusions regarding a continental source for a portion of the solute budget in the brine of MB140.

Based on its geology and normative salt assemblage, a conceptual model for the deposition of MB140 may be developed. Holt (1993) summarized the depositional environment for the Salado sulfate interbeds as a shallow saline lagoon environment periodically flooded by eustatic sea level changes or meteoric-driven basin-wide floods. Following flooding, evaporative concentration would precipitate a sequence of sulfates followed by halite before another flooding event inundated the basin. Based on the core logs of two boreholes in Room C1, C1H07 and C1X05, Holt described the depositional environment for MB140, which is summarized in Wawersik et al. (1997). Room C1 is approximately 670 m due east of Room L4. To summarize Holt's interpretation: Two separate flooding events were necessary to produce the observed MB140 lithologic sequence. The first flood event brought mud into the basin, deposited as a mudstone at the base of MB140. Subsequent evaporation deposited gypsum which is now the basal anhydrite of MB140. Halite saturation may or may not have been reached and halite deposited above the basal anhydrite. A second flood event carried additional mud into the basin, as shown by a 10-cm-thick mudstone included within MB140. Evaporation of the basinal brine deposited the remainder of MB140, which consisted of prismatic gypsum and detrital gypsum re-

worked by wave action. Halite saturation was reached and the overlying halite unit was deposited. During deposition of the overlying halite, gypsum was being replaced by anhydrite and halite as pseudomorphs.

Holt's interpretation of the MB140 geology is consistent with the interpretation based on the normative mineral assemblage as predicted by SNORM. Both interpretations require two separate flood events. Based on the normative mineral assemblage, one flood event must have been a transgression of the Permian sea, and the second a meteoric-driven continental flood event carrying an input of sulfatic weathering solution. The sulfatic weathering solution was probably derived from the erosion of backreef evaporite deposits. Thus, the brine currently found in MB140 was trapped during or shortly after deposition of the unit during the Permian and is not part of an active flow system involving meteoric recharge at the ground surface and discharge to some other surface location.

9.4 Comparison of MB140 Brine to Other WIPP Brines

The MB140 brine composition was compared to those of other WIPP brines (Stein and Krumhansl, 1986; Deal et al., 1989, 1991a, 1991b, 1993; Krumhansl et al., 1991) to evaluate similarities and differences. Figures 9-23 and 9-24 show Na/Cl versus Ca/SO_4 and Na/Cl versus K/Mg, respectively, for various WIPP brines including the MB140 brine analyses. Also shown are mixing lines calculated with PHRQPITZ 1.10 (Plummer et al., 1988) and an experimental evaporation line (Krumhansl et al., 1991).

These figures show that the chemistries of the brines from MB140 in L4P51, from boreholes G090 and H090, and from GSEEP are very similar. GSEEP is a location in Room G between boreholes G090 and H090 where brine has been observed to accumulate on the floor (Figure 5-1). Deal et al. (1991b) state that the brines from G090, H090, and GSEEP are probably native WIPP brines contaminated with water spread on the floor to control dust, and this dust-control brine is either "construction" brine, for which the composition is poorly defined, or water from the overlying Culebra dolomite that flowed into the underground facility through the AIS. If the GSEEP, G090, or H090 brines were mixtures of AIS and native Salado (e.g., Map Unit 0) brine, then they would plot near the mixing lines on Figures 9-23 and 9-24. In fact, both G090 and H090 were drilled through MB140, which is the likely source of the brine in those holes.

The source of the GSEEP brine has been the topic of much speculation (Deal et al., 1991b). Figure 9-25 is a column bar chart of the normative salt assemblages for brines from L4P51, G090, H090, and GSEEP. The similarity of their normative salt assemblages suggests a common origin for this group of brines. Figures 9-26, 9-27, and 9-28 are column bar charts of the normative salt assemblages for brines originating from MB139, Map Unit 0, and the AIS, respectively. The salt norms for MB139, Map Unit 0, and AIS brines are distinctive compared to the MB140 norm and distinctive compared to each other. If GSEEP brines were derived from a combination of two WIPP brines, then common mineralogic denominators should be present between the GSEEP and constituent brines. For example, because kainite occurs in the norm for GSEEP, it would also have to occur in the norm of at least one constituent brine. However, kainite is not present in the norms of any other brines.

Figure 9-29 shows the salt norms for mixtures of AIS brine and OH20 brine (dashed line on Figure 9-24). Notice that the OH20 chemistry

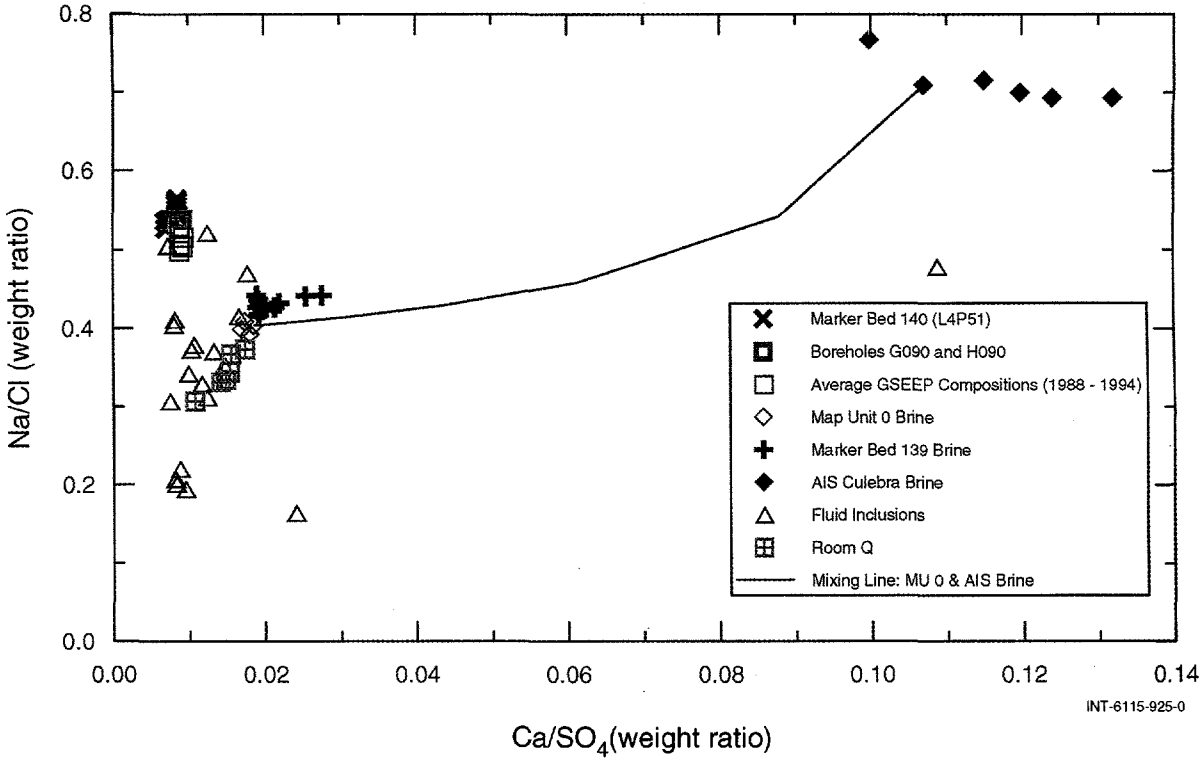

Figure 9-23. Na/Cl ratio versus Ca/SO_4 ratio.

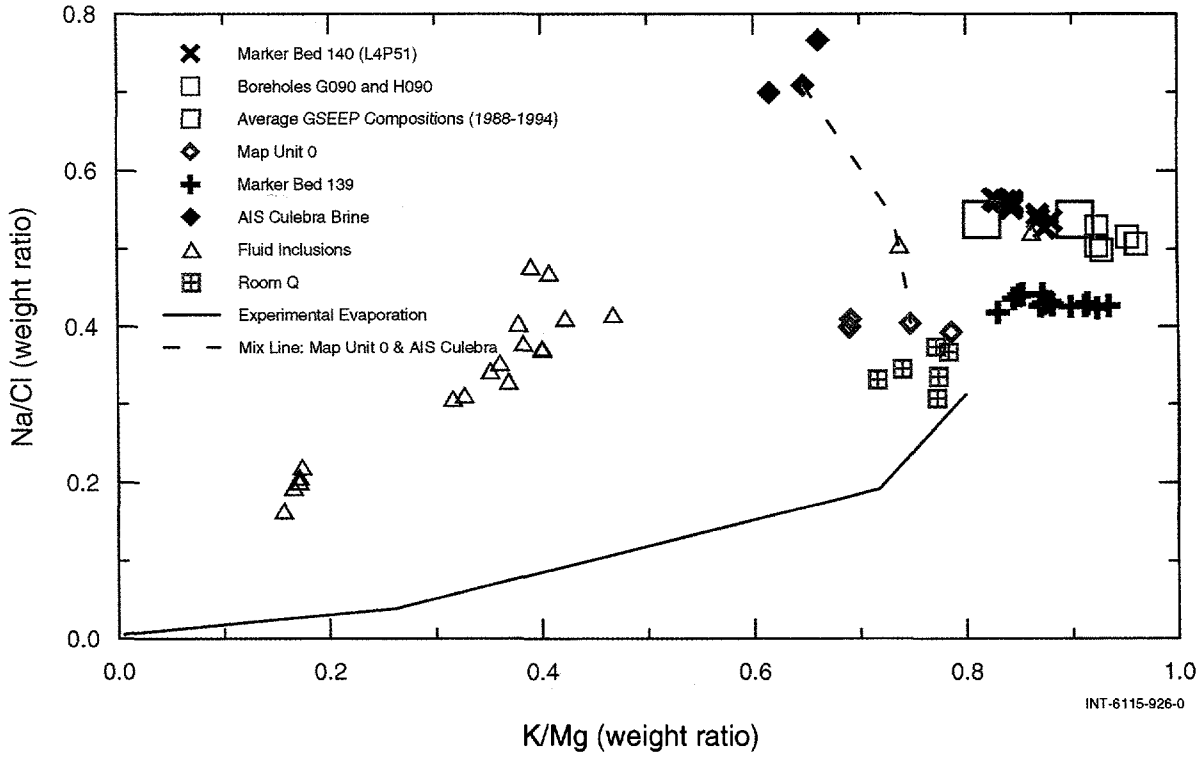

Figure 9-24. Na/Cl ratio versus K/Mg ratio.

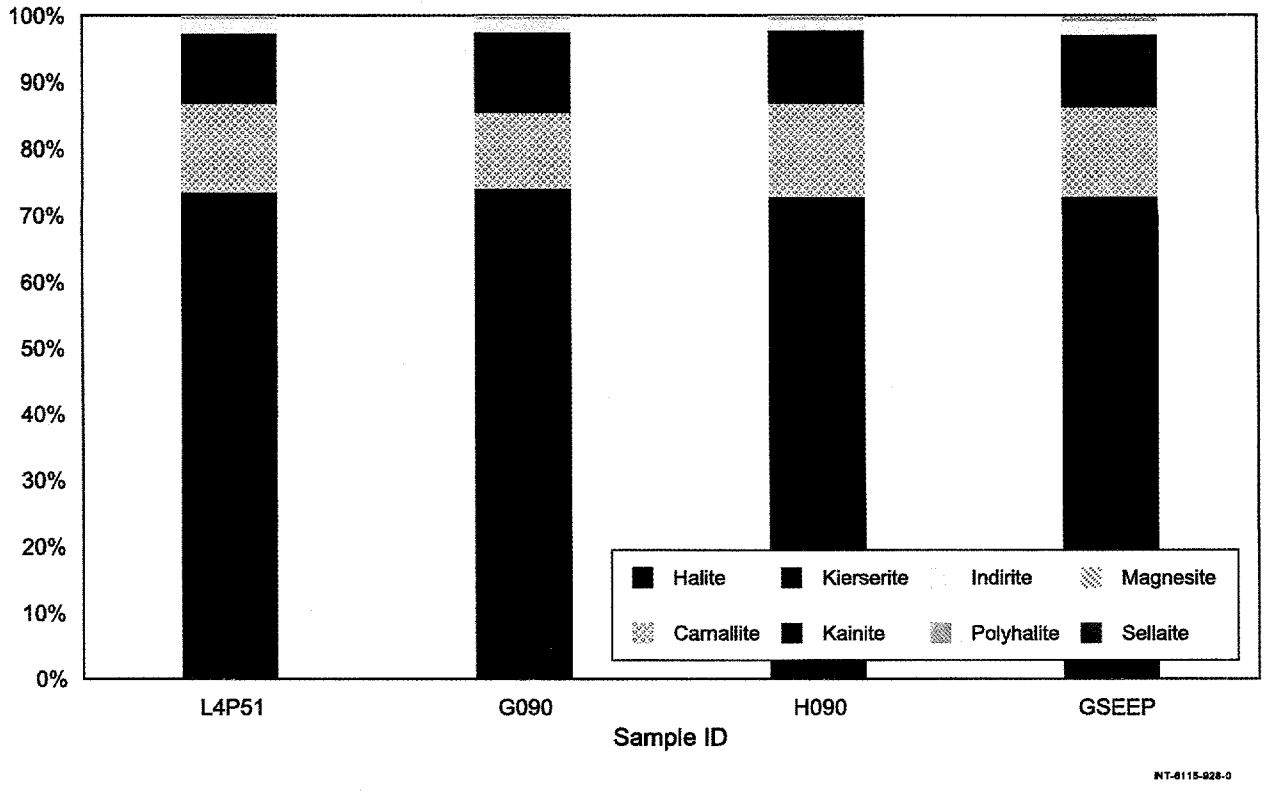

Figure 9-25. Normative salt assemblages for L4P51, G090, H090, and GSEEP brines.

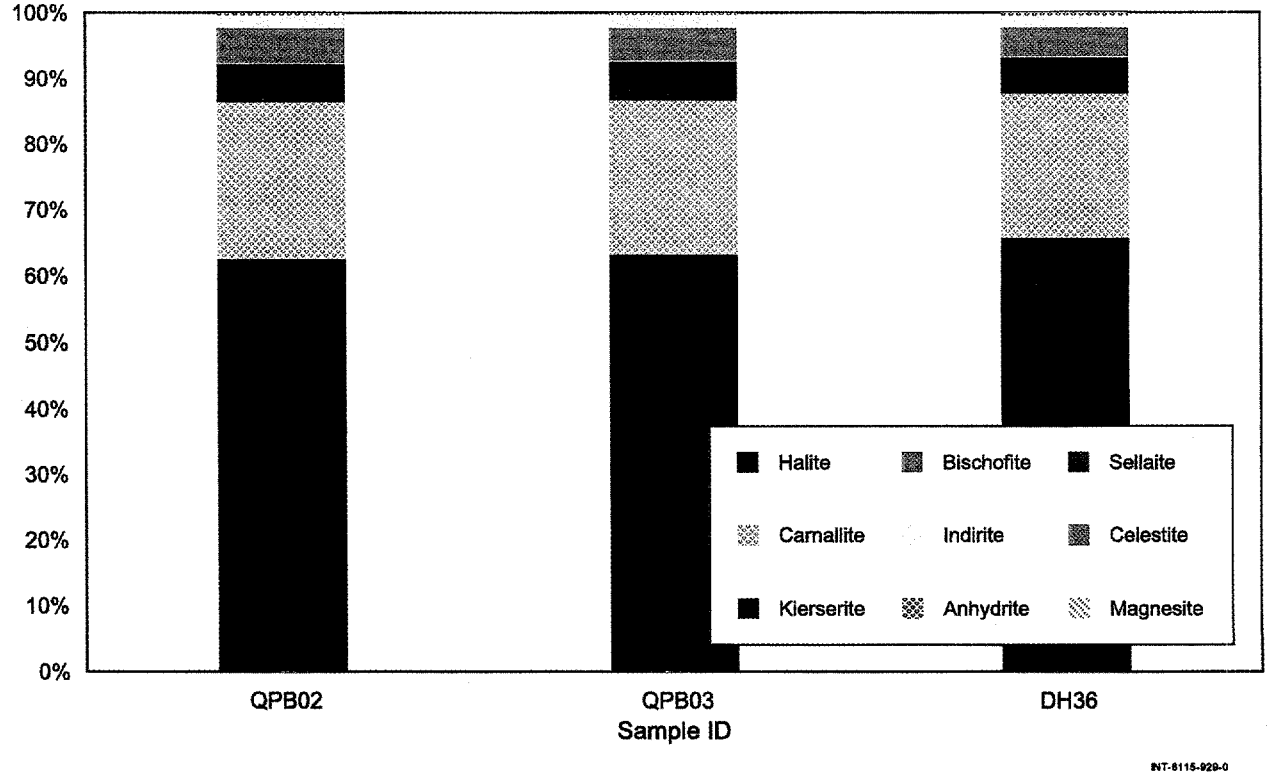

Figure 9-26. Normative salt assemblages for Marker Bed 139 brines.

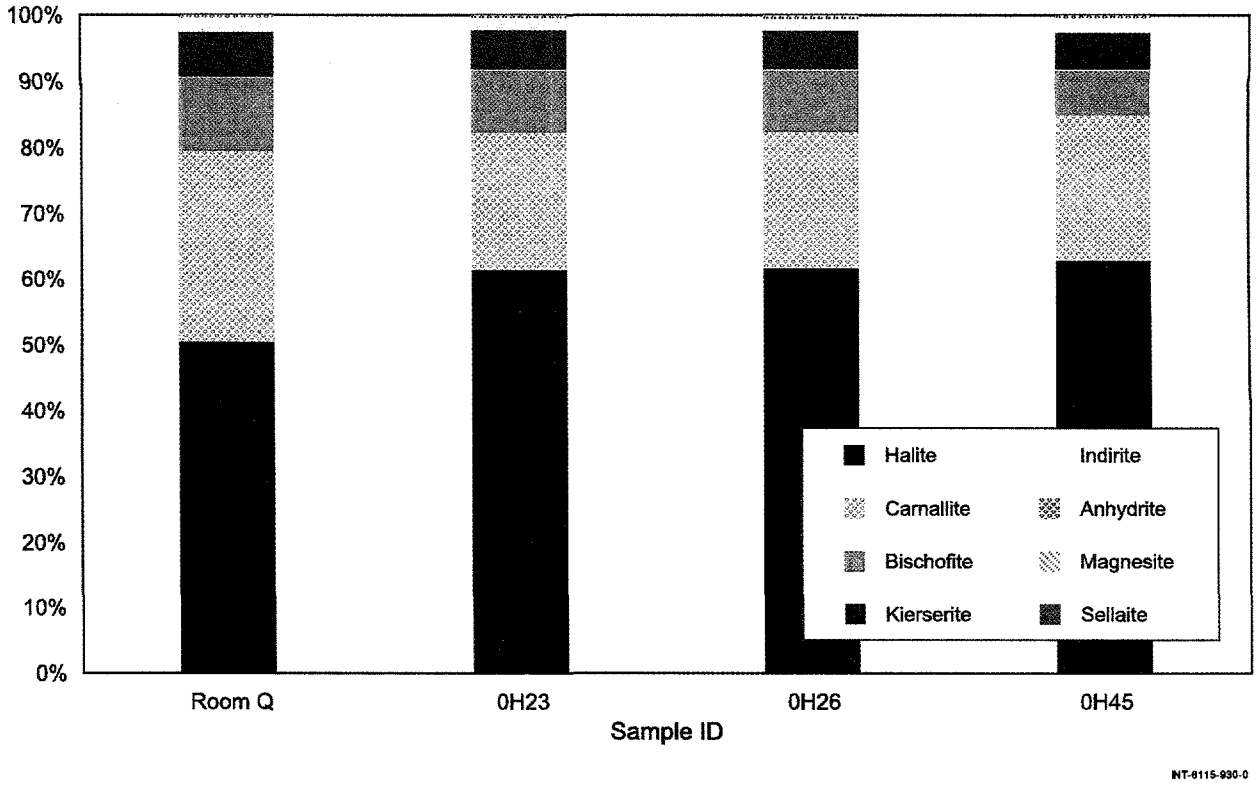

Figure 9-27. Normative salt assemblages for Map Unit 0 brines.

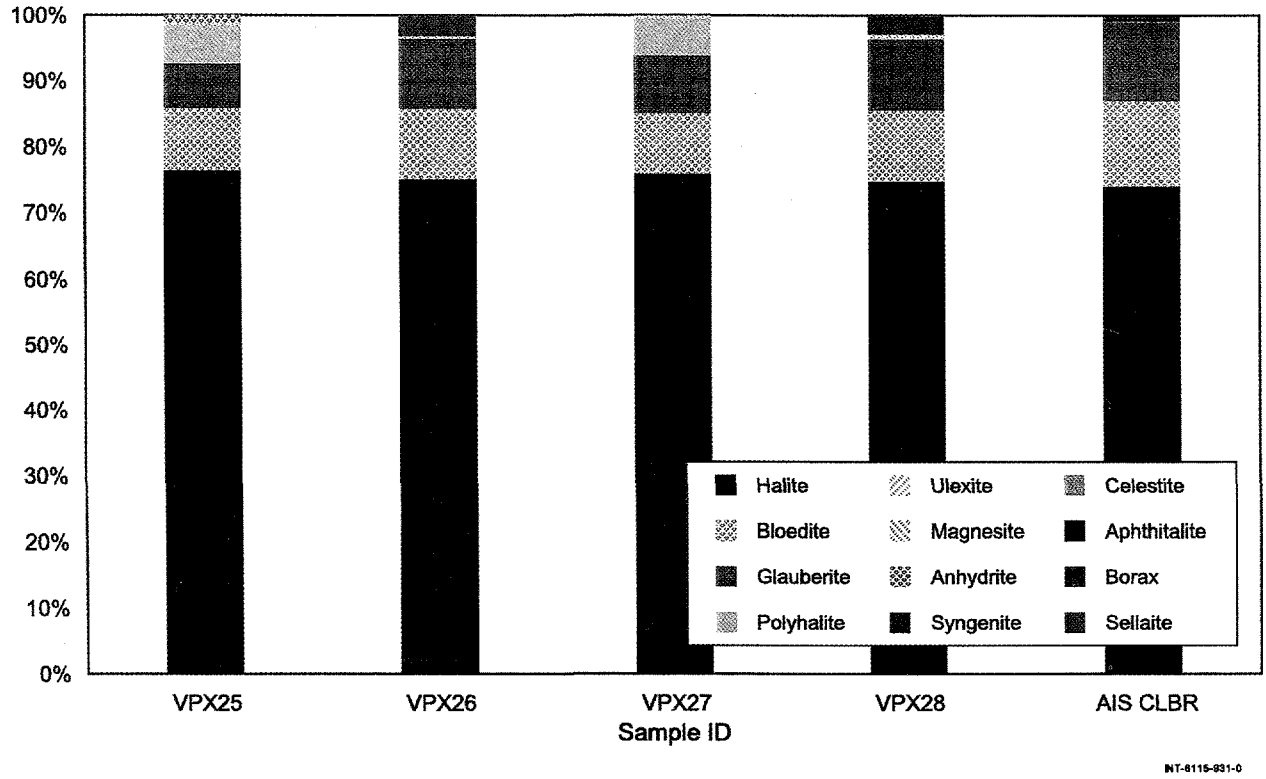

Figure 9-28. Normative salt assemblages for AIS Culebra brines.

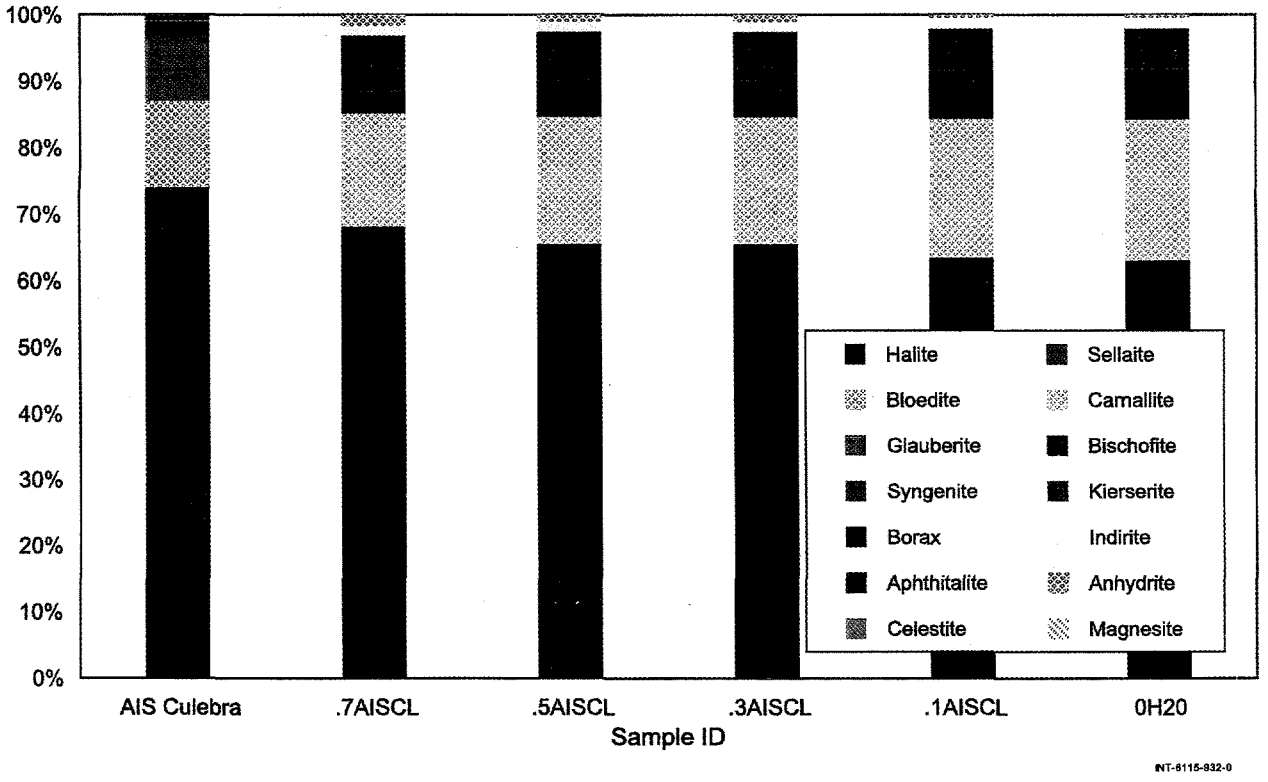

Figure 9-29. Normative salt assemblages for mixing of halite-type brine (OH20) and AIS Culebra brine.

controls the mineralogy of the salt norms and the AIS brine only influences the proportions of the phases. The reason for this is that brine from OH20 contains tens of times more solutes than the AIS brine and, hence, has a greater influence on the normative assemblage. For this reason, a relatively dilute solution, such as AIS brine, cannot be responsible for altering the GSEEP brine to the degree that it differs from other WIPP brines.

The geochemical evidence indicates that the brines from L4P51, G090, H090, and GSEEP share a common origin, MB140, and that the MB140 brine is unique compared to other Salado brines sampled to date. The path by which brine from MB140 arrived at the GSEEP location is uncertain.

9.5 Summary and Conclusions

The gas and brine samples collected during hydraulic testing of MB140 provided a unique opportunity to investigate gas and brine chemistry of an important stratigraphic interval in the WIPP repository. Gas-saturation calculations show that at the temperature and pressure conditions of MB140, both nitrogen and methane were near saturated concentrations in the MB140 brine and carbon dioxide was undersaturated. The hydrocarbon gases probably arose from the *in situ* decay/maturation of the small amount of organic material that happened to be indigenous to the hypersaline lagoons from which the salts precipitated, while nitrogen and CO_2 could have originated as trapped atmospheric gases at the time of deposition of MB140.

The relatively high concentration of helium in the MB140 gas most likely is from the decay of naturally occurring radioactive uranium and thorium isotopes.

The solutes of the MB140 brine were interpreted as having been derived from two Permian sources: marine and continental. This theory is supported by geochemical and geologic evidence. Furthermore, the brine originating from MB140 has a unique chemical signature (based on available data) compared to other WIPP brines, both from within the Salado Formation and from the Culebra Dolomite Member of the Rustler Formation. Brines from GSEEP, G090, and H090 that had been thought to be anomalous in their composition by Deal et al. (1991b) have been identified to originate from MB140. The identification of these brines as originating from MB140 is based on their compositional similarity to the MB140 brine from borehole L4P51 as well as on information about the units penetrated by the boreholes.

10. SUMMARY AND CONCLUSIONS

This report presents interpretations of hydraulic tests conducted in bedded evaporites of the Salado Formation from April 1992 through May 1995. The report supplements two previous reports on tests conducted from 1988 through early 1990 (Beauheim et al., 1991) and from mid-1989 through mid-1992 (Beauheim et al., 1993a) and a report on similar testing performed before and after the mining of Room Q (Domski et al., 1996). The tests discussed in this report were conducted on six intervals in three boreholes drilled from the underground WIPP facility. A summary of the test-interpretation results from this report and conclusions about the hydraulic properties and behavior of the Salado Formation based on all available test results are presented below.

10.1 Results of Most Recent Testing

The primary objectives of the hydraulic tests were to estimate the hydraulic conductivities, specific-storage values, and formation pore pressures of different stratigraphic intervals in the Salado Formation around the WIPP facility. Pressure-pulse, constant-pressure-injection/withdrawal, and/or pressure-buildup/falloff tests of six stratigraphic units were successfully conducted. Interpreted average hydraulic conductivities for four anhydrite layers range from 8×10^{-14} to 3×10^{-11} m/s ($k = 1 \times 10^{-20}$ to 6×10^{-18} m^2). The average hydraulic conductivities of the two halite intervals tested range from 2×10^{-11} to 7×10^{-10} m/s ($k = 4 \times 10^{-18}$ to 1×10^{-16} m^2).

The average specific-storage values of the anhydrite intervals tested range from 9×10^{-11} to 2×10^{-4} m^{-1}. Most of these specific-storage values are outside the theoretical range of 1×10^{-7} to 2×10^{-7} m^{-1} given in Beauheim et al. (1993a). As discussed in Section 6.2.3.8, specific storage cannot be reliably estimated from single-borehole tests. These estimates are assumed to be anomalous due to the presence of skin zones of altered permeability around the boreholes related to stress relief and/or the high compressibility of fractures in the anhydrite. The average specific-storage values of the halite intervals tested range from 5×10^{-9} to 4×10^{-7} m^{-1}. The lowest value falls below the theoretical minimum value of halite specific storage of 3×10^{-8} m^{-1} given in Beauheim et al. (1993a). These estimates, however, are affected by the same uncertainties discussed with respect to the anhydrite specific-storage values above.

The formation pore pressures of the anhydrite intervals tested range from a minimum of 4 MPa in anhydrite "b" in a hole angled upward and away from Room 7 of Waste Panel 1 to 10.3 MPa in MB138 in the same borehole after it was deepened for the S1P74-B testing sequence. Pore pressures in halite intervals range from greater than 4.8 MPa to 8.7 MPa.

Another objective of the Salado hydraulic testing program was to determine the radii of influence of the tests in order to define the scales at which the interpreted properties are representative. Unfortunately, the radii of influence of the tests cannot be reliably determined for the following reasons. The estimated radius of influence is highly dependent on the estimated specific storage, which cannot be reliably estimated for the reasons discussed above. In addition, flow in some of the tests appears to be nonradial, so the radius of influence, as it is typically conceptualized within the context of a radial system, is not well defined. Wawersik et al. (1997) indicate that fluorescent dye injected during hydraulic fracturing tests followed preferential flow paths from the back of Room C1 to a

distance of at least 10 m toward the front of the room. No dye, however, was found at the same distance in a borehole drilled at an angle away from the room, under the back rib (wall), providing direct evidence of nonsymmetric flow.

The responses of several tested intervals, both anhydrite and halite, indicated that the hydraulic conductivity of those intervals was dependent on the driving pressures of the tests performed. Analyses of the test responses indicated that the hydraulic conductivity increased as the driving pressure increased and decreased as the driving pressure decreased. Interpreted pressure-dependent hydraulic conductivities varied by approximately one order of magnitude (L4P52-B test zone) to as much as four orders of magnitude (S1P74-A test zone) during individual testing sequences. We believe that the changes in hydraulic conductivity correspond to changes in fracture aperture(s) as the fluid pressure in the fracture(s) changes. This pressure-dependent behavior was observed in both a vertical borehole in the floor of Room L4 (L4P51-C) and in two boreholes angled upward into ribs of excavations (L4P52-B, S1P74-A). We are uncertain why some tested intervals behave in a pressure-dependent manner and others do not.

Flow was interpreted as nonradial in five of the six newly tested intervals. The interpreted flow dimensions during the constant-pressure-withdrawal tests of H-m2 in L4P51 were initially subradial to radial and then decreased further, suggesting channeling of flow through fracture networks, or portions of fractures, that occupy a diminishing proportion of the radially available space. The interpreted flow dimensions from the MB140 testing, however, increased during the course of the constant-pressure-withdrawal tests, suggesting a fractured system in which connectivity increases with distance/time.

10.2 Discussion of All Salado Test Results

The results of the hydraulic tests discussed both in this report and by Beauheim et al. (1991, 1993a) and Domski et al. (1996) were used to evaluate how the presence of the WIPP facility has affected hydraulic conductivities and formation pore pressures in the surrounding rock. No simple correlation appears to exist between average hydraulic conductivity and distance from an excavation (Figure 8-1), either in anhydrite or halite. Correlations are not seen even when the angled-hole tests are considered separately from the vertical-hole tests. This is not to argue that hydraulic conductivity is **not** affected by the excavations. As discussed in Section 8.1.3, changes in the stress field around excavations likely cause both increases and reductions in hydraulic conductivity at different locations and times. But the complex nature of the hydromechanical coupling, as well as additional factors affecting hydraulic conductivity (e.g., mineralogy, natural heterogeneity, orientation of the tested zone with respect to an excavation), preclude precise definition of the changes that have occurred at specific locations.

As shown in Figure 8-1, typical average hydraulic-conductivity values for anhydrite range from approximately 10^{-13} to 5×10^{-11} m/s ($k \approx 10^{-20}$ to 10^{-17} m^2). Average hydraulic-conductivity values for halite are typically less than 10^{-13} m/s. Higher values have been inferred from tests conducted within 5 m of excavations and/or of intervals containing significant clay seams, as well as from the anomalous test of H-m2 in L4P51.

Pore pressures tend to increase with distance from the excavations, both in halite and an-

hydrite (Figure 8-2). Pore pressures tend to be most reduced within a few meters directly above and below excavations, as shown by atmospheric conditions encountered in two test intervals 1-2 m into the floor and in two test intervals 1-4 m into the roof of excavations. Beyond approximately 3 m, no systematic difference can be seen between pore-pressure measurements made above and below an excavation and those made in the ribs of excavations. However, the highest pore pressures (>12 MPa) have all been measured in holes drilled outward into virgin rock from the extreme edges of the WIPP excavations. Wawersik et al. (1997) interpret hydraulic-fracturing data to show that the stress state (and presumably the pore pressure) in MB140, over 23 m below the floor of the excavation, was clearly affected by the excavation. They note, however, that conditions were much more disturbed directly below the excavation than they were under the rib. We are, therefore, uncertain to what distance pore pressures in angled boreholes are affected by the excavations.

10.3 Summary of MB140 Gas and Brine Chemistry

Solute assemblages present in brine from MB140 at borehole L4P51 suggest a dual marine and continental source for the solutes. The chemical signature of the MB140 brine from L4P51 is distinct from that of all other Salado brines sampled except for that from GSEEP in Room G and two other boreholes drilled through MB140, G090 and H090. The brine sampled from MB140 contained abundant dissolved gas, primarily nitrogen and methane, with lesser amounts of carbon dioxide, ethane, propane, and helium. The data suggest that the brine was saturated with respect to nitrogen and methane, but undersaturated with respect to carbon dioxide. Based on the available data, no definite conclusions can be drawn as to the source(s) of the gases.

10.4 Conclusions

Pressure-pulse, constant-pressure flow, and pressure-recovery tests have been performed in bedded evaporites of the Salado Formation at the WIPP site to evaluate the hydraulic properties controlling brine flow through the Salado. New numerical methods have been developed to interpret these tests that allow definition of the dimensionality of flow and quantification of uncertainty in parameter estimates. Hydraulic conductivities ranging from approximately 1×10^{-16} to 2×10^{-9} m/s ($k \approx 2 \times 10^{-23}$ to 3×10^{-16} m^2) have been interpreted from tests conducted on 30 stratigraphic intervals within 24 m of the WIPP underground excavations. Typical average hydraulic-conductivity values for anhydrite range from approximately 10^{-13} to 5×10^{-11} m/s ($k \approx 10^{-20}$ to 10^{-18} m^2), while those of halite are less than 10^{-13} m/s. Apparent specific-storage values of the tested intervals range from about 6×10^{-12} to 2×10^{-4} m^{-1}. The specific-storage estimates are potentially affected by permeability changes around the borehole resulting from stress changes and are not considered quantitatively reliable. Pore pressures in 47 stratigraphic intervals range from atmospheric to 13.5 MPa.

Hydraulic conductivities of some tested intervals have been found to be dependent on the pressures at which the tests were conducted. We interpret this as the result of fracture apertures changing in response to changes in effective stress. Flow dimensions inferred from some test responses are subradial, which we believe reflects channeling of flow through fracture networks, or portions of fractures, that occupy a diminishing proportion of the radially available space. Other test responses indicate flow dimensions between radial and spherical, which may reflect propa-

gation of pressure transients above or below the plane of the test interval or into regions of increased permeability. The variable stress and pore-pressure fields around the WIPP excavations probably contribute to the apparent nonradial flow dimensions.

Inferred values of hydraulic conductivity cannot be separated from their associated flow dimensions. Therefore, numerical models of flow and transport should include heterogeneity that is structured to provide the same flow dimensions as are observed in hydraulic tests. Modeling of the Salado Formation around the WIPP repository should also include coupling between hydraulic properties and the evolving stress field.

11. REFERENCES

Argüello, J.G. 1990. *Pretest 3D Finite Element Analysis of the WIPP Intermediate Scale Borehole Test.* SAND90-2055. Albuquerque, NM: Sandia National Laboratories.

Barker, J.A. 1988. "A Generalized Radial Flow Model for Hydraulic Tests in Fractured Rock," *Water Resources Research.* Vol. 24, no. 10, 1796-1804.

Beauheim, R.L., G.J. Saulnier, Jr., and J.D. Avis. 1991. *Interpretation of Brine-Permeability Tests of the Salado Formation at the Waste Isolation Pilot Plant Site: First Interim Report.* SAND90-0083. Albuquerque, NM: Sandia National Laboratories.

Beauheim, R.L., R.M. Roberts, T.F. Dale, M.D. Fort, and W.A. Stensrud. 1993a. *Hydraulic Testing of Salado Formation Evaporites at the Waste Isolation Pilot Plant Site: Second Interpretive Report.* SAND92-0533. Albuquerque, NM: Sandia National Laboratories.

Beauheim, R.L., W.R. Wawersik, and R.M. Roberts. 1993b. "Coupled Permeability and Hydrofracture Tests to Assess the Waste-Containment Properties of Fractured Anhydrite," *International Journal of Rock Mechanics and Mining Sciences & Geomechanics Abstracts.* Vol. 30, no. 7, 1159-1163.

Bechtel National, Inc. 1986. *Interim Geotechnical Field Data Report, Fall 1986.* DOE-WIPP 86-012. Carlsbad, NM: US DOE.

Black, J.H., J.A. Barker, and D.J. Noy. 1986. *Crosshole Investigations – The Method, Theory and Analysis of Crosshole Sinusoidal Pressure Tests in Fissured Rock.* Stripa Project IR 86-03. Stockholm, Sweden: SKB.

Bodine, M.W., Jr., and B.F. Jones. 1986. *THE SALT NORM: A Quantitative Chemical-Mineralogical Characterization of Natural Waters.* Water Resources Investigations Report 86-4086. Reston, VA: US Geological Survey.

Bourdet, D., J.A. Ayoub, and Y.M. Pirard. 1989. "Use of Pressure Derivative in Well-Test Interpretation," *SPE Formation Evaluation.* Vol. 4, no. 2, 293-302.

Bredehoeft, J.D., and S.S. Papadopulos. 1980. "A Method for Determining the Hydraulic Properties of Tight Formations," *Water Resources Research.* Vol. 16, no. 1, 233-238.

Butler, J.J., Jr., and W.Z. Liu. 1991. "Pumping Tests in Non-Uniform Aquifers - The Linear Strip Case," *Journal of Hydrology.* Vol. 128, 69-99.

Chace, D.A., R.M. Roberts, J.B. Palmer, M.B. Kloska, M.D. Fort, G.J. Martin, and W.A. Stensrud. 1998. *Waste Isolation Pilot Plant Salado Hydrology Program Data Report #3.* SAND97-1880. Albuquerque, NM: Sandia National Laboratories.

Chem-Nuclear Geotech Analytical Laboratory. 1993. "Analytical Report." Grand Junction, CO: Chem-Nuclear Geotech. (On file in the SWCF under WPO#43913.)

Chem-Nuclear Geotech Analytical Laboratory. 1994. "Analytical Report." Grand Junction, CO: Chem-Nuclear Geotech. (On file in the SWCF under WPO#43913.)

Cook, N.G.W. 1992. "Natural Joints in Rock: Mechanical, Hydraulic and Seismic Behaviour and Properties under Normal Stress," *International Journal of Rock Mechanics and Mining Sciences & Geomechanics Abstracts.* Vol. 29, no. 3, 198-223.

Cooper, H.H., Jr., and C.E. Jacob. 1946. "A Generalized Graphical Method for Evaluating Formation Constants and Summarizing Well-Field History," *Transactions, American Geophysical Union.* Vol. 27, no. IV, 526-534.

Cygan, R.T. 1991. *The Solubility of Gases in NaCl Brine and a Critical Evaluation of Available Data.* SAND90-2848. Albuquerque, NM: Sandia National Laboratories.

Darcy, H. 1856. *Les Fontaines Publiques de la Ville de Dijon.* Paris, France: Victor Dalmont.

Deal, D.E., R.J. Abitz, D.S. Belski, J.B. Case, M.E. Crawley, R.M. Deshler, P.E. Drez, C.A. Givens, R.B. King, B.A. Lauctes, J. Myers, S. Niou, J.M. Pietz, W.M. Roggenthen, J.R. Tyburski, and M.G. Wallace. 1989. *Brine Sampling and Evaluation Program 1988 Report.* DOE/WIPP 89-015. Carlsbad, NM: US DOE Waste Isolation Pilot Plant Project Office.

Deal, D.E., R.J. Abitz, D.S. Belski, J.B. Clark, M.E. Crawley, and M.L. Martin. 1991a. *Brine Sampling and Evaluation Program 1989 Report.* DOE/WIPP 91-009. Carlsbad, NM: US DOE Waste Isolation Pilot Plant Project Office.

Deal, D.E., R.J. Abitz, J. Myers, J.B. Case, D.S. Belski, M.L. Martin, and W.M. Roggenthen. 1991b. *Brine Sampling and Evaluation Program 1990 Report.* DOE/WIPP 91-036. Carlsbad, NM: US DOE Waste Isolation Pilot Plant Project Office.

Deal, D.E., R.J. Abitz, J. Myers, D.S. Belski, M.L. Martin, D.J. Milligan, R.W. Sobocinski, and P.P.J. Lipponer. 1993. *Brine Sampling and Evaluation Program 1991 Report.* DOE/WIPP 93-026. Carlsbad, NM: US DOE Waste Isolation Pilot Plant Project Office.

Detournay, E., and H.-D. Cheng. 1993. "Fundamentals of Poroelasticity," *Comprehensive Rock Engineering.* Eds. J. Hudson and C. Fairhurst. Oxford, UK; New York, NY: Pergamon Press. Vol. II, 113-171.

Doe, T.W. 1991. "Fractional Dimension Analysis of Constant-Pressure Well Tests," *Proceedings: 1991 SPE Annual Technical Conference and Exhibition, Formation Evaluation & Reservoir Geology, Dallas, TX, October 6-9, 1991.* SPE 22702. Richardson, TX: Society of Petroleum Engineers. 461-467.

Domski, P.S., D.T. Upton, and R.L. Beauheim. 1996. *Hydraulic Testing Around Room Q: Evaluation of the Effects of Mining on the Hydraulic Properties of Salado Evaporites.* SAND96-0435. Albuquerque, NM: Sandia National Laboratories.

Earlougher, R.C., Jr. 1977. *Advances in Well Test Analysis. Monograph Volume 5.* Dallas, TX: Society of Petroleum Engineers of AIME. 264 p.

Ehlig-Economides, C.A. 1979. "Well Test Analysis for Wells Produced at a Constant Pressure." PhD dissertation. Palo Alto, CA: Department of Petroleum Engineering, Stanford University. 117 p.

Ehlig-Economides, C.A., and H.J. Ramey, Jr. 1981. "Transient Rate Decline Analysis for Wells Produced at Constant Pressure," *Society of Petroleum Engineers Journal.* Vol. 21, no. 1, 98-104.

Faure, G. 1986. *Principles of Isotope Geology.* 2nd ed. New York, NY: John Wiley & Sons.

Ferris, J.G., D.B. Knowles, R.H. Brown, and R.W. Stallman. 1962. *Theory of Aquifer Tests.* Water-Supply Paper 1536-E. Washington, DC: U.S. Government Printing Office.

Fetkovich, M.J. 1980. "Decline Curve Analysis Using Type Curves," *Journal of Petroleum Technology.* Vol. 32, no. 6, 1065-1077.

Gale, J.E. 1977. *A Numerical, Field and Laboratory Study of Flow in Rocks with Deformable Fractures.* Scientific Series No. 72. Ottawa, Canada: Fisheries and Environment Canada, Inland Waters Directorate, Water Resources Branch.

Geier, J.E., T.W. Doe, A. Benabderrahman, and L. Hässler. 1996. *Generalized Radial Flow Interpretation of Well Tests for the SITE-94 Project.* SKI Report 96:4. Stockholm, Sweden: Swedish Nuclear Power Inspectorate.

Gringarten, A.C., D.P. Bourdet, P.A. Landel, and V.J. Kniazeff. 1979. "A Comparison Between Different Skin and Wellbore Storage Type Curves for Early-Time Transient Analysis," *Society of Petroleum Engineers 54th Annual Technical Conference & Exhibition, Las Vegas, NV, September 23-26, 1979.* SPE 8205. Richardson, TX: Society of Petroleum Engineers. 17 p.

Holt, R.M. 1993. *Sedimentary Textures, Structures, and Lithofacies in the Salado Formation: A Guide for Recognition, Classification, and Interpretation.* DOE/WIPP 93-056. Carlsbad, NM: US DOE Waste Isolation Pilot Plant Project Office.

Holt, R.M., and D.W. Powers. 1990. *Geologic Mapping of the Air Intake Shaft at the Waste Isolation Pilot Plant.* DOE/WIPP 90-051. Carlsbad, NM: US DOE.

Horne, R.N. 1995. *Modern Well Test Analysis: A Computer-Aided Approach.* 2nd ed. Palo Alto, CA: Petroway, Inc. 257 p.

Horner, D.R. 1951. "Pressure Build-Up in Wells," *Proceedings of the Third World Petroleum Congress, The Hague, Netherlands, May 29, 1951.* Leiden, The Netherlands: E.J. Brill. Sec. II, 503-521. Reprinted 1967. *Pressure Analysis Methods.* SPE Reprint Series Vol. 9. Richardson, TX: Society of Petroleum Engineers. 25-43.

Jacob, C.E., and S.W. Lohman. 1952. "Nonsteady Flow to a Well of Constant Drawdown in an Extensive Aquifer," *Transactions, American Geophysical Union.* Vol. 33, no.4, 559-569.

Jensen, A.L. 1990. *Borehole Closure and Test Zone Volume Determination Program for Brine-Permeability Test Results Within the Waste Isolation Pilot Plant Underground Facility.* SAND90-0228. Albuquerque, NM: Sandia National Laboratories.

Jones, B., and S.K. Anderholm. 1996. "Some Geochemical Considerations of Brines Associated with a Bedded Salt Repository," *Proceedings: Fourth International Symposium on the Geochemistry of the Earth's Surface, Ilkley, Yorkshire, England, July 22-28, 1996.* Ed. S.H. Bottrell. [Leeds]: University of Leeds, Department of Earth Sciences. 343-353.

Jones, C.L., C.G. Bowles, and K.G. Bell. 1960. *Experimental Drill Hole Logging in Potash Deposits of the Carlsbad District, New Mexico.* USGS Open-File Report 60-84. Washington, DC: U.S. Government Printing Office. 25 p.

Krumhansl, J.L., K.M. Kimball, and C.L. Stein. 1991. *Intergranular Fluid Compositions from the Waste Isolation Pilot Plant (WIPP), Southeastern New Mexico.* SAND90-0584. Albuquerque, NM: Sandia National Laboratories.

Lee, W.J. 1982. *Well Testing.* SPE Textbook Series Volume 1. Dallas TX: Society of Petroleum Engineers of AIME. 159 p.

Matthess, G. 1982. *The Properties of Groundwater.* Translated by J.C. Harvey. New York, NY: Wiley-Interscience.

McTigue, D.F., S.J. Finley, and E.J. Nowak. 1989. "Brine Transport in Polycrystalline Salt: Field Measurements and Model Considerations," *Eos Transactions.* Vol. 70, no. 43, 1111.

McTigue, D.F. 1993. *Permeability and Hydraulic Diffusivity of Waste Isolation Pilot Plant Repository Salt Inferred from Small-Scale Brine Inflow Experiments.* SAND92-1911. Albuquerque, NM: Sandia National Laboratories.

Noy, D.J., J.A. Barker, J.H. Black, and D.C. Holmes. 1988. *Crosshole Investigations – Implementation and Fractional Dimension Interpretation of Sinusoidal Tests.* Stripa Project TR 88-01. Stockholm, Sweden: Swedish Nuclear Fuel and Waste Management Co.

Olsson, W.A., and S.R. Brown. 1993. "Hydromechanical Response of a Fracture Undergoing Compression and Shear," *International Journal of Rock Mechanics and Mining Sciences & Geomechanics Abstracts.* Vol. 30, no. 7, 845-851.

Peres, A.M.M., M. Onur, and A.C. Reynolds. 1989. "A New Analysis Procedure for Determining Aquifer Properties From Slug Test Data," *Water Resources Research.* Vol. 25, no. 7, 1591-1602.

Pickens, J.F., G.E. Grisak, J.D. Avis, D.W. Belanger, and M. Thury. 1987. "Analysis and Interpretation of Borehole Hydraulic Tests in Deep Boreholes: Principles, Model Development, and Applications," *Water Resources Research.* Vol. 23, no. 7, 1341-1375.

Plummer, L.N., D.L. Parkhurst, G.W. Fleming, and S.A. Dunkle. 1988. *A Computer Program Incorporating Pitzer's Equations for Calculation of Geochemical Reactions in Brines.* Water-Resources Investigations Report 88-4153. Reston, VA: US Geological Survey.

Press, W.H., S.A. Teukolsky, W.T. Vetterling, and B.P. Flannery. 1992. *Numerical Recipes in FORTRAN: The Art of Scientific Computing.* 2nd ed. New York, NY: Cambridge University Press.

Rutqvist, J., J. Noorishad, O. Stephansson, and C.F. Tsang. 1992. "Theoretical and Field Studies of Coupled Hydromechanical Behaviour of Fractured Rocks—2. Field Experiment and Modelling," *International Journal of Rock Mechanics and Mining Sciences & Geomechanics Abstracts.* Vol. 29, no. 4, 411-419.

Saulnier, G.J., Jr. 1988. "Field Operations Plan for Permeability Testing in the WIPP Underground Facility." Albuquerque, NM: Sandia National Laboratories. (On file in the SWCF under WPO#5399.)

Saulnier, G.J., Jr. 1991. "Field Operations Plan for Permeability Testing in the WIPP Underground Facility, Addendum I." Albuquerque, NM: Sandia National Laboratories. (On file in the SWCF under WPO#6587.)

Skempton, A.W. 1954. "The Pore-Pressure Coefficients A and B," *Géotechnique.* Vol. IV, 143-147.

Stein, C.L., and J.L. Krumhansl. 1986. *Chemistry of Brines in Salt from the Waste Isolation Pilot Plant (WIPP), Southeastern New Mexico: A Preliminary Investigation.* SAND85-0897. Albuquerque, NM: Sandia National Laboratories.

Stensrud, W.A., T.F. Dale, P.S. Domski, J.B. Palmer, R.M. Roberts, M.D. Fort, G.J. Saulnier, Jr., and A.L. Jensen. 1992. *Waste Isolation Pilot Plant Salado Hydrology Program Data Report #2.* SAND92-7072. Albuquerque, NM: Sandia National Laboratories.

Stormont, J.C., C.L. Howard, and J.J.K. Daemen. 1991. *In Situ Measurements of Rock Salt Permeability Changes Due to Nearby Excavation.* SAND90-3134. Albuquerque, NM: Sandia National Laboratories.

Theis, C.V. 1935. "The Relation Between the Lowering of the Piezometric Surface and the Rate and Duration of Discharge of a Well Using Ground-Water Storage," *Transactions, American Geophysical Union.* Vol. 16, 519-524.

Uraiet, A.A., and R. Raghavan. 1980. "Unsteady Flow to a Well Producing at a Constant Pressure," *Journal of Petroleum Technology.* Vol. 32, no. 10, 1803-1812.

US Department of Energy. 1996. *Title 40 CFR Part 191 Compliance Certification Application for the Waste Isolation Pilot Plant.* DOE/CAO-1996-2184. Carlsbad, NM: US DOE Waste Isolation Pilot Plant, Carlsbad Area Office.

Warpinski, N.R., L.W. Teufel, and D.C. Graf. 1991. "Effect of Stress and Pressure on Gas Flow Through Natural Fractures," *Proceedings: 1991 SPE Annual Technical Conference and Exhibition, Dallas, TX, October 6-9, 1991.* SPE 22666. Richardson, TX: Society of Petroleum Engineers. 105-118.

Wawersik, W.R., and C.M. Stone. 1989. "A Characterization of Pressure Records in Inelastic Rock Demonstrated by Hydraulic Fracturing Measurements in Salt," *International Journal of Rock Mechanics and Mining Sciences & Geomechanics Abstracts.* Vol. 26, no. 6, 613-627.

Wawersik, W.R., L.W. Carlson, J.A. Henfling, D.J. Borns, R.L. Beauheim, C.L. Howard, and R.M. Roberts. 1997. *Hydraulic Fracturing Tests in Anhydrite Interbeds in the WIPP, Marker Beds 139 and 140.* SAND95-0596. Albuquerque, NM: Sandia National Laboratories.

Westinghouse Electric Corporation. 1989. *Geotechnical Field Data and Analysis Report, July 1987-June 1988, Volume II.* DOE/WIPP 89-009. Carlsbad, NM: US DOE.

Westinghouse Electric Corporation. 1990. *Geotechnical Field Data and Analysis Report, July 1988-June 1989, Volume II.* DOE/WIPP 90-006. Carlsbad, NM: US DOE.

Wolery, T.J. 1983. *EQ3NR, A Computer Program for Geochemical Aqueous Speciation-Solubility Calculations: User's Guide and Documentation.* UCRL-53414. Livermore, CA: Lawrence Livermore National Laboratory.

Zartman, R.E., G.J. Wasserburg, and J.H. Reynolds. 1961. "Helium, Argon, and Carbon in Some Natural Gases," *Journal of Geophysical Research.* Vol. 66, no. 1, 277-306.

APPENDIX A

REANALYSES OF PREVIOUS TESTS

THIS PAGE INTENTIONALLY LEFT BLANK

APPENDIX A: REANALYSES OF PREVIOUS TESTS

A.1 Introduction

The permeability tests presented in this appendix were previously analyzed and discussed in Beauheim et al. (1991 and 1993a). The tests have been subsequently re-analyzed utilizing the GTFM inverse-solver and statistical routines that were not available when the original analyses were done. Analyses of the tests have also incorporated the variable-flow-dimension methodology discussed in Section 6.2.2 of this report. Corrections (pressure offsets) have been applied to all pressure data to compensate for the difference in elevation of the tested interval and the pressure transducer.

A.2 C2H01-A Test Zone, 7/88 – 8/88

The two pulse-injection (PI) tests could not be matched adequately with a single parameter set and were, consequently, analyzed separately. The results of these analyses are presented in Table A-1. Quantitative estimates of the fitting-parameter uncertainty (95% joint-confidence regions) and the corresponding correlation matrices are presented in Appendix C. Figures A-1a and A-2a show the best-fit GTFM simulations compared to the PI1 and PI2 normalized-

Table A-1. Summary of Reanalyses of Previous Salado Permeability Tests

Hole/ Zone	Map Unit	Test	Map Unit Thickness (m)	Average Hydraulic Conductivity K (m/s)	Average Permeability k (m^2)	Average Specific Storage S_s (m^{-1})	Formation Pore Pressure P_f (MPa)	Flow Dimension
C2H01-A Test	4-5	PI1	0.83	1.7E-9	3.0E-16	7.1E-5	0.00	2.9E-2
		PI2	0.83	2.1E-9	3.6E-16	6.2E-5	0.00	0.31
C2H01-B Test	0	PI1 & PW1	1.08	6.9E-15	1.2E-21	6.2E-9	3.11	2.49
C2H01-B Guard	0-4	PW1	1.10	3.3E-14	5.7E-21	6.2E-9	4.49	1.83
C2H01-C Test	MB139	PW2	0.96	1.1E-12	1.9E-19	2.1E-6	8.00	2.71
C2H02 Test	MB139	PW3	0.87	8.8E-14	1.5E-20	1.4E-7	9.28	2.12
S0P01 Test	PH-3 and clay D	SI & PW2	1.43	1.3E-13	2.2E-20	2.8E-9	4.82	1.88
S1P71-B Test	Anhydrite "c"	PW1	0.08	2.2E-13	3.9E-20	3.4E-7	4.80	2.41
		PW2	0.08	1.3E-13	2.3E-20	5.6E-7	4.80	2.62
S1P73-B Test	MB138	CPW	0.17	2.0E-12	3.5E-19	7.7E-7	4.34	1.83
SCP01-A Test	MB139	CPW2 & PB2	0.96	4.9E-11	8.6E-18	5.5E-12	13.50	1.53
L4P52-A Test	Anhydrite "a"	PW2	0.24	4.8E-13	8.3E-20	4.5E-8	6.84	1.95

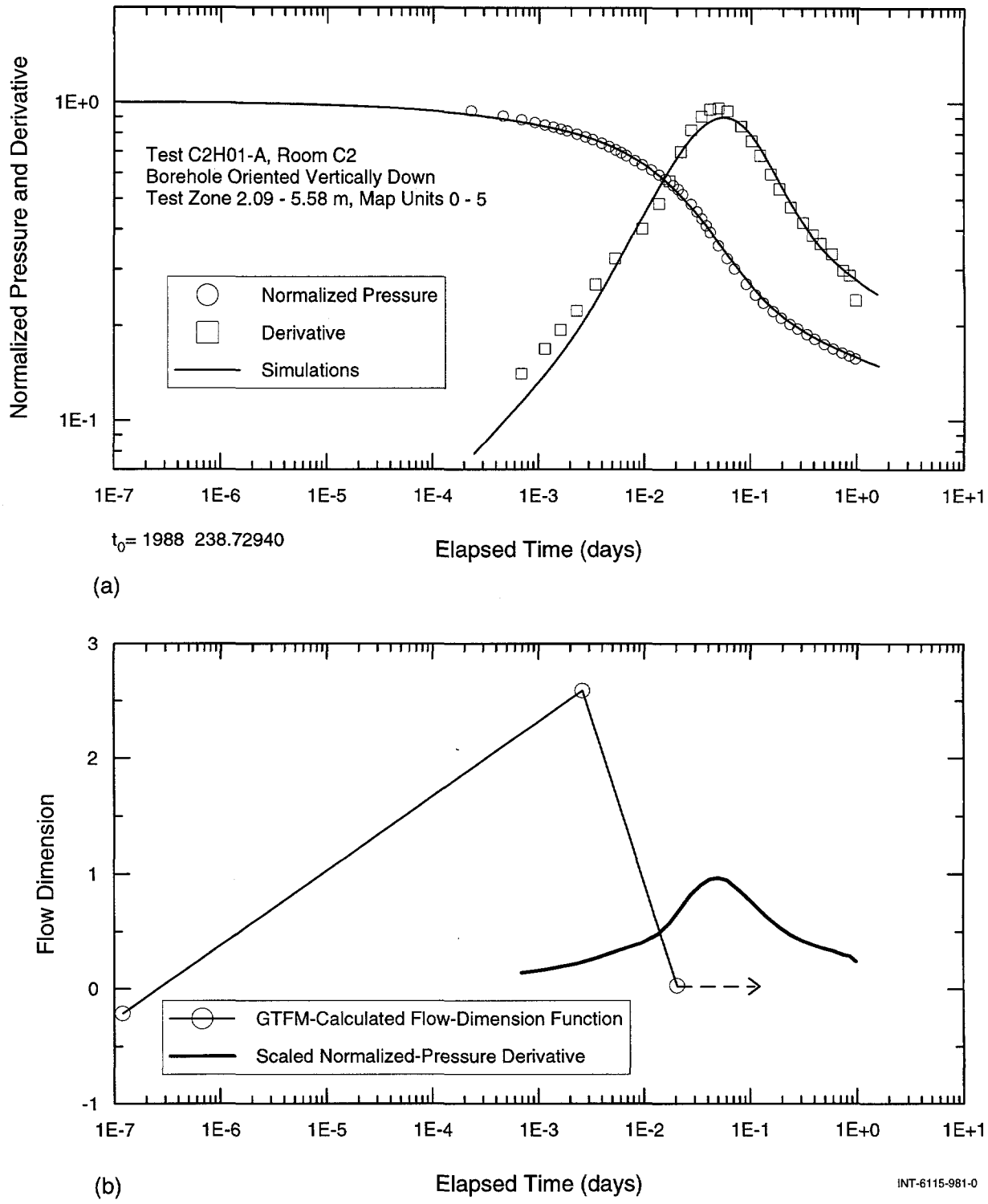

Figure A-1. Log-log and semilog plots of GTFM simulation (a) and flow-dimension function (b) of the C2H01-A test-zone pulse-injection test #1.

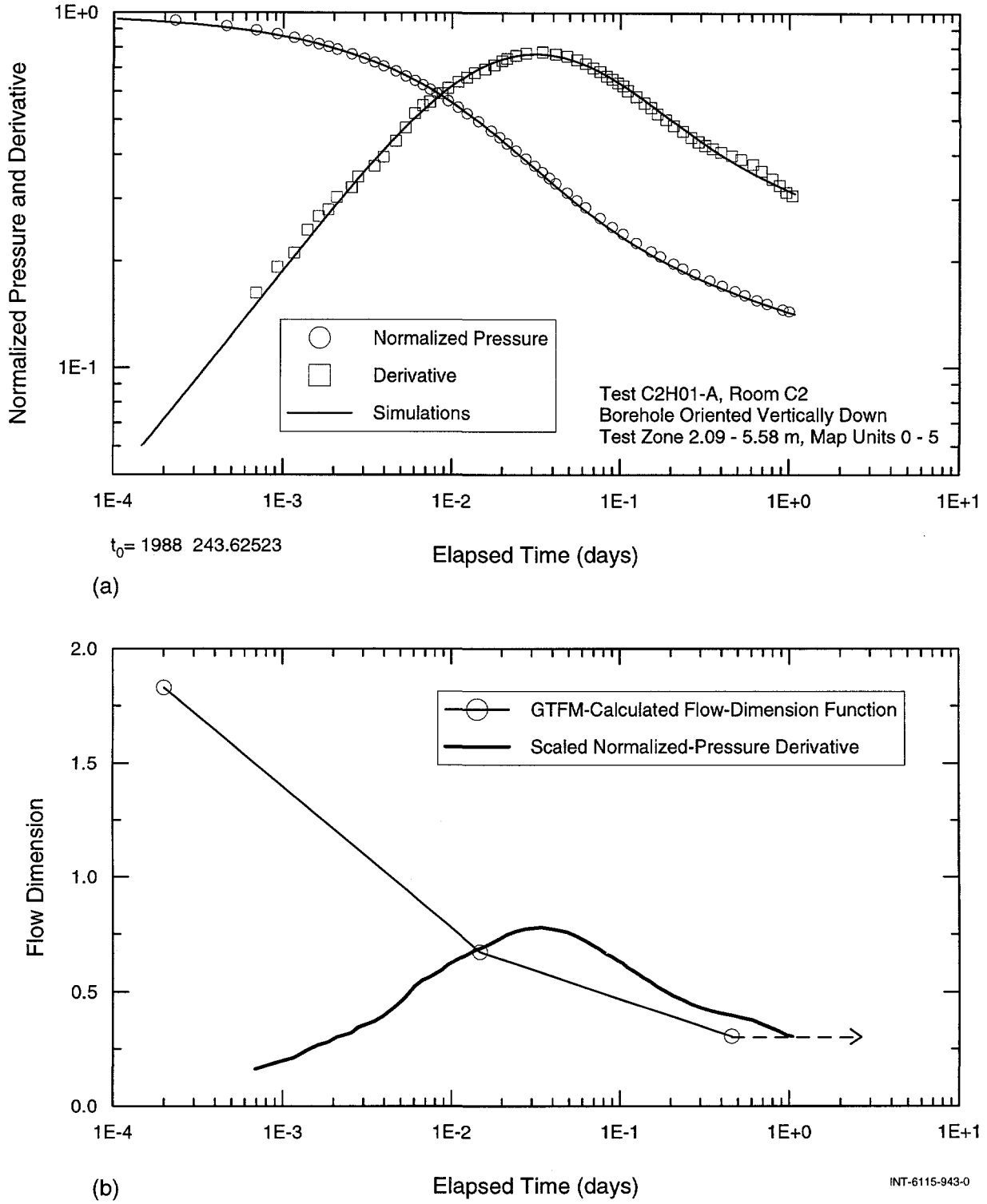

Figure A-2. Log-log and semilog plots of GTFM simulation (a) and flow-dimension function (b) of the C2H01-A test-zone pulse-injection test #2.

pressure data and derivatives, respectively. Figures A-1b and A-2b show the flow-dimension functions calculated by GTFM for each of the simulations. Both of the PI tests were simulated as variable-flow-dimension systems (*n(r)*), with both tests exhibiting low *n* at late times. Figures A-1b and A-2b also show that the low late-time GTFM estimates of *n* are in qualitative agreement with those indicated by the late-time flow-dimension diagnostic plots (Section 6.2.2.2). Figure A-3 shows the best-fit GTFM simulations compared to the observed pressures for the C2H01-A PI tests for the two analyses discussed above. The test-zone pressures were compensated by adding 0.058 MPa to the pressures measured by the pressure transducers.

A.3 C2H01-B Test Zone, 9/88 – 2/89

Estimates of the C2H01-B test-zone fitting parameters presented in Table A-1 were obtained by simultaneously matching the PI test and the first pulse-withdrawal test (PW1). Quantitative estimates of the fitting-parameter uncertainty (95% joint-confidence regions) and the corresponding correlation matrices are presented in Appendix C. Figures A-4 and A-5 show the best-fit GTFM simulations compared to the PI and PW1 normalized-pressure data and derivatives, respectively, along with the flow-dimension functions calculated by GTFM. Figure A-6 shows the best-fit GTFM simulation compared to the observed pressures for the C2H01-B test zone. The test-zone pressures were compensated by adding 0.073 MPa to the pressures measured by the pressure transducers.

A.4 C2H01-B Guard Zone, 9/88 – 2/89

Estimates of the C2H01-B guard-zone fitting parameters presented in Table A-1 were obtained by matching the guard-zone response to the first PW test performed in the test zone. (The guard zone responded to a test in the test zone because of tool compliance.) Quantitative estimates of the fitting-parameter uncertainty (95% joint-confidence regions) and the corresponding correlation matrices are presented in Appendix C. Figure A-7a shows the best-fit GTFM simulation compared to the "pulse-withdrawal" normalized-pressure data and derivative. The flow-dimension function calculated by GTFM is shown in Figure A-7b. Figure A-8 shows the best-fit GTFM simulation compared to the observed pressures for the C2H01-B guard zone. The guard-zone pressures were compensated by adding 0.053 MPa to the pressures measured by the pressure transducers.

A.5 C2H01-C Test Zone, 2/89 – 5/89

Estimates of the C2H01-C test-zone fitting parameters presented in Table A-1 were obtained by matching the first 0.6 days of the PW2 response, prior to the development of a leak in the system. Quantitative estimates of the fitting-parameter uncertainty (95% joint-confidence regions) and the corresponding correlation matrices are presented in Appendix C. Figure A-9 shows the best-fit GTFM simulation compared to the PW2 normalized-pressure data and derivative along with the flow-dimension function calculated by GTFM. Figure A-10 shows the best-fit GTFM simulation compared to the observed pressures for the C2H01-C test zone along

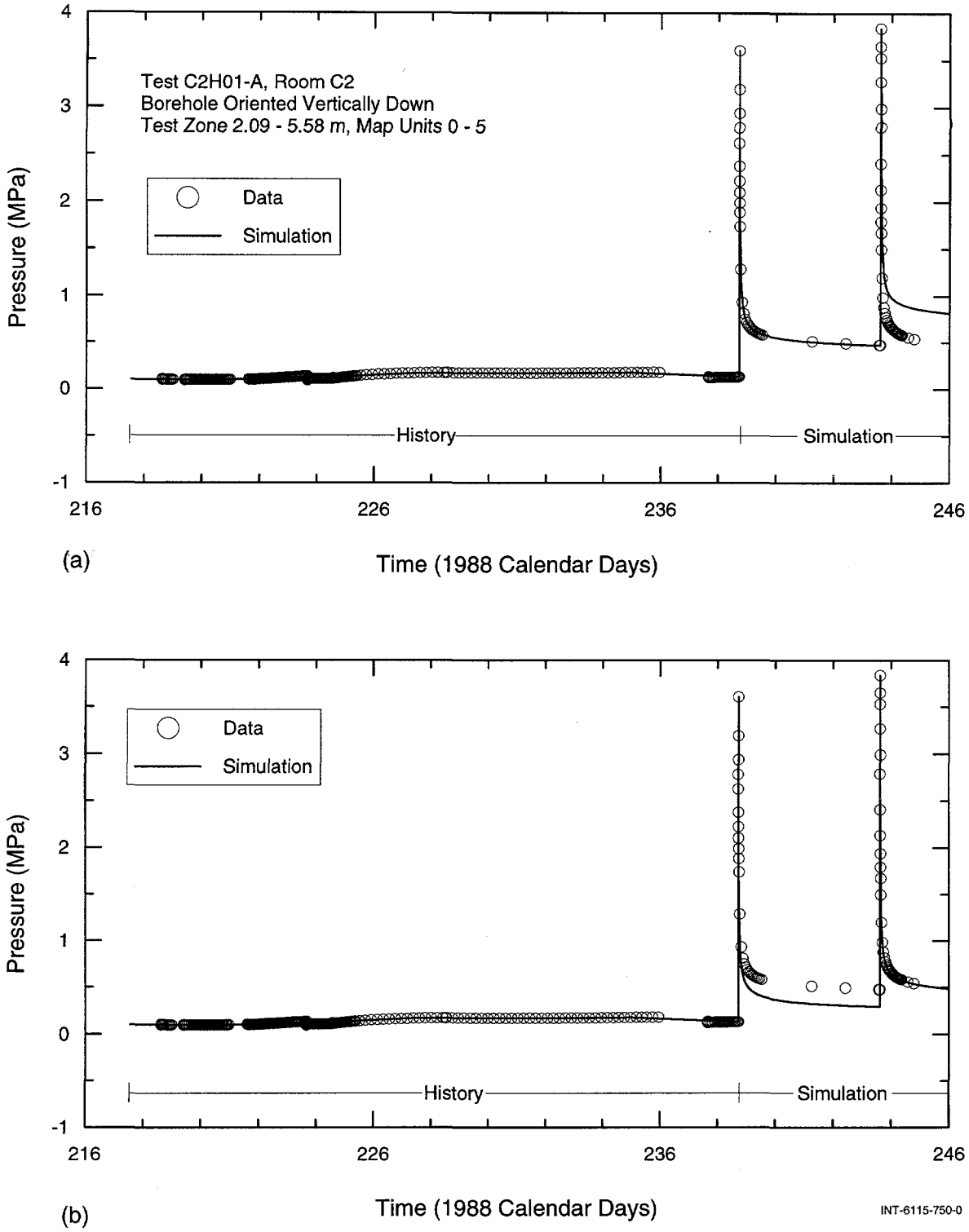

Figure A-3. Linear-linear plots of GTFM simulations of pressures during the C2H01-A test-zone pulse-injection tests #1 (a) and #2 (b).

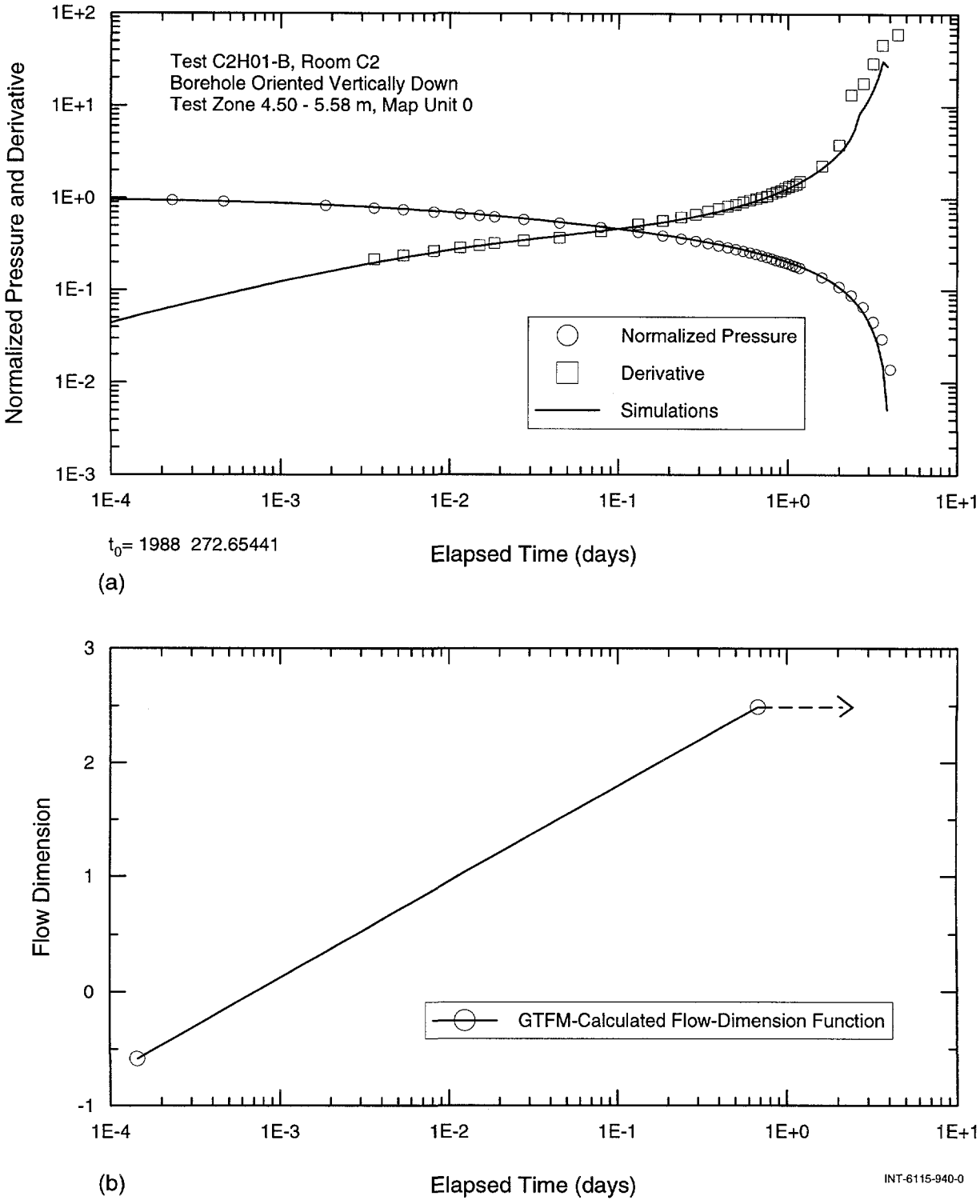

Figure A-4. Log-log and semilog plots of GTFM simulation (a) and flow-dimension function (b) of the C2H01-B test-zone pulse-injection test.

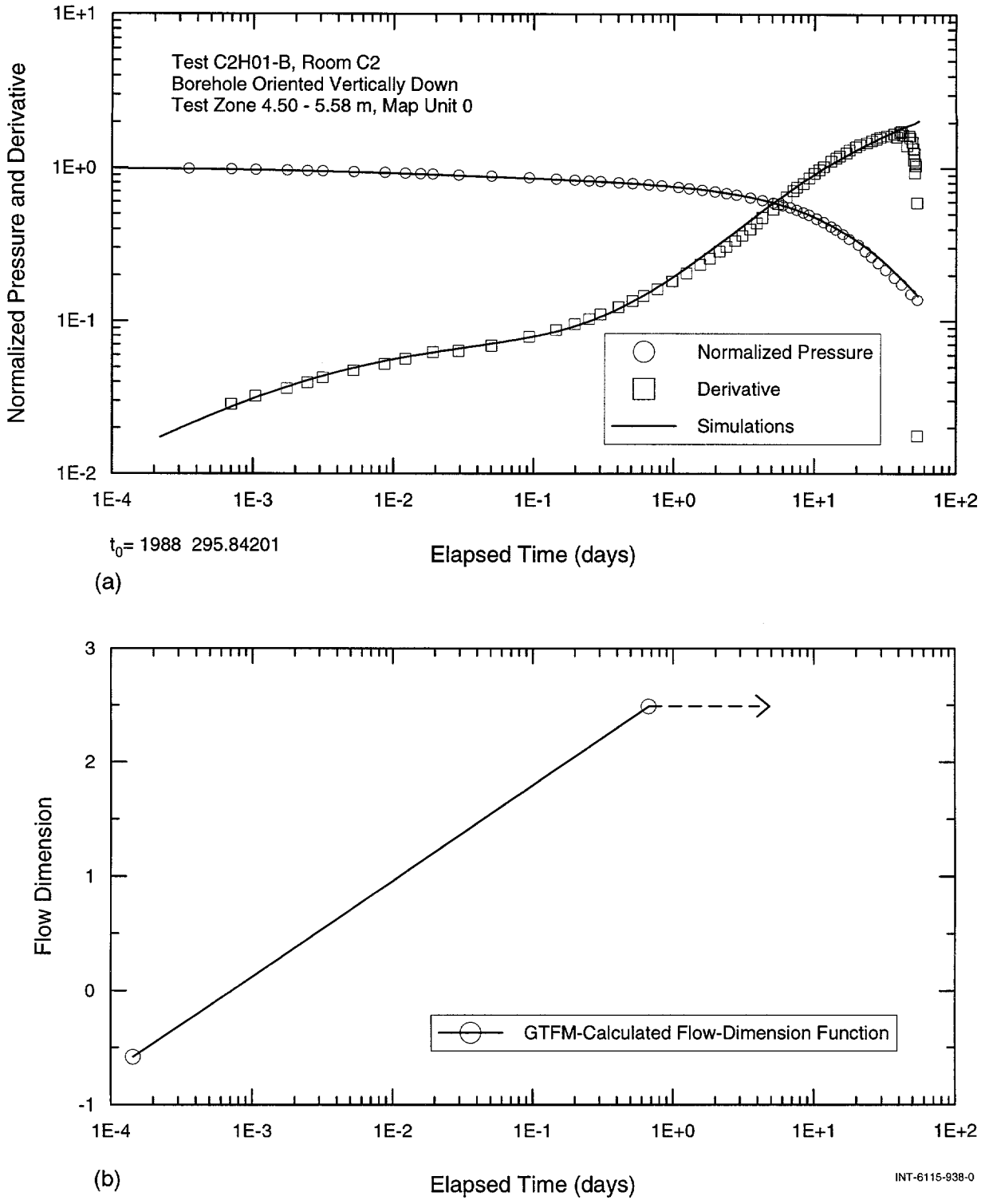

Figure A-5. Log-log and semilog plots of GTFM simulation (a) and flow-dimension function (b) of the C2H01-B test-zone pulse-withdrawal test #1.

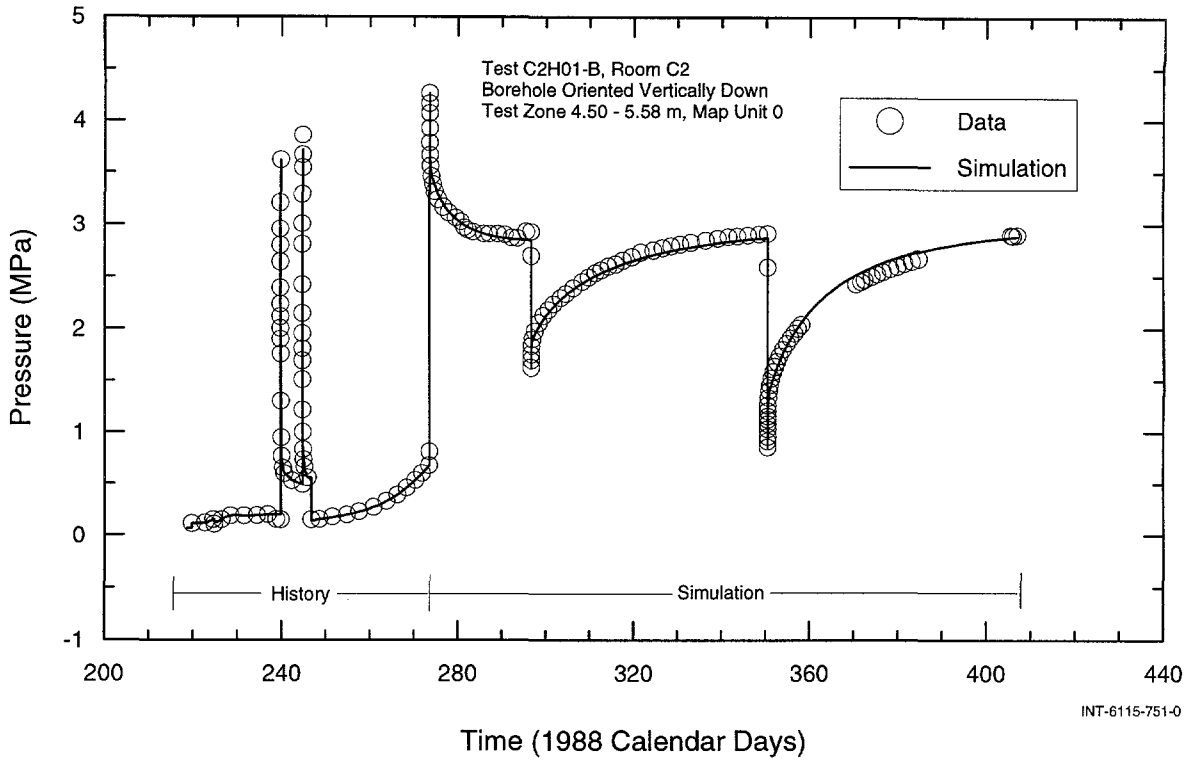

Figure A-6. Linear-linear plot of GTFM simulation of the C2H01-B test-zone test-sequence pressures.

with an inset showing the leak-dominated portion of the response. The test-zone pressures were compensated by adding 0.099 MPa to the pressures measured by the pressure transducers.

A.6 C2H02 Test Zone, 4/89 – 12/89

Estimates of the C2H02 test-zone fitting parameters presented in Table A-1 were obtained by matching the PW3 response. Quantitative estimates of the fitting-parameter uncertainty (95% joint-confidence regions) and the corresponding correlation matrices are presented in Appendix C. Figure A-11 shows the best-fit GTFM simulation compared to the PW3 normalized-pressure data and derivative along with the flow-dimension function calculated by GTFM. Figure A-12 shows the best-fit GTFM simulation compared to the observed pressures for the C2H02 test zone. The test-zone pressures were compensated by adding 0.098 MPa to the pressures measured by the pressure transducers.

A.7 S0P01 Test Zone, 1/89 – 7/89

Estimates of the S0P01 test-zone fitting parameters presented in Table A-1 were obtained by simultaneously matching the shut in and PW2 responses. Quantitative estimates of the fitting-

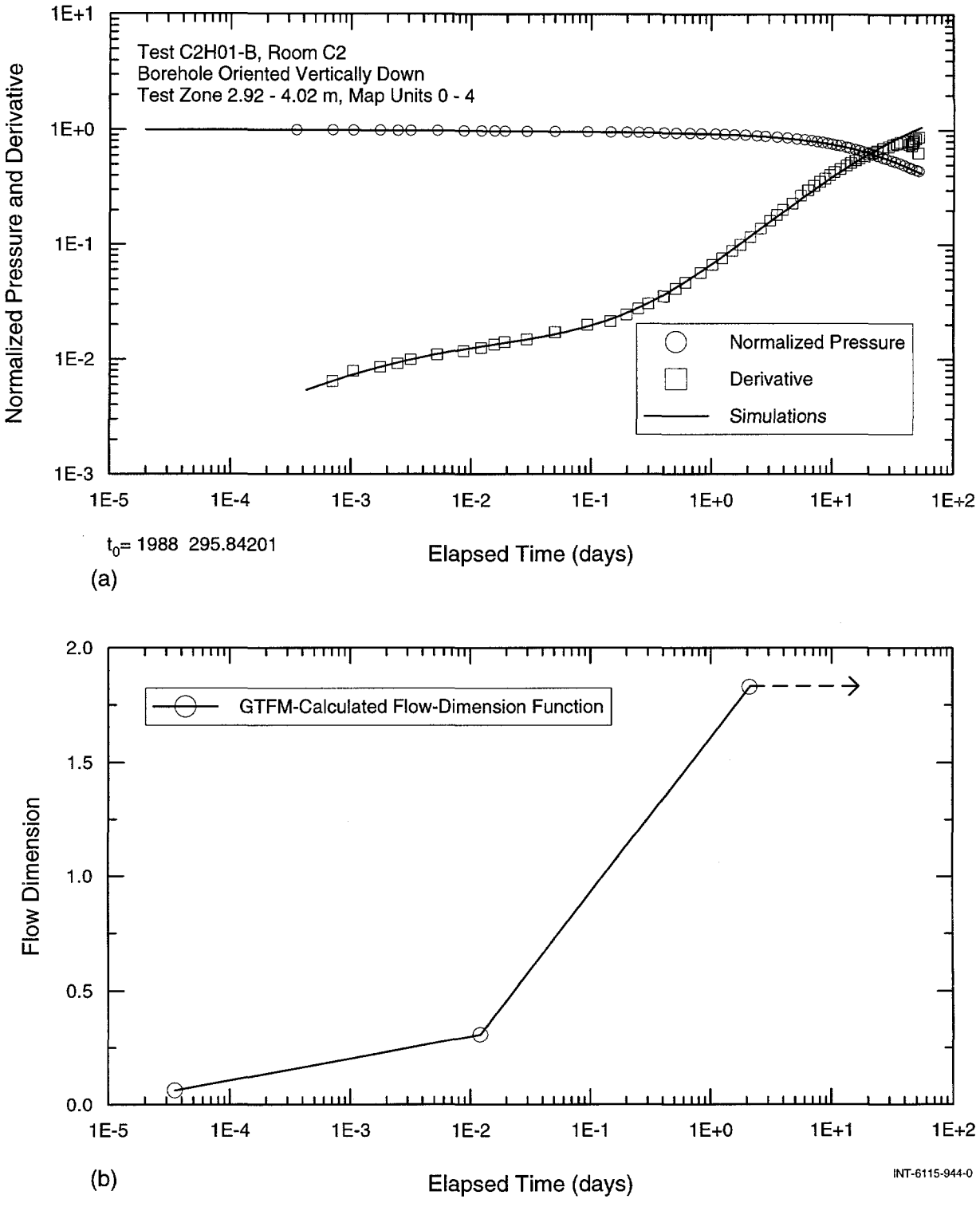

Figure A-7. Log-log and semilog plots of GTFM simulation (a) and flow-dimension function (b) of the C2H01-B guard-zone pulse-withdrawal test #1.

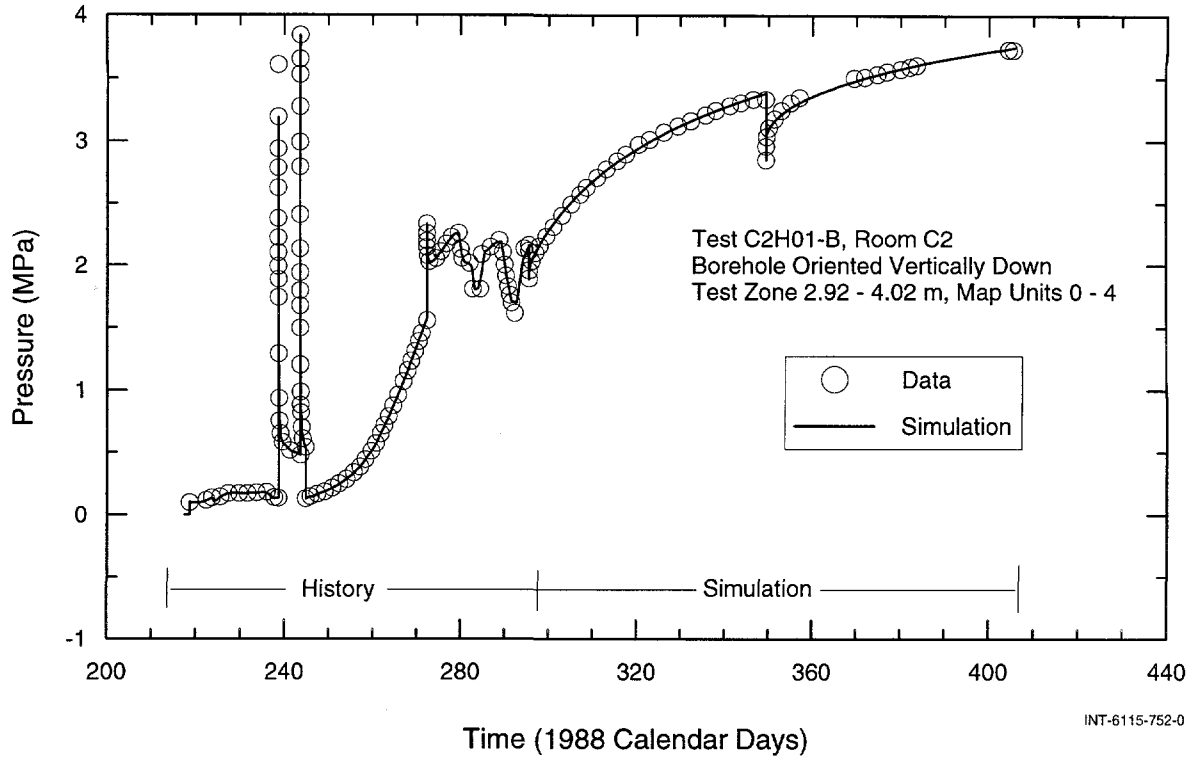

Figure A-8. Linear-linear plot of GTFM simulation of the C2H01-B guard-zone test-sequence pressures.

parameter uncertainty (95% joint-confidence regions) and the corresponding correlation matrices are presented in Appendix C. Figure A-13 shows the best-fit GTFM simulation compared to the PW2 normalized-pressure data and derivative along with the flow-dimension function calculated by GTFM. Figure A-14 shows the best-fit GTFM simulation compared to the observed pressures for the S0P01 test zone. The test-zone pressures were compensated by adding 0.065 MPa to the pressures measured by the pressure transducers.

A.8 S1P71-B Test Zone, 7/89 – 3/90

The two PW tests could not be matched adequately with a single parameter set and were, consequently, analyzed separately. The estimates of the fitting parameters from these two analyses are presented in Table A-1. Quantitative estimates of the fitting-parameter uncertainty (95% joint-confidence regions) and the corresponding correlation matrices are presented in Appendix C. Figures A-15 and A-16 show the best-fit GTFM simulations compared to the PW1 and PW2 normalized-pressure data and derivatives, respectively, along with the flow-dimension functions calculated by GTFM. The inability to match pulse responses of different magnitudes simultaneously was also noted in the S1P74-B test zone 2 analysis (Section 7.5.2). In both cases, we believe that the larger magnitude pulses were more affected by compliance than the smaller magnitude pulses. As with the S1P74-B test zone 2 pulse analyses, similar estimates

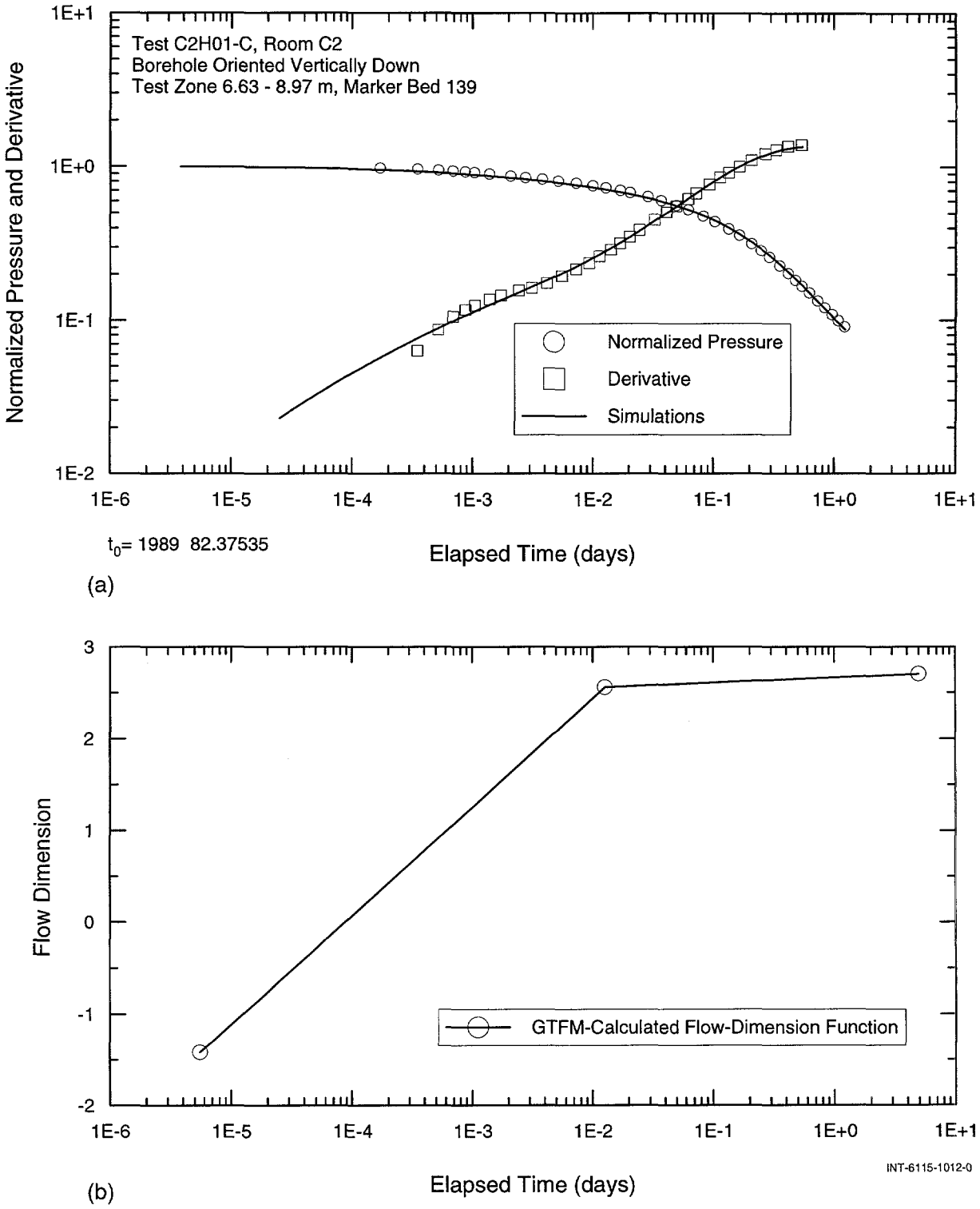

Figure A-9. Log-log and semilog plots of GTFM simulation (a) and flow-dimension function (b) of the C2H01-C pulse-withdrawal test #2.

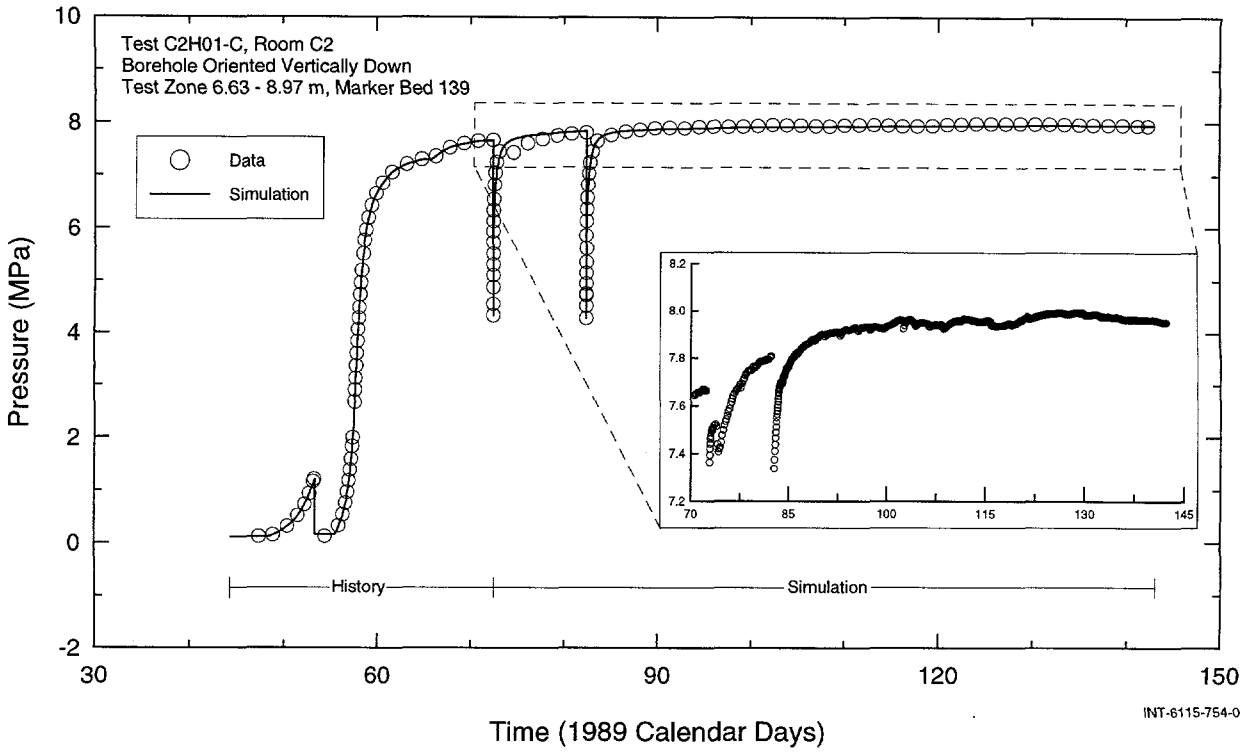

Figure A-10. Linear-linear plot of GTFM simulation of the C2H01-C test-sequence pressures.

of K were obtained from each of the S1P71-B pulse analyses, even with the varying compliance effects (Table A-1). Figure A-17 shows GTFM simulations using the parameter sets derived from both analyses compared to the observed pressures for the S1P71-B test zone. The test-zone pressures were compensated by adding 0.131 MPa to the pressures measured by the pressure transducers.

A.9 S1P73-B Test Zone, 1/91 – 6/91

The responses of the various types of tests (PW, CPW, and pressure buildup (PB)) performed during the S1P73-B testing sequence could not be simultaneously matched with a single parameter set. Possible reasons include a leak observed in the pressure response when the test-zone pressure exceeded approximately 4.15 MPa (Figure A-18). Consequently, estimates of the S1P73-B test-zone fitting parameters presented in Table A-1 were obtained by matching only the CPW response. Quantitative estimates of the fitting-parameter uncertainty (95% joint-confidence regions) and the corresponding correlation matrices are presented in Appendix C. Figures A-19 and A-20a show the best-fit GTFM simulations compared to the cumulative production for the CPW test and the calculated flow rates during the CPW test, respectively. The flow-dimension function calculated by GTFM is shown in Figure A-20b. Figure A-20b also shows the flow dimension calculated from the scaled derivative of the CPW data (Section 6.2.2.2). The test-zone pressures were compensated by subtracting 0.168 MPa from the pressures measured by the pressure transducers.

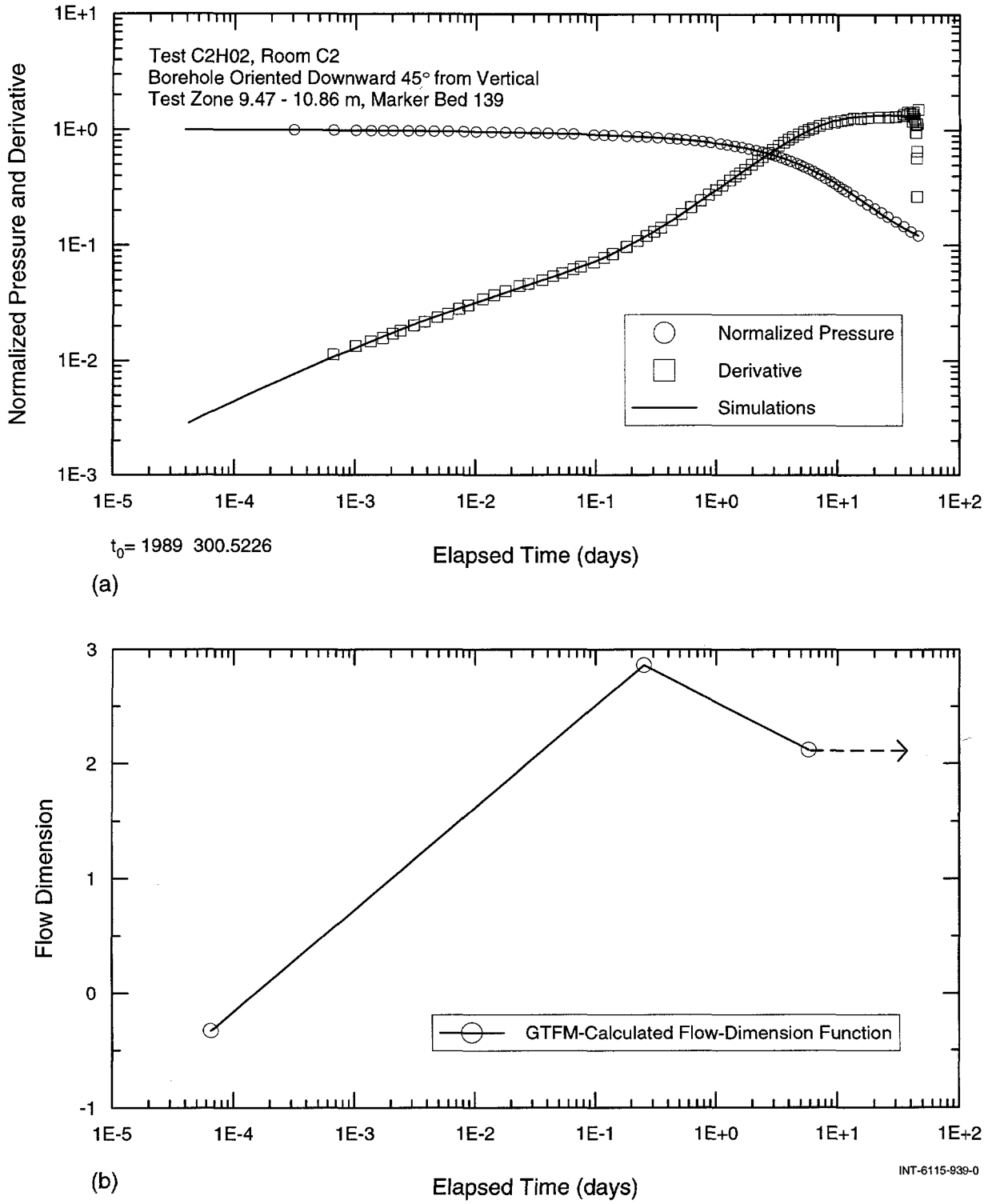

Figure A-11. Log-log and semilog plots of GTFM simulation (a) and flow-dimension function (b) of the C2H02 pulse-withdrawal test #3.

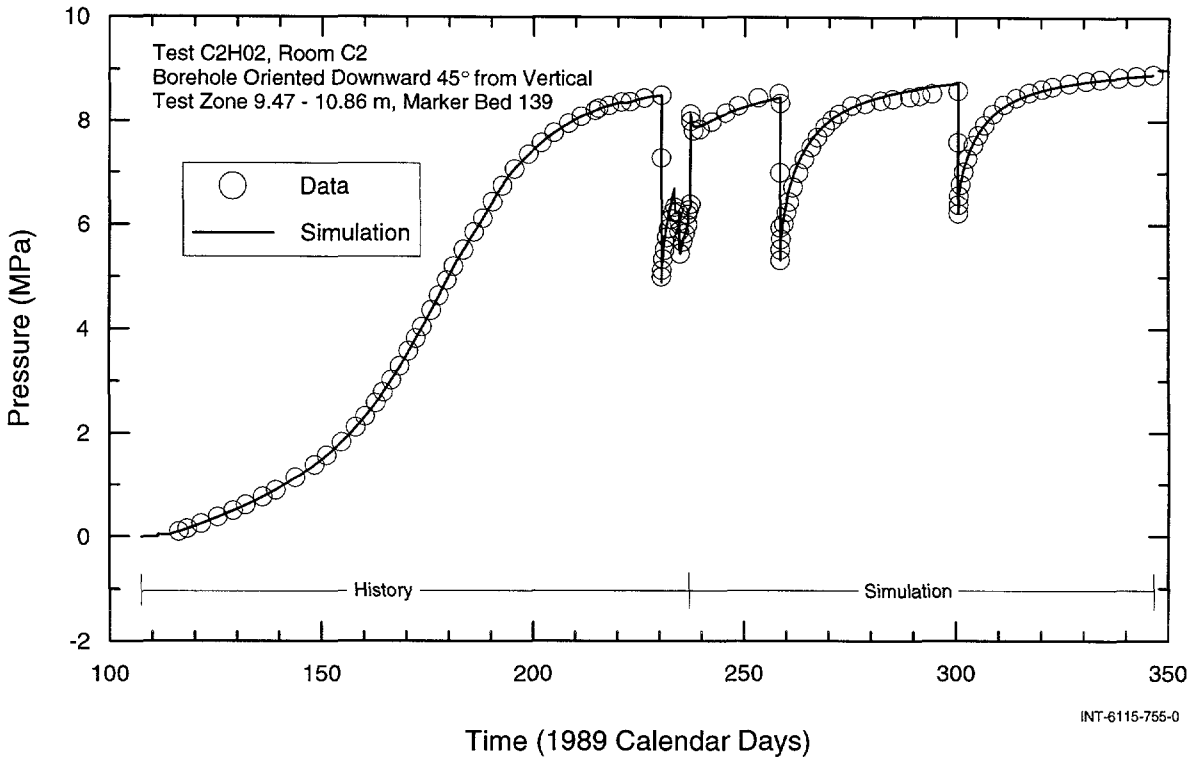

Figure A-12. Linear-linear plot of GTFM simulation of the C2H02 test-sequence pressures.

A.10 SCP01-A Test Zone, 4/90 – 10/90

The estimates of the SCP01-A test-zone fitting parameters presented in Table A-1 were obtained by simultaneously matching the CPW2 and PB2 responses. All of the previous test events were affected by leaks and/or test-tool movement. Quantitative estimates of the fitting-parameter uncertainty (95% joint-confidence regions) and the corresponding correlation matrices are presented in Appendix C. The best-fit GTFM simulations compared to the cumulative production for the CPW2 test, the calculated flow rates during the CPW2 test, the pressure change and derivative from the PB2 test, and the observed pressures for the SCP01-A testing period are shown in Figures A-21, A-22, A-23, and A-24, respectively. Figure A-25 shows the GTFM-estimated flow-dimension value along with the flow-dimension diagnostic plots calculated from the CPW2 and PB2 test data (Section 6.2.2.2). The test-zone pressures were compensated by adding 0.040 MPa to the pressures measured by the pressure transducers.

A.11 L4P51-B Test Zone, 10/90 – 12/91

Previous analysis could not be improved.

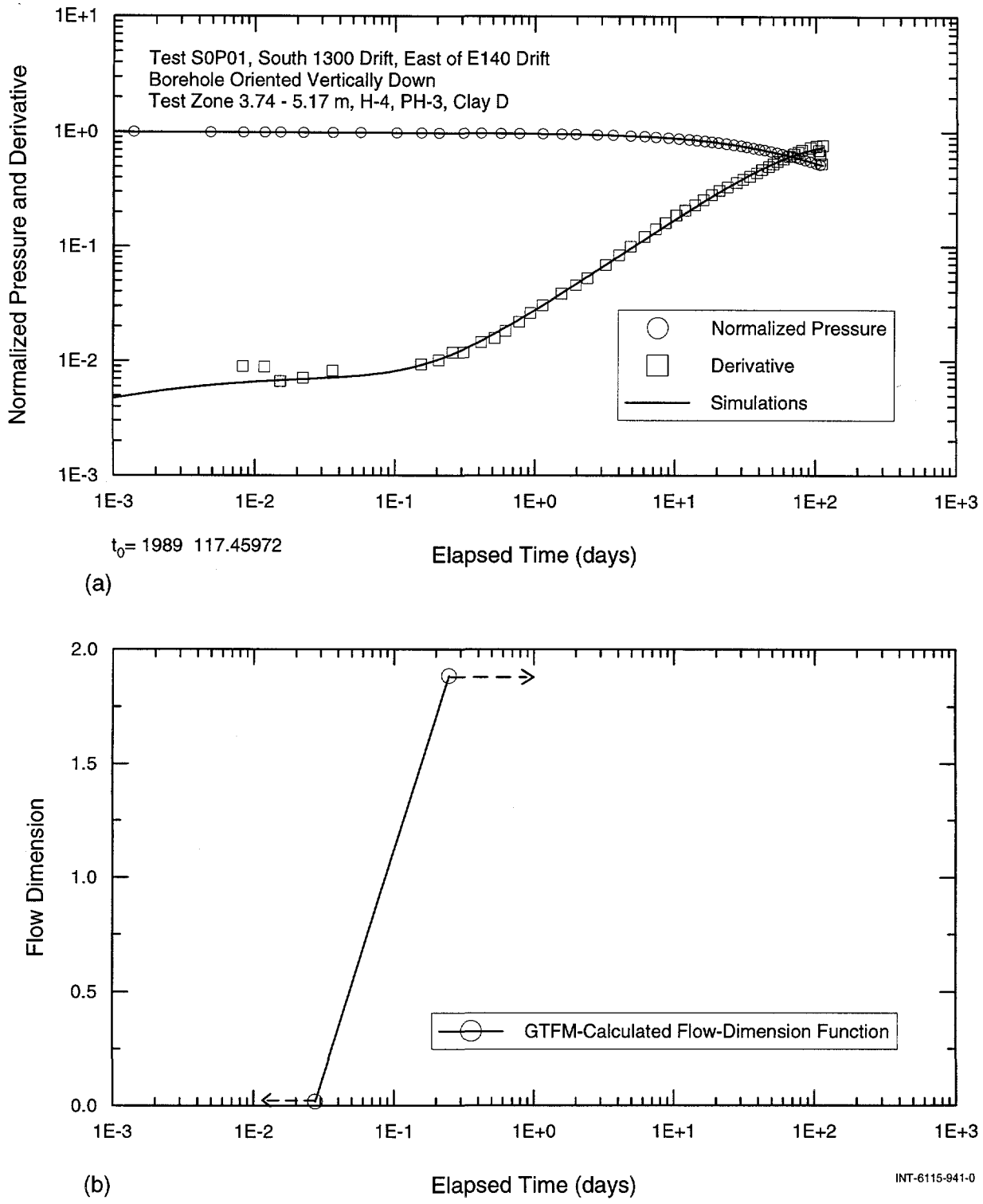

Figure A-13. Log-log and semilog plots of GTFM simulation (a) and flow-dimension function (b) of the S0P01 pulse-withdrawal test #2.

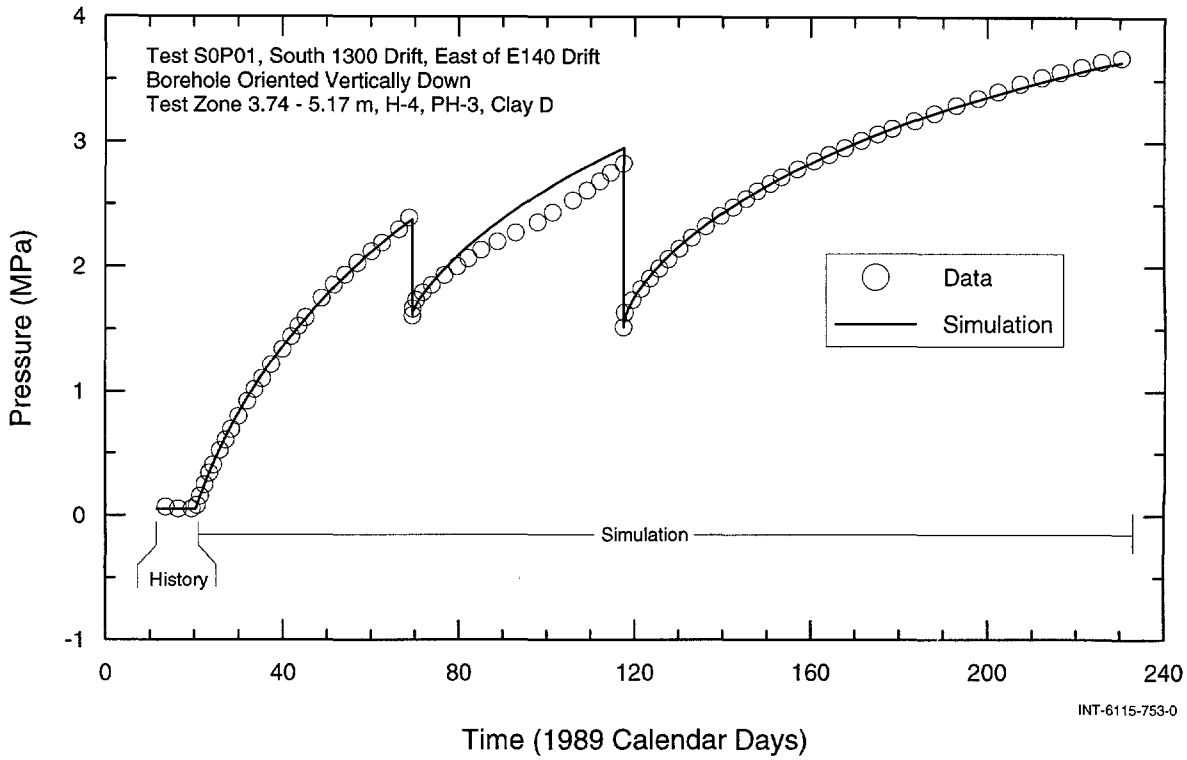

Figure A-14. Linear-linear plot of GTFM simulation of the S0P01 test-sequence pressures.

A.12 L4P52-A Test Zone, 4/91 – 7/92

The estimates of the L4P52-A test-zone fitting parameters presented in Table A-1 were obtained by matching the PW2 response. The data from the remaining tests were either too noisy to be used or affected by leaks in the system. Quantitative estimates of the fitting-parameter uncertainty (95% joint-confidence regions) and the corresponding correlation matrices are presented in Appendix C. Figure A-26 shows the best-fit GTFM simulations compared to the PW2 normalized-pressure data and derivative along with the flow-dimension function calculated by GTFM. Figure A-27 shows the best-fit GTFM simulation compared to the observed pressures for the L4P52-A test zone. The test-zone pressures were compensated by subtracting 0.078 MPa from the pressures measured by the pressure transducers.

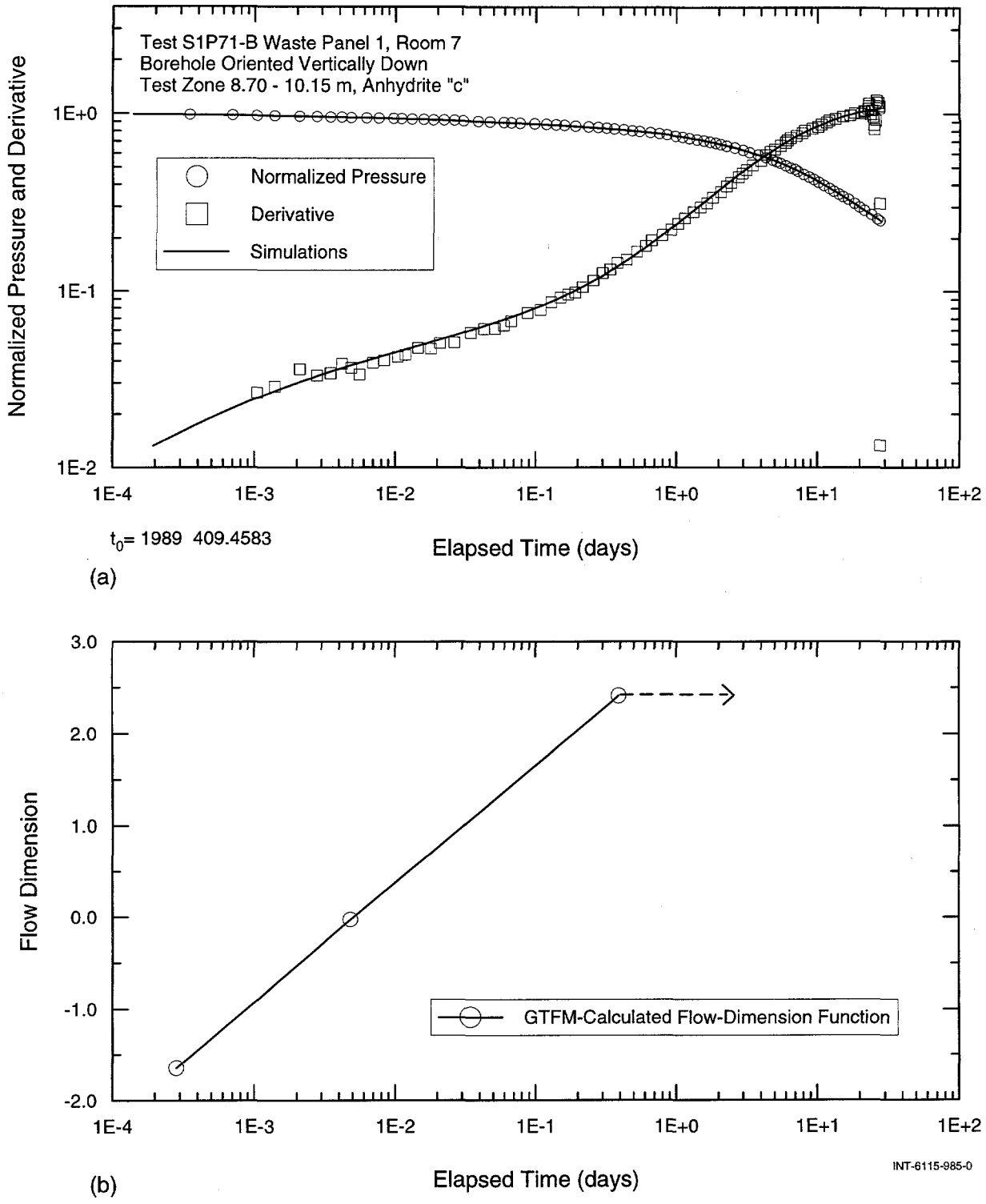

Figure A-15. Log-log and semilog plots of GTFM simulation (a) and flow-dimension function (b) of the S1P71-B pulse-withdrawal test #1.

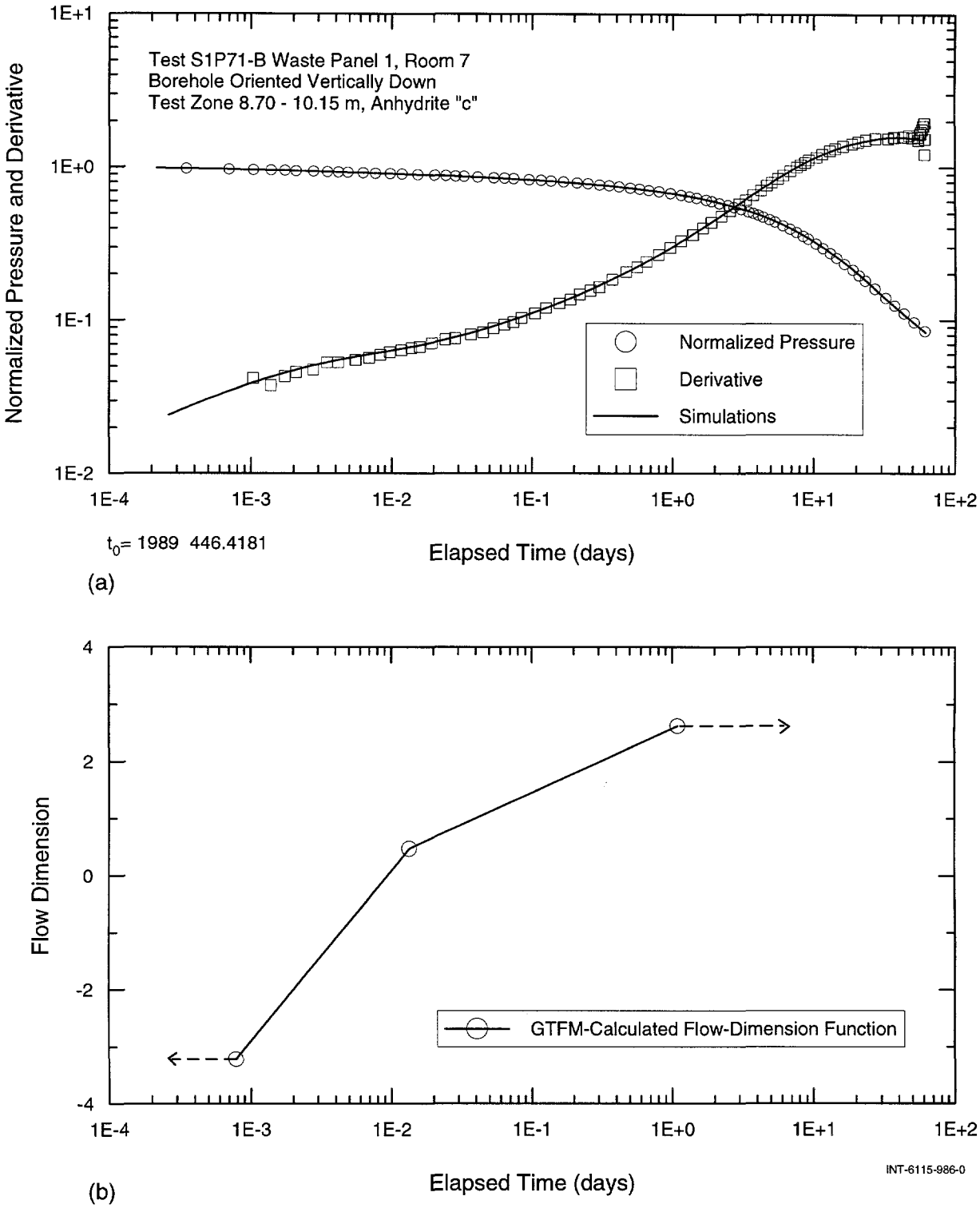

Figure A-16. Log-log and semilog plots of GTFM simulation (a) and flow-dimension function (b) of the S1P71-B pulse-withdrawal test #2.

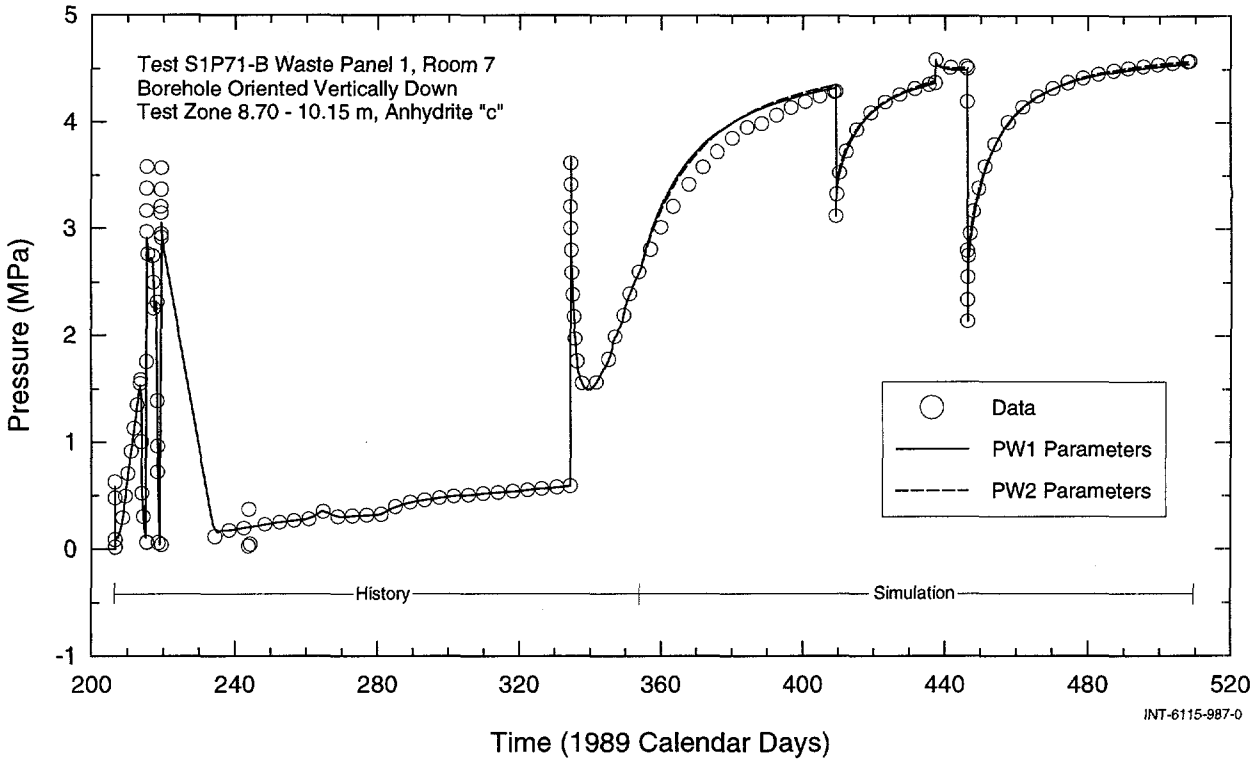

Figure A-17. Linear-linear plot of GTFM simulations of the S1P71-B test-sequence pressures.

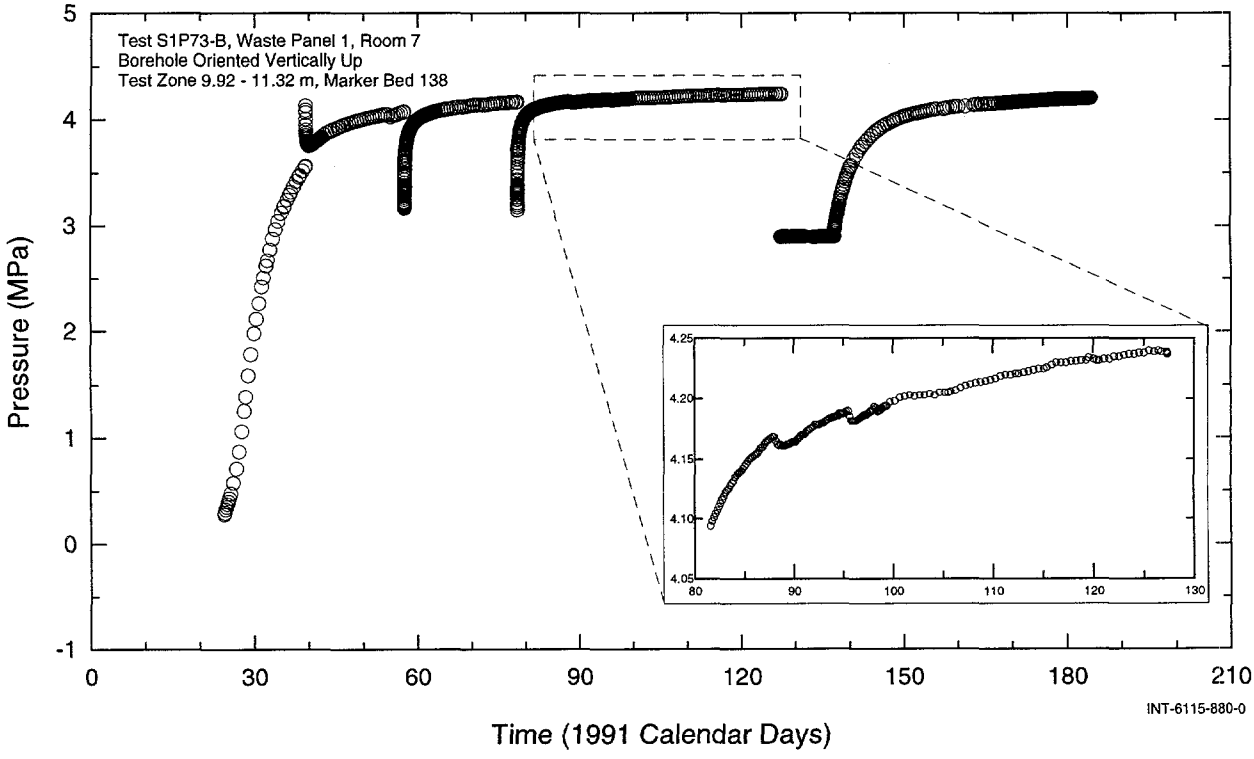

Figure A-18. Pressures observed during S1P73-B test sequence.

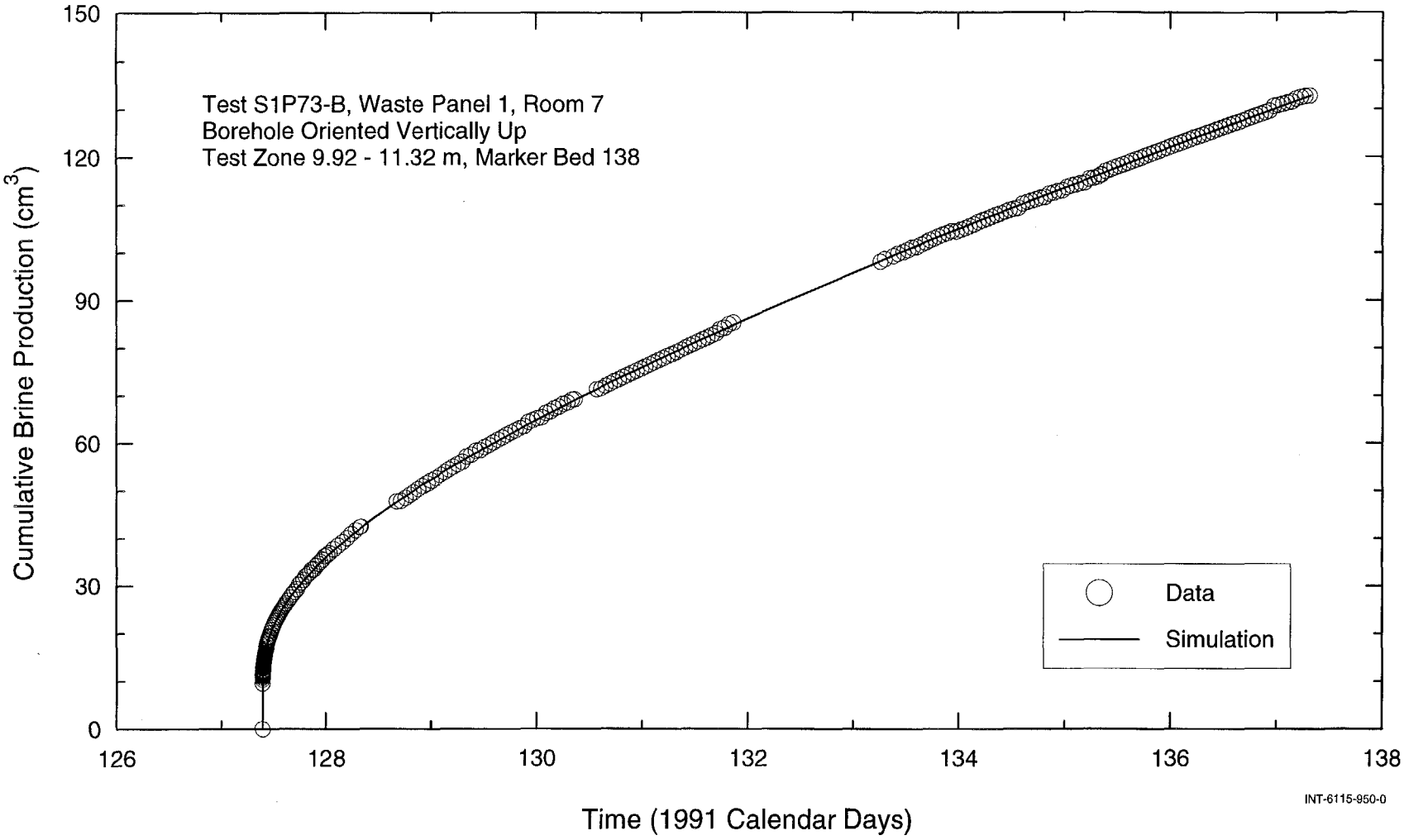

Figure A-19. GTFM simulation of cumulative brine production during the S1P73-B constant-pressure-withdrawal test.

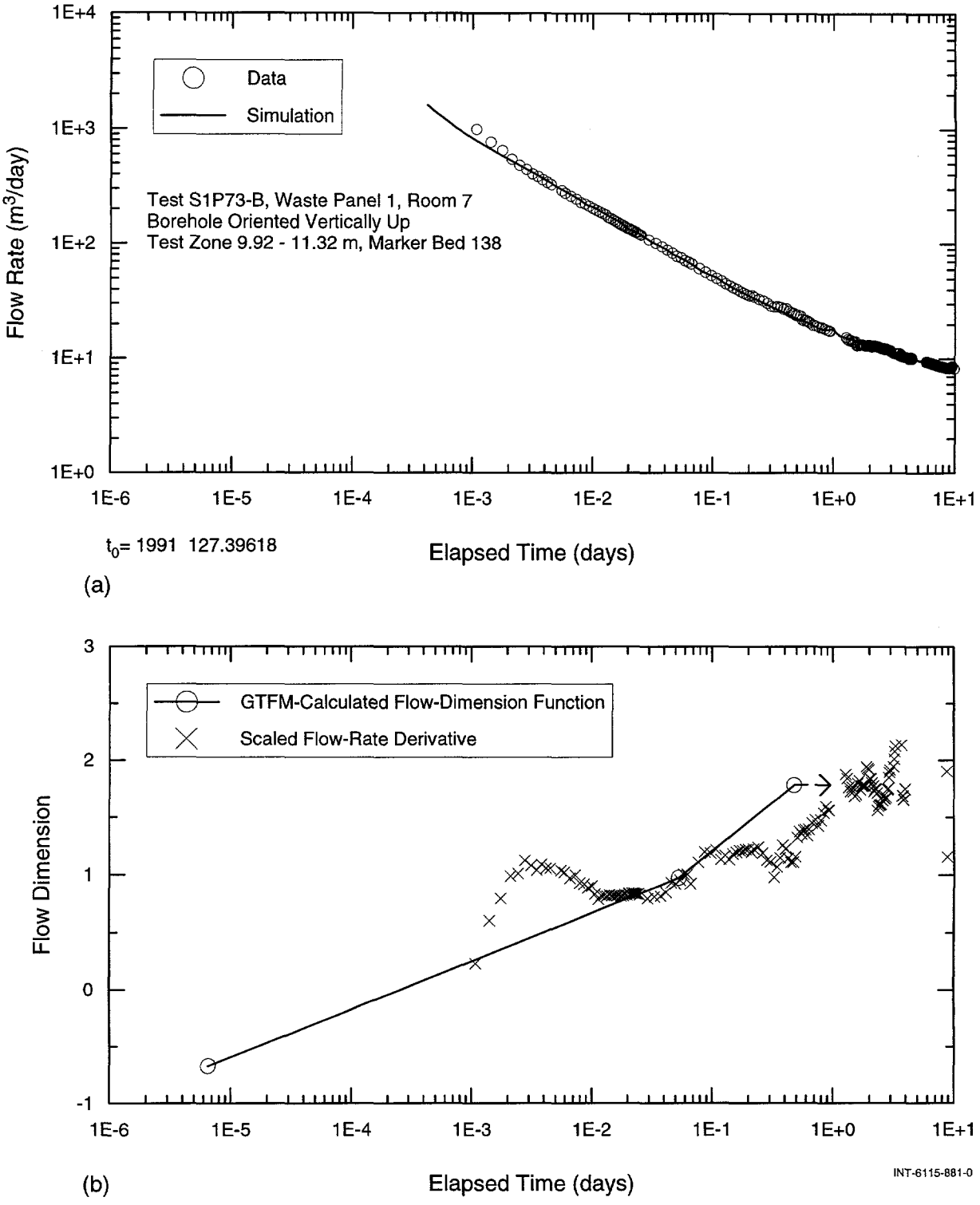

Figure A-20. Log-log and semilog plots of GTFM simulation of flow rates (a) and flow-dimension function (b) during the S1P73-B constant-pressure-withdrawal test.

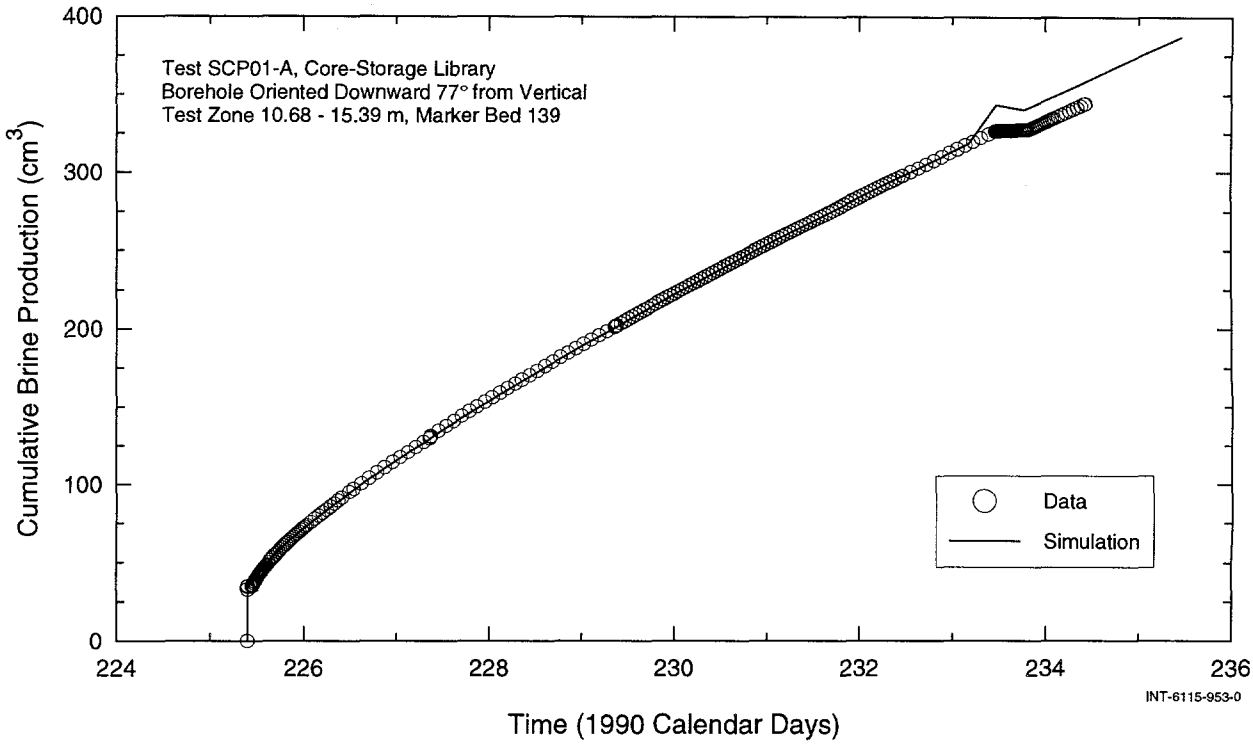

Figure A-21. GTFM simulation of cumulative brine production during the SCP01-A constant-pressure-withdrawal test #2.

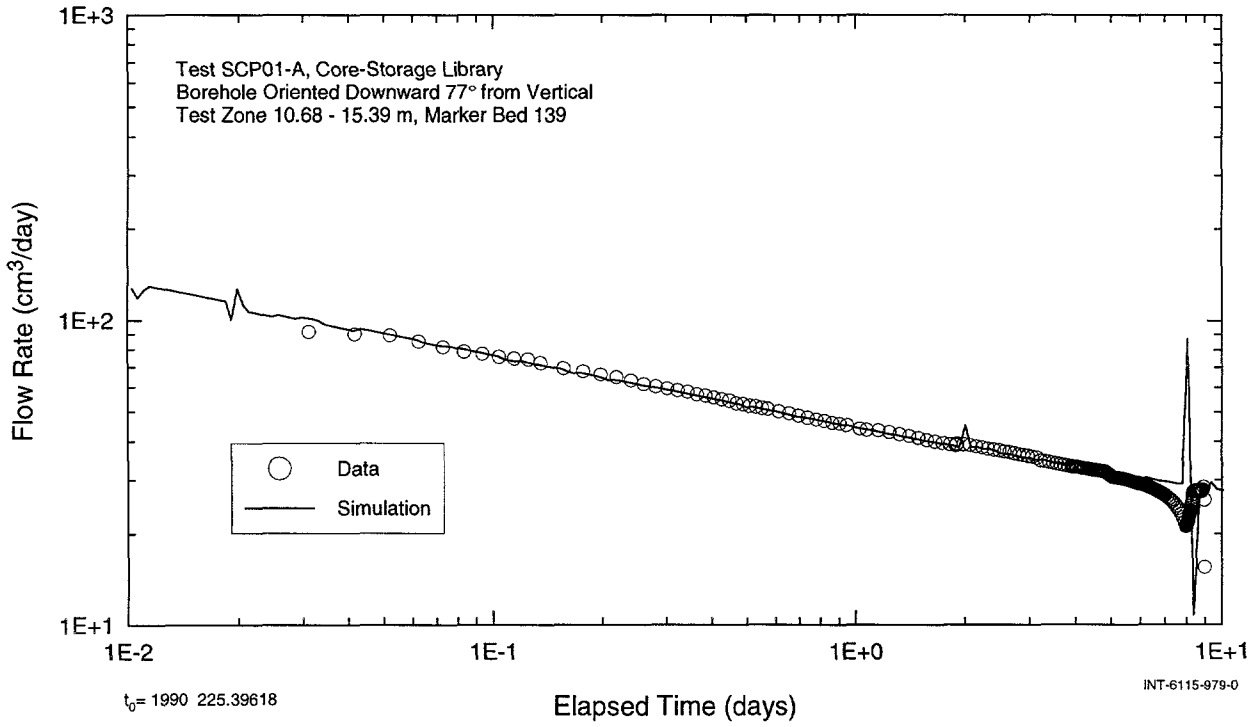

Figure A-22. Log-log plot of GTFM simulation of flow rates during the SCP01-A constant-pressure-withdrawal test #2.

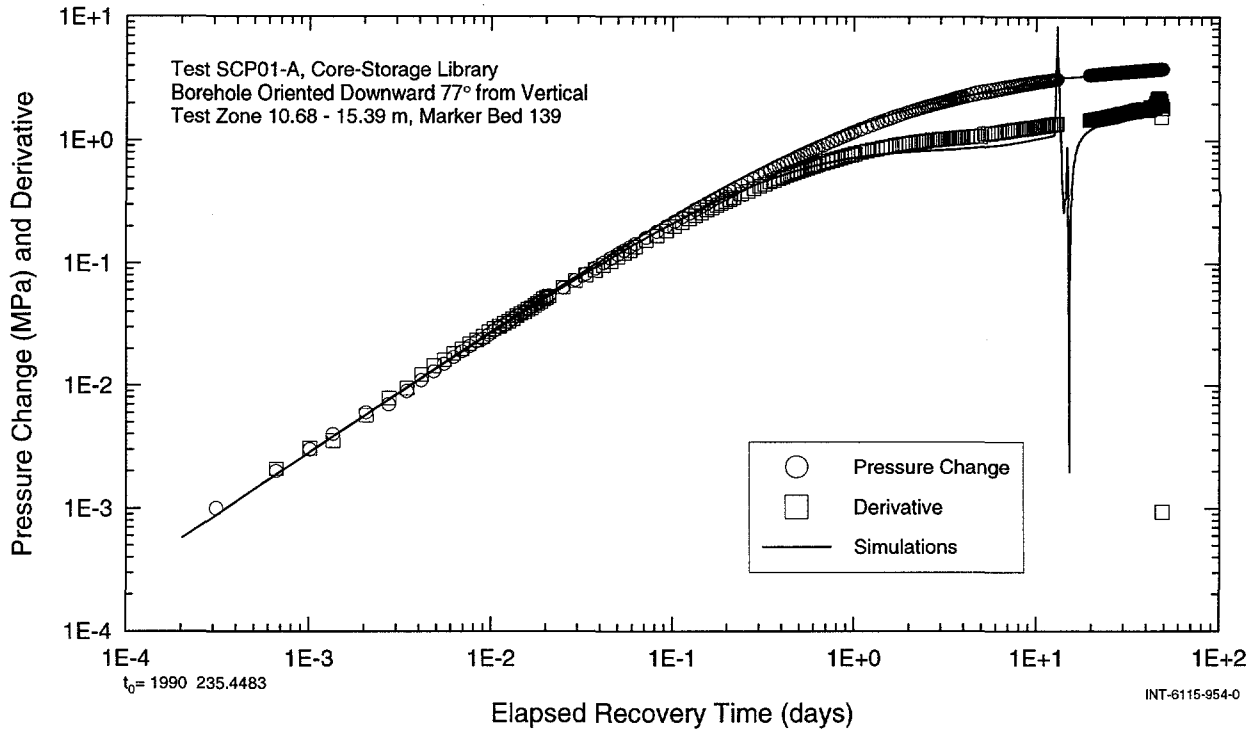

Figure A-23. Log-log plot of GTFM simulation of pressure change and derivative during the SCP01-A pressure-buildup test #2.

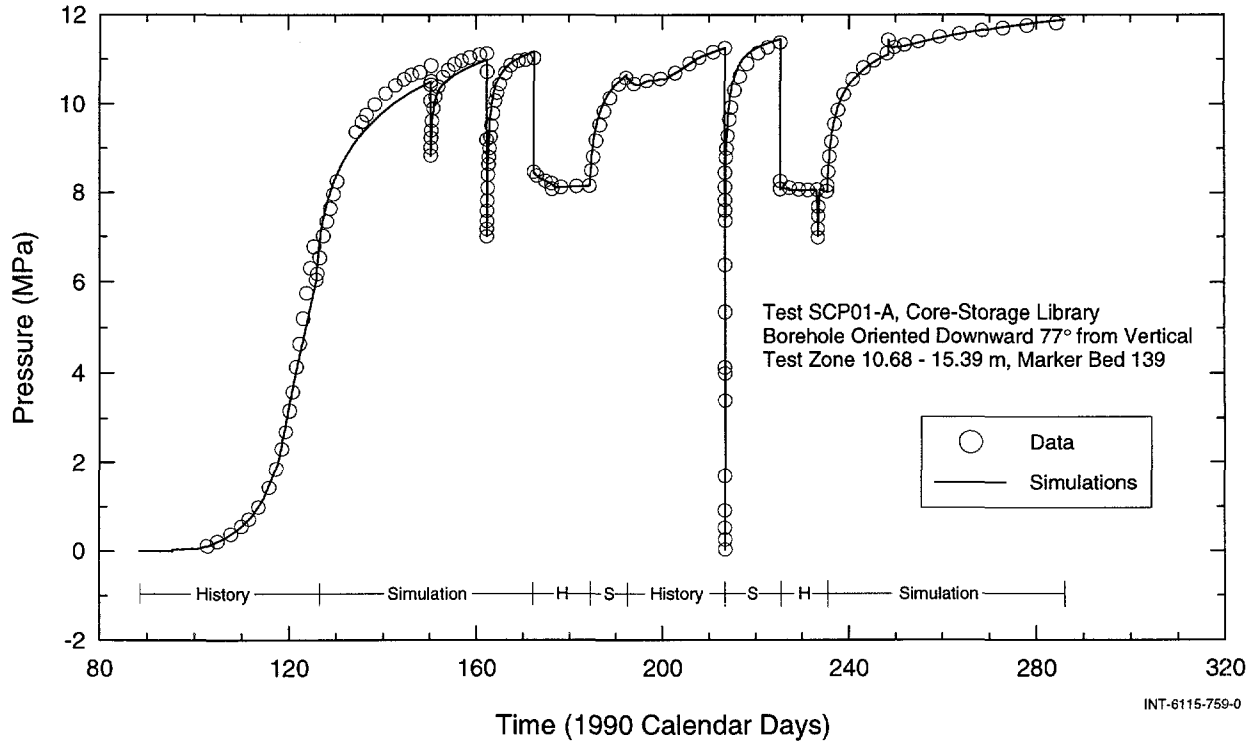

Figure A-24. Linear-linear plot of GTFM simulation of the SCP01-A test-sequence pressures.

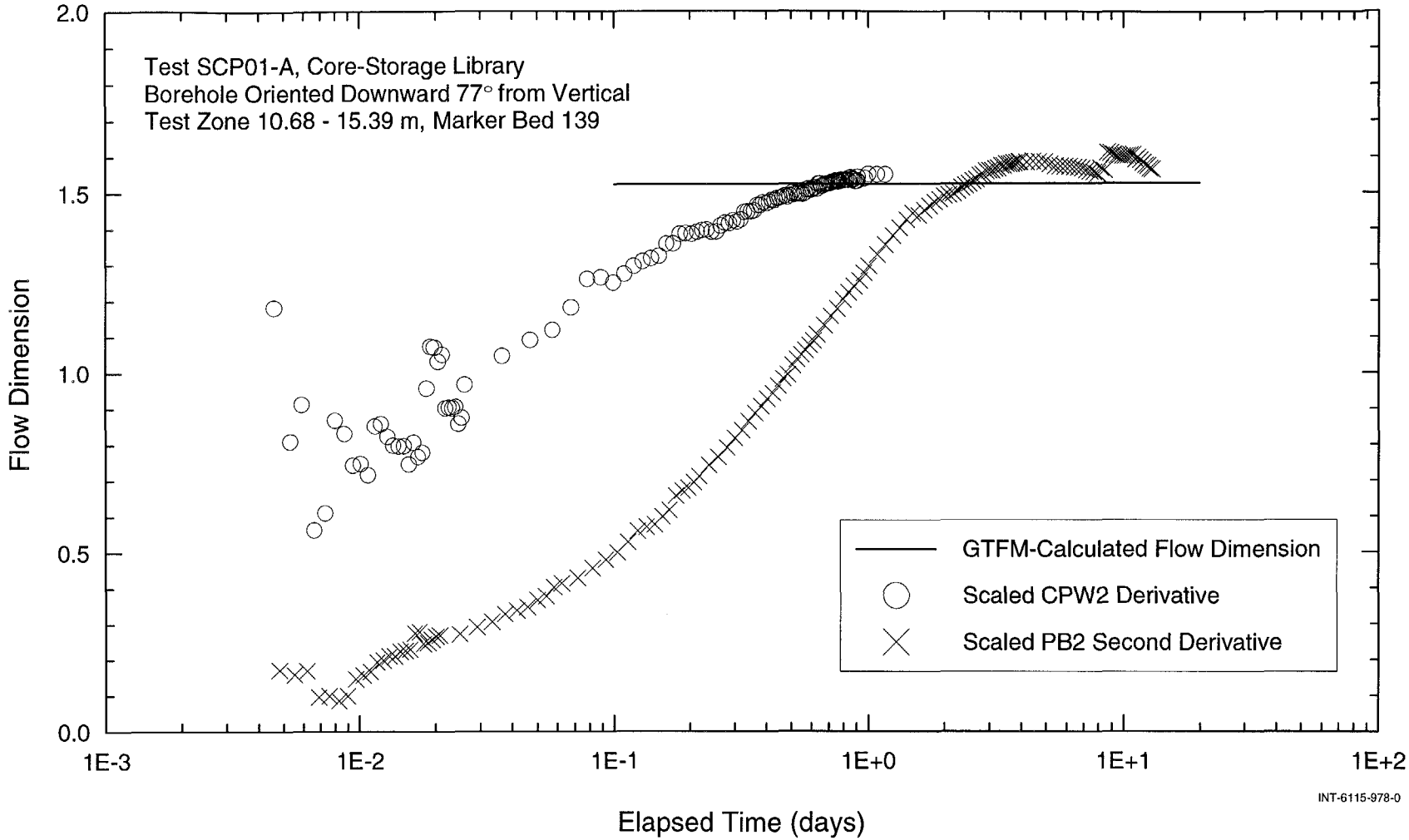

Figure A-25. Semilog plot of GTFM-calculated flow dimension and scaled derivatives from the SCP01-A constant-pressure-withdrawal test #2 and pressure-buildup test #2.

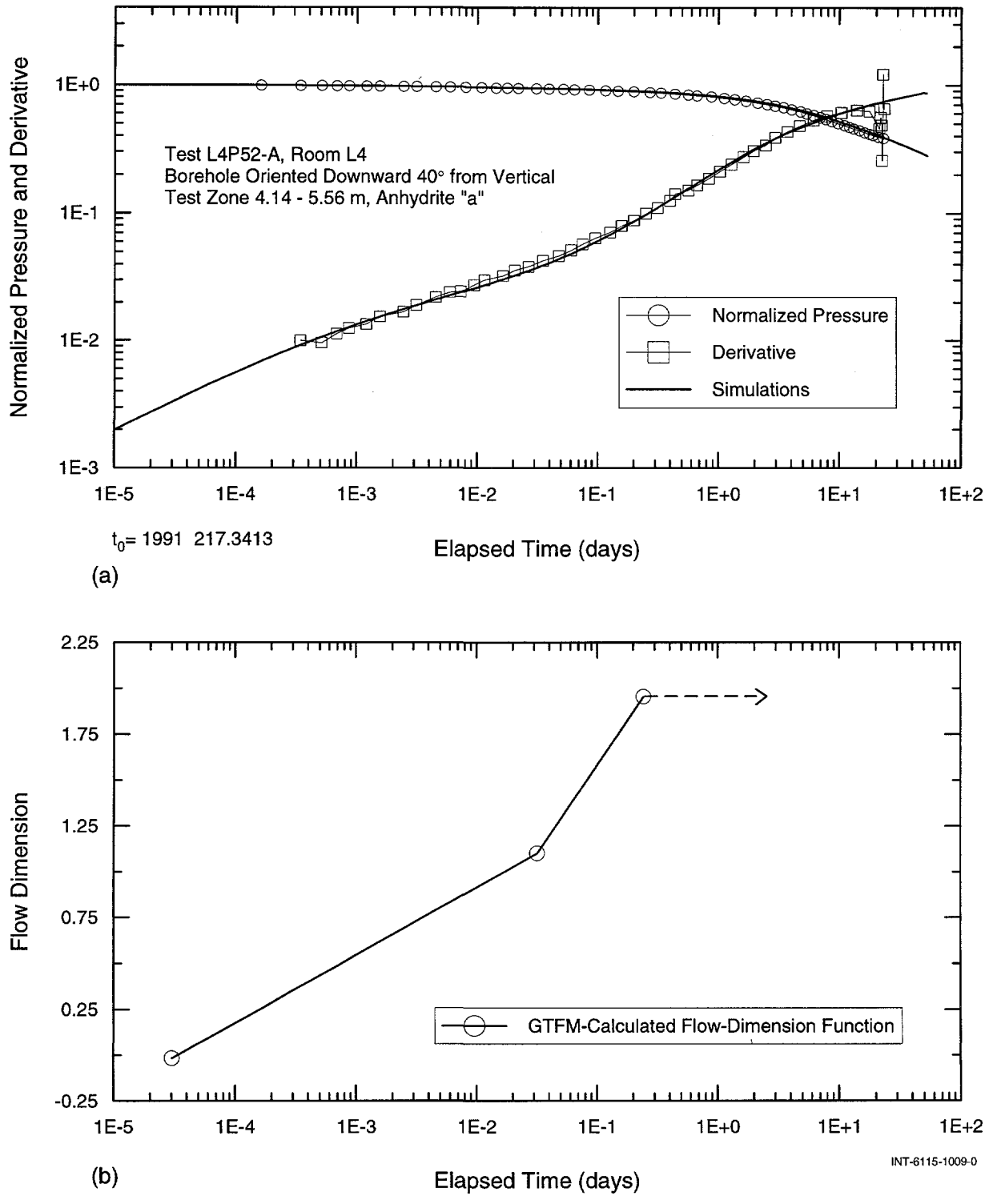

Figure A-26. Log-log and semilog plots of GTFM simulation (a) and flow-dimension function (b) of the L4P52-A pulse-withdrawal test #2.

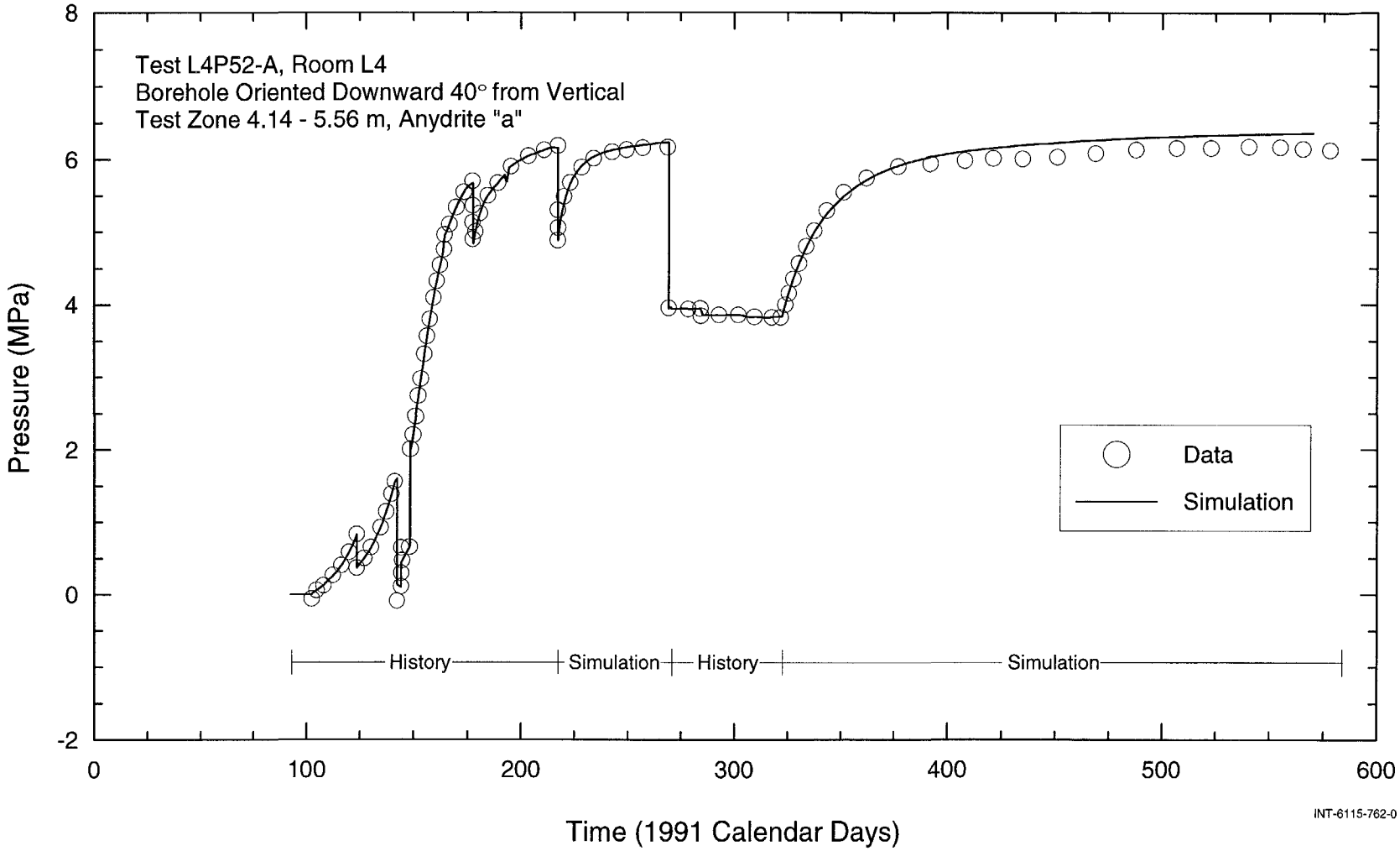

Figure A-27. Linear-linear plot of GTFM simulation of the L4P52-A test-sequence pressures.

APPENDIX B

DESCRIPTION OF GENERALIZED STRATIGRAPHY NEAR THE REPOSITORY HORIZON

THIS PAGE INTENTIONALLY LEFT BLANK

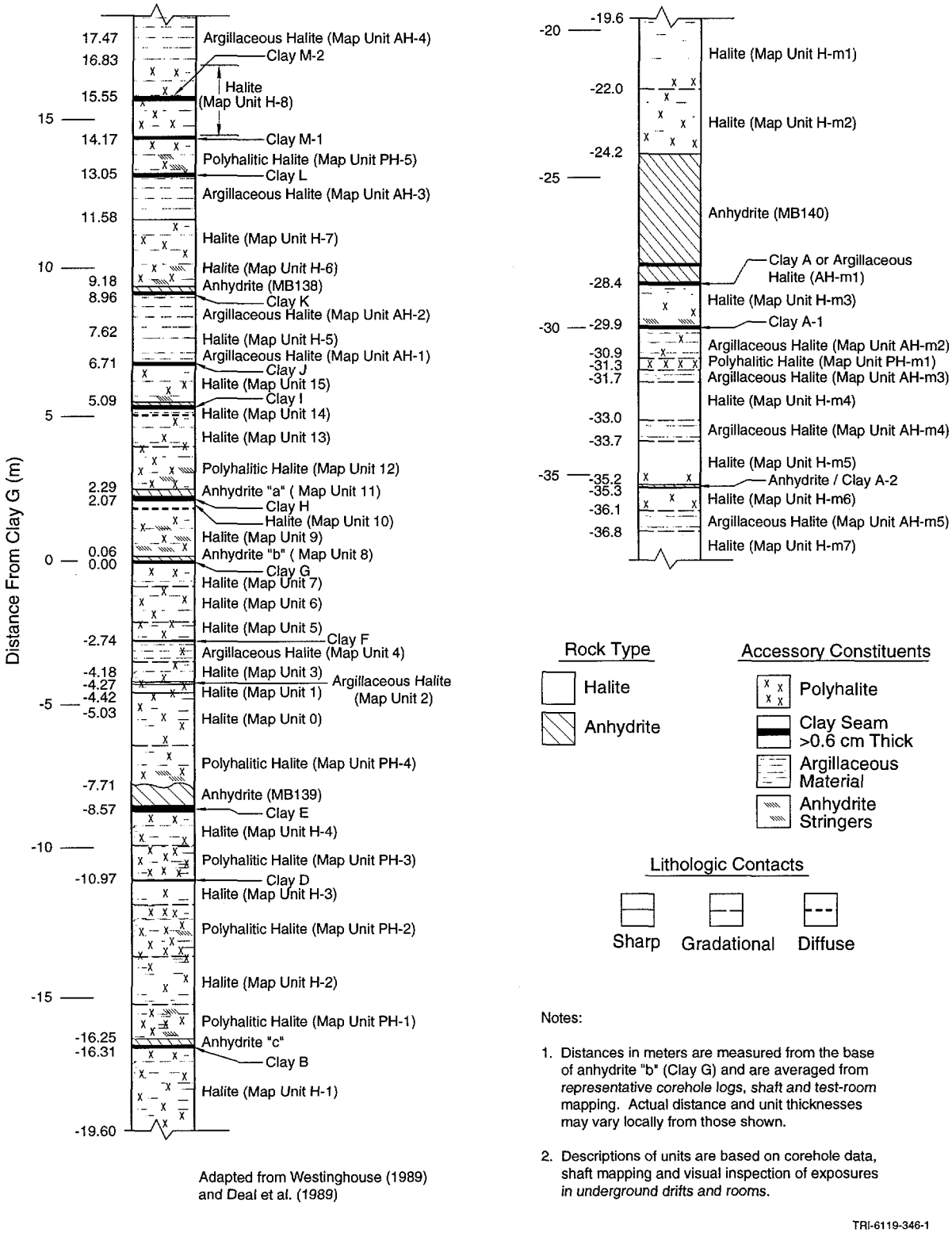

Adapted from Westinghouse (1989) and Deal et al. (1989)

Notes:

1. Distances in meters are measured from the base of anhydrite "b" (Clay G) and are averaged from *representative corehole logs, shaft and test-room* mapping. Actual distance and unit thicknesses may vary locally from those shown.

2. Descriptions of units are based on corehole data, shaft mapping and visual inspection of exposures *in underground drifts and rooms.*

TRI-6119-346-1

Figure B-1. Detailed stratigraphy near the WIPP underground facility.

Table B-1. Description of Generalized Stratigraphy near the Repository Horizon*

Approximate Distance from Clay G (m)	Stratigraphic Unit	Description
20.1 to 21.2	Polyhalitic halite (PH-7)	Clear to moderate reddish orange/brown. Fine to coarsely crystalline. <1-3% polyhalite.
19.3 to 20.1	Halite (H-9)	Clear to light moderate reddish orange. Medium to coarsely crystalline. ≤1% polyhalite. May contain ≤1% brown and gray clay.
17.5 to 19.3	Polyhalitic halite (PH-6)	Clear to moderate reddish orange/brown. Medium to coarsely crystalline. <1-3% polyhalite. May contain traces of gray clay and/or scattered anhydrite.
16.8 to 17.5	Argillaceous halite (AH-4)	Clear to moderate brown. Medium to coarsely crystalline. <1 to 3% brown clay. Intercrystalline and discontinuous breaks. In one core hole, consists of a 2.5-cm-thick clay seam. Unit can vary up to 1.2 m in thickness. Contact with lower unit is gradational.
14.2 to 16.8	Halite (H-8)	Clear to moderate reddish orange and moderate brown. Coarsely crystalline, some medium. ≤1% brown clay, locally argillaceous (clays M-1 and M-2). Scattered anhydrite stringers locally.
13.0 to 14.2	Polyhalitic halite (PH-5)	Clear to moderate reddish orange, some moderate brown. Coarsely crystalline. <1 to 3% polyhalite. None to 1% brown and some gray clay. Scattered anhydrite locally. Contact with unit below is typically sharp at clay L.
11.6 to 13.0	Argillaceous halite (AH-3)	Clear to moderate brown. Medium to coarsely crystalline, some fine. <1 to 5% brown clay. Locally contains 10% clay. Intercrystalline and scattered breaks. Locally contains partings and seams. Upper contact is clay L. Contact with lower unit is gradational based on increased clay content. Average range of unit is 11.6 to 13.0 m above clay G but varies from 10.3 to 14.0 m.

*Modified from Deal et al. (1989).

Table B-1. Description of Generalized Stratigraphy near the Repository Horizon (continued)

Approximate Distance from Clay G (m)	Stratigraphic Unit	Description
10.4 to 11.6	Halite (H-7)	Clear to moderate brown, some moderate reddish brown. Coarsely crystalline, some fine and medium. ≤1% brown clay, trace gray clay locally. Scattered breaks. Locally argillaceous. <1% polyhalite. Contact with unit below is gradational based on clay and polyhalite content.
9.2 to 10.4	Halite (H-6)	Clear to moderate reddish orange. Coarsely crystalline. <1 to 3% polyhalite. Commonly polyhalitic. Scattered anhydrite stringers with anhydrite layers up to 1.3 cm thick locally. Scattered brown clay locally. Contact with MB138 below is sharp.
9.0 to 9.2	Anhydrite (MB138)	Light to medium gray. Microcrystalline. Partly laminated. Scattered halite growths. Clay seam K found at base of unit.
7.6 to 9.0	Argillaceous halite (AH-2)	Clear to moderate brown, some light moderate reddish orange. Medium to coarsely crystalline. <1 to 3% brown clay, some gray. Locally up to 5% clay. Clay is intercrystalline with scattered breaks and partings present. <1/2% dispersed polyhalite. Contact with lower unit is gradational based on clay content. Upper contact with clay K is sharp.
7.0 to 7.6	Halite (H-5)	Clear, some light moderate brown. Coarsely crystalline. <1/2% brown clay. Contact with clay J below varies from sharp to gradational depending if clay J is a distinct seam or merely an argillaceous zone.
6.4 to 7.0	Argillaceous halite (clay J; AH-1)	Usually consists of scattered breaks or argillaceous zone containing <1 to 3% brown clay. In C&SH shaft, it is a 1.3-cm-thick brown clay seam.
5.1 to 6.4	Halite (map unit 15)	Clear. Coarsely crystalline, scattered medium. Up to 1% dispersed polyhalite and brown clay. Scattered anhydrite. Lower contact is sharp with clay I.

Table B-1. Description of Generalized Stratigraphy near the Repository Horizon (continued)

Approximate Distance from Clay G (m)	Stratigraphic Unit	Description
4.8 to 5.1	Halite (map unit 14)	Clear to grayish orange-pink. Coarsely crystalline, some medium. <1/2% dispersed polyhalite. Scattered discontinuous gray clay stringers. Clay I is along upper contact. Contact with lower unit is diffuse.
3.5 to 4.8	Halite (map unit 13)	Clear to moderate reddish orange and moderate brown. Medium to coarsely crystalline, some fine. ≤1% brown clay, locally up to 3%. Trace of gray clay. Scattered discontinuous breaks. <1% dispersed polyhalite and polyhalite blebs. Contact with unit below is gradational based on clay and polyhalite content.
2.3 to 3.5	Polyhalitic halite (map unit 12)	Clear to moderate reddish orange. Coarsely crystalline. ≤1 to 3% dispersed polyhalite and polyhalite blebs. Scattered anhydrite stringers. Contact is sharp with unit below.
2.1 to 2.3	Anhydrite ("a" - map unit 11)	Light to medium gray, light brownish gray and sometimes light moderate reddish orange. Microcrystalline. Halite growths within. Partly laminated. Locally contains clear, coarsely crystalline halite layer up to 5 cm wide. Thin gray clay seam H at base.
1.7 to 2.1	Halite (map unit 10)	Clear to moderate reddish orange/brown. Fine to coarsely crystalline. ≤1% brown and/or gray clay and dispersed polyhalite. Discontinuous clay stringers locally. Contact with lower unit is diffuse based on crystal size and varying amounts of clay and polyhalite.
0.1 to 1.7	Halite (map unit 9)	Clear to light moderately reddish orange. Coarsely crystalline, some medium. None to <1% polyhalite. Trace of gray clay locally. Scattered anhydrite stringers. Contact with unit below is sharp.
0.0 to 0.1	Anhydrite ("b" - map unit 8)	Light to medium gray. Microcrystalline. Scattered halite growths. Thin gray clay seam G at base of unit.

Table B-1. Description of Generalized Stratigraphy near the Repository Horizon (continued)

Approximate Distance from Clay G (m)	Stratigraphic Unit	Description
0.0 to -0.7	Halite (map unit 7)	Clean to light/medium gray, some moderate reddish orange/brown. Coarsely crystalline, some fine and medium. ≤1% brown and gray clay. Locally up to 2% clay. <1% dispersed polyhalite. Upper contact is sharp with clay G. Contact with lower unit is gradational.
-0.7 to -2.1	Halite (map unit 6)	Clear, some moderate reddish orange. Coarsely crystalline, some fine to medium locally. <1/2% gray clay and polyhalite. Contact with lower unit gradational and/or diffuse.
-2.1 to -2.7	Halite (map unit 5)	Clear. Coarsely crystalline. <1/2% gray clay. Contact with lower unit usually sharp with clay F.
-2.7 to -3.5	Argillaceous halite (map unit 4)	Clear to moderate brown and moderate reddish brown. Coarsely crystalline. <1% polyhalite. <1 to 5% argillaceous material; predominantly brown, some gray, locally. Intercrystalline and discontinuous breaks and partings common in upper part of unit. Decreasing argillaceous content downward. Contact with lower unit is gradational.
-3.5 to -4.2	Halite (map unit 3)	Clear to moderate reddish orange. Coarsely crystalline. ≤1% dispersed polyhalite and polyhalite blebs. Locally polyhalitic. Scattered gray clay locally. Contact with lower unit is sharp.
-4.2 to -4.3	Argillaceous halite (map unit 2)	Moderate reddish brown to medium gray. Medium to coarsely crystalline. <1 to 3% argillaceous material. Contact with lower unit is usually sharp.
-4.3 to -4.4	Halite (map unit 1)	Light reddish orange to moderate reddish orange. Medium to coarsely crystalline. ²1% dispersed polyhalite. Contact with lower unit is sharp.

Table B-1. Description of Generalized Stratigraphy near the Repository Horizon (continued)

Approximate Distance from Clay G (m)	Stratigraphic Unit	Description
-4.4 to -6.7	Halite (map unit 0)	Clear to moderate reddish orange/brown, moderate brown and grayish brown. Medium to coarsely crystalline. <1 to 5% argillaceous material. Predominantly brown, some gray, intercrystalline argillaceous material and discontinuous breaks and partings. Upper 0.6 m of unit is argillaceous halite decreasing in argillaceous content downward. None to <1% polyhalite. Contact with lower unit is gradational based on polyhalite content.
-6.7 to -7.7	Polyhalitic halite (PH-4)	Clear to moderate reddish orange. Coarsely crystalline, some medium locally. <1 to 3% polyhalite. Scattered anhydrite. Scattered gray clay locally. Contact with lower unit (MB139) is sharp, but commonly irregular and undulating. Trace of gray clay locally present along this contact.
-7.7 to -8.6	Anhydrite (MB139)	Moderate reddish orange/brown to light and medium gray. Microcrystalline. "Swallowtail" pattern, consisting of halite growths within anhydrite, common in upper part of unit. Locally, hairline, clay-filled, low-angle fractures found in lower part of unit. Thin halite layer common close to lower contact. Clay seam E found at base of unit. Upper contact is irregular, undulating and sometimes contains <0.2 cm gray clay.
-8.6 to -9.5	Halite (H-4)	Clear to moderate reddish orange, and light gray. Coarsely crystalline, some fine and medium. ≤1% polyhalite and intercrystalline gray clay. Contact with lower unit is gradational based on increased polyhalite content.
-9.5 to -11.0	Polyhalitic halite (PH-3)	Clear to moderate reddish orange. Coarsely crystalline. <1 to 3% polyhalite. Contact with lower unit is usually sharp along clay D.
-11.0 to -11.5	Halite (H-3)	Clear to moderate reddish orange, some light gray. Medium to coarsely crystalline. ≤1% polyhalite and gray clay. Contact with lower unit is gradational based on increased polyhalite content.

Table B-1. Description of Generalized Stratigraphy near the Repository Horizon (continued)

Approximate Distance from Clay G (m)	Stratigraphic Unit	Description
-11.5 to -13.0	Polyhalitic halite (PH-2)	Clear to moderate reddish orange/brown. Coarsely crystalline. <1 to 3% polyhalite. Trace of clay and scattered anhydrite locally. Lower contact is gradational, based on decreased polyhalite content.
-13.0 to -14.4	Halite (H-2)	Clear to moderate reddish orange. Medium to coarsely crystalline. <1% dispersed polyhalite. <1% brown and/or gray clay. Contact with lower unit is gradational and/or diffuse.
-14.4 to -16.2	Polyhalitic halite (PH-1)	Clear to moderate reddish orange. Coarsely crystalline with some medium sometimes present close to lower contact. <1 to 3% polyhalite. Scattered anhydrite especially common close to anhydrite "c". Lower contact is sharp with anhydrite "c".
-16.2 to -16.3	Anhydrite ("c")	Light to medium gray. Microcrystalline. Scattered halite growths. Faintly laminated locally. Clay seam B found at base of unit.
-16.3 to –19.6	Halite (H-1)	Clear to medium gray and moderate brown. Medium to coarsely crystalline, some fine locally. ≤1% polyhalite, locally polyhalitic. <1 to 3% clay, both brown and gray. Intercrystalline clay with discontinuous breaks and partings. Zones of argillaceous halite found within unit. Seams of clay mixed with halite crystals present locally. Upper contact of this unit is sharp with clay B.
-19.6 to –22.0	Halite (H-m1)	Colorless to gray. Medium to coarsely crystalline. Minor gray clay decreasing with depth. Minor polyhalite in lower 0.4 m.
-22.0 to –24.2	Halite (H-m2)	Colorless to orange. Medium crystalline. Trace gray clay. Polyhalite increasing with depth.
-24.2 to –28.3	Anhydrite (MB140)	Gray, orange, red. Microcrystalline. Halite pseudomorphs after gypsum 0.4 to 1.2 m from top. Halite abundant from 1.6 to 2.2 m from top. 5- to 12-cm gray clay seam ~0.6 m above base.

Table B-1. Description of Generalized Stratigraphy near the Repository Horizon (continued)

Approximate Distance from Clay G (m)	Stratigraphic Unit	Description
-28.3 to –28.4	Clay (A) and/or argillaceous halite (AH-m1)	Gray, soft clay seam typically 5 to 16 cm thick, but locally 0.1 m argillaceous halite.
-28.4 to –29.8	Halite (H-m3)	Colorless to pale orange. Medium to coarsely crystalline. Trace intercrystalline gray clay near top. Trace polyhalite. Anhydrite stringer 0.3 m above base.
-29.8 to –29.9	Clay (A-1)	Gray. Overlain by 1 cm gray anhydrite.
-29.9 to –30.9	Argillaceous halite (AH-m2)	Podular muddy halite. Gray clay. Medium to coarsely crystalline. Minor polyhalite.
-30.9 to –31.3	Polyhalitic halite (PH-m1)	Orange. Coarsely crystalline.
-31.3 to –31.7	Argillaceous halite (AH-m3)	Podular muddy halite. Brown clay. Finely to coarsely crystalline.
-31.7 to –33.0	Halite (H-m4)	Colorless. Finely to coarsely crystalline.
-33.0 to –33.7	Argillaceous halite (AH-m4)	Podular muddy halite. Gray clay. Finely to coarsely crystalline.
-33.7 to –35.2	Halite (H-m5)	Colorless to orange. Coarsely crystalline. Trace polyhalite increasing in lower 0.6 m.
-35.2 to –35.3	Anhydrite	Gray to white. Microcrystalline. Clay A-2 at base.
-35.3 to –36.1	Halite (H-m6)	Pale orange. Coarsely crystalline. Minor polyhalite.
-36.1 to –36.8	Argillaceous halite (AH-m5)	Brown. Coarsely to medium crystalline.
-36.8 to -?	Halite (H-m7)	Colorless. Medium crystalline.

APPENDIX C

FITTING-PARAMETER UNCERTAINTY AND CORRELATION INFORMATION

THIS PAGE INTENTIONALLY LEFT BLANK

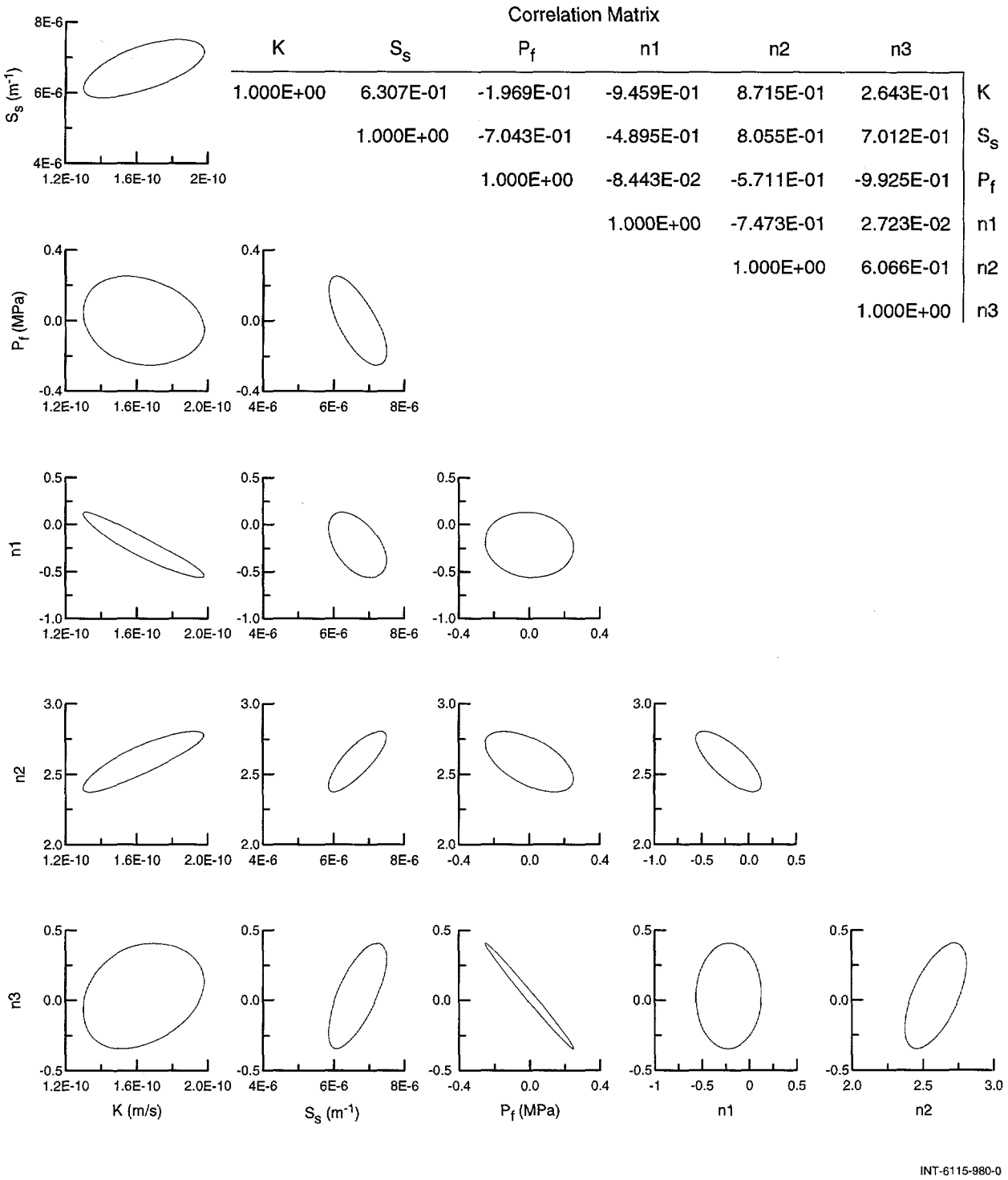

Figure C-1. Correlation matrix and 95% joint-confidence regions for C2H01-A PI1 analysis.

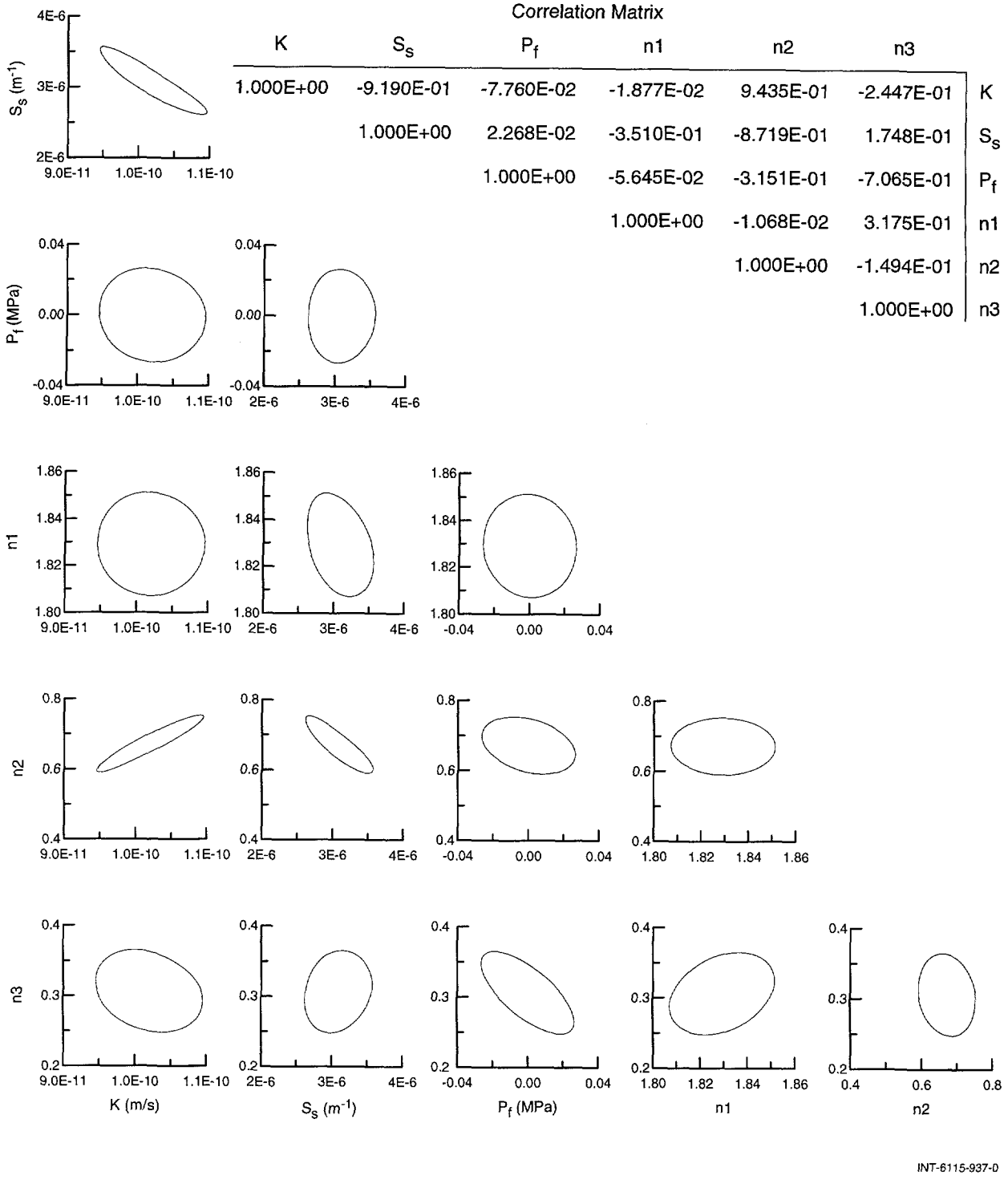

Figure C-2. Correlation matrix and 95% joint-confidence regions for C2H01-A PI2 analysis.

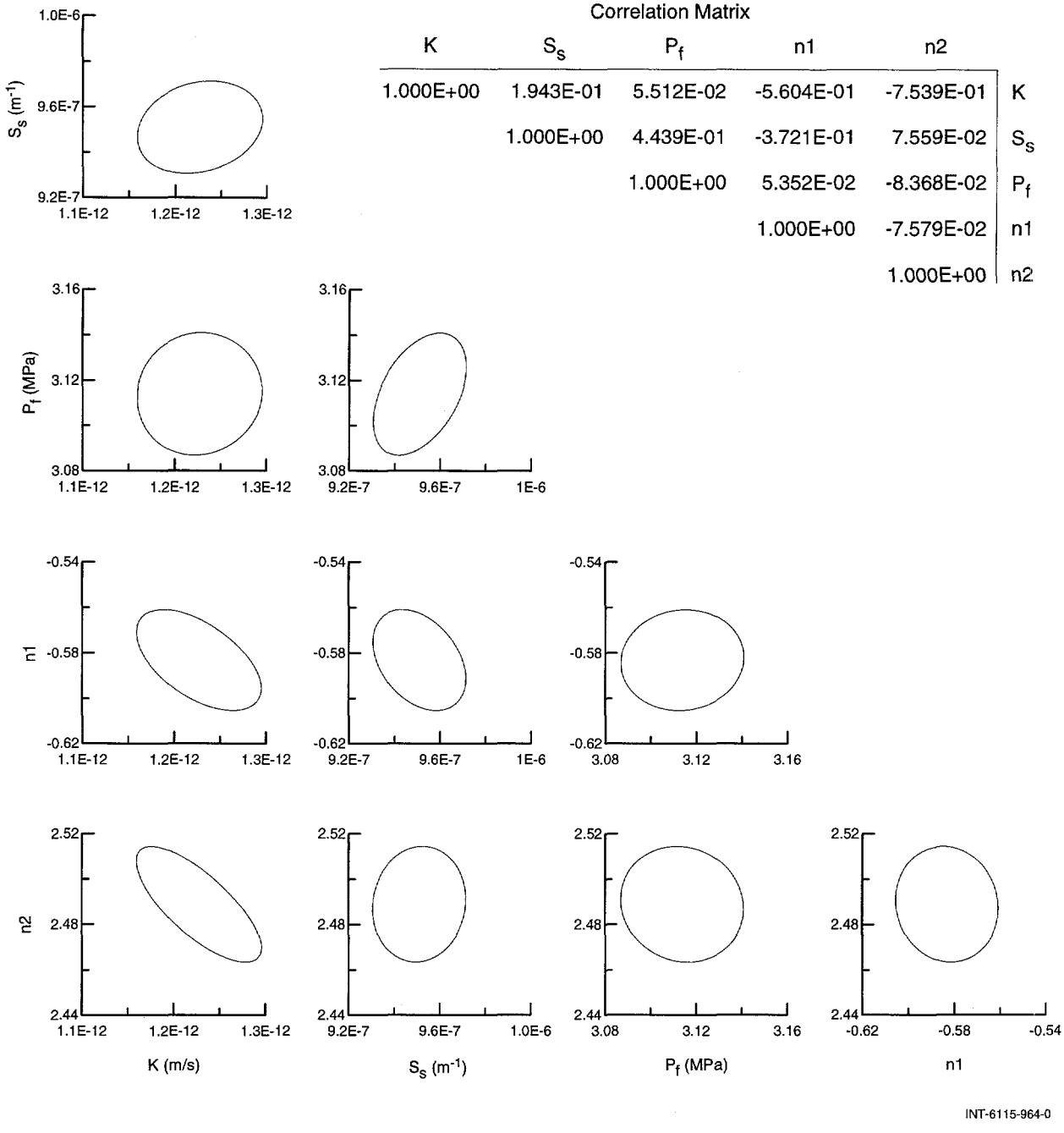

Figure C-3. Correlation matrix and 95% joint-confidence regions for C2H01-B analysis.

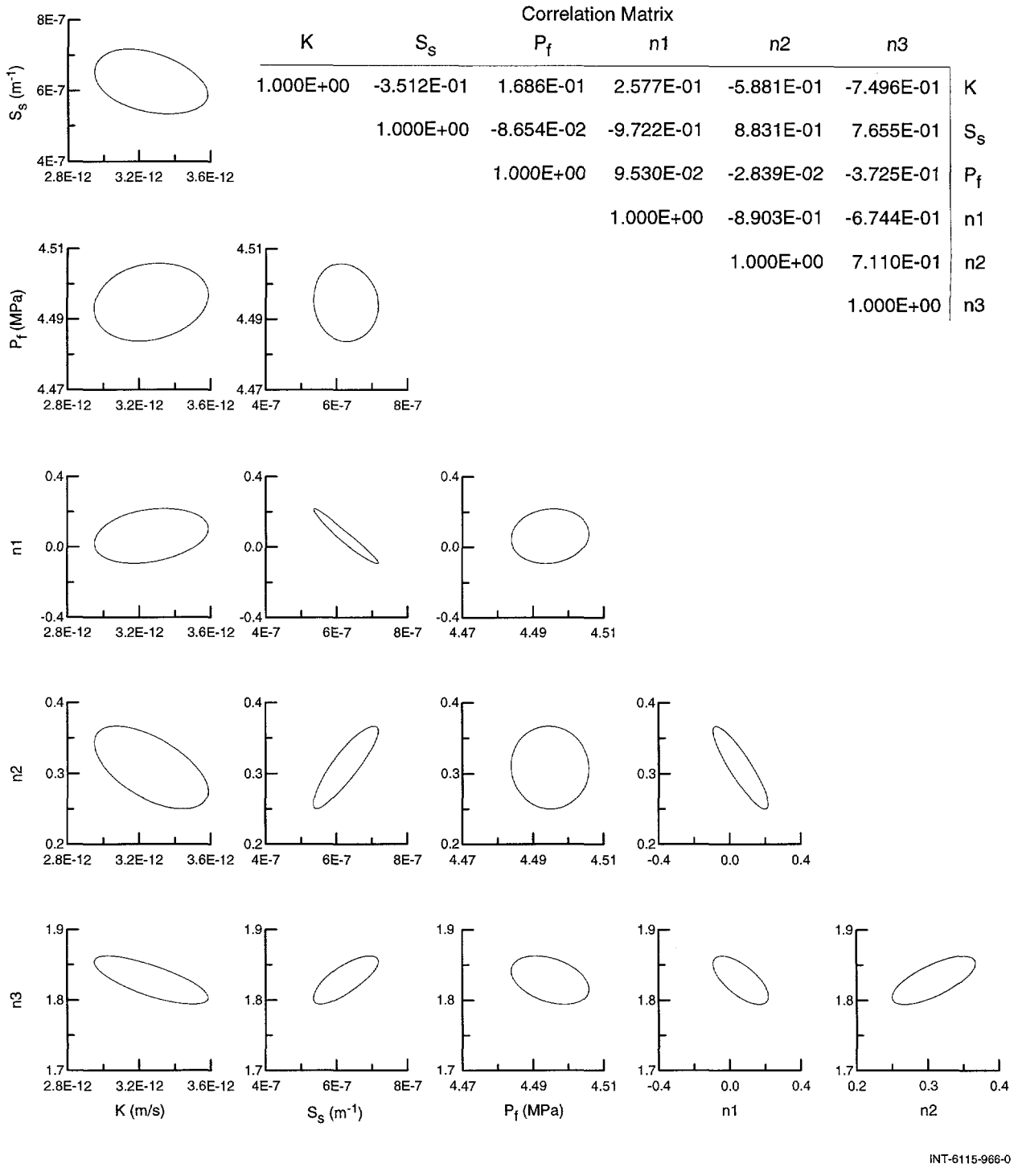

Figure C-4. Correlation matrix and 95% joint-confidence regions for C2H01-B-GZ analysis.

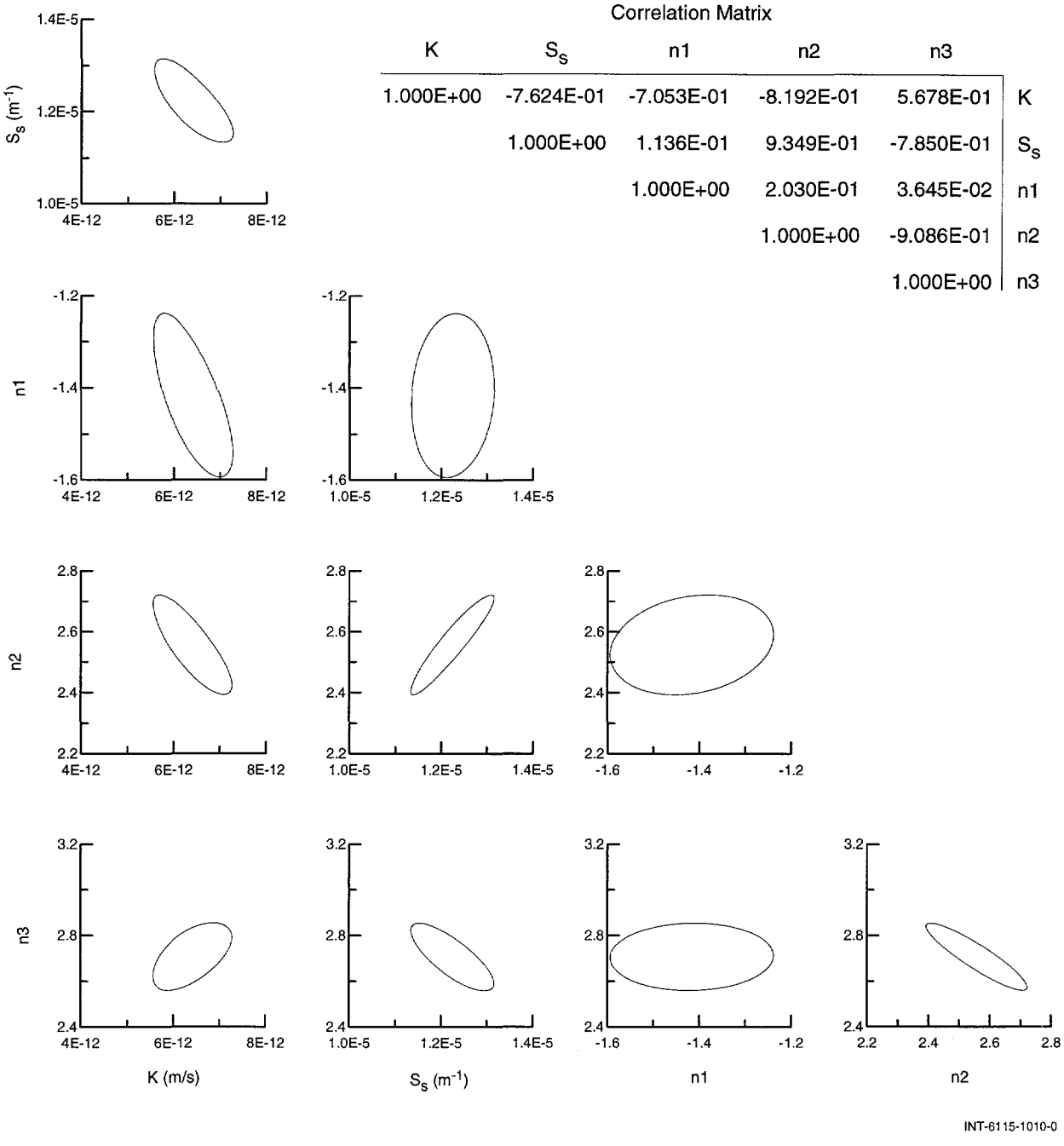

Figure C-5. Correlation matrix and 95% joint-confidence regions for C2H01-C analysis.

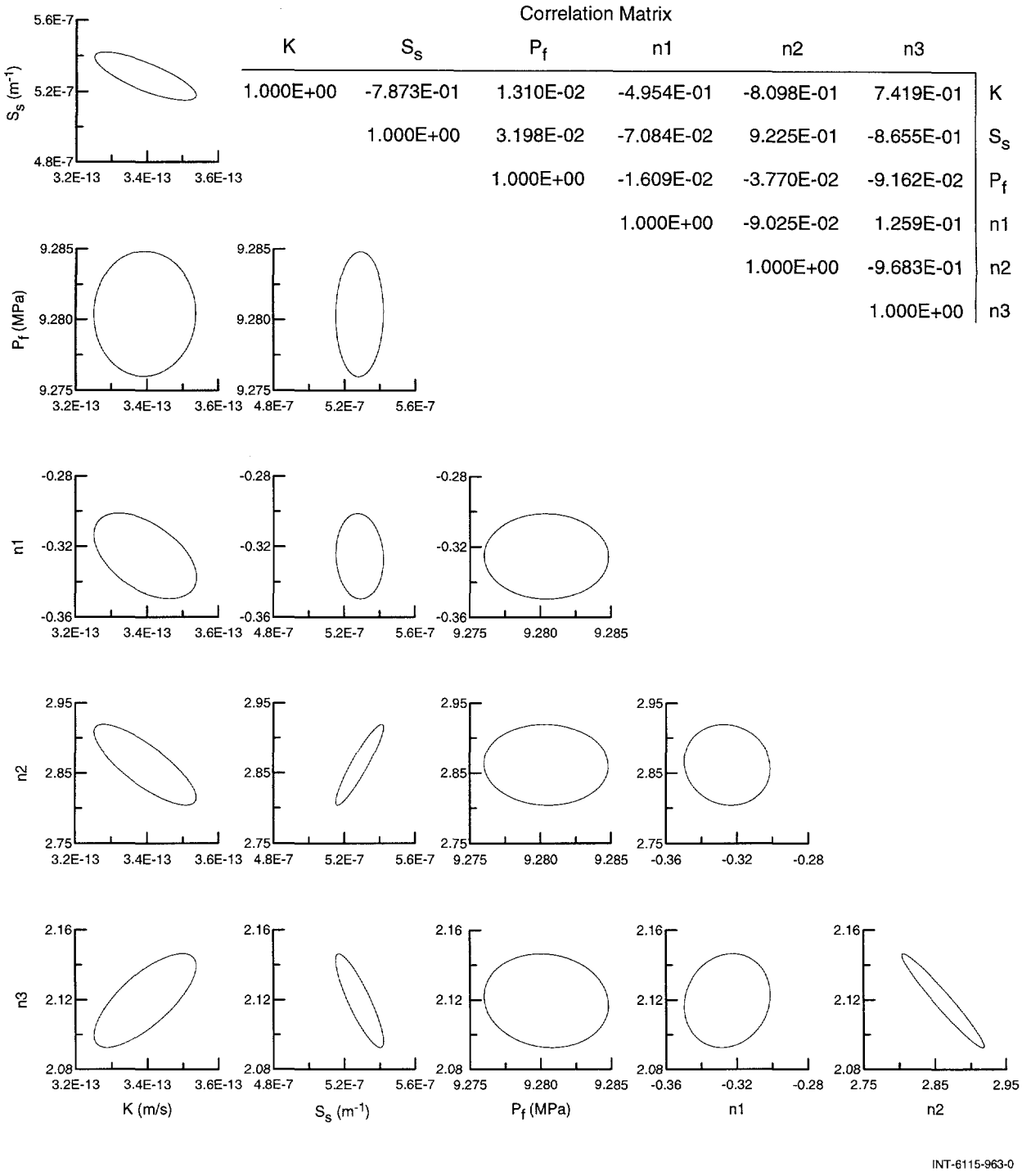

Figure C-6. Correlation matrix and 95% joint-confidence regions for C2H02 analysis.

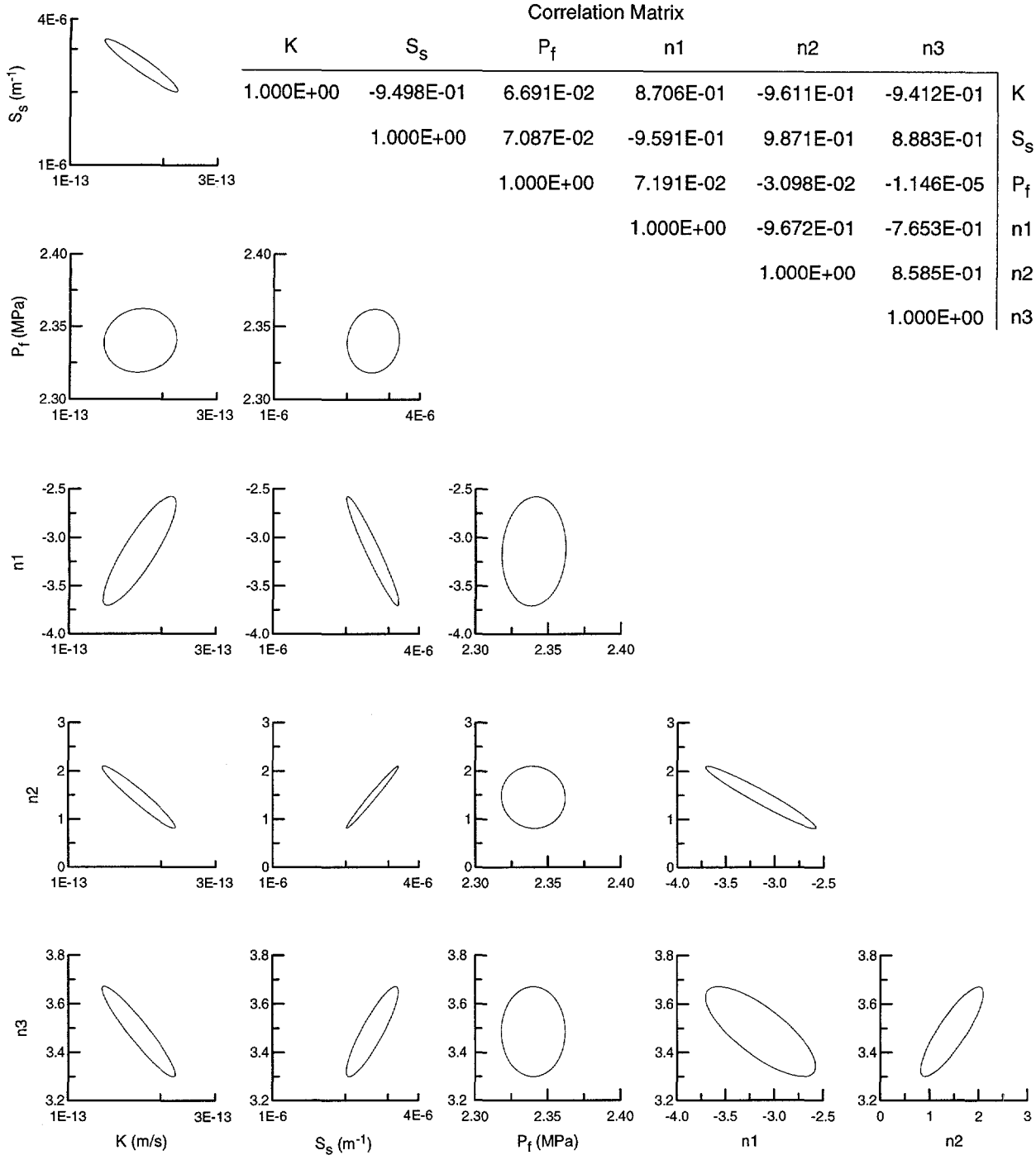

Figure C-7. Correlation matrix and 95% joint-confidence regions for L4P51-A analysis.

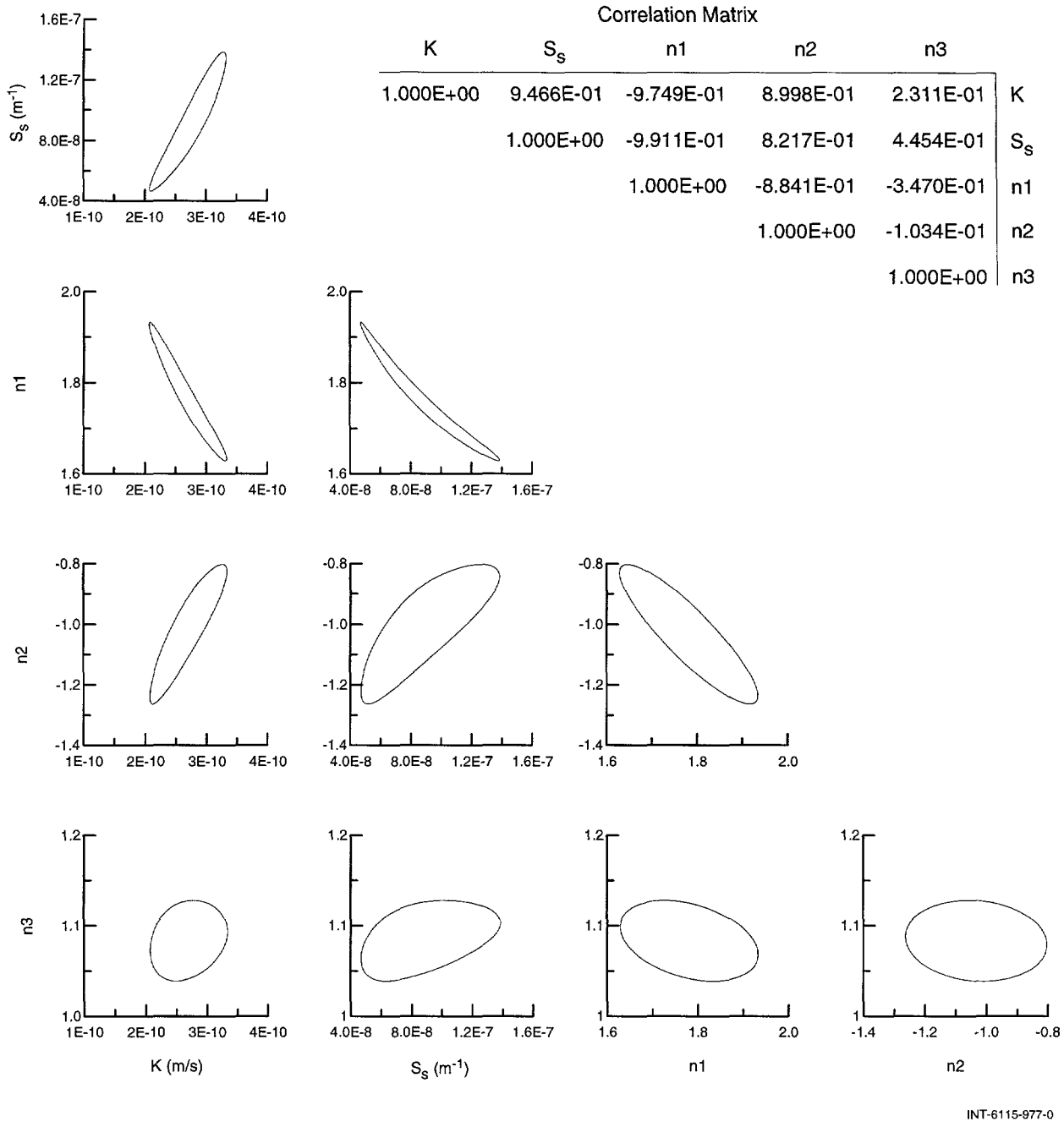

Figure C-8. Correlation matrix and 95% joint-confidence regions for L4P51-C1-GZ CPW analysis.

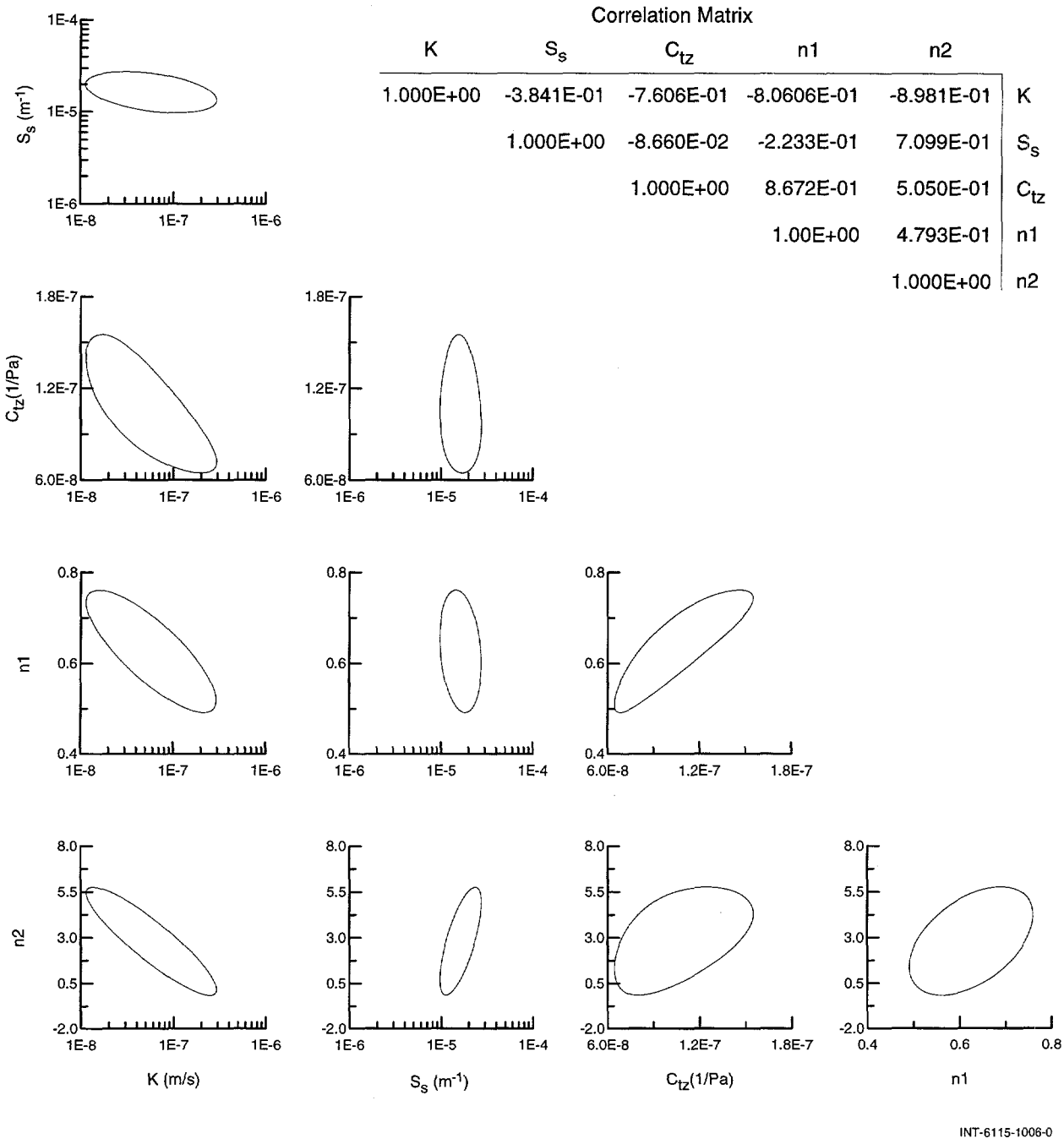

Figure C-9. Correlation matrix and 95% joint-confidence regions for L4P51-C1-TZ CPW1 analysis.

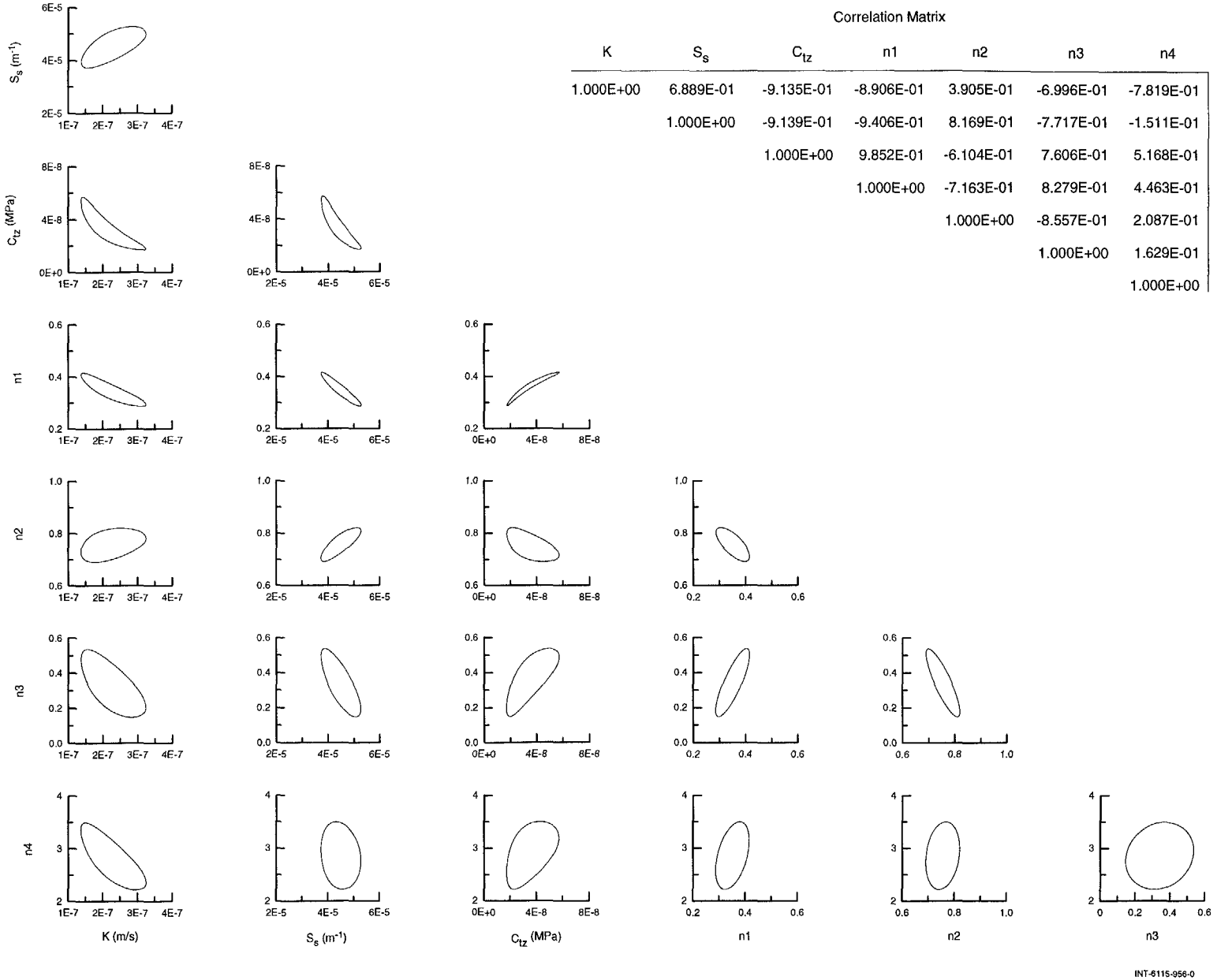

Correlation Matrix

K	S_s	C_{tz}	n1	n2	n3	n4	
1.000E+00	6.889E-01	-9.135E-01	-8.906E-01	3.905E-01	-6.996E-01	-7.819E-01	K
	1.000E+00	-9.139E-01	-9.406E-01	8.169E-01	-7.717E-01	-1.511E-01	S_s
		1.000E+00	9.852E-01	-6.104E-01	7.606E-01	5.168E-01	C_{tz}
			1.000E+00	-7.163E-01	8.279E-01	4.463E-01	n1
				1.000E+00	-8.557E-01	2.087E-01	n2
					1.000E+00	1.629E-01	n3
						1.000E+00	n4

Figure C-10. Correlation matrix and 95% joint-confidence regions for L4P51-C1-TZ CPW2 analysis.

Correlation Matrix

K	S_s	n1	n2	
1.000E+00	-5.599E-01	-6.125E-01	-9.147E-01	K
	1.000E+00	-2.979E-01	8.327E-01	S_s
		1.000E+00	2.420E-01	n1
			1.000E+00	n2

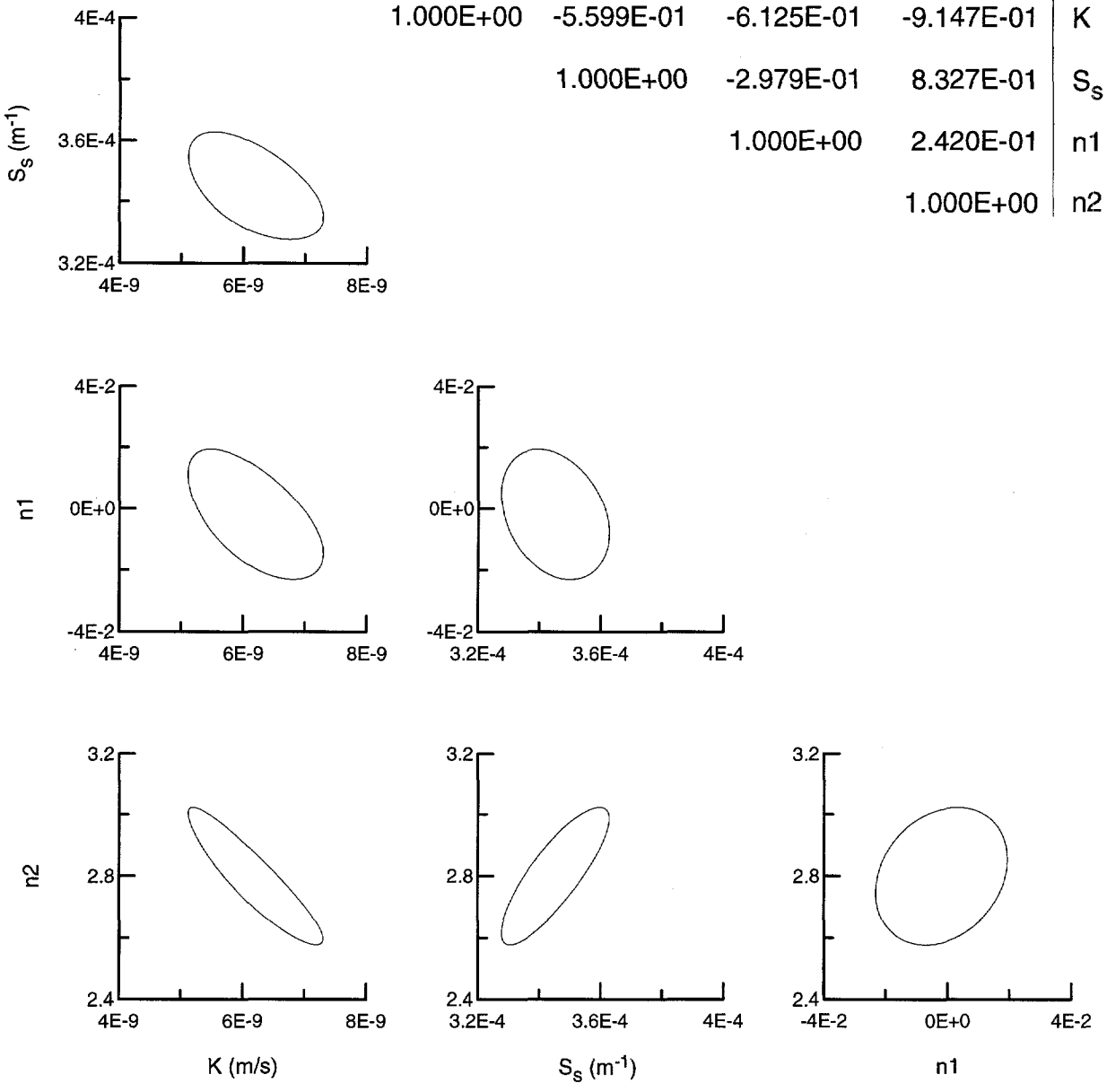

INT-6115-835-0

Figure C-11. Correlation matrix and 95% joint-confidence regions for L4P51-C1-TZ CPW3 analysis.

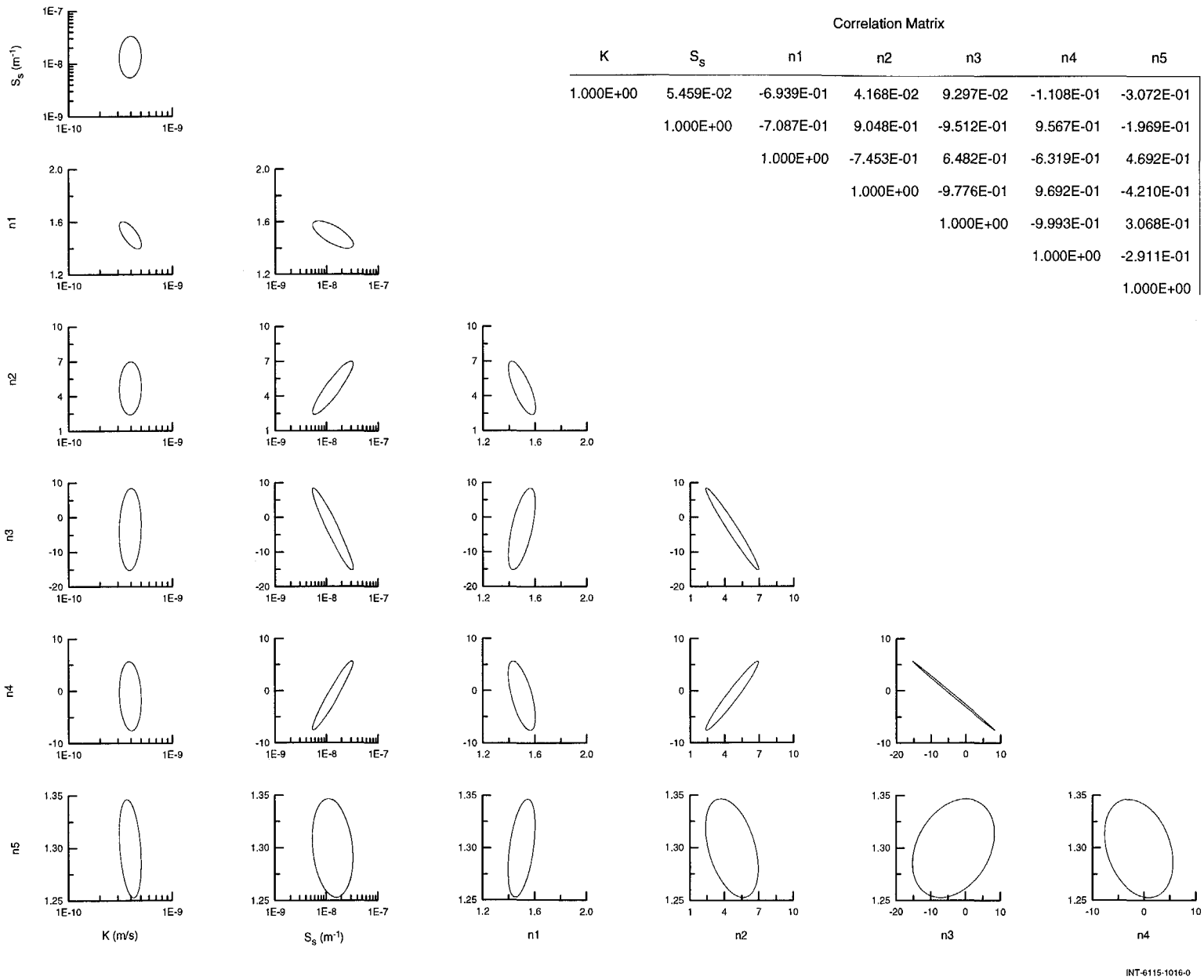

Figure C-12. Correlation matrix and 95% joint-confidence regions for L4P51-C2 CPW analysis.

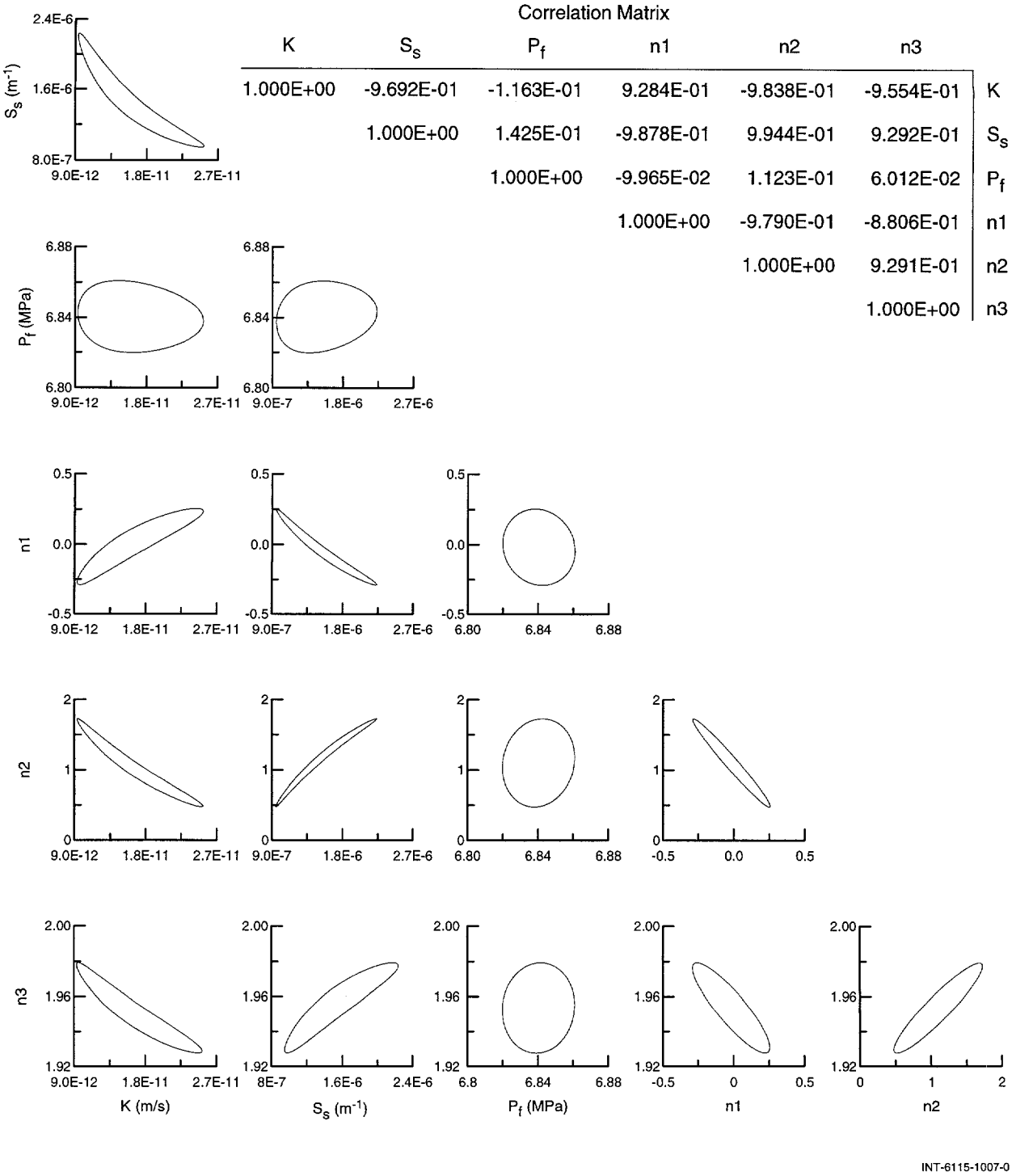

Figure C-13. Correlation matrix and 95% joint-confidence regions for L4P52-A analysis.

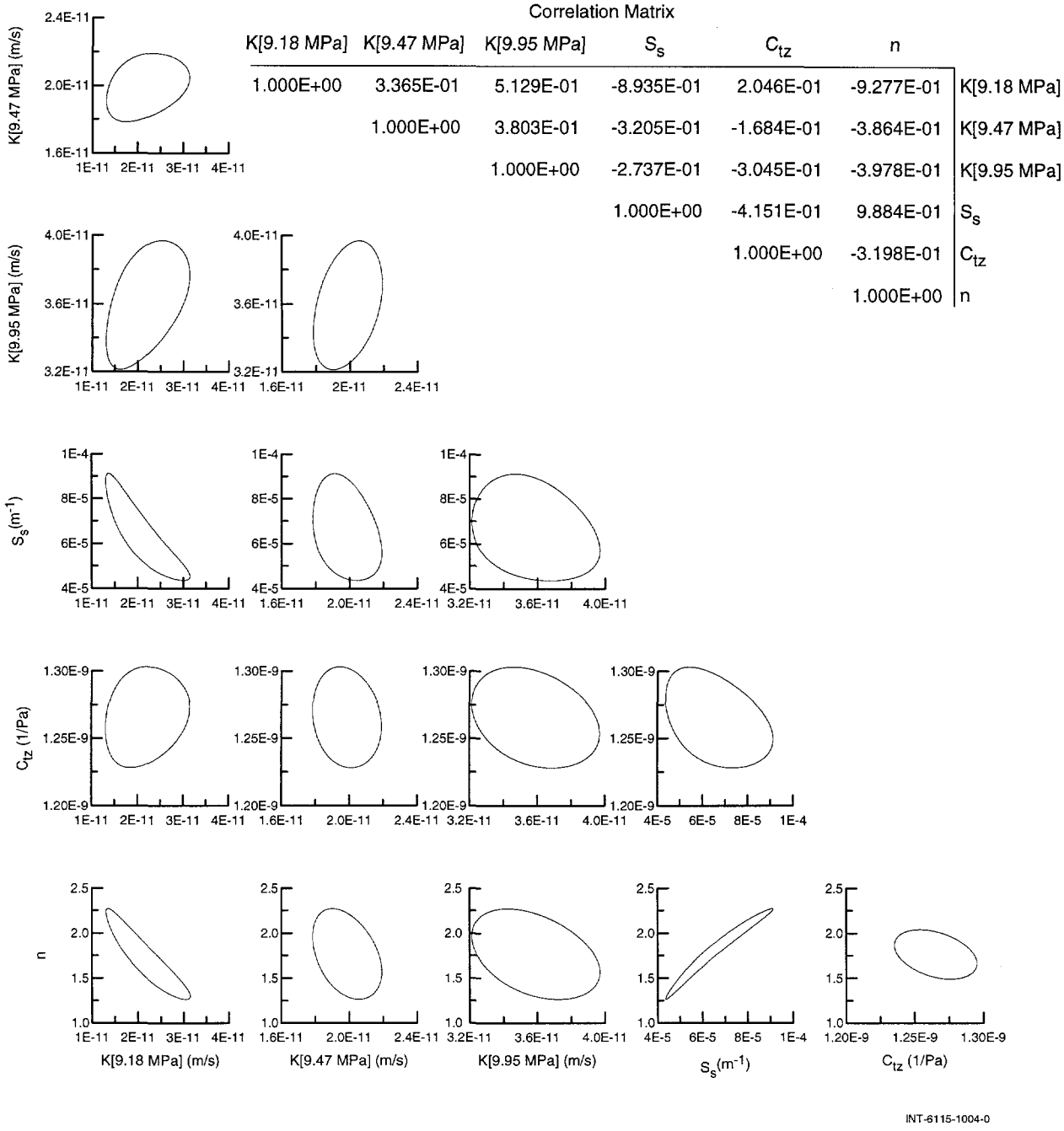

Figure C-14. Correlation matrix and 95% joint-confidence regions for L4P52-B analysis.

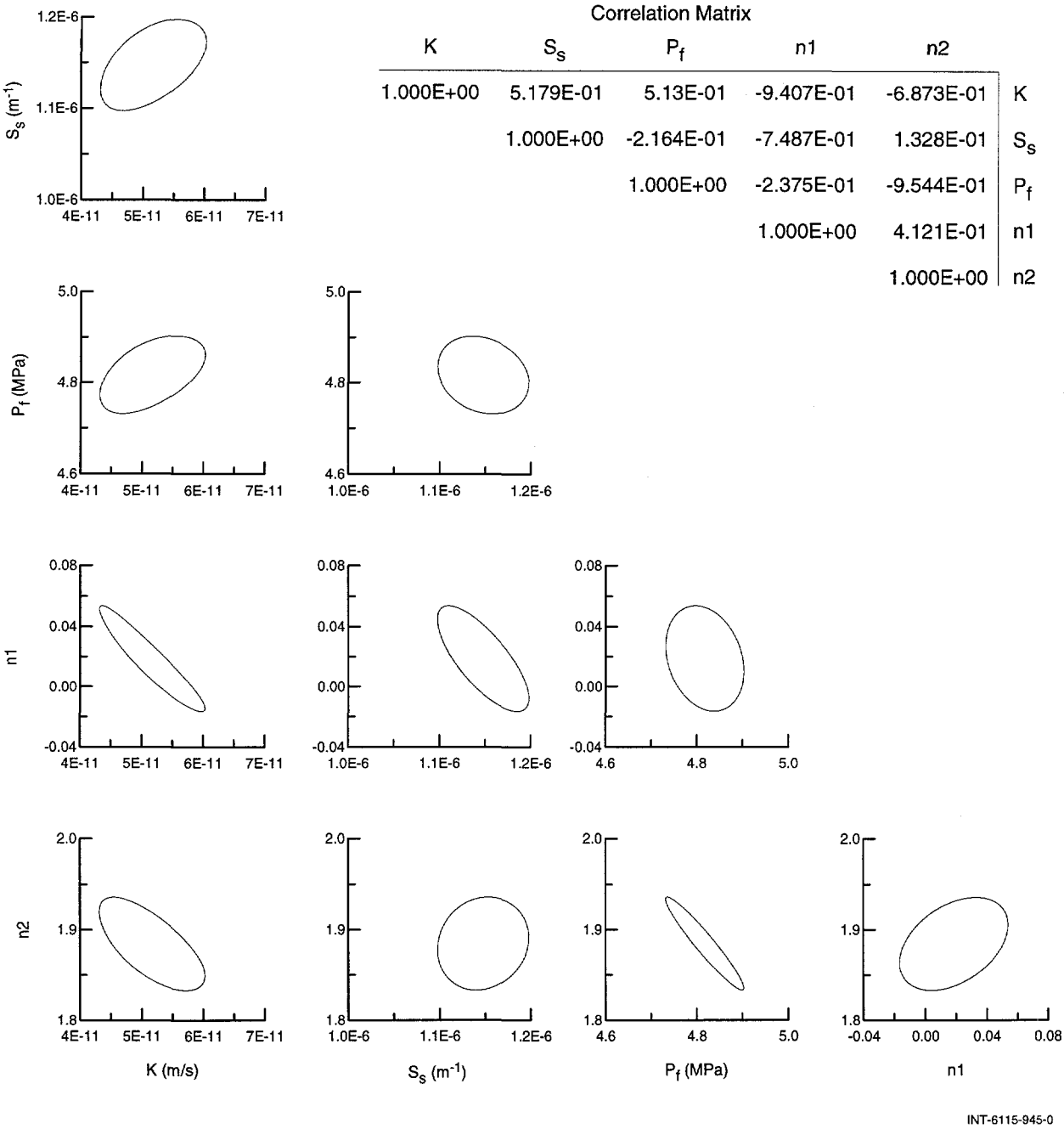

Figure C-15. Correlation matrix and 95% joint-confidence regions for S0P01 analysis.

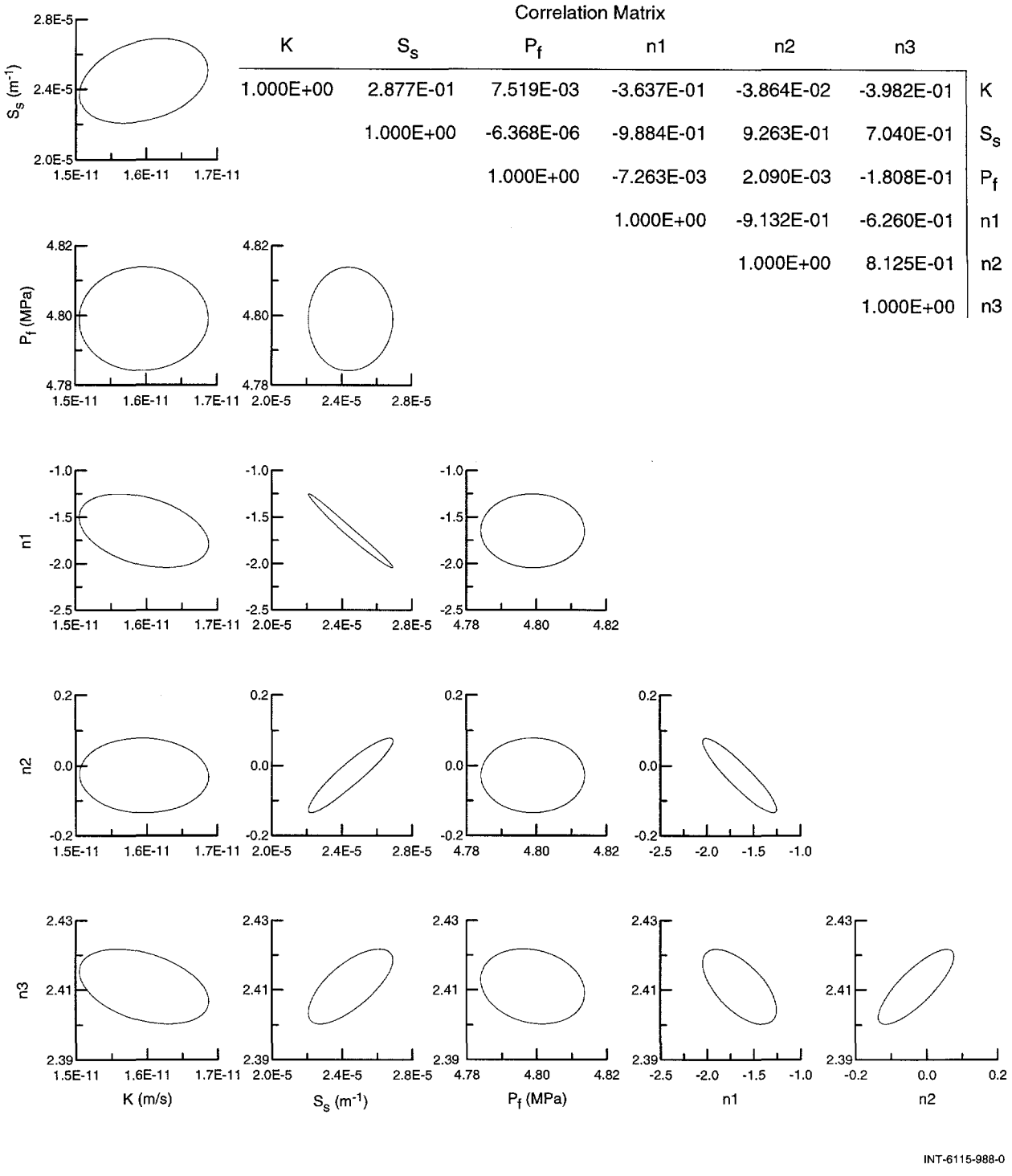

Figure C-16. Correlation matrix and 95% joint-confidence regions for S1P71-B PW1 analysis.

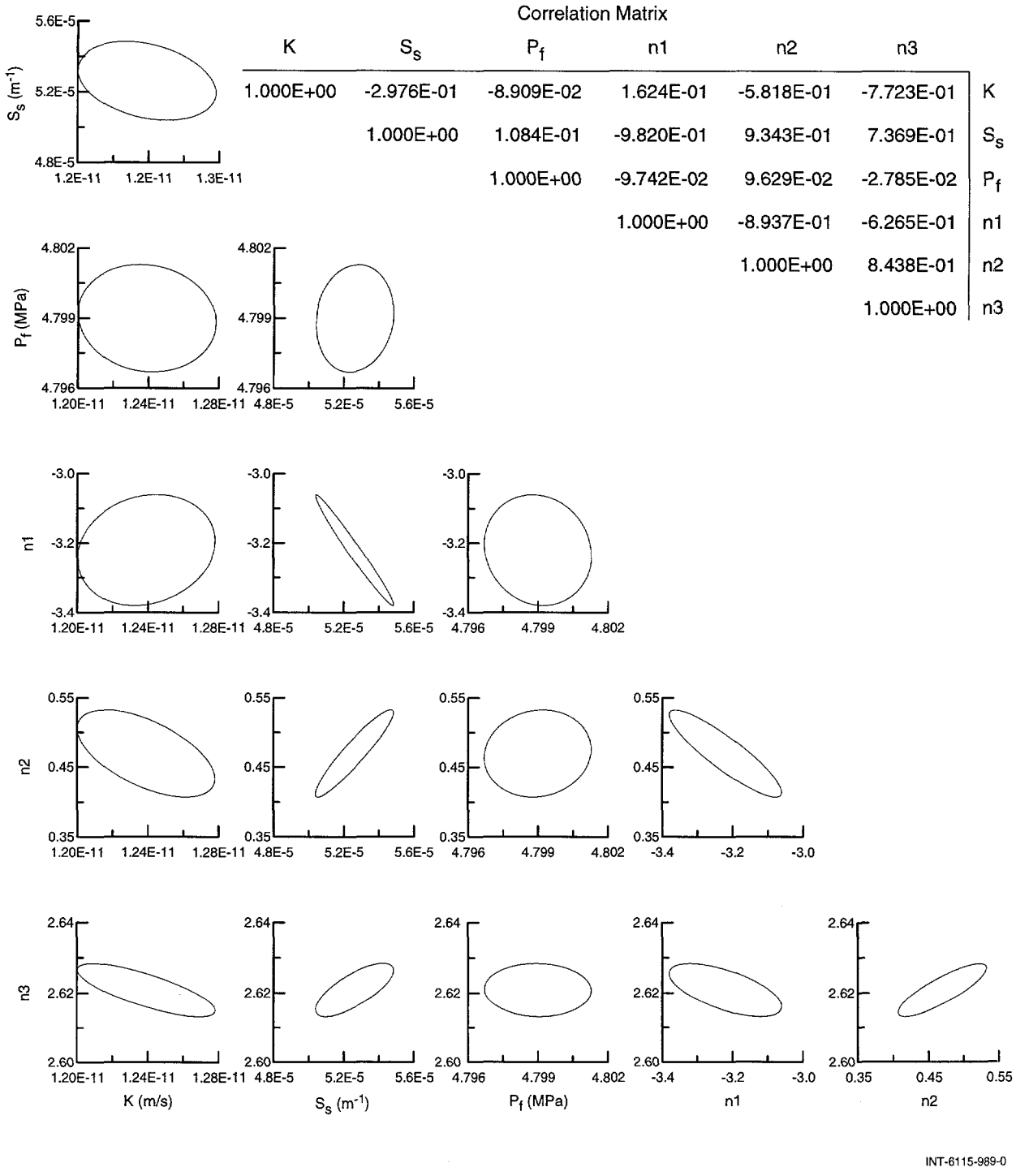

Figure C-17. Correlation matrix and 95% joint-confidence regions for S1P71-B PW2 analysis.

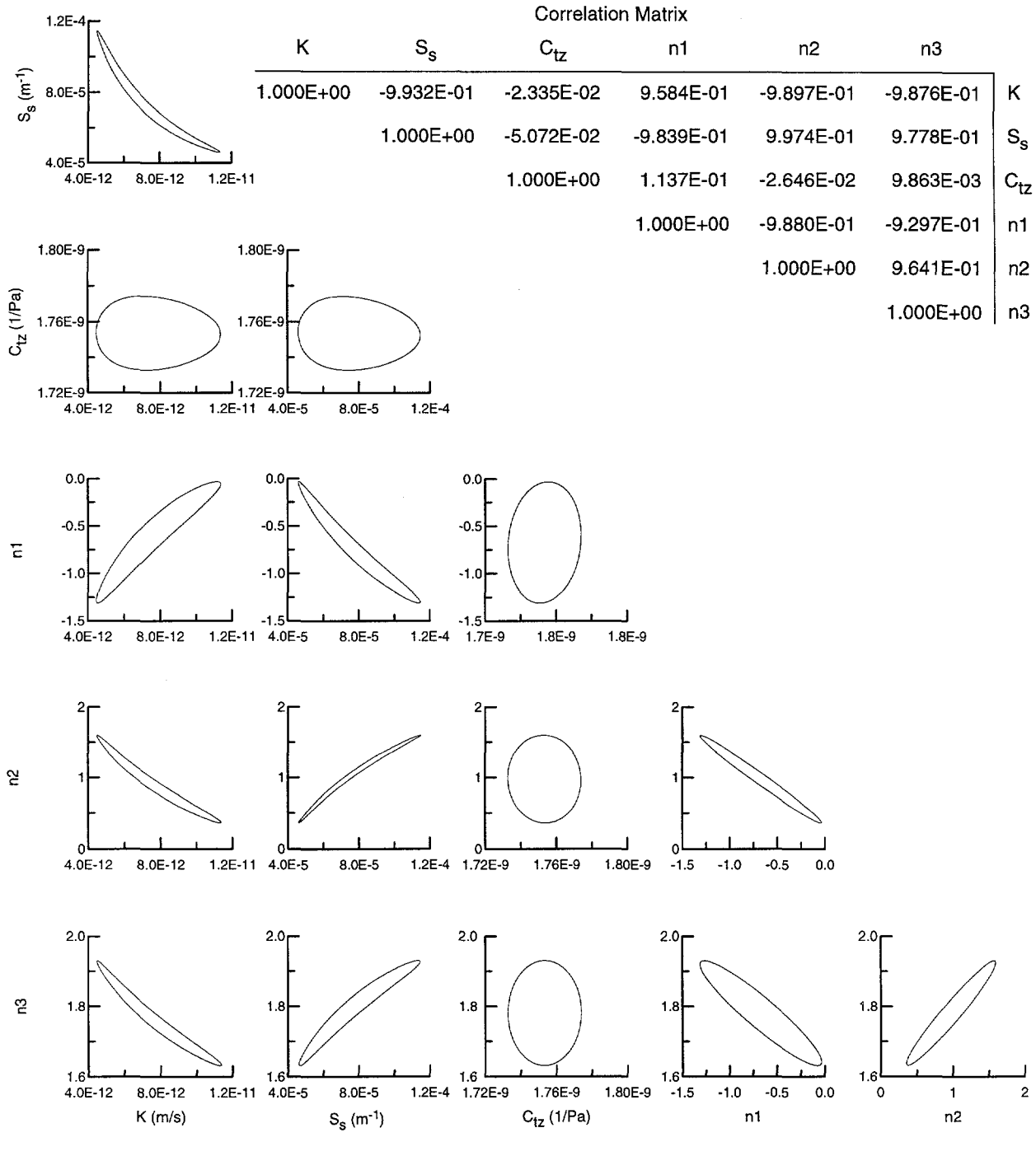

Figure C-18. Correlation matrix and 95% joint-confidence regions for S1P73-B analysis.

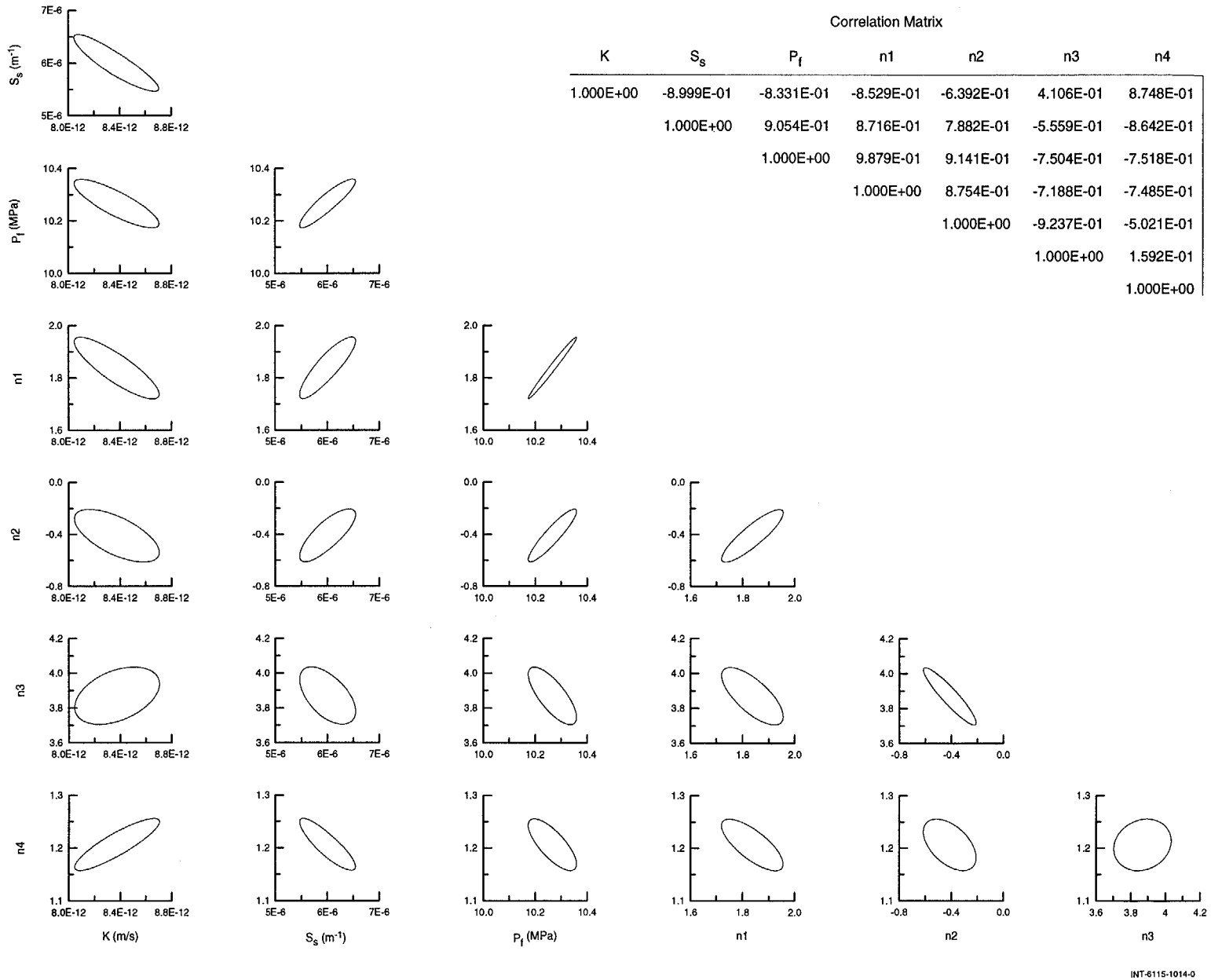

Figure C-19. Correlation matrix and 95% joint-confidence regions for S1P74-B-TZ1 analysis.

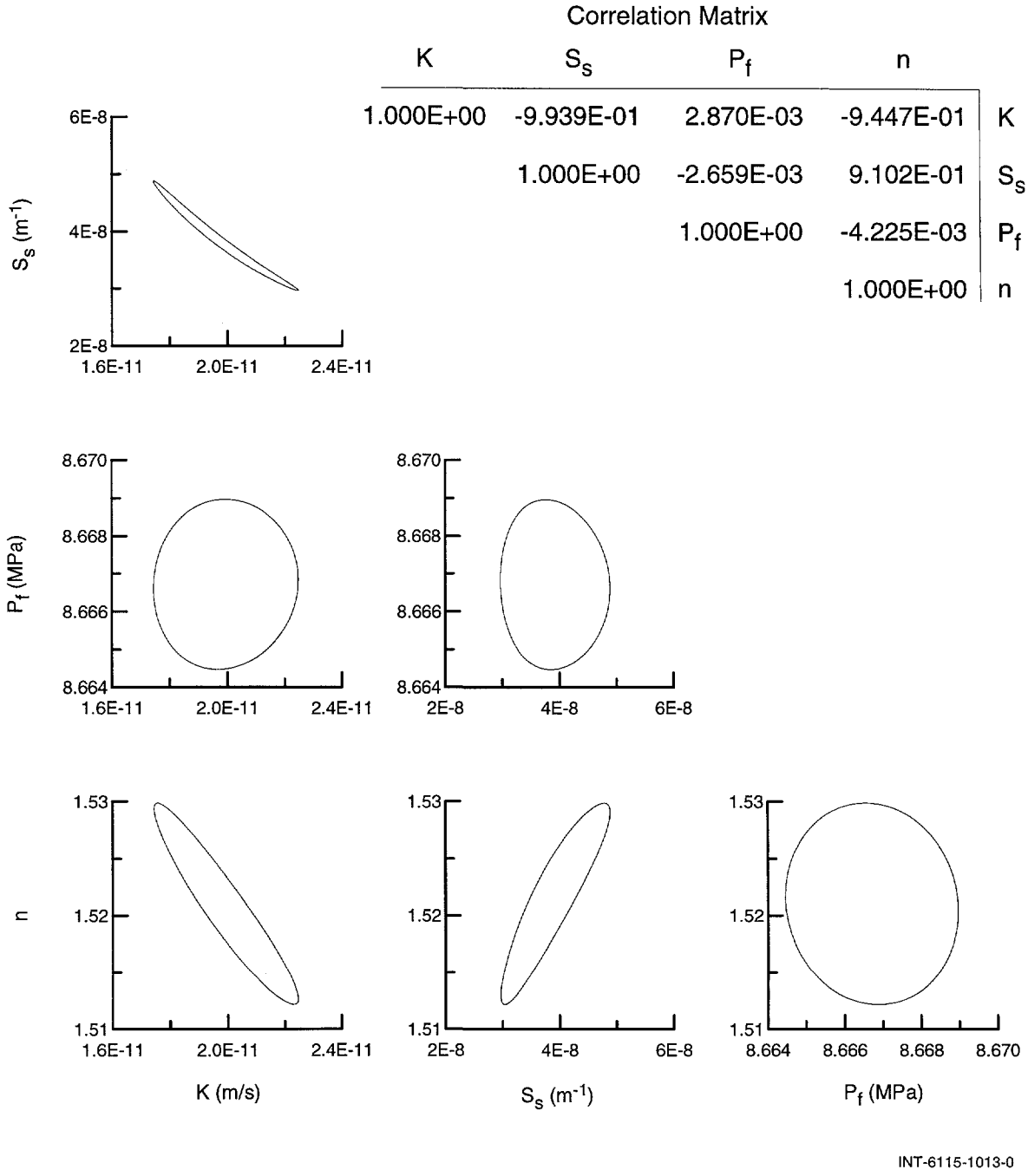

Figure C-20. Correlation matrix and 95% joint-confidence regions for S1P74-B-TZ2 PW1 analysis.

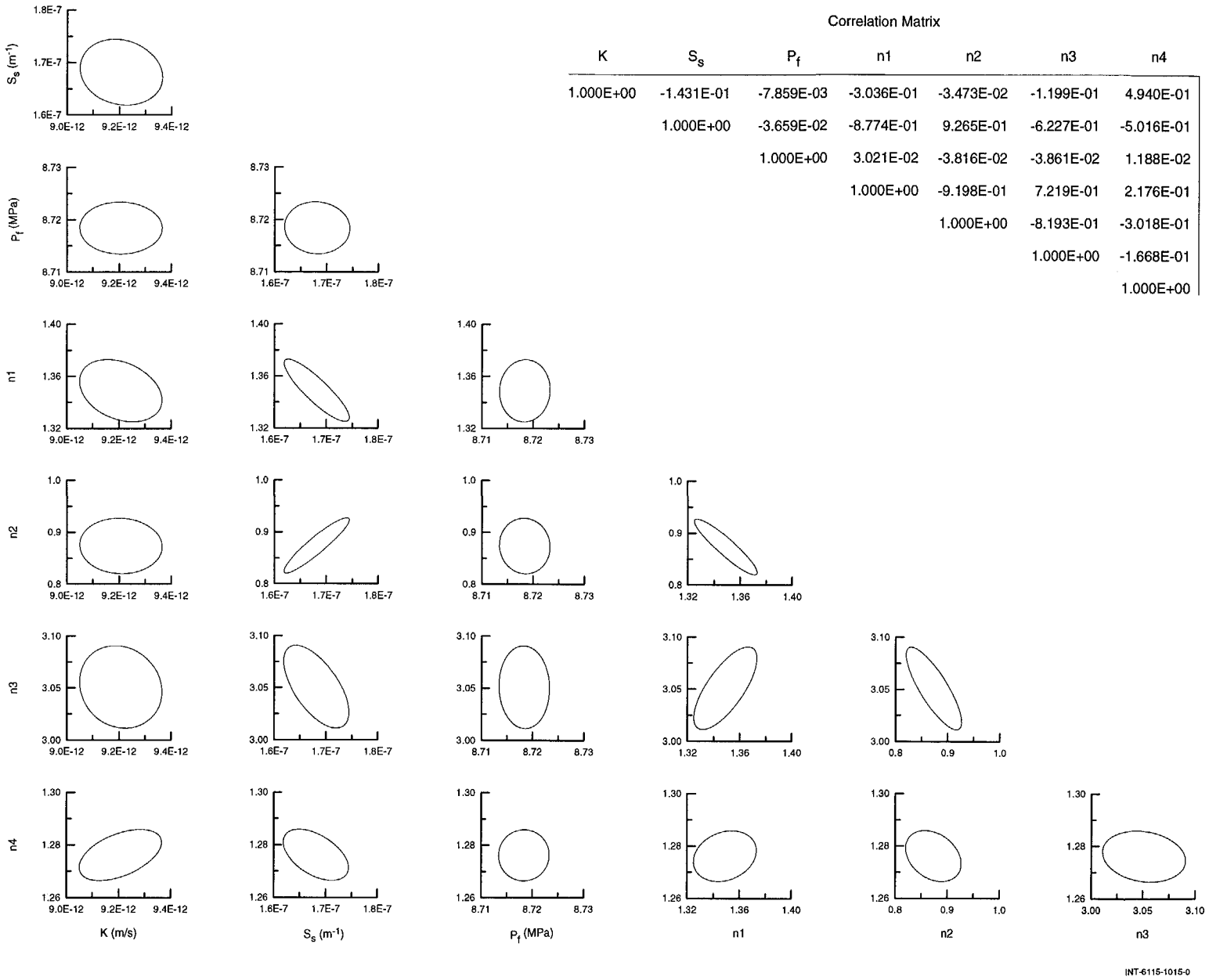

Figure C-21. Correlation matrix and 95% joint-confidence regions for S1P74-B-TZ2 PW2 analysis.

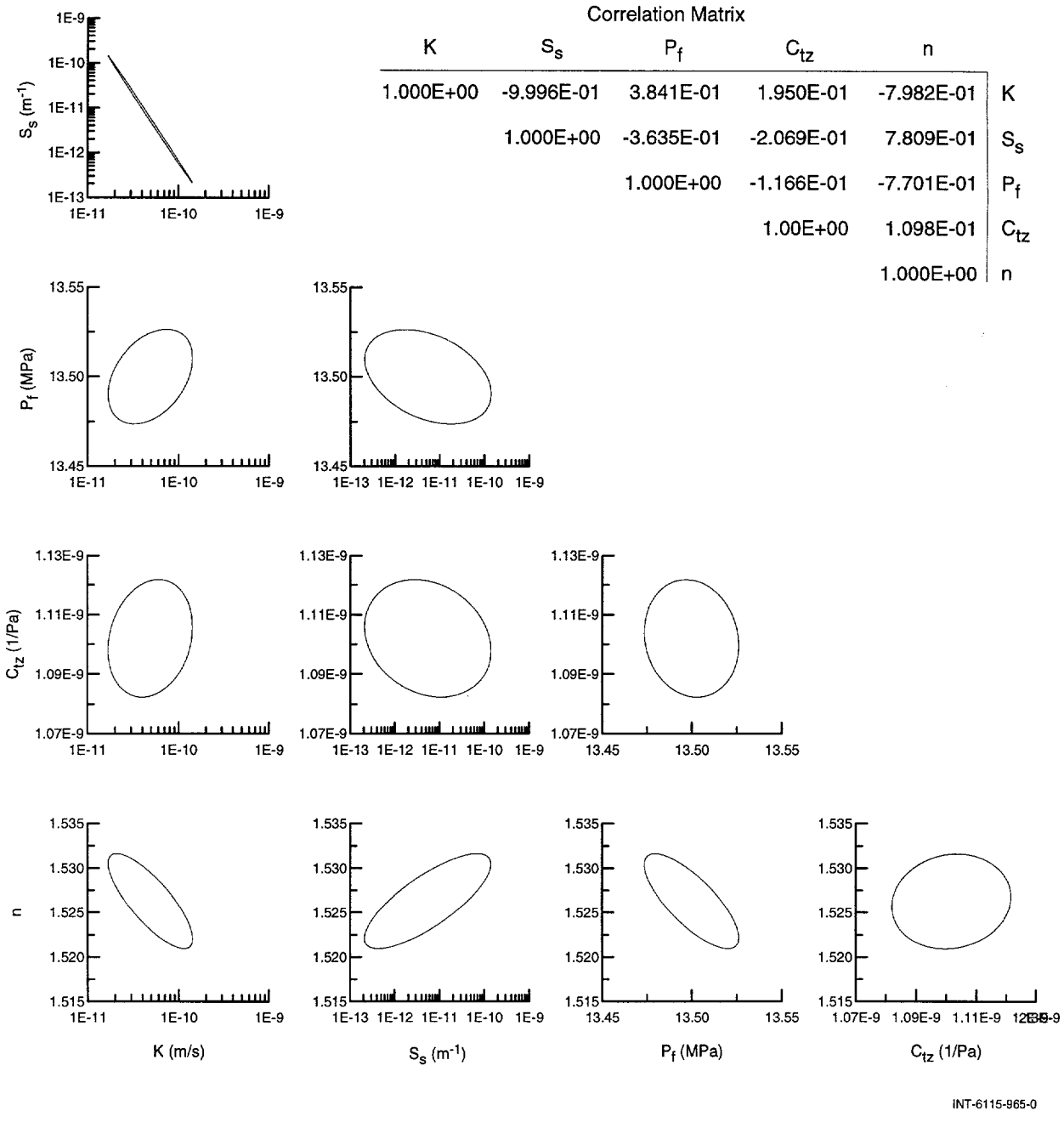

Figure C-22. Correlation matrix and 95% joint-confidence regions for SCP01 analysis.

APPENDIX D

PACKER-PRESSURE PLOTS

THIS PAGE INTENTIONALLY LEFT BLANK

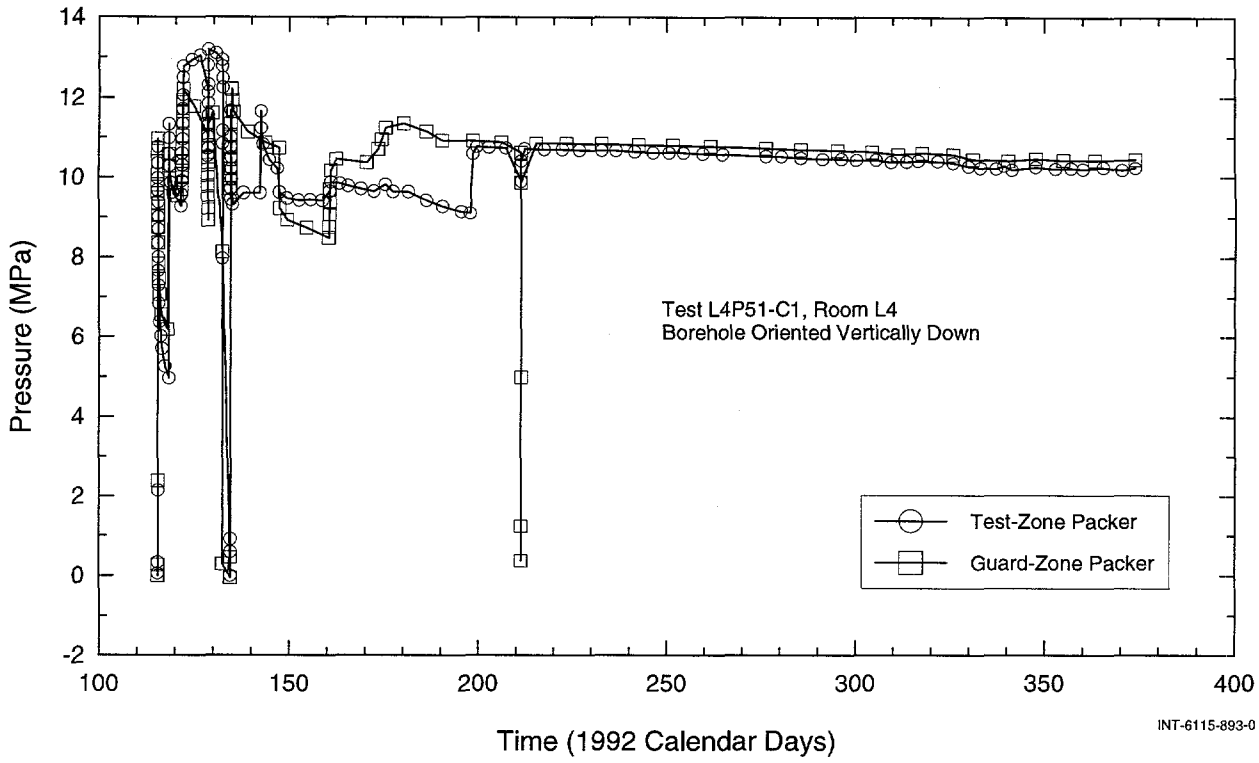

Figure D-1. Test- and guard-zone packer-inflation pressures during L4P51-C1 testing.

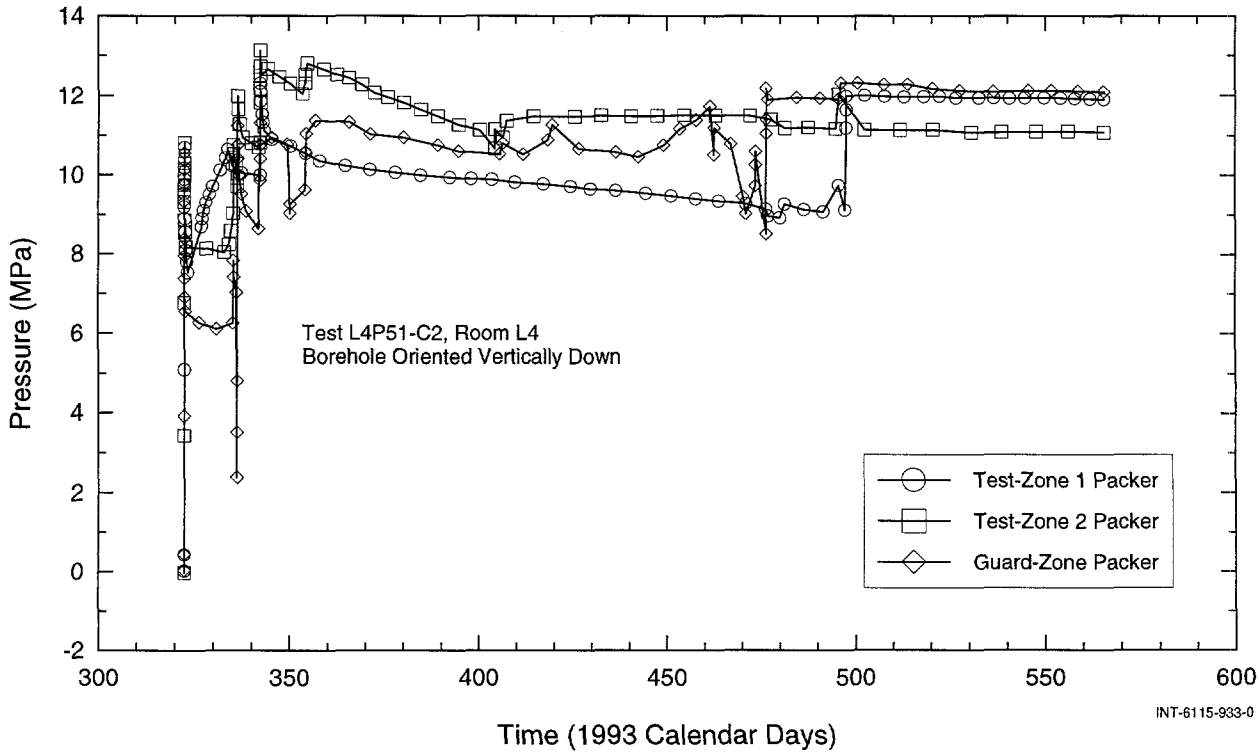

Figure D-2. Test- and guard-zone packer-inflation pressures during L4P51-C2 testing.

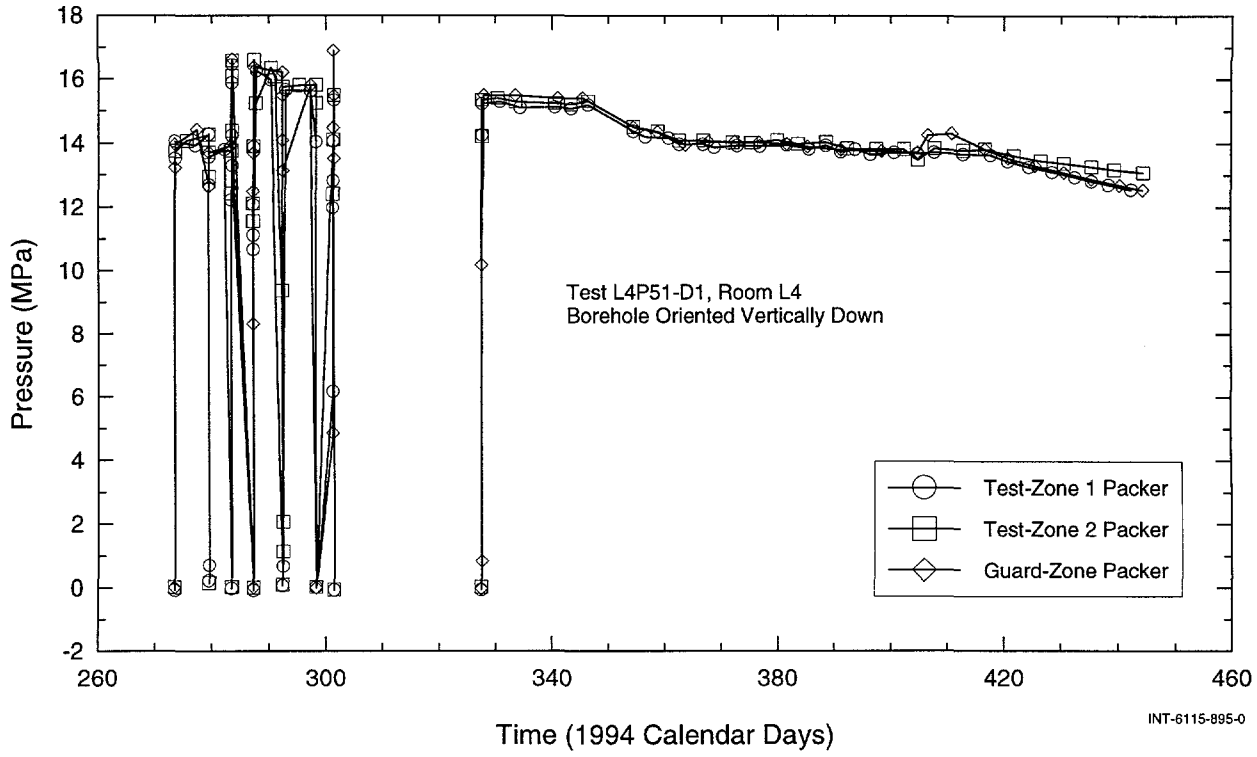

Figure D-3. Test- and guard-zone packer-inflation pressures during L4P51-D1 testing.

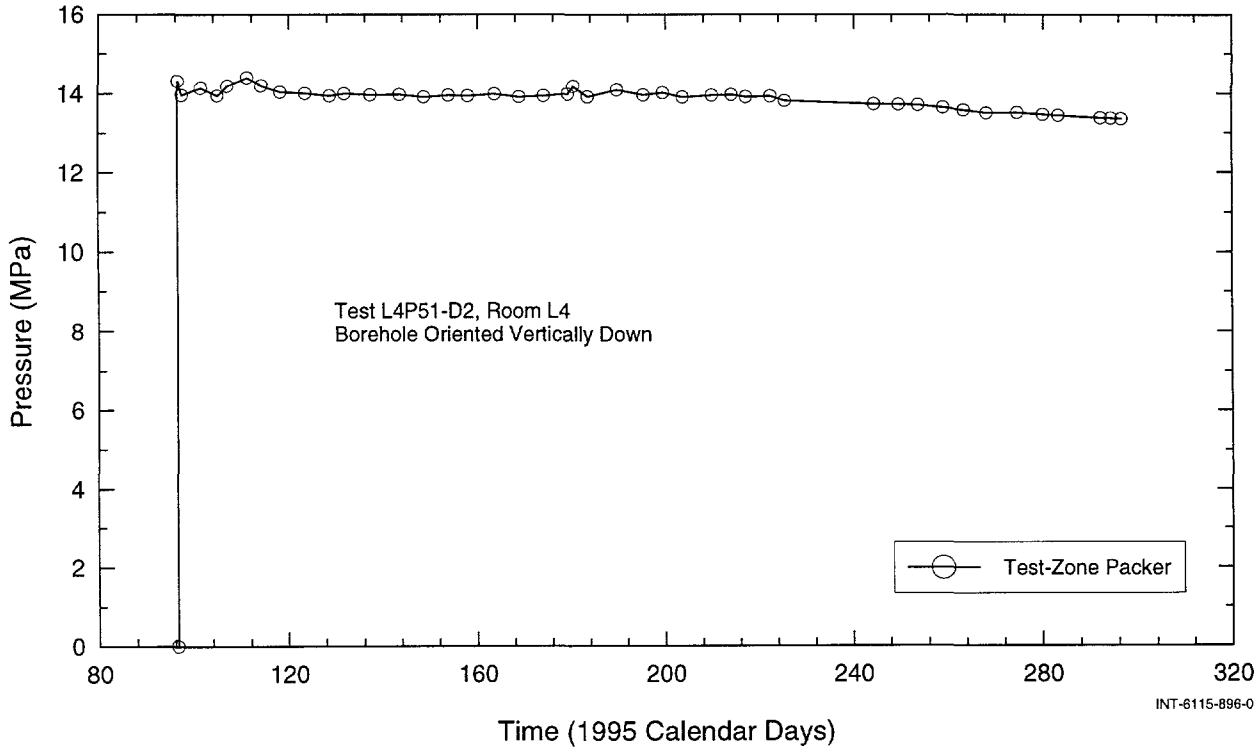

Figure D-4. Test-zone packer-inflation pressure during L4P51-D2 testing.

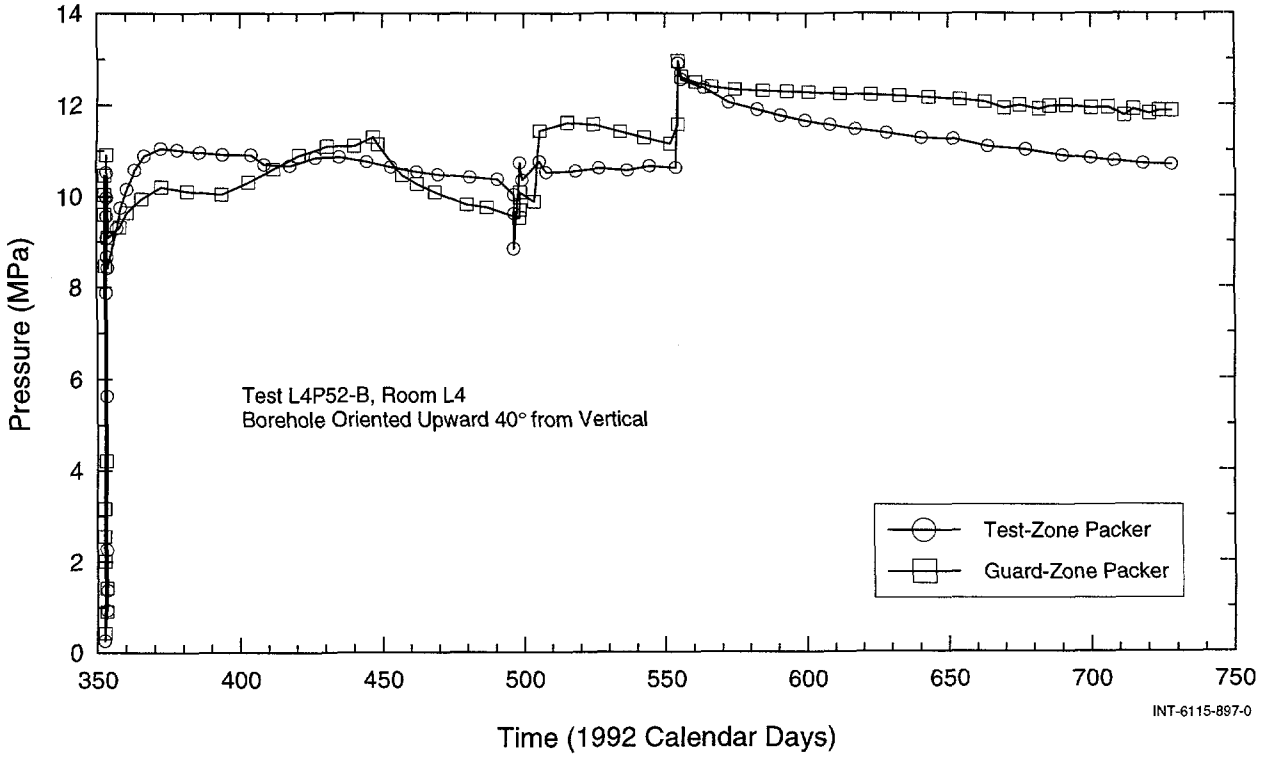

Figure D-5. Test- and guard-zone packer-inflation pressures during L4P52-B testing.

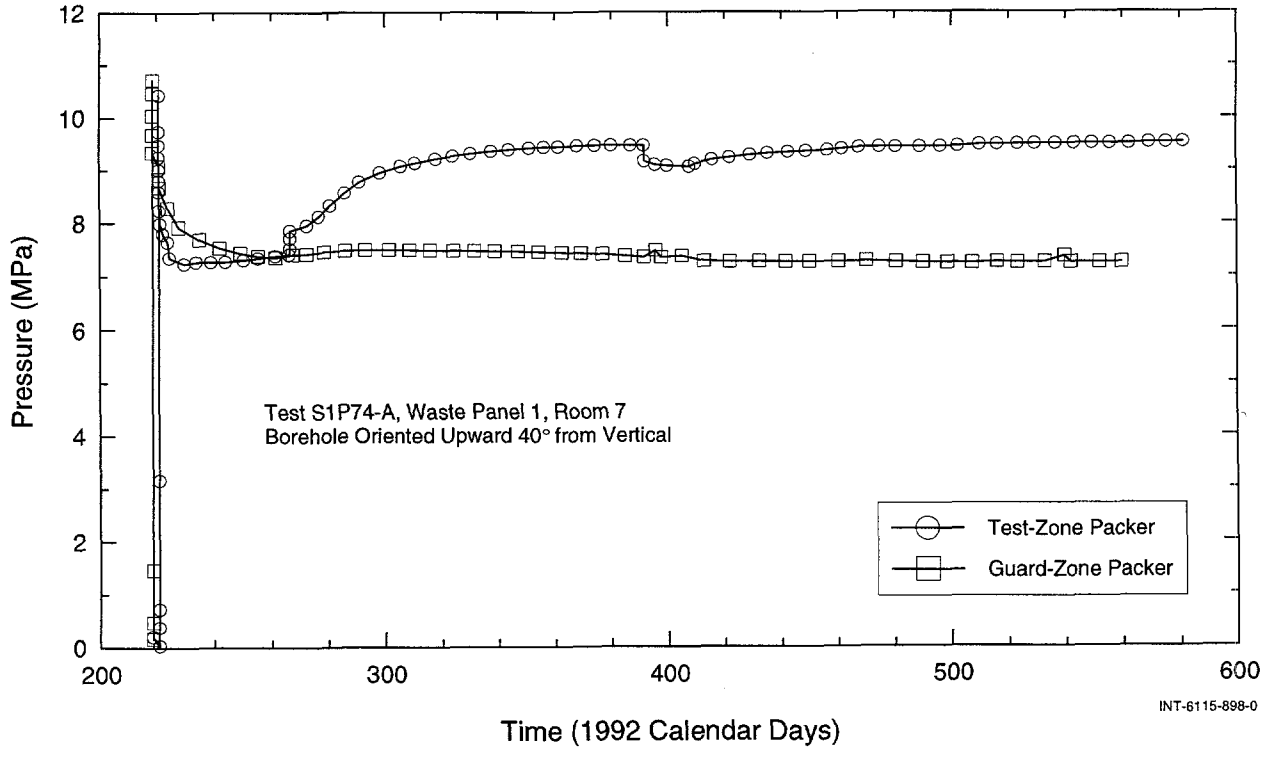

Figure D-6. Test- and guard-zone packer-inflation pressures during S1P74-A testing.

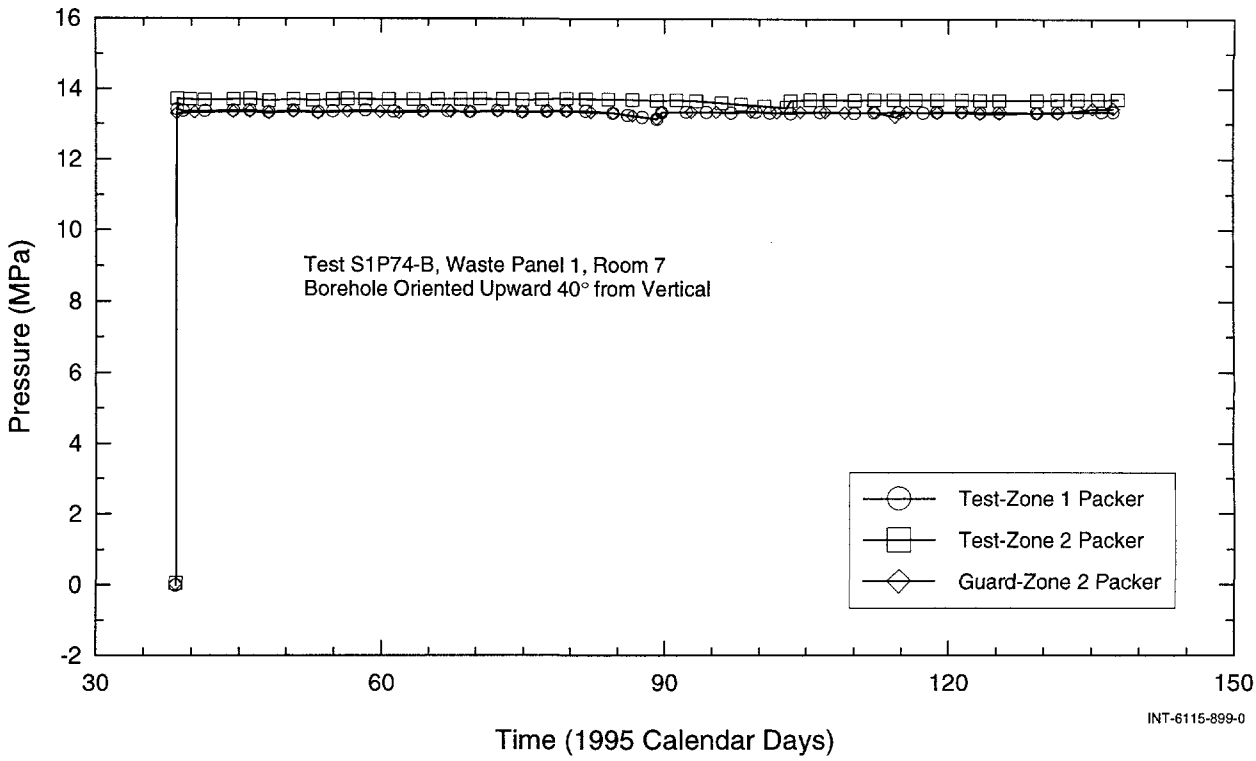

Figure D-7. Test- and guard-zone packer-inflation pressures during S1P74-B testing.

APPENDIX E

GAS-THRESHOLD-PRESSURE TESTING

THIS PAGE INTENTIONALLY LEFT BLANK

APPENDIX E: GAS-THRESHOLD-PRESSURE TESTING

Gas-threshold-pressure testing of anhydrite interbeds was performed at three locations in the WIPP underground facility under a Test Plan by Saulnier (1992). The specific objectives of the tests were:

- to estimate the gas-threshold pressure of different anhydrite interbeds in the Salado Formation around the WIPP facility; and
- to determine if the gas-threshold pressure is related to formation intrinsic permeability.

Gas-threshold-pressure tests (GTPTs) were performed in borehole C2H02 in Room C2 (one test), borehole L4P52 in Room L4 (one test), and borehole SCP01 in the core-storage library (two tests). The tests were performed in the anhydrite interbeds MB138 and MB139. The tests in boreholes C2H02 and SCP01 were in MB139 and the L4P52 test was in MB138.

The GTPTs were performed either immediately after the completion of a brine-permeability-test sequence (L4P52) or later following a long pressure-monitoring period (C2H02 and SCP01). With a test tool installed, the interval to be tested for gas-threshold pressure was shut in and the borehole pressure allowed to equilibrate with the formation pressure. Upon achieving stable borehole pressure conditions, the brine in the test interval was exchanged with nitrogen gas and a period of constant-rate gas-injection was initiated. Typically, the borehole was shut in following the gas-injection period and the borehole pressure was allowed to stabilize.

In GTPT sequences, a gas (nitrogen) is introduced at a constant rate into a confined zone of a borehole. The maintenance of a constant gas-injection rate is critical to the successful completion of a GTPT. For the GTPTs conducted in the WIPP underground facility, this constant injection rate was achieved using a Bronkhorst Model F-230C-FA-22-V mass-flow meter with a high-pressure nitrogen reservoir as the gas source. This DAS-controlled mass-flow meter allowed for a constant gas-injection rate of 0 to 5 mL/min (at STP) to be maintained. All calibrations of the mass-flow meters that were used during the GTPT sequences were performed by the manufacturer. The gas-injection system used is shown in Figure E-1. Chace et al. (1998) describe the instrumentation and procedures used for the GTPTs in greater detail and also document the test data.

E.1 L4P52

Gas-threshold-pressure testing was performed in MB138 following the completion of the L4P52-B permeability-testing sequence (Section 7.3.1). The brine in the test zone was replaced with nitrogen at a pressure of approximately 8.6 MPa. After a 10-day stabilization period, nitrogen was injected into the test zone at a constant mass rate of 2 mL/min (at STP). When the test-zone pressure exceeded 10.5 MPa approximately 1.2 days later, the injection rate was decreased to 0.8 mL/min to avoid hydraulic fracturing of the marker bed. This

injection rate was maintained for four days and was followed by a 13-day pressure-falloff period. Pressure and injection-rate data from this test are shown in Figures E-2 and E-3, respectively.

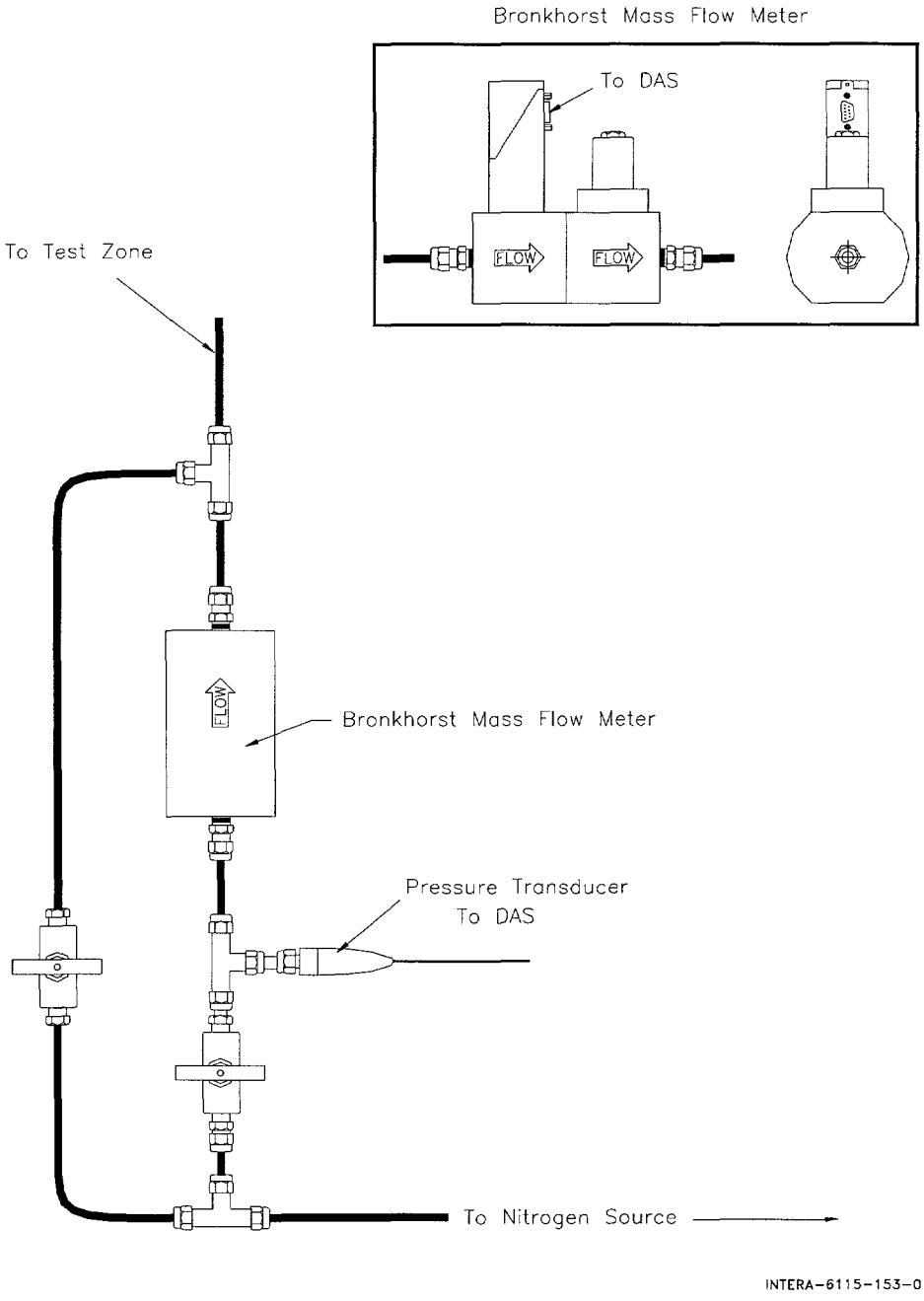

Figure E-1. Schematic illustration of the constant-rate gas-injection system.

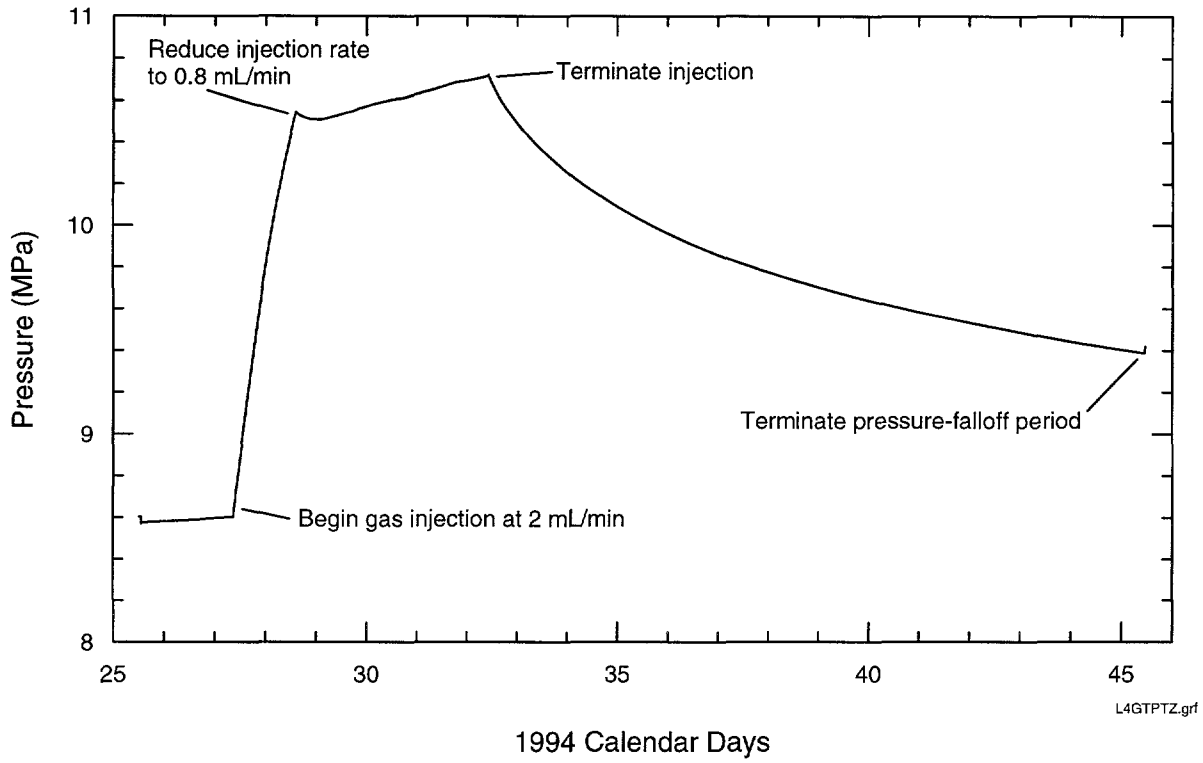

Figure E-2. Pressures during L4P52-B gas-threshold-pressure test.

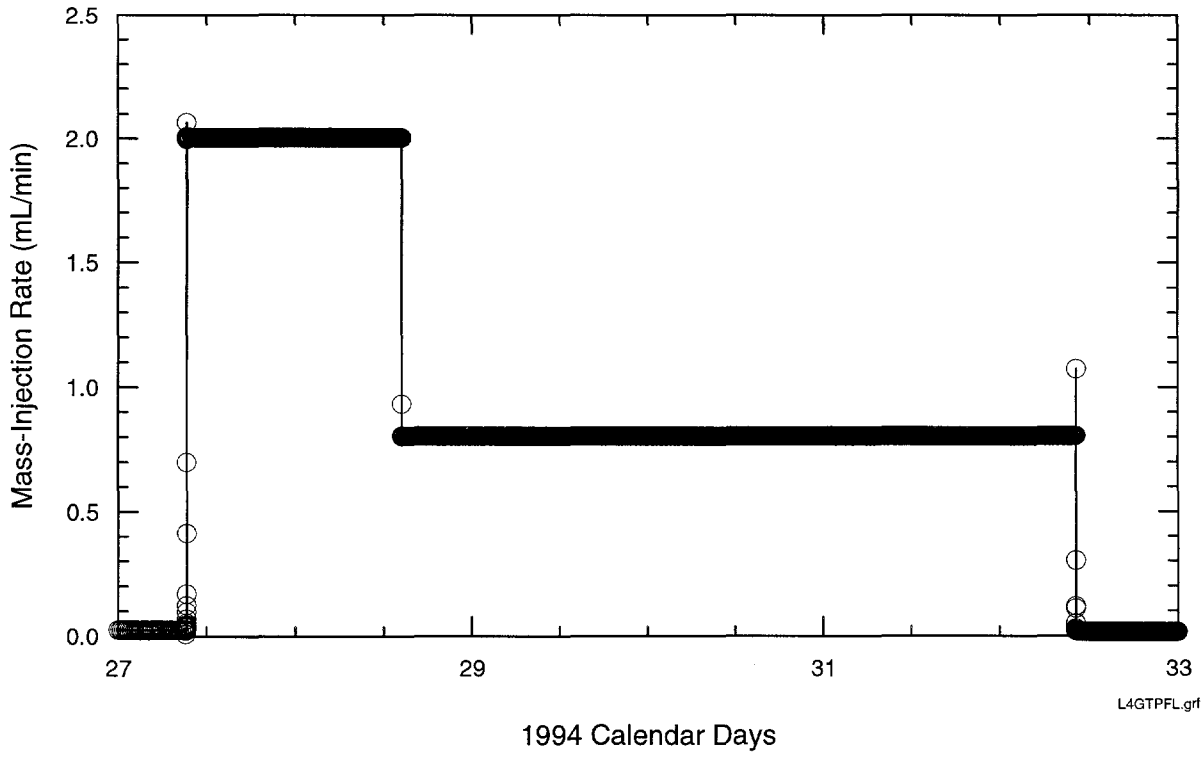

Figure E-3. Injection rates during L4P52-B gas-threshold-pressure test.

The gas-threshold pressure can be inferred from a log-log plot of the pressure change and derivative of pressure change versus elapsed time during the injection period. Initially, the pressure change and derivative will follow a unit-slope line that is indicative of compression of gas in the borehole, or wellbore storage. As gas flow into the formation begins, the slopes of the pressure-change and derivative traces will decrease, with the derivative diverging more rapidly from the unit-slope line than the pressure change. The pressure change at which the derivative trace separates from the unit-slope line provides an estimate of the gas-threshold pressure. Definition of the gas-threshold pressure in this way is affected by data noise and is somewhat subjective.

Only the data from the initial injection period into L4P52-B can be analyzed using the method discussed above. Qualitatively, however, the pressure falloff shows clearly that the threshold pressure was exceeded during the test and gas was flowing into the formation. Figure E-4 shows a log-log plot for the first gas-injection phase into MB138 in L4P52-B. The pressure-derivative data clearly deviated from the unit-slope line by the time the pressure change reached approximately 0.22 MPa, and possibly slightly sooner. Therefore, the gas-threshold pressure appears to be no greater than 0.22 MPa.

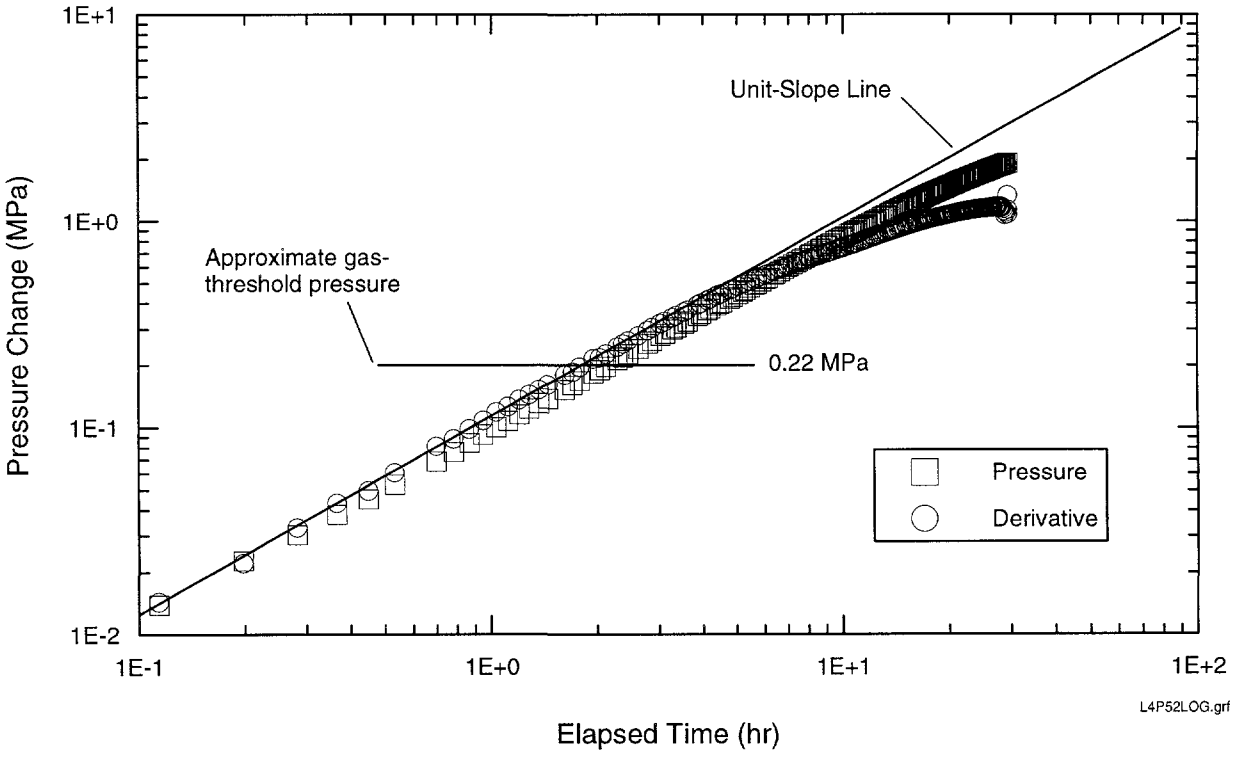

Figure E-4. Log-log plot for first gas-injection phase into MB138 in L4P52-B.

Davies (1991) developed an empirical relationship between the intrinsic permeability of anhydrite and threshold pressure as follows:

$$P_t\,(\text{MPa}) = 2.6 \times 10^{-7}\,[k\,(m^2)]^{-0.348} \qquad \text{(E-1)}$$

From the analyses presented in Section 7.3.1.2, the permeability of MB138 at L4P52-B at a pressure of approximately 9 MPa is approximately 3.4×10^{-18} m^2, which leads to a threshold pressure of 0.31 MPa using Eq. E-1. The value inferred from the log-log plot shown in Figure E-4, 0.22 MPa, is slightly lower than predicted using the relationship established by Davies (1991), but is still consistent with values estimated for the WIPP Compliance Certification Application (US DOE, 1996). Video logging of borehole L4P52 (WPO#45907) revealed fractures in MB138. Davies (1991) suggested that fractures may have threshold pressures lower than predicted by his correlation. The estimate from this analysis is consistent with that hypothesis.

E.2 C2H02

The exchange of gas for brine at the beginning of the test in C2H02 was unsuccessful in exposing the entire surface of MB139 to gas. We estimate that approximately the lower 30 cm of the 115 cm of MB139 within the test zone were still exposed to brine when the constant-rate gas injection began. Consequently, as the gas pressure increased, brine may have been pushed into the lower portion of the marker bed. As a result, the volume of borehole being pressurized with gas would have been slowly increasing. We cannot separate the response due to brine potentially leaving the borehole from that of gas entering the formation and, therefore, cannot interpret the gas-threshold-pressure test in C2H02 uniquely. Gas leakage around the test-zone packer during portions of the constant-rate injection phase also rendered the test data difficult to interpret.

E.3 SCP01

Two gas-threshold-pressure tests were attempted on MB139 in borehole SCP01. During the first testing sequence, designated SCP01-1, three attempts were made to obtain a pressure-tight packer seat, all of which failed. Problems were also encountered during the second testing sequence, designated SCP01-2. The tool had to be replaced once before a test at a gas-injection rate of 2 mL/min could be performed. This test was terminated sooner than desired to avoid hydraulic fracturing of the formation. Fluctuations in the flow rate are evident in both the pressure and derivative data, and no information on threshold pressure can be obtained from the test. A second CRI test at a gas-injection rate of 0.2 mL/min was unsuccessful. That rate was below the calibrated range of the Bronkhorst mass-flow meter/controller. Pressure cycled instead of increasing steadily during this test, which indicated failure of the meter/controller to deliver a constant rate. No further analysis of the data from SCP01 is warranted.

E.4 Conclusions

Of the three attempted gas-threshold-pressure tests of Salado anhydrites, only the testing of MB138 in borehole L4P52 was successful. The gas-threshold pressure of MB138 was interpreted to be approximately 0.2 MPa from this test. This value is slightly lower than the value that would be predicted using the correlation of Davies (1991) relating gas-threshold pressure to permeability, probably because of the presence of fractures in MB138. The test of MB139 attempted in borehole C2H02 could not be interpreted because the exchange of brine for gas failed to remove enough brine to expose the entire anhydrite bed to gas. The tests of MB139 attempted in borehole SCP01 were unsuccessful because of equipment problems and fluctuating injection rates. Because only one test was successful, we are unable to determine if the *in situ* gas-threshold pressures of Salado anhydrites are correlated with the values of permeability inferred from hydraulic tests.

A number of lessons were learned from both the successful and unsuccessful gas-threshold-pressure tests that would be helpful in planning future tests. First, all brine must be removed from the test zone to provide certainty that the pressure responses observed during testing reflect the behavior of gas. Second, the pressure in the borehole should be allowed to equilibrate completely with the formation pressure before exchanging brine for gas, and the gas pressure should then be set exactly at that stabilized pressure. This will remove uncertainty as to whether or not pre-existing pressure transients in the formation are affecting the estimation of threshold pressure. Third, all other system elements (e.g., packer and guard-zone pressures) should be completely stabilized before gas injection begins and should not be altered during injection. This is necessary to provide certainty that changes observed in the pressure derivative during injection are caused by gas flow into the formation rather than by volume changes in the test zone. Fourth, the gas injection should be performed at the lowest constant rate the system can provide, which must be determined during compliance (or bench) testing. This will provide maximum resolution of the threshold pressure while minimizing the possibility of hydraulically fracturing the formation. Fifth, data acquisition should be rapid and continuous enough to allow calculation of pressure derivatives from a few seconds after the test begins until the end of the test. This will also act to maximize resolution of the threshold pressure. Sixth, only a single injection should be performed, during which the threshold pressure is unambiguously exceeded, followed by a long pressure-falloff period in which either the pressure is allowed to stabilize or the pressure derivative is allowed to stabilize such that an accurate extrapolation to the final stabilized pressure can be made. Additional test elements such as repeated injections at different rates will not be uniquely interpretable because of uncertainties about the saturation state in the formation. Therefore, emphasis should be placed on collecting adequate, high-quality data from a single simple test rather than on designing a complex test sequence that likely will provide only ambiguous results.

E.5 References

Chace, D.A., R.M. Roberts, J.B. Palmer, M.B. Kloska, M.D. Fort, G.J. Martin, and W.A. Stensrud. 1998. *Waste Isolation Pilot Plant Salado Hydrology Program Data Report #3.* SAND97-1880. Albuquerque, NM: Sandia National Laboratories.

Davies, P.B. 1991. *Evaluation of the Role of Threshold Pressure in Controlling Flow of Waste-Generated Gas into Bedded Salt at the Waste Isolation Pilot Plant.* SAND90-3246. Albuquerque, NM: Sandia National Laboratories.

Saulnier, G.J., Jr. 1992. "Test Plan: Gas-Threshold-Pressure Testing of the Salado Formation in the WIPP Underground Facility." Albuquerque, NM: Sandia National Laboratories. (On file in the SWCF under WPO#7685.)

US Department of Energy. 1996. *Title 40 CFR Part 191 Compliance Certification Application for the Waste Isolation Pilot Plant.* DOE/CAO-1996-2184. Carlsbad, NM: US DOE Waste Isolation Pilot Plant, Carlsbad Area Office.

THIS PAGE INTENTIONALLY LEFT BLANK

WIPP
DISTRIBUTION LIST
SAND98-2537

Federal Agencies

US Department of Energy (4)
Office of Civilian Radioactive Waste Mgmt.
Attn: Deputy Director, RW-2
Acting Director, RW-10
Office of Human Resources & Admin.
Director, RW-30
Office of Program Mgmt. & Integ.
Director, RW-40
Office of Waste Accept., Stor., & Tran.
Forrestal Building
Washington, DC 20585

Yucca Mountain Site Characterization Office
Director, RW-3
Office of Quality Assurance
Attn: Project Director
P. O. Box 30307
North Las Vegas, NV 89036-0307

US Department of Energy
Research & Waste Management Division
Attn: Director
P.O. Box E
Oak Ridge, TN 37831

US Department of Energy (6)
Carlsbad Area Office
Attn: I. Triay
M. McFadden
D. Galbraith
D. Mercer
J. A. Mewhinney
G. T. Basabilvazo
Mailroom
P.O. Box 3090
Carlsbad, NM 88221-3090

US Department of Energy
Office of Environmental Restoration and
Waste Management
Attn: M. Frei, EM-30
Forrestal Building
Washington, DC 20585-0002

US Department of Energy (3)
Office of Environmental Restoration and
Waste Management
Attn: J. Juri, EM-34, Trevion II
Washington, DC 20585-0002

US Department of Energy
Office of Environmental Restoration and
Waste Management
Attn: S. Schneider, EM-342, Trevion II
Washington, DC 20585-0002

US Department of Energy (2)
Office of Environment, Safety & Health
Attn: C. Borgstrom, EH-25
R. Pelletier, EH-231
Washington, DC 20585

US Department of Energy (2)
Idaho Operations Office
Fuel Processing & Waste Mgmt. Division
785 DOE Place
Idaho Falls, ID 83402

US Environmental Protection Agency (2)
Radiation Protection Programs
Attn: M. Oge
ANR-460
Washington, DC 20460

US Geological Survey
Water Resources Division
Attn: S. F. Richey
4501 Indian School Rd. NE, Suite 200
Albuquerque, NM 87110-3929

Boards

Defense Nuclear Facilities Safety Board
Attn: D. Winters
625 Indiana Ave. NW, Suite 700
Washington, DC 20004

Nuclear Waste Technical Review Board (2)
Attn: Chairman
J. L. Cohon
2300 Clarendon Blvd. Ste 1300
Arlington, VA 22201-3367

State Agencies

Attorney General of New Mexico
P.O. Drawer 1508
Santa Fe, NM 87504-1508

Environmental Evaluation Group (3)
Attn: Library
7007 Wyoming NE
Suite F-2
Albuquerque, NM 87109

NM Environment Department (3)
Secretary of the Environment
1190 St. Francis Drive
Santa Fe, NM 87503-0968

NM Bureau of Mines & Mineral Resources
Socorro, NM 87801

Laboratories/Corporations

Battelle Pacific Northwest Laboratories
Battelle Blvd.
Richland, WA 99352

Los Alamos National Laboratory
Attn: B. Erdal, INC-12
P.O. Box 1663
Los Alamos, NM 87544

Tech Reps, Inc. (3)
Attn: J. Chapman (1)
Loretta Robledo (2)
5000 Marble NE, Suite 222
Albuquerque, NM 87110

Westinghouse Electric Corporation (7)
Attn: Library
J. Epstein
J. Lee
R. Kehrman
R. G. Richardson
S. Patchet
N. Rempe
P.O. Box 2078
Carlsbad, NM 88221

S. Cohen & Associates
Attn: Bill Thurber
1355 Beverly Road
McLean, VA 22101

Golder Associates
Attn: T. W. Doe
4104 148th Avenue, NE
Redmond, WA 98052

Golder Associates (2)
Attn: W. Thompson
J. Wozniewicz
44 Union Blvd., Suite 300
Lakewood, CO 80228

Duke Engineering & Services, Inc. (5)
Attn: G. A. Freeze
D. A. Chace
P. S. Domski (3)
1650 University Blvd. NE. Suite 300
Albuquerque, NM 87102-1732

Duke Engineering and Services, Inc. (2)
Attn: J. F. Pickens
9111 Research Blvd.
Austin, TX 78758

E. O. Berkeley National Laboratory (2)
Attn: A. Cohen
C. F. Tsang
Earth Sciences Division
1 Cyclotron Road
Berkeley, CA 94720

IT Corporation
Attn: R. J. Abitz
5301 Central Ave. NE, Suite 700
Albuquerque, NM 87108

National Academy of Sciences
WIPP Panel

Tom Kiess (15)
Staff Study Director
GF456
2101 Constitution Ave.
Washington, DC 20418

Universities

University of New Mexico
Geology Department
Attn: Library
141 Northrop Hall
Albuquerque, NM 87131

University of Washington
College of Ocean & Fishery Sciences
Attn: G. R. Heath
583 Henderson Hall, HN-15
Seattle, WA 98195

New Mexico Tech
Department of Geoscience
Attn: J. Wilson
Socorro, NM 87801

Texas A&M University
Department of Geology
Attn: P. A. Domenico
College Station, TX 77843

University of Arizona
Department of Hydrology
Attn: S. P. Neuman
Tucson, AZ 85721

University of Kansas
Kansas Geological Survey
Attn: J. Butler
1930 Constant Ave.
Campus West
Lawrence, KS 66046

University of Wisconsin-Madison (2)
Department of Geology and Geophysics
Attn: M. P. Anderson
H. F. Wang
1215 Dayton St.
Madison, WI 53706

Stanford University
Dept. of Petroleum Engineering
Attn: Jaime Gomez-Hernandez
Green Earth Sciences Building
Stanford, CA 94305-2220

Libraries

Thomas Brannigan Library
Attn: D. Dresp
106 W. Hadley St.
Las Cruces, NM 88001

Government Publications Department
Zimmerman Library
University of New Mexico
Albuquerque, NM 87131

New Mexico Junior College
Pannell Library
Attn: R. Hill
Lovington Highway
Hobbs, NM 88240

New Mexico State Library
Attn: N. McCallan
325 Don Gaspar
Santa Fe, NM 87503

New Mexico Tech
Martin Speere Memorial Library
Campus Street
Socorro, NM 87810

WIPP Information Center
Attn: Y. Acosta
4021 National Parks Highway
Carlsbad, NM 88220

Foreign Addresses

Martin Put
SCK/CEN
Geological Waste Disposal Project
Boeretang, 200
B-2400 MOL
BELGIUM

Atomic Energy of Canada, Ltd. (2)
Whiteshell Laboratories
Attn: B. Goodwin
C. C. Davison
Pinawa, Manitoba, R0E 1L0
CANADA

Environment Canada
National Water Research Institute
Canada Centre for Inland Waters
Attn: K. S. Novakowski
867 Lakeshore Road
P.O. Box 5050
Burlington, Ontario, L7R 4A6
CANADA

Peter Flavelle
AECB
Waste and Decommissioning Division
P.O. Box 1046, Station B
280 Slater Street
Ottawa, Ontario K1P 5S9
CANADA

Mark Jensen
Ontario Power Generation
700 University Ave., H16-E27
Toronto, Ontario M5G 1X6
CANADA

Aimo Hautojarvia
VTT Energy
Teckniikantie 4 C, Espoo
P.O. Box 1604
FIN-02044 VTT
FINLAND

Francois Chenevier (2)
ANDRA
Parc de la Croix Blanche
1-7 rue Jean Monnet
92298 Chatenay-Malabry Cedex
FRANCE

Gerard Bruno
IPSN
IPSN/DPRE/SERGD – BP6
92265 Fontenay-aux-Roses Cedex
FRANCE

Scott Altman (3)
ANDRA
Parc de la Croix Blanche
1-7 rue Jean Monnet
92298 Chatenay-Malabry Cedex
FRANCE

Claude Sombret
Centre d'Etudes Nucleaires de la Vallee Rhone
CEN/VALRHO
S.D.H.A. B.P. 171
30205 Bagnols-Sur-Ceze
FRANCE

Commissariat a L'Energie Atomique
Attn: D. Alexandre
Centre d'Etudes de Cadarache
13108 Saint Paul Lez Durance Cedex
FRANCE

Ghislain de Marsily
Universite Paris VI
Laboratoire de Geologie Appliquee
4 place Jussien
75230 Cedex 05
FRANCE

Bundesanstalt fur Geowissenschaften und
Rohstoffe (2)
Attn: M. Langer
K. Schelkes
Postfach 510 153
D-30631 Hannover
GERMANY

Bundesministerium fur Forschung und
Technologie
Postfach 200 706
5300 Bonn 2
GERMANY

WBI
Attn: B. Wittke
Henricistrasse 50
D-52072 Aachen
GERMANY

Christian Enachescu
Golder Associates, Ltd
Vorbruch 3
D-29227 Celle
GERMANY

Institut fur Tieflagerung
Attn: K. Kuhn
Theodor-Heuss-Strasse 4
D-3300 Braunschweig
GERMANY

Gesellschaft fur Anlagen und Reaktorsicherheit
(GRS)
Attn: B. Baltes
Schwertnergasse 1
D-50667 Cologne
GERMANY

Shingo Tashiro
Japan Atomic Energy Research Institute
Tokai-Mura, Ibaraki-Ken, 319-11
JAPAN

Netherlands Energy Research Foundation ECN
Attn: J. Prij
3 Westerduinweg
P.O. Box 1
1755 ZG Petten
THE NETHERLANDS

Jesus Carrerra
Universidad Politechnica de Catalunya
E. T. S. I. Caminos
Jordi, Girona 31
E-08034 Barcelona
SPAIN

Carmen Bajos
ENRESA
Emilio Vargas 7
28043 Madrid
SPAIN

Javier Rodriguez
CSN
C/Justo Dorado 11
28040 Madrid
SPAIN

Conterra AB
Attn: A. Winberg
Ogardesvagen 4
S-433 30 Partille
SWEDEN

Mansueto Morosini
SKB
Aspo Hard Rock Laboratory
PI 300
S-572 95 Figeholm
SWEDEN

GEOSIGMA AB
Attn: P. Anderson
P.O. Box 894
S-751 08 Uppsala
SWEDEN

Svensk Karnbransleforsorjning AB
Attn: F. Karlsson
Project KBS (Karnbranslesakerhet)
Box 5864
S-102 48 Stockholm
SWEDEN

Nationale Genossenschaft fur die Lagerung
Radioaktiver Abfalle (3)
Attn: S. Vomvoris
P. Zuidema
B. Frieg
Hardstrasse 73
CH-5430 Wettingen
SWITZERLAND

Erik Frank
HSK
5232 Villigen-HSK
SWITZERLAND

AEA Technology
Attn: J. H. Rees
D5W/29 Culham Laboratory
Abington, Oxfordshire OX14 3DB
UNITED KINGDOM

AEA Technology
Attn: W. R. Rodwell
044/A31 Winfrith Technical Centre
Dorchester, Dorset DT2 8DH
UNITED KINGDOM

AEA Technology
Attn: J. E. Tinson
B4244 Harwell Laboratory
Didcot, Oxfordshire OX11 ORA
UNITED KINGDOM

John Black
Golder Associates, Ltd.
Landmere Lane
Edwalton, Nottingham
NG12 4DE
UNITED KINGDOM

Other

D. W. Powers
HC 12
Box 87
Anthony, TX 79821

Internal

MS	Org.	
0701	6100	P. B. Davies
0779	6849	D. R. Anderson
0779	6848	H. N. Jow
0771	6800	M. Chu
1395	6821	M. Marietta
1395	6821	R. L. Beauheim (5)
1395	6821	R. Roberts (5)
1395	6821	P. Vaughn
1395	6821	M. K. Knowles
1395	6821	F. D. Hansen
1395	6821	R. A. Jepsen
0735	6115	A. R. Lappin
0735	6115	L. C. Meigs
0735	6115	T. F. Corbet
0735	6115	R. M. Holt
0735	6115	S. J. Altman
0735	6115	S. A. McKenna
0735	6115	P.C. Reeves
0731	6811	K. Hart (2)
0731	4415	NWM Library (20)
9018	8940-2	Central Technical Files
0899	4916	Technical Library (2)
0619	15102	Review and Approval Desk, For DOE/OSTI (2)